

**Pattern formation and hydrogen
production in suspensions of
swimming green algae.**

by

Charlotte R. Williams

A thesis submitted to the
Faculty of Information and Mathematical Sciences
at the University of Glasgow
for the degree of
Doctor of Philosophy

September 2009

© C R Williams 2009

Abstract

This thesis concerns two aspects of microorganism behaviour. Firstly, the phenomenon of bioconvection is explored, where suspensions of motile microorganisms that are denser than the fluid in which they swim spontaneously form concentrated aggregations of cells that drive fluid motion, forming intricate patterns. The cells considered herein orientate by gyrotaxis, a balance between a gravitational torque due to uneven starch deposits causing cells to be bottom heavy and a viscous torque due to fluid flow gradients, and phototaxis, biased movement towards or away from a light source. In Chapters 2 and 3, a stochastic continuum model for gyrotaxis is extended to include phototaxis using three physically diverse and novel methods. A linear stability analysis is performed for each model and the most unstable wavenumber for a range of parameter values is predicted. For two of the models, sufficiently strong illumination is found to stabilize all wavenumbers compared to the gyrotaxis only case. Phototaxis is also found to yield non-zero critical wavenumbers under such strong illumination. Two mechanisms that lead to oscillatory solutions are presented. Dramatically different results are found for the third model, where instabilities arise even in the absence of fluid flow. In Chapter 4, an experimental study of pattern formation by the photo-gyrotactic unicellular green alga species *Chlamydomonas nivalis* is presented. Fourier analysis is used to extract the wavelength of the initial dominant mode. Variations in red light illumination are found to have no significant effect on the initial pattern wavelength. However, fascinating trends for the effects of cell concentration and white light intensity on cells illuminated either from above or below are described. This work concludes with comparisons between theoretical predictions and experimental results, between which good agreement is found.

Secondly, we investigate the intracellular pathways and processes that lead to hydrogen production upon implementation of a two-stage sulphur deprivation method in the green alga *C. reinhardtii*. In Chapter 5, a novel model of this system is constructed from a

consideration of the main cellular processes. Model results for a range of initial conditions are found to be consistent with published experimental results. In Chapter 6, a parameter sensitivity of the model is performed and a study in which different sulphur input functions are used to optimize the yield of hydrogen gas over a set time is presented, with the aim of improving the commercial and economic viability of algal hydrogen production. One such continuous sulphur input function is found to significantly increase the yield of hydrogen gas compared to using the discontinuous two-stage cycling of Ghirardi *et al.* 2000 [41].

To Will

Acknowledgments

I am greatly indebted to my supervisor, Dr Martin Bees, for all his help, encouragement and support over the last four years. His expertise, attention to detail and dedication to this project have been invaluable. I would also like to thank the other members of the algae group, in particular, Otte Croze, for his reading of an early version of the hydrogen chapter, Stephen O'Malley, for all the Matlab help and advice, and Jean-Baptiste Provost, for his patient help in designing the initial bioconvection experiments. I am grateful to Christina Cobbold for acting as my temporary supervisor and offering support and assistance with the hydrogen project in my first year. I am also indebted to the EPSRC for funding this research and the Department of Mathematics at Glasgow for allowing me to attend international conferences. Thanks also to the various people I have shared an office with over the years who have made studying at Glasgow an experience to remember.

Four years can seem like a very long time and I certainly couldn't have got through it without the support of my family and friends. I am indebted to my Mum and Dad, not only for the continued encouragement, support and advice they have given, but also for all the wonderful meals, the DIY and the relaxing weekends we had together in Seaton Ross and Glasgow. Dad's stories about his own time as a research student inspired me to complete this manuscript and often made me laugh. I'm pleased to have carried on the family tradition, started by my mother, of programming in Fortran, and even more pleased that this didn't involve punch cards! I am also very grateful to my sisters, Emily and Hannah, for their willingness to listen to me talk about this thesis endlessly, and to my very useful brother, Robby, who kindly acquired for me the most difficult to find papers. Finally, I owe a great debt of gratitude to Will, who encouraged me to start this project in the first place, and whose endless patience, constant encouragement and unwavering belief in me over the last four years have been unbelievable.

Statement

This thesis is submitted in accordance with the regulations for the degree of Doctor of Philosophy at the University of Glasgow. Chapter 1 is an introductory chapter. Chapters 2, 3, 4, 5, 6 and 7 are the authors original and novel work (done under the supervision of Dr. Martin Bees), except where explicitly credited to others.

Contents

1	Introduction	1
1.1	General background	1
1.2	Morphology and swimming behaviour of motile microorganisms	2
1.3	What determines the direction in which <i>Chlamydomonas</i> cells swim?	5
1.4	How do <i>Chlamydomonas</i> cells photo-orientate?	10
1.5	Bioconvection: a brief summary of observations and theory	12
1.5.1	Instability mechanisms in suspensions of <i>Chlamydomonas</i> cells	14
1.5.2	Early models of bioconvection	16
1.5.3	A new continuum model for stochastic gyrotactic bioconvection, Pedley and Kessler 1990 [130]	20
1.5.4	Modelling phototactic bioconvection	23
1.5.5	Current challenges in bioconvection research	25
1.6	The use of microorganisms in the energy industry	25
1.7	Links between bioconvection and hydrogen production	28
1.8	An overview of this thesis	28
2	Modelling photo-gyrotactic bioconvection in suspensions of green algae	
	- Part I	31
2.1	Introduction	31
2.2	Modelling photo-gyrotactic bioconvection.	34
2.2.1	Three new photo-gyrotactic models	34
2.2.2	Modelling light	38
2.2.3	Non-dimensionalization of the general model	39
2.2.4	Table of parameters	41
2.2.5	Solving the Fokker-Planck equation without the phototaxis terms	43

2.3	Model A: modelling phototaxis in a photokinesis manner	46
2.3.1	Equilibrium solution	47
2.3.2	Exploring the effects of using a diffusion tensor dependent on light, $\mathbf{D}(\mathbf{I})$	48
2.3.3	Analytical approximation to the equilibrium solution for weak ab- sorption	49
2.3.4	Numerical and analytical equilibrium profiles	50
2.3.5	Linear stability analysis	52
2.4	Asymptotic analysis in Model A for weak illumination and large layer depth	58
2.4.1	Equilibrium solution	59
2.4.2	Linear Stability Analysis	60
2.5	Numerical and asymptotical results for Model A	67
2.5.1	Comparison of asymptotical and numerical results	69
2.5.2	Exploring changes in layer depth d	72
2.5.3	Exploring the effects of the phototaxis parameter χ on the critical wavenumber k_c and Rayleigh number R_c	72
2.5.4	Exploring the effects of the gyrotaxis parameter η on the critical wavenumber k_c and Rayleigh number R_c	78
2.5.5	Exploring the effects of the absorption parameter κ on the critical wavenumber k_c and Rayleigh number R_c	81
2.5.6	Using a stress-free boundary condition for $\chi < 1$	81
2.5.7	Exploring the bifurcation from steady solutions with one branch to oscillating solutions with two double loop branches	82
2.5.8	Table of Results	85
2.6	Discussion	85
3	Modelling photo-gyrotactic bioconvection in suspensions of green algae	
	- Part II	92
3.1	Model B, where the centre of mass offset h varies with light intensity.	92
3.2	Solving the Fokker-Planck equation for Model B	94
3.2.1	Solution for zero flow	95
3.2.2	First order perturbation for spherical and aspherical cells	97
3.2.3	Summary	103
3.3	Equilibrium solution and linear analysis for Model B	105

3.3.1	Analytical approximation to the equilibrium solution for weak absorption	106
3.3.2	Numerical and analytical equilibrium profiles	107
3.3.3	Linear stability analysis	107
3.3.4	Taylor Expansions of K_i and J_i	112
3.4	Asymptotic analysis for a deep layer and weak illumination in Model B . . .	112
3.4.1	Equilibrium solution	112
3.4.2	Linear stability analysis	115
3.5	Numerical and asymptotical results for Model B	119
3.5.1	Comparison of asymptotical and numerical solutions	119
3.5.2	Exploring the effects of the phototaxis parameter χ on the critical wavenumber k_c and Rayleigh number R_c	121
3.5.3	Exploring the effects of the gyrotaxis parameter η on the critical wavenumber k_c and Rayleigh number R_c	122
3.5.4	Table of Results	123
3.6	Model C, where a new torque due to phototaxis is introduced	123
3.7	Model C, Case 1, where the torque due to phototaxis is caused by illumination from above	126
3.7.1	Solving the Fokker-Planck equation	127
3.7.2	Equilibrium solution and linear stability analysis	129
3.8	Model C, Case II, where cells respond to gradients in light intensity	131
3.8.1	Solving the Fokker Planck equation	132
3.8.2	Equilibrium solution and linear stability analysis	139
3.9	Numerical results for Model C	142
3.9.1	Model C, Case I	142
3.9.2	Model C, Case II	145
3.10	Model comparisons	153
3.11	Discussion	156
4	An experimental study of the effects of light and concentration on pattern formation	161
4.1	Introduction	161
4.2	Materials and Methods	163
4.2.1	Cell Culture	163

4.2.2	Concentrating cells	164
4.2.3	Transfer of culture	164
4.2.4	Measuring depth and concentration	165
4.2.5	Culture mixing	166
4.2.6	Calibration of the light source	168
4.2.7	Image Capture	169
4.2.8	Varying concentration in the suspension	169
4.2.9	Controlling illumination	170
4.2.10	Statistical Analysis	171
4.3	Image Analysis	171
4.3.1	Fourier transformation	172
4.3.2	Dominant wavenumber extraction	174
4.4	Results and discussion	176
4.4.1	Exploring the effects of mixing on initial pattern formation	176
4.4.2	Exploring the effects of concentration on initial pattern wavelength	179
4.4.3	Does red light illumination affect the initial pattern wavelength?	183
4.4.4	Exploring the effects of white light illumination from below on initial pattern wavelength	188
4.4.5	Exploring the effects of white light illumination from above on initial pattern wavelength	196
4.4.6	Exploring the start time of pattern formation, t_0	205
4.5	Comparing experiment results with predictions from the three photo-gyrotaxis models	208
4.6	Predicting I_c from Experiments	215
4.7	Conclusions	217
5	Modelling hydrogen production in suspensions of <i>Chlamydomonas reinhardtii</i>.	220
5.1	Introduction	220
5.1.1	Background	221
5.1.2	Challenges to commercial hydrogen production	227
5.1.3	Previous modelling methodologies	229
5.1.4	Modelling methodology in this study	229
5.1.5	Hypotheses	230

5.2	Model construction	232
5.2.1	Main modelling assumptions	232
5.2.2	Internal concentrations	235
5.2.3	External sulphur concentration	241
5.2.4	Oxygen concentration	241
5.2.5	Growth and decay of cell volume fraction	243
5.2.6	The effects of culture density on light availability	245
5.2.7	Hydrogen production	247
5.2.8	The standard model, SM	250
5.3	Parameter Estimation	251
5.3.1	The critical values s_0 , s_1 , ω_1 , ω_2 , ω_p and p_r	252
5.3.2	Parameters in the sulphur equations	253
5.3.3	Parameters in the oxygen and hydrogen equations	256
5.3.4	Parameters in the cell volume fraction equation	257
5.3.5	Parameters in the light function	259
5.3.6	Standard parameter values	259
5.4	Non-dimensionalization of the standard model	262
5.4.1	Initial conditions	264
5.5	Numerical model results for the standard parameter values	264
5.5.1	Numerical Method	264
5.5.2	A numerical check	266
5.5.3	The sulphur-deprived case	268
5.5.4	The sulphur-replete case	271
5.5.5	Varying the initial concentration of external sulphur, S_0	273
5.5.6	Comparing initial rates of hydrogen production as S_0 varies	279
5.5.7	Varying the initial cell volume fraction, Λ_0	280
5.6	Discussion	280
6	Investigating parameter sensitivity and optimizing hydrogen yield for the mechanistic hydrogen model	285
6.1	Parameter sensitivity	285
6.1.1	Parameters in the sulphur uptake equation	285
6.1.2	Parameters in substrate equations for sulphur and protein	287
6.1.3	Parameters relating to oxygen and hydrogen production	287

6.1.4	Parameters in the growth equation	292
6.1.5	Investigation into the light parameters I_0 , I_{sat} and D_C	293
6.1.6	Brief conclusions from parameter sensitivity analysis	296
6.2	Optimizing the yield of hydrogen gas	297
6.2.1	Numerical optimization	300
6.2.2	Two-stage sulphur cycling (as in Ghirardi <i>et al.</i> [41])	300
6.2.3	Sulphur cycling using a sine wave	304
6.2.4	Sulphur cycling using a square wave	306
6.2.5	Controlling sulphur addition using the gradient of H_2 production: a gradient switch function	309
6.2.6	Controlling sulphur input using the gradient of H_2 production: a linear and a two-step switch function	314
6.2.7	A novel two-stage feedback spike sulphur input function	319
6.2.8	Optimizing the initial sulphur concentration, S_0	323
6.2.9	Investigating k_3 , the dimensional rate constant for protein production.	326
6.2.10	Summary of Optimization Results	328
6.3	Discussion	328
7	Concluding remarks	335
A	Analytic equilibrium solution for the case of weak absorption in Models A and B	340
B	Solving terms in the Fokker-Planck equation using associated Legendre polynomials	344
B.1	Definitions and identities for associated Legendre polynomials	344
B.2	An example of using associated Legendre polynomials to solve a term in the Fokker-Planck equation	345
C	Definitions of constants used in the asymptotic analysis for a deep layer and weak illumination for Model B	347
	References	350

List of Figures

1.1	A schematic diagram of the structure of a typical <i>Chlamydomonas reinhardtii</i> cell.	3
1.2	A schematic diagram to show the forces acting on a <i>Chlamydomonas</i> cell.	6
1.3	A simple sketch to show how a cell may vary the flagellar beat pattern during positive phototaxis.	11
1.4	Examples of collective motions caused by cell swimming in cultures of <i>C. nivalis</i>	12
1.5	A schematic diagram of an overturning Rayleigh-Taylor instability.	15
1.6	A schematic diagram of a gyrotactic instability in the absence of an upper boundary.	15
1.7	A simple diagram of an experimental set-up to produce and collect hydrogen gas.	27
2.1	A comparison between numerical (solid lines) and analytical (dashed lines) equilibrium solutions, where $d = 20$, $\chi = 1.2$ and κ varies.	51
2.2	Concentration profiles for the equilibrium solution in Model A, where $d = 20$, $\kappa = 1.2$ and χ varies.	52
2.3	Concentration profiles for the equilibrium solution in Model A, where $d = 200$, $\kappa = 1.2$ and χ varies.	53
2.4	Concentration profiles for the equilibrium solution in Model A, where $d = 20$, $\chi = 1.02$ and $\kappa = 0.5, 1.0$ and 2.0	53
2.5	Asymptotic (dashed) and numerical (solid) curves of neutral stability for Model A, where $d = 40$, $\kappa = 1$, and $\chi = d^{-1}$. The three curves are for $d^2\eta = 0, 2$ and 3	70

2.6	Asymptotic (dashed) and numerical (solid) curves of neutral stability for Model A, where $d = 200$, $\kappa = 1$ and $\chi = d^{-1}$. The five curves are $d^2\eta = 0, 2, 4, 8$ and 16 . Numerical oscillatory solutions are shown by dot-dashed lines.	71
2.7	Asymptotic (dashed) and numerical (solid) curves of neutral stability for Model A, where $d = 200$, $\kappa = 1$ and $\chi = d^{-1}$ - a close up of the cases $d^2\eta = 8$ and 16 .	71
2.8	Flow and concentration profiles for Model A, where $d = 0.1$, $\kappa = 1.2$, $\eta = 0.1$ and $k = 10$, with $\chi = 0.1$ in Figures (a) and (b), and $\chi = 1.03$ in Figure (c) and (d).	73
2.9	Flow and concentration profiles for Model A, where $d = 20$, $\kappa = 1.2$, $d^2\eta = 4$ and $k = 10$, with $\chi = 0.1$ in Figures (a) and (b), and $\chi = 1.03$ in Figures (c) and (d).	73
2.10	Curves of neutral stability for Model A, where $d = 20$, $\kappa = 1.2$, $d^2\eta = 2$ and χ varies.	74
2.11	Curves of neutral stability for Model A, where $d = 20$, $\kappa = 1.2$, $d^2\eta = 4$ and χ varies.	75
2.12	Plots of critical Rayleigh number (circles) and critical wavenumbers (crosses) for Model A, where $d = 20$, $\kappa = 1.2$, $d^2\eta = 4$ and χ varies.	76
2.13	Figure (a) shows curves of neutral stability, where $d = 20$, $d^2\eta = 2$, $\chi = 0.5$ and $R_c = 6.20 \times 10^4$ for Model A. Figure (b) shows the growth rate σ plotted against wavenumber.	76
2.14	Equilibrium solutions and streamlines for Model A, where $d = 20$, $\kappa = 1.2$, $d^2\eta = 4$ and $\chi = 1.03$ and $\chi = 1.04$.	77
2.15	Curves of neutral stability for Model A, where $d = 20$, $\kappa = 1.2$, $\chi = 0.5$ and η varies.	79
2.16	Curves of neutral stability for Model A, where $d = 20$, $\kappa = 1.2$, $\chi = 1.03$ and η varies.	79
2.17	Flow profiles for Model A, where $d = 20$, $\kappa = 1.2$, $\chi = 1.03$, and $d^2\eta = 64$, with $k = 2.5$ in (a) and $k = 5$ in (b).	81
2.18	Curves of neutral stability for Model A, where $d = 20$, $\chi = 1.03$, $d^2\eta = 2$ and $\kappa = 0.8, 1.2$ and 1.6 .	82

2.19	A comparison of curves of neutral stability for the rigid (solid lines) and the stress-free (dashed) boundary conditions for Model A, where $d = 20$, $d^2\eta = 2$, and $\kappa = 1.2$, and $\chi = 0.0, 0.1$ and 0.5	83
2.20	Curves of neutral stability for Model A, where $d = 200$, $\kappa = 1$, and $\chi = 0$, and $d^2\eta = 7.5$ (solid lines), $d^2\eta = 8$ (dashed lines), or $d^2\eta = 8.5$ (bold dashed lines).	84
2.21	A schematic diagram to show how oscillations arise for photo-gyrotactic cells in Model A	90
3.1	A comparison between numerical (solid lines) and analytical (dashed lines) equilibrium solutions for Model B, where $d = 20$, $\chi = 1.0$ and κ varies. . . .	108
3.2	Concentration profiles for the equilibrium solution in Model B, where $d = 20$, $\kappa = 1.2$ and χ varies.	108
3.3	Asymptotic and numerical curves of neutral stability for Model B, where $d = 200$, $\kappa = 1$, $\chi = d^{-1}$ and $d^2\eta$ varies.	120
3.4	Curves of neutral stability for Model B, where $d = 200$, $\kappa = 1.2$, $d^2\eta = 8$ and χ varies.	121
3.5	Curves of neutral stability for Model B, where $d = 200$, $\kappa = 1.2$, $d\chi = 40$ and $d^2\eta$ varies.	122
3.6	Curves of neutral stability for Model B, where $d = 20$, $\kappa = 1.2$, $d^2\eta = 4$ and χ varies.	123
3.7	Curves of neutral stability for Model B, where $d = 20$, $\kappa = 1.2$, $\chi = 1.03$ and $d^2\eta$ varies.	125
3.8	Concentration profiles for the equilibrium solution in Model C, Case I, where $d = 20$, $\kappa = 1.0$ and χ varies with $\zeta = 0.236$	143
3.9	Curves of neutral stability for Model C, Case I, where $d = 20$, $\kappa = 1.0$, $d^2\eta = 4$, $\zeta = 0.236$ and χ varies.	144
3.10	Concentration profiles for the equilibrium solution in Model C, Case I, where $d = 20$, $\kappa = 1.0$, $\zeta = 0.236$ and $\chi = 0.5$ (dashed) or $\chi = 0$ (solid line).	145
3.11	Curves for $g(I)$ for Models B and C, where $\zeta = 0.236$ is set so that the gradients at $g(I) = 0$ are the same, and $\chi = 0.5$	146
3.12	Curves of neutral stability for Model C, Case I, where $d = 20$, $\kappa = 1.0$ and $\zeta = 0.236$, for a both a stress-free and a no-flow condition for $\chi = 0.0$ and $\chi = 0.5$	146

3.13	Concentration profiles for the equilibrium solution for Model C, Case II, where $d = 20$, $\kappa = 1.2$, $\chi = 2.0$, $d^2\eta = 4$ and ζ varies.	147
3.14	Curves of neutral stability for Model C, Case II, where $d = 20$, $\kappa = 1.2$, $\chi = 2.0$, $d^2\eta = 4$ and ζ varies.	148
3.15	Curves of neutral stability for Model C, Case II, where $d = 20$, $\kappa = 1.2$, $\chi = 2.0$, $d^2\eta = 4$ and ζ varies.	148
3.16	Growth rate curves for Model C, Case II when there is no fluid flow, so that $U = R = 0$, $d = 20$, $\kappa = 1.2$, $\chi = 2.0$, $d^2\eta = 4$, and ζ varies.	149
3.17	Neutral stability curve of wavenumber versus the phototaxis parameter ζ , where ζ is used as the eigenvalue for the case of zero flow, $U = 0$, in Model C, Case II, where $d = 20$, $\kappa = 1.2$, $\chi = 2.0$ and $d^2\eta = 4$	150
3.18	Concentration profiles for the equilibrium solution for Model C, Case II, where $d = 20$, $\kappa = 1.2$, $\chi = 0.5$, $d^2\eta = 4$ and ζ varies.	151
3.19	Curves of neutral stability for Model C, Case II, where $d = 20$, $\kappa = 1.2$, $\chi = 0.5$, $d^2\eta = 4$, and ζ varies.	152
3.20	Curves of neutral stability for Model C, Case II, where $d = 20$, $\kappa = 1.2$, $d^2\eta = 4$ and χ varies, with $\zeta = 0.1$ in Figure (a) and $\zeta = 4.0$ in Figure (b).	153
3.21	A comparison of equilibrium solutions for Model A (solid lines) and Model B (dashed lines), where $d = 20$, $\kappa = 1.2$ and $\chi = 1.0$, $\chi = 1.02$ and $\chi = 1.04$	154
3.22	A comparison of curves of neutral stability for Model A (solid lines) and Model C, Case I (dashed lines), where $d = 20$, $\kappa = 1.2$ and $\chi = 0$ or $\chi = 0.5$, with $\zeta = 0.236$ in Model C, Case I.	155
3.23	A comparison of curves of neutral stability for Model A (solid lines) and Model B (dashed lines), where $d = 200$, $\kappa = 1.2$, $\chi = 32d^{-1}$, and $d^2\eta = 8$	155
4.1	Calibrating the absorbance measurement, A , from the colourimeter with cell concentration, C , found using a haemocytometer to count cells.	166
4.2	Light calibration curves for the red (crosses) and white (stars) light.	168
4.3	A schematic diagram of the experimental set-up for illuminating the culture from below.	170
4.4	A schematic diagram of the experimental set-up for illuminating the culture from above.	172
4.5	A sample bioconvection image where the culture is illuminated from above with white light.	173

4.6	Sample bioconvection images where the culture was mixed using $m_1 = 2$, $t_1 = 10$ and $t_2 = m_2 = 0$.	177
4.7	Sample images from Experiment CA, with white light illumination from above, $I = 645$ lux, where $d = 0.306$ cm and $I_w = 2.47$ cm. Figure (a) shows a case where concentration $C = 8.11 \times 10^6$ cells / cm ³ and Figure (b) a case where $C = 3.33 \times 10^6$ cells / cm ³ . Images were captured every 2 seconds, starting 10 seconds after mixing ended.	180
4.8	Experiment CA: The effects of concentration on dominant initial pattern wavelength for a culture illuminated from above with a white light, where $I = 645$ lux and $d = 0.306$ cm.	182
4.9	Experiment CB: The effects of concentration on dominant initial pattern wavelength for a culture illuminated from below with a white light, where $I = 645$ lux and $d = 0.345$ cm.	182
4.10	Action spectra for <i>C. reinhardtii</i> cells; the relationship between wavelength of light, λ nm, and relative response. This figure is reproduced from data in Nultsch <i>et al.</i> [125].	184
4.11	Sample images from Experiment RA, with red light illumination from above, $I = 101$ lux, where $C = 5.05 \times 10^6$ cells / cm ³ , $d = 0.306$ cm, and $I_w = 2.33$ cm. Images were captured every 2 seconds, starting 10 seconds after mixing ended.	184
4.12	A sample set of Fourier spectra from Experiment RA, with red light illumination from above, where $I = 101$ lux, $C = 5.05 \times 10^6$ cells / cm ³ and $d = 0.306$ cm. Images were captured every 2 seconds, starting 10 seconds after mixing ended.	185
4.13	A sample contour plot from Experiment RA, with red light illumination from above, where $I = 101$ lux, $C = 5.05 \times 10^6$ cells / cm ³ and $d = 0.306$ cm. Images were captured every 2 seconds, starting 10 seconds after mixing ended. Time is measured from the start of image recording, and is not the time since mixing.	186
4.14	Experiment RA: The effect of red light from above on dominant initial pattern wavelength, where $d = 0.306$ cm and $C = 5.05 \times 10^6$ cells / cm ³ .	187
4.15	Spectrum of the white light box.	188

4.16	Experiment LB1: The effect of white light illumination from below on dominant initial pattern wavelength, where $d = 0.306$ cm and $C = 5.35 \times 10^6$ cells / cm ³	189
4.17	Experiment LB2: The effect of white light illumination from below on dominant initial pattern wavelength, where $d = 0.306$ cm and $C = 5.18 \times 10^6$ cells / cm ³	191
4.18	Experiment LB3: The effect of white light illumination from below on dominant initial pattern wavelength, where $d = 0.306$ cm and $C = 9.46 \times 10^6$ cells / cm ³	191
4.19	The effect of illumination from below on dominant initial pattern wavelength, where linear regression fits have been plotted for all experiments, separately for the first three points and the last four points in each data set.	194
4.20	Sample images from Experiment LA1, with white light illumination from above, where $C = 5.05 \times 10^6$ cells / cm ³ , $d = 0.306$ cm and $I_w = 2.47$ cm. Figure (a) shows a case where $I = 645$ lux and Figure (b) a case where $L = 4770$ lux. Images were captured every 2 seconds, starting 12 seconds after mixing ended.	198
4.21	A sample set of Fourier spectra from Experiment LA1, with white light illumination from above, where $I = 645$ lux, $C = 5.05 \times 10^6$ cells / cm ³ and $d = 0.306$ cm. Images were captured every 2 seconds, starting 12 seconds after mixing ended.	199
4.22	A sample set of Fourier spectra from Experiment LA1, with white light illumination from above, where $I = 4770$ lux, $C = 5.05 \times 10^6$ cells / cm ³ and $d = 0.306$ cm. Images were captured every 2 seconds, starting 12 seconds after mixing ended.	200
4.23	A sample 3D surface from Experiment LA1, with white light illumination from above, where $I = 645$ lux, $C = 5.05 \times 10^6$ cells / cm ³ and $d = 0.306$ cm. Images were captured every 2 seconds, starting 12 seconds after mixing ended. ‘Time’ is time since recording started.	201
4.24	Experiment LA1: The effect of white light illumination from above on dominant initial pattern wavelength, where $d = 0.306$ cm and $C = 5.05 \times 10^6$ cells / cm ³ . A linear regression fit is plotted for all points except the first, $I = 645$ lux.	202

4.25	Experiment LA2: The effect of white light illumination from above on dominant initial pattern wavelength, where $d = 0.306$ cm and $C = 4.86 \times 10^6$ cells / cm ³ . A linear regression fit is plotted for all points except the first, $I = 645$ lux.	202
4.26	Experiment LA3: The effect of white light illumination from above on the dominant initial pattern wavelength, where $d = 0.306$ cm and $C = 5.69 \times 10^6$ cells / cm ³ . A linear regression fit is plotted for all points except the first, $I = 645$ lux.	203
4.27	Plots of average initial start time t_0 for (a) Experiment LB1 and (b) Experiment LA1 for different light intensities, where the average start time for $I = 325$ lux for the red light experiment RA is included as $I = 0$ lux, since red light has no effect on photo-motility. In both cases, $d = 0.306$ cm, and for LA1 and LB1 images were captured every 2 seconds, starting 12 seconds after mixing ended.	205
4.28	Results from experiment LA1, where the dimensional wavelengths have been non-dimensionalized, for comparison with the theoretical predictions, and converted to a non-dimensional wavenumber, \tilde{k}_0	212
4.29	Critical wavenumber, k_c , plotted against χ for Model A in Figure (a) and for Model B in Figure (b), where $\kappa = 20.3$ and $d = 34.6$	212
4.30	Curves of neutral stability for Model B, where $d = 20$, $\kappa = 20.3$, $d^2\eta = 16$ and $\chi = 0.0$, $\chi = 0.1$ and $\chi = 0.2$	214
5.1	A schematic diagram showing the basic internal structure of a <i>C. reinhardtii</i> cell.	222
5.2	A schematic diagram of the intracellular processes and pathways that occur under normal, sulphur-replete conditions.	225
5.3	A schematic diagram of the intracellular processes and interactions that occur during sulphur-deprivation.	226
5.4	A simple schematic diagram of the variables in novel mechanistic model, showing the interactions between them.	233
5.5	An example of a ramp function $R(s, s_0) = sH_1(s_0 - s) + s_0H(s - s_0)$, where $s_0 = 1.0$, used to model the rate of sulphur used to repair PSII in equation 5.7.	237

5.6	A simple schematic diagram to show the cyclic relationship between protein and sulphur.	238
5.7	A simple schematic diagram of the transport of electron flow from photosystem I, via electrons donated from PSII and from protein breakdown, to the final location.	240
5.8	The function for growth dependent on protein, shown with the standard parameter values in Table 5.1	244
5.9	The normalized light function $L(\Lambda)$, where $I_{sat} = 150$ and $I_0 = 49.6$ (dotted), $I_0 = 99.2$ (solid) and $I_0 = 148.8$ (dashed lines).	248
5.10	Reproduced protein data for $S_0 = 0 \mu\text{M}$ from Figure 5 for unsynchronized cells in Kosourov <i>et al.</i> [92].	254
5.11	Numerical (solid lines) and analytical (dashed lines) solutions for a simplified version of the model. Good agreement is found between numerical and analytical solutions for early times, $t < 4$	268
5.12	Results for the model with standard parameter values under sulphur deprivation, with initial condition $S_0 = 0$	269
5.13	Results for the model with standard parameter values under sulphur-replete conditions, with initial condition $S_0 = 100$ in non-dimensional units.	272
5.14	Data reproduced from Figure 6b in Kosourov <i>et al.</i> 2002 [92] for hydrogen production per 1.2 L of unsynchronized culture against time, where the cultures were deprived of sulphur at $t = 0$, and data points every 20 hours were manually measured from smooth curves in [92].	273
5.15	Results for the model with standard parameter values, with initial conditions of external sulphur of $S_0 = 0$ (solid lines), $S_0 = 1.725$ (dotted lines) and $S_0 = 3.45$ (dashed lines). These correspond to $0 \mu\text{M}$, $25 \mu\text{M}$, and $50 \mu\text{M}$, respectively.	274
5.16	Hydrogen and cell volume fraction curves for the model with standard parameter values and with initial conditions $S_0 = 0$ (solid lines), 3.45 (dashed lines), 6.9 (dot-dashed lines), 13.8 (dotted lines), and 20.7 (thick dashed lines).	275
5.17	Hydrogen yield at time $t = T$ as a function of initial condition S_0 where $T = 5.74$ (solid line), $T = 10$ (dotted line) and $T = 15$ (dashed line).	276

5.18	Results for the model with standard parameter values where $T = 15$, with initial conditions of $S_0=15.2$ (solid line), $S_0 = 18.5$ (dotted) and $S_0 = 22.0$ (dashed). These results illustrate the behaviour of the model for values of S_0 around the undulating regions on the curve for hydrogen yield as a function of S_0 in Figure 5.17.	277
5.19	Initial amount of external sulphur, S_0 , plotted against the start time of hydrogen production, T_H	278
5.20	Initial rates of hydrogen production (in the first 14.6 hours) plotted against the initial amount of external sulphur.	279
5.21	Results for the model with standard parameter values, with initial condition $S_0 = 3.45$ and $\Lambda_0 = 0.00225$ (solid lines), $\Lambda_0 = 0.0045$ (dotted lines) and $\Lambda_0 = 0.001125$ (dashed lines).	281
6.1	Model results when the sulphur uptake parameter A_1 is increased (dashed lines) and decreased (dotted lines) by a factor of 2, compared to model results for the standard parameter values (solid lines).	286
6.2	Model results when K_2 is increased (dashed lines) and decreased (dotted lines) by a factor of 2, compared to model results for the standard parameter values (solid lines).	288
6.3	Model results when K_6 is increased (dashed lines) and decreased (dotted lines) by a factor of 2, compared to model results for the standard parameter values (solid lines).	290
6.4	Model results when S_1 is increased (dashed lines) and decreased (dotted lines) by a factor of 2, compared to model results for the standard parameter values (solid lines).	291
6.5	Model results when I_0 is increased (dashed lines) and decreased (dotted lines) by a factor of 2, compared to model results for the standard parameter values (solid lines)	294
6.6	Model results when D_C is decreased (dotted lines) and increased (dashed lines) by a factor of 2 for $I_0 = 300 \mu\text{mol m}^{-2}\text{s}^{-1}$, compared to model results for the standard parameter values (solid lines)	296

6.7	Data reproduced from Ghirardi <i>et al.</i> [41] for hydrogen production using the two-stage sulphur cycling method, where cells are deprived of sulphur at $t = 0$ and re-suspended in a sulphur-replete medium for 30 hours at $t = 100$ and $t = 220$ hours, before being deprived of sulphur once more.	301
6.8	Results for the model with standard parameters using the two-stage cycling regime from Ghirardi <i>et al.</i> [41] until $t = 14.7$. Here, $S_R = 62.1$ ($S_R = 0.9$ mM) in sulphur-replete conditions, and $t_1 = 4.1$, $t_2 = 1.23$	302
6.9	Model results to $t = 40$ using optimal parameters $t_1 = 3.04$, $t_2 = 0.941$ with $S_R = 62.1$ for the two-stage cycling from Ghirardi <i>et al.</i> [41].	303
6.10	Contour plot of optimal hydrogen yield at $t = 15$ using the sine wave sulphur input, with $S_0 = 0$, varying amplitude and frequency.	305
6.11	Model results to $t = 15$ using optimal parameters $F = 1.09$ and $A = 0.154$ for the sine wave sulphur input.	305
6.12	Contour plot of optimal hydrogen yield at $t = 40$ using the sine wave sulphur input, with $S_0 = 0$, varying amplitude and frequency.	306
6.13	An example of a square wave function used in the optimization where $A = 2$, $F = 2$ and $P = 25$	307
6.14	Model results to $t = 15$ using optimal parameters $F = 5.11$, $A = 35.2$ and $P = 3.44$ for the square wave sulphur input.	308
6.15	Contour plot of optimal hydrogen yield at $t = 15$ using the square wave sulphur input, with $S_0 = 0$, varying A and P and setting $F = 5.11$	309
6.16	Model results to $t = 15$ using optimal parameter values $h_c = 0.0031$ and $a_1 = 1.4117$ for the hydrogen gradient switch sulphur input.	311
6.17	Surface plot of optimal hydrogen yield at $t = 15$ using the hydrogen gradient switch sulphur input, with $S_0 = 0$, varying a_1 and h_c	312
6.18	An example of the linear switch sulphur input dependant on $\frac{dh}{dt}$, where $h_c = 0.005$, $a_1 = 0.5$ and $a_2 = 2$	315
6.19	A comparison of optimization strategies for the linear switch sulphur input, with optimal parameters $a_1 = 0.0002$, $a_2 = 1.44$ and $h_c = 0.0051$ (solid lines), and $a_1 = 0.936$, $a_2 = 0.0661$ and $h_c = 0.006$ (dashed lines). The dashed line optimization is not continuous and for long times it is no longer optimal and hydrogen production stops around $t = 14$	316

6.20	Model results to $t = 15$ using optimal parameters $a_1 = 0.522$, $a_2 = 1.868$, $h_c = 0.0051$ and $h_{c2} = 0.0001$ (solid lines) with $h_{c2} = 0.001$ (dashed lines) for the two-step sulphur input.	318
6.21	Surface plot of optimal hydrogen yield at $t = 15$ using the two-step sulphur input, with $S_0 = 0$ and $h_c = 0.0051$, varying a_1 and a_2	319
6.22	Contour plot of optimal hydrogen yield at $t = 15$ using the two-step sulphur input, with $S_0 = 0$. In Figure (a) $a_1 = 0.552$, and a_2 and h_c are varied, and in Figure (b) $a_2 = 1.87$, and a_1 and h_c are varied.	320
6.23	Contour plot of optimal hydrogen yield at $t = 15$ using the feedback spike optimization function, with $S_0 = 0$ and $h_c = 0.0051$, varying S_I and a_1	321
6.24	Model results to $t = 15$ using optimal parameters $S_I = 5.75$, $h_c = 0.0051$ and $a_1 = 0.614$ for the feedback spike cycling method. A significant increase in yield at $t = 15$ is seen compared to the previous optimization functions.	322
6.25	Model results to $t = 15$ using optimal parameters $S_I = 5.75$, $h_c = 0.0051$ and $a_1 = 0.614$ for the feedback spike cycling method: a close up of the external sulphur (S) behaviour.	324
6.26	Model results to $t = 15$ using optimal parameters $S_0 = 2.81$, $h_c = 0.0051$, $S_I = 6.54$ and $a_1 = 0.557$ for the feedback spike cycling method, where the initial condition for external sulphur was also varied.	325
6.27	The difference in yield per cycle between the second and third cycles of hydrogen production, h_{23} , as a function of the rate of protein production, k_3 . Negative regions indicate a decrease in yield per cycle. Here, $t_1 = 4.1$ and $t_2 = 1.23$ as in Ghirardi <i>et al.</i> [41].	327
6.28	A bar chart to show the values of hydrogen in mL H_2 /L culture at approximately 15 days for the different optimization strategies tested. Standard parameter values from Table 5.3 were used.	328

List of Tables

2.1	Table of the standard parameter estimates for the green algae species <i>C. nivalis</i> .	42
2.2	Table of values of K_i and J_i for use in Model A, where $\lambda = 2.2$ and $\alpha_0 = 0.2$. The $a_{i,j}$, $\tilde{a}_{i,j}$ and $\bar{a}_{i,j}$ values are defined in Chapter 3.	45
2.3	Values and definitions of constants A_i , P_V and P_H when $\lambda = 2.2$ and $\alpha_0 = 0.2$.	58
2.4	Summary of asymptotic and numerical results for a deep layer with weak illumination, where $\kappa = 1$ and standard parameters were used.	72
2.5	Summary of the linear stability results for Model A, in terms of critical wavenumber, k_c , and Rayleigh number, R_c , for $\lambda = 2.2$ and $\alpha_0 = 0.2$. The star indicates the solution at the critical wavenumber, k_c , is mode two.	85
3.1	Summary of the linear stability results for Model B, in terms of critical wavenumber, k_c , and Rayleigh number, R_c , for $\lambda = 2.2$ and $\alpha_0 = 0.2$. The star indicates the solution at the critical wavenumber, k_c , is mode two.	124
4.1	Summary of the different mixing methods used in the experimental results. The last column is a sequence of seconds with order mixing, waiting and is either (m_1, t_1) , (m_2, t_2) or (m_1, t_1) , (m_2, t_2) , (m_3, t_3) in cases where more mixing is required.	178
4.2	Summary of results for the initial pattern wavelength, where cell concentration varies. White light from above was used in experiment CA and white light from below in CB.	179
4.3	Summary of results for initial pattern wavelength when the suspension was illuminated with a red light from above.	186
4.4	Summary of results for initial pattern wavelength when the suspension was illuminated with a white light from below.	190

4.5	Summary of results for initial pattern wavelength when the suspension was illuminated with a white light from above.	197
4.6	Summary of initial start time t_0 for the Experiments LA1 and LB1 and for a sample red light intensity $I = 325$ lux from Experimental RA.	206
4.7	Results from experiment LA1 with white light from above and RA with red light from above, where wavelength has been converted into non-dimensional wavenumbers in order to compare with theoretical results.	211
4.8	Theoretical predictions of critical wavenumber, k_c , and critical Rayleigh number, R_c , for Models A and B.	213
4.9	Summary of curve fitting results when cells are illuminated with a white light from above for the three experiments in Section 4.4.5. Separate curves were fit for the data points $I = 645$ lux and $I = 1330$ lux and for the data points $I \geq 2020$ lux. The point at which the curves meet, for each experiment, is used as an estimate of I_c	216
5.1	Table of standard model parameters for the hydrogen model. Estimates parameters, such as those calculated using the model, are marked with a star.	261
5.2	The values of the gradients, g , used in each tanh function. Here, H_{light} is the Heaviside function used in the expression for light intensity in equation 5.57.	263
5.3	Table of all non-dimensional parameter values for the hydrogen model. Parameters that were already non-dimensionalized are included here for completeness.	265
6.1	Summary of functional forms used as input functions in equation 6.1 in an attempt to optimize hydrogen yield.	299
6.2	The yield of hydrogen gas at $t = 15$. The * indicates that this optimal strategy is non-sustainable, as discussed in the relevant section.	329
C.1	Summary of constants needed to compute the asymptotic solution for Model B in equation 3.188, where $\alpha_0 = 0.2$	349

Nomenclature

Chapter 1

a	Cell length
b	Cell breadth
B	Gyrotactic orientation parameter in Pedley and Kessler [129]
c	Cell concentration in Childless <i>et al.</i> [22]
C	Position at which $I = I_c$ in Vincent and Hill 1996 [172]
D	Cell diffusion tensor
D_h	Horizontal component of orthotropic cell diffusion
D_r	Rotational diffusivity
D_v	Vertical component of orthotropic cell diffusion
E	Dimensional rate-of-strain tensor
$f(\mathbf{p})$	Cell swimming direction probability density function
g	Acceleration due to gravity
h	Distance between the centre of mass and the geometric center of a cell along \mathbf{p}
i,j,k	Unit vector coordinate system
I	Light intensity
I_c	Critical light intensity
I_s	Light intensity at the source
J	Flux of organisms through the fluid
\mathbf{L}_g	Gravitational torque acting on a cell
\mathbf{L}_T	Total torque acting on a cell
\mathbf{L}_v	Viscous torque acting on a cell
m	Mass of a cell
n	Cell concentration

p	Pressure in Childless <i>et al.</i> [22]
p_e	Excess pressure above hydrostatic (at density ρ)
\mathbf{p}	Unit vector in direction of swimming cell
$\langle \mathbf{p} \rangle$	Mean cell swimming direction
$\mathbf{P}, \mathbf{R}, \mathbf{Y}$	Tensors depending on the surface geometry of the cell
\mathbf{q}, \mathbf{r}	Unit vectors perpendicular to cell swimming direction
\mathbf{r}	Vector from the cell to the light source in Vincent and Hill [172]
r	Radius of a cell modelled as sphere in the sedimentation velocity approximation (equation 1.1)
S	Surface of the unit sphere
t	Time
$T(I)$	Taxis function in Vincent and Hill [172]
\mathbf{u}	Fluid velocity
U_s	Sedimentation speed of a non-swimming cell
$U(c, z)$	Function for cell swimming speed in Childless <i>et al.</i> [22]
v	Mean volume of a cell
\mathbf{v}	Cell swimming velocity
\mathbf{V}_r	Velocity of a cell relative to its mean value
V_c	Cell swimming velocity in Vincent and Hill [172]
V_s	Average cell swimming speed
α	Extinction coefficient
α_e	Extra density due to microorganisms relative to the fluid in Childless <i>et al.</i> [22]
α_{\parallel}	Dimensionless resistance coefficient for rotation about \mathbf{p}
α_{\perp}	Dimensionless resistance coefficient for rotation about an axis perpendicular to \mathbf{p}
α_0	Cell eccentricity
δ_{ij}	Kronecker delta
ϵ_{ijl}	Levi-Civita tensor
μ	Fluid viscosity
ϕ	Cell orientation angle in the horizontal plane
ρ	Fluid density
ρ_{fluid}	Density of the fluid in equation 1.1
ρ_{sphere}	Density of a cell in equation 1.1
$\Delta\rho$	Extra density of cell relative to the fluid
Σ	Stress tensor

$\Sigma^{(d)}$	Batchelor stresses
$\Sigma^{(p)}$	Stresses associated with the effective particle rotation caused by rotational diffusion
$\Sigma^{(s)}$	Stresslets associated with the swimming motions of individual cells
τ	Direction correlation time
θ	Cell orientation angle from the vertical
Ω	Dimensional vorticity
ω^c	Angular velocity of a cell

Chapter 2

Notation as previously defined, plus the following amendments and additions.

a_i, b_i, A_i, B_i	Constants from the asymptotic analysis
$a_{i,j}, b_{i,j}$	Constants in linear expansion of the Fokker-Planck equation
$\tilde{a}_{i,j}, \tilde{b}_{i,j}$	Constants in linear expansion of the Fokker-Planck equation
$\bar{a}_{i,j}, \bar{b}_{i,j}$	Constants in linear expansion of the Fokker-Planck equation
A_i	Functions in linear analysis equations which are dependent on K_i, J_i and α_0
B_n	Gyrotactic orientation parameter as in Pedley and Kessler [129] but based on h_n instead of h
C	Position at which $I = I_c$ for an individual cell
d	Dimensionless layer depth parameter
D_0	Diffusion scale
\mathbf{e}	Dimensionless rate-of-strain tensor
$f^0(\theta, \phi)$	No-flow component of cell swimming probability density function, $f(\theta, \phi)$
$f^1(\theta, \phi)$	First order perturbation to cell swimming probability density function, $f(\theta, \phi)$
G_1	Constant in the analytical equilibrium solution
$h(I)$	Centre of mass offset that varies with light intensity
h_n	Centre of mass offset in the dark
H	Suspension depth
$H_i(\alpha_0, \eta)$	Functions of J_i, K_i, α_0 and η involved in the linear stability analysis
$\tilde{\mathbf{k}}(I)$	Function dependent on light intensity that appears in the Fokker-Planck equation in Model C

k	Dimensionless wavenumber
k_c	Dimensionless critical wavenumber
K	Constant obtained from the transcendental equation for the analytical equilibrium solution
K_i, J_i	Functions of λ in the mean cell swimming direction and cell swimming diffusion tensor
\mathbf{L}_p	New phototactic torque
m	Integral of concentration, n
$M(z)$	Amplitude of perturbation to integral of cell concentration
\bar{n}	Mean cell concentration
N	Scaling of cell concentration
P_V, P_H	Functions in linear analysis equations which are dependent on K_i and λ
$P_i(z)$	Functions in linear analysis equations that depend on $z, K_i, J_i, A_i, \kappa, \chi$ and d
R	Rayleigh number
R_c	Critical Rayleigh number
S_c	Schmidt number
V_n	Average cell swimming speed (obtained from Hill and Häder [61] for <i>C. nivalis</i>)
$V_s(I)$	Mean cell swimming speed dependent on light intensity
$U(z)$	Amplitude of perturbation to fluid velocity
α^*	Cellular extinction coefficient
ϵ	Perturbation parameter
η	Dimensionless gyrotaxis number
κ	Dimensionless measure of absorption
λ	$= (2B_n D_r)^{-1}$
μ_λ	Function of λ
ν	Kinematic fluid viscosity
σ	Linear growth rate
$\Phi(z)$	Amplitude of perturbation to cell concentration
χ	Dimensionless phototaxis parameter
ω	Dimensionless vorticity vector
\bullet^i	Perturbation of order i
\bullet_{-i}	Component of asymptotic solution
\bullet_I	Denotes scaling z with d (or inner asymptotic solution)

$\bullet\zeta$	Denotes intermediate region in matched asymptotic solution
$\partial\bullet \equiv \frac{\partial}{\partial\bullet}$	Abbreviation
$\partial_i \equiv \frac{\partial}{\partial x_i}$	Abbreviation
\prime	Differentiation with respect to the dependent variable

Chapter 3

Notation as previously defined, plus the following amendments and additions.

$\hat{a}_{i,j}, \hat{b}_{i,j}$	Constants in linear expansion of the Fokker-Planck equation
$A_K, B_K,$ C_K, N_K	Constants of integration in the asymptotic analysis for Model B
$A_i(z)$	Functions of z in linear analysis equations which are dependent on $K_i(z), J_i(z)$ and α_0
$A_{(i,j)}$	Terms of order j in the Taylor expansion of A_i for small d^{-1}
$C(z)$	Function of $I(z), \zeta$ and χ in the phototactic torque
$f(I)$	Function of light intensity in the phototaxis torque
f_m	Maximum of the function $f(I)$
$f^{1(*)}(\theta, \phi)$	First order perturbation to cell swimming probability density function, $f(\theta, \phi)$ arising from the asymmetry of the cell or from phototaxis
F_0	Constant in $f(I)$
$\hat{\mathbf{G}}$	Unit vector in ∇I
$g_i(\theta, \phi),$ $h_i(\theta, \phi)$	Components of $f^1(\theta, \phi)$ and $f^{1(*)}(\theta, \phi)$
$g(I)$	Function multiplied by the combined gravitactic and phototactic torque term
$G_n(\theta, \phi)$	$= \sum_{r=1}^n a_{n,r} P_r^1(\theta, \phi)$
$H_i(z, \alpha_0, \eta)$	Functions of $J_i(z), K_i(z), \alpha_0$ and η involved in the linear stability analysis
$\hat{\mathbf{k}}(I)$	Unit vector dependent on light intensity in Model C
\bar{K}_i, \bar{J}_i	Value of $K_i(z)$ or $J_i(z)$ when $\Lambda = \Lambda_C = \Lambda_{C2} = 2.2$
$K_i(z), J_i(z)$	Functions of z in the mean cell swimming direction and cell swimming diffusion tensor
$K_{(i,j)},$ $J_{(i,j)}$	Terms of order j in the Taylor expansion of K_i or J_i for small d^{-1}

$P_V(z),$	Functions in linear analysis equations which are dependent on $K_i(z)$ and
$P_H(z)$	$\Lambda(z)$
$P_{i,j}$	Terms of order j in the Taylor expansion of P_i for small d^{-1}
$P_r^m(x)$	Associated Legendre polynomials
β_1, β_2	Constants in the phototaxis torque
ζ	Dimensionless measure of the strength of the phototactic torque
$\hat{\theta}$	Unit vector in direction of varying θ
Λ	Function of z in the linear expansion to the Fokker-Planck equation for Model B
Λ_C	Function of z in the linear expansion to the Fokker-Planck equation for Model C, Case I
Λ_{C2}	Function of z in the linear expansion to the Fokker-Planck equation for Model C, Case II
π	Direction of illumination in Model C
$\hat{\phi}$	Unit vector in direction of varying ϕ
χ_c	Value of χ above which purely non-hydrodynamic modes first exist

Chapter 4

Notation as previously defined, plus the following amendments and additions.

A	Absorbance measured using the colourimeter
BBM	Bold's Basal Medium
c	Constant in double logarithmic fit
C	Concentration (in cells/cm ³)
CA	Experiment in which concentration is varied when the culture is illuminated with white light from above
CB	Experiment in which concentration is varied when the culture is illuminated with white light from below
$d(\text{cm})$	Suspension depth
d	Dimensionless measure of depth in Models A, B and C
E	Ekman number
$I(k)$	Fourier intensity in Czirók <i>et al.</i> [26]
I	Light intensity
I_R	Red light intensity

I_W	White light intensity
I_w	Image width
k	wavenumber
k_0	Dimensional dominant initial wavenumber (or dominant wavenumber in Cziráok <i>et al.</i> [26])
\tilde{k}_0	Dimensionless dominant initial wavenumber
l	Path length of light through the substance when measuring absorbance
LA _{1,2,3}	Experiments in which white light intensity is varied when the culture is illuminated from above
LB _{1,2,3}	Experiments in which white light intensity is varied when the culture is illuminated from below
m_i	Mixing time
n	Number of experimental runs
N	Image size
p	Significance value from T-test
P	Percentage illumination
R	Correlation coefficient
R^2	Coefficient of determination
RA	Experiment in which red light intensity is varied when the culture is illuminated from above
S.D.	Standard deviation calculated over n runs
t_0	Time from the end of mixing to the start of pattern formation
t_i	Time between periods of mixing
$W_H(x, y)$	Two-dimensional Hahn windowing function
α	Fitting parameter in the double logarithmic function
β	Fitting parameter in the double logarithmic function
ϵ_{KS}	Kolmogorov-Smirnov statistic
ϵ_m	Sum modulus error statistic
κ_1^{-1}	Sublayer depth
λ	Dimensional wavelength
λ_0	Dimensional dominant initial wavelength
$\tilde{\lambda}_0$	Dimensionless dominant initial wavelength
ρ_n	Discrete Fourier spectrum at wavenumber n
$\phi(X = n)$	Fitting function distribution (either double logarithmic or double Gaussian distribution)
Ω	Angular velocity of Petri dish in solid body rotation

Chapter 5

Notation is re-defined in Chapter 5 as follows.

a	Maximum rate of uptake of external sulphur
A_1	Dimensionless ratio of sulphur uptake rates
A_2	Dimensionless ratio of sulphur uptake rates
ATP	Adenosine triphosphate
b_i	Rate constants for sulphur uptake
B	Dimensionless ratio of S uptake rates
c_1	Gradient of the linear part of the growth function
c_i	Constants in simplified analytic solution
C_L	Measure of absorbance of the cells
d	Width of the bio-reactor
d_i	Constants in simplified analytical solution
D_C	$D_C = C_L d$, dimensionless absorption measure
e^-	Electron
E_L	Fraction of electrons from PSII-dependent path
g	Constant in the tanh approximations for the Heaviside functions
G	Rate constant for sulphur uptake
h	Hydrogen gas
H^+	Proton
H_{name}	Heaviside function to model process, 'name'
$I(S, h, \frac{dh}{dt}, t)$	Input of external sulphur function.
I_0	Dimensionless light intensity at the source
I_{sat}	Dimensionless saturation level of light
$I(z)$	Function for total light intensity
$\langle I \rangle_d$	Function for total light intensity averaged over depth if the suspension is instantaneously well mixed
k	Constant used in Henry's law, with units of L.atm/mol, to calculate ω_2
k_1	Rate constant for PSII repair
k_2	Rate constant for protein breakdown
k_3	Rate constant for protein production
k_4	Rate constant for hydrogen production

k_5	Rate constant for oxygen consumption by respiration
k_6	Rate constant for oxygen production from PSII
k_{chl}	Cellular extinction coefficient
k_w	Absorbance coefficient of the medium
K_3	Dimensionless measure of rate of protein production
K_2	Dimensionless protein breakdown rate
K_5	Dimensionless respiration rate
K_6	Dimensionless photosynthesis rate
K_Λ	Maximum packing capacity of spheres
l	Constant in expression for useable light, $L(\Lambda)$
$L(\Lambda)$	Function for useable light intensity
L_1	Constant values of $L(\Lambda)$ from Kosourov <i>et al.</i> [92] used to estimate k_1 and k_3
L_{e1}	Value of the useable light function in Kosourov <i>et al.</i> [92]
n	Cell concentration
n_0	Uniform cell concentration throughout the layer
N	Number of cells
NADP ⁺	Nicotinamide adenine dinucleotide phosphate
NADPH	Reduced form of NADP ⁺
p	Protein
p_0	Protein level when growth is zero
p_1	Protein below which maximum decay occurs
p_2	Protein required for maximum growth
p_{atm}	Partial pressure, measured in atm, used in Henry's law to calculate ω_2
p_h	Normalization of PSII-independent electron pathway
p_r	Basic protein needed for cell survival
P_G	Dimensionless protein gradient
P_H	Dimensionless reciprocal of p_h
P_R	Dimensionless protein required for survival
PSI/PSII	Photosystem I/II
r_{decay}	Maximum rate for cell decay
r_{exp}	Maximum growth rate
$R(s, s_0)$	Ramp function
R_D	Dimensionless decay rate
R_G	Dimensionless growth rate

s	Internal sulphur
s_0	Normal level of sulphur in a cell
s_1	Sulphur level above which Calvin cycle is active
s_g	Gradient of Rubisco switch function
s_h	Normalization of PSII-dependent electron pathway
S	External sulphur
S_1	Ratio of sulphur required for Calvin cycle compared to normal sulphur concentration
S_H	Dimensionless reciprocal of s_h
t	Time
$t_{1/2}$	Half life of sulphur from Melis <i>et al.</i> [114]
t_i	Time at start of i^{th} stage of analytic solution
T	Time at which total hydrogen yield h is output
T_H	Start time of hydrogen production
v_{O_2}	Oxygen mass transfer coefficient
V_{cell}	Volume of a single cell
$V_{\text{container}}$	Volume of the container
V_L	Dimensionless oxygen mass transfer
$\alpha(s)$	Function for the maximum uptake rate of external sulphur
$\beta(s)$	Function for the substrate concentration when the sulphur uptake rate is half of its maximum
β	Average moles of sulphur in one mole of protein
γ_0	Dimensionless protein switch p_0
γ_1	Dimensionless protein switch p_1
γ_2	Dimensionless protein switch p_2
Λ	Cell volume fraction
Λ_1	Constant values of Λ from Kosourov <i>et al.</i> [92] used to estimate k_1 and k_3
Λ_{T_H}	Cell volume fraction when hydrogen production begins
χ	Oxygen saturation in water
ω	Oxygen
ω_1	Oxygen level required for full respiration
ω_2	Oxygen level required to inhibit H_2 production
ω_p	Oxygen level below which protein breakdown occurs

Ω_1	Dimensionless oxygen switch ω_1
Ω_2	Dimensionless oxygen switch ω_2
• $_0$	Initial condition at $t_0 = 0$ (unless otherwise stated)
• <i>initial</i>	Protein concentration or time at the start of a period of protein breakdown in Kosourov <i>et al.</i> [92]
• <i>final</i>	Protein concentration or time at the end of a period of protein breakdown in Kosourov <i>et al.</i> [92]

Chapter 6

Notation as defined in Chapter 5, plus the following amendments and additions.

a_i	Rates of sulphur addition in the gradient switch, linear switch, two-step switch and feedback spike sulphur input functions
A	Amplitude of sulphur addition in the sine wave and square wave sulphur input functions
$f(S, h, \frac{dh}{dt}, t)$	Sulphur input function used in optimization study
F	Frequency of sulphur addition in the sine wave and square wave sulphur input functions
h_c, h_{c2}	Critical hydrogen gradients in the gradient switch, linear switch, two-step switch and feedback spike sulphur input functions
h_{tol}	Small parameter in the feedback spike sulphur input function such that if $\frac{dh}{dh}(T + 1) < h_{tol}$ then sulphur is added
I_C	Initial conditions in the feedback spike sulphur input function
P	Percentage of frequency for which sulphur is input in the square wave sulphur input function
S_D	External sulphur concentration during the sulphur-deprived period in the two-stage sulphur input function
S_I	External sulphur concentration added when hydrogen production stops in the feedback spike sulphur input function
S_R	External sulphur concentration during the sulphur-replete period in the two-stage sulphur input function
t_1	Time in sulphur-deprived medium in the two-stage sulphur input function
t_2	Time in sulphur-replete medium in the two-stage sulphur input function

Chapter 1

Introduction

1.1 General background

Microorganisms comprise a major proportion of the biomass on Earth, although the scale of such creatures means they can not be seen by the naked eye (Madigan *et al.* 2003 [107]). From the bacteria found in the stomachs of mammals, to the algae and plankton found in rivers and oceans worldwide, an enormous and diverse range of microorganism species has been evolving for many millions of years. Such microorganisms not only modulate their own lifecycles and populations, but have a significant impact on phenomena on scales much greater than that of an individual cell. Species of algae and plankton are at the bottom of the food chain in aquatic ecosystems (Pomeroy 1974 [137]), and population variations can affect fishing harvests, cause large-scale species extinctions, and can even contribute to weather conditions and climate change (for example, Charlson *et al.* 1987 [20]). Researching aspects of these fundamentally important organisms is crucial for building a thorough understanding of the world in which we live. Microorganism swimming behaviour, which can lead to local aggregations of high cell density, is no exception, especially since it appears to be a vital part of the natural lifecycle of the cells, in terms of regulation of nutrients, controlling light levels and reproduction. Additionally, aspects of the collective motions caused by cell swimming may mirror large-scale phenomena, such as migration and self-ordering of populations and, as such, techniques and information gained through microorganism research may be useful when considering a wide range of other problems.

Some species of microorganisms also have exciting commercial and industrial applications. By-products produced during intracellular photosynthesis and respiration, such as ethanol, are commercially valuable, and the high lipid content of species such as *Botryococ-*

cus braunii indicate the potential of microorganisms in the lipid energy market (Metzger and Largeau 2005 [118]). Various species of microorganism are able to produce hydrogen gas and, hence, are a potential source of renewable energy. It has been known for decades that the algal species *Chlamydomonas reinhardtii* has the ability to produce hydrogen gas transiently (Gaffron and Rubin 1942 [37]). However, it was not until recent discoveries by Melis and co-workers in 2000 [114], who found a novel method for increasing the yield of gas, that the exciting prospect of substantial algal hydrogen production from this species started to become a reality. Melis's discovery was a hugely significant one, since hydrogen production by microorganisms has the potential to produce renewable, green energy from the Earth's most plentiful resources: light and water. With modern advances in genetics, thousands of genes which code for hydrogen-metabolizing proteins in microorganisms have now been identified, promising exciting new sources of future energy.

This thesis is concerned with both pattern formation by motile, uni-cellular microorganisms and the intracellular processes that lead to hydrogen production in green algae.

1.2 Morphology and swimming behaviour of motile microorganisms

In this thesis, we are concerned only with swimming, uni-cellular microorganisms. The taxonomy of such organisms has been the source of much debate for hundreds of years (for example, Stewart *et al.* 1975 [160]). Microorganisms fit into two broad generalizations: prokaryotic cells, which lack a cell nucleus, such as cyanobacteria, and eukaryotic cells, which have a nucleus, such as green algae. Distinctions between eukaryotic microorganisms are loosely based on the presence or absence of chloroplasts (phytoplankton versus zooplankton, for example) and broadly reflect plant versus animal lineages, respectively. However, recent genetic developments have led to the construction of phylogenetic trees based on molecular genetic evidence which reflect the evolutionary history of microorganisms (Falkowski *et al.* 2004 [30]). Combined with morphological studies, this has allowed the grouping of species into more accurate taxonomic divisions. Such studies have shown that the chlorophytes (including green algae, which are the predominant focus of this thesis) diverged from the embryophytes (land plants) over 1 billion years ago and subsequent subphyla have been traced (Merchant *et al.* 2007 [117]). However, there is substantial conservation of biochemical pathways and mechanical structures between the

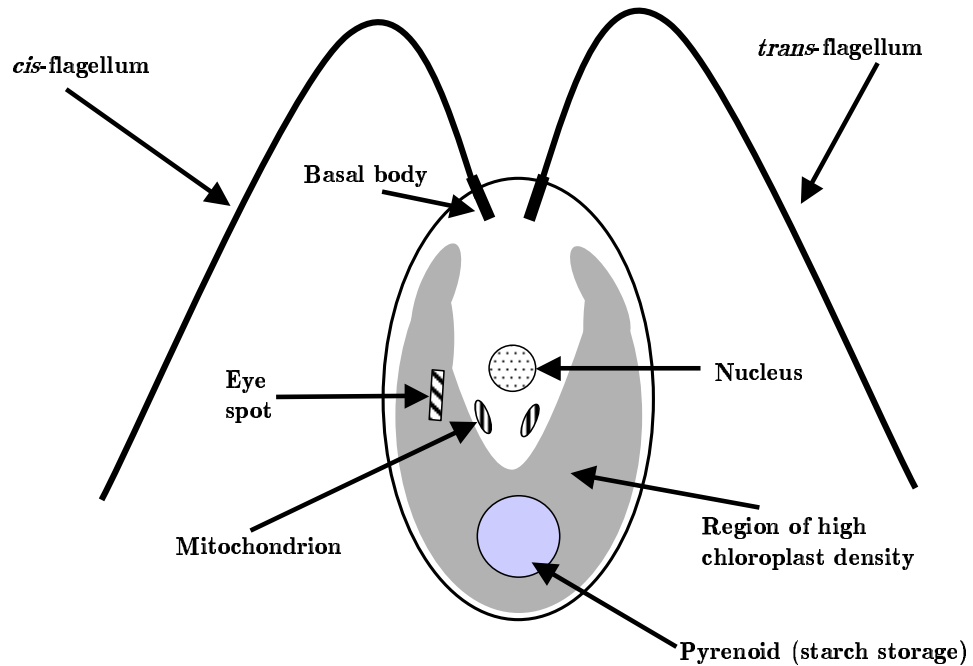


Figure 1.1: A simple schematic diagram of the structure of a typical *Chlamydomonas reinhardtii* cell. The cell is approximately $10 \mu\text{m}$ long, with two flagella of approximately the same length.

Chlorophytes and other microorganisms. For this reason, many of the descriptions below are independent of the precise taxonomic classifications.

Different species of motile microorganisms display an astonishing variety of shapes, structures and swimming apparatus. Regardless of the cell morphology and swimming method, all microorganisms considered in this work swim at low Reynolds number due to the relative size of the cell compared to the fluid [102, 103, 142]. This is very different to conditions for humans swimming in water, and Childress 1981 [21] likened low Reynolds swimming to swimming through a vat of warm pitch. In such cases, inertia is extremely small, and the reversible fluid flow prevents sustained directional movement if a time-symmetric, ‘reciprocal’ swimming stroke is used (in which a cell changes its swimming apparatus into a certain shape and then changes back to the original shape by going through exactly the same sequence in reverse; Purcell 1977 [142]). Thus motile microorganisms have developed swimming strokes that are non-time-symmetric and allow swimming in the desired direction of travel.

One of the most studied microorganisms is the uni-cellular green alga species *Euglena gracilis*. Cells are elongated and measure between 50 and $80 \mu\text{m}$ in length. A single

flagellum attached at the anterior of the cell is rotated in a screw-like manner by passing a helical wave down its length [98], resulting in a swimming speed of around $50 - 100 \mu\text{m}$ per second (Ascoli *et al.* 1978 [4]). In contrast, the genus *Chlamydomonas*, including the species *C. nivalis* and *C. reinhardtii*, possesses cell bodies which are typically spheroidal, and approximately $10 \mu\text{m}$ in length. A schematic diagram of such a cell is shown in Figure 1.1, indicating that many chloroplasts and the pyrenoid, which stores starch, are located towards the posterior of the cell. An eye-spot for light detection is located close to the surface of the cell near the cell equator (the precise location is discussed further in Section 1.3). Two flagella are attached to the anterior of the cell body and are approximately $10 \mu\text{m}$ long. The *cis*-flagellum is located closer to the eye-spot than the *trans* flagellum. Cells propel themselves through the fluid by beating the two flagella in a non-time-reversible (or non-reciprocal) breaststroke-like motion, which may be modelled as a simple power and a recovery stroke (Jones *et al.* 1994 [74]). During the power stroke, the cell starts with both flagella pointing in the direction of cell swimming (vertically upwards in the geometry presented in Figure 1.1). The cell then pushes the flagella down and back towards to the cell body, hence gaining ground. During the recovery stroke ground is lost while a bend travels from the base to the tip of each flagellum, causing both flagella to be pulled in towards the cell and re-positioned at the original location to start the power stroke again. This approximate breaststroke has been observed in many studies, such as Hyams and Boris 1978 [69] and Brokaw *et al.* 1982 [14], although in reality the two phases of the beat actually overlap with each other (Rüffer and Nultsch 1985 [149]). Since more ground is gained during the power stroke than is lost during the recovery stroke, the net movement is in the desired direction of travel, and an individual cell swims at $55 - 67 \mu\text{m}$ per second on average (measured in a series of experiments by Hill and Häder 1997 [61]). The frequency of the beat is approximately 45 Hz [149].

Rüffer and Nultsch found that for *C. reinhardtii* cells the flagella beat outside of the flagella plane and cells employ a slightly unequal beating pattern between the *cis*- and the *trans*-flagella [149, 150]. The *cis*-flagellum moves closer to the axis of the cell body than the *trans* flagellum, and the bending during the recovery stroke happens earlier. The *trans* flagellum beats with a greater distance from the cell body, and generates a stronger rotational component about the cell swimming direction by beating further out of the flagella plane, leading to a helical swimming path [149, 150]. The cell utilizes this rotation since it allows the cell to measure light intensity periodically over a full rotation and then

control photo-orientation accordingly (Nultsch and Häder 1988 [124], Crenshaw 1993 [25]), discussed further in Section 1.4. The frequency of rotation is approximately 1.4-2 Hz. Although the flagellar beat pattern is not symmetric, it is predominantly synchronous, because each flagellum usually beats with approximately the same frequency. However, synchronous beating is sometimes interrupted by single transient asynchronous beating between the flagella (Rüffer and Nultsch 1987 [149, 150]), and it was recently found that cells can stochastically switch between synchronous and asynchronous beating (Polin *et al.* 2009 [134]).

Other species of microorganism have significantly different morphology and swimming behaviours. The genus *Tetrahymena* consists of ciliated microorganisms with elongated cell bodies with diameters of approximately $35\ \mu\text{m}$. The entire surface of the cell is covered with small cilia that are used to propel the cell with a swimming speed of around $500\ \mu\text{m}$ per second [131]. On a much smaller scale, the bacterium *Bacillus subtilis* are rod-like shaped cells, only $2 - 4\ \mu\text{m}$ in length (a clear image of such a cell is shown in [62]). Each cell is peritrichously flagellated (with flagella uniformly distributed over the cell body). These flagella come together to form a helical bundle that is used to propel the cell forward at speeds of up to 10 body lengths per second [62].

The microorganisms discussed above are examples taken from a diverse range of cell species. However, despite the differences in cell morphology and swimming mechanisms, many of the physical behavioural aspects of these cells, such as their orientation towards external stimuli, are similar. Thus using a generic body morphology for simplification purposes seems appropriate. In this thesis, we analyse in detail a cell morphology type based on the genus *Chlamydomonas* shown in Figure 1.1, where we assume that cells are self-propelled spheroids. This is used in many studies of cell motility and pattern formation (for example, Pedley and Kessler 1990 [130] and Bees and Hill 1998 [9]). From here on, we only discuss *Chlamydomonas* cells in detail, except where explicitly stated otherwise.

1.3 What determines the direction in which *Chlamydomonas* cells swim?

It has been known for many years that the direction in which green algae swim is not solely random (for example, Wagner 1911 [174], Buder 1917 [15] and, more recently, Kessler and co-workers [81, 82, 84, 85], to name but a few). *Chlamydomonas* cells respond to stim-

uli using simple ‘rules’ that bias the swimming direction in order to guide cells towards more favorable locations. These ‘rules’ are termed taxes, where a taxis is defined as an innate behavioural response by a freely motile organism towards (positive) or away from (negative) a directional stimulus or gradient of stimulus intensity (or, simply “an orientation behaviour related to a directional stimulus” [68]). The term ‘taxis’ includes both the measurement of the environment and the physical mechanism employed in response to the stimulus. Cells that exhibit no taxes swim in a random manner, with no preferred direction, so can not swim toward preferred areas (such as those high in nutrients or light). This is not advantageous to the cell, thus cells have evolved to use a combination of random movement and biased swimming directions in order to ensure they have the best chance of reaching the optimal location. Examples of taxes are phototaxis, movement towards or away from light, gravitaxis, a bias in direction due to gravity, and chemotaxis, observed mainly in bacteria, which is a directional response to gradients in chemical concentrations (for example, Berg 1983 [13]).

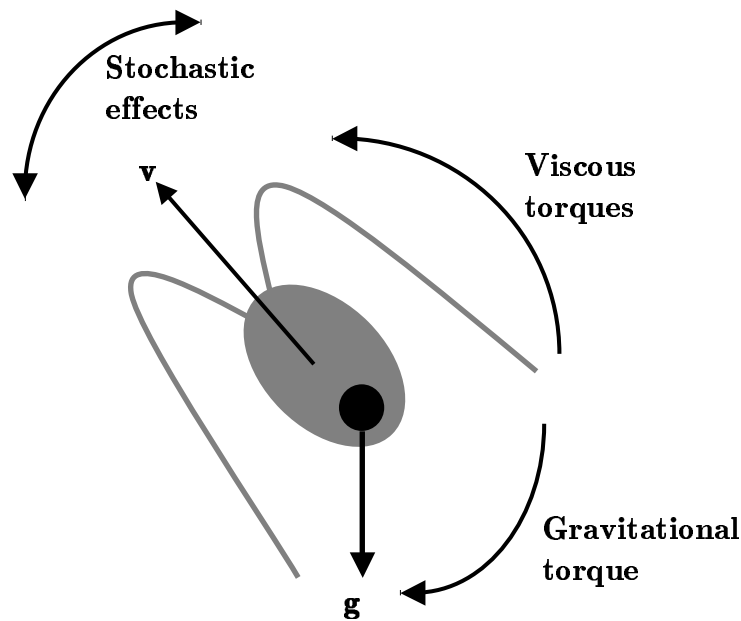


Figure 1.2: A schematic diagram to show the forces acting on a *Chlamydomonas* cell. \mathbf{v} is the cell velocity and \mathbf{g} is the force due to gravity. Viscous torques arise due to strain and vorticity in the fluid. The gravitational torque is caused by the off centre mass distribution arising from uneven starch deposits throughout the cell.

Negative gravitaxis has been observed many times in suspensions of *Chlamydomonas*

[8, 61, 81, 82]. *Chlamydomonas* cells have an anisotropic mass distribution because the pyrenoid, a store for dense starch produced in the chloroplast, is located towards the posterior of the cell (Figure 1.1). Thus the centre of mass is offset from the geometric centre of the cell (i.e. they are bottom heavy). Hence, *Chlamydomonas* cells are negatively gravitactic, so they swim upwards on average (in the absence of other orientation strategies). Kessler defined the term ‘gyrotaxis’ to describe a balance between viscous and gravitational torques that arises due to the cells’ geometry and centre of mass distribution [87] (see Figure 1.2). In the absence of fluid flow, gyrotactic cells swim vertically upwards on average due to gravitaxis. However, if there is a fluid flow with a horizontal component of vorticity then the viscous torque that arises will cause cells to be tipped away from the vertical. Thus the preferred swimming direction of gyrotactic cells is towards regions of locally downwelling fluid and away from locally upwelling fluid (discussed further in Section 1.5.1. Kessler demonstrated this by setting up a Poiseuille flow of *C. nivalis* cells through a U-tube container [81, 82]. In the section of the pipe in which the fluid flowed upwards, the cells swam towards the edge of the container and formed incoherent structures. In the section of the pipe in which the fluid flowed downwards, cells swam towards the centre of the fluid and formed a focused beam, or ‘plume’ (as shown in Figure 1.6). This is an example of gyrotactic focussing.

Both the sedimentation velocity of non-swimming cells and the rotational torque due to sedimentation need to be considered. The sedimentation velocity of a sphere in a viscous fluid can be calculated using the expression for Stokes drag on a sphere,

$$6\pi\mu r U_s = \frac{4}{3}\pi r^3(\rho_{sphere} - \rho_{fluid})g, \quad (1.1)$$

where μ is fluid viscosity, r is the radius of the sphere, U_s is the sedimentation speed, ρ_{sphere} is the density of the sphere, ρ_{fluid} is the density of the fluid, and g is the acceleration due to gravity. We assume that a *Chlamydomonas* cell is a sphere with radius $r = 5.2 \mu\text{m}$ (estimating r for a cell with major axis length of $a = 8 - 10 \mu\text{M}$ and minor axis of $b = 3 - 5 \mu\text{M}$ using the relation for an equivalent sphere of radius r , $r^3 = a \times b^2$) and density $\rho_{sphere} = 1.05 \text{ gm cm}^{-3}$ falling through a fluid with viscosity $\mu = 10^{-2} \text{ gm cm}^{-1} \text{ s}^{-1}$ and density $\rho_{fluid} = 1.0 \text{ gm cm}^{-3}$. We calculate the sedimentation velocity of a non-swimming cell as approximately $U_s = 3 \mu\text{m s}^{-1}$, using equation 1.1. This is much smaller than the cell swimming velocity, by an order of magnitude, thus we neglect this aspect of sedimentation (following many of the theoretical developments described in Pedley and Kessler 1992 [131] and Hill and Pedley [62]). In a series of publications by Roberts [145–148], the idea that

bottom heaviness alone is not responsible for negative gravitaxis is discussed. Roberts proposes that asymmetry of cell body and flagella causes rotational orientation during sedimentation, even when the cell has a uniform mass distribution, because the large cell body sediments faster than the flagella (due to the viscous drag of the flagella on the cell), causing the cell to point upwards. The relative magnitudes of the shape orientation and bottom heavy mechanisms are unclear, but both mechanisms result in orientation to the vertical described by the relation

$$\frac{d\theta}{dt} = \beta \sin \theta, \quad (1.2)$$

where θ is the instantaneous angle of inclination of the cell axis to the upward vertical at time t , and the constant β is the maximum orientation rate which occurs when the long axis of the cell is horizontal (Roberts 2006 [147]). Thus the two mechanisms give similar orientational terms and it is largely irrelevant which mechanism or combination of mechanisms negative gravitaxis is attributed to. In this thesis, gravitaxis is modelled as purely due to the asymmetric mass distribution that causes the cell to be bottom heavy, in line with theoretical developments described in reviews by Pedley and Kessler 1992 [131] and Hill and Pedley 2005 [62], and any rotational torque due to sedimentation is neglected.

Most species of green, motile microorganism have been found to respond to light (Nultsch and Häder 1988 [124]), which is not surprising since these organisms require light for energy production via photosynthesis. Genera such as *Chlamydomonas* and *Euglena* swim towards weak light (termed positive phototaxis) and away from strong light (negative phototaxis), so that there is some light intensity in between at which cells can obtain the optimal light intensity [35, 52, 83]. This is termed the critical light intensity. Phototaxis is different to gravitaxis and gyrotaxis because, rather than being a mechanical effect, it involves complex detection and response processes (for a review of *Chlamydomonas* phototaxis, see Witman 1993 [178]). How a cell photo-orientates during phototaxis is described in detail in Section 1.4. Apart from phototaxis, other photoresponses by microorganisms include photokinesis, where the speed of movement depends on light intensity (Casey *et al.* 2003 [17]), and photophobic responses, where sudden increases or decreases in light intensity cause transient motor responses that can also change the direction of travel (Nultsch and Häder 1988 [124] and Pazour *et al.* 1995 [127]). For example, a sudden increase of light causes *Chlamydomonas* cells to swim backwards transiently (Hegemann and Bruck 1989 [57]). This thesis is predominantly concerned with phototaxis, although in Chapter 2 a model in which phototaxis occurs in a photokinesis-like manner is considered.

Of course, if a cell exhibits multiple orientation taxes then these taxes can act in opposition to each other under certain conditions. For example, under strong illumination from above *C. nivalis* cells are both negatively gravitactic, causing the cells to swim upwards, and negatively phototactic, causing the cells to swim downwards to escape the light. Interestingly, Häder 1987 [52] found that negative phototaxis is sufficient to overcome negative gravitaxis under strong illumination from above, and the cells swim steadily downwards under these conditions.

The orientation of swimming *Chlamydomonas* cells is intrinsically random. This was demonstrated by Hill and Häder 1997 [61], who tracked *C. nivalis* cells and then plotted their swimming trajectories. For trajectories in the vertical plane, it is clear that the cells swim upwards on average, but that there is significant noise resulting in a spread of trajectories. This ‘noise’ was also investigated by Vladimirov *et al.* 2004 [173] using sophisticated laser velocimetry techniques to track hundreds of cells.

Although translational and rotational Brownian motion caused by collisions with water molecules are insignificant for *Chlamydomonas* cells when compared to other orientation influences, due to the relatively large cell size [35, 131], there are many other possible explanations for randomness in swimming direction. Firstly, if growth is not synchronized cells will be different ages and at different stages of their lifecycle, hence size, shape and behaviour will be intrinsically different between individuals. These effects are shown by the wide range of individual swimming speeds in the cell tracking experiments of Vladimirov *et al.* 2004 [173]. Secondly, cells may interact hydrodynamically with the side of the container and, in concentrated suspensions, with each other. In addition, cells exhibit rotational variations due to slight random changes in flagella beating from one beat to the next [35], which may be due to noise in biochemical reactions within the cell [172]. Fluctuations in light, for example due to waves on the surface of the suspensions, light scattering caused by any debris, or even scattering by the cells themselves, may transiently alter the light intensity at a given location, which can also introduce noise. The combination of all these factors introduces a stochastic element to the cell swimming direction. Correlated and biased random walks have been successfully used to describe the trajectories of such microorganisms (Lovely and Dahlquist 1975 [106] for *E. coli* and Hill and Häder [61] and Vladimirov *et al.* [173] for *C. nivalis*).

1.4 How do *Chlamydomonas* cells photo-orientate?

In order to perform phototaxis, *Chlamydomonas* cells must be able to respond directionally to light. There are three basic stages to any such photo-response: detection of light, processing of the stimulus via signal transduction pathways, and a mechanical re-orientation response. These three steps are repeated over and over again so that the cell can move towards a preferred location at which the light intensity is optimal (Foster and Smyth 1980 [35]).

In order to ‘decide’ which direction to move in, *Chlamydomonas* cells detect a signal in illumination using an eye-spot and a photoreceptor. The precise location of the eye-spot (and photoreceptor) is controversial, probably because it differs between species, as discussed by Ruffer and Nultsch 1985 [149]. For *C. reinhardtii* the eye-spot is located near the cell equator and is displaced out of the flagella plane by an angle of 45° (Gruber and Rosario 1974 [51], Ruffer and Nultsch 1985 [149]). The eye-spot location may be different in *C. nivalis*, as in Hill and Vincent 1993 [64] the eye-spot is modelled as located at 45° to the cell’s major axis (rather than 90°). However, explicit experimental evidence of this location is lacking. In both cases, the photoreceptor is located between the eye-spot and the cell surface and directly detects the illumination [35, 124]. The eye-spot organelle consists of stacked layers of pigmented granules within the chloroplast (Foster and Smyth 1980 [35]) and, although the eye-spot does not directly detect the light, it is crucial in phototactic orientation; cells without eye-spots are less able to photo-orientate, as shown by Morel-Laurens and Feinleib 1983 [120]. The eye-spot may work as an interference reflector (Foster and Smyth 1980 [35]). Since cells rotate as they swim, they receive a different light signal depending on the angle, or stage, of rotation [35]. The light signal is strongest when the eye-spot is normal to the light source and weakest when the light strikes the cell from directly behind the eye-spot, since it is shaded by the cell body. Thus rotation during swimming is exploited by the cell since it enables it to scan the environment and obtain a periodic signal of light intensity over one rotation, which is then processed within the cell and used for propulsion in the desired direction [25, 124].

How do cells re-orient with respect to the light once the signal has been received? In a series of papers, Ruffer and Nultsch explored aspects of flagella beating under illumination in both free swimming cells and cells held on micropipettes to try and explain what mechanisms a cell uses to photo-orientate [149–155]. They found that changes in flagella beat frequencies during illumination can not be responsible for phototactic reorientation,

as previously thought, because frequencies changed in both flagella concurrently (Rüffer and Nultsch 1990 [151]). However, changes in beat pattern between the flagella were found to coincide with cell steering either towards or away from the light (Rüffer and Nultsch 1991 [152]). Thus it was proposed that an asymmetric beat pattern during illumination, in which inverse (or opposite) amplitude shifts occur between the *cis*- and *trans*-flagellum, leads to cell reorientation and phototaxis. This is illustrated schematically in Figure 1.3. Convincing support for this argument was found by studying a *C. reinhardtii* mutant that does not exhibit phototaxis (Rüffer and Nultsch 1997 [154]). In this mutant, both flagella always responded to light in the same way and no phototactic steering was found. More complex examination of flagella behaviour have recently been performed, with aspects such as the velocity of the response, helical swimming and the relative phase of the flagella all thought to contribute in some as yet unclear way to phototaxis [76, 77].

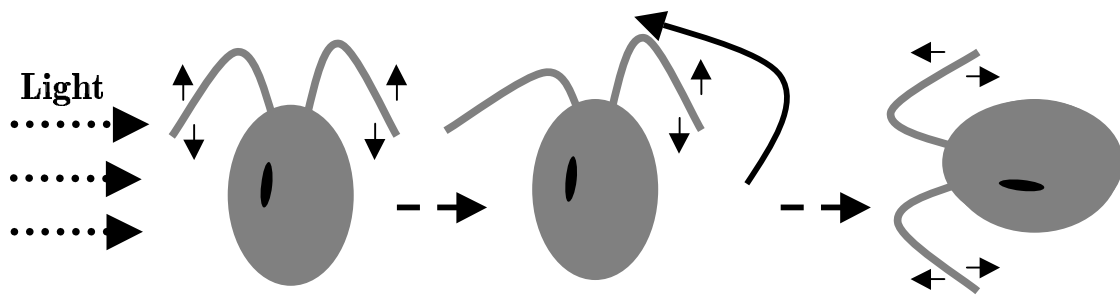


Figure 1.3: A simple sketch to show how a cell may vary the flagella beat pattern during positive phototaxis. The black region represents the eye-spot and photoreceptor. Solid arrows indicate flagella beating, dotted arrows indicate light and dashed arrows show the sequence of events. A signal of light intensity collected by the eye-spot is processed, which causes the flagella beat pattern to change in a non-symmetric way for each flagellum. This allows the cell body to rotate so that it is directed towards the light. The flagellar beat patterns are then re-synchronized again and the cell swims towards the light.

The method by which the change in flagella beat pattern is implemented is still not fully elucidated. Light striking the photoreceptor leads to signal transduction involving transmembrane Ca^{2+} fluxes that cause temporary changes in the beating of the two flagella (good reviews can be found in Sineshcekov 1991 [158] and Witman 1993 [178]). Kamiya and Witman 1984 [78] were among the first to suggest that the *cis*- and *trans*-flagellum are differently controlled by these calcium fluxes, leading to the asymmetric flagella beat

responsible for phototactic turning. In this chiefly mathematical thesis, we are more interested in behaviour resulting from changes in illumination, and not in the details of how these changes occur through biological transduction and, as such, the simple mechanism described in Ruffer and Nultsch 1991 [152] is sufficient to explain phototaxis on a basic mechanical level.

1.5 Bioconvection: a brief summary of observations and theory

Platt coined the term ‘bioconvection’ in 1961 to describe the phenomenon of pattern formation in shallow suspensions of motile microorganisms that are denser than the fluid in which they swim [132]. Patterns are formed by swimming cells with some orientational bias and generally consist of quasi-regular square or hexagonal arrays of falling sheets of cells, or semi-regular arrays of concentrated falling plumes that appear as dots when the fluid surface is viewed from above. Figure 1.4 shows a typical bioconvection pattern in a

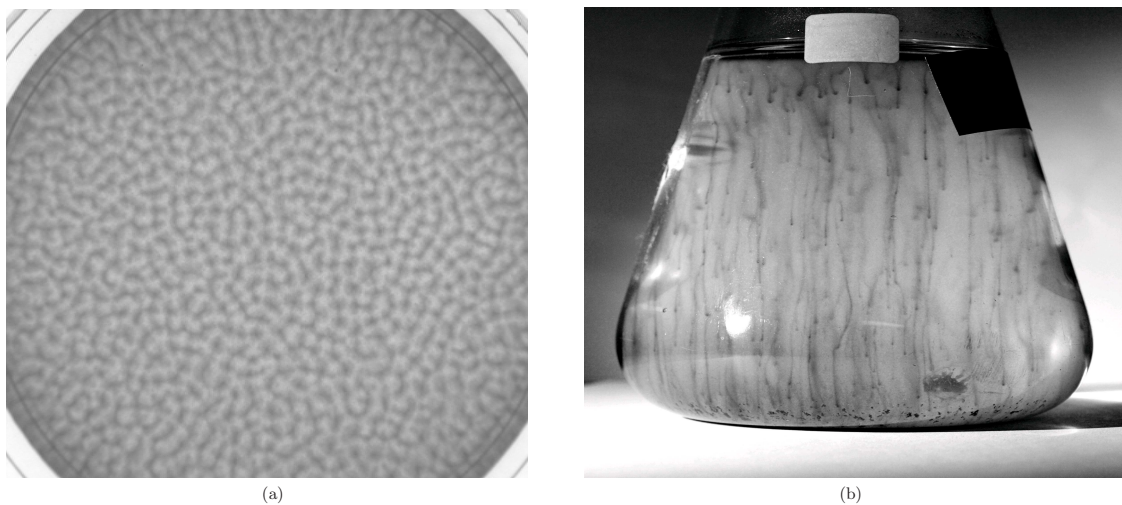


Figure 1.4: Examples of collective motions caused by cell swimming in cultures of *C. nivalis*. Panel (a) shows a sample bioconvection pattern in a Petri dish, taken from above. The depth is approximately 3 mm and the concentration 4×10^6 cells/mL. Dark regions indicate high cell concentration. Panel (b) shows many interesting vertical plumes formed in a relatively dilute suspension in a conical flask, where blip instabilities are present and plumes form both from the fluid surface and deep within the layer.

Petri dish viewed from above, and a flask in which many plumes can be seen when viewed from the side, both for the species *C. nivalis*.

Species found to exhibit bioconvection include *E. gracilis* and *viridis* [144,174], *Tetrahymena* [22, 105, 132, 133], *C. nivalis* [8, 81, 84, 174], *Heterosigma akashiwo* [6], and various species of bacteria [26, 70, 71, 86, 115, 116], to name but a few. For pattern formation by green algae, the following common features are usually found. Firstly, the cells are a different density to the fluid in which they swim. Secondly, cells need a mechanism to aggregate somewhere within the suspension. Finally, the patterns die away if cell swimming stops. The size and shape of the patterns formed in the dark by *Chlamydomonas* cells have been found to principally depend on the cell concentration and the depth of the suspension layer [8, 131].

Early studies of bioconvection were focused on observations of patterns formed by various species of microorganisms in laboratory conditions and the effects on pattern formation of illumination, depth and concentration, temperature and pH were explored [22, 105, 144, 174]. In a series of studies in the 1980s, Kessler explored aspects of gyrotactic focussing and plume formation in *C. nivalis*, such as the U-tube experiment described in Section 1.3 [81–84]. Blip instabilities were also investigated, where localized regions of high concentration form on downwelling plumes, thus falling faster than the plumes themselves. These can be seen on some of the plumes in Figure 1.4(b).

Self-shading, where cells close to the light source absorb and scatter light, so that those further away from the light receive less light than those closer, creates a non-uniform distribution of light intensity throughout a suspension layer. By only illuminating a suspension of *Chloromonas rosae* from one side and not the other, Kessler showed that illumination significantly affects pattern formation, since shading within the layer leads to interesting patterns (which are very different at the side closest to the light compared to the far side) as cells seek shelter behind each other [83]. Kessler [85] also suggested that illumination through a layer of microorganisms could be modelled by the Beer-Lambert law, which relates the absorption of light to the properties of the layer through which the light is travelling (see Section 2.2.2).

Bees and Hill 1997 [8] performed one of the first quantitative studies of aspects of bioconvective patterns in suspensions of *C. nivalis*. The wavelength of the initial pattern to form before any non-linear effects arose and the long term wavelength, measured approximately 5 minutes after mixing, were extracted using computational image analysis

techniques for a range of concentrations and depths. The initial pattern wavelength was found to be predominantly determined by suspension depth and not by cell concentration. Cziráková *et al.* 2000 [26] performed a similar study, this time using the bacteria *Bacillus subtilis*, and found the opposite results for the significance of depth and concentration. The techniques presented in [8] and [26] are used to investigate initial pattern wavelength as a function of concentration and light intensity in Chapter 4, and a detailed discussion of these quantitative studies can be found in Section 4.1. Other quantitative studies include Taylor *et al.* [164], who derive novel statistical measures for the regularity of patterns and use bioconvection as an example, and Yamamoto *et al.* 1992 [180], who find the critical depth and concentration needed for pattern formation in suspensions of *C. reinhardtii*.

1.5.1 Instability mechanisms in suspensions of *Chlamydomonas* cells

Both gravitaxis and gyrotaxis can result in instabilities that lead to pattern formation in a suspension of microorganisms that are denser than the fluid in which they swim. A schematic description for a gravitactic instability is as follows (depicted in Figure 1.5). Gravitaxis causes cells to swim upwards on average, so that in the presence of an upper boundary cells will accumulate at the upper surface and form a sublayer that is denser than the fluid below (*C. nivalis* cells are approximately 5% denser than the medium). This creates a Rayleigh-Taylor overturning type of instability, where the cells start to drip down due to the density difference, and the fluid around these cells pulls more cells into the drip as it descends (Figure 1.5). These drip-like structures happen all along the fluid sublayer, forming long vertical plumes as they descend (shown clearly in Figure 1.4(b)). Viewed from above, the plumes form bioconvection patterns (shown in Figure 1.4(a)).

Gyrotaxis can cause an instability to occur even in the absence of a fluid boundary, as depicted in Figure 1.6. Gyrotactic cells swim towards regions of locally downwelling fluid Kessler [81] (created by small perturbations, or by the gravitactic instability in Figure 1.5). The added mass of these cells amplifies the downwelling and makes the fluid sink faster, again creating plumes. This is an example of gyrotactic focusing.

Instabilities arising from gravitaxis and gyrotaxis can also occur when the suspension is illuminated from above, in which case phototaxis has an effect on the form of the instabilities leading to patterns formation [81, 83, 174]. If the light intensity at the source is greater than the critical light intensity then cells near the source will swim downwards and away from the light (negative phototaxis), while those further away are shaded by

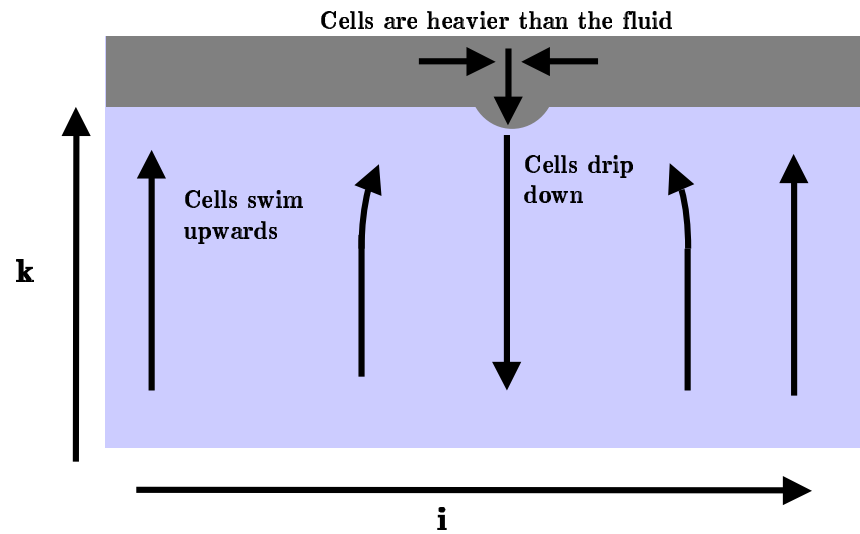


Figure 1.5: A schematic diagram of an overturning Rayleigh-Taylor instability. Upwardly swimming cells that are denser than the fluid collect in a concentrated sublayer at the boundary that has a mean density which is greater than that of the fluid below. This may be unstable.

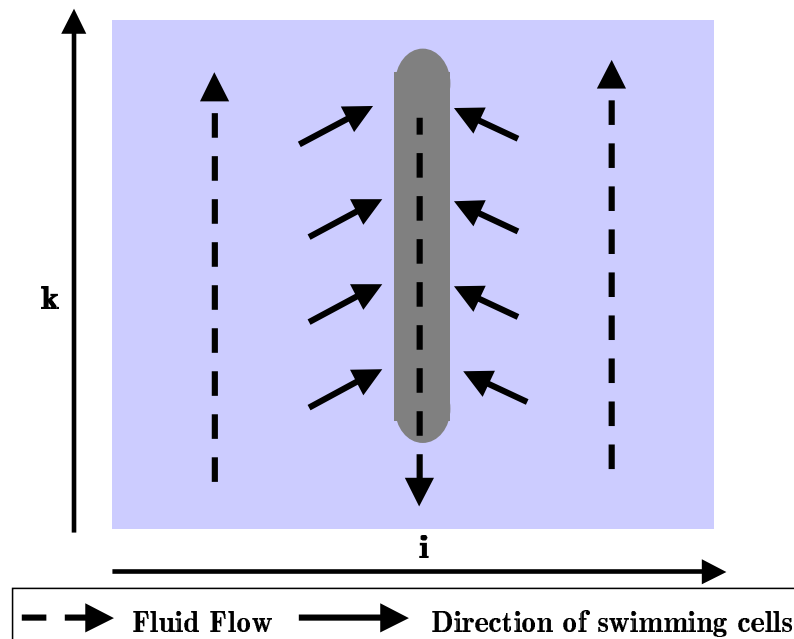


Figure 1.6: A schematic diagram of a gyrotactic instability in the absence of an upper boundary. Cells swim towards a region of downwelling fluid, the added mass amplifies the downwelling and the fluid sinks faster, forming a plume of concentrated cells (shown by the dark region in the centre of the diagram).

cells above and so swim upwards (positive phototaxis). This results in a concentrated, dense sublayer of cells located at some point within the fluid layer, not necessarily at the upper boundary, and only the region below the sublayer is gravitationally unstable. A Rayleigh-Taylor instability caused by the density difference between the cells and the fluid can still occur here, but the size of the unstable region is reduced if the sublayer forms below the upper boundary. This can result in penetrative bioconvection, where flows from the unstable region penetrate into the stable region and result in motions that utilize the whole fluid layer. This is similar to other types of penetrative convection problems, such as the thermal convection problem described by Veronis in 1963 [170] for a layer of water, the bottom of which is maintained at 0°C and the top at a temperature greater than 4°C . Since water reaches its maximum density at 4°C , a dense sublayer forms away from the upper boundary, resulting in a gravitationally stable layer overlying an unstable layer. A thorough review of mathematical aspects of penetrative convection can be found in Straughan 1993 [161].

Why microorganisms have evolved to form these intricate patterns is still not clear. Current theories include that of Tomson and Demets 1989 [166], who postulate that these self-concentrating mechanisms help cells, which are present in very small cell volume fractions in the wild, to meet and mate sexually. Also, the circulations caused by the instabilities stir the medium, resulting in nutrient mixing, and cause variations in light intensity (due to shading) for cells at different locations within the fluid. Kessler 1989 [85] postulates that it could be that the effects of this stirring “improves the cells’ chances of survival”.

Of course, in reality many species, such as *Chlamydomonas*, are gravitactic, gyrotactic and phototactic, and patterns are formed due to combinations of these different instability mechanisms. It is this bioconvection by photo-gyrotactic cells that Chapters 2, 3 and 4 of this thesis explore.

1.5.2 Early models of bioconvection

Microorganism bioconvection has many similarities with thermal convection (except that in bioconvection energy is provided by the cells themselves) and, as such, many of the techniques employed in thermal problems (such as those presented in Chandrasekar 1961 [19]) can be employed.

Plesset and Winet 1974 [133] were among the first to suggest modelling bioconvection as a Rayleigh-Taylor instability. They used a two-layer model of an unstable density dis-

tribution in which a small, uniform dense layer overlies a deeper uniform layer of lower density, assumed to be caused by cells swimming upwards. However, there was no diffusion between the layers and cell swimming was only modelled implicitly, not explicitly. The most unstable wavelength (the one that grows most rapidly from an equilibrium solution) was computed as a function of depth and concentration. Some good agreement was found between theoretical values and visually estimated dominant wavelengths from observations of pattern formation in finite depth suspensions of upwardly swimming *Tetrahymena pyriformis*.

Moving on from phenomenological models, the first self-consistent hydrodynamic theory for the onset of bioconvection, by Childress *et al.* 1975 [22] and Levandowsky *et al.* 1975 [99], incorporated purely upward swimming cells in a suspension layer between $z = 0$ and $z = -H$ for both stress-free and rigid upper boundaries. They assumed that the sides of the container are sufficiently far apart that the layer effectively has an infinite width. They replaced the discrete microorganism distribution by a continuous density distribution and modelled cells as denser than the fluid in which they swim. The fluid was assumed to incompressible and the suspension was modelled as dilute, so cell to cell interactions were neglected. The velocity of a cell relative to the media was assumed to consist of both a random motion and a steady upward drift [99]. It was assumed that the length scale of the bulk motions are large compared to typical cell spacing and cell size, so that the effects of non-Newtonian stresses and flow around individual cells are negligible. The Boussinesq approximation was used (as in Chandrasekar 1961 [19]), so that the only way in which the cells affect the fluid flow is through the density difference between the cells and the fluid. Thus the Navier-Stokes equation with an incompressibility condition is

$$\rho \frac{D\mathbf{u}}{Dt} = -\nabla p - g\rho(1 + \alpha_e c)\mathbf{k} + \mu\nabla^2\mathbf{u}, \quad (1.3)$$

$$\text{and} \quad \nabla \cdot \mathbf{u} = 0, \quad (1.4)$$

respectively, where $\mathbf{u}(\mathbf{x}, t)$ is fluid velocity, $p(\mathbf{x}, t)$ is pressure, ρ is the density of the fluid, μ is fluid viscosity, $-g\mathbf{k}$ is acceleration due to gravity and $\rho\alpha_e c$ is the extra density due to microorganisms of concentration $c(\mathbf{x}, t)$ at a point. D/Dt is the convective derivative. Since the total number of cells is conserved, they used a cell conservation equation of the form

$$\frac{Dc}{Dt} + \nabla \cdot \mathbf{J} = 0, \quad (1.5)$$

to describe the evolution of cell concentration, c , where \mathbf{J} is the flux of organisms through the fluid and has two components: flux due to random motions (diffusion) and flux due to negatively gravitactic drift. Hence,

$$\mathbf{J} = cU(c, z)\mathbf{k} - \mathbf{D} \cdot \nabla c, \quad (1.6)$$

where $U(c, z)$ is a function for cell swimming speed and \mathbf{D} is the orthotropic diffusion tensor, given in Childress *et al.* [22] by

$$\mathbf{D} = \kappa_1(c, z)(\mathbf{ii} + \mathbf{jj}) + \kappa(c, z)\mathbf{kk}, \quad (1.7)$$

where $\kappa_1(c, z)$ and $\kappa(c, z)$ are functions of c and z . For the majority of Childress *et al.* [22], $\kappa_1(c, z)$ and $\kappa(c, z)$ were taken as constant horizontal and vertical diffusivities D_h and D_v , respectively. Note equations 1.3 and 1.6 are very similar to those of Chandrasekar [19] for the thermal convection problem. In Childress *et al.*, an equilibrium solution for the case of no flow was calculated, and linear analysis of this model predicted the critical wavenumber (the smallest wavenumber on the neutral curve, on which the growth rate is zero) was zero, corresponding to an infinite wavelength. Good agreement between model predictions and experimental results using *Tetrahymena* cells for the critical depth and concentration required for pattern formation were found in Childress *et al.* [22] and Levandowsky *et al.* [99].

The next major development in bioconvection modelling was to include gyrotaxis in the upswimming only models. Before this could be done, a rational way of modelling gyrotaxis was required. The framework for this was presented by Pedley and Kessler 1987 [129], who considered the orientation of spheroidal microorganisms in a flow field. Following their analysis, the total torque, \mathbf{L}_T , is given by

$$\mathbf{L}_T = \mathbf{L}_g + \mathbf{L}_v, \quad (1.8)$$

where \mathbf{L}_v is the viscous torque and \mathbf{L}_g is the gravitational torque due to bottom heaviness. Using summation convention with repeated indices, the torques for negatively gravitactic and gyrotactic bottom heavy *Chlamydomonas* cells are given by

$$L_{gi} = hmg\epsilon_{ijl}p_jk_l, \quad (1.9)$$

$$L_{vi} = -\mu v \left[P_{ij}(v_j - u_j) + Y_{ij} \left(\omega_j^c - \frac{1}{2}\Omega_j \right) + R_{ijl}E_{jl} \right], \quad (1.10)$$

where h is the centre of mass offset between the cell's centre of mass and its geometrical centre along the swimming direction \mathbf{p} , m is the mass of the cell, g is the magnitude of

the acceleration due to gravity, \mathbf{k} is the unit vector in the vertical direction and ϵ_{ijl} is the Levi-Civita tensor. The expression for L_v comes from Rallison 1978 [143] for the viscous torque on a solitary body with zero Reynolds number, where v is the cell volume, μ is the fluid viscosity, \mathbf{v} is the cell velocity, $\boldsymbol{\omega}^c$ the angular velocity of the cell, $\boldsymbol{\Omega}$ the vorticity and \mathbf{E} the rate-of-strain tensor. Tensors \mathbf{P} , \mathbf{Y} and \mathbf{R} depend only on the orientation and surface geometry of the cell. For a rigid prolate spheroid (Batchelor 1970 [5]),

$$P_{ij} = 0, \quad (1.11)$$

$$Y_{ij} = \alpha_{\parallel} p_i p_j + \alpha_{\perp} (q_i q_j + r_i r_j), \quad (1.12)$$

$$R_{ijk} = -\alpha_0 Y_{il} (r_l p_j q_k - q_l p_k r_j), \quad (1.13)$$

for the orthonormal right-handed set of coordinates $\mathbf{p}, \mathbf{q}, \mathbf{r}$, where α_{\parallel} is the dimensionless resistance coefficient for rotation about \mathbf{p} , α_{\perp} is the dimensionless resistance coefficient for rotation about an axis perpendicular to \mathbf{p} , and the eccentricity for a cell with length a and breadth b given by

$$\alpha_0 = \frac{a^2 - b^2}{a^2 + b^2}. \quad (1.14)$$

Since the rate-of-strain tensor is symmetric, the viscous torque in equation 1.10 can be written as

$$L_{vi} = -\mu v \left[Y_{ij} \left(\omega_j^c - \frac{1}{2} \Omega_j \right) - \alpha_0 Y_{il} \epsilon_{klm} p_m p_j E_{jk} \right]. \quad (1.15)$$

Substituting equations 1.15 and 1.9 into equation 1.8 and setting $\mathbf{L}_{\mathbf{T}} = \mathbf{0}$ gives

$$hmg \epsilon_{ijl} p_j k_l - \mu v \left[(\alpha_{\parallel} p_i p_j + \alpha_{\perp} (q_i q_j + r_i r_j)) \left(\omega_j^c - \frac{1}{2} \Omega_j - \alpha_0 \epsilon_{kjm} p_m p_l E_{lk} \right) \right] = 0. \quad (1.16)$$

On multiplying the expression by $\epsilon_{ist} p_s$ and using the identity $\epsilon_{ijk} \epsilon_{stk} = \delta_{is} \delta_{jt} - \delta_{it} \delta_{js}$, where δ_{ij} is the Kronecker delta, equation 1.16 can be written as

$$\dot{\mathbf{p}} = \frac{1}{2B} [\mathbf{k} - (\mathbf{k} \cdot \mathbf{p}) \mathbf{p}] + \frac{1}{2} \boldsymbol{\Omega} \wedge \mathbf{p} + \alpha_0 [\mathbf{E} \cdot \mathbf{p} - \mathbf{p} \mathbf{p} \cdot \mathbf{E} \cdot \mathbf{p}], \quad (1.17)$$

since $\dot{\mathbf{p}} = \boldsymbol{\omega}^c \wedge \mathbf{p}$, and

$$B = \frac{\mu \alpha_{\perp}}{2h\rho g} \quad (1.18)$$

is the gyrotaxis number with units of seconds, as in Pedley and Kessler 1987 [129]. Equation 1.17 is essentially a combination of expressions from Leal and Hinch 1972 [96] and Hinch and Leal 1972 [66].

The first models for gyrotactic bioconvection were explored by Pedley *et al.* 1988 [128] for an infinite suspension and by Hill *et al.* 1989 [63] for a suspension of finite depth. Both models were based on the upswimming only models [22, 99], but the cell swimming direction, \mathbf{p} , was calculated as a function of vorticity and the rate-of-strain tensor using the gyrotactic theory of Pedley and Kessler 1987 [129] (using similar analysis to that shown above). Thus the Navier-Stokes equation with an incompressibility condition takes the same form as in the upswimming model (equations 1.3 and 1.4), and the cell conservation equation takes the form of equation 1.5, where the cell flux \mathbf{J} is now defined as

$$\mathbf{J} = nV_s\mathbf{p} - \mathbf{D} \cdot \nabla n, \quad (1.19)$$

where cell concentration is now written as $n(\mathbf{x}, t)$ and V_s is the constant swimming speed. Random motions were modelled by cell diffusion with a constant isotropic tensor \mathbf{D} , such that $D_{11} = D_{22} = D_{33} = D_h = D_v$ (denoted simply D in [63]) in equation 1.7.

Both Pedley *et al.* [128] and Hill *et al.* [63] found a finite, non-zero critical wavenumber for gyrotactic cells, compared to a zero critical wavenumber for the upswimming only models [22, 99]. Hill *et al.* [63] also found the existence of oscillatory modes of instability. These were attributed to the interaction of gyrotaxis and shear at the rigid upper boundary causing the cells' horizontal components of velocity to be in the opposite direction to that of the convective flow.

1.5.3 A new continuum model for stochastic gyrotactic bioconvection, Pedley and Kessler 1990 [130]

In what is often referred to as a 'new' continuum model, Pedley and Kessler 1990 [130] proposed that using a strongly random isotropic diffusion tensor that is independent of gyrotaxis is inconsistent with modelling swimming velocity as deterministic and not random. In other words, if the swimming direction of the cells is deterministic then it is inconsistent to assume that the direction of diffusion of the cells is stochastic and not affected by swimming velocity. Thus Pedley and Kessler [130] modelled the cell swimming direction in a probabilistic fashion, using techniques similar to those of colloidal particles subject to Brownian motion (for example, Hinch and Leal 1972 [66, 96]). They considered a cell swimming direction probability density function, $f(\mathbf{p})$, defined on a unit sphere, where \mathbf{p}

is the cell swimming direction unit vector, given by

$$\mathbf{p} = \begin{pmatrix} \sin \theta \cos \phi \\ \sin \theta \sin \phi \\ \cos \theta \end{pmatrix}, \quad (1.20)$$

and θ, ϕ are spherical polar angles. θ is the colatitude measured relative to \mathbf{k} and ϕ is the cell orientation angle in the horizontal plane. $f(\mathbf{p}(\theta, \phi))$ satisfies the Fokker-Planck equation

$$\frac{\partial f}{\partial t} + \nabla \cdot (\dot{\mathbf{p}}f) = D_r \nabla^2 f, \quad (1.21)$$

where D_r is rotational diffusivity, which models randomness in cell orientation due to the intrinsically imperfect cell motion (see Section 1.3). The first term in equation 1.21 can be disregarded if it is assumed that D_r^{-1} is much less than the timescale for variation of the flow. This is also used in Bees and Hill 1998 [9]. The rate of change of \mathbf{p} , $\dot{\mathbf{p}}$, calculated from the torque balance equation in 1.17, can be substituted in to equation 1.21, which can then be solved to calculate $f(\mathbf{p})$. In Pedley and Kessler 1990 [130], the mean cell swimming speed and diffusivity tensor are defined using

$$\langle \mathbf{p} \rangle = \int_S \mathbf{p} f(\mathbf{p}) dS, \quad (1.22)$$

$$\mathbf{D}(t) = \int_0^\infty \langle \mathbf{V}_r(t) \mathbf{V}_r(t-t') \rangle dt', \quad (1.23)$$

where S is the surface of the unit sphere and \mathbf{V}_r is the velocity of a cell relative to its mean value. Equation 1.23 is difficult to calculate since it requires a knowledge of all previous cell velocities. For simplicity, Pedley and Kessler [130] assumed the average cell swimming speed, defined as V_s , to be constant, and removed the integral over time by assuming that it takes a cell τ seconds to settled to a preferred direction. Thus equation 1.23 can be evaluated to give

$$\mathbf{D} \approx V_s^2 \tau \langle (\mathbf{p} - \langle \mathbf{p} \rangle) (\mathbf{p} - \langle \mathbf{p} \rangle) \rangle, \quad (1.24)$$

where τ is termed the direction correlation time.

The main model equations for the stochastic gyrotaxis model proposed by Pedley and Kessler [130] for an infinite layer are, again, based on the continuum upswimming model of Childress *et al.* [22, 99]. The main modelling assumptions are the same in Pedley and Kessler [130] as in Childress *et al.* [22], discussed in Section 1.5.2, except where explicitly

stated otherwise. Thus the model consists of the Navier-Stokes equations with an extra term due to the negative buoyancy of the cells. Hence,

$$\nabla \cdot \mathbf{u} = 0, \quad (1.25)$$

$$\rho \left(\frac{\partial \mathbf{u}}{\partial t} + (\mathbf{u} \cdot \nabla) \mathbf{u} \right) = -\nabla p_e + nv\Delta\rho\mathbf{g} + \nabla \cdot \boldsymbol{\Sigma}, \quad (1.26)$$

where $\mathbf{u}(\mathbf{x}, t)$ is fluid velocity, $\boldsymbol{\Sigma}(\mathbf{x}, t)$ the fluid stress tensor, $p_e(\mathbf{x}, t)$ is the pressure excess above hydrostatic (at density ρ), $n(\mathbf{x}, t)$ is local cell concentration, v is the volume of an alga cell, ρ is the density of the fluid and $\Delta\rho$ the density difference between the cell and the fluid. As in Childress *et al.* [22] and Pedley *et al.* [128], cell concentration is modelled using a conservation equation of the form

$$\frac{\partial n}{\partial t} = -\nabla \cdot [n\mathbf{u} + nV_s\langle\mathbf{p}\rangle - \mathbf{D} \cdot \nabla n]. \quad (1.27)$$

The first term on the right hand side is due to advection of the cells by the fluid, the second is due to the swimming of the cells, and $\langle\mathbf{p}(\mathbf{x}, t)\rangle$ the mean cell swimming direction calculated from equation 1.22, and the third term is due to diffusion, where $\mathbf{D}(\mathbf{x}, t)$ is the cell swimming diffusion tensor calculated from equation 1.24.

Unlike Childress *et al.* 1975 [22] and Pedley *et al.* [128] 1988, who ignored all effects that cells may have on the bulk fluid motion (apart from their negative buoyancy) by assuming that $\boldsymbol{\Sigma} = 2\mu\mathbf{E}$, Pedley and Kessler [130] considered a variety of ways in which the cells can affect the fluid. They wrote the fluid stress tensor as

$$\boldsymbol{\Sigma} = 2\mu\mathbf{E} + \boldsymbol{\Sigma}^{(p)} + \boldsymbol{\Sigma}^{(d)} + \boldsymbol{\Sigma}^{(s)}, \quad (1.28)$$

where $\boldsymbol{\Sigma}^{(p)}$ are Batchelor stresses that arise because rigid cells do not allow the fluid to deform in the same way as it would in the absence of cells [5], $\boldsymbol{\Sigma}^{(d)}$ are stresses associated with the effective particle rotation caused by rotational diffusion, and $\boldsymbol{\Sigma}^{(s)}$ are stresslets associated with the swimming motions of individual cells. Aside from the basic Newtonian stress, they found that only $\boldsymbol{\Sigma}^{(s)}$ makes a significant contribution to $\boldsymbol{\Sigma}$, but even this contribution is small compared to the Newtonian stress.

The expressions for $\langle\mathbf{p}\rangle$ and \mathbf{D} in equations 1.22 and 1.24, along with the expression for fluid stress in equation 1.28, can then be substituted into equations 1.25, 1.26 and 1.27 to complete the continuum model of Pedley and Kessler 1990 [130].

Using this model to assess linear stability, Pedley and Kessler 1990 [130] found similar results to Pedley *et al.* 1988 [128] for the old gyrotaxis continuum model analysed in an

infinite layer. Bees and Hill 1998 [9] used the ‘new’ model of Pedley and Kessler [130] to find an equilibrium solution and conduct a linear stability analysis for a layer of finite depth with a rigid boundary. They found, as for the ‘old’ gyrotaxis models in Pedley *et al.* 1988 [128] and Hill *et al.* 1989 [63], that the introduction of gyrotaxis creates a non-zero critical wavenumber associated with a finite wavelength and, furthermore, found that increasing gyrotaxis destabilizes the system for sufficiently large wavenumbers. They predicted wavelengths ≈ 1 mm at the onset of bioconvection (compared to experimentally measured estimates of 4-7 mm Bees and Hill 1997 [8]).

Bees *et al.* 1998 [11] obtained analytic solutions of the Fokker-Planck equation for the orientation of dipolar particles in a steady, shear flow with a uniform external field by expanding the Fokker-Planck in terms of spherical harmonics. Computer algebra was used to solve a truncated set of equations. In Bees and Hill 1999 [10], a weakly non-linear analysis of the model of Pedley and Kessler [130] was performed for a infinitely deep layer, from which it was found that the bifurcation to the gyrotactic instability is supercritical, unlike the gravitactic instability which is subcritical (Childress and Spiegel 1978 [23]). This gives some justification to using linear stability theory to predict initial bioconvection pattern wavelengths in suspensions of gyrotactic cells.

1.5.4 Modelling phototactic bioconvection

The first model for phototactic bioconvection was presented by Vincent and Hill 1996 [172] for a suspension of microorganisms in a shallow layer of infinite horizontal extent illuminated from above. Both upswimming (negative gravitaxis) and gyrotaxis were neglected. They followed the generic model of Childress *et al.* [22], using a Navier-Stokes equation and a cell conservation equation. The model equations are essentially the same as equations 1.25, 1.26 and 1.27 for the Pedley and Kessler model [130], with the following exceptions. Unlike previous models, Vincent and Hill [172] modelled cell swimming velocity, $V_s \langle \mathbf{p} \rangle$ in equation 1.27, as dependent only on light reaching the photoreceptor, so that

$$V_s \langle \mathbf{p} \rangle = V_s T(I) \mathbf{k}, \quad (1.29)$$

where the taxis function $T(I)$ depends on the light intensity $I(\mathbf{x}, t)$ and is written

$$T(I) \begin{cases} \geq 0 & \text{if } I(\mathbf{x}, t) \leq I_c \\ < 0 & \text{if } I(\mathbf{x}, t) > I_c \end{cases}, \quad (1.30)$$

where I_c is the critical, or optimal, light intensity, above which cells swim away from the light. Diffusion was modelled as a constant orthotropic tensor as in equation 1.7, where $D_{11} = D_{22} = D_h$ and $D_{33} = D_v$, and the Fokker-Planck equation from Pedley and Kessler [130] was not used in this case. They assumed that the only effect the cells have on the suspension is due to their negative buoyancy, and other contributions to the bulk stress are neglected, so that $\Sigma = 2\mu\mathbf{E}$ in equation 1.26 (as in Childress *et al.* 1975 [22] and Pedley *et al.* [128] 1988).

Vincent and Hill [172] modelled light intensity using a self-shading model with light from above. They used the Beer-Lambert law for weak scattering, as suggested by Kessler [85], where light intensity at position \mathbf{x} is given by

$$I(\mathbf{x}) = I_s e^{-\alpha \int_0^{\mathbf{r}} n(\mathbf{r}') d\mathbf{r}'}, \quad (1.31)$$

where I_s is light intensity at the source, α is the cellular extinction coefficient and \mathbf{r} is the vector from the cell to the light source. Vincent and Hill [172] found that if $I = I_c$ at depth $z = -C$, say, then cells above $z = -C$ swim down and cells below swim up, so that the concentrated sublayer occurs somewhere within the fluid layer, creating a stable region overlying an unstable region. Using a linear stability analysis, they found that this leads to penetrative bioconvection, where fluid motions utilize the entire fluid layer. The critical wavenumber was found to be non-zero in some regions of parameter space and oscillatory modes of instability were also found.

Ghorai and Hill 2005 [46] used the phototaxis model proposed by Vincent and Hill [172] in a two-dimensional layer confined between a rigid bottom and a stress-free top. They numerically investigated convection cycles over a range of parameter values, having set the Rayleigh number to be constant. Transitions from steady state to periodic oscillations, and back, were found and the mechanism for oscillations was discussed. As yet, no consistent model to combine phototaxis with gravitaxis and gyrotaxis has been published. (Vincent 1995 [171] presents a combined photo-gyrotactic model, but cell swimming direction is modelled deterministically and the effects of phototaxis and gyrotaxis on cell orientation are assumed additive. Also, errors in the work have subsequently been found.) This is addressed in Chapters 2 and 3 of this thesis.

1.5.5 Current challenges in bioconvection research

Many recent notable developments that could further improve the feasibility of bioconvection models have been made. Bees and Hill 2002 [60] calculated the first rational expression for the diffusion coefficients of *C. nivalis*, by using generalized Taylor dispersion theory and considering cells in a vertical shear flow. They found that as vorticity tends to infinity, the effective diffusivity in the shear plane tends to zero due to the rapid tumbling of the cells, in contradiction to previous expressions for \mathbf{D} in Bees *et al.* [11] and Pedley and Kessler [130]. This rational theory could be used to model diffusion in bioconvection problems. Manela and Frankel 2003 [108] extended aspects of this theory to axisymmetric microorganisms (including local rate-of-strain as well as vorticity).

In a series of numerical papers, Ghorai and Hill study gyrotactic bioconvection using a vorticity-streamfunction formulation of the basic model of Pedley *et al.* 1988 [128] in 2D and 3D [42–45, 47]. In 2000, Ghorai and Hill [44] found the first computational examples of the bottom-standing plumes that are often observed in bioconvection and suggested that they are always transient, which may explain why analytic solutions for such structures have not been found. Other current challenges in theoretical studies of bioconvection include studying thermo-bioconvection and bioconvection in a porous media [2, 94, 95], analyzing cell swimming near boundaries [168] and pattern formation in different geometries [1, 123, 163].

1.6 The use of microorganisms in the energy industry

It has been known for many decades that various species of microorganism have the ability to produce hydrogen gas (for example, Gaffron 1942 [37]). Research in this area has accelerated in recent years due to the possibility of using microorganisms to produce hydrogen for the renewable energy industry. There are two main pathways to hydrogen production in microorganisms: photobiological processes in the light and fermentative processes in the dark.

Photobiological hydrogen production describes a wide range of biological processes that all require three things: light as the energy source, a substrate to donate electrons to the hydrogen production complex, and a catalyst to combine protons and electrons to produce H_2 [40]. In green algae and some cyanobacteria, light energy is used to split water and release electrons and protons during oxygenic photosynthesis. This process

is coupled via the photosynthetic chain to either a nitrogenase or hydrogenase enzyme that can combine protons and electrons to produce hydrogen gas if specific conditions are met (a thorough review of these processes can be found in Ghirardi *et al.* 2009 [40] and Hallenbeck and Benemann 2002 [54]). A major difficulty with oxygenic photosynthetic production of hydrogen gas is that all green algal nitrogenase and hydrogenase enzymes need the photosynthetic chain in operation to pass electrons to the enzyme, but these nitrogenase and hydrogenase enzymes are highly sensitive to oxygen co-produced from the photosynthetic pathway and will only function under anaerobic conditions (Fay and Cox 1967 [31] and Ghirardi *et al.* 1997 [39]). For many years, this dichotomy prevented substantial hydrogen production via this method. Another process for photobiological hydrogen generation is non-oxygenic photosynthesis coupled to nitrogenase-catalyzed H₂ production, found in purple photosynthetic bacteria (for example, Lee *et al.* 2002 [97]). In this case, photosynthesis uses organic acids instead of water as electron donors for hydrogen production via the nitrogenase (shown by Hillmer and Gest 1977 [65] and Lee 2002 *et al.* [97]). This has the advantage that oxygen is not produced and so the sensitivity of the nitrogenase to oxygen production is not an issue [40].

Many anaerobic microorganisms, such as the genus *Bacillus*, can produce hydrogen through dark fermentation, where anaerobic bacteria grow on carbohydrate-rich substrates and produce H₂ and CO₂ as fermentation end products (a good review can be found in Hawkes *et al.* 2002 [56]). This process holds many advantages over photobiological processes, as it requires a simple bio-reactor design for which illumination is not necessary, the required microbes are readily available in sewage, soils and other waste products, and the substrates required for fermentation can come from waste water (Ghirardi *et al.* 2009 [40]). Additionally, rates of hydrogen production have found to be higher than those during photobiological production (Datar *et al.* 2007 [27]).

Despite many recent advancements in genetics and technology, neither photobiological or fermentative processes alone are able to produce sufficiently high yields of hydrogen gas from microorganisms for cost-effective industrial scale-up (Ghirardi *et al.* 2009 [40], Prince and Kheshgi 2005 [141]). This is due to a relatively low production rate of H₂ compared to the theoretical maximum [111], inefficient use of light energy [135], high cost of substrates and bio-reactors [141], and the fact that issues such as the sensitivity of the hydrogenase to oxygen have not been overcome [33]. Integrated systems, in which two or more of the biological processes described above are used together in bio-reactors for H₂ production,

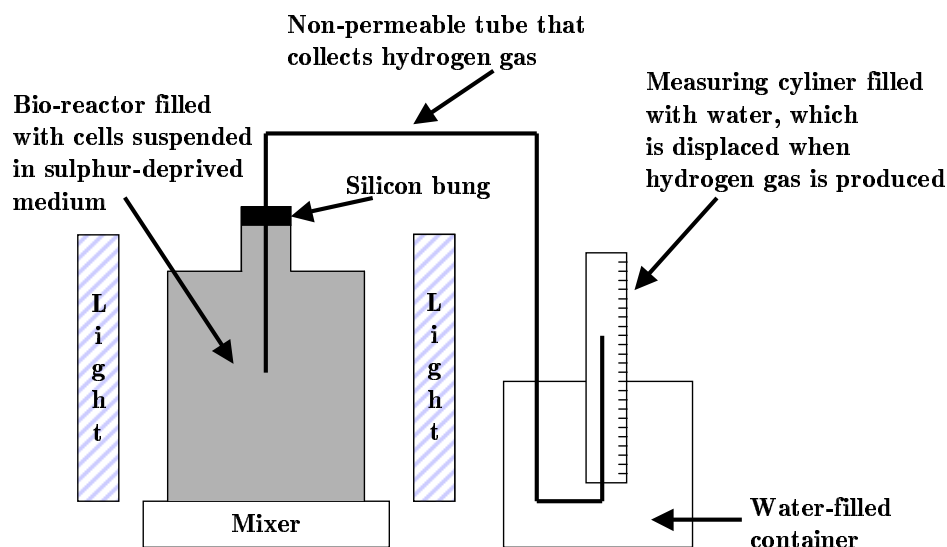


Figure 1.7: A simple experimental set-up to produce and collect hydrogen gas. A sulphur-deprived culture of *C. reinhardtii* is incubated in a sealed container under illumination and is placed on a mixing device. Hydrogen gas is collected using a non-permeable tube that leaves the bio-reactor and enters a measuring cylinder filled with water. When hydrogen is produced water is displaced from the cylinder and gas production is quantified.

are currently in the processes of development and testing (see Ghirardi *et al.* 2009 for a review [40]).

In this thesis, we are concerned with photobiological hydrogen production from the green algae species *Chlamydomonas reinhardtii* via the coupled oxygenic photosynthesis and the oxygen-sensitive iron-hydrogenase pathway, first discovered by Gaffron and Rubin 1942 [37]. In 2000 Melis and co-workers [114] found that sulphur depriving a culture of cells reversibly inactivates only the oxygen-producing component of the photosynthetic chain (photosystem II), so that the remaining photosynthetic activity continues (for a full description of the biochemical pathways and biological processes, see Section 5.1.1). This bypasses the sensitivity of the hydrogenase to oxygen and temporally separates oxygen and hydrogen production. Thus hydrogen can be produced and collected under sulphur deprivation in an illuminated and sealed container, depicted in Figure 1.7. However, substantial endogenous substrate is catabolized during hydrogen production, and H_2 production stops when these substrates run out (Melis 2002 [111]). In this way the H_2 production process is not continuous due to the need to cycle cultures between anaerobic, sulphur-deprived conditions to allow hydrogen production and aerobic, sulphur-replete conditions to allow cellular repair and growth. Under current cycling conditions, yields of H_2 produced

using this process are too low to be industrially successful [40, 111], allowing scope for technological and theoretical optimization. We investigate these issues in Chapters 5 and 6.

1.7 Links between bioconvection and hydrogen production

Although not immediately obvious, there are two main ways in which hydrogen production and bioconvection can interact in a suspension of cells. Firstly, starch (deposits of which determine the centre of mass offset) is one of the endogenous substrates that is catabolized during hydrogen production [139, 156, 182]. This causes the cells to change from ellipsoids to small spheroids (Zhang *et al.* 2002 [182]) which, together with changes in mass distribution as starch stores are mobilized, will clearly affect the centre of mass of the individual cells. This in turn affects the gravitactic and gyrotactic swimming behaviour of the cells and will have a profound effect on bioconvection and pattern formation. Secondly, plume formation during bioconvection creates an uneven distribution of cells throughout the bio-reactor, which creates a non-uniform distribution of light and could potentially improve the yield of hydrogen gas. This has not yet been considered as a feature of photobiological hydrogen production using motile cells. Thus the processes of bioconvection and hydrogen production, the two main areas of research in this thesis, are inherently linked.

1.8 An overview of this thesis

In this thesis, experimental and theoretical aspects of bioconvection in suspensions of the photo-gyrotactic microorganism *Chlamydomonas nivalis* are explored, and a novel model is built from scratch and used to investigate hydrogen production via the sulphur-deprived pathway found for *Chlamydomonas reinhardtii* by Melis *et al.* 2000 [114].

Chapter 2 describes three novel models that extend the continuum model of Pedley and Kessler 1990 [130] for gyrotactic cells to include phototaxis. Light is modelled using the Beer-Lambert law for weak scattering. The first of these models (Model A), in which phototaxis is modelled photokinetically on top of gyrotaxis, is formulated and a linear analysis is performed, both analytically and numerically, to assess stability in a container of finite depth. Phototaxis is found to significantly affect both the equilibrium solution and the critical wavenumber of the instability, and oscillatory solutions are found in certain regions of parameter space.

Chapter 3 details the two remaining photo-gyrotaxis models: in Model B the gyrotactic centre-of-mass offset is modelled as function of light intensity, and Model C describes the effects of including a new phototaxis torque dependent on gradients of light intensity in the gyrotactic torque balance equation (equation 1.8). For both models the solution to the Fokker-Planck is different to the gyrotaxis only case in Pedley and Kessler 1990 [130], since new terms dependent on light are introduced. Similar techniques to those laid out in Chapter 2 are used to analyse the models. Trends in stability as the phototaxis and gyrotaxis parameters are varied in Model B are qualitatively similar to those for Model A in the majority of cases. However, Model C produces drastically different stability predictions; instabilities are found even in the absence of fluid flow due to horizontal components of velocity arising from shading induced gradients of light intensity in the phototaxis torque.

Chapter 4 is an experimental study of *C. nivalis* swimming behaviour. First, experiments and techniques are described to capture images of bioconvection and to extract the initial wavelength of patterns. Experiments were repeated, both for the same cells and for different cells, allowing some simple statistical measures to be employed. Trends in initial wavelength as a function of either concentration or light intensity are then investigated. Results for variations in concentration of cells illuminated from above and below are consistent with results presented in Bees and Hill 1997 [8]. Variations in red light intensity, with a wavelength of 660 nm, are found to have no significant effect on the initial pattern wavelength. This is because cells exhibit a considerably reduced response to light intensity with wavelengths greater than 550 nm (Nultsch *et al.* 1971 [125]). However, intriguing significant trends are found as the intensity of the white light increases. These trends are qualitatively different when the suspension is illuminated from above compared to from below. Experimental results are then compared with model predictions and good agreement is found between the two methods.

Chapter 5 describes the biology and bio-chemistry involved in hydrogen production by sulphur deprived *C. reinhardtii* cells in detail, and a new mechanistic model to describe this system is constructed. Parameters are estimated and results for a non-dimensional model are computed. Encouragingly, the model is found to be consistent with published experimental results under a range of initial conditions. Hypotheses postulated by biologists in experimental studies are tested for consistency using the model.

Chapter 6 investigates ways to increase the yield of hydrogen gas using the hydrogen

production model of Chapter 5, initially by conducting a parameter sensitivity analysis. The yield of hydrogen gas produced after a specified time is optimized using a range of functions to input external sulphur. One such novel sulphur-input function, where sulphur is added at a low rate during hydrogen production and then in a one-off block addition to facilitate repair, is found to significantly increase the yield compared to using the current state-of-the-art, two-stage cycling of Ghirardi *et al.* 2000 [41].

Chapter 2

Modelling photo-gyrotactic bioconvection in suspensions of green algae - Part I

Summary

In this chapter, three models designed to incorporate phototaxis into the stochastic gyrotaxis model of Pedley and Kessler 1990 [130] in a novel and rational manner are described. Light is modelled using the Beer-Lambert law for light transmission through a self-shading suspension. The simplest model, which incorporates phototaxis in a photokinesis manner, is explored here. Analytical and numerical equilibrium solutions are presented and perturbation theory is applied in order to perform a linear stability analysis. Stability is analysed numerically and the code is verified using an asymptotic analysis in a deep layer for weak illumination. Good agreement between these methods is found and interesting results are presented for the development of instabilities as the key model parameters for phototaxis and gyrotaxis are varied.

2.1 Introduction

In recent decades, many theoretical studies to describe bioconvective pattern formation in suspensions of motile microorganisms have been presented. Previous rational theoretical models have either been for cultures with no illumination, in which case the cells will only be exhibiting negative gravitaxis and gyrotaxis, such as Hill *et al.* 1989 [63], Pedley and

Kessler 1990 [130] and later Bees and Hill 1998 [9], or for illuminated suspensions where phototaxis is exhibited but the effects of gravitaxis and gyrotaxis are neglected, such as in Vincent and Hill 1996 [172] and Ghorai and Hill 2005 [46]. No rational combined model for all three taxes has yet been published due to the difficulty of incorporating this complex balance of taxes, and a lack of information on precisely how these taxes interact under different conditions (Vincent 1995 [171] presents a combined photo-gyrotactic model, but errors have subsequently been found). If all three taxes were exhibited then we envisage that in certain situations the taxes would compete. For example, under bright light illumination from above, cells will swim downwards due to negative phototaxis but will also be inclined to swim upwards due to negative gravitaxis. This balance between the three taxes, along with the effects of self-shading within the suspension (where cells closer to the light source absorb and scatter light so that those further away get less), will affect the equilibrium solution and the stability of the system. Here, we formulate three rational models for bioconvection in a suspension of phototactic, gyrotactic and gravitactic green algae that is illuminated from above. The proposed models are applicable to many species and demonstrate general principals of modelling photo-gyrotactic behaviour.

We base the three photo-gyrotactic models on the continuum model of Pedley and Kessler 1990 [130], in which gravitaxis and gyrotaxis are modelled using a torque balance equation and the cell swimming direction is modelled probabilistically using a Fokker-Planck equation (detailed in Chapter 1). To model light we make use of the self-shading model presented in Vincent and Hill [172], where cells nearer the light source absorb and scatter the light.

We propose three different ways of incorporating phototaxis into the gyrotaxis model of Pedley and Kessler 1990 [130]. The first is to model cell swimming speed as a function of light intensity, so that cells regulate the amount of light they receive photo-kinetically. The second is to model the centre of mass offset, which controls gyrotaxis, as a function of light intensity, where we stipulate that the cells act as though their centre of mass offset varies (although it may not physically change). The third is to include a new torque due to phototaxis in the gyrotactic torque balance equation that is then used in the Fokker-Planck equation. These three models for phototaxis are fundamentally different, and this multi-model approach is used because we do not know precisely how the taxes interact, especially when they are competing. In this study, we choose to investigate in detail the green alga *Chlamydomonas nivalis*, which may exhibit aspects of all three models;

in particular, cells may respond to light by varying their swimming speed in conjunction with orientating via a phototactic torque. By exploring three somewhat phenomenological models we are able to get an indication of how modelling the effects of illumination in three significantly different ways effects the stability of the fluid layer. It also allows us to investigate whether a different modelling approach introduces behaviour not seen before, and to make some direct comparisons between modelling strategies.

The same methodology for all three models is followed, which is based on the analysis of the Pedley and Kessler 1990 [130] model applied to a layer of finite depth by Bees and Hill in 1998 [9]. The Fokker-Planck equation is solved and used to calculate the mean cell swimming direction and an estimate for the cell swimming diffusion tensor which are used in the cell conservation equation. Analytical and numerical equilibrium solutions for the case of no fluid flow are then found and perturbed to linearize the model equations and assess stability. The key non-dimensional parameters that are investigated and which characterize the suspension are the layer depth, d , the gyrotaxis parameter, η , the phototaxis parameter, $\chi = \frac{I_s}{I_c}$, which is a ratio of the light intensity at the source to the critical light intensity (the preferred light intensity for an individual cell), the strength of the phototaxis torque, ζ (in Model C), a measure of the absorption of the cells, κ , and the Rayleigh number, R . Neutral stability curves, on which the linear growth rate is zero, are plotted, with the region in parameter space below the curve indicating stability and above, instability.

Only Model A is explored in this chapter. We find that at equilibrium, increasing the phototaxis parameter moves the concentrated sublayer down through the suspension to a level at which there is a balance between phototaxis, gravitaxis, diffusion and cell shading. For $\chi < 1$, small wavenumbers are relatively destabilized and the critical wavenumber (the minimum wavenumber on the neutral curve) becomes zero, but for $\chi > 1$ all wavenumbers are relatively stabilized, and a non-zero critical wavenumber occurs for all η and κ , if χ is sufficiently large. As the gravitationally unstable region shrinks with increasing χ , penetrative convection occurs, where motions from the unstable region penetrate into the stable region. Looping neutral curves, which change mode as they turn, and oscillatory solutions are also found when η is sufficiently large. The chapter concludes with a discussion of results, in which comparisons with previous work, especially Bees and Hill 1998 [9] and Vincent and Hill 1996 [172], are made.

2.2 Modelling photo-gyrotactic bioconvection.

All three combined photo-gyrotactic models are based on the model proposed by Pedley and Kessler in 1990 [130] for gyrotactic and gravitactic cells (itself based on the gravitaxis model of Childress *et al.* [22]). This model was discussed in Section 1.5.3, where the main model equations are given in equations 1.17, 1.21, 1.25 1.26, 1.27, 1.22 and 1.24, along with an expression for the fluid stress tensor, Σ . We use the same modelling assumptions to construct the three photo-gyrotactic models, such as the suspension is dilute and incompressible, so cell to cell interactions are neglected, unless explicitly stated otherwise. Here, we present the three modelling approaches and then give the general equations for the new combined photo-gyrotaxis models to show how phototaxis is incorporated into the Pedley and Kessler model in each case.

2.2.1 Three new photo-gyrotactic models

In Chapters 2 and 3, I_c denotes critical light intensity, which is the preferred light intensity for an individual cell such that when $I > I_c$ cells are negatively phototactic and when $I < I_c$ they are positively phototactic. The three model approaches to include phototaxis in the stochastic gyrotaxis model of Pedley and Kessler 1990 [130], denoted Model A, B, and C, are:

- **Model A** A photokinesis-like model in which cell swimming speed V_s varies as a function of light intensity, I , so that cells swim faster when the light intensity is less than the critical intensity, I_c , and slower when $I > I_c$. For simplicity we choose $V_s(I) = -\xi(I - I_c)$, where ξ is constant. This is a somewhat phenomenological way of modelling, as V_s is generally not negative. The new, non-constant V_s is only included in the cell swimming term in the cell conservation equation of Pedley and Kessler, equation 1.27. The coefficient of the cell swimming diffusion tensor (equation 1.24) is kept as a constant, the implications of which are explored in Section 2.3.2
- **Model B** A phenomenological model in which the cells act as though their centre of mass offset h (the distance between the cell's geometric centre and centre of mass) varies with light intensity. Here, $h(I)$ is modelled as a linear function of I , $h(I) = -\xi(I - I_c)$. This non-constant $h(I)$ will appear in the previously constant B in the gravitational torque term in $\dot{\mathbf{p}}$, shown in equations 1.17 and 1.18 of the Pedley and Kessler model [130]. Thus the solution to the Fokker-Planck equation and,

hence, $\langle \mathbf{p} \rangle$ and \mathbf{D} , will depend on light intensity. This will affect the deterministic-stochastic balance of each cell such that when $|h|$ is large the cell will swim more deterministically upwards and when $|h|$ is small the cell will swim more stochastically. When the cell is at the preferred light intensity, I_c , $h = 0$, and there will be no gravitaxis or gyrotaxis, so the cell will move stochastically, with no preferred direction.

- **Model C** In this model a new effective torque due to phototaxis, \mathbf{L}_p , is included in the torque-balance equation, changing the derivation of $\dot{\mathbf{p}}$ in Section 1.5.3 and, hence, the solution to the Fokker-Planck equation, so that again $\langle \mathbf{p} \rangle$ and \mathbf{D} depend on I . We denote this in the main model equations by using $\tilde{\mathbf{k}}(I)$ instead of \mathbf{k} in Equation 1.17, since there is a way to combine the gravitaxis and phototaxis torque terms to give a unit vector dependent on light multiplied by a function to describe the strength of the torque (shown in Chapter 3). If $I = I_c$ in Model B there is no gyrotaxis, but in this model the phototaxis torque disappears and gyrotaxis remains, since separate phototaxis and gyrotaxis torques are modelled. This allows the phototaxis and gyrotaxis torques to exist independently. Different forms for the effective phototactic torque are investigated, depending on what assumptions we make about the direction of the light and the response.

These three models operate at different levels in the system and are fundamentally different. While Model A does not affect the solution to the Fokker-Planck equation from Pedley and Kessler [130] and only affects the cell swimming velocity, Model B incorporates phototaxis into the gravitactic torque. Model C, on the other hand, includes a separate torque due to phototaxis in the torque balance equation and affects the derivation of $\dot{\mathbf{p}}$ and, like Model B, the solution to the Fokker Planck equation. The most general form of the main model equations in dimensional terms are shown in equations 2.1, 2.2, 2.3, 2.4 and 2.5, where all three ways of including phototaxis in the model of Pedley and Kessler [130] in Section 1.5.3 are included. The Navier-Stokes equation with an incompressibility condition is

$$\nabla \cdot \mathbf{u} = 0, \quad (2.1)$$

$$\rho \left(\frac{\partial \mathbf{u}}{\partial t} + (\mathbf{u} \cdot \nabla) \mathbf{u} \right) = -\nabla p_e + nv\Delta\rho\mathbf{g} + \nabla \cdot \boldsymbol{\Sigma}, \quad (2.2)$$

where $\mathbf{u}(\mathbf{x}, t)$ is the fluid velocity, $\boldsymbol{\Sigma}(\mathbf{x}, t)$ the fluid stress tensor, $p_e(\mathbf{x}, t)$ is the excess pressure above hydrostatic (at density ρ), $n(\mathbf{x}, t)$ is local cell concentration, v is the volume of a cell, ρ is the density of the fluid and $\rho + \Delta\rho$ is the density of a cell. The second term on the right-hand side of equation 2.2 is the Boussinesq approximation due to the difference in density between the fluid and the cell, denoted $\Delta\rho$, and g is the acceleration due to gravity. These equations are the same as the Navier-Stokes equations in Pedley and Kessler, shown in equations 1.25 and 1.26.

The cell conservation equation of Pedley and Kessler shown in equation 1.27 becomes

$$\frac{\partial n}{\partial t} = -\nabla \cdot [n\mathbf{u} + nV_s(I)\langle\mathbf{p}(\boldsymbol{\Omega}, \mathbf{E}, I)\rangle - \mathbf{D}(\boldsymbol{\Omega}, \mathbf{E}, I) \cdot \nabla n], \quad (2.3)$$

where t is time, $\mathbf{x} = (x, y, z)$ is the cartesian coordinate system where z points vertically upwards, $\boldsymbol{\Omega}(\mathbf{x}, t)$ is the dimensional vorticity and $\mathbf{E}(\mathbf{x}, t)$ the dimensional rate-of-strain tensor, and I denotes light intensity. The first term on the right hand side of equation 2.3 is due to advection of the cells by the fluid. The second is due to cell swimming, where $V_s(I)$ is mean cell swimming speed dependent on light intensity, and $\langle\mathbf{p}(\boldsymbol{\Omega}, \mathbf{E}, I)\rangle$ is the mean cell swimming direction. The third term is due to diffusion, where $\mathbf{D}(\boldsymbol{\Omega}, \mathbf{E}, I)$ is the cell swimming diffusion tensor.

The expression for $\dot{\mathbf{p}}$, the rate of change of cell swimming direction \mathbf{p} , and the Fokker-Planck equation are given by

$$\begin{aligned} \dot{\mathbf{p}} &= \frac{1}{2B(h(I))} [\tilde{\mathbf{k}}(I) - (\tilde{\mathbf{k}}(I) \cdot \mathbf{p})\mathbf{p}] + \frac{1}{2}\boldsymbol{\Omega} \wedge \mathbf{p} \\ &+ \alpha_0[\mathbf{E} \cdot \mathbf{p} - \mathbf{p}\mathbf{p} \cdot \mathbf{E} \cdot \mathbf{p}], \end{aligned} \quad (2.4)$$

$$\frac{\partial f}{\partial t} + \nabla_p \cdot (\dot{\mathbf{p}}f) = D_r \nabla_p^2 f, \quad (2.5)$$

where α_0 is a measure of cell eccentricity. The subscript p in the Fokker-Planck equation (equation 2.5) indicates that the derivatives are in orientation space, and $f(\mathbf{p})$ is the cell swimming direction probability density function defined on a unit sphere, where D_r is rotational diffusivity. The function $B(h(I))$ is defined as

$$B(h(I)) = \frac{\mu\alpha_\perp}{2h(I)\rho g}, \quad \text{where } h(I) = -\xi(I - I_c) \quad (2.6)$$

is the centre of mass offset which depends on light intensity, μ is the fluid viscosity, α_\perp is the dimensionless resistance coefficient for rotation about an axis perpendicular to \mathbf{p} and ξ is a constant. B was previously a constant in the model of Pedley and Kessler [130], shown in equation 1.18, but now depends on light intensity because the centre of mass offset h now depends on I .

In reality, the effect of the cells on the fluid motion does not come only from their negative buoyancy. These other contributors are discussed fully in Pedley and Kessler 1990 [130], where the most significant was found to be the contribution to the bulk stress from the swimming motion, although this had only marginal effects. We neglect all contributions to the bulk stress except the negative buoyancy and assume Newtonian stress, so that

$$\boldsymbol{\Sigma} = 2\mu\mathbf{E}. \quad (2.7)$$

The mean cell swimming direction, $\langle \mathbf{p} \rangle$, and the cell swimming diffusion tensor, \mathbf{D} , are calculated from the solution to the Fokker-Planck using an expression similar to those in Pedley and Kessler [130], where the expressions for diffusion in equation 1.23 is approximated as in equation 1.24 (described in Section 1.5.3), so that

$$\langle \mathbf{p} \rangle = \int_S \mathbf{p} f(\mathbf{p}) dS, \quad (2.8)$$

$$\mathbf{D} \approx D_0 \langle (\mathbf{p} - \langle \mathbf{p} \rangle)(\mathbf{p} - \langle \mathbf{p} \rangle) \rangle, \quad (2.9)$$

where S is a unit sphere and D_0 is a diffusion scale that varies between models ($D_0 = V_s^2 \tau$ in Pedley and Kessler [130], where V_s is defined as the average cell swimming speed and τ the direction correlation time). The diffusion should really be calculated from a swimming velocity autocorrelated function using generalized Taylor dispersion theory [60, 108] but no general theory for all flows exists, so this expression is used for simplicity and to allow feasible computations.

The new terms in equations 2.1 to 2.5 (compared to the gyrotaxis model of Pedley and Kessler [130]) are $V_s(I)$ and $h(I)$, which were previously constants, and $\tilde{\mathbf{k}}(I)$, which was previously the constant unit vector in the vertical direction, \mathbf{k} . The models are formulated so that if there is no light, $I = 0$, hence no phototaxis, then $V_s(I) = V_s$, $h(I) = h$ and $\tilde{\mathbf{k}}(I) = \mathbf{k}$, and the model equations are the same as in the Pedley and Kessler model [130] for gyrotactic and gravitactic cells and as in Bees and Hill 1998 [9] for a suspension layer of finite depth. Although all models are included in these general photo-gyrotactic model equations, we study each model individually and do not use all of the new terms together.

We consider a layer of depth H cm. A rigid no-flow boundary condition is used at both the upper and the lower boundaries, which seems reasonable as cells form an almost solid boundary of mats of cells at the fluid surface fairly quickly. However, a mixed stress-free and no-flow boundary condition at $z = 0$ may be a better approximation. We also specify

zero flux perpendicular to the boundaries. Thus

$$\mathbf{u} = \mathbf{0} \quad \text{at} \quad z = 0, -H \quad \text{and} \quad (2.10)$$

$$\mathbf{k} \cdot (n(\mathbf{u} + V_s(I)\langle \mathbf{p} \rangle) - \mathbf{D} \cdot \nabla n) = 0 \quad \text{at} \quad z = 0, -H, \quad (2.11)$$

as used by Bees and Hill 1998 [9].

2.2.2 Modelling light

To model the effects of light from above on bioconvection we include the effects of self-shading, where cells close to the light source absorb and scatter light before it reaches those cells further away. This shading model is based on that presented in Vincent and Hill 1996 [172] and further explored by Ghorai and Hill 2005 [46]. We assume that light scattering and absorption by the medium is weak and, hence, can be disregarded, which seems reasonable as the medium is similar to water and the layer depth is relatively small. We also assume that all cells are homogeneous and possess the same transmittance of light in every direction, and disregard multiple scattering by stipulating that a cell only receives light travelling to it in a straight line from the source. We assume that absorption across the suspension does not affect the wavelength of the light. Finally, we assume that the timescales for changes in light intensity as the cell rotates are longer than the time required for the cell to detect those changes (i.e. the cell detects changes in I quickly).

We use the same expression for light intensity I for each model (as used in Vincent and Hill [172]), derived from the Beer-Lambert law, that states that there is a logarithmic relationship between light intensity I and the distance the light has travelled through the suspension. This is commonly used to calculate absorption in suspensions. The expression for the light intensity I at a depth z is

$$I(z) = I_s e^{[-\alpha^* \int_z^0 n(z) dz]} \quad (2.12)$$

where α^* is the cellular extinction coefficient (a measure of light absorption per cell), n is the concentration of cells and I_s is the light intensity at the source ($z = 0$). The integral of the concentration between 0 and z is a measure of how much a cell at position z is shaded by the sum of all cells between it and the light source. Equation 2.12 can only be used if the total volume of particles per unit volume multiplied by the light absorbed by a single particle is small and, as in Vincent and Hill [172], we conclude that this is the case in our system since the cell volume fraction and light absorption are both relatively small.

One might question whether equation 2.12 would represent the actual intensity perceived by an algal cell at z at a given time, as the transduction process is probably not totally efficient and the partially shaded eyespot is likely to be at some non-zero angle to the light source. However, over several rotations the mean intensity measured by the cell is likely to be approximately $I(z)$.

2.2.3 Non-dimensionalization of the general model

The non-dimensionalization for the general model in equations 2.1 to 2.5 is presented here. We non-dimensionalize the cell conservation and Navier-Stokes equation as in Bees and Hill 1998 [9], where length is scaled on H and, for now, diffusivity on D_0 , which is defined separately in each model. $V_s(I)$ is non-dimensionalized with the constant average cell swimming speed, denoted V_n (obtained from Hill and Häder 1996 [61] for *C. nivalis*). To allow direct comparisons between these results and those of Bees and Hill [9] we non-dimensionalize n with N , where $N = \frac{d\bar{n}}{1-e^{-d}}$ and $d = \frac{K_1 H V_n}{K_2 D_0}$, which arises from the solution to the equilibrium solution (see Section 2.3.1), where \bar{n} is the mean cell concentration and K_1 and K_2 are constants from the Fokker-Planck equation in equations 2.38 and 2.40. Although this is not an obvious choice it allows comparison with previous work. We non-dimensionalize I using light intensity at the source, I_s . This gives the following scalings:

$$\begin{aligned} \tilde{x} &= \frac{x}{H}, & \tilde{n} &= \frac{n}{N}, & \tilde{\mathbf{D}} &= \frac{\mathbf{D}}{D_0}, & \tilde{t} &= \frac{tD_0}{H^2}, & \tilde{\mathbf{u}} &= \frac{\mathbf{u}H}{D_0}, \\ \tilde{\Sigma} &= \frac{\Sigma H^2}{D_0 \mu}, & \tilde{p}_e &= \frac{p_e H^2}{\mu D_0}, & \tilde{I} &= \frac{I}{I_s}, & \tilde{V}_s &= \frac{V_s}{V_n}. \end{aligned} \quad (2.13)$$

On dropping tildes, the non-dimensional incompressibility condition (2.1), the Navier-Stokes equation (2.2) and the cell conservation equation (2.3) become

$$\nabla \cdot \mathbf{u} = 0, \quad (2.14)$$

$$S_c^{-1} \frac{D\mathbf{u}}{Dt} = -\nabla p_e - \gamma n \mathbf{k} + \nabla \cdot \Sigma, \quad (2.15)$$

$$\frac{\partial n}{\partial t} = -\nabla \cdot \left[n \left(\mathbf{u} + \frac{V_n H}{D_0} V_s(I) \langle \mathbf{p} \rangle \right) - \mathbf{D} \cdot \nabla n \right], \quad (2.16)$$

where the Schmidt number S_c and γ are given by

$$S_c = \frac{\nu}{D_0} \quad \text{and} \quad \gamma = \frac{N \nu g \Delta \rho H^3}{\nu \rho D_0}, \quad (2.17)$$

where ν is the kinematic viscosity. The non-dimensional stress tensor is

$$\Sigma = 2\mathbf{e}, \quad (2.18)$$

and the non-dimensional function for light intensity is

$$I(z) = e^{[-\kappa \int_z^0 n(z) dz]}, \quad (2.19)$$

where $\kappa = \alpha^* HN$ is a dimensionless measure of light absorption by the cells. As in Vincent and Hill 1996 [172] and Ghorai and Hill 2005 [46] we remove the integral and thus increase the order of the system by defining

$$m = - \int_z^0 n(z) dz \quad \text{so} \quad n(z) = \frac{dm}{dz}. \quad (2.20)$$

The no-flow and no-flux boundary conditions are now

$$\mathbf{u} = \mathbf{0} \quad \text{at} \quad z = 0, -1 \quad \text{and} \quad (2.21)$$

$$\mathbf{k} \cdot \left(n\mathbf{u} + \frac{V_n H}{D_0} V_s(I) n(\mathbf{p}) - \mathbf{D} \cdot \nabla n \right) = 0 \quad \text{at} \quad z = 0, -1. \quad (2.22)$$

Increasing the order of the system means we need another boundary condition. This comes from setting $z = 0$ in equation 2.20, so that

$$m = 0 \quad \text{at} \quad z = 0. \quad (2.23)$$

The expression for $\dot{\mathbf{p}}$ and the Fokker-Planck equation are non-dimensionalized using the same scalings as Pedley and Kessler [130] and Bees and Hill [9], so that

$$\boldsymbol{\Omega} = \frac{D_0}{H^2} \boldsymbol{\omega} \quad \text{and} \quad \mathbf{E} = \frac{D_0}{H^2} \mathbf{e}, \quad (2.24)$$

where $\boldsymbol{\omega}$ is the dimensionless vorticity and \mathbf{e} the dimensionless rate-of-strain tensor. We use the steady version of the Fokker-Planck equation, as in Pedley and Kessler [130] and Bees and Hill [9], since we also assume that the timescale for unsteadiness in the flow is large compared to D_r^{-1} (discussed in Chapter 1). Substituting the scalings into equations 2.4 and 2.5 gives

$$\begin{aligned} \frac{D_0}{H^2} \dot{\mathbf{p}} &= \frac{1}{2B(h(I))} [\tilde{\mathbf{k}}(I) - (\tilde{\mathbf{k}}(I) \cdot \mathbf{p})\mathbf{p}] + \frac{1}{2} \frac{D_0}{H^2} \boldsymbol{\omega} \wedge \mathbf{p} \\ &+ \alpha_0 \frac{D_0}{H^2} [\mathbf{e} \cdot \mathbf{p} - \mathbf{p}\mathbf{p} \cdot \mathbf{e} \cdot \mathbf{p}], \end{aligned} \quad (2.25)$$

$$\frac{D_0}{H^2} \nabla_p \cdot (\dot{\mathbf{p}} f) = D_r \nabla_p^2 f. \quad (2.26)$$

Here, I in $\tilde{\mathbf{k}}(I)$ is non-dimensionalized and the constants in the definition for $\tilde{\mathbf{k}}(I)$ are redefined so that $\tilde{\mathbf{k}}(I)$ is now dimensionless, which is discussed in full detail in Section 3.6.

We also non-dimensionalize $h(I)$ in equation 2.6 with the average centre of mass offset in the dark, h_n , so that $\tilde{h}(I) = \frac{h}{h_n}$. Thus we can re-write $B(h(I))$ in equation 2.6 as

$$B(h(I)) = \frac{\mu\alpha_{\perp}}{2h_n\tilde{h}(I)\rho g} = \frac{\mu\alpha_{\perp}}{2h_n\rho g} \frac{1}{\tilde{h}(I)} = \frac{B_n}{\tilde{h}(I)}, \quad (2.27)$$

where

$$B_n = \frac{\mu\alpha_{\perp}}{2h_n\rho g} \text{ and } \tilde{h}(I) = \frac{\xi}{h_n}(I_s\tilde{I} - I_c), \quad (2.28)$$

so that B_n is a constant and $\tilde{h}(I)$ a function dependent on I . This can be substituted into equations 2.25, and if we substitute the expression for $\dot{\mathbf{p}}$ into the Fokker-Planck equation then, on dropping tildes, we have

$$\begin{aligned} & h(I)\nabla_p \cdot [(\tilde{\mathbf{k}}(I) - (\tilde{\mathbf{k}}(I) \cdot \mathbf{p})\mathbf{p})f] + \eta\nabla_p \cdot [(\boldsymbol{\omega} \wedge \mathbf{p})f] \\ & + 2\alpha_0\eta\nabla_p \cdot [(\mathbf{e} \cdot \mathbf{p} - \mathbf{p}\mathbf{p} \cdot \mathbf{e} \cdot \mathbf{p})f] = \lambda^{-1}\nabla_p^2 f, \end{aligned} \quad (2.29)$$

where

$$\lambda = \frac{1}{2D_r B_n} \text{ and } \eta = \frac{B_n D_0}{H^2}. \quad (2.30)$$

η is the dimensionless gyrotaxis parameter. h_n is the centre of mass offset in the dark, or the normal centre of mass offset, and this is the same as h in Bees and Hill [9]. Thus the parameter B_n and those parameters containing B_n can be directly compared with the corresponding parameters in [9].

Equations 2.14, 2.15, 2.16, 2.19, 2.29, along with equations 2.8 for $\langle \mathbf{p} \rangle$, 2.9 for \mathbf{D} and 2.18 for $\boldsymbol{\Sigma}$, complete the most general non-dimensional form of the combined photo-gyrotaxis model, with boundary conditions given in equations 2.21, 2.22 and 2.23.

2.2.4 Table of parameters

The model so far has been for any general swimming green algae species. Table 2.1 lists standard parameter values that will be used in all three models for *Chlamydomonas nivalis*. Other parameters are discussed in each model separately. Most of these values are the same as in Bees and Hill 1998 [9], to allow comparisons between the models, and come from [130], [73], [61] and [63]. Typically the cells have a cell diameter of 10 μm , with an average distance between cells of 100 μm , while the length scale for pattern formation is much larger, at around 0.1 – 0.5 cm (found experimentally in Chapter 4).

Name	Description	Standard value	Units
ρ	Density of fluid	1.0	gm/cm ³
$\rho + \Delta\rho$	Cell density	1.05	gm/cm ³
v	Cell volume	5×10^{-10}	cm ³
g	Acceleration due to gravity	10^3	cm/s ²
μ	Viscosity	10^{-2}	gm /cm s
V_n	Average cell swimming speed	63	$\mu\text{m} / \text{s}$
D_0	Diffusivity	$5 \times 10^{-5} - 5 \times 10^{-4}$	cm ² /s
h	Centre of mass offset	0 – 0.5	μm
B	Gyrotaxis parameter	3.4	s
B	Gyrotaxis parameter (with flagella)	6.3	s
α_0	Cell eccentricity	0.2 – 0.31	N/A
D_r	Rotational diffusivity of cells	0.067	s ⁻¹
α_{\perp}	Dimensionless resistance coefficient for rotation about an axis perpendicular to \mathbf{p}	6.8	N/A
λ	Deterministic-stochastic parameter	2.2	N/A
τ	Direction correlation time	1.3 – 5	s
S_c	Schmidt number	19	N/A
α^*	Cellular extinction coefficient	$3.67 \times 10^{-7} - 6.74 \times 10^{-7}$	cm ²

Table 2.1: A table of the standard parameter estimates for the green algae species *Chlaydomonas nivalis*.

2.2.5 Solving the Fokker-Planck equation without the phototaxis terms

Pedley and Kessler 1990 [130] solved the non-dimensional Fokker-planck equation for the gyrotaxis and gravitaxis only case (corrected in Bees and Hill 1998 [9]). The presence of $h(I)$ and $\tilde{\mathbf{k}}(I)$ in equation 2.29 creates extra terms in the solution to the Fokker-Planck for Models B and C, and for this reason the Fokker-Planck equation in equation 2.29 with all the terms is solved in full in Chapter 3. For Model A, $h(I) = 1$ and $\tilde{\mathbf{k}}(I) = \mathbf{k}$, and so we can quote the solutions to the Fokker-Planck directly from Pedley and Kessler [130]. To understand where these terms originate, here we indicate, in brief, the process for solving equation 2.29 in the case of no phototaxis.

If $h(I) = 1$ and $\tilde{\mathbf{k}}(I) = \mathbf{k}$ then equation 2.29 becomes

$$\nabla_p \cdot [(\mathbf{k} - (\mathbf{k} \cdot \mathbf{p})\mathbf{p})f] + \eta \nabla_p \cdot [(\boldsymbol{\omega} \wedge \mathbf{p})f] \quad (2.31)$$

$$+ 2\alpha_0 \eta \nabla_p \cdot [(\mathbf{e} \cdot \mathbf{p} - \mathbf{p}\mathbf{p} \cdot \mathbf{e} \cdot \mathbf{p})f] = \lambda^{-1} \nabla_p^2 f. \quad (2.32)$$

This is an equation in orientational space; so \mathbf{k} , $\boldsymbol{\omega}$ and \mathbf{e} are constants and $tr(\mathbf{e}) \equiv \nabla \cdot \mathbf{u} = 0$. \mathbf{p} is the cell swimming direction and is the unit vector perpendicular to the unit sphere, so that for any function $g(\mathbf{p})$, ∇g is perpendicular to \mathbf{p} , so $(\mathbf{p} \cdot \nabla)g = 0$. We calculate $\nabla \cdot \mathbf{p} = 2$, $\nabla \mathbf{p} = \mathbf{I} - \mathbf{p}\mathbf{p}$ and $(\nabla \wedge \mathbf{p})_i = \epsilon_{ijk} p_{j,k} = \frac{1}{2} \epsilon_{ijk} (p_{j,k} + p_{k,j}) = 0$ as $\nabla \mathbf{p} = (\nabla \mathbf{p})^T$. Following the term by term analysis in Bees and Hill [9], the non-dimensional Fokker-Planck equation simplifies to

$$(\mathbf{k} \cdot \nabla_p f - 2(\mathbf{k} \cdot \mathbf{p})f) + \eta \boldsymbol{\omega} \cdot (\mathbf{p} \wedge \nabla_p f) + 2\eta \alpha_0 [\mathbf{p} \cdot \mathbf{e} \cdot \nabla_p f - 3\mathbf{p} \cdot \mathbf{e} \cdot \mathbf{p} f] = \lambda^{-1} \nabla_p^2 f. \quad (2.33)$$

Equation 2.33 is solved by first considering the equilibrium state of no-flow, denoted with superscript 0, where $\mathbf{u} = \boldsymbol{\omega} = \mathbf{e} = \mathbf{0}$, $f = f^0$ and $m = m^0$, so that on writing $\mathbf{p} = (\sin \theta \cos \phi, \sin \theta \sin \phi, \cos \theta)$ and $\mathbf{k} = (0, 0, 1)$,

$$\lambda (\mathbf{k} \cdot \nabla_p f^0 - 2(\mathbf{k} \cdot \mathbf{p})f^0) = \nabla_p^2 f^0, \quad (2.34)$$

where θ is the colatitude measured relative to \mathbf{k} and ϕ is the cell orientation angle in the horizontal plane. This is solved to calculate f^0 , which is then used in equations 2.8 and 2.9 to calculate the equilibrium components of the mean cell swimming direction and cell swimming diffusion tensor, denoted $\langle \mathbf{p} \rangle^0$ and \mathbf{D}^0 , respectively. We then consider an infinitesimal perturbation, denoted by superscript 1, where

$$\mathbf{u} = \epsilon \mathbf{u}^1, \quad \boldsymbol{\omega} = \epsilon \boldsymbol{\omega}^1, \quad \mathbf{e} = \epsilon \mathbf{e}^1, \quad f = f^0 + \epsilon f^1 \text{ and } m = m^0 + \epsilon m^1, \quad (2.35)$$

where $0 < \epsilon \ll 1$. Equation 2.32 at order ϵ is

$$\begin{aligned} & \lambda [\mathbf{k} \cdot \nabla_p f^1 - 2(\mathbf{k} \cdot \mathbf{p}) f^1] + \eta \lambda \boldsymbol{\omega}^1 \cdot (\mathbf{p} \wedge \nabla_p f^0) \\ & + 2\eta \lambda \alpha_0 [\mathbf{p} \cdot \mathbf{e}^1 \cdot \nabla_p f^0 - 3\mathbf{p} \cdot \mathbf{e}^1 \cdot \mathbf{p} f^0] = \nabla_p^2 f^1, \end{aligned} \quad (2.36)$$

which is solved to calculate f^1 . This is then used to calculate the weak ambient flow components of the mean cell swimming direction and cell swimming diffusion tensor, denoted $\langle \mathbf{p} \rangle^1$ and \mathbf{D}^1 , respectively. The solutions take the form

$$\langle \mathbf{p} \rangle = \langle \mathbf{p} \rangle^0 + \epsilon \langle \mathbf{p} \rangle^1 \quad (2.37)$$

$$= \begin{pmatrix} 0 \\ 0 \\ K_1 \end{pmatrix} + \epsilon \left[\eta J_1 \begin{pmatrix} \omega_2 \\ -\omega_1 \\ 0 \end{pmatrix} - 2\alpha_0 \eta \begin{pmatrix} e_{13} J_4 \\ e_{23} J_4 \\ \frac{3}{2} e_{33} K_4 \end{pmatrix} \right] + O(\epsilon^2), \quad (2.38)$$

and the dimensionless diffusion tensor is

$$\mathbf{D} = \mathbf{D}^0 + \epsilon \mathbf{D}^1 \quad (2.39)$$

$$\begin{aligned} & = \begin{pmatrix} \frac{K_1}{\lambda} & 0 & 0 \\ 0 & \frac{K_1}{\lambda} & 0 \\ 0 & 0 & K_2 \end{pmatrix} + \epsilon \left[\eta (J_2 - J_1 K_1) \begin{pmatrix} 0 & 0 & \omega_2 \\ 0 & 0 & -\omega_1 \\ \omega_2 & -\omega_1 & 0 \end{pmatrix} - 2\alpha_0 \eta \right. \\ & \left. \begin{pmatrix} -\frac{3}{4} e_{33} K_5 + \frac{1}{4} (e_{11} - e_{22}) J_6 & \frac{1}{2} e_{12} J_6 & e_{13} (J_5 - K_1 J_4) \\ \frac{1}{2} e_{12} J_6 & -\frac{3}{4} e_{33} K_5 - \frac{1}{4} (e_{11} - e_{22}) J_6 & e_{23} (J_5 - K_1 J_4) \\ e_{13} (J_5 - K_1 J_4) & e_{23} (J_5 - K_1 J_4) & \frac{3}{2} e_{33} (K_5 - 2K_1 K_4) \end{pmatrix} \right] \\ & + O(\epsilon^2). \end{aligned} \quad (2.40)$$

A full explanation of these solutions can be found in Chapter 3. Definitions for the constants K_i and J_i (which depend on λ) and values of these constants when $\lambda = 2.2$ (from the range computed by Pedley and Kessler [130] and used by Bees and Hill [9]) are shown in Table 2.2. An error in the calculation of the values J_4 and J_5 was found when computing the Fokker-Planck solution for Model B; the corrected values are $J_4 = -0.22$ and $J_5 = -0.17$. However, this only makes a quantitative difference to results and, since Model A results had already been computed with the original J_i values, they were not re-computed for this chapter (except when exploring bifurcations in Section 2.5.7); results presented here use J_4 and J_5 values as in Table 2.2, allowing direct comparison with Pedley and Kessler [130] and Bees and Hill [9]. However, the corrected J_i values are used in Chapter 3, and, when direct comparisons are made between models, Model A results

Name	Definition	Value
μ_λ	$\frac{\lambda}{4\pi \sinh \lambda}$	0.039
K_1	$\coth \lambda - \frac{1}{\lambda}$	0.57
K_2	$1 - \coth^2 \lambda + \frac{1}{\lambda^2}$	0.16
K_4	$K_2 - \frac{K_1}{\lambda}$	-0.10
K_5	$-\frac{2}{\lambda} \left[1 + K_2 - \frac{4K_1}{\lambda} \right]$	-0.11
J_1	$\frac{4}{3}\pi\lambda\mu_\lambda \sum_{l=0}^{\infty} \lambda^{2l+1} a_{2l+1,1}$	0.45
J_2	$\frac{4}{5}\pi\lambda\mu_\lambda \sum_{l=1}^{\infty} \lambda^{2l} a_{2l,2}$	0.16
J_4	$\frac{4}{3}\pi\lambda\mu_\lambda \sum_{l=0}^{\infty} \lambda^{2l+1} \tilde{a}_{2l+1,1}$	-0.26*
J_5	$\frac{4}{5}\pi\lambda\mu_\lambda \sum_{l=0}^{\infty} \lambda^{2l} \tilde{a}_{2l,2}$	-0.13*
J_6	$\frac{16}{5}\pi\lambda\mu_\lambda \sum_{l=0}^{\infty} \lambda^{2l} \bar{a}_{2l,2}$	-0.20

Table 2.2: A table of values of K_i and J_i for use in Model A, where $\lambda = 2.2$ and $\alpha_0 = 0.2$. The $a_{i,j}$, $\tilde{a}_{i,j}$ and $\bar{a}_{i,j}$ values are defined in Chapter 3. The star indicates these values were wrongly calculated in [130]; the correct values are $J_4 = -0.23$ and $J_5 = -0.17$. K_4 shown here is the corrected form from Bees and Hill 1998 [9], since Pedley and Kessler had incorrectly concluded $K_4 = 1 - \coth^2 \lambda - \frac{2}{K_1}$ [130].

are re-computed with the correct J_i values. The error in the critical Rayleigh number when using the incorrect values is only approximately 5.7%.

2.3 Model A: modelling phototaxis in a photokinesis manner

In Model A, we investigate modelling swimming speed as a function of light intensity, $V_s(I)$. We set $h(I) = 1$ and $\tilde{\mathbf{k}}(I) = \mathbf{k}$ in equation 2.29, so that centre of mass offset is modelled as a constant, h_n , and there is no torque due to phototaxis. As stated in section 2.2, the analysis is simplified if we choose a non-dimensional V_s as a linear function of I , so that $V_s(I) = -\xi(I_s I - I_c)$, where ξ is a constant. On setting the non-dimensional cell swimming speed to be 1 when the light intensity is zero, we obtain $\xi = \frac{1}{I_c}$. The assumption that V_s depends linearly on I is only really valid when the light intensity is close to the critical light intensity, $I \approx I_c$, but is used here for simplicity. On substituting in the non-dimensional equation for light intensity 2.19 and re-arranging, this gives the non-dimensional variable cell swimming speed as

$$V_s(I) = - \left(\chi e^{-\kappa \int_z^0 n(z) dz} - 1 \right). \quad (2.41)$$

Here, $\chi = \frac{I_s}{I_c}$ is the ratio of the light intensity at the source to the critical light intensity I_c and is referred to as the phototaxis parameter. When $\chi = 0$ there is no light, $V_s = 1$ and the model is identical to that of Bees and Hill [9].

The effect of light only appears in the term for cell swimming in the cell conservation equation. The Navier-Stokes equation, the torque balance and Fokker-Planck equations are the same as in Pedley and Kessler [130]. For the majority of this chapter we define diffusion using a constant average cell swimming speed V_n , and equation 2.9 gives $D_0 = V_n^2 \tau$, where τ is the direction correlation time (the time it takes a cell to re-orientate). However, we investigate using a light dependent average swimming speed $V_s(I)$ in the diffusion

approximation in Section 2.3.2. This gives the non-dimensional equations for Model A as

$$\nabla \cdot \mathbf{u} = 0, \quad (2.42)$$

$$S_c^{-1} \frac{D\mathbf{u}}{Dt} = -\nabla p_e - \gamma n \mathbf{k} + \nabla \cdot \boldsymbol{\Sigma}, \quad (2.43)$$

$$\frac{\partial n}{\partial t} = -\nabla \cdot \left[n \mathbf{u} + \frac{dK_2}{K_1} \left(1 - \chi e^{-\kappa \int_z^0 n(z) dz} \right) n \langle \mathbf{p} \rangle - \mathbf{D} \cdot \nabla n \right], \quad (2.44)$$

$$n(z) = \frac{dm}{dz}, \quad (2.45)$$

$$\begin{aligned} \nabla_p \cdot [(\mathbf{k} - (\mathbf{k} \cdot \mathbf{p})\mathbf{p})f] + \eta \nabla_p \cdot [(\boldsymbol{\omega} \wedge \mathbf{p})f] \\ + 2\alpha_0 \eta \nabla_p \cdot [(\mathbf{e} \cdot \mathbf{p} - \mathbf{p}\mathbf{p} \cdot \mathbf{e} \cdot \mathbf{p})f] = \lambda^{-1} \nabla_p^2 f. \end{aligned} \quad (2.46)$$

Here, d is the ratio of layer depth H to sublayer depth $\left(\frac{K_1}{K_2 V_n \tau}\right)^{-1}$, defined by

$$d = \frac{K_1 H}{K_2 V_n \tau}, \quad (2.47)$$

where K_1 and K_2 come from the solution to the Fokker-Planck and are defined in Table 2.2, and d can be thought of as a non-dimensional layer depth. When $d \ll 1$ the layer is ‘shallow’ and when $d \gg 1$ the layer is ‘deep’. This is the same expression for d as in [9]. Solutions to the Fokker-Planck equation used to calculate $\langle \mathbf{p} \rangle$ and \mathbf{D} do not differ from those found by Pedley and Kessler [130], corrected in Bees and Hill [9], thus are given in equations 2.38 and 2.40. The only difference is we define constant average cell swimming speed as V_n (instead of V_s in [130] and [9]).

Boundary conditions 2.21, 2.22 and 2.23 become

$$\mathbf{u} = \mathbf{0} \quad \text{at} \quad z = 0, -1 \quad (2.48)$$

$$\mathbf{k} \cdot \left(n \mathbf{u} + \frac{dK_2}{K_1} \left(1 - \chi e^{-\kappa \int_z^0 n(z) dz} \right) n \langle \mathbf{p} \rangle - \mathbf{D} \cdot \nabla n \right) = 0 \quad \text{at} \quad z = 0, -1, \quad (2.49)$$

$$\text{and} \quad m = 0 \quad \text{at} \quad z = 0. \quad (2.50)$$

Following the general analysis of Bees and Hill [9], we find an equilibrium solution and then perturb about this solution. This gives two coupled linear equations which are solved numerically and analytically in certain parameter ranges to assess the stability of the system for different values of the main model parameters.

2.3.1 Equilibrium solution

We look for an equilibrium solution for the case of no fluid flow, $\mathbf{u} = \mathbf{0}$, $\boldsymbol{\omega} = \mathbf{0}$, $\mathbf{e} = \mathbf{0}$, where $n = n(z)$. The mean cell swimming direction and diffusion tensor become $\langle \mathbf{p} \rangle = \langle \mathbf{p} \rangle^0$ and $\langle \mathbf{D} \rangle = \langle \mathbf{D} \rangle^0$, where the superscript 0 indicates that we take only the part of the vector or

tensor for zero flow. If we consider a steady solution that only depends on z then equation 2.44 becomes

$$0 = -\frac{d}{dz} \cdot \left[\frac{dK_2}{K_1} n \left(1 - \chi e^{-\kappa \int_z^0 n(z) dz} \right) \langle \mathbf{p} \rangle^0 - \mathbf{D}^0 \cdot \nabla n \right], \quad (2.51)$$

with non-dimensional boundary conditions

$$\mathbf{u} = \mathbf{0} \quad \text{on } z = 0, -1 \quad (2.52)$$

and

$$\mathbf{k} \cdot \left(\frac{dK_2}{K_1} \left(1 - \chi e^{-\kappa \int_z^0 n(z) dz} \right) \langle \mathbf{p} \rangle^0 - \mathbf{D}^0 \cdot \nabla n \right) = 0 \quad \text{at } z = 0, -1. \quad (2.53)$$

Integrating equation 2.51 with respect to the boundary conditions and substituting in the solutions to the Fokker-Planck equation for zero flow from equations 2.38 and 2.40 gives

$$\frac{d^2 m(z)}{dz^2} - d \left(1 - \chi e^{\kappa m(z)} \right) \frac{dm(z)}{dz} = 0, \quad (2.54)$$

where equation 2.20 is used to increase the order of the system. The boundary condition for $z = -1$ comes from applying the non-dimensional normalization condition

$$\int_{-1}^0 n(z) dz = \frac{\bar{n}}{N}, \quad (2.55)$$

(i.e. $\int_{-H}^0 n(z) dz = \bar{n}H$), which gives $m = \frac{e^{-d}-1}{d}$ at $z = -1$. We also have the boundary condition that $m = 0$ at $z = 0$. Equation 2.54 is hard to solve analytically for all parameter values and so is solved numerically in Section 2.3.4. Note that if $\chi = 0$ then the solution is an exponential distribution for $n(z)$, as for the gyrotaxis only case presented in Bees and Hill [9], and others [63]. (For comparison with the phototaxis only model of Ghorai and Hill 2005 [46], here our $\frac{V_n H}{D_0} = \frac{dK_2}{K_1}$ is the same as $V_c = \frac{W_c H}{D}$ in [46], where W_c is the average cell swimming speed and D a constant diffusion coefficient, and the only difference in the constant d is that we multiply by $\frac{K_1}{K_2}$ since we use the Fokker-Planck equation instead of a constant isotropic diffusion tensor.) Whether either of these basic equilibrium states are achieved in laboratory cultures is discussed in Chapter 4.

2.3.2 Exploring the effects of using a diffusion tensor dependent on light, $\mathbf{D}(\mathbf{I})$

In the main body of Model A we do not consider the diffusion tensor \mathbf{D} as a function of light. This is inconsistent in a way because swimming diffusion should be a function of

swimming speed, and in Model A the average cell swimming speed, $V_s(I)$, is dependent on light. If we consider the diffusion tensor as a function of I , so that $\mathbf{D}(I) = V_s^2(I)\mathbf{D}$, where $V_s(I)$ and \mathbf{D} are non-dimensional and are given in equations 2.41 and 2.40, respectively, then the equilibrium profile is a solution of

$$(1 - \chi e^{\kappa m}) \frac{dn}{dz} - dn(z) = 0. \quad (2.56)$$

When $\chi = 1$ and $m = 0$ at $z = 0$ this equation is singular, and this problem will also arise for other values of $\chi > 1$ and m . Thus this does not seem like a realistic model as it is not consistent for $\chi > 1$. Furthermore, solutions for $\chi < 1$ show that increasing χ from zero causes the equilibrium solution to retain an almost exponential shape with increasing maximum concentration at $z = 0$ as χ increases. This increasing maximum is the opposite trend to that found from equation 2.54 for the equilibrium solution if diffusion is based on a constant average cell swimming speed V_n (where the maximum decreases for small χ), and is physically unrealistic. For these reasons we do not model the diffusion tensor as a function of light intensity, and instead define diffusion using a constant average mean cell swimming speed V_n , so that $D_0 = V_n^2 \tau$ in equation 2.9.

2.3.3 Analytical approximation to the equilibrium solution for weak absorption

As in Vincent and Hill [172] and Ghorai and Hill [46], if we assume the case of weak absorption, so that $0 < \kappa \ll 1$ and I is close to I_c , then we can find an analytical equilibrium solution. For small κ we re-write equation 2.54 as

$$\frac{dn}{dz} + \frac{d}{dz} \left(I_s e^{[-\kappa \int_z^0 n(z) dz]} - I_c \right) n(z) = 0 \quad (2.57)$$

and expand the exponential in equation 2.57 to give

$$I_s e^{[-\kappa \int_z^0 n(z) dz]} - I_c \approx I_s \left[1 - \kappa \int_z^0 n(z) dz \right] - I_c \quad (2.58)$$

The critical intensity I_c occurs at position $z = -C$ ($0 \leq C \leq 1$) for an individual cell for the vertically uniform concentration profile $n = 1$. Thus at $I = I_c$,

$$I_c = I_s e^{-\kappa \int_{-C}^0 1 dz} \approx I_s (1 - \kappa C), \quad (2.59)$$

which can be used in equation 2.58 to give

$$I_s e^{[-\kappa \int_z^0 n(z) dz]} - I_c \approx -I_s \kappa \left[\int_z^0 n(z) dz - C \right]. \quad (2.60)$$

Since $I_c = I_s + O(\kappa)$, $I_c \approx I_s$, and we can replace I_s with I_c . The equilibrium solution for weak absorption in equation 2.57 becomes

$$\frac{dn}{dz} - d\kappa \left[\int_z^0 n(z) dz - C \right] n(z) = 0. \quad (2.61)$$

The unique solution of equation 2.61 is

$$n(z) = \frac{\frac{K^2}{2G_1} [(K^2/G_1^2) - C^2] \operatorname{sech}^2(Kz/2)}{[(K/G_1) + C \tanh(Kz/2)]^2} \quad (2.62)$$

where $G_1 = d\kappa$ is a new constant defined for convenience so that a general solution to equation 2.61 can be computed in Appendix A (this is useful in Chapter 3 for Model B, where the analytic equilibrium solution has the same form as equation 2.61 but with different constants outside the bracket). Note that this definition does not affect the form of the solution found in Appendix A and $G_1 = d\kappa$ can be substituted back into equation 2.62 to provide the full solution. K is a constant obtained from the transcendental equation

$$\left(\frac{K^2}{G_1^2} - C^2 + d^{-1} (1 - e^{-d}) C \right) \tanh\left(\frac{K}{2}\right) - \frac{d^{-1} (1 - e^{-d}) K}{G_1} = 0, \quad (2.63)$$

on using the non-dimensional normalization condition

$$\int_{-1}^0 n(z) dz = d^{-1} (1 - e^{-d}). \quad (2.64)$$

Details of this solution can be found in Appendix A. This solution (with different constants) was originally found by Kamke 1967 [79] and is similar to the solution presented in Ghorai and Hill 2005 [46], which was the corrected version of that found in Vincent and Hill 1996 [172], except that we have a different value for the constant G_1 and we use a non-dimensionalization of n leading to a different boundary condition at $m = -1$.

To plot the analytical solutions we need to first calculate C and K . C is straightforward, since when $I = I_c$, $I_c = I_s e^{-\kappa C}$, hence $C = -\frac{1}{\kappa} \ln\left(\frac{1}{\chi}\right)$. K is more complicated but can be approximated using a numerical Newton-Raphson routine.

2.3.4 Numerical and analytical equilibrium profiles

For all equilibrium and linear stability results, the non-dimensional z coordinate is scaled with non-dimensional layer depth d , so that $z_I = dz$. This improves the numerics when d is large and χ is small, since the top region of the layer is expanded, but most importantly it allows us to directly compare results with Bees and Hill [9]. z_I derivatives are denoted as $\frac{d}{dz_I} = D_I$ throughout, and the layer depth is now $0 \geq z \geq -d$.

In Figure 2.1, $d = 20$, $\chi = 1.2$ and numerical and analytical equilibrium solutions for $\kappa = 0.1$, $\kappa = 0.5$ and $\kappa = 0.75$ are plotted. Although the analytical solution technically is valid only for small κ , we see good agreement between numerical and analytical results up to $\kappa = 0.75$ and indeed beyond. This comparison gives us confidence that the numerical code works as expected.

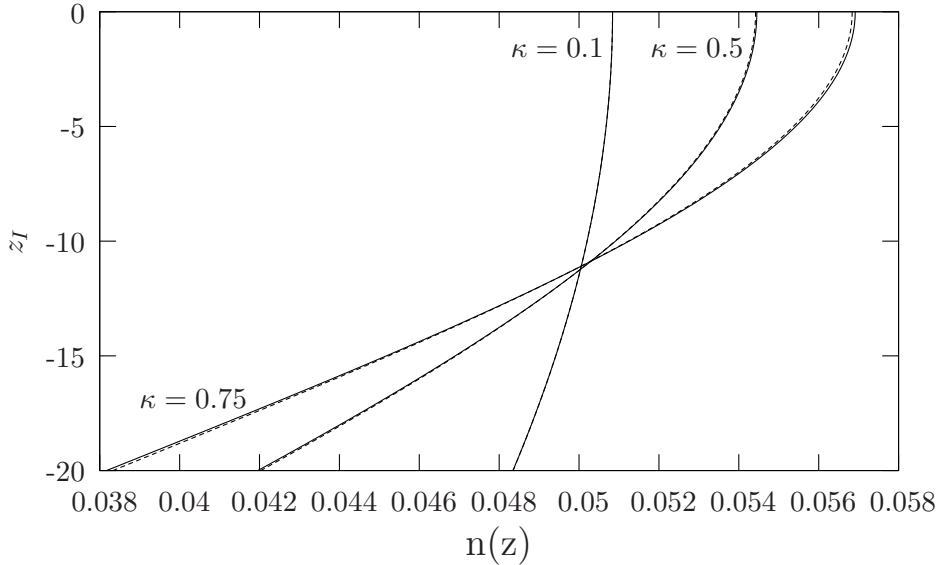


Figure 2.1: A comparison between numerical (solid lines) and analytical (dashed lines) equilibrium solutions where $d = 20$, $\chi = 1.2$ and κ varies. The non-dimensional coordinate z is scaled with non-dimensional layer depth d . The agreement between methods is good, even when κ is close to 1.

In Figure 2.2, $\kappa = 1.2$ and $d = 20$, and equilibrium solutions for different values of χ are plotted. The case $\chi = 0$ is equivalent to there being no light in the system, $I_s = 0$, and we have the gyrotaxis only case such that the equilibrium profile is an exponential function with maximum at $z = 0$, as in Bees and Hill 1998 [9] and Hill *et al.* 1989 [63]. As χ is increased to $\chi = 0.75$ the peak of the concentration profile is still at $z = 0$ but the value of the maximum is smaller and there is a greater spread of cells throughout the top region. When $\chi = 1$, $I_c = I_s$ the maximum remains at the top of the fluid layer but the distribution is less peaked, as shown in Figure 2.2(b). For $\chi > 1$ the cells near the light source have too much light and start to swim downwards, so the peak of the distribution moves down the fluid layer and the distribution becomes wider. When the peak gets half way down the layer the maximum value of n is at its smallest. When I and χ are large most cells swim downwards and the distribution is almost exponential with maximum at

$z = -d$, as shown in Figure 2.2(d).

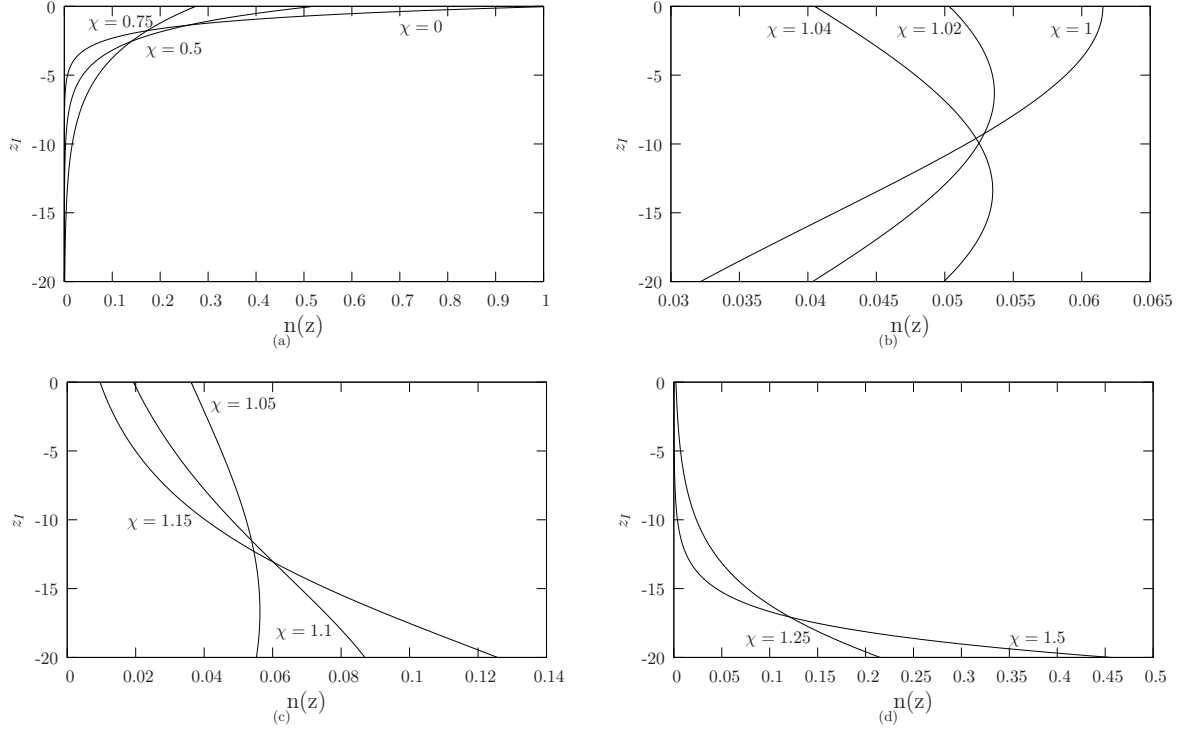


Figure 2.2: Concentration profiles for the equilibrium solution in Model A, where $d = 20$, $\kappa = 1.2$ and χ varies.

Figure 2.3 shows that increasing layer depth d to $d = 200$ gives qualitatively the same results as in Figure 2.2. Due to the depth of the layer we see (in Figure 2.3(a)) a very sharp distribution with most cells at the very top for small χ . The solution becomes more sensitive to χ , since a value of $\chi = 1.005$ provides a solution with a maximum in the bottom half of the layer in Figure 2.3(b).

Figure 2.4 shows that for $\chi = 1.02$, increasing κ from $\kappa = 1$ causes the maximum of the equilibrium profile to move upwards and become more peaked, which is the opposite effect to increasing χ . Large κ also makes solutions less sensitive to changes in χ , so that larger changes in χ are needed to move the peak of $n(z)$.

2.3.5 Linear stability analysis

Consider a small perturbation from the equilibrium solution such that

$$\begin{aligned}
 \mathbf{u} &= \epsilon \mathbf{u}^1, & \langle \mathbf{p} \rangle &= \langle \mathbf{p} \rangle^0 + \epsilon \langle \mathbf{p} \rangle^1, & n &= n^0 + \epsilon n^1, \\
 p_e &= p_e^0 + \epsilon p_e^1, & \Sigma &= \epsilon \Sigma^1, & \mathbf{D} &= \mathbf{D}^0 + \epsilon \mathbf{D}^1, \\
 m &= m^0 + \epsilon m^1,
 \end{aligned} \tag{2.65}$$

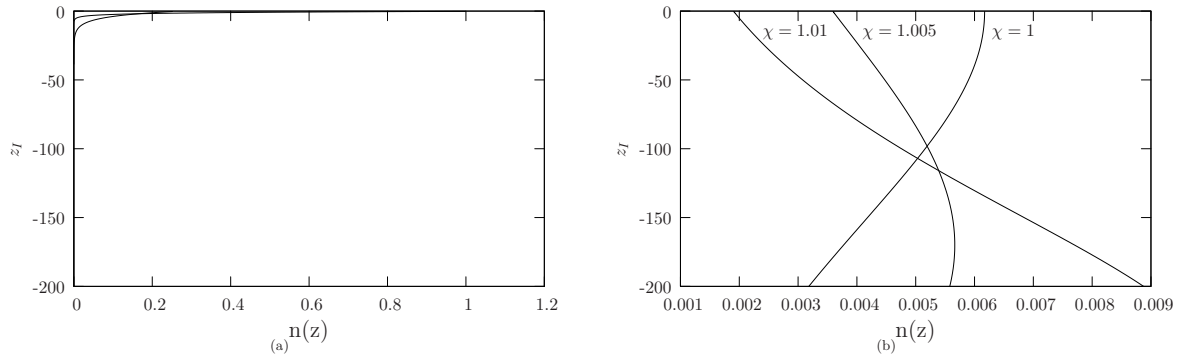


Figure 2.3: Concentration profiles for the equilibrium solution in Model A, where $d = 200$, $\kappa = 1.2$ and χ varies. In the first plot the top curve is $\chi = 0$ and the bottom $\chi = 0.75$

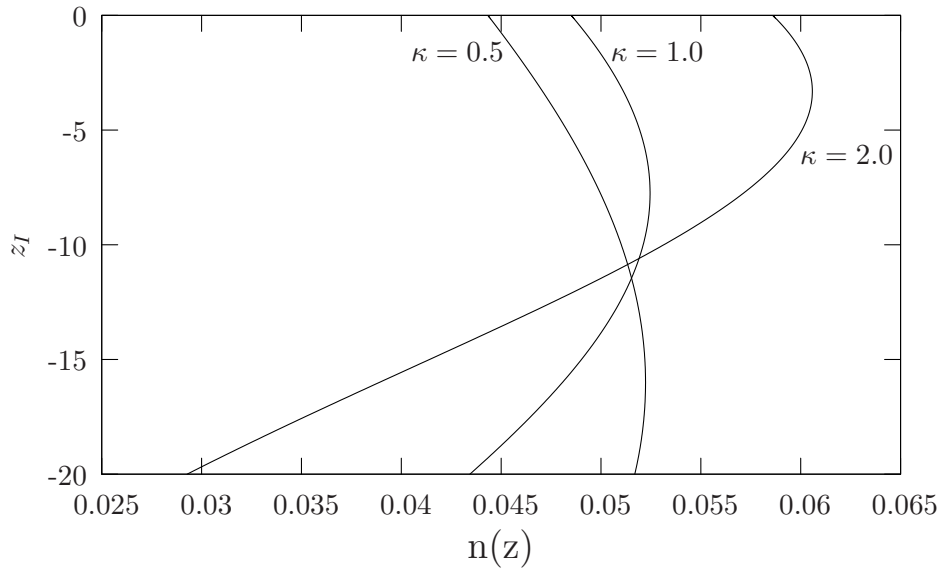


Figure 2.4: Concentration profiles for the equilibrium solution in Model A, where $d = 20$, $\chi = 1.02$ and $\kappa = 0.5, 1.0$ and 2.0

where $\epsilon \ll 1$, and the superscript 0 indicates the zeroth order, no-flow equilibrium solution and 1 indicates the first order perturbation. Looking first at the effect of the perturbation on m , $V_s(I)$ in equation 2.41 becomes

$$V_s(I) = 1 - \chi e^{\kappa(m^0 + \epsilon m^1)} = 1 - \chi e^{\kappa m^0} e^{\epsilon \kappa m^1} + O(\epsilon^2). \quad (2.66)$$

Expanding the exponential in ϵ gives

$$V_s(I) = 1 - \chi e^{\kappa m^0} - \epsilon \chi \kappa m^1 e^{\kappa m^0} + O(\epsilon^2). \quad (2.67)$$

On substituting the perturbations into the main model equations (equations 2.42, 2.43, 2.44, and 2.45), the governing equations to order ϵ become

$$\nabla \cdot \mathbf{u}^1 = 0, \quad (2.68)$$

$$S_c^{-1} \frac{\partial \mathbf{u}^1}{\partial t} = -\nabla p_e^1 - \gamma n^1 \mathbf{k} + \nabla \cdot \boldsymbol{\Sigma}^1, \quad (2.69)$$

$$\begin{aligned} \frac{\partial n^1}{\partial t} = & -\nabla \cdot \left[n^0 \mathbf{u}^1 + \frac{dK_2}{K_1} \left((1 - \chi e^{\kappa m^0}) n^1 \langle \mathbf{p} \rangle^0 + (1 - \chi e^{\kappa m^0}) n^0 \langle \mathbf{p} \rangle^1 \right. \right. \\ & \left. \left. - \chi \kappa m^1 e^{\kappa m^0} n^0 \langle \mathbf{p} \rangle^0 \right) - \mathbf{D}^0 \cdot \nabla n^1 - \mathbf{D}^1 \cdot \nabla n^0 \right], \end{aligned} \quad (2.70)$$

$$n^1 = \frac{dm^1}{dz}. \quad (2.71)$$

We rewrite $\nabla \cdot \boldsymbol{\Sigma}^1$ as $\nabla^2 \mathbf{u}^1$ (since we consider only Newtonian stress and we use the definition of $\boldsymbol{\Sigma}$ in equation 2.18). We then take the divergence of equation 2.69 and the Laplacian of the third component. This gives

$$0 = -\nabla^2 p_e^1 - \gamma \partial_3 n^1, \quad (2.72)$$

$$S_c^{-1} \frac{\partial}{\partial t} (\nabla^2 u_3^1) = -\partial_3 \nabla^2 p_e^1 + \nabla^2 \nabla^2 u_3^1 - \gamma \nabla^2 n^1, \quad (2.73)$$

and on putting the two together

$$S_c^{-1} \frac{\partial}{\partial t} (\nabla^2 u_3^1) = \nabla^4 u_3^1 - \gamma \nabla^2 n^1 + \gamma \partial_3 \partial_3 n^1. \quad (2.74)$$

Expanding the cell conservation equation (equation 2.70) gives

$$\begin{aligned} \frac{\partial n^1}{\partial t} = & -\partial_3 n^0 u_3^1 - \frac{dK_2}{K_1} \left[\partial_i \left((1 - \chi e^{\kappa m^0}) n^1 \right) \langle \mathbf{p} \rangle_i^0 \right. \\ & + \partial_3 \left((1 - \chi e^{\kappa m^0}) n^0 \right) \langle \mathbf{p} \rangle_3^1 + (1 - \chi e^{\kappa m^0}) n^0 \partial_i \langle \mathbf{p} \rangle_i^1 \\ & \left. - \partial_i \left(\chi \kappa m^1 e^{\kappa m^0} n^0 \right) \langle \mathbf{p} \rangle_i^0 \right] + D_{ij}^0 \partial_i \partial_j n^1 + D_{33}^1 \partial_3 \partial_3 n^0 + \partial_3 n^0 \partial_i D_{i3}^1. \end{aligned} \quad (2.75)$$

To continue, we consider the terms $\partial_i \langle \mathbf{p} \rangle_i^1$ and $\partial_i D_{i3}^1$. We know that

$$\partial_1 \omega_2 = \partial_3 \partial_1 u_1^1 - \partial_1 \partial_1 u_3^1 \quad \text{and} \quad \partial_2 \omega_1 = \partial_2 \partial_2 u_3^1 - \partial_3 \partial_2 u_2^1. \quad (2.76)$$

Because $\partial_3(\partial_i u_i^1) = 0$, $\partial_1 \omega_2 - \partial_2 \omega_1 = -\partial_i \partial_i u_3^1$ and

$$\begin{aligned} \partial_1 e_{13} + \partial_2 e_{23} &= \frac{1}{2}(\partial_3 \partial_1 u_1^1 + \partial_1 \partial_1 u_3^1 + \partial_3 \partial_2 u_2^1 + \partial_2 \partial_2 u_3^1) \\ &= \frac{1}{2}(-\partial_3 \partial_3 u_3^1 + \partial_1 \partial_1 u_3^1 + \partial_2 \partial_2 u_3^1) \\ &= \frac{1}{2} \nabla^2 u_3^1 - \partial_3 \partial_3 u_3^1. \end{aligned} \quad (2.77)$$

From the solution for the Fokker-Planck equation in equations 2.38 and 2.40 (with rearrangement) we have

$$\partial_i \langle \mathbf{p} \rangle_i^1 = -\eta(J_1 + \alpha_0 J_4) \nabla^2 u_3^1 + \eta \alpha_0 (2J_4 - 3K_4) \partial_3 \partial_3 u_3^1, \quad (2.78)$$

$$\partial_i D_{i3}^1 = -\eta(J_2 - J_1 K_1 + \alpha_0(J_5 - K_1 J_4)) \nabla^2 u_3^1 \quad (2.79)$$

$$+ \eta \alpha_0 (2(J_5 - K_1 J_4) - 3(K_5 - 2K_1 K_4)) \partial_3 \partial_3 u_3^1. \quad (2.80)$$

We define the functions H_i as

$$H_1 = -\eta(J_1 + \alpha_0 J_4), \quad (2.81)$$

$$H_2 = \eta \alpha_0 (2J_4 - 3K_4), \quad (2.82)$$

$$H_3 = -\eta(J_2 - J_1 K_1 + \alpha_0(J_5 - K_1 J_4)), \quad (2.83)$$

$$H_4 = \eta \alpha_0 (2(J_5 - K_1 J_4) - 3(K_5 - 2K_1 K_4)), \quad (2.84)$$

which gives

$$\partial_i \langle \mathbf{p} \rangle_i^1 = H_1 \nabla^2 u_3^1 + H_2 \partial_3 \partial_3 u_3^1, \quad (2.85)$$

$$\partial_i D_{i3}^1 = H_3 \nabla^2 u_3^1 + H_4 \partial_3 \partial_3 u_3^1. \quad (2.86)$$

Substituting equations 2.85 and 2.86 into equation 2.75 gives

$$\begin{aligned} \frac{\partial n^1}{\partial t} &= \left\{ -\partial_3 n^0 + \left[\partial_3 n^0 H_3 - \frac{dK_2}{K_1} (1 - \chi e^{\kappa m^0}) n^0 H_1 \right] \nabla^2 \right. \\ &+ \left[\partial_3 n^0 H_4 - \frac{dK_2}{K_1} (1 - \chi e^{\kappa m^0}) n^0 H_2 \right] \partial_3 \partial_3 \\ &+ 3\alpha_0 \eta \left[\partial_3 \left(\frac{dK_2}{K_1} (1 - \chi e^{\kappa m^0}) n^0 \right) K_4 - (K_5 - 2K_1 K_4) \partial_3^2 n^0 \right] \partial_3 \left. \right\} u_3^1 \\ &+ \left\{ \frac{K_1}{\lambda} (\partial_1 \partial_1 + \partial_2 \partial_2) + K_2 \partial_3 \partial_3 \frac{dK_2}{K_1} K_1 \left[(1 - \chi e^{\kappa m^0}) \partial_3 + \partial_3 (1 - \chi e^{\kappa m^0}) \right] \right\} n^1 \\ &+ dK_2 \chi \kappa \partial_3 (m^1 e^{\kappa m^0} n^0). \end{aligned} \quad (2.87)$$

Equations 2.74 and 2.87 are two equations in two unknowns, the independent variables u_3^1 and n^1 . We introduce sinusoidal perturbations in x and y and an exponential component in t by choosing the normal modes

$$u_3^1 = U(z) e^{i(lx+my)+\sigma t}, \quad n^1 = \Phi(z) e^{i(lx+my)+\sigma t}, \quad m^1 = M(z) e^{i(lx+my)+\sigma t}, \quad (2.88)$$

where σ is the growth rate of the perturbation and $k = \sqrt{l^2 + m^2}$ is the wavenumber. This non-dimensional wavenumber is related to the non-dimensional wavelength via $\lambda = \frac{2\pi}{k}$. Substituting these modes into equation 2.74 gives

$$\left(\frac{\sigma}{S_c} + k^2 - \frac{d^2}{dz^2}\right) \left(k^2 - \frac{d^2}{dz^2}\right) U = -Rd^{-1}k^2\Phi, \quad (2.89)$$

where the Rayleigh number R is defined by

$$R = \gamma d = \frac{Nvg\Delta\rho H^4 K_1}{\nu\rho V_n^3 \tau^2 K_2} \quad (2.90)$$

and can be thought of as a ratio of the buoyancy forces that drive the instability to the viscous forces that inhibit it. R is based on the depth of the full fluid layer as in Hill *et al.* 1989 [63]. Since N is chosen to be the same as in Bees and Hill 1998 [9], R is also the same as R in [9], except with average cell swimming speed defined as V_n instead of V_s . Substituting the normal modes in equation 2.88 into the cell conservation equation 2.87 gives

$$\begin{aligned} & \left(P_V \frac{d^2}{dz^2} - P_H k^2 - \sigma - dP_V \left[(1 - \chi e^{\kappa m^0}) \frac{d}{dz} + \frac{d}{dz} (1 - \chi e^{\kappa m^0}) \right] \right) \Phi \quad (2.91) \\ & + dP_V \frac{d}{dz} \left(\chi \kappa e^{\kappa m^0} n^0 M(z) \right) = \left\{ \frac{d}{dz} n^0 - \eta \left[A_1 \frac{d}{dz} n^0 + \frac{dK_2}{K_1} A_2 (1 - \chi e^{\kappa m^0}) n^0 \right] \frac{d^2}{dz^2} \right. \\ & - \eta \left[\frac{dK_2}{K_1} A_3 \frac{d}{dz} \left((1 - \chi e^{\kappa m^0}) n^0 \right) - A_4 \frac{d^2}{dz^2} n^0 \right] \frac{d}{dz} \\ & \left. + \left[A_5 \frac{d}{dz} n^0 - \frac{dK_2}{K_1} A_6 (1 - \chi e^{\kappa m^0}) n^0 \right] \eta k^2 \right\} U(z), \end{aligned}$$

where the definitions for the H_i from equations 2.81 - 2.84 are substituted back in and we define new constants

$$P_V = K_2, \quad (2.92)$$

$$P_H = \frac{K_1}{\lambda}, \quad (2.93)$$

$$A_1 = J_1 K_1 - J_2 + \alpha_0 (-J_5 + K_1 J_4 + 2(J_5 - K_1 J_4) - 3(K_5 - 2K_1 K_4)), \quad (2.94)$$

$$A_2 = J_1 - \alpha_0 (J_4 - 3K_4), \quad (2.95)$$

$$A_3 = 3\alpha_0 K_4, \quad (2.96)$$

$$A_4 = 3\alpha_0 (K_5 - 2K_1 K_4), \quad (2.97)$$

$$A_5 = -(J_2 - J_1 K_1 + \alpha_0 (J_5 - K_1 J_4)), \quad (2.98)$$

$$A_6 = -J_1 - \alpha_0 J_4. \quad (2.99)$$

To make comparisons between this expression and that of the gyrotaxis only case in Bees and Hill [9] we write equation 2.91 as

$$\begin{aligned} & \left(P_V \frac{d^2}{dz^2} - P_H k^2 - \sigma - P_V dP_Q(z) \frac{d}{dz} + 2P_V d\chi\kappa P_R(z) \right) \Phi(z) + P_V d\chi\kappa P_M(z) M(z) \\ & = \left(\frac{dn^0}{dz} - \eta P_5(z; d) \frac{d^2}{dz^2} - \eta P_6(z; d) \frac{d}{dz} + \eta P_7(z; d) k^2 \right) U(z), \end{aligned} \quad (2.100)$$

and we use the same labels, P_i , but now allow them to be functions of z , such that

$$P_Q(z) = \left(1 - \chi e^{\kappa m^0} \right), \quad (2.101)$$

$$P_R(z) = e^{\kappa m^0} n^0, \quad (2.102)$$

$$P_M(z) = e^{\kappa m^0} \left(\frac{dn^0}{dz} + \kappa (n^0)^2 \right), \quad (2.103)$$

$$P_5(z; d) = A_1 \frac{dn^0}{dz} + \frac{dK_2}{K_1} A_2 \left(1 - \chi e^{\kappa m^0} \right) n^0, \quad (2.104)$$

$$\begin{aligned} P_6(z; d) &= \frac{dK_2}{K_1} A_3 \frac{d}{dz} \left(\left(1 - \chi e^{\kappa m^0} \right) n^0 \right) - A_4 \frac{d^2}{dz^2} n^0 \\ &= \frac{dK_2}{K_1} A_3 \left[-\chi \kappa e^{\kappa m^0} (n^0)^2 + \left(1 - \chi e^{\kappa m^0} \right) \frac{dn^0}{dz} \right] - A_4 \frac{d^2 n^0}{dz^2}, \end{aligned} \quad (2.105)$$

$$P_7(z; d) = A_5 \frac{dn^0}{dz} - \frac{dK_2}{K_1} A_6 \left(1 - \chi e^{\kappa m^0} \right) n^0, \quad (2.106)$$

where $n^0 = n^0(z)$ and $m^0 = m^0(z)$. At $\chi = 0$ these equations are exactly the same as the linear stability equations in [9] for the gyrotaxis only case, and can be used to verify numerical results for this case by directly comparing neutral curves. The new terms on the left hand side, compared to [9], are those involving $P_R(z)$ and $P_M(z)$. The no-flow boundary condition $\mathbf{u} = \mathbf{0}$ on $z = 0, -1$ becomes

$$U = 0, \quad \frac{dU}{dz} = 0 \quad \text{on} \quad z = 0, -1. \quad (2.107)$$

The no-flux boundary conditions 2.49 become

$$\frac{d\Phi}{dz} - d(1 - \chi) \Phi = 0 \quad \text{on} \quad z = 0 \quad \text{and} \quad (2.108)$$

$$\frac{d\Phi}{dz} - d \left(1 - \chi e^{\kappa m^0} \right) \Phi + d\kappa \chi e^{\kappa m^0} n^0 M = 0 \quad \text{on} \quad z = -1. \quad (2.109)$$

The boundary condition for M in equation 2.50 becomes

$$M = 0 \quad \text{at} \quad z = 0. \quad (2.110)$$

The linear stability equations can be solved numerically or asymptotically in restricted parameter ranges. Typical values of A_1 to A_6 , P_H and P_V are shown in Table 2.3.

Name	Definition	Value
A_1	$J_1 K_1 - J_2 + \alpha_0(-J_5 + K_1 J_4 + 2(J_5 - K_1 J_4) - 3(K_5 - 2K_1 K_4))$	0.0977
A_2	$J_1 - \alpha_0(J_4 - 3K_4)$	0.442
A_3	$3\alpha_0 K_4$	-0.06
A_4	$3\alpha_0(K_5 - 2K_1 K_4)$	0.0054
A_5	$-(J_2 - J_1 K_1 + \alpha_0(J_5 - K_1 J_4))$	0.0929
A_6	$-J_1 - \alpha_0 J_4$	-0.398
P_V	K_2	0.16
P_H	$\frac{K_1}{\lambda}$	0.26

Table 2.3: Values and definitions of constants A_i , P_V and P_H when $\lambda = 2.2$ and $\alpha_0 = 0.2$.

2.4 Asymptotic analysis in Model A for weak illumination and large layer depth

In this section, we perform an asymptotic analysis for a deep layer, $d^{-1} \ll 1$, and a small value of χ , using similar techniques to Bees and Hill [9]. This allows us to learn more about which terms dominate in the linear stability equations and can be used as a check for the numerical code. What does large d mean physically? Using standard parameter values from Table 2.1 we find $d \approx 435H$ (or $d \approx 113H$ for $\tau = 5$). For an average experimental depth of 4 mm, $d = 174$, which is sufficiently large to be used in the expansions for large d . Shallow layers are not investigated, because although numerical solutions could be verified in this way it is not a realistic parameter ($d = 0.1$ would give $H = 2.3\mu\text{m}$, which is much smaller than any experimental depth). van Dyke 1964 [169] presents a full description of the ideas involved in this analysis, where an outer solution far from the upper boundary is matched to an inner solution.

We consider the case when $\sigma = 0$, $k \sim 1$, $d^{-1} \ll 1$ and $\chi \ll 1$, so that illumination is weak. We write $\chi = \chi_{-1} d^{-1}$, where χ_{-1} is order 1. Since χ is small this analysis is similar to that of Bees and Hill [9] up to third order, so the gyrotaxis parameter is of the order d^n and P_V, P_H, P_5, P_6 and P_7 are constants, not dependent on z , assumed to be order one up to third order. This is valid as long as d is sufficiently large.

First, an asymptotic equilibrium solution for equation 2.54 must be found, after which the asymptotic solutions for the linear stability equations 2.89 and 2.100 with boundary conditions 2.107 to 2.110 are calculated for outer and inner solutions. These are then

matched, and an expression for the Rayleigh number as a function of wavenumber $R(k)$ is found. Note that the asymptotic equilibrium solution calculated in Section 2.4.1 is not the same as the analytic equilibrium solution calculated in Section 2.3.3, since the latter was for the case of weak absorption, $\kappa \ll 1$, and the solution required in this analysis is for a deep layer with weak illumination, $d \gg 1$ and $\chi \ll 1$.

2.4.1 Equilibrium solution

Multiplying the equilibrium equation 2.54 by d^{-1} and writing $\chi = \chi_{-1}d^{-1}$ gives

$$d^{-1} \frac{d^2 m}{dz^2} + (d^{-1} \chi_{-1} e^{\kappa m} - 1) \frac{dm}{dz} = 0, \quad (2.111)$$

with boundary conditions $m = 0$ at $z = 0$ and $m = \frac{e^{-d}-1}{d}$ at $z = -1$. χ does not appear at leading order. For the **outer** solution, we expand m in powers of d^{-1} , so that $m = m_0 + d^{-1}m_{-1} + d^{-2}m_{-2} + O(d^{-3})$. At leading order

$$-m'_0 = 0, \quad (2.112)$$

where prime denotes differentiation with respect to z . Solving gives $m_0 = \text{constant}$. At the next order

$$\frac{d^2 m_0}{dz^2} + \chi_{-1} e^{\kappa m_0} m'_0 - m'_{-1} = 0, \quad (2.113)$$

which gives $m_{-1} = \text{constant}$. Proceeding in this way we see that all the m_{-n} will be constants. We assume that d is sufficiently large that e^{-d} is small and then, since $m = -d^{-1}$ at $z = -1$, we have that $m_{-1} = -1$ and $m_0 = m_{-2} = m_{-n} = 0$.

For the **inner** solution we scale $z_I = dz$ to magnify the top region of the fluid and write the equilibrium equation as

$$m'' + (d^{-1} \chi_{-1} e^{\kappa m} - 1) m' = 0. \quad (2.114)$$

We expand m in powers of d ,

$$m = \sum_{n=0}^{\infty} d^{-n} m_{-n}, \quad (2.115)$$

and, on expanding the exponential, we find the solution at leading order is

$$m_0 = A_0(e^{z_I} - 1) \quad (2.116)$$

and at the next order

$$m''_{-1} + \chi_{-1} e^{\kappa m_0} m'_0 - m'_{-1} = 0. \quad (2.117)$$

On matching the inner and outer solutions up to second order we consider the intermediate region such that $z_\zeta \sim 1$ as $d^{-1} \rightarrow 0$, where $z_\zeta = \frac{z}{\zeta(d^{-1})}$ and $\zeta(d^{-1}) \rightarrow 0$ as $d^{-1} \rightarrow 0$ and satisfies $0 < d^{-1} \ll \zeta \ll 1 \ll d$. Expanding the outer solution gives

$$m = -d^{-1} + O(d^{-1}e^{-d}), \quad (2.118)$$

and expanding the inner solution using $z_\zeta = z_I \frac{d^{-1}}{\zeta}$ gives

$$m = A_0(e^{d\zeta z_\zeta} - 1) + d^{-1}m_{-1} + O(d^{-2}) + \dots O(d^{-1}e^{-d}) + \dots \quad (2.119)$$

This leads to $A_0 = 0$ (since there is no $O(1)$ part of the outer solution), so we solve equation 2.117 to give $m_{-1} = A_1(e^{z_I} - 1)$. The matching condition gives $A_1 = 1$. At next order

$$m''_{-2} - m'_{-2} + \chi_{-1}e^{\kappa m_0}m'_{-1} + \chi_{-1}e^{\kappa m_0}m'_0 = 0. \quad (2.120)$$

Hence, we use the integrating factor e^{-z_I} to solve equation 2.120 for m_{-2} such that

$$m'_{-2}e^{-z_I} = -\chi_{-1}z_I + B_2, \text{ hence} \quad (2.121)$$

$$m_{-2} = -\chi_{-1}(z_I - 1)e^{z_I} + B_2e^{z_I} - A_2. \quad (2.122)$$

To find the constants we can apply the boundary condition that $m = 0$ at $z_I = 0$, which gives

$$\chi_{-1} + B_2 - A_2 = 0. \quad (2.123)$$

To find the other constant we can then match to the outer solution at third order, which we know just gives $m = 0$, so

$$A_2 = 0, \quad (2.124)$$

hence $B_2 = -\chi_{-1}$, and

$$m_{-2} = -\chi_{-1}z_Ie^{z_I}. \quad (2.125)$$

2.4.2 Linear Stability Analysis

As in linear stability analysis in Section 2.3.5, the equilibrium components from Section 2.4.1 are now denoted with a superscript 0. Writing equations 2.89 and 2.100 so that terms can be expanded for large d and small κ , with $\sigma = 0$, gives

$$(D^2 - k^2)^2U = -k^2d^{-1}R\Phi, \quad (2.126)$$

and

$$\begin{aligned}
& \left(P_V D^2 - P_H k^2 - P_V d \left(1 - \chi e^{\kappa m^0} \right) D + 2P_V G \chi \kappa e^{\kappa m^0} \frac{dm^0}{dz} \right) \Phi \quad (2.127) \\
& + \left(P_V d \chi \kappa e^{\kappa m^0} \left(\frac{dn^0}{dz} + \kappa n^0 \frac{dm^0}{dz} \right) \right) M = \left[\frac{dn^0}{dz} - \eta \left(A_1 \frac{dn^0}{dz} \right. \right. \\
& + \frac{dK_2}{K_1} A_2 \left(1 - \chi e^{\kappa m^0} \right) n^0 \left. \right) D^2 - \eta \left(\frac{dK_2}{K_1} A_3 \left[-\chi \kappa e^{\kappa m^0} \frac{dm^0}{dz} n^0 \right. \right. \\
& + \left. \left. \left(1 - \chi e^{\kappa m^0} \right) \frac{dn^0}{dz} \right] - A_4 \frac{d^2 n^0}{dz^2} \right) D \\
& \left. + \eta \left(A_5 \frac{dn^0}{dz} - \frac{dK_2}{K_1} A_6 \left(1 - \chi e^{\kappa m^0} \right) n^0 \right) k^2 \right] U.
\end{aligned}$$

Outer solution

We use the equilibrium solution from the outer solution, which was simply $m^0 = -d^{-1}$ (since e^{-d} will be exponentially small). Since $\frac{dm^0}{dz} = n^0$, n^0 and any further derivatives are zero. This simplifies the cell conservation equation so that we have

$$\left(P_V D^2 - P_H k^2 - P_V d \left(1 - d^{-1} \chi_{-1} e^{-\kappa d^{-1}} \right) D \right) \Phi = 0. \quad (2.128)$$

Note that this has the same form as in Bees and Hill [9] where it is assumed that e^{dz} is infinitesimally small. Expanding for d large gives

$$\left(P_V D^2 - P_H k^2 - P_V d \left(1 - d^{-1} \chi_{-1} \left(1 - d^{-1} \kappa + \frac{d^{-2} \kappa^2}{2} - \dots \right) \right) D \right) \Phi = 0. \quad (2.129)$$

If we expand Φ in powers of d^{-1} then at leading order

$$-P_V D \Phi_0 = 0, \quad \text{hence } \Phi_0 = \text{constant}. \quad (2.130)$$

Using our boundary condition 2.109 on $z = -1$ we have that, since $n^0 = 0$,

$$\frac{d\Phi}{dz} - d \left(1 - d^{-1} \chi_{-1} e^{-\kappa} \right) \Phi = 0. \quad (2.131)$$

At leading order this gives $\Phi_0 = 0$. At the next order

$$P_V D^2 \Phi_0 - P_H k^2 \Phi_0 - P_V D \Phi_{-1} + P_V \chi_{-1} D \Phi_0 = 0, \quad (2.132)$$

so that $\Phi_{-1} = 0$, using the boundary condition. At the next order

$$P_V D^2 \Phi_{-1} - P_H k^2 \Phi_{-1} - P_V D \Phi_{-2} - \kappa \chi_{-1} P_V D \Phi_0 + P_V \chi_{-1} \chi_{-1} D \Phi_{-1} = 0, \quad (2.133)$$

which also gives $\Phi_{-2} = 0$. In this way we can see that all the components of Φ are going to be zero, since the previous two components are zero, which will always lead to $\Phi_{-n} = 0$.

Using this in the Navier Stokes equation 2.126 gives

$$(D^2 - k^2)^2 U = 0, \quad (2.134)$$

with $U = DU = 0$ on $z = -1$, which has solution

$$U = -kA(z+1) \cosh k(z+1) + (A+B(z+1)) \sinh k(z+1), \quad (2.135)$$

where A and B are constants that can be expanded in terms of d^{-1} . Note that this outer solution is exactly the same as in Bees and Hill [9], which is as expected because in both cases the concentration is very small, or zero, in the outer region due to an almost exponential profile near the upper boundary.

Inner solution

For the inner solution we re-scale $z_I = dz$ to give the main model equations 2.126 and 2.127 as

$$(D_I^2 - d^{-2}k^2)^2 U = -k^2 d^{-5} R \Phi, \quad (2.136)$$

and

$$\begin{aligned} & \left(P_V D_I^2 - P_V \left(1 - \chi e^{\kappa m^0} \right) D_I - P_H k^2 d^{-2} + 2P_V d^{-1} \chi \kappa e^{\kappa m^0} n^0 \right) \Phi \quad (2.137) \\ & + \left(P_V d^{-1} \chi \kappa e^{\kappa m^0} \left(d \frac{dn^0}{dz_I} + \kappa (n^0)^2 \right) \right) M \\ & = \left\{ d^{-1} \frac{dn^0}{dz_I} - d\eta \left(A_1 \frac{dn^0}{dz_I} + \frac{K_2}{K_1} A_2 \left(1 - \chi e^{\kappa m^0} \right) n^0 \right) D_I^2 \right. \\ & - \eta \left(\frac{K_2}{K_1} A_3 \left[-\chi \kappa e^{\kappa m^0} (n^0)^2 + d \left(1 - \chi e^{\kappa m^0} \right) \frac{dn^0}{dz_I} \right] - dA_4 \frac{d^2 n^0}{dz_I^2} \right) D_I \\ & \left. + \eta d^{-1} \left(A_5 \frac{dn^0}{dz_I} - \frac{K_2}{K_1} A_6 \left(1 - \chi e^{\kappa m^0} \right) n^0 \right) k^2 \right\} U. \end{aligned}$$

For the inner equilibrium solution in the variable z_I ,

$$m^0 = d^{-1} (e^{z_I} - 1) - d^{-2} \chi_{-1} z_I e^{z_I} + O(d^{-3}). \quad (2.138)$$

Thus

$$n^0 = d \frac{dm^0}{dz_I} = e^{z_I} - d^{-1} \chi_{-1} (z_I e^{z_I} + e^{z_I}) + O(d^{-2}), \quad (2.139)$$

$$\frac{dn^0}{dz_I} = e^{z_I} - d^{-1} \chi_{-1} (z_I e^{z_I} + 2e^{z_I}) + O(d^{-2}), \quad (2.140)$$

$$\frac{d^2 n^0}{dz_I^2} = e^{z_I} - d^{-1} \chi_{-1} (z_I e^{z_I} + 3e^{z_I}) + O(d^{-2}). \quad (2.141)$$

We expand the exponential $e^{\kappa m^0}$,

$$e^{\kappa m^0} = e^{\kappa d^{-1} (e^{z_I} - 1) - \kappa d^{-2} \chi_{-1} (z_I e^{z_I})} = e^{\kappa d^{-1} (e^{z_I} - 1)} e^{-d^{-2} \chi_{-1} \kappa z_I e^{z_I}} + h.o.t., \quad (2.142)$$

and expanding again in powers of d^{-1} gives

$$e^{\kappa m^0} \approx 1 + d^{-1}\kappa(e^{z_I} - 1) + d^{-2}\kappa\left(\frac{\kappa}{2}(e^{z_I} - 1)^2 - \chi_{-1}z_I e^{z_I}\right) \quad (2.143)$$

$$+ d^{-3}\left(\frac{\kappa^3(e^{z_I} - 1)^3}{6} - \kappa^2\chi_{-1}z_I e^{z_I}(e^{z_I} - 1)\right) + O(d^{-3}).$$

Substituting these expressions into equation 2.137 and re-writing by collecting terms of each order in d together (separately on each side) gives

$$(P_V D_I^2 - P_V D_I) \Phi + d^{-1} [P_V \chi_{-1} D_I \Phi + P_V \chi_{-1} \kappa e^{z_I} M] \quad (2.144)$$

$$+ d^{-2} [-P_H k^2 \Phi + P_V \chi_{-1} \kappa (e^{z_I} - 1) D_I \Phi + 2P_V \chi_{-1} \kappa e^{z_I} \Phi$$

$$+ P_V \kappa \chi_{-1} (\kappa e^{2z_I} - \chi_{-1} (z_I e^{z_I} + 2e^{z_I}) + \kappa e^{z_I} (e^{z_I} - 1)) M]$$

$$+ d^{-3} [P_V \chi_{-1} \kappa \left(\frac{\kappa}{2}(e^{z_I} - 1)^2 - \chi_{-1} z_I e^{z_I}\right) D_I \Phi + 2P_V \chi_{-1} \kappa (\kappa e^{z_I} (e^{z_I} - 1)$$

$$- \chi_{-1} (z_I e^{z_I} + e^{z_I})) \Phi + P_V \kappa \chi_{-1} \left(\kappa e^{z_I} \left(\frac{\kappa}{2}(e^{z_I} - 1)^2 - \chi_{-1} z_I e^{z_I}\right)$$

$$+ \kappa (e^{z_I} - 1) (\kappa e^{2z_I} - \chi_{-1} (z_I e^{z_I} + 2e^{z_I})) - 2\kappa \chi_{-1} e^{z_I} (z_I e^{z_I} + e^{z_I})\right) M] + h.o.t$$

$$= -\eta d e^{z_I} [P_5 D_I^2 + P_6 D_I] U + \eta \chi_{-1} [(z_I e^{z_I} + 2e^{z_I}) P_5 D_I^2 + (z_I e^{z_I} + 3e^{z_I}) P_6 D_I] U$$

$$+ d^{-1} \left[e^{z_I} + \eta \chi_{-1} \frac{K_2 A_2}{K_1} (\kappa e^{z_I} (e^{z_I} - 1) - \chi_{-1} (z_I e^{z_I} + e^{z_I})) D_I^2 \right.$$

$$\left. + \eta \chi_{-1} \frac{K_2 A_3}{K_1} (\kappa e^{2z_I} + \kappa e^{z_I} (e^{z_I} - 1) - \chi_{-1} (z_I e^{z_I} + 2e^{z_I})) D_I + \eta k^2 e^{z_I} P_7 \right] U$$

$$+ d^{-2} \left[-\chi_{-1} (z_I e^{z_I} + 2e^{z_I}) + \eta \chi_{-1} \left(\frac{K_2 A_2}{K_1} \left(\kappa \left(\frac{\kappa}{2} (e^{z_I} - 1)^2 - \chi_{-1} z_I e^{z_I} \right) e^{z_I} \right. \right.$$

$$\left. - \kappa \chi_{-1} (e^{z_I} - 1) (z_I e^{z_I} + e^{z_I}) \right) D_I^2$$

$$\left. + \frac{K_2 A_3}{K_1} \left(\kappa^2 e^{2z_I} (e^{z_I} - 1) - 2\chi_{-1} \kappa e^{z_I} (z_I e^{z_I} + e^{z_I}) + \kappa e^{z_I} \left(\frac{\kappa}{2} (e^{z_I} - 1)^2 - \chi_{-1} z_I e^{z_I} \right) \right. \right.$$

$$\left. - \kappa \chi_{-1} (e^{z_I} - 1) (z_I e^{z_I} + 2e^{z_I}) \right) D_I - k^2 (z_I e^{z_I} + 2e^{z_I}) P_7 \right] U.$$

The boundary conditions for the inner solution become

$$U = 0 \quad \text{and} \quad D_I U = 0 \quad \text{on} \quad z_I = 0, \quad (2.145)$$

$$D_I \Phi - (1 - d^{-1} \chi_{-1}) \Phi = 0 \quad \text{on} \quad z_I = 0. \quad (2.146)$$

As in Bees and Hill [9] for the gyrotaxis only case, equation 2.136 implies that for a non-trivial solution $R \sim d^5 U$, and we examine the parameter space where the right hand side of equation 2.144 does not appear at leading order. This requires $U \leq O(1)$ and $\eta U \leq O(d^{-2})$ to eliminate the first two terms on the right hand side and, since the rest of the terms are at most order d^{-1} , they will also not appear. Since we are looking for solutions $\sigma = 0$, we expect there to be a self-consistent region where the model is valid. If

we consider terms at third order then if none of the terms on the right hand side appear we will obtain $P_H k^2 = 0$, which is not useful. If any terms appear before third order then we will obtain $R = 0$ or $\eta = 0$, which is again unhelpful. Although these results are not obvious at first glance they are quickly found by solving using the boundary conditions. Thus we need terms at third order and not before and so we consider $U \approx d^{-n}$ where $n = 1, 2, 3, \dots$ and write

$$U = \sum_{m=n}^{\infty} U_{-m} d^{-m}, \quad \Phi = \sum_{m=0}^{\infty} \Phi_{-m} d^{-m}, \quad M = \sum_{m=0}^{\infty} M_{-m} d^{-m}, \quad (2.147)$$

and

$$R = d^{5-n} R_{5-n} + d^{5-n-1} R_{5-n-1} + \dots \quad (2.148)$$

To first order equation 2.136 gives

$$D_I^4 U_{-n} + R_{5-n} k^2 \Phi_0 = 0 \quad (2.149)$$

and equation 2.144 gives

$$P_V D_I (D_I - 1) \Phi_0 = 0, \quad (2.150)$$

with boundary condition on $z = 0$ at order one as

$$D_I \Phi_0 - \Phi_0 = 0. \quad (2.151)$$

Solving equation 2.150 with this boundary condition gives

$$\Phi_0 = e^{z_I} \quad (2.152)$$

and substituting this into equation 2.149 gives

$$U_{-n} = a_{-n} z_I^3 + b_{-n} z_I^2 + R_{5-n} k^2 (z_I + 1 - e^{z_I}). \quad (2.153)$$

Since $d \frac{dM}{dz_I} = \Phi$ then

$$\frac{dM_0}{dz_I} = \frac{e^{z_I}}{d}, \quad \text{hence } M_0 = d^{-1} (e^{z_I} - 1) \quad (2.154)$$

and M_0 will appear at a higher order than Φ_0 as it is multiplied by d^{-1} from the scaling for z_I . At second order equations 2.136 and 2.144 become

$$D^4 U_{-n-1} + k^2 R_{5-n} \Phi_{-1} + k^2 R_{5-n-1} \Phi_0 = 0 \quad (2.155)$$

and

$$P_V D_I (D_I - 1) \Phi_{-1} + P_V \chi_{-1} D_I \Phi_0 = 0, \quad (2.156)$$

where the M_0 term in equation 2.144 is omitted because it is a higher order than Φ_0 . This has solutions

$$\Phi_{-1} = -\chi_{-1} z_I e^{z_I} + B e^{z_I}, \quad \text{and} \quad (2.157)$$

$$U_{-n-1} = a_{-n-1} z_I^3 + b_{-n-1} z_I^2 + k^2 R_{5-n-1} (z_I + 1 - e^{z_I}) \quad (2.158)$$

$$+ k^2 R_{5-n} (\chi_{-1} (z_I e^{z_I} - 4e^{z_I}) - B e^{z_I} + (3\chi_{-1} + B) z_I + 4\chi_{-1} + B).$$

where B is a constant of integration. As before, to match the inner and outer solutions up to second order we consider the intermediate region such that $z_\zeta \sim 1$ as $d^{-1} \rightarrow 0$, where $z_\zeta = \frac{z}{\zeta(d^{-1})}$ and $\zeta(d^{-1}) \rightarrow 0$ as $d^{-1} \rightarrow 0$, and satisfies $0 < d^{-1} \ll \zeta \ll 1 \ll d$. If we expand the inner solution by writing $z_\zeta = z_I \frac{d^{-1}}{\zeta}$, then writing the terms in order of size

$$U = d^{-n+2} [\zeta^3 da_{-n} z_\zeta^3 + \zeta^2 b_{-n} z_\zeta^2 + \zeta^3 a_{-n-1} z_\zeta^3 + d^{-1} z_\zeta \zeta R_{5-n} k^2 + d^{-1} \zeta^2 b_{-n-1} z_\zeta^2] \quad (2.159)$$

$$+ O(d^{-n}, \zeta^4 d^{-n}).$$

For the outer solution we expand by writing $z = \zeta z_\zeta$, so

$$U = d^{-\xi} \left[-k \cosh k A_{-\xi} + \sinh k A_{-\xi} + \sinh k B_{-\xi} + (-k^2 \sinh k A_{-\xi} \right. \quad (2.160)$$

$$+ \sinh k B_{-\xi} + k \cosh k B_{-\xi}) \zeta z_\zeta + \left(-k^3 \frac{\cosh k}{2} A_{-\xi} - k^2 \frac{\sinh k}{2} A_{-\xi} \right. \quad (2.161)$$

$$\left. + k^2 \frac{\sinh k}{2} B_{-\xi} + k \cosh k B_{-\xi} \right) \zeta^2 z_\zeta^2 \Big] + \text{h.o.t.}$$

We proceed by matching terms in z_ζ . If we try and match any of the first three terms in the inner solution then at least the first two terms of the outer solution will have to be zero, which leads to the trivial solution. This leads us to conclude that $a_{-n} = a_{-n-1} = b_{-n} = 0$ and we match the fourth term in the inner solution, which implies $\xi = n - 1$ and

$$(A_{-n+1} + B_{-n+1}) \sinh k - k A_{-n+1} \cosh k = 0, \quad (2.161)$$

$$B_{-n+1} \sinh k + B_{-n+1} k \cosh k - k^2 A_{-n+1} \sinh k = k^2 R_{5-n}, \quad (2.162)$$

$$-k^3 \frac{\cosh k}{2} A_{-n+1} - k^2 \frac{\sinh k}{2} A_{-n+1} + k^2 \frac{\sinh k}{2} B_{-n+1} \quad (2.163)$$

$$+ k \cosh k B_{-n+1} = b_{-n-1}.$$

We proceed by looking in the region of parameter space where $\eta \sim d^{-2}$ and $n = 1$, since this is the most general region of parameter space, as shown by Bees and Hill [9]. The cell

conservation equation at third order in equation 2.144 becomes

$$\begin{aligned} & P_V D_I (D_I - 1) \Phi_{-2} + P_V \chi_{-1} D_I \Phi_{-1} + P_V \chi_{-1} \kappa e^{z_I} M_0 - P_H k^2 \Phi_0 + P_V \chi_{-1} \kappa (e^{z_I} - 1) D_I \Phi_0 \\ & + 2P_V \chi_{-1} \kappa e^{z_I} \Phi_0 = e^{z_I} U_{-1} - \eta_{-2} e^{z_I} (P_5 D_I^2 + P_6 D_I) U_{-1}. \end{aligned}$$

M is a higher order than Φ and so the M term in equation 2.144 for d^{-1} is used, and for d^{-2} is omitted. To obtain the solvability condition we integrate from $-\infty$ to 0 which gives

$$R_4 = \frac{2P_H}{(1 - \eta_{-2}(P_5 - P_6))}, \quad (2.164)$$

where

$$P_5 = A_1 + \frac{K_2 A_2}{K_1} \quad \text{and} \quad P_6 = \frac{K_2 A_3}{K_1} - A_4. \quad (2.165)$$

The asymptotics break down for sufficiently large $\eta_{-2}(P_5 - P_6)$. This expression, at third order, is the same as in the gyrotaxis case in Bees and Hill [9], since the effects of phototaxis through the χ term have not yet appeared. Solving for the constants in equations 2.161, 2.162 and 2.163 gives

$$A_0 = \frac{R_4 k^2 \sinh k}{k^2 - \sinh^2 k}, \quad (2.166)$$

$$B_0 = \frac{k^2 R_4 (k \cosh k - \sinh k)}{k^2 - \sinh^2 k}, \quad (2.167)$$

$$b_{-2} = \frac{k^3 R_4 (k - \cosh k \sinh k)}{k^2 - \sinh^2 k}. \quad (2.168)$$

At fourth order the cell conservation equation is

$$\begin{aligned} & (P_V D_I^2 - P_V D_I) \Phi_{-3} + P_V \chi_{-1} D_I \Phi_{-2} + P_V \chi_{-1} \kappa e^{z_I} M_{-1} - P_H k^2 \Phi_{-1} \\ & + P_V \kappa \chi_{-1} (e^{z_I} - 1) D_I \Phi_{-1} + 2P_V \chi_{-1} \kappa e^{z_I} \Phi_{-1} + P_V \chi_{-1} \kappa (2\kappa e^{2z_I} \\ & - \chi_{-1} (z_I e^{z_I} + 2e^{z_I}) - \kappa e^{z_I}) M_0 + P_V \kappa \chi_{-1} \left(\frac{\kappa}{2} (e^{2z_I} - 2e^{z_I} + 1) - \chi_{-1} z_I e^{z_I} \right) D_I \Phi_0 \\ & + 2P_V \chi_{-1} \kappa (\kappa e^{2z_I} - \kappa e^{z_I} - \chi_{-1} (z_I e^{z_I} + e^{z_I})) \Phi_0 \\ & = e^{z_I} U_{-2} - \chi_{-1} (z_I e^{z_I} + 2e^{z_I}) U_{-1} - \eta_{-2} e^{z_I} [P_5 D_I^2 + P_6 D_I] U_{-2} \\ & + \eta \chi_{-1} ((z_I e^{z_I} + 2e^{z_I}) P_5 D_I^2 + (z_I e^{z_I} + 3e^{z_I}) P_6 D_I) U_{-1}, \end{aligned} \quad (2.169)$$

where we recalculate M_{-1} from the new expression for Φ_{-1} as

$$M_{-1} = \chi_{-1} e^{z_I} (1 - z_I) + B e^{z_I} - B - \chi_{-1}. \quad (2.170)$$

To get the solvability condition we integrate from $-\infty$ to 0 which gives

$$R_3 = \frac{4b_{-2}}{k^2} - \frac{2R_4 \chi_{-1}}{(1 - \eta_{-2}(P_5 - P_6))}. \quad (2.171)$$

Thus we obtain the expression for the Rayleigh number as a function of wavenumber for a deep layer and weak illumination, by putting all the above information together, as

$$R = \frac{2P_H d^4}{(1 - \eta_{-2}(P_5 - P_6))} \left[1 + d^{-1} \left(\frac{4k(k - \cosh k \sinh k)}{k^2 - \sinh^2 k} - \frac{2\chi_{-1}}{(1 - \eta_{-2}(P_5 - P_6))} \right) + O(d^{-2}) \right].$$

This equation can be used directly to plot asymptotic solutions to the linear stability problem for comparison with numerical solutions when d is large and χ is small. This expression is only valid for $k \leq O(1)$, and cannot predict the global most unstable wavenumber over all k . For small χ this predicts the critical wave wavenumber (the smallest wavenumber on the neutral curve) as zero, since the function is monotonically increasing in k .

As in Bees and Hill [9] we can also explore other areas of parameter space to build up a full picture of all feasible space. For $\eta \sim d^{-1}$ with $U \sim d^{-1}$, the solvability conditions at third order gives

$$R = -\frac{2P_H}{(P_5 - P_6)\eta_{-1}}, \quad (2.172)$$

which gives a negative constant for $R(k)$ and implies the asymptotics break down for small k . If we use $\eta \sim d^{-3}$ and $U \sim d^{-1}$ the solvability conditions gives

$$R = 2P_H d^4 \left(1 + d^{-1} \left(\eta_{-3}(P_5 - P_6) + \frac{4k(k - \sinh k \cosh k)}{k^2 - \sinh^2 k} - \chi_{-1} \right) + O(d^{-2}) \right), \quad (2.173)$$

which is monotonically increasing in k and has zero critical wavenumber for $k \leq O(1)$.

2.5 Numerical and asymptotical results for Model A

In this section we solve the linear stability equations valid for all parameter values numerically using FORTRAN 77. We use a fourth order finite difference numerical scheme called ‘NRK’, implemented by Cash and Moore 1980 [18], which iterates using a Newton-Raphson-Kantorovich algorithm. The linear stability equations are seventh order and the Rayleigh number R is the eigenvalue for the problem. We investigate at what values of R and k the solution becomes unstable by plotting neutral curves, which are defined as the locus of points where the real part of the growth rate is zero, $\text{Re}(\sigma) = 0$. If $\text{Re}(\sigma) < 0$ the perturbation dies away and the equilibrium solution is stable, but if $\text{Re}(\sigma) > 0$ the perturbation grows and the system is unstable, so that the region under the neutral curve is stable and above is unstable. If the imaginary part of σ is also zero then the principle of exchange of stabilities is said to be valid (Chandrasekhar 1961 [19]) and the perturbation

is stationary or non-oscillatory. However, if $\text{Im}(\sigma) \neq 0$ then overstable, or oscillatory, solutions exist. Such solutions were found in this model. For each choice of the key parameters there are an infinite number of branches of the neutral curve $R^n(k)$, where $n = 1, 2, 3, \dots$. We look for the branch on which R has its minimum at (k_c, R_c) , which describes the initial disturbance before non-linear effects occur. If $k_c \neq 0$, the critical wavenumber is also the most unstable mode to grow from equilibrium (when $R > R_c$). However, if the critical wavenumber is zero then k_c is not the most unstable mode, since if the Rayleigh number is increased above R_c the growth rate for $k_c = 0$ is still zero, as the neutral curve in this case includes the R axis, and this mode will never grow. Thus a different, non-zero mode would have the maximum growth rate and would be the most unstable mode. Solutions consist of stacked convection cells and are mode n if there are n convection cells (or if the solution for U crosses the x -axis $n - 1$ times). The critical wavenumber was usually on the $R^1(k)$ branch (mode one) in this model.

Short routines to find the neutral curves for a range of values of wavenumber k were used. Initial guesses for the cell concentration Φ and the fluid velocity U , as well as an initial guess for the Rayleigh number, were input into the program and these trial solutions were modified until good convergence was achieved. The solution for the first wavenumber k was then employed as the trial solution for the next step in k , so that as long as the steps between wavenumbers were sufficiently small a smooth neutral curve could be traced out. Providing a good guess for the Rayleigh number for the mode one solution was important, and the asymptotics helped to provide a suitable range. Convergence was always found to at least six significant figures. When the parameter d , the non-dimensional layer depth, was large and χ small, the size of mesh was particularly important. For this reason, and to allow comparisons with Bees and Hill 1998 [9], we scale the linear stability equations 2.89 and 2.100 using $z_I = dz$ (as was done for the equilibrium solution), so that the new layer depth is $-d \leq z_I \leq 0$, and we use a variety of grids to find smooth solutions. This scaling improves the numerics when d is large and χ small. Changing the grid structure or grid size beyond a certain level did not alter the form of converged solutions, helping to verify the program. Up to 513 grid points were used to obtain convergence, although this was not always necessary and the program often converged well with less. Convergence was hard to obtain for more extreme parameter values, such as for large χ or η . In these cases the parameter in question had to be increased by a small amount each time and the solution for a particular k was saved and used as the initial guess for the increased value

of the parameter in next run. In this way, solutions for the full range of interest of the parameters were found.

The large number of parameters make it unfeasible to investigate the full parameter space. The parameters from the Fokker-Planck equation, P_V , P_H , and A_1 to A_6 depend on λ and α_0 , and were not varied in this study, since it is predominately the balance between phototaxis and gyrotaxis we want to explore. We fix $\lambda = 2.2$, as in Bees and Hill 1998 [9], which is within the range suggested by Pedley and Kessler 1990 [130]. We also fix $\alpha_0 = 0.2$. We vary the non-dimensional layer depth, d , the wavenumber, k , the gyrotaxis parameter, η , the phototaxis parameter, χ , and the measure of the strength of absorption of the cells, κ , using specific values to illustrate the general behaviour of the system. Where possible, parameters were chosen so that comparisons with Bees and Hill 1998 [9] and Vincent and Hill 1996 [172] can be made. However, direct comparisons with [9] can only be made when $\chi = 0$, and direct comparisons can not be made between model results for χ compared to results using the phototaxis parameter C in [172]. This is because the phototaxis parameter C , the position at which $I = I_c$, and χ cannot be directly compared, since at $C = 0$ the cells collect at the upper boundary and are still phototactic, so that shading occurs, whereas in this model $\chi = 0$ is equivalent to the case of no illumination, so there is only gyrotaxis and gravitaxis and no phototaxis. Note also that results in [172] are only valid for the case of weak absorption, $\kappa \ll 1$, and there are errors that mean solutions are only correct when C is at the upper or lower boundary or located at the mid-point of the layer. However, qualitative rather than quantitative comparisons can still be made with both Vincent and Hill [172] and Bees and Hill [9].

2.5.1 Comparison of asymptotical and numerical results

Figures 2.5 and 2.6 show asymptotical and numerical neutral curves for a deep layer (d^{-1} small) where $\chi = d^{-1}$, $\kappa = 1$ and $d = 40$ (in Figure 2.5) or $d = 200$ (in Figure 2.6). Good agreement is found between asymptotics and numerics when $k \leq O(1)$, with better matchings found for smaller values of $d^2\eta$ and larger d , as expected (since the asymptotics are valid as $d \rightarrow \infty$). The numerics and asymptotics show the same trend as η is increased from $d^2\eta = 0$ in both cases, where the system is slightly stabilized for $k \leq O(1)$. The numerical results for $k > O(1)$ show that increasing η destabilizes the system, and a non-zero critical wavenumber appears in all cases when η is sufficiently large. The asymptotics cannot predict this as they are not valid for $k > O(1)$.

The asymptotics break down when $d = 40$ with $d^2\eta = 4$, as R is negative for $k = O(1)$. When $d = 200$ a larger $d^2\eta$ is required for the order one term to become negative. For $d^2\eta > 4$ the Rayleigh number tends to infinity for small k , and the value of η for which this first occurs can be found from equation 2.172 as

$$\eta_c = \frac{d^{-2}}{P_5 - P_6}, \quad (2.174)$$

since this is where the expression for R becomes singular. For $\lambda = 2.2$ and $\alpha = 0.2$, $\eta_c = 4.2$, so for $\eta > 4.2$ the asymptotic break down for $k \leq O(1)$. This is consistent with numerical results (shown in Figure 2.6, for example, where for small k , R tends to infinity when $d^2\eta > 4$).

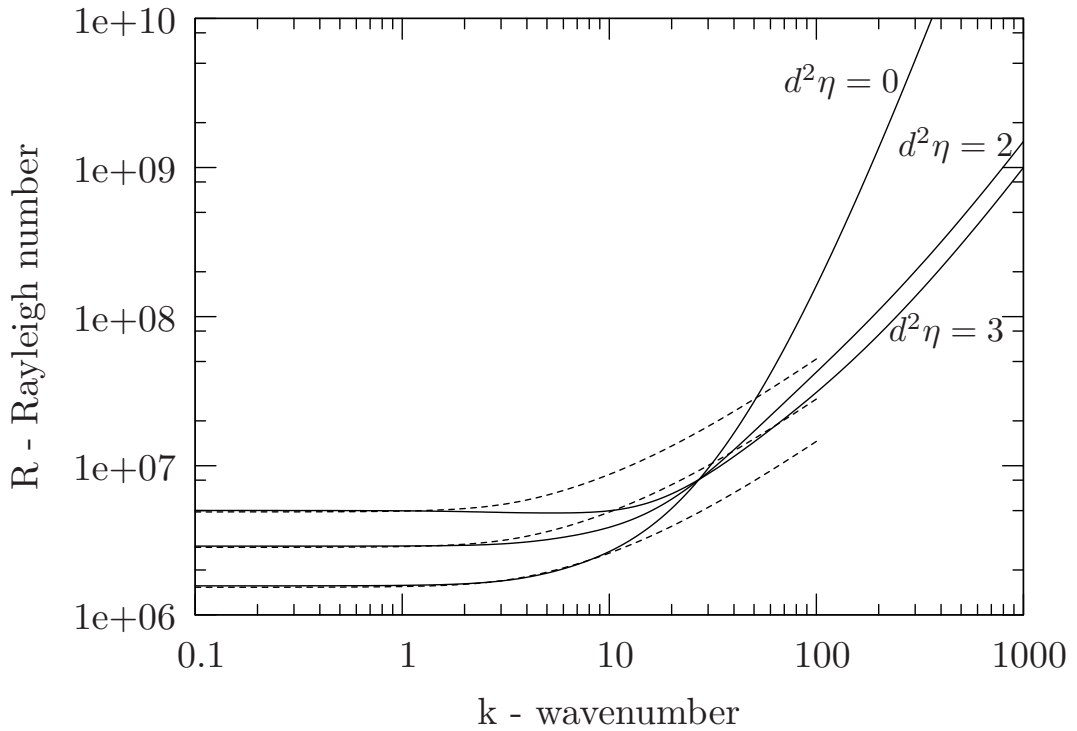


Figure 2.5: Asymptotic (dashed) and numerical (solid) curves of neutral stability for Model A, where $d = 40$, $\kappa = 1$, and $\chi = d^{-1}$. The three curves are for $d^2\eta = 0, 2$ and 3 .

On setting $d^2\eta = 2$ and varying $d\chi < 2$ good agreement is found between asymptotic and numerical results, with closer matches found for $d = 200$ compared to $d = 40$. Larger values of χ destabilize the system. The χ term in the asymptotic expansion in equation 2.172 is negative and so, if χ is large, the Rayleigh number becomes negative and the asymptotics are not valid for large χ_{-1} .

The good agreement between asymptotic and numerical results, as shown in Table 2.4,

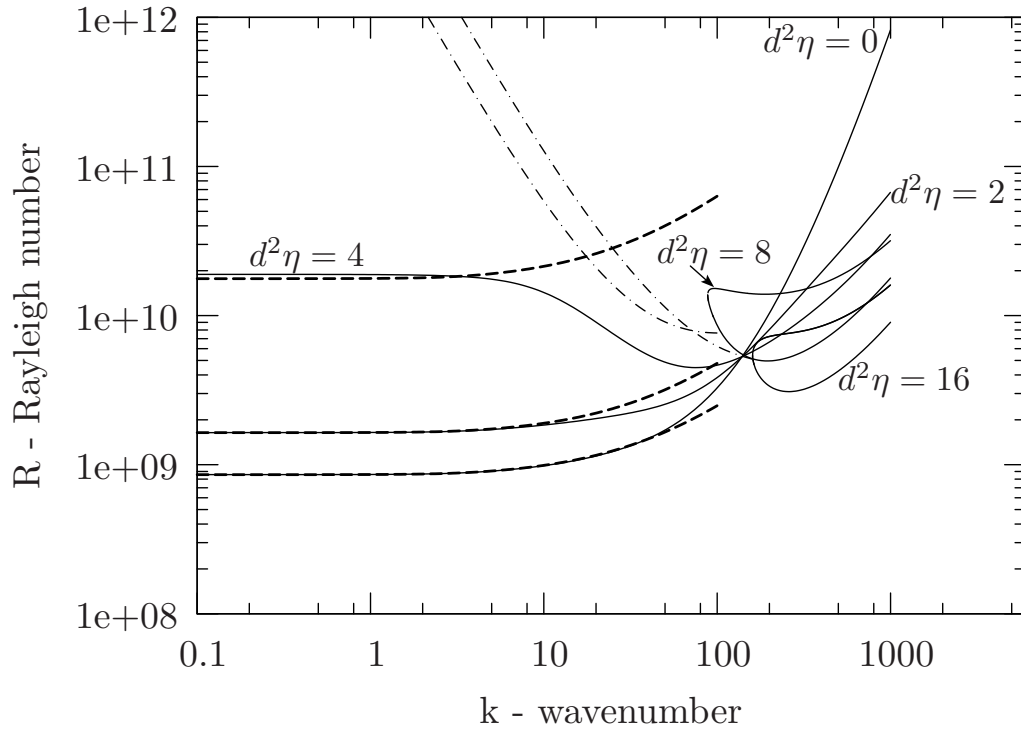


Figure 2.6: Asymptotic (dashed) and numerical (solid) curves of neutral stability for Model A, where $d = 200$, $\kappa = 1$ and $\chi = d^{-1}$. The five curves are $d^2\eta = 0, 2, 4, 8$ and 16 . Numerical oscillatory solutions are shown by dot-dashed lines.

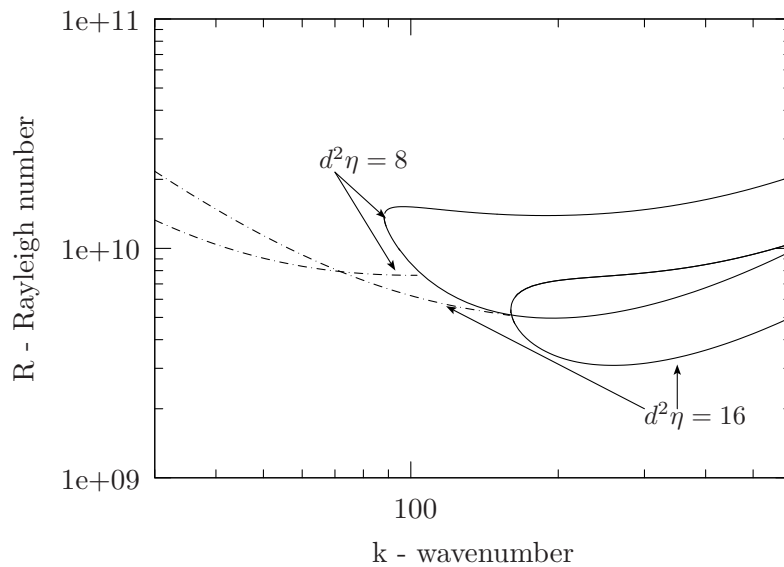


Figure 2.7: Asymptotic (dashed) and numerical (solid) curves of neutral stability for Model A, where $d = 200$, $\kappa = 1$ and $\chi = d^{-1}$ - a close up of the cases $d^2\eta = 8$ and 16 . Numerical oscillatory solutions are shown by dot-dashed lines, and here the enlarged region shows more clearly that there is one oscillatory branch for each value of $d^2\eta$.

d	$d^2\eta$	$d\chi$	k	R_c numerical	R_c asymptotical
40	2	0	0.1	3.16×10^6	3.08×10^6
40	2	1	0.1	2.89×10^6	2.84×10^6
200	2	0	0.1	1.67×10^9	1.67×10^9
200	2	1	0.1	1.64×10^9	1.64×10^9
200	2	2	0.1	1.61×10^9	1.61×10^9

Table 2.4: Summary of asymptotic and numerical results for a deep layer with weak illumination, where $\kappa = 1$ and standard parameters were used.

and the similar trends of behaviour for small χ and η when $k \leq O(1)$, help to verify the numerical analysis.

2.5.2 Exploring changes in layer depth d

Asymptotic and numerical results are shown in Figures 2.5 and 2.6 for two different layer depths, $d = 40$ and $d = 200$, and for small values of $\chi = d^{-1}$. Large values of d stabilizes the suspension, as in Bees and Hill [9], so that for all values of χ increasing the layer depth will increase R_c .

Flow and concentration profiles in Figures 2.8 and 2.9 show that for large layer depth d (Figure 2.9) the perturbations for small χ are closer to the surface of the fluid layer than for smaller d (Figures 2.8). Perturbations for large χ ($\chi = 1.03$) move down the fluid layer as d increases, so that large χ has a greater effect on the perturbation profile (compared to the case $\chi = 0$) when d is also large.

To study the effects of varying η and χ in the following sections we choose layer depth as $d = 20$, since this seems a reasonable depth when considered dimensionally ($H = 0.18\text{cm}$ if $\tau = 5\text{s}$, which is an approximate typical layer depth used experimentally) and gives good convergence when solving using the numerical program.

2.5.3 Exploring the effects of the phototaxis parameter χ on the critical wavenumber k_c and Rayleigh number R_c

Figure 2.10 shows results for a range of χ values when $d^2\eta = 2$, and Figure 2.11 for $d^2\eta = 4$, where the bold line is the neutral curve for $\chi = 0$ and is the only curve that can be directly compared with the results of Bees and Hill [9]. These values of η were chosen to see how χ affects the neutral stability curve when the critical wavenumber is zero in the gyrotaxis

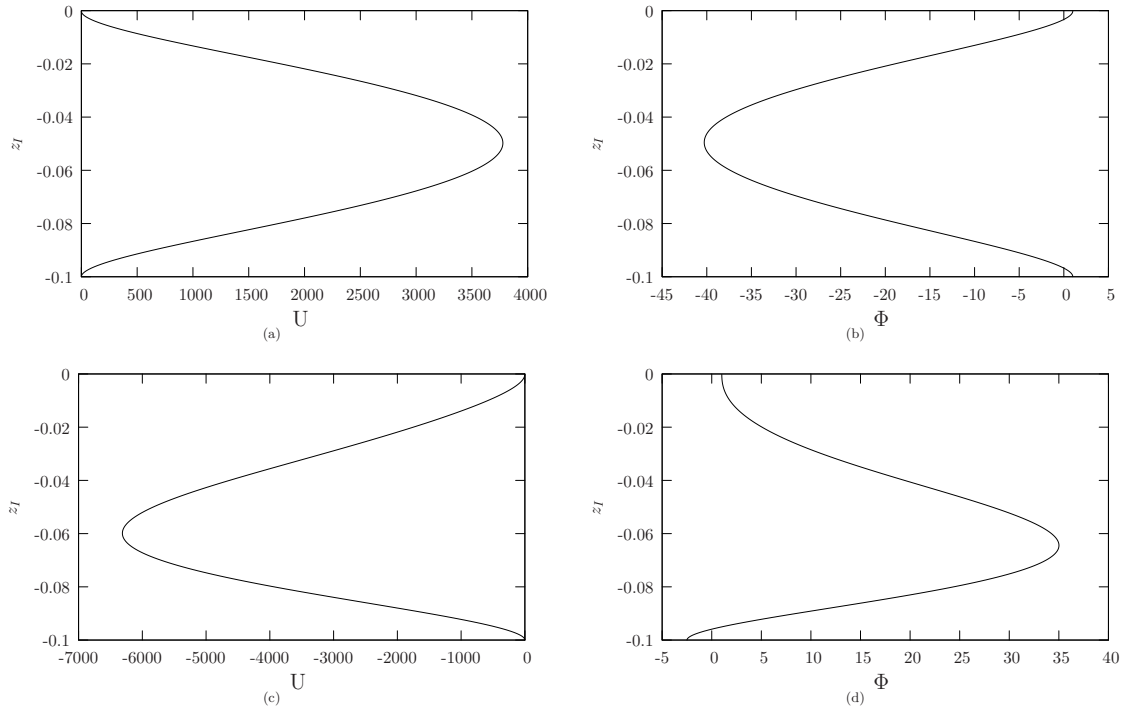


Figure 2.8: Flow and concentration profiles for Model A, where $d = 0.1$, $\kappa = 1.2$, $\eta = 0.1$ and $k = 10$, with $\chi = 0.1$ in Figures (a) and (b), and $\chi = 1.03$ in Figure (c) and (d). These solutions are mode one.

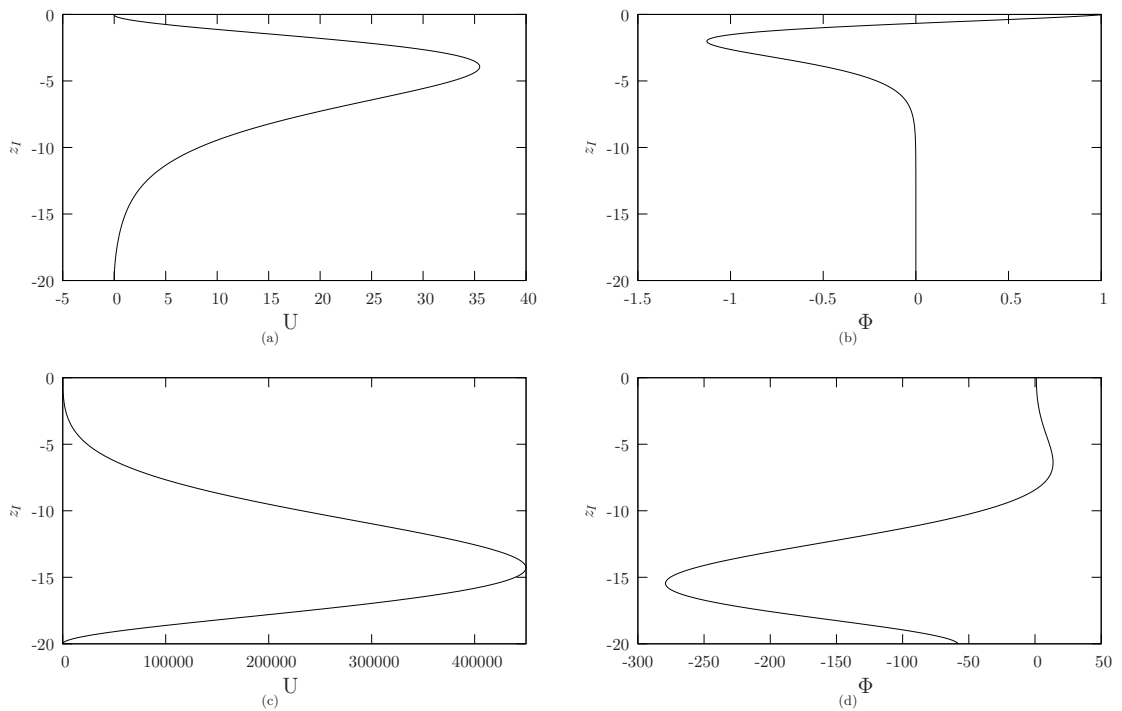


Figure 2.9: Flow and concentration profiles for Model A, where $d = 20$, $\kappa = 1.2$, $d^2\eta = 4$ and $k = 10$, with $\chi = 0.1$ in Figures (a) and (b), and $\chi = 1.03$ in Figures (c) and (d). These solutions are mode one.

only case $\chi = 0$ ($d^2\eta = 2$), compared to a case for which there is a non-zero wavenumber when $\chi = 0$ ($d^2\eta = 4$).

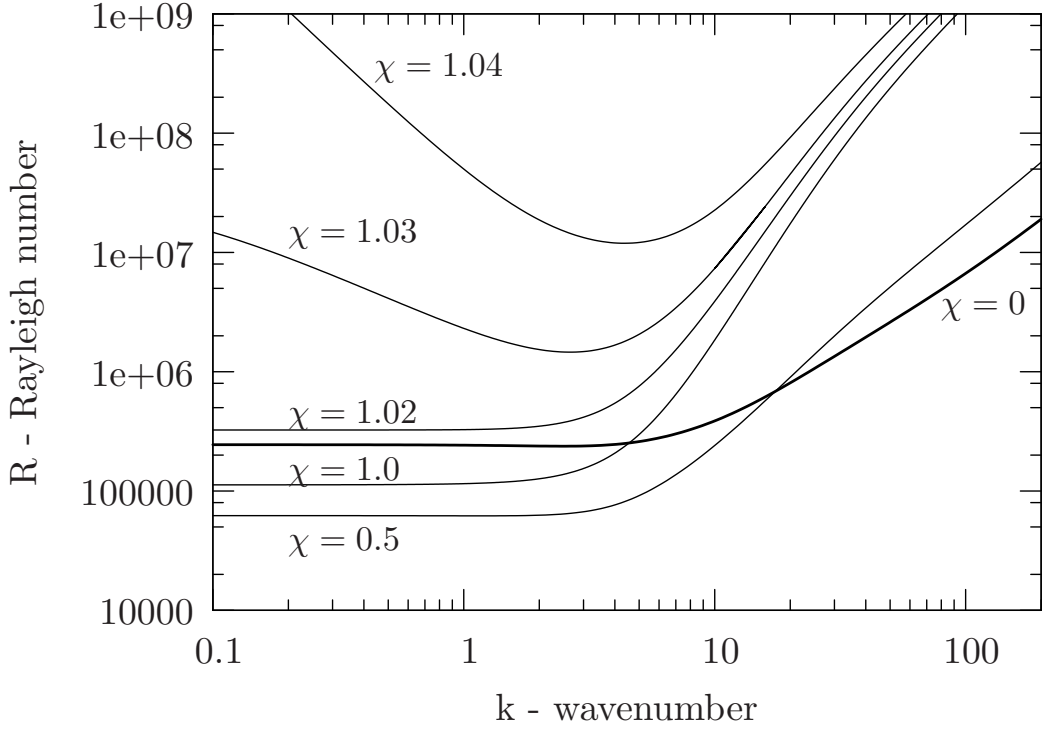


Figure 2.10: Curves of neutral stability for Model A, where $d = 20$, $\kappa = 1.2$, $d^2\eta = 2$ and χ varies. The bold line is the special case $\chi = 0$ where there is no phototaxis.

For both values of η , as $\chi < 1$ is increased from zero (and the equilibrium sublayer is located at $z = 0$), the neutral curve is first destabilized for small wavenumbers and stabilized for larger wavenumbers, leading to $k_c = 0$. This destabilization of small k indicates there is a region in parameter space where setting $\chi > 0$ causes the critical wavenumber to be zero when it was previously non-zero for gyrotaxis and gravitaxis only (i.e. when $\chi = 0$). This is demonstrated in Figure 2.12 for $d^2\eta = 4$, where k_c and R_c are plotted against χ , and both decrease and then increase, and k_c begins as non-zero and becomes zero for some $0 < \chi < 1$. Vincent and Hill [172] also find that R_c initially decreases as C increases, although in that case the position of the sublayer was not at $z = 0$.

As χ increases further from $\chi = 1$, the sublayer at equilibrium moves down from $z = 0$, creating a stable region overlying an unstable region and the peak of the concentration profile at equilibrium decreases for $\chi > 1$, so that there is a greater spread of cells throughout the layer at equilibrium. The appearance of the stable region and the greater spread

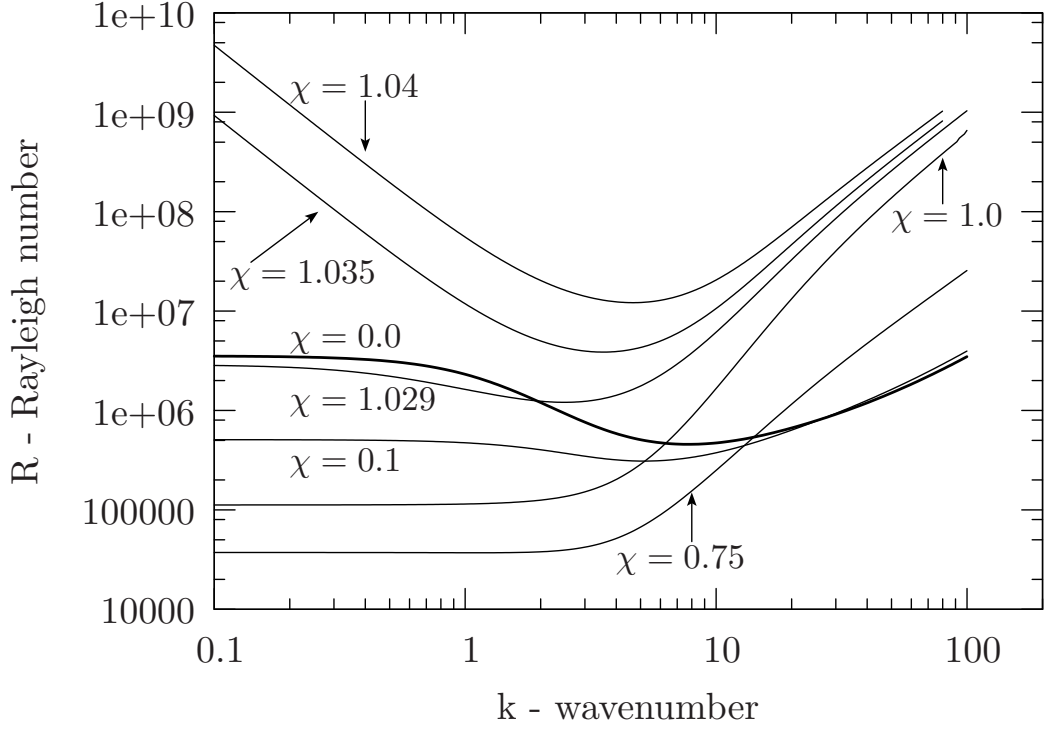


Figure 2.11: Curves of neutral stability where $d = 20$, $\kappa = 1.2$, $d^2\eta = 4$ and χ varies. The bold line is the special case $\chi = 0$ where there is no phototaxis.

of cells at equilibrium will naturally stabilize the system. When $\chi \geq 1.02$ for $d^2\eta = 2$ and $\chi \geq 1.03$ for $d^2\eta = 4$ the Rayleigh number at every wavenumber is larger than for the case $\chi = 0$, so all wavenumbers are stabilized for χ sufficiently large. Small wavenumbers are stabilized more than large wavenumbers, which results in a dip forming on the neutral curve so that for every η the critical wavenumber, k_c , becomes non-zero as χ is increased. Growth rates and the neutral curve for various values of R when $\chi = 0.5$ and $d^2\eta = 2$ are shown in Figure 2.13.

These results are qualitatively similar to the case for $\eta = 0$ (no gyrotaxis; results not shown). Thus for every d and η , if χ is sufficiently large there exists a non-zero value of the critical wavenumber k_c . Similarly, in the phototaxis only model of Vincent and Hill [172], critical wavenumbers such that $k_c > 0$ were found as the position, $z = -C$, at which $I = I_c$ for an individual was varied (although direct comparisons cannot be made and errors were found in that work). However, we do not find loop or oscillatory solutions for any χ when η is small, unlike Vincent and Hill [172].

We also investigate the mode of the solutions, in terms of how many vertically stacked convection cells there are, as χ is varied. We find that for both $d^2\eta = 2$ and $d^2\eta = 4$, as

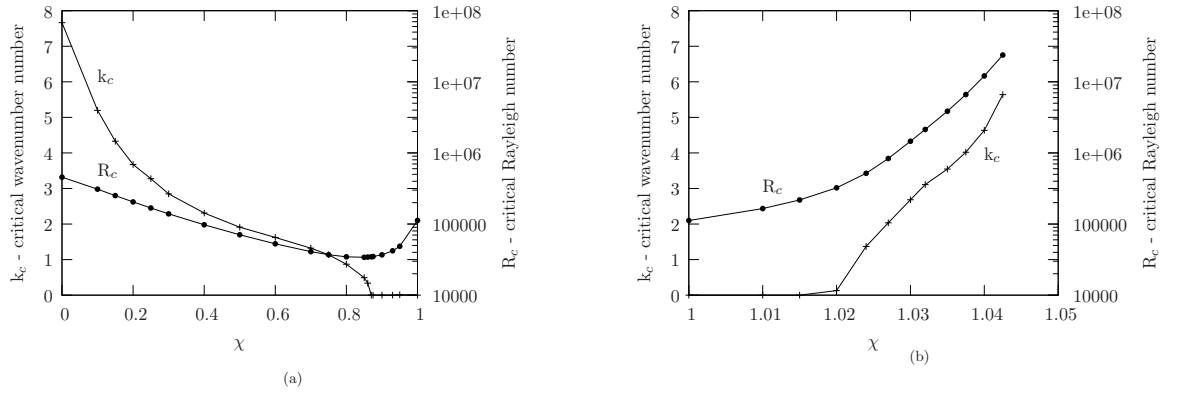


Figure 2.12: Plots of critical Rayleigh number (circles) and critical wavenumbers (crosses) for Model A, where $d = 20$, $\kappa = 1.2$, $d^2\eta = 4$ and χ varies.

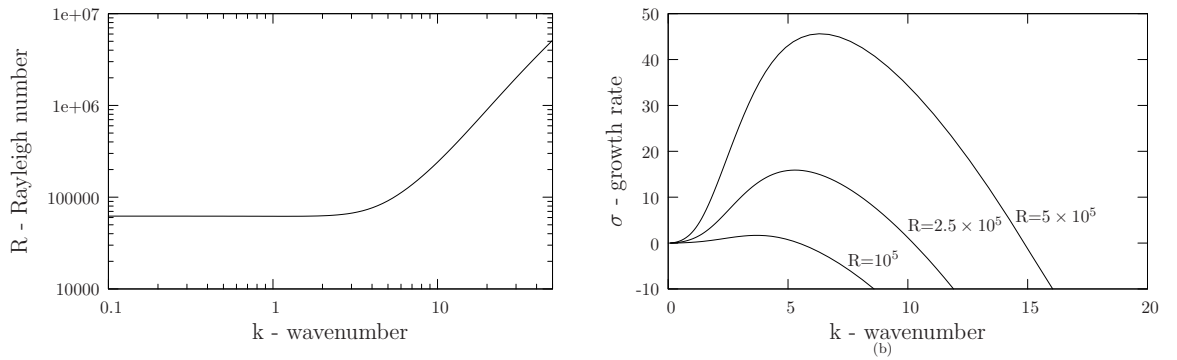
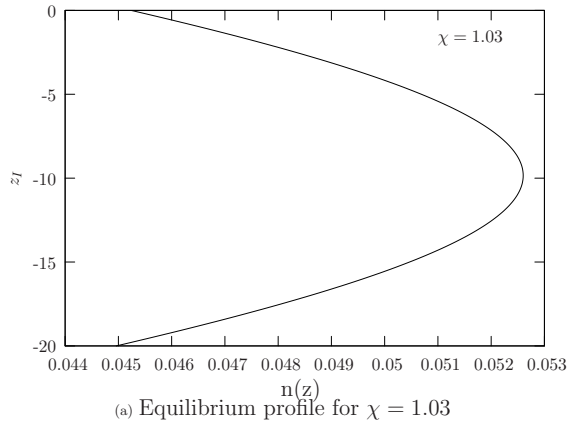
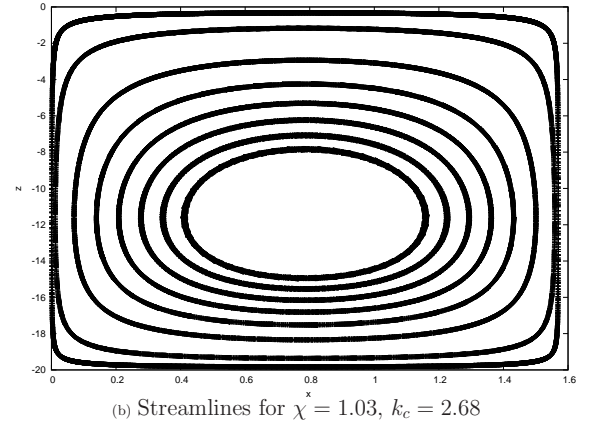


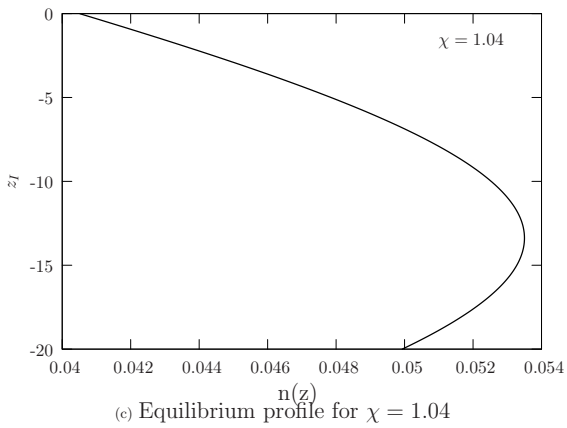
Figure 2.13: Figure (a) shows curves of neutral stability, where $d = 20$, $d^2\eta = 2$, $\chi = 0.5$ and $R_c = 6.20 \times 10^4$ for Model A. Figure (b) shows the growth rate σ plotted against wavenumber.



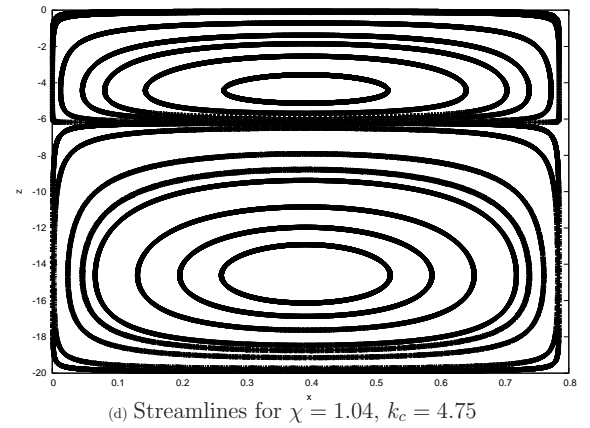
(a) Equilibrium profile for $\chi = 1.03$



(b) Streamlines for $\chi = 1.03$, $k_c = 2.68$



(c) Equilibrium profile for $\chi = 1.04$



(d) Streamlines for $\chi = 1.04$, $k_c = 4.75$

Figure 2.14: Equilibrium solutions and streamlines for Model A, where $d = 20$, $\kappa = 1.2$, $d^2\eta = 4$ and $\chi = 1.03$ and $\chi = 1.04$. The wavenumber in each case is the critical wavenumber k_c .

χ increases from $\chi = 1$ the solutions change from mode one to mode two for small k and the critical wavenumber k_c switches to mode two for sufficiently large χ . For $d^2\eta = 4$ and $\chi = 1.03$ the equilibrium in Figure 2.14(a) shows a region with stable cell density gradient overlying an unstable region. The flow profiles in Figure 2.14(b) show the solution at k_c is mode one (and is also mode one for $0.1 < k < 10$), with only one convection cell filling the whole fluid layer. This is an example of penetrative convection that occurs in a wide range of situations (Straughan 1993 [161]), where convection motions from the unstable layer penetrate into the stable layer and drive fluid motions throughout the whole layer. For $\chi = 1.04$ a small convection cell appears at the top of the fluid layer for small k and k_c and the solution becomes mode two since full penetrative convection does not occur; the path of least resistance is two separate convection cells. Vincent and Hill also found mode two solutions, with the second convection cell forming at the bottom of the layer for $k < k_c$ when $C \leq 0.5$ and at the top for large C , with k_c mode two. The parameters χ used here and C in [172] are similar and, interestingly, we find that our results for large χ follow similar trends to large C .

2.5.4 Exploring the effects of the gyrotaxis parameter η on the critical wavenumber k_c and Rayleigh number R_c

In this section, the effects of varying η for the case of weak illumination, where $\chi = 0.5$ and the peak of the equilibrium concentration is at the top of the layer, and strong illumination, where $\chi = 1.03$ and the peak of the equilibrium concentration profile is approximately half way down the suspension, are shown in Figure 2.15 and Figure 2.16.

For $\chi = 0.5$ in Figure 2.15 (and $\chi = d^{-1}$, where $d = 40$, in Figure 2.5) increasing $d^2\eta$ from $d^2\eta = 0$ stabilizes small wavenumbers and destabilizes large wavenumbers. The results for $\chi = 1.03$ and small η are somewhat different to those for weak illumination (small χ). In Figure 2.16, the initial wavelength when $d^2\eta = 0$ is non-zero, and little difference is found between the neutral curves for $d^2\eta \leq 32$. This shows that for strong illumination (large χ) large values of η are needed to have a substantial effect on the system. For $d^2\eta = 32$, small wavenumbers are slightly stabilized ($k < 0.1$), wavenumbers between $k = 0.1$ and $k = 2.9$ are slightly destabilized and wavenumbers $k > 2.9$ are stabilized. For $d^2\eta > 32$, large wavenumbers are stabilized more than small wavenumbers, as is the case when $\chi = 0.5$. Thus for all χ there is a non-zero critical wavenumber k_c for $d^2\eta$ sufficiently large, or all $d^2\eta$ if χ is sufficiently large, and k_c increases and R_c decreases as η increases

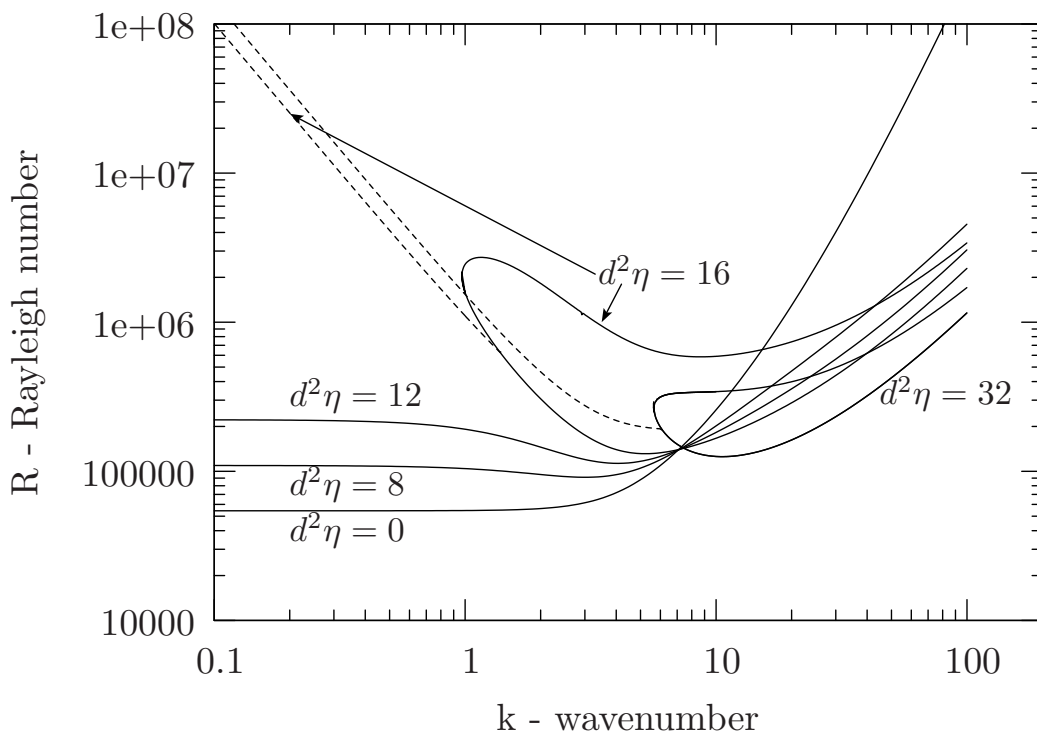


Figure 2.15: Curves of neutral stability for Model A, where $d = 20$, $\kappa = 1.2$, $\chi = 0.5$ and η varies.

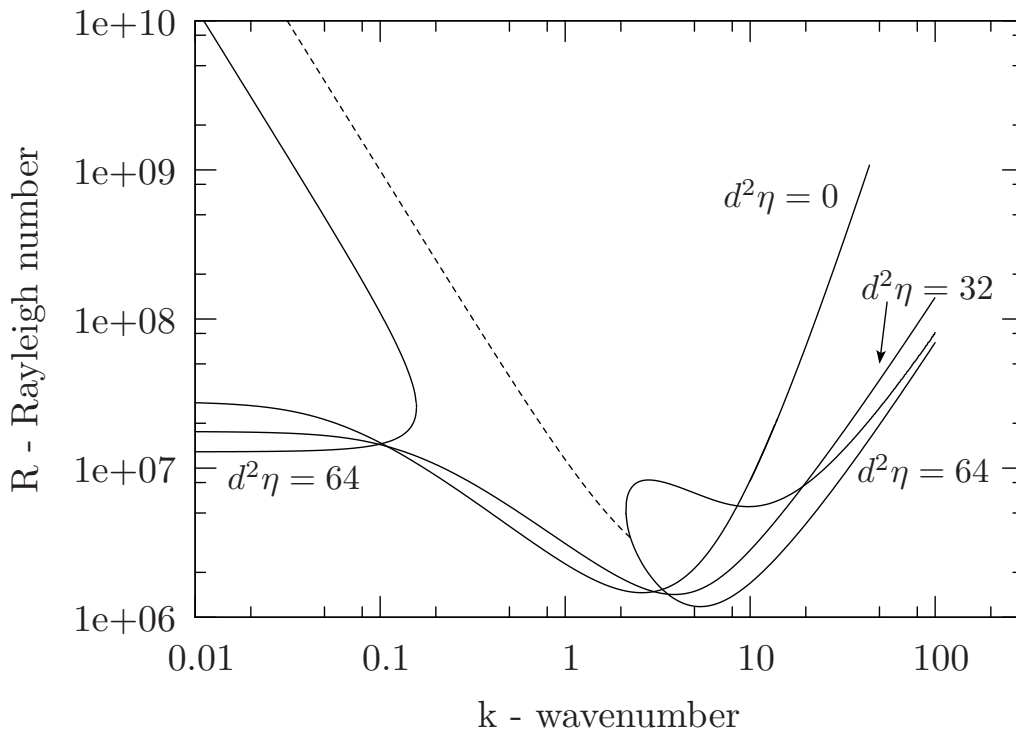


Figure 2.16: Curves of neutral stability for Model A, where $d = 20$, $\kappa = 1.2$, $\chi = 1.03$ and η varies. Dashed lines are oscillatory solutions.

(so that the system is destabilized). This is the same trend as in the gyrotaxis only case in Bees and Hill [9].

For $d^2\eta \geq 16$ for $\chi = 0.5$, and $d^2\eta \geq 64$ for $\chi = 1.03$, the neutral curves break into two sections, which turn back on themselves to form loops. The lower branches of these loops have mode one solutions for all k , but this smoothly adjusts to a mode two as the loops turn into the upper branch, with the second, smaller, convection cell at the top of the layer for $\chi = 0.5$ and the bottom of the layer for $\chi = 1.03$. This is shown in the flow profiles for $\chi = 1.03$ in Figure 2.17. For both values of χ , the critical wavenumber appeared on the bottom branch of the loop and was mode one. These looped solutions were not found in Bees and Hill [9], although they do exist for the gyrotaxis only case. Similar solutions were found in the phototaxis only model of Vincent and Hill [172], where the second convection cell was found at the top of the suspension layer for large C and the bottom for small C , which is the opposite to the trend in χ found here. Vincent and Hill [172] also found loop solutions for small C , but here loop solutions are found only if η is sufficiently large, regardless of χ . The mode one section of the neutral curve for small k was found for $d^2\eta = 64$ when $\chi = 1.03$, but was only partially found for $d^2\eta \geq 16$ for $\chi = 0.5$ and so is not shown in Figure 2.15.

Oscillatory solutions were found for $d^2\eta \geq 16$ when $\chi = 0.5$ and $d^2\eta \geq 64$ when $\chi = 1.03$. Neutral curves that loop back on themselves were always found to have oscillatory solutions (as in Vincent and Hill [172]) with a single oscillatory branch bifurcating from the stationary branch at a point k_0 , and with $k < k_0$ for all values of k on this oscillatory branch. In all cases investigated the oscillatory branch did not have a smaller minimum than the stationary branch. The oscillatory branch for $\chi = 1.03$ and $d^2\eta = 64$ bifurcated from the stable solution at $k_0 = 2.25$ and was found to be mode one at this point, changing smoothly to mode two as k decreased. Hill *et al.* 1989 [63] found oscillatory solutions for the gyrotaxis only case due to the interaction of gyrotaxis and fluid shear close to the rigid upper boundary. Vincent and Hill [172] also found oscillatory solutions in the phototaxis only model. In the model presented here, the mechanisms for overstability can not be solely explained by either explanation, since overstability only occurs when gyrotaxis is strong and can occur even when the peak of the equilibrium solution is not located at the upper boundary. The two mechanisms for overstability are presented in section 2.6.

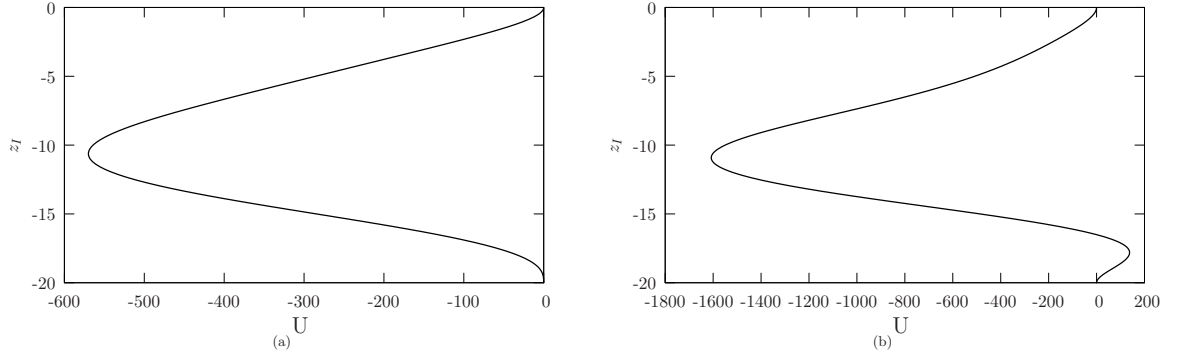


Figure 2.17: Flow profiles for Model A, where $d = 20$, $\kappa = 1.2$, $\chi = 1.03$, and $d^2\eta = 64$, with $k = 2.5$ in (a) and $k = 5$ in (b).

2.5.5 Exploring the effects of the absorption parameter κ on the critical wavenumber k_c and Rayleigh number R_c

Figure 2.18 shows neutral curves for different values of κ when $d = 20$, $\chi = 1.03$ and $d^2\eta = 2$. κ and χ act in similar but opposite ways, where large κ destabilizes the system compared to $\kappa = 0.8$, so that R_c and k_c both decrease as a function of increasing κ . This is what we would expect because κ and χ also have similar but opposite effects on the equilibrium solutions.

2.5.6 Using a stress-free boundary condition for $\chi < 1$

To further investigate the destabilization of the neutral curves for small χ , we compute stability solutions for small χ with a stress-free boundary condition at the upper surface given by

$$\frac{d^2U}{dz^2} = 0 \text{ at } z = 0. \quad (2.175)$$

From results shown in Figure 2.19, it is clear that for $\chi < 1$ using the stress-free boundary condition the curves of neutral stability are not destabilized as much compared to the same parameter values using the rigid, no-flow boundary condition. This implies that the destabilization found for small χ is in part due to the no-flow boundary condition on the upper surface.

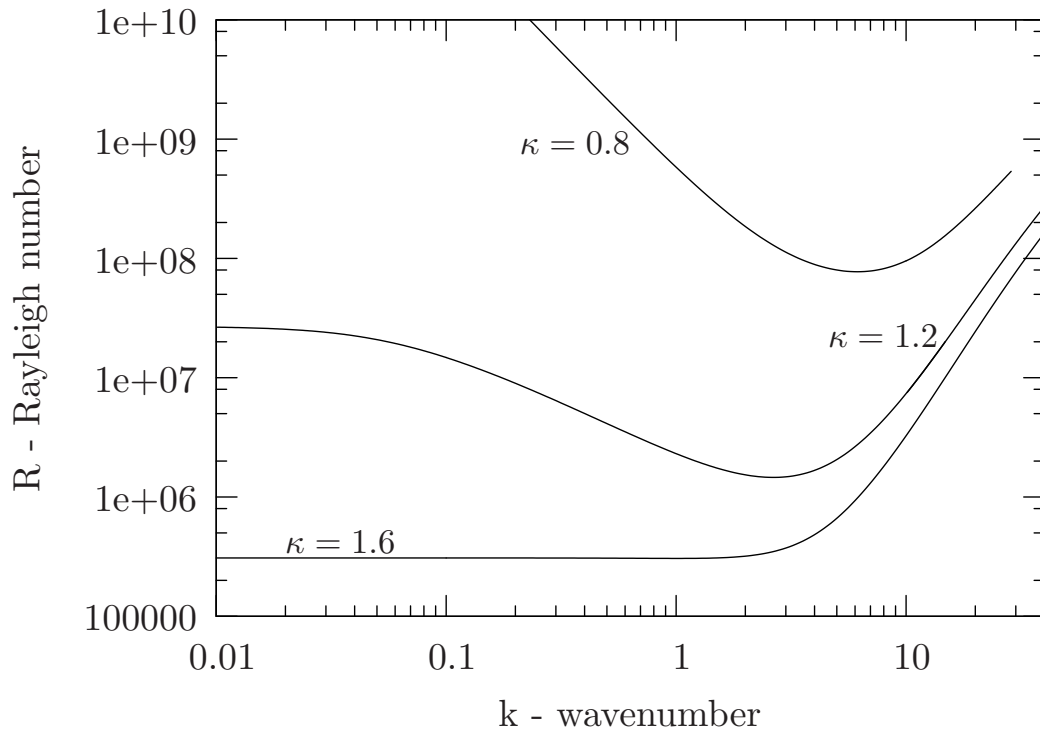


Figure 2.18: Curves of neutral stability for Model A, where $d = 20$, $\chi = 1.03$, $d^2\eta = 2$ and $\kappa = 0.8, 1.2$ and 1.6 .

2.5.7 Exploring the bifurcation from steady solutions with one branch to oscillating solutions with two double loop branches

Using the values of J_4 and J_5 corrected from Bees and Hill [9] with $\chi = 0$ (for the case of no phototaxis), we find that as η varies there is a bifurcation between two neutral curves of different modes, to two loops which are mixed mode. This is shown in Figure 2.20, where for $d^2\eta = 7.5$ there are two separate branches of the neutral curve, the top of which is mode two and the lower mode one. For $d^2\eta = 8$ these two branches are close together, and as $d^2\eta$ is increased further the mode one and mode two neutral curves split and two separate loops form. Both loops are mode one on the lower part and change smoothly to mode two as they cycle to the upper section. The loop for large k has an oscillatory solution, which is mode one where it meets the stationary curve, and as k decreases it smoothly changes to mode two.

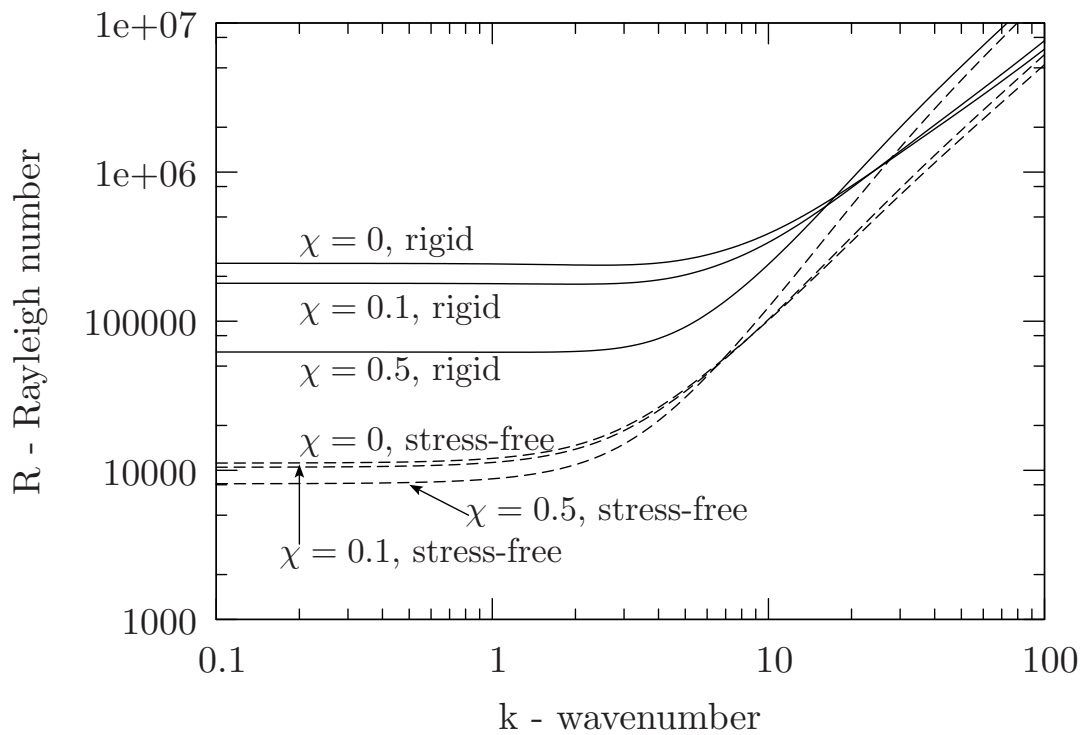


Figure 2.19: A comparison of curves of neutral stability for the rigid (solid lines) and the stress-free (dashed) boundary conditions for Model A, where $d = 20$, $d^2\eta = 2$, and $\kappa = 1.2$, and $\chi = 0.0, 0.1$ and 0.5 .

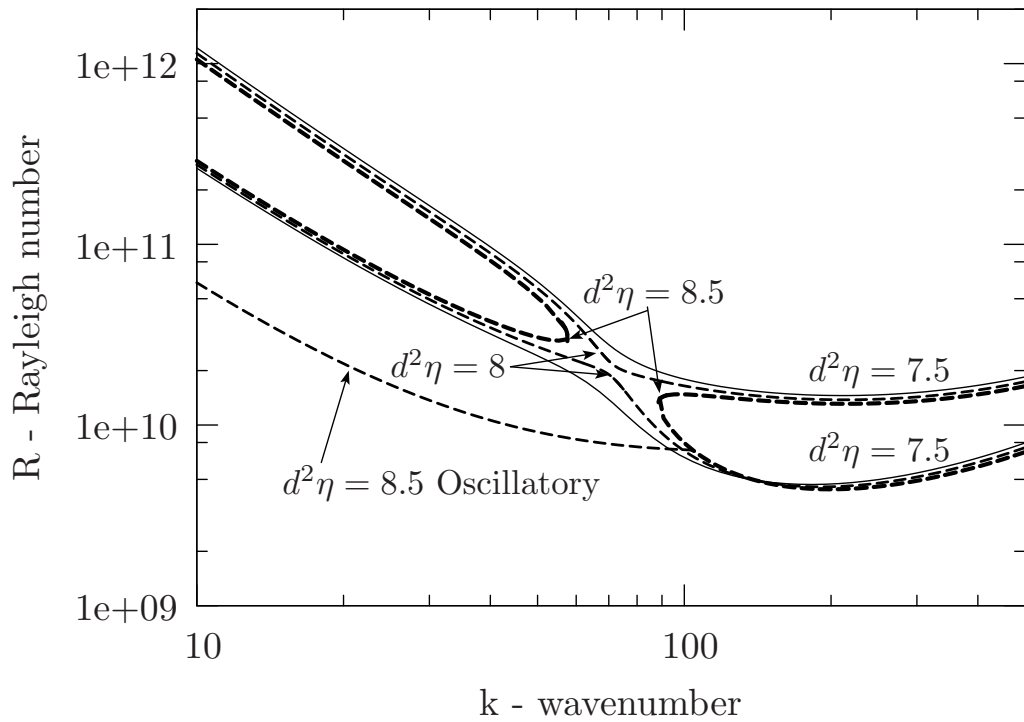


Figure 2.20: Curves of neutral stability for Model A, where $d = 200$, $\kappa = 1$, and $\chi = 0$, and $d^2\eta = 7.5$ (solid lines), $d^2\eta = 8$ (dashed lines), or $d^2\eta = 8.5$ (bold dashed lines). The oscillatory branch is labelled accordingly, and the corrected J_4 and J_5 values are used.

d	$d^2\eta$	χ	κ	k_c	R_c
200	0	$\frac{1}{d}$	1.0	0	8.58×10^8
200	16	$\frac{1}{d}$	1.0	257.71	3.09×10^9
40	0	$\frac{1}{d}$	1.0	0	1.56×10^6
40	2	$\frac{1}{d}$	1.0	0	2.88×10^6
20	2	0	1.2	2.44	2.38×10^5
20	2	0.5	1.2	1.16	6.19×10^4
20	2	1.0	1.2	0	1.27×10^5
20	2	1.02	1.2	0	3.25×10^5
20	2	1.04	1.2	4.40	1.19×10^7
20	4	0	1.2	7.66	4.56×10^5
20	4	0.5	1.2	1.91	7.07×10^4
20	4	1.0	1.2	0.0	1.12×10^5
20	4	1.02	1.2	0.29	3.22×10^5
20	4	1.04	1.2	4.75*	1.21×10^7

Table 2.5: Summary of the linear stability results for Model A, in terms of critical wavenumber, k_c , and Rayleigh number, R_c , for $\lambda = 2.2$ and $\alpha_0 = 0.2$. The star indicates the solution at the critical wavenumber, k_c , is mode two.

2.5.8 Table of Results

Sample results for Model A are summarized in Table 2.5. The critical wavenumber k_c and the corresponding critical Rayleigh number R_c are shown for a variety of parameter values. The critical wavenumber was mode one unless indicated by a star, in which case it was mode two. In all cases, even when oscillatory solutions were found, k_c was on the non-oscillatory section of the curve.

2.6 Discussion

In this chapter, three novel modelling approaches were presented in order to extend the stochastic gyrotaxis model of Pedley and Kessler 1990 [130] to include phototaxis. Light intensity was modelled using the Beer-Lambert law for a self-shading description of light through a layer. In particular, a photo-kinesis like model was explored, where the cells change their swimming speed with light intensity I (termed Model A). Equilibrium so-

lutions were found and perturbed to conduct a linear stability analysis. The stability equations were then solved numerically and asymptotically for a deep layer. Good agreement was found between results using these methods and trends in neutral curves, and flow and concentration perturbation profiles, were shown in section 2.5 for a range of parameter values. Here, we discuss the physical interpretation of these curves and compare these results to other works, specifically the phototaxis only model of Vincent and Hill 1996 [172] and the gravitactic and gyrotactic model of Pedley and Kessler 1990 [130] that was analysed in a layer of finite depth by Bees and Hill 1998 [9].

At equilibrium, when $\chi = 0$, there is no light and the cells exhibit only gravitaxis, and the equilibrium profile is an exponential function with maximum cell concentration at the top of the layer, as in Bees and Hill [9]. For $0 < \chi < 1$, the maximum is still at $z = 0$ but the spread of cells throughout the top of the layer is greater than for $\chi = 0$, because there is some light to which the cells respond, so that the swimming speed is slightly reduced. $\chi = 1$ refers to the case where the light intensity at the surface is equal to the critical light intensity ($I_s = I_c$), so if there was just one cell in the layer then it could be at any vertical position and still get the optimum light I_c . It is, therefore, the effect of the cells creating their own gradient in light due to shading that determines the position of maximum concentration.

For $\chi > 1$, the cells near the top, close to the light source, have too much light and swim backwards ($V_s(I) < 0$) whereas the cells below do not have enough light due to shading and swim upwards. This results in the concentrated sublayer at equilibrium being located below the upper boundary, not at $z = 0$, which creates a gravitationally stable layer overlying an unstable layer (the location of which is dependent on χ). The concentration profile has the highest spread and smallest maximum when the maximum concentration is around $z = -\frac{d}{2}$ and the concentration profile is symmetric. This was also found by Ghorai and Hill [46]. When χ is large the majority of cells swim downwards, resulting in an almost exponential distribution with maximum at $z = -d$. $d = 200$ gives qualitatively the same trend, with a more peaked distribution for $\chi = 0$ and a higher sensitivity to $\chi > 1$. For the linear stability analysis, increasing d increases the critical Rayleigh number R_c , as also observed in Bees and Hill [9] and Vincent and Hill [172].

Equilibrium profiles for the absorption coefficient, κ , exhibit opposite trends to those found for χ . Large κ moves the concentrated sublayer upwards and makes it more peaked, because increased absorption causes more shading of the cells lower down in the layer,

which induces those cells to swim upwards. Thus the linear stability results for κ increasing show similar but opposite trends to χ increasing, as shown in Figure 2.18. These trends for χ are discussed below.

This model is designed so that when $\chi = 0$, there is no light and we return to the case of gravitaxis and gyrotaxis only in a finite layer, as in Bees and Hill [9]. As such, we find exactly the same stability solutions as [9]. Vincent and Hill 1996 [172] find loop solutions with mode two sections when the position of the sublayer, denoted C , is close to the upper boundary. These solutions were not found here, but solutions are not expected to be similar as their model does not include gravitaxis or gyrotaxis.

The interactions between phototaxis and gyrotaxis are the main focus of this work. For weak light intensity (small χ) increasing η from zero slightly stabilizes small wavenumbers and destabilizes large wavenumbers. Small wavelength instabilities are destabilized because the gravitactic instability is reinforced by the gyrotactic instability, in which cells swim towards the downwelling regions and the added mass of these cells amplifies the downwelling, so the plumes become denser and more focussed. As η increases a minimum appears on the neutral curve and we find that for all layer depths d , if η is sufficiently large the critical wavenumber k_c is non-zero. This is consistent with results in Bees and Hill [9] for the gravitactic and gyrotactic only model.

From the case $\chi = 0$ we conclude that small wavenumber instabilities are caused by overturning at the boundary and large wavenumber instabilities by gyrotaxis, since the dip on the curve for large wavenumbers is formed when the gyrotaxis parameter η is increased from zero, and the small wavenumber instability is relatively unaffected by η . The upper no-slip boundary causes viscous damping and inhibits fluid motions, hence helping to prevent unstable flows near the boundary. We hypothesize that the greater spread of cells away from the boundary for $\chi < 1$ at equilibrium permits greater fluid flow associated with any emergent overturning instability. Thus even though the concentration gradient is slightly reduced, the overturning instability is enhanced and the system is less stable than if $\chi = 0$. The gyrotactic instability for large wavenumbers is not dependent on the boundary, and so large wavenumbers due to gyrotaxis are not destabilized as χ increases and are, in fact, slightly stabilized. As χ increases further the spread of cells at equilibrium also increases, and gradients drop sufficiently to stabilize the system. Less destabilization occurs for the stress-free boundary at $z = 0$ for small χ compared to the rigid boundary, backing the hypothesis that it is the greater spread of cells away from the

upper boundary permitting greater fluid flow that destabilizes small wavenumbers when χ is small. This initial decrease and subsequent increase in stability was also found in Vincent and Hill [172] as C , the position of the sublayer, moved down the fluid layer. In that case, the formation of a small stable region at the top of the layer relaxed the effect of the boundary condition at $z = 0$ and stabilized the system. Although the trend in C is similar to the trend found here for χ , the destabilization mechanism is not same, as the destabilization occurs in this model when the peak of n is still at the top of the layer and there is no stable region.

The appearance of the stable region overlying an unstable region at equilibrium for $\chi > 1$ naturally stabilizes the system for all wavelengths, so that R_c increases as χ increases, and we find there is a direct relationship between the size of the unstable region and the stability of the system. Similarly, in Vincent and Hill [172], R_c also increased as the sublayer at equilibrium moved further down the fluid layer, because the effect of destabilization away from the boundary was offset by the increasingly large stable region. Similar effects were also described by Veronis [170] and discussed by Matthews 1988 [109] and Whitehead and Chen 1970 [177] for thermal instability and convection of a thin fluid layer bounded by a stable stratified region. The decrease in size of the unstable region as χ increases means that it is harder for the convection cells to circulate due to the proximity of the lower boundary. The small wavelength instabilities do not take up the whole layer, so will not be as affected by the appearance of a stable region compared to the large wavelengths, which would rather utilize more of the layer and, hence, are more restricted. This leads to large wavelengths stabilizing more rapidly than small wavelengths as χ increases, resulting in a non-zero critical wavenumber for sufficiently large χ . As χ increases, the system tries to drive smaller and smaller wavelength instabilities in the shrinking unstable region, so that the critical wavenumber increases from $k_c = 0$ with $\chi > 1$ (see Figure 2.12, which summarizes these results). When the concentrated layer of cells is at the bottom of the suspension, $z = -d$, we expect the system to be almost fully stable, since there is no unstable density stratification within the layer. Neutral curves become hard to trace for large χ , and for large values of R , and are likely mainly due to gyrotaxis (which does not require a density gradient).

We hypothesize that there are at least two different destabilizing processes, one from phototaxis combined with gravitaxis and one from gyrotaxis. These instabilities combine to give a wider neutral curve than those found for the gravitactic and gyrotactic only cases

in Bees and Hill [9], and the critical wavenumber k_c increases as $\chi > 1$ increases. In one respect, gyrotaxis and phototaxis act in opposite ways in this model, since sufficiently large gyrotaxis destabilizes the system compared to the case $\eta = 0$, but introducing phototaxis for any η stabilizes the system compared to $\chi = 0$ if χ is large enough.

For $1 < \chi < 1.03$ penetrative convection occurs at the critical wavelength, where circulation in the unstable region penetrates into the stable region and the resulting fluid motion uses the whole suspension depth. As the stable region increases in size with χ , the energy required for the instabilities to penetrate into the stable region is more than the energy required to cycle round in the unstable region, and the critical wavelength becomes mode two when χ is sufficiently large. Penetrative convection and mode two solutions for k_c , when C is sufficiently large, were also found by Vincent and Hill [172].

We find that for all values of χ with large values of η the neutral curve splits in two and the neutral curve loops back on itself for high wavenumbers. Such loops were found for the phototaxis only case in Vincent and Hill [172] but not for the gravitaxis and gyrotaxis only case with $\chi = 0$ in Bees and Hill [9]. The upper branch changes smoothly from a mode one to a mode two solution by the formation of a second convection cell at the top for small χ and $\chi = 0$, and at the bottom of the layer for large χ .

For large η , when the neutral curves were found to form loops, oscillatory solutions were always found. However, the critical wavenumber k_c was always found to be on the steady, non-oscillatory branch. Oscillatory solutions occur when there is competition between a stabilizing and a destabilizing process. Unlike Bees and Hill [9], we find oscillatory solutions even when $\chi = 0$ for the gravitactic and gyrotactic only case. Hill *et al.* [63] found that overstability can occur in a suspension of purely gyrotactic algae using a deterministic model, as long as the upper boundary of the layer is rigid. They showed that the interaction of gyrotaxis and fluid shear close to the rigid surface can result in a net flux of cells away from the concentrated downwelling regions. If the flux were big enough it would eventually reverse the direction of the bioconvection cell and cause overstability. We hypothesize that this is also the mechanism for overstability in Model A, using the Fokker-Planck equation for orientation, when $\chi = 0$.

Oscillating solutions were also found in Model A when η was large and $\chi \neq 0$. We expect that the oscillating solutions when $0 < \chi \leq 1$ are also caused by the interaction with the boundary, since the peak of the equilibrium concentration profile is at $z = 0$. For η large and $\chi > 1$, oscillating solutions can not be attributed to the effect of the boundary,

since the sublayer forms at $z \neq 0$ due to the balance between diffusion, upswimming due to gravitaxis and the flux due to phototaxis. Vincent and Hill [172] found oscillations in their phototaxis only model and proposed a mechanism. However, this mechanism is not apparent in our system.

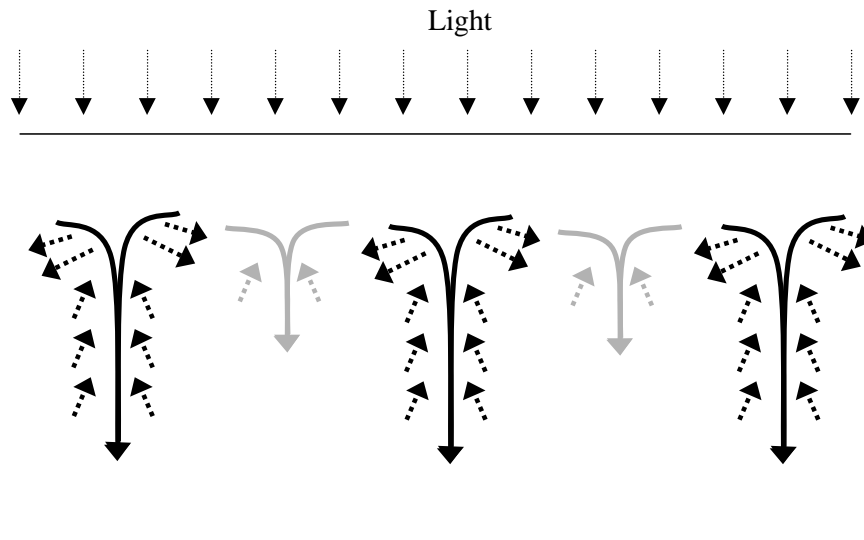


Figure 2.21: A schematic diagram to show how oscillations arise for photo-gyrotactic cells. Black lines show the initial instabilities and light grey lines indicate instabilities at a later time. Dashed lines are cell swimming, solid lines are fluid flow and dotted lines indicate illumination. When an instability arises, cells deep in the fluid layer are shaded by those above and swim upwards, towards downwelling fluid. Cells at the top of the plume receive too much light and swim backwards, away from the plume. If sufficient movement away from two adjacent plumes occurs a new plume forms in between them, shown in light grey. This reverses the flow of the convection cell and causes oscillations, as the plumes shift from side to side.

We hypothesize that the mechanisms for overstability caused by phototaxis in the absence of a boundary is as follows. First, perturbation leads to an overturning Rayleigh Taylor instability. Due to shading by cells within the fluid layer, cells further from the light source do not have enough light and swim upwards on average. Gyrotaxis causes these cells to swim towards any downwelling fluid, and the added mass amplifies the downwelling, forming plumes. However, cells at the top of the resulting plumes are closer to the light source and actually have too much light. Phototaxis causes these cells to swim backwards in order to avoid the light, even though the cells are gyrotactically orientated to point towards the plume, so that cells swim downwards and away from the concentrated

downwelling fluid. This de-focuses the plume. If the light intensity is sufficiently bright that enough cells swim away from the plume, and if this is happening concurrently in adjacent plumes, the backwards swimming cells from each plume eventually create an unstable plume between the original structures. The cells further down the layer then swim towards this newly created region of downwelling fluid and the direction of the convection cell has been reversed. This is shown schematically in Figure 2.21, where the original instabilities are black and the later plumes caused by shading and phototaxis are light grey. This cycle of shading and backwards swimming repeats until the plume is again located in its original place. These oscillations are only found for large η because strong gyrotaxis is needed for the horizontal components of velocity that are necessary to draw cells both into and away from the descending plumes. Oscillations like this will not necessarily be found experimentally because the timescale for overstability may be larger than the timescale for the convective motions to become fully non-linear.

The validity of Model A needs to be questioned. The model is formulated so that cells react to a bright light by swimming with a negative swimming speed $-V_s(I)$. This implies that the cells swim backwards to get away from bright light, an effect which is not seen in laboratory cultures, although cells can swim backwards during a photophobic response (Hegemann and Bruck 1989 [57]). By phenomenologically setting the variable swimming speed dependent on I we obtain qualitative results that investigate the interactions between gyrotaxis and phototaxis in self-propelled microorganisms. A more general discussion of the key assumptions and modelling processes can be found in Chapter 3, in which the remaining modelling approaches are explored using the same techniques as in this chapter, and results are analysed and compared between the models. Model results are compared to experimental results in Chapter 4, where we consider whether the equilibrium solutions would have time to form, and some of the issues involved in comparing theoretical and experimental results are discussed in detail. Some agreement between experimental and theoretical trends is found.

Chapter 3

Modelling photo-gyrotactic bioconvection in suspensions of green algae - Part II

Summary

In this chapter, the two remaining photo-gyrotaxis models, Models B and C, are formulated, equilibrium solutions are found and a linear stability analysis performed using the same techniques presented in Chapter 2. For Model B only, asymptotic solutions for a large layer depth are compared to numerical solutions and good agreement is found. For both models, numerical solutions are computed for a range of phototactic and gyrotactic parameter values. Model B results are generally similar to those in Chapter 2, whereas for Model C non-hydrodynamic modes of oscillation are found. This work concludes with model comparisons between all three models, followed by a discussion of the modelling techniques and results.

3.1 Model B, where the centre of mass offset h varies with light intensity.

In Model B, each cell's centre of mass offset varies with light intensity, $h = h(I)$. We set $V_s(I) = 1$ in equation 2.16 and $\tilde{\mathbf{k}}(I) = \mathbf{k}$ in equation 2.29. $h(I)$ is chosen as a linear function of I , so that, in non-dimensional terms, $h(I) = -\frac{\xi}{h_n}(I_s I - I_c)$, where ξ is a

constant (see Section 2.2.3 for details of the non-dimensionalization). We set $h(I) = 1$ at $I = 0$, where h_n is the normal centre of mass offset in the dark used, so that $\xi = \frac{h_n}{I_c}$. Substituting in the non-dimensional equation for light intensity I (equation 2.19) gives non-dimensional $h(I)$ as

$$h(I) = \left(1 - \chi e^{-\kappa \int_z^0 n(z) dz}\right), \quad (3.1)$$

where $\chi = \frac{I_s}{I_c}$, as in Model A. As before, we remove integrals by increasing the order of the system by writing

$$m(z) = - \int_z^0 n(z) dz. \quad (3.2)$$

The effect of light only appears directly in the equation for $\dot{\mathbf{p}}$ (equation 2.4) that is used in the Fokker-Planck equation. Thus the solution to the Fokker-Planck equation in this model is not the same to the solution in Pedley and Kessler 1990 [130], and the mean cell swimming direction and diffusion tensor now depend on light intensity. Diffusion is calculated using equation 2.9, with constant average cell swimming speed, V_n , so that $D_0 = V_n^2 \tau$ (as in Model A). The non-dimensional layer depth d is

$$d = \frac{H \bar{K}_1}{V_n \tau \bar{K}_2}. \quad (3.3)$$

\bar{K}_1 and \bar{K}_2 are the constant values of $K_1(\Lambda(z))$ and $K_2(\Lambda(z))$ when $\Lambda(z) = \lambda = 2.2$ as used in Model A (so that \bar{K}_i here is the same as K_i in Model A), where Λ is defined in equation 3.16 and $K_1(z)$ and $K_2(z)$ come from the solution the Fokker-Planck and are defined in equations 3.84 and 3.85. This ensures that d is defined the same in every model, which permits comparisons between models to be made. The non-dimensional equations for Model B are thus

$$\nabla \cdot \mathbf{u} = 0, \quad (3.4)$$

$$S_c^{-1} \frac{D\mathbf{u}}{Dt} = -\nabla p_e - \gamma n \mathbf{k} + \nabla \cdot \boldsymbol{\Sigma}, \quad (3.5)$$

$$\frac{\partial n}{\partial t} = -\nabla \cdot \left[n \left(\mathbf{u} + \frac{d\bar{K}_2}{\bar{K}_1} \langle \mathbf{p} \rangle \right) - \mathbf{D} \cdot \nabla n \right], \quad (3.6)$$

$$n(z) = \frac{dm}{dz}, \quad (3.7)$$

$$\begin{aligned} & h(I) \nabla_p \cdot [(\mathbf{k} - (\mathbf{k} \cdot \mathbf{p}) \mathbf{p}) f] + \eta \nabla_p \cdot [(\boldsymbol{\omega} \wedge \mathbf{p}) f] \\ & + 2\alpha_0 \eta \nabla_p \cdot [(\mathbf{e} \cdot \mathbf{p} - \mathbf{p} \mathbf{p} \cdot \mathbf{e} \cdot \mathbf{p}) f] = \lambda^{-1} \nabla_p^2 f, \end{aligned} \quad (3.8)$$

where

$$\gamma = \frac{Nvg\Delta\rho H^3}{\nu\rho V_n^2\tau}, \quad \lambda = \frac{1}{2D_r B_n} \quad \text{and} \quad \eta = \frac{B_n D_0}{H^2}, \quad (3.9)$$

as defined in equation 2.30 in Chapter 2, with $D_0 = V_n^2 \tau$. The notation of the general photo-gyrotaxis models in Chapter 2 is used here (defined in Section 2.2). Since B_n contains constant h_n (see equation 2.28), which takes the same value as h in Bees and Hill [9], these parameters are identical to those in Bees and Hill [9]. The fluid stress tensor, Σ , is defined in equation 2.18. The no-flow and no-flux boundary conditions, together with the boundary condition for M , are defined in equations 2.21, 2.22 and 2.23 in Chapter 2, with $V_s(I) = 1$.

3.2 Solving the Fokker-Planck equation for Model B

In this section, the solution to the Fokker-Planck equation is found for Model B and used to calculate the mean cell swimming direction $\langle \mathbf{p} \rangle$ and diffusion tensor \mathbf{D} . We use the steady solution to the Fokker-Planck, as in Pedley and Kessler [130] and Bees and Hill [9], since we assume that the timescale for unsteadiness in the flow is large compared to D_r^{-1} . This analysis was only sketched for Model A in Chapter 2, since the solution in that case is the same as in Pedley and Kessler 1990 [130].

The steady, non-dimensional photo-gyrotactic Fokker-Planck equation is given in equation 3.8 (where we drop the subscript p) as

$$\begin{aligned} & h(I) \nabla \cdot [(\mathbf{k} - (\mathbf{k} \cdot \mathbf{p}) \cdot \mathbf{p})f] + \eta \nabla \cdot [(\boldsymbol{\omega} \wedge \mathbf{p})f] \\ & + 2\alpha_0 \eta \nabla \cdot [(\mathbf{e} \cdot \mathbf{p} - \mathbf{p}\mathbf{p} \cdot \mathbf{e} \cdot \mathbf{p})f] = \lambda^{-1} \nabla^2 f. \end{aligned} \quad (3.10)$$

This is an equation in orientational space, where \mathbf{k} , $\boldsymbol{\omega}$ and \mathbf{e} are constants and $tr(\mathbf{e}) \equiv \nabla \cdot \mathbf{u} = 0$. \mathbf{p} is the cell swimming direction and is the unit vector perpendicular to the unit sphere, so that for any function $g(\mathbf{p})$, ∇g is perpendicular to \mathbf{p} , so $(\mathbf{p} \cdot \nabla)g = 0$. We calculate $\nabla \cdot \mathbf{p} = 2$, $\nabla \mathbf{p} = \mathbf{I} - \mathbf{p}\mathbf{p}$ and $(\nabla \wedge \mathbf{p})_i = \epsilon_{ijk} p_{j,k} = \frac{1}{2} \epsilon_{ijk} (p_{j,k} + p_{k,j}) = 0$, as $\nabla \mathbf{p} = (\nabla \mathbf{p})^T$. Following the term by term analysis in Bees and Hill [9] gives the non-dimensional Fokker Plank equation in equation 3.10 as

$$\begin{aligned} & h(I) (\mathbf{k} \cdot \nabla f - 2(\mathbf{k} \cdot \mathbf{p})f) + \eta \boldsymbol{\omega} \cdot (\mathbf{p} \wedge \nabla f) \\ & + 2\eta \alpha_0 [\mathbf{p} \cdot \mathbf{e} \cdot \nabla f - 3\mathbf{p} \cdot \mathbf{e} \cdot \mathbf{p}f] = \lambda^{-1} \nabla^2 f. \end{aligned} \quad (3.11)$$

Substituting in the non-dimensional expression for $h(I)$ in equation 3.1 gives

$$\begin{aligned} & \lambda (1 - \chi e^{\kappa m}) (\mathbf{k} \cdot \nabla f - 2(\mathbf{k} \cdot \mathbf{p})f) + \eta \lambda \boldsymbol{\omega} \cdot (\mathbf{p} \wedge \nabla f) \\ & + 2\eta \lambda \alpha_0 [\mathbf{p} \cdot \mathbf{e} \cdot \nabla f - 3\mathbf{p} \cdot \mathbf{e} \cdot \mathbf{p}f] = \nabla^2 f. \end{aligned} \quad (3.12)$$

3.2.1 Solution for zero flow

If we consider the equilibrium state of zero flow, where $\mathbf{u} = \boldsymbol{\omega} = \mathbf{e} = \mathbf{0}$, $f = f^0$ and $m = m^0$, then on writing $\mathbf{p} = (\sin \theta \cos \phi, \sin \theta \sin \phi, \cos \theta)$, where θ is the colatitude measured relative to \mathbf{k} and ϕ is the cell orientation angle in the horizontal plane, and $\mathbf{k} = (0, 0, 1)$,

$$\lambda \left(1 - \chi e^{\kappa m^0}\right) (\mathbf{k} \cdot \nabla f^0 - 2(\mathbf{k} \cdot \mathbf{p})f^0) = \nabla^2 f^0, \quad (3.13)$$

$$\begin{aligned} \text{hence} \quad & \lambda \left(1 - \chi e^{\kappa m^0}\right) \left(\left(\frac{\partial f^0}{\partial \theta} \hat{\boldsymbol{\theta}} + \frac{\partial f^0}{\partial \phi} \frac{1}{\sin \theta} \hat{\boldsymbol{\phi}} \right) \cdot \mathbf{k} - 2f^0 \cos \theta \right) \\ & = \frac{1}{\sin \theta} \frac{\partial}{\partial \theta} \left(\sin \theta \frac{\partial f^0}{\partial \theta} \right) + \frac{1}{\sin^2 \theta} \frac{\partial^2 f^0}{\partial \phi^2}. \end{aligned} \quad (3.14)$$

Since $\hat{\boldsymbol{\theta}} = (\cos \theta \cos \phi, \cos \theta \sin \phi, -\sin \theta)^T$,

$$\frac{1}{\sin \theta} \frac{\partial}{\partial \theta} \left(\sin \theta \frac{\partial f^0}{\partial \theta} \right) + \frac{1}{\sin^2 \theta} \frac{\partial^2 f^0}{\partial \phi^2} = -\Lambda \left(\sin \theta \frac{\partial f^0}{\partial \theta} + 2f^0 \cos \theta \right), \quad (3.15)$$

where we define

$$\Lambda(z) = \lambda \left(1 - \chi e^{\kappa m^0(z)}\right), \quad (3.16)$$

which can be treated as a constant for partial differential equations in orientation space. For zero flow we assume axial symmetry, so f^0 is independent of ϕ and $f^0 = f^0(\theta)$. If we substitute $x = \cos \theta$ into equation 3.15 then

$$(1 - x^2)f^{0''} - 2xf^{0'} - \Lambda \left((1 - x^2)f^{0'} - 2f^0 x \right) = 0. \quad (3.17)$$

Integrating equation 3.17 gives

$$(1 - x^2) (f^{0'} - \Lambda f^0) = A, \quad (3.18)$$

where A is a constant, which is found to be zero since at $x = 1$, f^0 and $f^{0'}$ are both finite.

Integrating again gives the solution

$$f^0 = \mu_\Lambda e^{(\Lambda \cos \theta)}. \quad (3.19)$$

Applying the normalization condition, that the integral of f^0 over the unit sphere is 1, gives

$$\mu_\Lambda \left[-\Lambda^{-1} \exp(\Lambda \cos \theta) \right]_0^\pi = \frac{1}{2\pi}, \quad \text{hence, } \mu_\Lambda = \frac{\Lambda}{4\pi \sinh(\Lambda)}. \quad (3.20)$$

The mean of \mathbf{p} is given in equation 2.8 as

$$\langle \mathbf{p} \rangle = \int_S \mathbf{p} f(\mathbf{p}) d\mathbf{p}, \quad (3.21)$$

so that the zero flow component, denoted $\langle \mathbf{p} \rangle^0$ is given by

$$\begin{aligned} \langle \mathbf{p} \rangle^0 &= \int_S \mathbf{p} f^0(\mathbf{p}) d\mathbf{p} \\ &= \int_0^{2\pi} \int_0^\pi \begin{pmatrix} \sin \theta \cos \phi \\ \sin \theta \sin \phi \\ \cos \theta \end{pmatrix} \mu_\Lambda e^{\Lambda \cos \theta} \sin \theta d\theta d\phi. \end{aligned} \quad (3.22)$$

Integrating with respect to ϕ gives components equal to zero in the \mathbf{i} and the \mathbf{j} directions. Integrating by parts with respect to θ then gives

$$\langle \mathbf{p} \rangle^0(z) = \begin{pmatrix} 0 \\ 0 \\ K_1(z) \end{pmatrix} \quad (3.23)$$

where

$$K_1(z) = \coth(\Lambda(z)) - \frac{1}{\Lambda(z)}. \quad (3.24)$$

To find the zero flow solution for \mathbf{D} , denoted \mathbf{D}^0 , we use the approximation in equation 2.9 in Chapter 2 and non-dimensionalize to give

$$\mathbf{D}^0 = [\langle \mathbf{p}\mathbf{p} \rangle^0 - \langle \mathbf{p} \rangle^0 \langle \mathbf{p} \rangle^0]. \quad (3.25)$$

$\langle \mathbf{p}\mathbf{p} \rangle$ is given by

$$\langle \mathbf{p}\mathbf{p} \rangle = \int_S \mathbf{p}\mathbf{p} f(\mathbf{p}) d\mathbf{p}. \quad (3.26)$$

For the zero flow solution, $\langle \mathbf{p}\mathbf{p} \rangle^0$, equation 3.26 gives

$$\langle \mathbf{p}\mathbf{p} \rangle^0 = \int_S \mathbf{p}\mathbf{p} f^0(\mathbf{p}) d\mathbf{p} \quad (3.27)$$

$$= \int_0^{2\pi} \int_0^\pi \begin{pmatrix} \sin \theta \cos \phi \\ \sin \theta \sin \phi \\ \cos \theta \end{pmatrix} \begin{pmatrix} \sin \theta \cos \phi \\ \sin \theta \sin \phi \\ \cos \theta \end{pmatrix} \mu_\Lambda e^{\Lambda \cos \theta} \sin \theta d\theta d\phi. \quad (3.28)$$

When integrating the matrix $\langle \mathbf{p}\mathbf{p} \rangle^0$ with respect to ϕ , only the diagonal terms remain as their ϕ components are $\cos^2 \phi$, $\sin^2 \phi$ and 1, respectively. All other terms give zero when ϕ is integrated between 0 and 2π . This gives

$$\langle \mathbf{p}\mathbf{p} \rangle^0 = \mu_\Lambda \pi \int_0^\pi \begin{pmatrix} \sin^2 \theta & 0 & 0 \\ 0 & \sin^2 \theta & 0 \\ 0 & 0 & 2 \cos^2 \theta \end{pmatrix} e^{\Lambda \cos \theta} \sin \theta d\theta. \quad (3.29)$$

Integrating by parts twice gives

$$\langle \mathbf{pp} \rangle_{11}^0(z) = \langle \mathbf{pp} \rangle_{22}^0(z) = \frac{K_1(z)}{\Lambda(z)} \quad (3.30)$$

and

$$\langle \mathbf{pp} \rangle_{33}^0(z) = 1 - \frac{2K_1(z)}{\Lambda(z)}. \quad (3.31)$$

Substituting equations 3.23, 3.30 and 3.31 into equation 3.25 gives

$$\begin{aligned} \mathbf{D}_{11}^0(z) &= \mathbf{D}_{22}^0(z) = \frac{K_1(z)}{\Lambda(z)} \\ \text{and } \mathbf{D}_{33}^0(z) &= \left(1 - \frac{2K_1(z)}{\Lambda(z)} - K_1^2(z) \right) = K_2(z), \end{aligned} \quad (3.32)$$

where

$$K_2(z) = 1 - \coth^2(\Lambda(z)) + \frac{1}{\Lambda(z)^2}. \quad (3.33)$$

3.2.2 First order perturbation for spherical and aspherical cells

From the equilibrium state of no fluid flow we perturb using

$$\mathbf{u} = \epsilon \mathbf{u}^1, \quad \boldsymbol{\omega} = \epsilon \boldsymbol{\omega}^1, \quad \mathbf{e} = \epsilon \mathbf{e}^1, \quad f = f^0 + \epsilon f^1 \text{ and } m = m^0 + \epsilon m^1, \quad (3.34)$$

where $0 < \epsilon \ll 1$. Equation 3.12 at order ϵ is

$$\begin{aligned} \Lambda [\mathbf{k} \cdot \nabla f^1 - 2(\mathbf{k} \cdot \mathbf{p})f^1] - \lambda \chi \kappa m^1 e^{\kappa m^0} [\mathbf{k} \cdot \nabla f^0 - 2(\mathbf{k} \cdot \mathbf{p})f^0] \\ + \eta \lambda \boldsymbol{\omega}^1 \cdot (\mathbf{p} \wedge \nabla f^0) + 2\eta \lambda \alpha_0 [\mathbf{p} \cdot \mathbf{e}^1 \cdot \nabla f^0 - 3\mathbf{p} \cdot \mathbf{e}^1 \cdot \mathbf{p} f^0] = \nabla^2 f^1, \end{aligned} \quad (3.35)$$

where $\Lambda(z)$ is defined in equation 3.16. Expanding equation 3.35 gives

$$\begin{aligned} \frac{1}{\sin \theta} \frac{\partial}{\partial \theta} \left(\sin \theta \frac{\partial f^1}{\partial \theta} \right) + \frac{1}{\sin^2 \theta} \frac{\partial^2 f^1}{\partial \phi^2} - \Lambda \left(\mathbf{k} \cdot \hat{\boldsymbol{\theta}} \frac{\partial f^1}{\partial \theta} - 2 \cos \theta f^1 \right) \\ = \eta \lambda \left(\boldsymbol{\omega}^1 \cdot \mathbf{p} \wedge \hat{\boldsymbol{\theta}} \frac{\partial f^0}{\partial \theta} + 2\alpha_0 \mathbf{p} \cdot \mathbf{e}^1 \cdot \hat{\boldsymbol{\theta}} \frac{\partial f^0}{\partial \theta} - 6\alpha_0 \mathbf{p} \cdot \mathbf{e}^1 \cdot \mathbf{p} f^0 \right) \\ - \lambda \chi \kappa m^1 e^{\kappa m^0} \left(\mathbf{k} \cdot \hat{\boldsymbol{\theta}} \frac{\partial f^0}{\partial \theta} - 2 \cos \theta f^0 \right), \end{aligned} \quad (3.36)$$

where

$$\frac{\partial f^0}{\partial \theta} = -\mu_\Lambda \Lambda \sin \theta e^{\Lambda \cos \theta}, \quad (3.37)$$

$$\mathbf{p} \wedge \hat{\boldsymbol{\theta}} = (-\sin \phi, \cos \phi, 0)^T, \quad (3.38)$$

$$\begin{aligned} \mathbf{p} \cdot \mathbf{e}^1 \cdot \hat{\boldsymbol{\theta}} &= -\frac{3}{4} e_{33} \sin 2\theta + \left[\frac{1}{4} (e_{11} - e_{22}) \cos 2\phi + \frac{1}{2} e_{12} \sin 2\phi \right] \sin 2\theta \\ &+ [e_{13} \cos \phi + e_{23} \sin 2\phi] \cos 2\theta, \end{aligned} \quad (3.39)$$

$$\begin{aligned} \mathbf{p} \cdot \mathbf{e}^1 \cdot \mathbf{p} &= \frac{1}{2} e_{33} (3 \cos^2 \theta - 1) + \left[\frac{1}{2} (e_{11} - e_{22}) \cos 2\phi + e_{12} \sin 2\phi \right] \sin^2 \theta \\ &+ [e_{13} \cos \phi + e_{23} \sin 2\phi] \sin 2\theta. \end{aligned} \quad (3.40)$$

The last term in equation 3.36 is a new term due to phototaxis, not present in Bees and Hill [9], and the last term on the first line of equation 3.36 is adjusted from the gyrotaxis only case of [9], since here Λ is a function of z and in [9] $\Lambda = \lambda$ constant, given in equation 3.9.

First order perturbation for spherical cells, $\alpha_0 = 0$

For spherical cells, where $\alpha_0 = 0$, equation 3.36 simplifies to

$$\begin{aligned} & \frac{1}{\sin \theta} \frac{\partial}{\partial \theta} \left(\sin \theta \frac{\partial f^1}{\partial \theta} \right) + \frac{1}{\sin^2 \theta} \frac{\partial^2 f^1}{\partial \phi^2} - \Lambda \left(\mathbf{k} \cdot \hat{\boldsymbol{\theta}} \frac{\partial f^1}{\partial \theta} - 2 \cos \theta f^1 \right) \\ = & -\eta \lambda \Lambda \mu_\lambda (\omega_2^1 \cos \phi - \omega_1^1 \sin \phi) \sin \theta e^{\Lambda \cos \theta} \\ & - \lambda \chi \kappa \mu_\lambda m^1 e^{\kappa m^0} e^{\Lambda \cos \theta} (\Lambda \sin^2 \theta - 2 \cos \theta). \end{aligned} \quad (3.41)$$

We solve this equation in two parts (one for each term on the right hand side). Consider the first term on the right hand side of equation 3.41 (disregard the other term for now) and write

$$f^1 = \lambda \mu_\lambda \eta (\omega_2^1 \cos \phi - \omega_1^1 \sin \phi) g(\theta), \quad (3.42)$$

for some function $g(\theta)$. On substituting $x = \cos \theta$ and equation 3.42 into equation 3.41,

$$((1-x^2)g')' - \frac{g}{(1-x^2)} - \Lambda((1-x^2)g)' = -\Lambda(1-x^2)^{\frac{1}{2}} e^{\Lambda x}. \quad (3.43)$$

Since Λ can be treated as a constant in this coordinate system, this equation is the same as the corresponding aspherical flow term in Pedley and Kessler [130], except we have $\Lambda(z)$ instead of constant λ . The equation can be solved in the same way, using Legendre polynomials of order one. To summarize, we first expand the exponential on the right hand side of equation 3.43 and write $g(x)$ as a power series in Λ so that

$$\Lambda e^{\Lambda x} = \sum_{n=1}^{\infty} \frac{\Lambda^n x^{n-1}}{(n-1)!} \quad \text{and} \quad g(x) = \sum_{n=1}^{\infty} \Lambda^n G_n(x), \quad (3.44)$$

assuming convergence at this stage. Comparing the coefficients of Λ^n gives

$$((1-x^2)G'_n)' - \frac{G_n}{(1-x^2)} - ((1-x^2)G'_{n-1})' = -\frac{(1-x^2)^{\frac{1}{2}} x^{n-1}}{(n-1)!}. \quad (3.45)$$

This has the form of an associated Legendre equation of order one, $P_r^1(x)$, so we define

$$G_n(x) = \sum_{r=1}^n a_{n,r} P_r^1(x), \quad (3.46)$$

where $a_{n,r} = 0$ for $n < r$ or $n, r < 1$. Equation 3.45 is solved using the same techniques as in Pedley and Kessler [130] and Bees and Hill [9], details of which can be found in Appendix B. We find

$$a_{n,m} = -\frac{m+2}{(m+1)(2m+3)}a_{n-1,m+1} + \frac{m-1}{(2m-1)m}a_{n-1,m-1} + \frac{b_{n,m}}{m(m+1)} \quad (3.47)$$

where

$$b_{n,m} = \frac{2m+1}{2(n-1)!m(m+1)} \int_{-1}^1 (1-x^2)^{\frac{1}{2}} x^{n-1} P_m^1(x) dx. \quad (3.48)$$

Quoting from Gradshteyn and Ryzhik [50],

$$b_{n+1,m} = \begin{cases} 0 & \forall \quad n+m \text{ even} \\ \frac{(2m+1)\Gamma(\frac{n+1}{2})\Gamma(\frac{n+2}{2})}{4\Gamma(n+1)\Gamma(\frac{n-m+3}{2})\Gamma(\frac{n+m+4}{2})} & \forall \quad n+m \text{ odd} \end{cases} \quad (3.49)$$

where $n+1 \geq m$, which implies that for $n+m$ even, $a_{n+1,m} = 0$. Γ represents the gamma function. We can then calculate $a_{i,j}$ for $i \geq j \geq 1$ by substituting the values of $b_{i,j}$ into the expression 3.47.

To calculate the contribution of this weak ambient flow to $\langle \mathbf{p} \rangle$, we use equations 3.44 and 3.46 in equation 3.21, so that

$$\begin{aligned} \langle \mathbf{p} \rangle^1 &= \int_S \mathbf{p} f^1(\mathbf{p}) \quad (3.50) \\ &= \mu_\Lambda \lambda \eta \int_0^{2\pi} \int_0^\pi (\omega_2 \cos \phi - \omega_1 \sin \phi) \begin{pmatrix} \sin \theta \cos \phi \\ \sin \theta \sin \phi \\ \cos \theta \end{pmatrix} \\ &\quad \times \left[\sum_{n=1}^{\infty} \Lambda^n \sum_{r=1}^n a_{n,r} P_r^1(\cos \theta) \right] \sin \theta d\theta d\phi, \end{aligned}$$

where the superscript 1 denotes the weak ambient flow component of $\langle \mathbf{p} \rangle$. Integrating with respect to ϕ gives

$$\langle \mathbf{p} \rangle^1(z) = \begin{pmatrix} \omega_2 \\ -\omega_1 \\ 0 \end{pmatrix} \eta J_1(z), \quad (3.51)$$

where J_1 is given by

$$J_1(z) = \mu_\Lambda(z) \lambda \pi \int_0^\pi \sum_{n=1}^{\infty} \Lambda^n(z) \sum_{r=1}^n a_{n,r} P_r^1(\cos \theta) \sin^2 \theta d\theta. \quad (3.52)$$

If we assume the series to be uniformly convergent, which seems reasonable, then we can integrate term by term and use equation B.3 (from Appendix B) with $k = 1$ to give

$$J_1(z) = \frac{4}{3}\pi\lambda\mu_\Lambda(z) \sum_{l=0}^{\infty} \Lambda^{2l+1}(z) a_{2l+1,1}. \quad (3.53)$$

To calculate the weak ambient flow contribution to the diffusion tensor, denoted \mathbf{D}^1 , we first use equation 3.26 to find $\langle \mathbf{pp} \rangle^1$, the diagonal terms of which are zero, which is symmetric. Quoting from Pedley and Kessler [130], but with $\Lambda(z)$ instead of λ , gives

$$\langle \mathbf{pp} \rangle_{13}^1(z) = \langle \mathbf{pp} \rangle_{31}^1(z) = \omega_2 \eta J_2(z), \quad (3.54)$$

$$\langle \mathbf{pp} \rangle_{23}^1(z) = \langle \mathbf{pp} \rangle_{32}^1(z) = -\omega_1 \eta J_2(z), \quad (3.55)$$

but here

$$J_2(z) = \frac{4}{5}\pi\lambda\mu_\Lambda(z) \sum_{l=1}^{\infty} \Lambda^{2l}(z) a_{2l,2}, \quad (3.56)$$

hence J_2 is not a constant. For $\lambda = 2.2$, if $0 \leq \chi \leq 1.5$ with $\kappa = 1.0$ then, using the boundary conditions on m , the range for Λ is

$$-1.1 \leq \Lambda \leq 2.2. \quad (3.57)$$

In this range, the $a_{i,j}$ values decay quickly for increasing i, j , and the series converges rapidly.

For the new term due to phototaxis on the right hand side of equation 3.41, we suppose

$$f^{1(2)} = \lambda\chi\kappa\mu_\lambda m^1 e^{\kappa m^0} h(\theta). \quad (3.58)$$

On substituting $x = \cos \theta$ and equation 3.58 into equation 3.41, we have

$$((1-x^2)h')' - \Lambda((1-x^2)h)' = -[e^{\Lambda x}(1-x^2)]'. \quad (3.59)$$

Substituting $h = H(x)e^{\Lambda x}$ into equation 3.59 and integrating once gives

$$(1-x^2)H'(x)e^{\Lambda x} = -e^{\Lambda x}(1-x^2) + C \quad (3.60)$$

We require $C = 0$ to avoid a singularity at $x = 1$. Hence, $H'(x) = -1$ so that

$$h = (B-x)e^{\Lambda x}. \quad (3.61)$$

B is determined from the normalization condition $\int_{-1}^1 h(x)dx = 0$, which gives

$$B(z) = \coth \Lambda(z) - \frac{1}{\Lambda(z)} = K_1(z), \quad (3.62)$$

which is constant in this orientation. Substituting B into equation 3.61 then gives

$$h(x, z) = e^{\Lambda x} (K_1(z) - x). \quad (3.63)$$

To find the contributions to $\langle \mathbf{p} \rangle$ for this new phototaxis term, we use equation 3.21, such that

$$\langle \mathbf{p} \rangle^{1(2)} = \lambda \chi \kappa \mu_\Lambda m^1 e^{\kappa m^0} \int_0^{2\pi} \int_0^\pi \begin{pmatrix} \sin \theta \cos \phi \\ \sin \theta \sin \phi \\ \cos \theta \end{pmatrix} (K_1(z) - \cos \theta) \sin \theta e^{\Lambda \cos \theta} d\theta d\phi. \quad (3.64)$$

Integrating with respect to ϕ shows that all but the z component of equation 3.64 are zero, and substituting $x = \cos \theta$ provides

$$\langle \mathbf{p} \rangle^{1(2)} = 2\pi \lambda \chi \kappa \mu_\Lambda m^1 e^{\kappa m^0} \mathbf{k} \int_{-1}^1 (K_1 - x) x e^{\Lambda x} dx. \quad (3.65)$$

Integrating by parts and substituting for μ_Λ from equation 3.20 gives

$$\langle \mathbf{p} \rangle^{1(2)} = \lambda \chi \kappa m^1 e^{\kappa m^0} \mathbf{k} \left(K_1^2 - 1 + \frac{2K_1}{\Lambda} \right). \quad (3.66)$$

We write this contribution to $\langle \mathbf{p} \rangle$ as

$$\langle \mathbf{p} \rangle^{1(2)}(z) = \lambda \chi \kappa m^1(z) e^{\kappa m^0(z)} \begin{pmatrix} 0 \\ 0 \\ K_6(z) \end{pmatrix} \quad (3.67)$$

where

$$K_6(z) = K_1^2(z) - 1 + \frac{2K_1(z)}{\Lambda(z)}. \quad (3.68)$$

Substituting equation 3.63 into the expression 3.26 for $\langle \mathbf{pp} \rangle$ gives the contribution of the new phototactic terms to $\langle \mathbf{pp} \rangle$ as

$$\begin{aligned} \langle \mathbf{pp} \rangle^{1(2)} &= \int_0^{2\pi} \int_0^\pi \begin{pmatrix} \sin \theta \cos \phi \\ \sin \theta \sin \phi \\ \cos \theta \end{pmatrix} \begin{pmatrix} \sin \theta \cos \phi \\ \sin \theta \sin \phi \\ \cos \theta \end{pmatrix} \\ &\quad \times \lambda \chi \kappa \mu_\Lambda m^1 e^{\kappa m^0} (K_1 - \cos \theta) e^{\Lambda \cos \theta} \sin \theta d\theta d\phi. \end{aligned} \quad (3.69)$$

As before, when we integrate with respect to ϕ only the diagonal terms remain, so that

$$\begin{aligned} \langle \mathbf{pp} \rangle^{1(2)} &= \pi \int_0^\pi \begin{pmatrix} \sin^2 \theta & 0 & 0 \\ 0 & \sin^2 \theta & 0 \\ 0 & 0 & 2 \cos^2 \theta \end{pmatrix} \\ &\quad \times \lambda \chi \kappa \mu_\Lambda m^1 e^{\kappa m^0} (K_1 - \cos \theta) e^{\Lambda \cos \theta} \sin \theta d\theta d\phi. \end{aligned} \quad (3.70)$$

Integrating by parts twice gives

$$\begin{aligned} \langle \mathbf{pp} \rangle_{11}^{1(2)}(z) &= \langle \mathbf{pp} \rangle_{22}^{1(2)}(z) = \lambda \chi \kappa m^1(z) e^{\kappa m^0(z)} \left(\frac{K_1^2(z)}{\Lambda(z)} + \frac{3K_1(z)}{\Lambda^2(z)} - \frac{1}{\Lambda(z)} \right) \quad (3.71) \\ &= \lambda \chi \kappa m^1(z) e^{\kappa m^0(z)} K_7(z) \end{aligned}$$

and

$$\begin{aligned} \langle \mathbf{pp} \rangle_{33}^{1(2)}(z) &= \lambda \chi \kappa m^1(z) e^{\kappa m^0(z)} \left(\frac{2}{\Lambda(z)} - \frac{2K_1^2(z)}{\Lambda} - \frac{6K_1(z)}{\Lambda^2(z)} \right) \quad (3.72) \\ &= \lambda \chi \kappa m^1(z) e^{\kappa m^0(z)} K_8(z), \end{aligned}$$

where

$$K_7(z) = \frac{K_1^2(z)}{\Lambda(z)} + \frac{3K_1(z)}{\Lambda^2(z)} - \frac{1}{\Lambda(z)}, \quad (3.73)$$

$$\text{and } K_8(z) = \frac{2}{\Lambda(z)} - \frac{2K_1^2(z)}{\Lambda(z)} - \frac{6K_1(z)}{\Lambda^2(z)}. \quad (3.74)$$

First order perturbation for aspherical cells ($\alpha_0 \neq 0$)

Next, we consider the terms in equation 3.36 that are present when $\alpha_0 \neq 0$ and the cells are aspherical. We write

$$\begin{aligned} f^{1(3)} &= -2\alpha_0 \lambda \mu_\Lambda \eta \left(\frac{3}{4} e_{33} g_2(x) + \left[\frac{1}{2} (e_{11} - e_{22}) \cos 2\phi + e_{12} \sin 2\phi \right] g_4(x) \right. \quad (3.75) \\ &\quad \left. + [e_{13} \cos \phi + e_{23} \sin \phi] g_3(x) \right), \end{aligned}$$

for some functions $g_2(x)$, $g_3(x)$ and $g_4(x)$, and $x = \cos \theta$. As in Bees [7], we define the operator L so that

$$L\bullet = \frac{\partial}{\partial x} \left((1-x^2) \frac{\partial}{\partial x} \bullet \right) - \Lambda \frac{\partial}{\partial x} ((1-x^2)\bullet). \quad (3.76)$$

Hence, equation 3.75 can be split into three parts,

$$Lg_2 = 2e^{\Lambda x} [-\Lambda x(1-x^2) + 3x^2 - 1], \quad (3.77)$$

$$Lg_3 - \frac{g_3}{1-x^2} = e^{\Lambda x} (1-x^2)^{\frac{1}{2}} [2x^2\Lambda - \Lambda + 6x], \quad (3.78)$$

$$Lg_4 - \frac{4g_4}{1-x^2} = e^{\Lambda x} (1-x^2) [\Lambda x + 3]. \quad (3.79)$$

Equation 3.77 is solved in the same way as the new term due to phototaxis in the previous section. Equation 3.78 is treated in the same way as the flow term in equation 3.41 in Section 3.2.2 but with a different right hand side. Equation 3.79 is solved in a similar fashion to the first term on the right hand side of equation 3.41 (solved using equation

3.43 in Section 3.2.2), but requires terms in $P_r^2(x)$ instead of $P_r^1(x)$. Equations 3.77 to 3.79 are the same as in Pedley and Kessler [130] except with $\Lambda(z)$ instead of constant λ on the right hand side (the z dependence does not affect the form of the solutions, however, as z is constant in this orientation). In Section 3.2.3, we quote the solutions for these equations from Bees and Hill [9] for the remaining components of $\langle \mathbf{p} \rangle$ and \mathbf{D} , changing λ to $\Lambda(z)$ where appropriate.

3.2.3 Summary

Summing the equilibrium and flow contributions (for spherical and aspherical cells), the mean cell swimming direction $\langle \mathbf{p} \rangle$ is given by

$$\begin{aligned} \langle \mathbf{p} \rangle = & \begin{pmatrix} 0 \\ 0 \\ K_1 \end{pmatrix} + \epsilon \left[\eta J_1 \begin{pmatrix} \omega_2 \\ -\omega_1 \\ 0 \end{pmatrix} - 2\alpha_0 \eta \begin{pmatrix} e_{13} J_4 \\ e_{23} J_4 \\ \frac{3}{2} e_{33} K_4 \end{pmatrix} + \lambda \chi \kappa m^1 e^{\kappa m^0} \begin{pmatrix} 0 \\ 0 \\ K_6 \end{pmatrix} \right] \\ & + O(\epsilon^2), \end{aligned} \quad (3.80)$$

and $\langle \mathbf{pp} \rangle$ is given by

$$\begin{aligned} \langle \mathbf{pp} \rangle = & \begin{pmatrix} \frac{K_1}{\Lambda} & 0 & 0 \\ 0 & \frac{K_1}{\Lambda} & 0 \\ 0 & 0 & 1 - 2\frac{K_1}{\Lambda} \end{pmatrix} + \epsilon \left[\eta J_2 \begin{pmatrix} 0 & 0 & \omega_2 \\ 0 & 0 & -\omega_1 \\ \omega_2 & -\omega_1 & 0 \end{pmatrix} \right. \\ & - 2\alpha_0 \eta \begin{pmatrix} -\frac{3}{4} e_{33} K_5 + \frac{1}{4} (e_{11} - e_{22}) J_6 & \frac{1}{2} e_{12} J_6 & e_{13} J_5 \\ \frac{1}{2} e_{12} J_6 & -\frac{3}{4} e_{33} K_5 - \frac{1}{4} (e_{11} - e_{22}) J_6 & e_{23} J_5 \\ e_{13} J_5 & e_{23} J_5 & \frac{3}{2} e_{33} K_5 \end{pmatrix} \\ & \left. + \lambda \chi \kappa m^1 e^{\kappa m^0} \begin{pmatrix} K_7 & 0 & 0 \\ 0 & K_7 & 0 \\ 0 & 0 & K_8 \end{pmatrix} \right] + O(\epsilon^2). \end{aligned} \quad (3.81)$$

Using the approximation for \mathbf{D} in equation 2.9, dimensionless \mathbf{D} up to order ϵ is

$$\mathbf{D} = [\langle \mathbf{pp} \rangle^0 - \langle \mathbf{p} \rangle^0 \langle \mathbf{p} \rangle^0] + \epsilon [\langle \mathbf{pp} \rangle^1 - (\langle \mathbf{p} \rangle^0 \langle \mathbf{p} \rangle^1 + \langle \mathbf{p} \rangle^1 \langle \mathbf{p} \rangle^0)]. \quad (3.82)$$

Substituting in the appropriate components of equations 3.80 and 3.81, we find the non-dimensional diffusion tensor as

$$\mathbf{D} = \begin{pmatrix} \frac{K_1}{\Lambda} & 0 & 0 \\ 0 & \frac{K_1}{\Lambda} & 0 \\ 0 & 0 & K_2 \end{pmatrix} + \epsilon \left[\eta(J_2 - J_1 K_1) \begin{pmatrix} 0 & 0 & \omega_2 \\ 0 & 0 & -\omega_1 \\ \omega_2 & -\omega_1 & 0 \end{pmatrix} - 2\alpha_0 \eta \right. \quad (3.83) \\ \left. \begin{pmatrix} -\frac{3}{4}e_{33}K_5 + \frac{1}{4}(e_{11} - e_{22})J_6 & \frac{1}{2}e_{12}J_6 & e_{13}(J_5 - K_1 J_4) \\ \frac{1}{2}e_{12}J_6 & -\frac{3}{4}e_{33}K_5 - \frac{1}{4}(e_{11} - e_{22})J_6 & e_{23}(J_5 - K_1 J_4) \\ e_{13}(J_5 - K_1 J_4) & e_{23}(J_5 - K_1 J_4) & \frac{3}{2}e_{33}(K_5 - 2K_1 K_4) \end{pmatrix} \right. \\ \left. + \lambda \chi \kappa m^1 e^{\kappa m^0} \begin{pmatrix} K_7 & 0 & 0 \\ 0 & K_7 & 0 \\ 0 & 0 & K_8 - 2K_1 K_6 \end{pmatrix} \right] + O(\epsilon^2).$$

We have thirteen functions dependent on $\Lambda(z) = \lambda \left(1 - \chi e^{\kappa m^0(z)}\right)$:

$$K_1(z) = \coth \Lambda(z) - \frac{1}{\Lambda(z)}, \quad (3.84)$$

$$K_2(z) = 1 - \coth^2 \Lambda(z) + \frac{1}{\Lambda^2(z)}, \quad (3.85)$$

$$K_4(z) = K_2(z) - \frac{K_1(z)}{\Lambda(z)}, \quad (3.86)$$

$$K_5(z) = -\frac{2}{\Lambda(z)} \left[1 + K_2(z) - \frac{4K_1(z)}{\Lambda(z)} \right], \quad (3.87)$$

$$K_6(z) = K_1^2(z) - 1 + \frac{2K_1(z)}{\Lambda(z)}, \quad (3.88)$$

$$K_7(z) = \frac{K_1^2(z)}{\Lambda(z)} + \frac{3K_1(z)}{\Lambda^2(z)} - \frac{1}{\Lambda(z)}, \quad (3.89)$$

$$K_8(z) = \frac{2}{\Lambda(z)} - \frac{2K_1^2(z)}{\Lambda(z)} - \frac{6K_1(z)}{\Lambda^2(z)}, \quad (3.90)$$

and

$$\mu_\Lambda(z) = \frac{\Lambda(z)}{4\pi \sinh \Lambda(z)}, \quad (3.91)$$

$$J_1(z) = \frac{4}{3}\pi\lambda\mu_\Lambda(z) \sum_{l=0}^{\infty} \Lambda^{2l+1}(z) a_{2l+1,1}, \quad (3.92)$$

$$J_2(z) = \frac{4}{5}\pi\lambda\mu_\Lambda(z) \sum_{l=1}^{\infty} \Lambda^{2l}(z) a_{2l,2}, \quad (3.93)$$

$$J_4(z) = \frac{4}{3}\pi\lambda\mu_\Lambda(z) \sum_{l=0}^{\infty} \Lambda^{2l+1}(z) \tilde{a}_{2l+1,1}, \quad (3.94)$$

$$J_5(z) = \frac{4}{5}\pi\lambda\mu_\Lambda(z) \sum_{l=0}^{\infty} \Lambda^{2l}(z) \tilde{a}_{2l,2}, \quad (3.95)$$

$$J_6(z) = \frac{16}{5}\pi\lambda\mu_\Lambda(z) \sum_{l=0}^{\infty} \Lambda^{2l}(z) \bar{a}_{2l,2}. \quad (3.96)$$

a , \tilde{a} and \bar{a} are defined as

$$a_{n,m} = -\frac{m+2}{(m+1)(2m+3)} a_{n-1,m+1} + \frac{m-1}{(2m-1)m} a_{n-1,m-1} + \frac{b_{n,m}}{m(m+1)},$$

where $b_{n+1,m} = \begin{cases} 0, & \forall n+m \text{ even}, \\ \frac{(2m+1)\Gamma_{\frac{n+1}{2}}\Gamma_{\frac{n+2}{2}}}{4\Gamma(n+1)\Gamma_{\frac{n-m+3}{2}}\Gamma_{\frac{n+m+4}{2}}}, & \forall n+m \text{ odd}, \end{cases} \quad (3.97)$

$$\tilde{a}_{n,m} = -\frac{m+2}{(m+1)(2m+3)} \tilde{a}_{n-1,m+1} + \frac{m-1}{(2m-1)m} \tilde{a}_{n-1,m-1} + \frac{\tilde{b}_{n,m}}{m(m+1)},$$

where $\tilde{b}_{n+1,m} = \begin{cases} 0, & \forall n+m \text{ even}, \\ -\frac{(2m+1)\Gamma_{\frac{n+1}{2}}\Gamma_{\frac{n+2}{2}}(n^2+5n+4+m+m^2)}{16\Gamma(n+1)\Gamma_{\frac{n-m+5}{2}}\Gamma_{\frac{n+m+6}{2}}}, & \forall n+m \text{ odd}, \end{cases} \quad (3.98)$

$$\bar{a}_{n,m} = -\frac{m+3}{(m+1)(2m+3)} \bar{a}_{n-1,m+1} + \frac{m-2}{(2m-1)m} \bar{a}_{n-1,m-1} + \frac{\bar{b}_{n,m}}{m(m+1)},$$

where $\bar{b}_{n+1,m} = \begin{cases} 0, & \forall n+m \text{ even}, \\ -\frac{(2m+1)\Gamma_{\frac{n+2}{2}}\Gamma_{\frac{n+3}{2}}(n+4)}{8\Gamma(n+2)\Gamma_{\frac{n-m+5}{2}}\Gamma_{\frac{n+m+6}{2}}}, & \forall n+m \text{ odd}. \end{cases} \quad (3.99)$

If $\chi = 0$, $\Lambda(z) = \lambda$, so that $K_6(z) = K_8(z) = 0$ and expressions 3.84 to 3.87 and 3.92 to 3.96 become exactly the same as for the gyrotaxis only case in Bees and Hill [9] and Pedley and Kessler [130], shown in Table 2.2. If this is the case, the solution to the Fokker-Planck equation is the same as that used in Model A in Chapter 2 and Bees and Hill [9], and direct comparisons can be made when $\chi = 0$.

3.3 Equilibrium solution and linear analysis for Model B

We find an equilibrium solution for the case of no fluid flow, $\mathbf{u} = \mathbf{0}$, with $n = n(z)$, using the same method as in Section 2.3.1. Integrating the cell conservation equation 3.6

with respect to z , applying the boundary conditions in equations 2.21, 2.22 and 2.23, and substituting in the solutions to the Fokker-Planck from equations 3.80 and 3.83 gives

$$\frac{dn}{dz} - \frac{d\bar{K}_2}{\bar{K}_1} \frac{K_1(z)}{K_2(z)} n(z) = 0, \quad (3.100)$$

with $K_1(z)$ and $K_2(z)$ defined in equations 3.84 and 3.85. We use the change of variables in equation 3.7 to remove the integral of $n(z)$ in the expression for light intensity that is present in $K_1(z)$ and $K_2(z)$, which increases the order of the system. Equation 3.100 then becomes

$$\frac{d^2 m(z)}{dz^2} - \frac{d\bar{K}_2}{\bar{K}_1} \frac{K_1(z)}{K_2(z)} \frac{dm(z)}{dz} = 0, \quad (3.101)$$

with boundary conditions $m = \frac{e^{-d}-1}{d}$ at $z = -1$, and $m = 0$ at $z = 0$, as in Model A.

3.3.1 Analytical approximation to the equilibrium solution for weak absorption

As in Vincent and Hill 1996 [172], Ghorai and Hill 2005 [46] and Model A, if we assume the case of weak absorption, so that $0 < \kappa \ll 1$ and I is close to I_c , then we can find an analytic equilibrium solution. The critical light intensity I_c occurs at position $z = -C$ ($0 \leq C \leq 1$) for an individual cell for the vertically uniform concentration profile $n = 1$. For small κ we can expand the exponential in the expression $\Lambda(z) = \lambda \left(1 - \chi e^{\kappa m^0}\right)$ such that

$$\Lambda = -\frac{\lambda}{I_c} \left(I_s - I_s \kappa \int_z^0 n(z) dz - I_c \right) + O(\kappa^2). \quad (3.102)$$

When $I = I_c$ we have $I_c = I_s e^{-\kappa C}$ which, expanding for small κ , gives $I_c = I_s - I_s \kappa C + O(\kappa^2)$. Equation 3.102 becomes

$$\Lambda = \frac{\lambda}{I_c} I_s \kappa \left(\int_z^0 n(z) dz - C \right) + O(\kappa^2), \quad (3.103)$$

and since $I_c = I_s + O(\kappa)$,

$$\Lambda = \lambda \kappa \left(\int_z^0 n(z) dz - C \right) + O(\kappa^2). \quad (3.104)$$

This shows that approximately $\Lambda \propto \kappa$ where $\kappa \ll 1$ and, hence, $\Lambda \ll 1$. To find an asymptotic equilibrium solution we need to expand $\frac{K_1(\Lambda(z))}{K_2(\Lambda(z))}$ in equation 3.101 for small Λ .

Using Taylor expansions we find

$$\frac{K_1(\Lambda)}{K_2(\Lambda)} = \frac{\coth(\Lambda) - \frac{1}{\Lambda}}{1 - \coth^2(\Lambda) + \frac{1}{\Lambda^2}} = \Lambda + O(\Lambda^3). \quad (3.105)$$

The equilibrium in equation 3.100 to order κ thus becomes

$$\frac{dn}{dz} - \frac{d\bar{K}_2}{\bar{K}_1} \lambda \kappa \left[\int_z^0 n(z) dz - C \right] n(z) = 0. \quad (3.106)$$

This is the same as in Vincent and Hill [172], Ghorai and Hill [46] and equation 2.61 in Chapter 2, except with different constants outside the bracket. We solve in the same way to give

$$n(z) = \frac{\frac{K^2}{2G_1} [(K^2/G_1^2) - C^2] \operatorname{sech}^2(Kz/2)}{[(K/G_1) + C \tanh(Kz/2)]^2}, \quad (3.107)$$

where $G_1 = \frac{d\bar{K}_2}{\bar{K}_1} \lambda \kappa$ is the new constant and K is a constant obtained from the transcendental equation 2.63 in Chapter 2. Full details can be found in Appendix A. K is calculated using a Newton-Raphson process.

3.3.2 Numerical and analytical equilibrium profiles

For use in the numerical programs for equilibrium solution and linear stability analysis, z is scaled with sublayer depth d , so that $z_I = dz$, as in Model A. This improves the numerics when d is large and χ is small, since the top region of the layer is expanded, but most importantly it allows us to directly compare results with Model A and Bees and Hill [9]. The layer depth is now $0 \geq z \geq -d$.

Figure 3.1 shows both analytical and numerical equilibrium solutions, where solutions are a closer match for small κ , but still match reasonably well when $\kappa = 1$. Equilibrium profiles are shown in Figure 3.2 for $d = 20$, $\kappa = 1.2$ and for various values of χ . These solutions show the same qualitative trends as equilibrium solutions for Model A. For $\chi < 1$, the maximum concentration at equilibrium is at the upper boundary and the maximum concentration decreases as χ increases. For increasing $\chi > 1$ the maximum concentration moves down the layer; the position decreases as χ increases. The smallest maximum occurs at the midheight of the layer, with the amplitude of the maximum increasing again in the bottom half of the layer.

3.3.3 Linear stability analysis

We consider a perturbation from the equilibrium solution such that

$$\begin{aligned} \mathbf{u} &= \epsilon \mathbf{u}^1, & \langle \mathbf{p} \rangle &= \langle \mathbf{p} \rangle^0 + \epsilon \langle \mathbf{p} \rangle^1, & n &= n^0 + \epsilon n^1, \\ p_e &= p_e^0 + \epsilon p_e^1, & \boldsymbol{\Sigma} &= \epsilon \boldsymbol{\Sigma}^1, & \mathbf{D} &= \mathbf{D}^0 + \epsilon \mathbf{D}^1, \\ m &= m^0 + \epsilon m^1, \end{aligned} \quad (3.108)$$

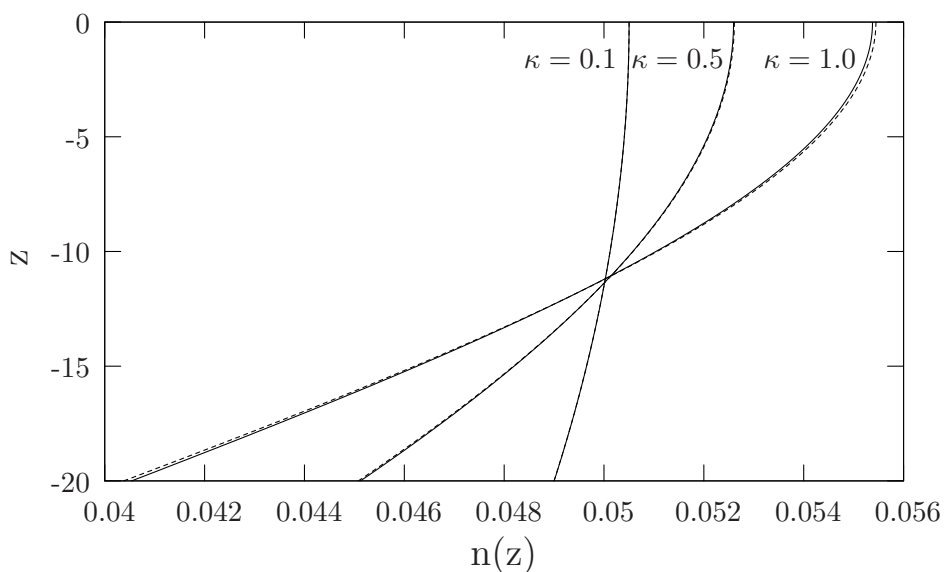


Figure 3.1: A comparison between numerical (solid lines) and analytical (dashed lines) equilibrium solutions for Model B, where $d = 20$, $\chi = 1.0$ and κ varies. The agreement between methods is good, even when κ is close to 1.

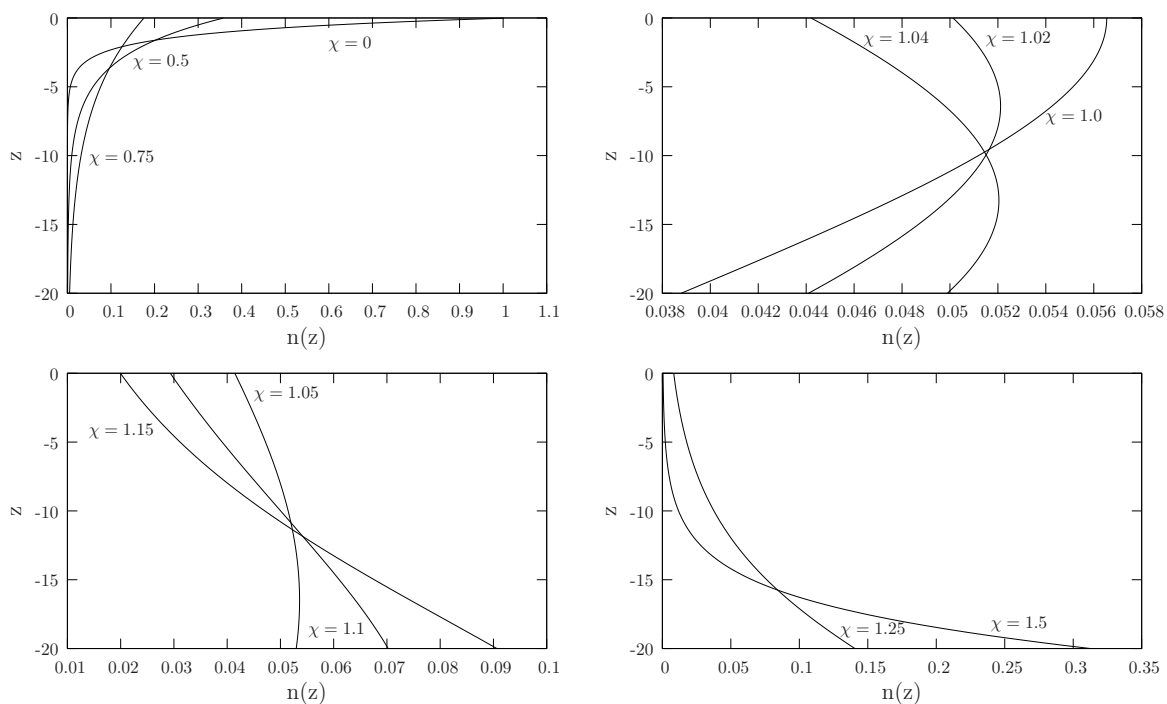


Figure 3.2: Concentration profiles for the equilibrium solution in Model B, where $d = 20$, $\kappa = 1.2$ and χ varies.

where $\epsilon \ll 1$. In this section, superscript 0 denotes the equilibrium solution (from Section 3.3) and superscript 1 the perturbation. On substituting the perturbations into the main model equations (equations 3.4, 3.5, 3.6 and 3.7), the governing equations to order ϵ become

$$\nabla \cdot \mathbf{u}^1 = 0, \quad (3.109)$$

$$S_c^{-1} \frac{\partial \mathbf{u}^1}{\partial t} = -\nabla p_e^1 - \gamma n^1 \mathbf{k} + \nabla \cdot \boldsymbol{\Sigma}^1, \quad (3.110)$$

$$\frac{\partial n^1}{\partial t} = -\nabla \cdot \left[n^0 \mathbf{u}^1 + \frac{d\bar{K}_2}{\bar{K}_1} n^0 \langle \mathbf{p} \rangle^1 + \frac{d\bar{K}_2}{\bar{K}_1} n^1 \langle \mathbf{p} \rangle^0 - \mathbf{D}^0 \cdot \nabla n^1 - \mathbf{D}^1 \cdot \nabla n^0 \right], \quad (3.111)$$

$$n^1 = \frac{dm^1}{dz}. \quad (3.112)$$

The Navier-Stokes equation 3.110 is the same as the corresponding Navier-Stokes equation 2.69 in Model A, so is not discussed here. Thus Rayleigh number is also the same as in Model A, defined in equation 2.90. Expanding equation 3.111, we find

$$\begin{aligned} \frac{\partial n^1}{\partial t} = & -\partial_3 n^0 u_3^1 - \frac{d\bar{K}_2}{\bar{K}_1} \partial_3 n^0 \langle \mathbf{p} \rangle_3^1 - \frac{d\bar{K}_2}{\bar{K}_1} n^0 \partial_i \langle \mathbf{p} \rangle_i^1 - \frac{d\bar{K}_2}{\bar{K}_1} \partial_i n^1 \langle \mathbf{p} \rangle_i^0 \\ & - \frac{d\bar{K}_2}{\bar{K}_1} n^1 \partial_i \langle \mathbf{p} \rangle_i^0 + D_{ij}^0 \partial_i \partial_j n^1 + \partial_i D_{ij}^0 \partial_j n^1 + D_{33} \partial_i \partial_j n^0 + \partial_i D_{i3}^1 \partial_3 n^0. \end{aligned} \quad (3.113)$$

From the solution for the Fokker-Planck equation in equation 3.80 and 3.83, using the method in Chapter 2, we have

$$\begin{aligned} \partial_i \langle \mathbf{p} \rangle_i^1 = & H_1 \nabla^2 u_3^1 + H_2 \partial_3 \partial_3 u_3^1 - 3\alpha_0 \eta \partial_3 u_3^1 \partial_3 K_4 \\ & + \lambda \chi \kappa \partial_3 \left(m^1 e^{\kappa m^0} K_6 \right), \end{aligned} \quad (3.114)$$

$$\begin{aligned} \partial_i D_{i3}^1 = & H_3 \nabla^2 u_3^1 + H_4 \partial_3 \partial_3 u_3^1 - 3\alpha_0 \eta \partial_3 u_3^1 \partial_3 (K_5 - 2K_1 K_4) \\ & + \lambda \chi \kappa \partial_3 ((K_8 - 2K_1 K_6) m^1 e^{\kappa m^0}), \end{aligned} \quad (3.115)$$

where H_i are defined in equations 2.81 to 2.84 in Chapter 2, and Λ , K_1 , K_2 , K_4 , K_5 , K_6 , K_7 and K_8 are all functions of z , whereas \bar{K}_1 and \bar{K}_2 are constants. Substituting

equations 3.114 and 3.115 in equation 3.113 gives

$$\begin{aligned}
\frac{\partial n^1}{\partial t} = & \left\{ -\partial_3 n^0 + \left[\partial_3 n^0 H_3 - \frac{d\bar{K}_2}{\bar{K}_1} n^0 H_1 \right] \nabla^2 \right. \\
& + \left[\partial_3 n^0 H_4 - \frac{d\bar{K}_2}{\bar{K}_1} n^0 H_2 \right] \partial_3 \partial_3 + 3\alpha_0 \eta \left[\frac{d\bar{K}_2}{\bar{K}_1} \partial_3 n^0 K_4 \right. \\
& \left. \left. - (K_5 - 2K_1 K_4) \partial_3 \partial_3 n^0 + \frac{d\bar{K}_2}{\bar{K}_1} n^0 \partial_3 K_4 - \partial_3 n^0 \partial_3 (K_5 - 2K_1 K_4) \right] \partial_3 \right\} u_3^1 \\
& \left\{ \frac{K_1}{\Lambda} (\partial_1 \partial_1 + \partial_2 \partial_2) + K_2 \partial_3 \partial_3 - \frac{d\bar{K}_2}{\bar{K}_1} K_1 \partial_3 - \frac{d\bar{K}_2}{\bar{K}_1} \partial_3 K_1 + \partial_3 K_2 \partial_3 \right\} n^1 \\
& + \lambda \chi \kappa e^{\kappa m^0} \left\{ -\frac{d\bar{K}_2}{\bar{K}_1} \left[\partial_3 n^0 K_6 + n^0 \left(\kappa \frac{dm^0}{dz} K_6 + \partial_3 K_6 + K_6 \partial_3 \right) \right] \right. \\
& + \partial_3 \partial_3 n^0 (K_8 - 2K_1 K_6) + \partial_3 n^0 \left[\kappa \frac{dm^0}{dz} (K_8 - 2K_1 K_6) + \partial_3 (K_8 - 2K_1 K_6) \right. \\
& \left. \left. + (K_8 - 2K_1 K_6) \partial_3 \right] \right\} m^1.
\end{aligned} \tag{3.116}$$

Consider normal modes, as in Chapter 2, so that

$$u_3^1 = U(z) e^{i(lx+my)+\sigma t}, \quad n^1 = \Phi(z) e^{i(lx+my)+\sigma t}, \quad m^1 = M(z) e^{i(lx+my)+\sigma t}, \tag{3.117}$$

where σ is the growth rate of the perturbation and $k = \sqrt{l^2 + m^2}$ is the wavenumber, and $\Phi(z) = \frac{dM}{dz}$. Equation 3.116 becomes

$$\begin{aligned}
& \left\{ P_V(z) \frac{d^2}{dz^2} - \frac{d\bar{K}_2}{\bar{K}_1} K_1(z) \frac{d}{dz} - P_H(z) k^2 - \sigma - \frac{d\bar{K}_2}{\bar{K}_1} \frac{dK_1}{dz} + \frac{dP_V(z)}{dz} \frac{d}{dz} \right. \\
& \left. + \lambda \chi \kappa e^{\kappa m^0} P_R(z; d) \right\} \Phi + \lambda \chi \kappa e^{\kappa m^0} P_M(z; d) M(z) \\
& = \left\{ \frac{dn^0}{dz} - \eta P_5(z; d) \frac{d^2}{dz^2} - \eta P_6(z; d) \frac{d}{dz} + \eta P_7(z; d) k^2 \right\} U(z),
\end{aligned} \tag{3.118}$$

where

$$P_V(z) = K_2(z), \quad P_H(z) = \frac{K_1(z)}{\Lambda(z)}, \quad (3.119)$$

$$P_R(z; d) = -\frac{d\bar{K}_2}{\bar{K}_1} n^0 K_6(z) + \frac{dn^0}{dz} (K_8(z) - 2K_1(z)K_6(z)), \quad (3.120)$$

$$P_M(z; d) = -\frac{d\bar{K}_2}{\bar{K}_1} \left[K_6(z) \frac{dn^0}{dz} + n^0 \left(\kappa \frac{dm^0}{dz} K_6(z) + \frac{dK_6(z)}{dz} \right) \right] \\ + \frac{d^2 n^0}{dz^2} (K_8(z) - 2K_1(z)K_6(z)) \\ + \frac{dn^0}{dz} \left[\kappa \frac{dm^0}{dz} (K_8(z) - 2K_1(z)K_6(z)) + \frac{d(K_8(z) - 2K_1(z)K_6(z))}{dz} \right], \quad (3.121)$$

$$P_5(z; d) = \frac{dn^0}{dz} A_1(z) + \frac{d\bar{K}_2}{\bar{K}_1} n^0 A_2(z), \quad (3.122)$$

$$P_6(z; d) = \frac{d\bar{K}_2}{\bar{K}_1} \frac{dn^0}{dz} A_3(z) - \frac{d^2 n^0}{dz^2} A_4(z) + \frac{d\bar{K}_2}{\bar{K}_1} n^0 \frac{dK_4(z)}{dz}, \\ - \frac{dn^0}{dz} \frac{d(K_5(z) - 2K_1(z)K_4(z))}{dz}, \quad (3.123)$$

$$P_7(z; d) = \frac{dn^0}{dz} A_5(z) - \frac{d\bar{K}_2}{\bar{K}_1} n^0 A_6(z), \quad (3.124)$$

where $n^0 = n^0(z)$ and $m^0 = m^0(z)$. $A_i(z)$ are the same as in Section 2.3.5 for Model A in Chapter 2, but are no longer constant and depend on z because they contain z -dependent expressions for $K_i(z)$ and $J_i(z)$. Equation 3.118 has a very similar form to equation 2.100 in Model A. The right hand sides of both equations are the same, although the definitions for $P_5(z; d)$, $P_6(z; d)$ and $P_7(z; d)$ are different. In this case, the non-constant K_i lead to extra terms on the left hand side with derivatives of $K_i(z)$. $P_M(z; d)$ and $P_R(z; d)$ are also defined differently. In both models, setting $\chi = 0$ gives the linear stability equation from Bees and Hill [9] for the gyrotaxis only case. The Navier-Stokes equation is given by equation 2.89 in Chapter 2. The boundary conditions are derived in the same way as Chapter 2, so that the no-flow boundary conditions in equation 2.21 become

$$U = 0 \quad \text{on } z = 0, -1, \quad \text{and} \quad \frac{dU}{dz} = 0 \quad \text{on } z = 0, -1. \quad (3.125)$$

By using these conditions, the no flux boundary conditions in equation 2.22 become

$$\frac{d\bar{K}_2}{\bar{K}_1} K_1 \Phi - K_2 \frac{d\Phi}{dz} \quad \text{on } z = 0, \quad (3.126)$$

and

$$\frac{d\bar{K}_2}{\bar{K}_1} K_1 \Phi - K_2 \frac{d\Phi}{dz} \quad (3.127)$$

$$+ \lambda \chi \kappa e^{\kappa m^0} \left(d \frac{\bar{K}_2}{\bar{K}_1} K_6 n^0 - \frac{dn^0}{dz} (K_8 - 2K_1 K_6) \right) M \quad \text{on } z = -1. \quad (3.128)$$

To complete the boundary conditions, we have the extra condition $M = 0$ at $z = 0$, from equation 2.23 (this is necessary as we increased the order of the system).

3.3.4 Taylor Expansions of K_i and J_i

Some parameter values, such as $I = I_c$, lead to values of Λ close to zero. This may cause problems when solving the model numerically, as many functions appear to involve division by Λ . However, Taylor expanding each K_i and J_i , as shown in equation 3.129 to 3.136, we find that every K_i and J_i is finite and converges as Λ tends to zero:

$$K_1(\Lambda) = \frac{1}{3}\Lambda - \frac{1}{45}\Lambda^3 + O(\Lambda^5), \quad (3.129)$$

$$K_2(\Lambda) = \frac{1}{3} - \frac{1}{15}\Lambda^2 + O(\Lambda^4), \quad (3.130)$$

$$K_4(\Lambda) = -\frac{2}{45}\Lambda^2 + \frac{8}{945}\Lambda^4 + O(\Lambda^6), \quad (3.131)$$

$$K_5(\Lambda) = -\frac{2}{45}\Lambda - \frac{4}{945}\Lambda^3 + O(\Lambda^5), \quad (3.132)$$

$$K_6(\Lambda) = -\frac{1}{3} + \frac{1}{15}\Lambda^2 - \frac{2}{189}\Lambda^4 + O(\Lambda^6), \quad (3.133)$$

$$K_7(\Lambda) = \frac{2}{45}\Lambda - \frac{8}{945}\Lambda^3 + O(\Lambda^5), \quad (3.134)$$

$$K_8(\Lambda) = -\frac{4}{45}\Lambda + \frac{16}{945}\Lambda^3 + O(\Lambda^5). \quad (3.135)$$

For each J_i , the part we need to expand for small Λ is

$$\frac{\Lambda}{\sinh(\Lambda)} = 1 - \frac{1}{6}\Lambda^2 + \frac{7}{360}\Lambda^4 + O(\Lambda^5). \quad (3.136)$$

These expressions are used in the numerical program to eliminate any problems when Λ is small.

3.4 Asymptotic analysis for a deep layer and weak illumination in Model B

In this section, we follow the asymptotic procedure for Model A in Chapter 2, and perform a deep layer analysis where $d \gg 1$ and χ small. We look for a solution when $\sigma = 0$, $k \sim 1$, $d^{-1} \ll 1$ and $\chi = d^{-1}\chi_{-1}$.

3.4.1 Equilibrium solution

Multiplying the equilibrium solution in equation 3.101 by d^{-1} gives

$$d^{-1} \frac{d^2 m}{dz^2} - \frac{\bar{K}_2}{\bar{K}_1} \frac{K_1(\Lambda)}{K_2(\Lambda)} \frac{dm}{dz} = 0, \quad (3.137)$$

with boundary conditions $m = 0$ at $z = 0$, and $m = d^{-1}(e^{-d} - 1)$ at $z = -1$. We re-write $\Lambda(z)$ in equation 3.16 as

$$\Lambda = \lambda(1 - d^{-1}\chi_{-1}e^{\kappa m}) = \lambda_0 + d^{-1}e^{\kappa m}\lambda_1, \quad (3.138)$$

where $\lambda_0 = \lambda$ and $\lambda_1 = -\lambda\chi_{-1}$. Using this expression to expand K_1 and K_2 in equations 3.84 and 3.85, using Taylor expansions for small d^{-1} , we have

$$K_1 = K_{(1,0)} + d^{-1}e^{\kappa m}K_{(1,-1)} + d^{-2}e^{2\kappa m}K_{(1,-2)}, \quad (3.139)$$

$$K_2 = K_{(2,0)} + d^{-1}e^{\kappa m}K_{(2,-1)} + d^{-2}e^{2\kappa m}K_{(2,-2)}, \quad (3.140)$$

where $K_{(i,j)}$ are constants not dependent on d , defined in Appendix C. If we expand $\frac{K_1}{K_2}$ for small d and define

$$K_{(1/2,0)} = \frac{K_{(1,0)}}{K_{(2,0)}}, \quad (3.141)$$

$$K_{(1/2,-1)} = \frac{1}{K_{(2,0)}} \left(K_{(1,-1)} - \frac{K_{(1,0)}K_{(2,-1)}}{K_{(2,0)}} \right), \quad (3.142)$$

$$K_{(1/2,-2)} = \frac{1}{K_{(2,0)}} \left(K_{(1,-2)} + \frac{K_{(1,0)}K_{(2,-2)}}{K_{(2,0)}} + \frac{K_{(2,-1)}(K_{(1,0)}K_{(2,-1)} - K_{(1,-1)}K_{(2,0)})}{K_{(2,0)}^2} \right), \quad (3.143)$$

then we can write

$$\frac{K_1(\Lambda)}{K_2(\Lambda)} \approx K_{(1/2,0)} + d^{-1}e^{\kappa m}K_{(1/2,-1)} + d^{-2}e^{2\kappa m}K_{(1/2,-2)} + O(d^{-3}). \quad (3.144)$$

Expanding m in powers of d^{-1}

$$m = \sum_{n=0}^{\infty} d^{-n}m_{-n}, \quad (3.145)$$

then

$$e^{\kappa m} = e^{\kappa m_0} \left(1 + d^{-1}\kappa m_{-1} + d^{-2}\kappa \left(m_{-2} + \frac{\kappa m_{-1}^2}{2} \right) + O(d^{-3}) \right), \quad (3.146)$$

as in equation 2.143 for Model A. Substituting equations 3.144 and 3.146 into equation 3.137 then gives

$$\begin{aligned} & d^{-1} \frac{d^2(m_0 d^{-1} m_{-1} + d^{-2} m_{-2} + \dots)}{dz^2} - \frac{\bar{K}_2}{\bar{K}_1} [K_{(1/2,0)} + d^{-1}e^{\kappa m_0}K_{(1/2,-1)}] \\ & + d^{-2}(e^{2\kappa m_0}K_{(1/2,-2)} + e^{\kappa m_0}\kappa m_{-1}K_{(1/2,-1)}) + O(d^{-3}) \\ & \times \frac{d(m_0 + d^{-1}m_{-1} + d^{-2}m_{-2} + \dots)}{dz} = 0. \end{aligned} \quad (3.147)$$

For the **outer** solution, we find $m_0 = \text{constant}$. Every subsequent m_{-n} will also be constant. The boundary condition at $z = -1$ gives that $m_0 = m_{-2} = \dots m_{-n} = 0$ and $m_{-1} = -1$.

For the **inner** solution we scale $z_I = dz$ so that the equilibrium solution becomes

$$\begin{aligned} & \frac{d^2(m_0 + d^{-1}m_{-1} + d^{-2}m_{-2} + \dots)}{dz_I^2} - \frac{\bar{K}_2}{\bar{K}_1} (K_{(1/2,0)} + d^{-1}e^{\kappa m_0} K_{(1/2,-1)}) \quad (3.148) \\ & + d^{-2}(e^{2\kappa m_0} K_{(1/2,-2)} + e^{\kappa m_0} \kappa m_{-1} K_{(1/2,-1)}) + O(d^{-3}) \\ & \frac{d(m_0 + d^{-1}m_{-1} + d^{-2}m_{-2} + \dots)}{dz_I} = 0. \end{aligned}$$

The solution at leading order is

$$m_0 = A_0(e^{z_I} - 1). \quad (3.149)$$

At next order we have

$$\frac{d^2 m_{-1}}{dz_I^2} - \frac{dm_{-1}}{dz_I} - \frac{\bar{K}_2}{\bar{K}_1} K_{(1/2,-1)} e^{\kappa m_0} \frac{dm_0}{dz_I} = 0. \quad (3.150)$$

In order to match with the outer solution we require $A_0 = 0$ (using the procedure described in Section 2.4). Solving equation 3.150 then gives

$$m_{-1} = A_1(e^{z_I} - 1). \quad (3.151)$$

The matching as z_I tends to $-\infty$ provides $A_1 = 1$. Equation 3.148 at the next order can be integrated with respect to z_I to give

$$\frac{dm_{-2}}{dz_I} - m_{-2} = \frac{\bar{K}_2}{\bar{K}_1} K_{(1/2,-1)} m_1 + A_2. \quad (3.152)$$

Substituting in m_{-1} and using the integrating factor e^{-z_I} gives

$$m_{-2} = \frac{\bar{K}_2}{\bar{K}_1} K_{(1/2,-1)} (z_I e^{z_I} + 1) - A_2 + B_2 e^{z_I}. \quad (3.153)$$

On applying the boundary condition at $z_I = 0$ and using the matching, we find $A_2 = \frac{\bar{K}_2}{\bar{K}_1} K_{(1/2,-1)}$ and $B_2 = 0$. Thus,

$$m_{-2} = \frac{\bar{K}_2}{\bar{K}_1} K_{(1/2,-1)} z_I e^{z_I}, \quad (3.154)$$

and we have the necessary components of the equilibrium solution for use in the linear stability analysis.

3.4.2 Linear stability analysis

The asymptotic linear stability theory is performed on the Navier-Stokes equation,

$$(D^2 - k^2)^2 U = -k^2 d^{-1} R\Phi, \quad (3.155)$$

and the cell conservation equation 3.118, with $P_i(z)$ and $K_i(z)$ defined in Section 3.3.3. As in linear stability analysis in Section 3.3.3, the equilibrium components are now denoted with a superscript 0. Since none of the K_i , J_i , P_i or A_i are constants, the asymptotic analysis involves much expanding. We write each expansion in the same way, as in the equilibrium solution. For example,

$$\begin{aligned} K_i = & K_{(i,0)} + d^{-1} K_{(i,-1)} + d^{-2} (\kappa m_{-1}^0 K_{(i,-1)} + K_{(i,-2)}) \\ & + d^{-3} \left(K_{(i,-1)} \kappa \left(m_{-2}^0 + \frac{\kappa (m_{-1}^0)^2}{2} \right) + K_{(i,-3)} + 2\kappa m_{-1} K_{(i,-2)} \right), \end{aligned} \quad (3.156)$$

and similarly for all J_i , P_i and A_i . Each component $K_{(i,j)}$ (and $J_{(i,j)}$, $P_{(i,j)}$, $A_{(i,j)}$) can be calculated directly using Taylor series to expand the expressions for K_i (and J_i , P_i and A_i) for $d \ll 1$, as for the equilibrium solution. Note that the leading order component of K_i and J_i do not depend on χ and are constants that depend on λ , and have the same form as K_i and J_i in Model A, defined in Table 2.2. For example, $K_{(1,0)} = \bar{K}_1$. The definitions of the relevant components for use in the asymptotic solution can be found in Appendix C.

Outer Solution

For the outer solution we use the outer equilibrium solution, which gives $m^0 = -d^{-1}$ (since we assume d is sufficiently large that e^{-d} is exponentially small) and, hence, $\frac{dm^0}{dz} = n^0 = 0$.

This simplifies equation 3.118 to

$$\left\{ K_2(z) \frac{d^2}{dz^2} - \frac{d\bar{K}_2}{\bar{K}_1} K_1(z) \frac{d}{dz} - \frac{K_1}{\Lambda(z)} k^2 - \sigma - \frac{d\bar{K}_2}{\bar{K}_1} \frac{dK_1}{dz} + \frac{dK_2(z)}{dz} \frac{d}{dz} \right\} \Phi = 0. \quad (3.157)$$

If we expand Φ in orders of d^{-1} then at leading order $\Phi_0 = \text{constant}$. The boundary condition on $z = -1$ at leading order gives $\Phi_0 = 0$. At next order, $\Phi_{-1} = 0$. This gives the same solution to the Navier-Stokes equation 3.155 as in the previous model, so

$$U = -kA(z+1) \cosh k(z+1) + (A + B(z+1)) \sinh k(z+1), \quad (3.158)$$

where A and B are constants that can be expanded in terms of d^{-1} .

Inner Solution

For the inner solution we re-scale equation 3.118 and the Navier-Stokes equation 2.89 using $z_I = dz$, so that

$$(D_I^2 - d^{-2}k^2)^2 U = -k^2 d^{-5} R\Phi, \quad (3.159)$$

$$\left\{ P_V(z_I) \frac{d^2}{dz_I^2} - \frac{\bar{K}_2}{\bar{K}_1} K_1(z_I) \frac{d}{dz_I} - d^{-2} P_H(z_I) k^2 - d^{-2} \sigma - \frac{\bar{K}_2}{\bar{K}_1} \frac{dK_1}{dz_I} + \frac{dP_V(z_I)}{dz_I} \frac{d}{dz_I} \right. \\ \left. + d^{-2} \lambda \chi_{-1} \kappa e^{\kappa m^0} P_R(z_I) \right\} \Phi + d^{-1} \lambda \chi_{-1} \kappa e^{\kappa m^0} P_M(z_I) = \left\{ d^{-1} \frac{dn^0}{dz_I} \right. \\ \left. - d\eta P_5(z_I) \frac{d^2}{dz_I^2} - d\eta P_6(z_I) \frac{d}{dz_I} + d^{-1} \eta P_7(z_I) k^2 \right\} U, \quad (3.160)$$

where

$$P_R(z_I) = -\frac{\bar{K}_2}{\bar{K}_1} n^0 K_6(z_I) + \frac{dn^0}{dz_I} (K_8(z_I) - 2K_1(z_I)K_6(z_I)), \quad (3.161)$$

$$P_M(z_I) = -\frac{\bar{K}_2}{\bar{K}_1} \left[K_6(z_I) \frac{dn^0}{dz_I} + n^0 \left(\kappa \frac{dm^0}{dz_I} K_6(z_I) + \frac{dK_6(z_I)}{dz_I} \right) \right] \\ + \frac{d^2 n^0}{dz_I^2} (K_8(z_I) - 2K_1(z_I)K_6(z_I)) \\ + \frac{dn^0}{dz_I} \left[\kappa \frac{dm^0}{dz_I} (K_8(z_I) - 2K_1(z_I)K_6(z_I)) + \frac{d(K_8(z_I) - 2K_1(z_I)K_6(z_I))}{dz_I} \right], \quad (3.162)$$

$$P_5(z_I) = \frac{dn^0}{dz_I} A_1(z_I) + \frac{\bar{K}_2}{\bar{K}_1} n^0 A_2(z_I), \quad (3.163)$$

$$P_6(z_I) = \frac{\bar{K}_2}{\bar{K}_1} \frac{dn^0}{dz_I} A_3(z_I) - \frac{d^2 n^0}{dz_I^2} A_4(z_I) + \frac{\bar{K}_2}{\bar{K}_1} n^0 \frac{dK_4(z_I)}{dz_I} \\ - \frac{dn^0}{dz_I} \frac{d(K_5(z_I) - 2K_1(z_I)K_4(z_I))}{dz_I}, \quad (3.164)$$

$$P_7(z_I) = \frac{dn^0}{dz_I} A_5(z_I) - \frac{\bar{K}_2}{\bar{K}_1} n^0 A_6(z_I), \quad (3.165)$$

and $n^0 = n^0(z_I)$ and $m^0 = m^0(z_I)$. Since $\frac{dm^0}{dz} = n^0$, then from the analytic equilibrium solution

$$d \frac{dm^0}{dz_I} = n^0(z_I) = e^{z_I} + d^{-1} \frac{\bar{K}_2}{\bar{K}_1} K_{(1/2,-1)}(z_I e^{z_I} + e^{z_I}), \quad (3.166)$$

$$\frac{dn^0}{dz_I} = e^{z_I} + d^{-1} \frac{\bar{K}_2}{\bar{K}_1} K_{(1/2,-1)}(z_I e^{z_I} + 2e^{z_I}), \quad (3.167)$$

$$\frac{d^2 n^0}{dz_I^2} = e^{z_I} + d^{-1} \frac{\bar{K}_2}{\bar{K}_1} K_{(1/2,-1)}(z_I e^{z_I} + 3e^{z_I}), \quad (3.168)$$

with boundary conditions

$$U = 0 \quad \text{and} \quad D_I U = 0 \quad \text{on} \quad z_I = 0, \quad (3.169)$$

$$\text{and} \quad K_2(z_I) D_I \Phi - \frac{K_{(2,0)}}{K_{(1,0)}} K_1(z_I) \Phi = 0 \quad \text{on} \quad z_I = 0. \quad (3.170)$$

The exponential terms on the right hand side of equation 3.160 complicate the expression and so we consider the case in which they do not appear at first order (as in Model A in Chapter 2 and in Bees and Hill [9]). This requires $U \leq O(1)$ and $\eta U \leq O(d^{-2})$. For a non-trivial solution we need $R \sim d^5 U$ and we follow the logic outlined in the asymptotic analysis for Model A in Section 2.4, Chapter 2. If we consider

$$U = \sum_{m=n}^{\infty} U_{-m} d^{-m}, \quad \Phi = \sum_{m=0}^{\infty} \Phi_{-m} d^{-m}, \quad \text{and} \quad M = \sum_{m=0}^{\infty} M_{-m} d^{-m}, \quad (3.171)$$

where $n = 1, 2, 3$, and

$$R = d^{5-n} R_{5-n} + d^{5-n-1} R_{5-n-1} + \dots, \quad (3.172)$$

then at first order we have

$$D_I U_{-n} + R_{5-n} k^2 \Phi_0 = 0 \quad (3.173)$$

$$\text{and} \quad K_{(2,0)} D_I (D_I - 1) \Phi_0 = 0. \quad (3.174)$$

Solving using the boundary conditions at order one gives

$$\Phi_0 = e^{z_I}, \quad (3.175)$$

$$U_{-n} = a_{-n} z_I^3 + b_{-n} z_I^2 + R_{5-n} k^2 (z_I + 1 - e^{z_I}). \quad (3.176)$$

At second order

$$D^4 U_{-n-1} + k^2 R_{5-n} \Phi_{-1} + k^2 R_{5-n-1} \Phi_0 = 0 \quad (3.177)$$

and

$$K_{(2,0)} D_I (D_I - 1) \Phi_{-1} + K_{(2,-1)} D_I^2 \Phi_0 - \frac{K_{(2,0)}}{K_{(1,0)}} K_{(1,-1)} D_I \Phi_0 = 0, \quad (3.178)$$

with the no flux boundary condition at this order given by

$$K_{(2,0)} D_I \Phi_{-1} - K_{(2,0)} \Phi_{-1} + K_{(2,-1)} D_I \Phi_0 - \frac{K_{(2,0)}}{K_{(1,0)}} K_{(1,-1)} \Phi_0 = 0. \quad (3.179)$$

Equation 3.178 can be written as

$$D_I^2 \Phi_{-1} - D_I \Phi_{-1} = -A_K e^{z_I}, \quad (3.180)$$

where

$$A_K = \frac{K_{(2,-1)} - \frac{K_{(2,0)}}{K_{(1,0)}} K_{(1,-1)}}{K_{(2,0)}}. \quad (3.181)$$

Integrating once gives

$$D_I \Phi_{-1} - \Phi_{-1} = -A_K e^{z_I} + B_K, \quad (3.182)$$

and, using the boundary condition, $B_K = 0$. Solving equation 3.182 gives

$$\Phi_{-1} = -A_K z_I e^{z_I} + C_K e^{z_I}, \quad (3.183)$$

where C_K is a constant. Solving equation 3.177 gives

$$\begin{aligned} U_{-n-1} = & a_{-n-1} z_I^3 + b_{-n-1} z_I^2 + k^2 R_{5-n-1} (z_I + 1 - e^{z_I}) \\ & + k^2 R_{5-n} (A_K (z_I e^{z_I} - 4e^{z_I}) - C_K e^{z_I} + (3A_K + C_K) z_I + 4A_K + C_K). \end{aligned} \quad (3.184)$$

To match the solutions we follow the procedure in Chapter 2, where we consider the intermediate region such that $z_\zeta \sim 1$ as $d^{-1} \rightarrow 0$, where $z_\zeta = \frac{z}{\zeta(d^{-1})}$ and $\zeta(d^{-1}) \rightarrow 0$ as $d^{-1} \rightarrow 0$ and $0 < d^{-1} \ll \zeta \ll 1 \ll d$. Expanding the inner solution, by writing $z_\zeta = z_I \frac{d^{-1}}{\zeta}$, we find that the terms due to phototaxis in Model B are small, and do not appear in the matching up to order d^{-n+1} . This means the matching is exactly the same as in Model A and, hence, $a_{-n} = a_{-n-1} = b_{-n} = 0$ (detailed in Section 2.4.2). If we look in the region of parameter space where $\eta \sim d^{-2}$ and $n = 1$, as for Model A, then A_0 , B_0 and b_{-2} are given by equations 2.161, 2.162 and 2.163 in Chapter 2. The cell conservation equation at third order is

$$\begin{aligned} & K_{(2,0)}(D_I^2 - D_I)\Phi_{-2} + K_{(2,-1)}D_I^2\Phi_{-1} + (\kappa m_{-1}^0 K_{(2,-1)} + K_{(2,-2)})D_I^2\Phi_0 \\ & - \frac{K_{(2,0)}}{K_{(1,0)}}(K_{(1,-1)}D_I\Phi_{-1} + (\kappa m_{-1}^0 K_{(1,-1)} + K_{(1,-2)})D_I\Phi_0) \\ & + \kappa \frac{dm_{-1}^0}{dz_I} K_{(2,-1)}D_I\Phi_0 - \frac{K_{(2,0)}}{K_{(1,0)}} \kappa \frac{dm_{-1}^0}{dz_I} K_{(1,-1)}D_I\Phi_0 - P_{H,0} k^2 \Phi_0 \\ & + \lambda_0 \chi_{-1} \kappa e^{z_I} (\Phi_0 + M_0) \left(-\frac{K_{(2,0)}K_{(6,0)}}{K_{(1,0)}} + (K_{(8,0)} - 2K_{(1,0)}K_{(6,0)}) \right) \\ = & e^{z_I} U_{-1} - \eta_{-2} e^{z_I} (P_{(5,0)} D_I^2 + P_{(6,0)} D_I) U_{-1}, \end{aligned} \quad (3.185)$$

with boundary condition

$$\begin{aligned} & K_{(2,0)}(D_I - 1)\Phi_{-2} + K_{(2,-1)}D_I\Phi_{-1} + (\kappa m_{-1}^0 K_{(2,-1)} + K_{(2,-2)})D_I\Phi_0 \\ & - \frac{K_{(2,0)}}{K_{(1,0)}}(K_{(1,-1)}\Phi_{-1} + (\kappa m_{-1}^0 K_{(1,-1)} + K_{(1,-2)})\Phi_0) = 0, \end{aligned} \quad (3.186)$$

where m^0 denotes the equilibrium solution components and upper case M denotes the linear stability analysis components. Substituting in $m_{-1}^0 = (e^{z_I} - 1)$ from the equilibrium

solution and integrating equation 3.185 from $-\infty$ to 0 gives

$$R_4 = \frac{2P_{(H,0)}}{(1 - \eta_{-2}(P_{(5,0)} - P_{(6,0)}))}. \quad (3.187)$$

Integrating the cell conservation equation between 0 and $-\infty$ at fourth order gives

$$\begin{aligned} R_3 = & 4b_{-2} + \frac{2(P_{(H,0)}(A_K + C_K) + P_{(H,-1)})}{(1 - \eta_{-2}(P_{(5,0)} - P_{(6,0)}))} \\ & + \frac{2R_4}{(1 - \eta_{-2}(P_{(5,0)} - P_{(6,0)}))} \left[\frac{N_K}{4} - \frac{5A_K}{4} - \frac{C_K}{2} + \eta_{-2} \left\{ \left(\frac{5A_K}{4} + \frac{C_K}{2} \right) \right. \right. \\ & \times (P_{(5,0)} - P_{(6,0)}) + \frac{3}{4}A_{(1,0)}N_K + \frac{1}{2}A_{(1,-1)} + \frac{A_{(4,-1)}}{2} + \frac{3N_K A_{(4,0)}}{4} + \\ & \left. \left. \frac{K_{(2,0)}}{K_{(1,0)}} \left(\frac{1}{2}A_{(2,-1)} + \frac{N_K}{4}A_{(2,0)} - \frac{1}{2}A_{(3,-1)} - \frac{N_K}{4}A_{(3,0)} \right) \right\} \right], \end{aligned} \quad (3.188)$$

where $N_k = \frac{K_{(2,0)}}{K_{(1,0)}}K_{(1/2,-1)}$ is a constant and the definitions of $A_{(i,j)}$, $P_{(i,j)}$ and all other constants can be found in Appendix C. The k dependance is due to $b_{-2}(k)$, shown in equation 2.163. The expression for the Raleigh number as a function of the wavenumber k is

$$R(k) = d^4 \left(\frac{2P_{(H,0)}}{1 - \eta_{-2}(P_{(5,0)} - P_{(6,0)})} + d^{-1}R_3 + O(d^{-2}) \right), \quad (3.189)$$

with R_3 given in equation 3.188. Note that to third order this is the same as the expression to third order for Model A and Bees and Hill [9], since $P_{(H,0)} = P_H$, $P_{(5,0)} = P_5$ and $P_{(6,0)} = P_H$, where P_H , P_5 and P_6 are defined in Chapter 2 as the same as in Bees and Hill [9]. Again, the effects of phototaxis only come in at fourth order. A full study of parameter space is possible here, as for Model A, but results would be similar and so are not shown.

3.5 Numerical and asymptotical results for Model B

A numerical study of parameter space in conducted using the same numerical procedure as described in Chapter 2, using a Newton-Raphson-Kantorovich algorithm in FORTRAN. The main parameters of interest are those involved in phototaxis and gyrotaxis: χ , η and κ . Again, z is scaled with d , so that $z_I = dz$, and the layer depth is $-d \leq z_I \leq 0$.

3.5.1 Comparison of asymptotical and numerical solutions

Figure 3.3 shows asymptotical and numerical neutral curves for $d = 200$. Good agreement is found between the two methods, helping to verify the numerical code. For $d^2\eta = 8$,

another minimum appears on the neutral curve for small k , where the solution is mode one at each minimum and changes to mode two on the connection between these minima. This was not found for smaller values of d , such as $d = 40$. The second convection cell appears at the top of the layer. For $d^2\eta = 16$ the neutral curve splits in two and a loop forms for large k , changing smoothly from mode one to mode two on the upper branch. The loop solution for small k could not be easily resolved, although it does exist.

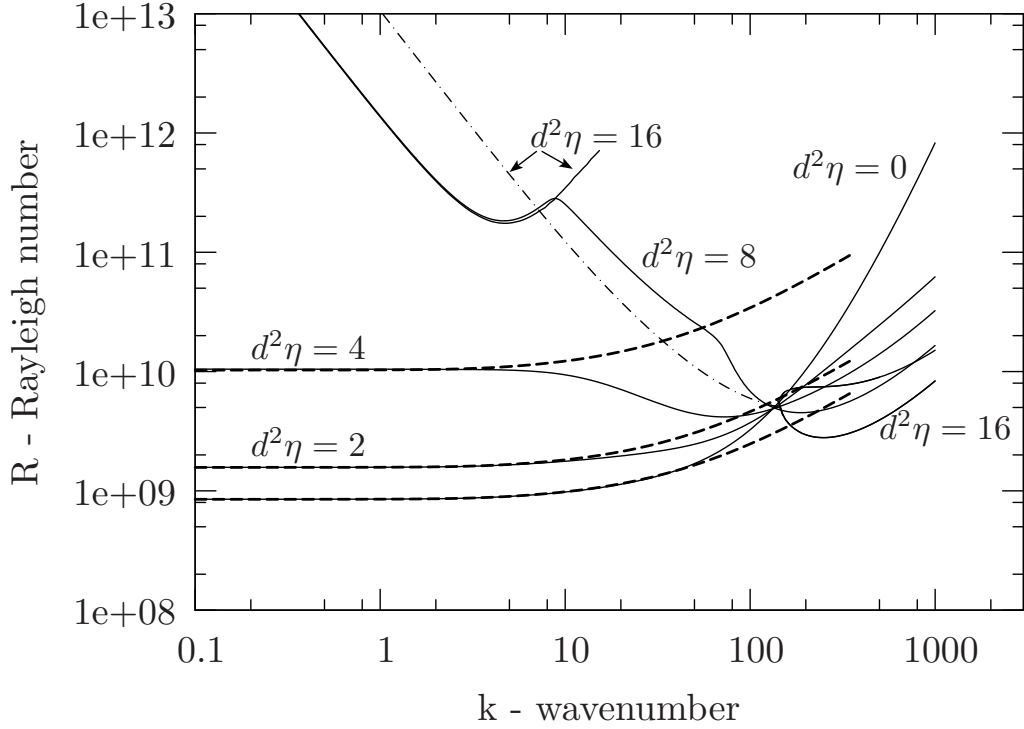


Figure 3.3: Asymptotic and numerical curves of neutral stability for Model B, where $d = 200$, $\kappa = 1$, $\chi = d^{-1}$ and $d^2\eta$ varies. Asymptotic solutions are dashed lines and oscillatory solutions dotted-dashed lines.

This double minimum effect was not found in Model A, nor was it present for the gyrotaxis only case, so must be related to the new method of modelling phototaxis. We investigate further by setting $d^2\eta = 8$ and varying χ for $d = 200$, as shown in Figure 3.4. As χ increases from $\chi = 0$ the minimum for large k is not significantly altered, but a second minimum forms for small k . These minima move closer together as χ is increased further, and both are destabilized. This eliminates the line connecting the two dips and, as χ approaches one, the minimum for small k is destabilized more than the minimum for large k . This flattens out the neutral curve. Hence, the critical wavenumber becomes zero as χ approaches one. For $\chi > 1$ all wavenumbers are stabilized compared to the case

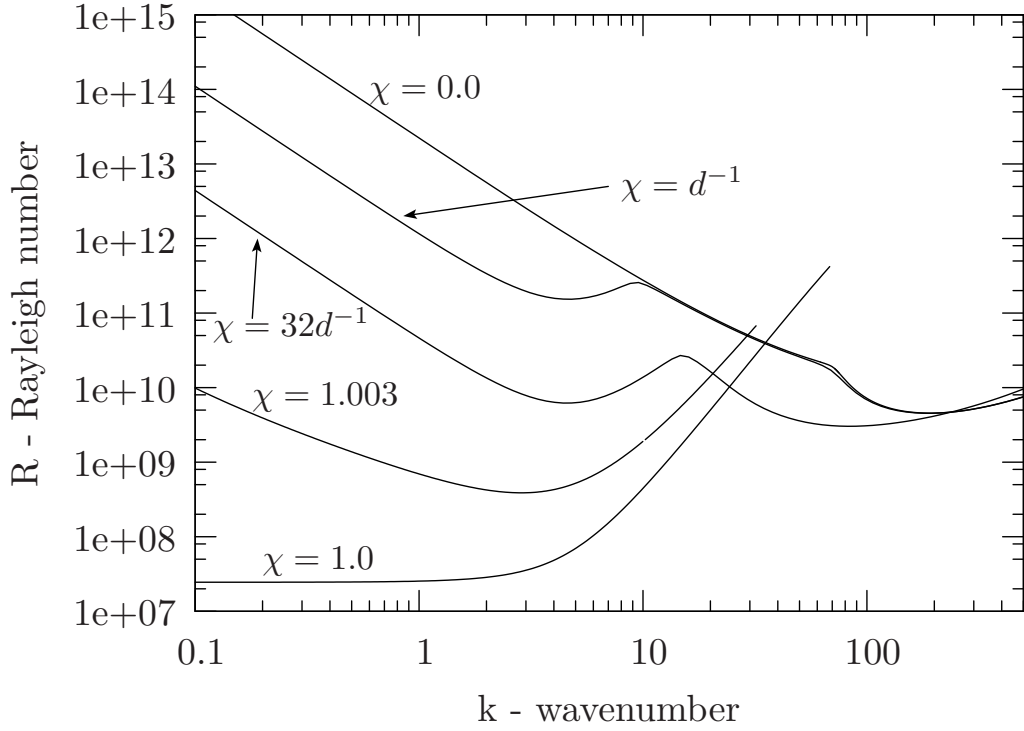


Figure 3.4: Curves of neutral stability for Model B, where $d = 200$, $\kappa = 1.2$, $d^2\eta = 8$ and χ varies.

$\chi = 1$, with small k stabilized more than large k , and k_c again becomes non-zero. R_c and k_c then both increase as a function of χ .

Results for $d = 200$, $\chi = 40d^{-1}$ and varying $d^2\eta$ are shown in Figure 3.5, where we find that decreasing η from $d^2\eta = 8.5$ stabilizes wavenumbers approximately $k < 90$. However, small wavenumbers are destabilized more than larger k , so that the lower minimum begins to flatten out and becomes smaller than the minimum for large k . Thus, k_c shifts from the large k curve to the small k curve just before both curves flatten out, and the critical wavenumber becomes zero.

3.5.2 Exploring the effects of the phototaxis parameter χ on the critical wavenumber k_c and Rayleigh number R_c

For $d^2\eta = 2$ and $d^2\eta = 4$, with $d = 20$ and $\kappa = 1.2$, varying χ gives qualitatively similar results to Model A, shown for $d^2\eta = 4$ in Figure 3.6. Small wavenumbers are destabilized and large wavenumbers stabilized for $\chi = 1$ compared to $\chi = 0$. This causes the critical wavenumber to become zero, even if it was non-zero in the gyrotaxis only case (when $\chi = 0$). For $\chi \geq 1.03$, all wavenumbers are stabilized compared to when $\chi = 0$, and the

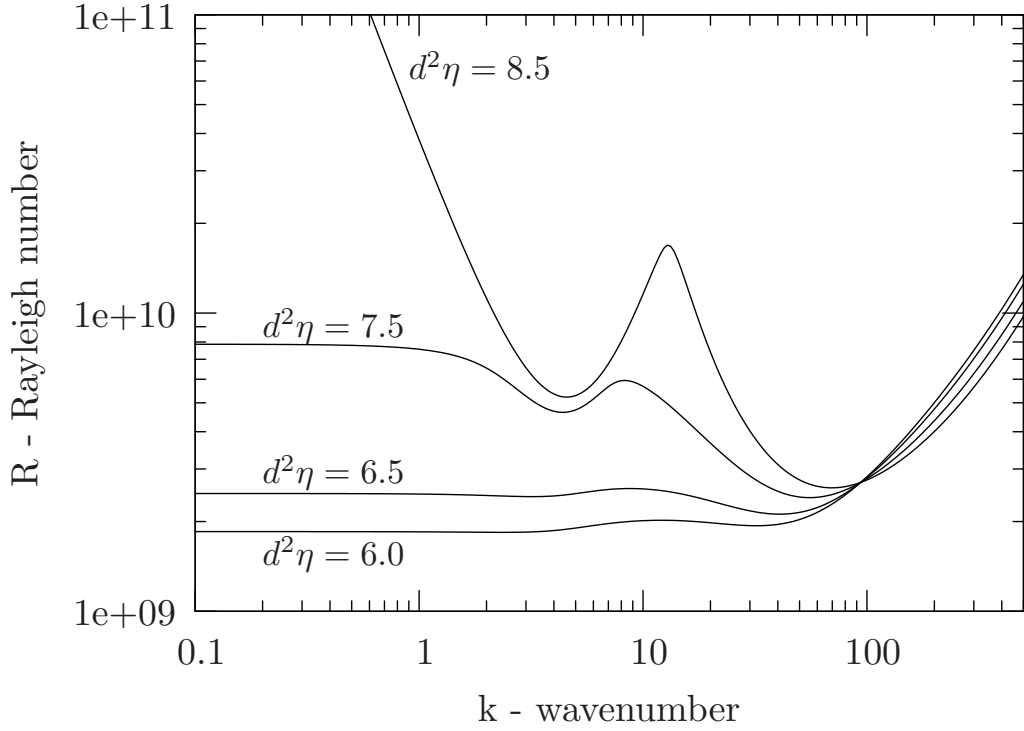


Figure 3.5: Curves of neutral stability for Model B, where $d = 200$, $\kappa = 1.2$, $d\chi = 40$ and $d^2\eta$ varies.

critical wavenumber becomes non-zero for sufficiently large χ . For large χ ($\chi > 1.03$ for $d^2\eta = 4$), the mode associated with the critical wavenumber becomes mode two, with the second convection cell forming at the top of the layer. This was also found in Chapter 2 for Model A. Different values of χ for $d^2\eta = 8$ were also explored but no double minima solutions were found.

3.5.3 Exploring the effects of the gyrotaxis parameter η on the critical wavenumber k_c and Rayleigh number R_c

For both $\chi = 0.5$ and $\chi = 1.03$, with $d = 20$ and $\kappa = 1.2$, the neutral curves are qualitatively similar to those for Model A for all values of $d^2\eta$, and the same trends are found as described in Chapter 2. Figure 3.7 shows solutions for $\chi = 1.03$, where loop and oscillatory solutions exist for sufficiently large η , and the critical wavenumber is always non-zero. In Model A, η was simply a constant measure of gyrotaxis, whereas here gyrotaxis varies with light intensity, since $h = h(I)$, so cells at different depths exhibit different levels of gyrotaxis, and η in this model is a measure of the ‘normal gyrotaxis’ (the magnitude of gyrotaxis when the centre of mass offset is h_n). We find that increasing

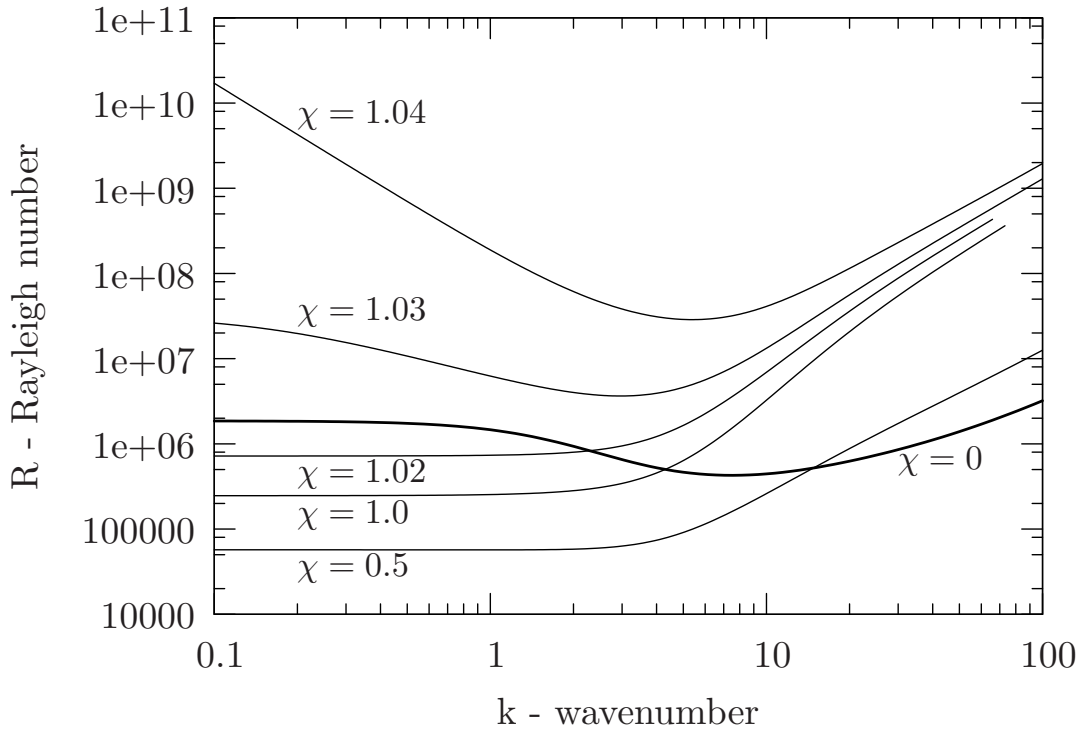


Figure 3.6: Curves of neutral stability for Model B, where $d = 20$, $\kappa = 1.2$, $d^2\eta = 4$ and χ varies. The bold line is the special case $\chi = 0$ where there is no phototaxis.

η in Model B has the same effect as increasing η in Model A (except where double loops form on the neutral curve when d is large).

3.5.4 Table of Results

Sample results for Model B are summarized in Table 3.1. The critical wavenumber, k_c , and the corresponding critical Rayleigh number, R_c , are shown for a variety of parameter values that illustrate the wider parameter space. The critical wavenumber k_c is mode one unless indicated by a star, in which case it is mode two. In all cases, even when oscillatory solutions were found, k_c was on the non-oscillatory section of the curve. We shall discuss these results further in Section 3.11.

3.6 Model C, where a new torque due to phototaxis is introduced

In Model C, we introduce a new torque due to phototaxis, \mathbf{L}_p , in the gyrotactic torque balance equation of Pedley and Kessler 1990 [130]. This is the only effect of phototaxis

d	$d^2\eta$	χ	κ	k_c	R_c
20	2	0	1.2	2.44	2.30×10^5
20	2	0.5	1.2	0.0	5.20×10^4
20	2	1.0	1.2	0.0	2.48×10^5
20	2	1.04	1.2	4.88*	2.83×10^7
20	4	0	1.2	7.56	4.27×10^5
20	4	1.0	1.2	0.00	2.47×10^5
20	4	1.04	1.2	5.36*	2.86×10^7
20	0	1.03	1.2	2.79	3.62×10^6
20	64	1.03	1.2	6.74	2.09×10^6
20	0	0.5	1.2	0.0	4.78×10^4
20	16	0.5	1.2	3.70	8.40×10^4
20	64	0.5	1.2	8.54	5.78×10^4
20	8	0.1	1.2	12.1	3.70×10^5
20	8	0.5	1.2	2.12	6.74×10^4
20	8	1.0	1.2	0.0	2.44×10^5
20	8	1.04	1.2	6.72*	2.78×10^7

Table 3.1: Summary of the linear stability results for Model B, in terms of critical wavenumber, k_c , and Rayleigh number, R_c , for $\lambda = 2.2$ and $\alpha_0 = 0.2$. The star indicates the solution at the critical wavenumber, k_c , is mode two.

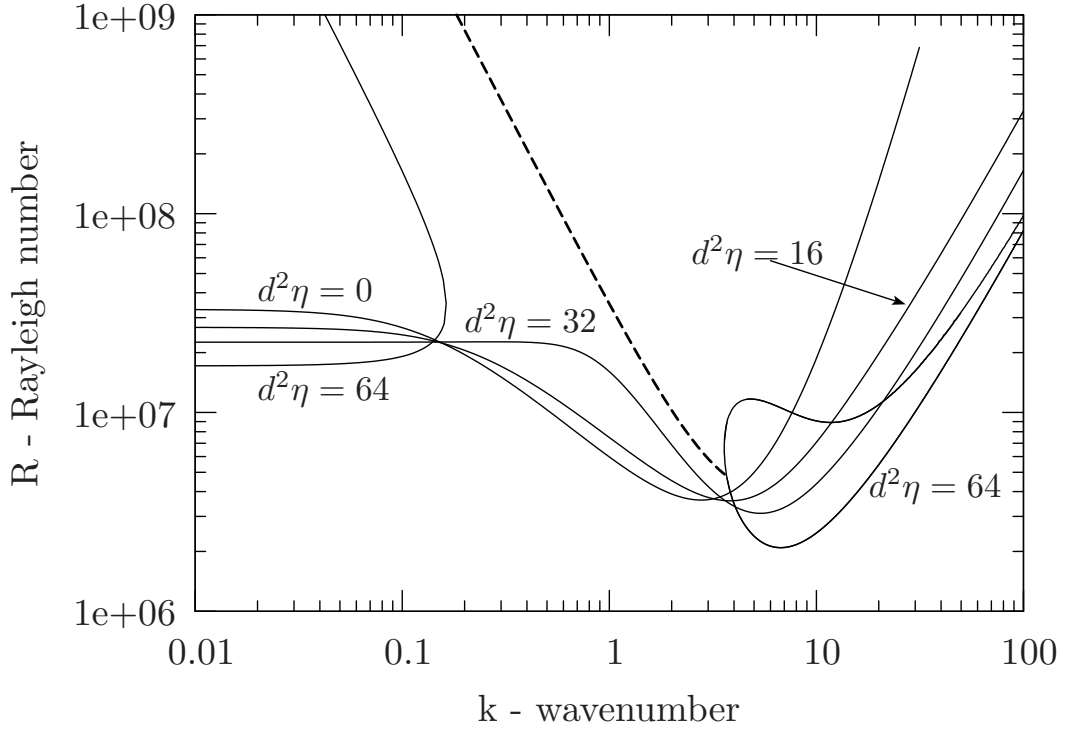


Figure 3.7: Curves of neutral stability for Model B, where $d = 20$, $\kappa = 1.2$, $\chi = 1.03$ and $d^2\eta$ varies.

in this model, so that the governing equations are equations 2.14, 2.15, 2.16, 2.19, 2.20 and 2.29 in Chapter 2 with $V_s(I) = 1$ constant and $\tilde{h}(I) = 1$. Here, we find that $\tilde{\mathbf{k}}(I)$ in equation 2.29 depends on the form of the phototaxis torque, \mathbf{L}_p . The new torque balance equation in equation 1.8 in Chapter 1 becomes

$$\mathbf{L}_T = \mathbf{L}_g + \mathbf{L}_v + \mathbf{L}_p, \quad (3.190)$$

where we propose a general dimensional phototactic torque of the form

$$\mathbf{L}_p = f(I)\mathbf{p} \wedge (\beta_1\boldsymbol{\pi} + \beta_2\nabla I), \quad (3.191)$$

with constant β_1 and β_2 , where $f(I)$ is a function for the strength of the phototaxis torque. Using this expression, we can investigate both the response of cells to light from an arbitrary global direction, $\boldsymbol{\pi}$, and also the possible effects of the cells reacting to local gradients in light intensity, ∇I .

We choose the simple functional response $f(I) = F_0 I(I - I_c)$, where F_0 is a constant, so that the phototaxis torque, \mathbf{L}_p , is zero both when there is no light *and* when the cells are at the critical light intensity, I_c . Thus the phototaxis torque is self-contained, so that

phototaxis and gyrotaxis are modelled separately, and at I_c the cells are still gyrotactic but the phototactic torque is turned off. F_0 is chosen so that between $I = 0$ and $I = I_c$ the strength of the torque is positive, so that the cells are biased to swim towards the light under low light conditions. The maximum torque is arbitrarily set to occur at $\frac{I_c}{2}$, so that

$$F_0 = \frac{4f_m}{I_c^2}, \quad (3.192)$$

where f_m is the maximum of the function $f(I)$. The torque in dimensional units is

$$\mathbf{L}_p = -\frac{4f_m}{I_c^2} I(I - I_c) \mathbf{p} \wedge (\beta_1 \boldsymbol{\pi} + \beta_2 \nabla I). \quad (3.193)$$

Mean cell swimming direction is calculated using equation 2.8, and we use the approximation for diffusion given in equation 2.9, and denote the average cell swimming speed as a constant, V_n , so that the diffusion scale is $D_0 = V_n^2 \tau$.

We split the analysis into two sections in order to explore both the response of the cells to light from an arbitrary direction and the effect of cells responding to local gradients in light intensity, so $(\beta_1, \beta_2) = (1, 0)$ and $(\beta_1, \beta_2) = \left(0, \frac{H}{I_s}\right)$, respectively.

3.7 Model C, Case 1, where the torque due to phototaxis is caused by illumination from above

Here we consider light from above, such that $\boldsymbol{\pi} = \mathbf{k}$, and we set $\beta_1 = 1$ and $\beta_2 = 0$. In Model B, phototaxis was included in the gravitaxis torque term in equation 3.8 by multiplying the original torque by the expression for centre of mass as a function of light intensity, $h(I) = (1 - \chi I)$. If we set $f(I) = -\chi I$ and also set the direction of the light as $\boldsymbol{\pi} = \mathbf{k}$ then Model B and this case of Model C would result in the same model equations. However, this is not the case for the form of $f(I)$ shown in equation 3.193, or if light is from any direction except the vertical.

Following the analysis of Pedley and Kessler 1987 [129], described in Chapter 1, we obtain

$$\begin{aligned} \dot{\mathbf{p}} = & \left(\frac{1}{2B_n} - \frac{4f_m I(I - I_c)}{I_c^2 \mu \alpha_{\perp} v} \right) [\mathbf{k} - (\mathbf{k} \cdot \mathbf{p}) \mathbf{p}] + \frac{1}{2} \boldsymbol{\Omega} \wedge \mathbf{p} \\ & + \alpha_0 [\mathbf{E} \cdot \mathbf{p} - \mathbf{p} \mathbf{p} \cdot \mathbf{E} \cdot \mathbf{p}], \end{aligned} \quad (3.194)$$

from the torque balance equation, where B_n is defined in equation 2.28. We non-dimensionalize I with I_s and use the same non-dimensionalizations as in equation 2.24, $\boldsymbol{\Omega} = \frac{V_n^2 \tau}{H^2} \boldsymbol{\omega}$ and

$\mathbf{E} = \frac{V_n^2 \tau}{H^2} \mathbf{e}$. Substituting equation 3.194 into the Fokker-Planck equation and simplifying the terms (described in Section 3.2) gives

$$(1 - \chi \zeta e^{\kappa m} (\chi e^{\kappa m} - 1)) (\mathbf{k} \cdot \nabla f - 2(\mathbf{k} \cdot \mathbf{p})f) + \eta \boldsymbol{\omega} \cdot (\mathbf{p} \wedge \nabla f) \quad (3.195)$$

$$+ 2\eta \alpha_0 [\mathbf{p} \cdot \mathbf{e} \cdot \nabla f - 3\mathbf{p} \cdot \mathbf{e} \cdot \mathbf{p} f] = \lambda^{-1} \nabla^2 f,$$

where

$$\lambda = \frac{1}{2D_r B_n}, \quad \zeta = \frac{4f_m}{h_n m g} \quad \text{and} \quad \eta = \frac{B_n V_n^2 \tau}{H^2}. \quad (3.196)$$

ζ is a new parameter only present in Model C and is a measure of the strength of the torque due to phototaxis. The definition for $\chi = \frac{I_s}{I_c}$ is the same as in Models A and B, as are the definitions for λ and η . Equation 3.195 replaces equation 2.29 in the general model, where here $\tilde{\mathbf{k}}(I) = (1 - \chi \zeta e^{\kappa m} (\chi e^{\kappa m} - 1)) \mathbf{k}$.

3.7.1 Solving the Fokker-Planck equation

If we consider the equilibrium state of zero flow, $\mathbf{u} = \boldsymbol{\omega} = \mathbf{e} = \mathbf{0}$, $f = f^0$ and $m = m^0$, then writing $\mathbf{p} = (\sin \theta \cos \phi, \sin \theta \sin \phi, \cos \theta)$ and $\mathbf{k} = (0, 0, 1)$, at equilibrium equation 3.195 becomes

$$\lambda \left(1 - \zeta \chi e^{\kappa m^0} (\chi e^{\kappa m^0} - 1) \right) (\mathbf{k} \cdot \nabla f^0 - 2(\mathbf{k} \cdot \mathbf{p})f^0) = \nabla^2 f^0. \quad (3.197)$$

If we define

$$\Lambda_C(z) = \lambda \left(1 - \zeta \chi e^{\kappa m^0(z)} (\chi e^{\kappa m^0(z)} - 1) \right), \quad (3.198)$$

then equation 3.197 has the same form as equation 3.13 for Model B, but with Λ_C instead of Λ , so the solution is $f^0 = \mu_{\Lambda_C} e^{\Lambda_C \cos \theta}$ with $\mu_{\Lambda_C} = \frac{\Lambda_C}{4\pi \sinh \Lambda_C}$.

Considering the first order perturbation for spherical cells ($\alpha_0 = 0$), then equation 3.195 at $O(\epsilon)$ becomes

$$\Lambda_C (\mathbf{k} \cdot \nabla f^1 - 2(\mathbf{k} \cdot \mathbf{p})f^1) - \zeta \chi \lambda e^{\kappa m^0} \kappa m^1 \left(2\chi e^{\kappa m^0} - 1 \right) (\mathbf{k} \cdot \nabla f^0 - 2(\mathbf{k} \cdot \mathbf{p})f^0)$$

$$+ \lambda \eta \boldsymbol{\omega}^1 \cdot (\mathbf{p} \wedge \nabla f^0) = \nabla^2 f^1. \quad (3.199)$$

On expanding, equation 3.199 becomes

$$\frac{1}{\sin \theta} \frac{\partial}{\partial \theta} \left(\sin \theta \frac{\partial f^1}{\partial \theta} \right) + \frac{1}{\sin^2 \theta} \frac{\partial^2 f^1}{\partial \phi^2} - \Lambda_C \left(\mathbf{k} \cdot \hat{\boldsymbol{\theta}} \frac{\partial f^1}{\partial \theta} - 2 \cos \theta f^1 \right) \quad (3.200)$$

$$= -\eta \lambda \Lambda_C \mu_\lambda (\omega_2^1 \cos \phi - \omega_1^1 \sin \phi) \sin \theta e^{\Lambda_C \cos \theta}$$

$$- \lambda \zeta \chi \kappa \mu_\lambda m^1 e^{\kappa m^0} \left(2\chi e^{\kappa m^0} - 1 \right) e^{\Lambda_C \cos \theta} (\Lambda_C \sin^2 \theta - 2 \cos \theta).$$

The solution to the flow term, the first line on the right hand side, is the same as in Model B (but with Λ_C instead of Λ), and so is merely quoted in expressions for $\langle \mathbf{p} \rangle$ and \mathbf{D} in equations 3.204 and 3.205. For the second term on the right hand side, which is the new term due to the phototactic torque, we solve by writing

$$f^1 = \lambda \zeta \chi \kappa \mu \Lambda m^1 e^{\kappa m^0} (2\chi e^{\kappa m^0} - 1) h(\theta). \quad (3.201)$$

Substituting into equation 3.200 and making the change of variable $x = \cos \theta$ gives

$$((1-x^2)h')' - \Lambda_C ((1-x^2)h)' = - [\Lambda_C e^{\Lambda_C x} (1-x^2) - 2x e^{\Lambda_C x}]. \quad (3.202)$$

This has the same form as equation 3.59 in Model B, hence

$$h(x, z) = e^{\Lambda_C x} (K_1(z) - x). \quad (3.203)$$

The contributions of this new term to $\langle \mathbf{p} \rangle$ and \mathbf{D} are found using the methods presented for Model B. The form of solution is the same, but with Λ_C instead of Λ and a different multiplier outside the brackets. This can be seen in the expressions for $\langle \mathbf{p} \rangle$ and \mathbf{D} in equations 3.204 and 3.205. The aspherical terms in this model are not altered by the new phototaxis torque, thus are also quoted in equations 3.204 and 3.205, where Λ from Model B is replaced by Λ_C .

Summing all the components of $\langle \mathbf{p} \rangle$ gives

$$\begin{aligned} \langle \mathbf{p} \rangle = & \begin{pmatrix} 0 \\ 0 \\ K_1 \end{pmatrix} + \epsilon \left[\eta J_1 \begin{pmatrix} \omega_2 \\ -\omega_1 \\ 0 \end{pmatrix} - 2\alpha_0 \eta \begin{pmatrix} e_{13} J_4 \\ e_{23} J_4 \\ \frac{3}{2} e_{33} K_4 \end{pmatrix} \right. \\ & \left. + \lambda \zeta \chi \kappa m^1 e^{\kappa m^0} (2\chi e^{\kappa m^0} - 1) \begin{pmatrix} 0 \\ 0 \\ K_6 \end{pmatrix} \right] + O(\epsilon^2). \end{aligned} \quad (3.204)$$

Similarly, we find the dimensionless diffusion tensor to be

$$\begin{aligned} \mathbf{D} = & \begin{pmatrix} \frac{K_1}{\Lambda_C} & 0 & 0 \\ 0 & \frac{K_1}{\Lambda_C} & 0 \\ 0 & 0 & K_2 \end{pmatrix} + \epsilon \left[\eta(J_2 - J_1 K_1) \begin{pmatrix} 0 & 0 & \omega_2 \\ 0 & 0 & -\omega_1 \\ \omega_2 & -\omega_1 & 0 \end{pmatrix} - 2\alpha_0 \eta \right. \\ & \begin{pmatrix} -\frac{3}{4}e_{33}K_5 + \frac{1}{4}(e_{11} - e_{22})J_6 & \frac{1}{2}e_{12}J_6 & e_{13}(J_5 - K_1 J_4) \\ \frac{1}{2}e_{12}J_6 & -\frac{3}{4}e_{33}K_5 - \frac{1}{4}(e_{11} - e_{22})J_6 & e_{23}(J_5 - K_1 J_4) \\ e_{13}(J_5 - K_1 J_4) & e_{23}(J_5 - K_1 J_4) & \frac{3}{2}e_{33}(K_5 - 2K_1 K_4) \end{pmatrix} \\ & \left. + \lambda \zeta \chi \kappa m^1 e^{\kappa m^0} (2\chi e^{\kappa m^0} - 1) \begin{pmatrix} K_7 & 0 & 0 \\ 0 & K_7 & 0 \\ 0 & 0 & K_8 - 2K_1 K_6 \end{pmatrix} \right] + O(\epsilon^2), \quad (3.205) \end{aligned}$$

where the $K_i(z)$ and $J_i(z)$ have the same form as equations 3.84 to 3.96, but now depend on $\Lambda_C(z)$ instead of $\Lambda(z)$. The last terms in equations 3.204 and 3.205 are the new terms due to the phototactic torque.

3.7.2 Equilibrium solution and linear stability analysis

To find an equilibrium solution we look at the case of no fluid flow, $\mathbf{u} = \mathbf{0}$ and $n = n(z)$. On integrating with respect to the boundary conditions in equations 2.21, 2.22 and 2.23 and using the change of variable in equation 3.7, the cell conservation equation 2.16 becomes

$$\frac{d^2 m}{dz^2} - \frac{d\bar{K}_2}{\bar{K}_1} \frac{K_1(\Lambda_C)}{K_2(\Lambda_C)} \frac{dm}{dz} = 0. \quad (3.206)$$

$d = \frac{\bar{K}_1 H}{\bar{K}_2 V_n \tau}$, where \bar{K}_1 and \bar{K}_2 are values of K_1 and K_2 for constant $\Lambda_C = \lambda = 2.2$. This is the same definition as in Models A and B and Bees and Hill [9], and is used so that results can be compared between models. The boundary conditions for m are the same as for Models A and B. The equilibrium solution has the same form as equation 3.101 in Model B, but K_1 and K_2 from the Fokker-Planck depend on $\Lambda_C(z)$ instead of $\Lambda(z)$.

The linear stability analysis follows the same procedure detailed in Chapter 2 and Section 3.3.3. The Navier-Stokes equation is not altered in this model, and so the version for use in the numerical program is given by equation 2.89 in Chapter 2, and the Rayleigh number is, again, defined in equation 2.90. If we perturb, using equations 3.108, and expand the cell conservation equation to order ϵ we obtain equation 3.113 from the Model

B analysis, but with different expression for $\partial_i \langle \mathbf{p} \rangle_i^1$ and $\partial_i \mathbf{D}_{i3}^1$, given for this case as

$$\begin{aligned} \partial_i \langle \mathbf{p} \rangle_i^1 &= H_1 \nabla^2 u_3^1 + H_2 \partial_3 \partial_3 u_3^1 - 3\alpha_0 \eta \partial_3 u_3^1 \partial_3 K_4 \\ &\quad + \lambda \zeta \chi \kappa \partial_3 \left(m^1 e^{\kappa m^0} (2\chi e^{\kappa m^0} - 1) K_6 \right), \end{aligned} \quad (3.207)$$

$$\begin{aligned} \partial_i D_{i3}^1 &= H_3 \nabla^2 u_3^1 + H_4 \partial_3 \partial_3 u_3^1 - 3\alpha_0 \eta \partial_3 u_3^1 \partial_3 (K_5 - 2K_1 K_4) \\ &\quad + \lambda \zeta \chi \kappa \partial_3 ((K_8 - 2K_1 K_6) m^1 e^{\kappa m^0} (2\chi e^{\kappa m^0} - 1)), \end{aligned} \quad (3.208)$$

where the equilibrium components are now denoted with a superscript 0, and the perturbations with a superscript 1. We substitute these equations into equation 3.113 and resolve into the normal modes as in equation 3.117, which gives

$$\begin{aligned} &\left\{ P_V(z) \frac{d^2}{dz^2} - \frac{d\bar{K}_2}{\bar{K}_1} K_1(z) \frac{d}{dz} - P_H(z) k^2 - \sigma - \frac{d\bar{K}_2}{\bar{K}_1} \frac{dK_1}{dz} + \frac{dP_V(z)}{dz} \frac{d}{dz} \right. \\ &\quad \left. + \lambda \zeta \chi \kappa e^{\kappa m^0} P_R(z; d) \right\} \Phi + \lambda \zeta \chi \kappa e^{\kappa m^0} P_M(z; d) M(z) \\ &= \left\{ \frac{dn^0}{dz} - \eta P_5(z; d) \frac{d^2}{dz^2} - \eta P_6(z; d) \frac{d}{dz} + \eta P_7(z; d) k^2 \right\} U(z), \end{aligned} \quad (3.209)$$

where

$$\begin{aligned} P_R(z; d) &= -\frac{d\bar{K}_2}{\bar{K}_1} n^0 K_6(z) (2\chi e^{\kappa m^0} - 1) + \frac{dn^0}{dz} (K_8(z) - 2K_1(z) K_6(z)) (2\chi e^{\kappa m^0} - 1), \quad (3.210) \\ P_M(z; d) &= -\frac{d\bar{K}_2}{\bar{K}_1} \left[K_6(z) \frac{dn^0}{dz} + n^0 \left(\kappa \frac{dm^0}{dz} K_6(z) (4\chi e^{\kappa m^0} - 1) + \frac{dK_6(z)}{dz} (2\chi e^{\kappa m^0} - 1) \right) \right] \\ &\quad + \frac{d^2 n^0}{dz^2} (K_8(z) - 2K_1(z) K_6(z)) + \frac{dn^0}{dz} \left[\kappa \frac{dm^0}{dz} (K_8(z) - 2K_1(z) K_6(z)) (4\chi e^{\kappa m^0} - 1) \right. \\ &\quad \left. + \frac{d(K_8(z) - 2K_1(z) K_6(z))}{dz} (2\chi e^{\kappa m^0} - 1) \right], \end{aligned} \quad (3.211)$$

and $n^0 = n^0(z)$ and $m^0 = m^0(z)$, and $P_V(z)$, $P_H(z)$, $P_5(z; d)$, $P_6(z; d)$ and $P_7(z; d)$ are the same as equations 3.119, 3.122, 3.123 and 3.124 in Model B. Equation 3.209 has the same form as equation 3.118 for Model, B but $P_M(z; d)$ and $P_R(z; d)$ are different and K_i now depend on $\Lambda_C(z)$ instead of $\Lambda(z)$. The no-flow boundary conditions are the same as in the previous models (shown in equations 3.125 for Model B). We also have $M = 0$ at $z = 0$, and the no flux condition becomes

$$\begin{aligned} &\frac{d\bar{K}_2}{\bar{K}_1} K_1 \Phi - K_2 \frac{d\Phi}{dz} \quad \text{on } z = 0, \quad (3.212) \\ \text{and} &\frac{d\bar{K}_2}{\bar{K}_1} K_1 \Phi - K_2 \frac{d\Phi}{dz} \\ &\quad + \lambda \zeta \chi \kappa e^{\kappa m^0} (2\chi e^{\kappa m^0} - 1) \left(\frac{d\bar{K}_2}{\bar{K}_1} K_6 n^0 - \frac{dn^0}{dz} (K_8 - 2K_1 K_6) \right) M(z) \\ &\quad \text{on } z = -1. \end{aligned}$$

3.8 Model C, Case II, where cells respond to gradients in light intensity

We now consider the case where the new phototaxis torque in equation 3.193 models cells responding to local gradients in light intensity. We set $\beta_1 = 0$ and $\beta_2 = \frac{H}{I_s}$, for convenience (since this is the reciprocal of the non-dimensionalization of ∇I), in equation 3.193. The phototaxis torque is non-dimensionalized in the same way as in Section 3.7 and the expression in equation 3.192 is used for F_0 , so that

$$\mathbf{L}_p = -4f_m\chi I(\chi I - 1)\mathbf{p} \wedge (\nabla I). \quad (3.213)$$

Summing all torques \mathbf{L}_T and following the procedure in Pedley and Kessler [130] as in Chapter 1, where $\mathbf{\Omega}$ and \mathbf{E} are non-dimensionalized using equation 2.24, gives

$$\begin{aligned} \frac{D_0}{H^2}\dot{\mathbf{p}} &= \frac{1}{2B_n}(\mathbf{k} - (\mathbf{k} \cdot \mathbf{p})\mathbf{p}) - \frac{4f_m}{\mu\alpha_\perp v}\chi I(\chi I - 1)(\nabla I - (\nabla I \cdot \mathbf{p})\mathbf{p}) \\ &+ \frac{1}{2}\frac{D_0}{H^2}\boldsymbol{\omega} \wedge \mathbf{p} + \alpha_0\frac{D_0}{H^2}[\mathbf{e} \cdot \mathbf{p} - \mathbf{p}\mathbf{p} \cdot \mathbf{e} \cdot \mathbf{p}]. \end{aligned} \quad (3.214)$$

Note the new terms in ∇I appearing in the second term on the right hand side. To combine the gravitational and phototaxis torques in one term we write

$$\hat{\mathbf{G}} = \frac{\nabla I}{|\nabla I|}, \quad (3.215)$$

where $\hat{\mathbf{G}}$ is a unit vector, and define $\zeta = \frac{4f_m}{h_nmg}$, as for Case I. Equation 3.214 thus yields

$$\begin{aligned} \frac{D_0}{H^2}\dot{\mathbf{p}} &= \frac{1}{2B_n} \left[(\mathbf{k} - (\mathbf{k} \cdot \mathbf{p})\mathbf{p}) - \zeta\chi I(\chi I - 1)|\nabla I|(\hat{\mathbf{G}} - (\hat{\mathbf{G}} \cdot \mathbf{p})\mathbf{p}) \right] \\ &+ \frac{1}{2}\frac{D_0}{H^2}\boldsymbol{\omega} \wedge \mathbf{p} + \alpha_0\frac{D_0}{H^2}[\mathbf{e} \cdot \mathbf{p} - \mathbf{p}\mathbf{p} \cdot \mathbf{e} \cdot \mathbf{p}]. \end{aligned} \quad (3.216)$$

If we define

$$C = \zeta\chi I(\chi I - 1)|\nabla I| \quad (3.217)$$

then equation 3.216 becomes

$$\begin{aligned} \frac{D_0}{H^2}\dot{\mathbf{p}} &= \frac{1}{2B_n}[\mathbf{k} - C\hat{\mathbf{G}} - (\mathbf{k} \cdot \mathbf{p})\mathbf{p} + C(\hat{\mathbf{G}} \cdot \mathbf{p})\mathbf{p}] \\ &+ \frac{1}{2}\frac{D_0}{H^2}\boldsymbol{\omega} \wedge \mathbf{p} + \alpha_0\frac{D_0}{H^2}[\mathbf{e} \cdot \mathbf{p} - \mathbf{p}\mathbf{p} \cdot \mathbf{e} \cdot \mathbf{p}]. \end{aligned} \quad (3.218)$$

We define a new dimensionless unit vector $\hat{\mathbf{k}}(I)$ such that

$$\hat{\mathbf{k}}(I) = \frac{\mathbf{k} - C\hat{\mathbf{G}}}{|\mathbf{k} - C\hat{\mathbf{G}}|}, \quad (3.219)$$

then substituting equation 3.219 into equation 3.218 gives

$$\begin{aligned} \frac{D_0}{H^2} \dot{\mathbf{p}} &= \frac{|\mathbf{k} - C\hat{\mathbf{G}}|}{2B_n} (\hat{\mathbf{k}} - (\hat{\mathbf{k}} \cdot \mathbf{p})\mathbf{p}) \\ &+ \frac{1}{2} \frac{D_0}{H^2} \boldsymbol{\omega} \wedge \mathbf{p} + \alpha_0 \frac{D_0}{H^2} [\mathbf{e} \cdot \mathbf{p} - \mathbf{p}\mathbf{p} \cdot \mathbf{e} \cdot \mathbf{p}]. \end{aligned} \quad (3.220)$$

In equation 3.219, if the denominator is zero then the numerator will also be zero, as here $\mathbf{k} = C\hat{\mathbf{G}}$, and at the singular point we define $\hat{\mathbf{k}} = \mathbf{0}$. Physically, this means that if $\mathbf{k} = C\hat{\mathbf{G}}$ then the phototactic torque term has cancelled out the gravitactic term and we are left only with viscous torques in the torque balance equation. In any case, $\hat{\mathbf{k}}$ is always multiplied by $|\mathbf{k} - C\hat{\mathbf{G}}|$, as shown in equation 3.220, and so singularity is not an issue.

On substituting equation 3.220 into the non-dimensional, steady Fokker Plank equation 2.26, we have

$$\begin{aligned} \nabla \cdot \left[|\mathbf{k} - C\hat{\mathbf{G}}| (\hat{\mathbf{k}} - (\hat{\mathbf{k}} \cdot \mathbf{p})\mathbf{p}) f \right. \\ \left. + \eta (\boldsymbol{\omega} \wedge \mathbf{p}) f + 2\eta\alpha_0 [\mathbf{e} \cdot \mathbf{p} - \mathbf{p}\mathbf{p} \cdot \mathbf{e} \cdot \mathbf{p}] f \right] = \lambda^{-1} \nabla^2 f, \end{aligned} \quad (3.221)$$

where λ and η are given in equation 3.196. Following the procedure in Bees and Hill [9] shown in Section 3.2, where $\nabla \cdot \hat{\mathbf{k}} = 0$ since $\hat{\mathbf{k}}(I)$ can be treated as a constant in orientational space, equation 3.221 becomes

$$\begin{aligned} |\mathbf{k} - C\hat{\mathbf{G}}| \left(\hat{\mathbf{k}} \cdot \nabla f - 2(\hat{\mathbf{k}} \cdot \mathbf{p}) f \right) + \eta \boldsymbol{\omega} \cdot (\mathbf{p} \wedge \nabla f) \\ + 2\eta\alpha_0 [\mathbf{p} \cdot \mathbf{e} \cdot \nabla f - 3\mathbf{p} \cdot \mathbf{e} \cdot \mathbf{p} f] = \lambda^{-1} \nabla^2 f. \end{aligned} \quad (3.222)$$

This completes the formulation for Model C Case II, with the governing equations as in equations 2.14, 2.15, 2.16, 2.19, 2.20 in Chapter 2, with $V_s(I) = 1$ constant and $\tilde{h}(I) = 1$, and equation 3.222 with $\hat{\mathbf{k}}(I)$ given in equation 3.219. $\hat{\mathbf{G}}(\nabla I)$ is given in equation 3.215 and $C(I, \nabla I)$ is given in equation 3.217 to complete the model. For comparison to the Fokker-Planck equation for the general model in Chapter 2, equation 2.29, we can write $\tilde{\mathbf{k}}(I) = |\mathbf{k} - C\hat{\mathbf{G}}| \hat{\mathbf{k}}(I)$.

3.8.1 Solving the Fokker Planck equation

To solve the Fokker-Planck equation for this case, we first separate out the zero flow and perturbation components in equation 3.220, denoted by superscript 0 and superscript 1, respectively, for the perturbations given in equation 3.108. We start by writing

$$\hat{\mathbf{k}} = \hat{\mathbf{k}}^0 + \epsilon \hat{\mathbf{k}}^1. \quad (3.223)$$

We calculate $\hat{\mathbf{k}}^0$ and $\hat{\mathbf{k}}^1$ by writing $C = C^0 + \epsilon C^1$ and $\hat{\mathbf{G}} = \hat{\mathbf{G}}^0 + \epsilon \hat{\mathbf{G}}^1$, so that equation 3.223 becomes

$$\hat{\mathbf{k}} = \frac{\mathbf{k} - C\hat{\mathbf{G}}}{|\mathbf{k} - C\hat{\mathbf{G}}|} = \frac{\mathbf{k} - C^0\hat{\mathbf{G}}^0 - \epsilon(C^0\hat{\mathbf{G}}^1 + C^1\hat{\mathbf{G}}^0) + O(\epsilon^2)}{|\mathbf{k} - C^0\hat{\mathbf{G}}^0 - \epsilon(C^0\hat{\mathbf{G}}^1 + C^1\hat{\mathbf{G}}^0) + O(\epsilon^2)|}. \quad (3.224)$$

Since $I = e^{\kappa(m^0 + \epsilon m^1)} = e^{\kappa m^0} + \epsilon \kappa m^1 e^{\kappa m^0} + O(\epsilon^2)$, we use Taylor series to expand ∇I for small ϵ , so that

$$\nabla I = \begin{pmatrix} 0 \\ 0 \\ \kappa \frac{dm^0}{dz} e^{\kappa m^0} \end{pmatrix} + \epsilon \kappa e^{\kappa m^0} \begin{pmatrix} \frac{dm^1}{dx} \\ \frac{dm^1}{dy} \\ \frac{dm^1}{dz} + \kappa m^1 \frac{dm^0}{dz} \end{pmatrix} + O(\epsilon^2), \quad (3.225)$$

and

$$|\nabla I| = \kappa e^{\kappa m^0} \left(\left(\frac{dm^0}{dz} \right)^2 + 2\epsilon \frac{dm^0}{dz} \left(\frac{dm^1}{dz} + \kappa m^1 \frac{dm^0}{dz} \right) + O(\epsilon^2) \right)^{\frac{1}{2}}. \quad (3.226)$$

Using the definition for $\hat{\mathbf{G}}$ in equation 3.215 and again expanding using Taylor series for small ϵ gives

$$\begin{aligned} \hat{\mathbf{G}} &= \frac{\nabla I}{|\nabla I|} = \left[\begin{pmatrix} 0 \\ 0 \\ \kappa \frac{dm^0}{dz} e^{\kappa m^0} \end{pmatrix} + \epsilon \kappa e^{\kappa m^0} \begin{pmatrix} \frac{dm^1}{dx} \\ \frac{dm^1}{dy} \\ \frac{dm^1}{dz} + \kappa m^1 \frac{dm^0}{dz} \end{pmatrix} \right] \\ &\times \left(\frac{1}{\kappa e^{\kappa m^0} \frac{dm^0}{dz}} - \epsilon \frac{\frac{dm^0}{dz} \left(\frac{dm^1}{dz} + \kappa m^1 \frac{dm^0}{dz} \right)}{\kappa e^{\kappa m^0} \left(\frac{dm^0}{dz} \right)^3} \right) + h.o.t. \\ &= \mathbf{k} - \epsilon \left(\frac{\left(\frac{dm^1}{dz} + \kappa m^1 \frac{dm^0}{dz} \right) \mathbf{k}}{\frac{dm^0}{dz}} - \frac{1}{\frac{dm^0}{dz}} \begin{pmatrix} \frac{dm^1}{dx} \\ \frac{dm^1}{dy} \\ \frac{dm^1}{dz} + \kappa m^1 \frac{dm^0}{dz} \end{pmatrix} \right) + O(\epsilon^2). \end{aligned} \quad (3.227)$$

Hence,

$$\hat{\mathbf{G}}^0 = \mathbf{k} \quad \text{and} \quad \hat{\mathbf{G}}^1 = \frac{1}{\frac{dm^0}{dz}} \begin{pmatrix} \frac{dm^1}{dx} \\ \frac{dm^1}{dy} \\ 0 \end{pmatrix}. \quad (3.228)$$

Expanding I in terms of ϵ in the definition of $C = \zeta \chi I (\chi I - 1) |\nabla I|$, and using equation 3.226, gives

$$C^0 = \zeta \chi \kappa e^{2\kappa m^0} (\chi e^{\kappa m^0} - 1) \frac{dm^0}{dz}, \quad (3.229)$$

$$\text{and} \quad C^1 = \zeta \chi \kappa e^{2\kappa m^0} \left(\kappa n^0 (3\chi e^{\kappa m^0} - 2) m^1 + (\chi e^{\kappa m^0} - 1) \frac{dm^1}{dz} \right).$$

To find $\hat{\mathbf{k}}$ we write

$$\hat{\mathbf{G}}^1 = \begin{pmatrix} \hat{G}^{11} \\ \hat{G}^{12} \\ 0 \end{pmatrix}, \quad (3.230)$$

since $\hat{G}^{13} = 0$, and substitute this equation into 3.224. Again, using Taylor series to expand equation 3.224 for small ϵ gives

$$\hat{\mathbf{k}} = \mathbf{k} - \frac{\epsilon}{1 - C^0} \begin{pmatrix} C^0 \hat{G}^{11} \\ C^0 \hat{G}^{12} \\ 0 \end{pmatrix} + O(\epsilon^2). \quad (3.231)$$

Equating this with equation 3.223 gives

$$\hat{\mathbf{k}}^0 = \mathbf{k} \text{ and } \hat{\mathbf{k}}^1 = -\frac{C^0 \hat{\mathbf{G}}^1}{1 - C^0}. \quad (3.232)$$

These can be used in the solution for the Fokker-Planck equation component wise, using the definition for \hat{G}^{11} and \hat{G}^{22} to write

$$\hat{k}^{11} = \frac{-C^0 \frac{dm^1}{dx}}{(1 - C^0) \frac{dm^0}{dz}}, \quad \hat{k}^{12} = \frac{-C^0 \frac{dm^1}{dy}}{(1 - C^0) \frac{dm^0}{dz}} \text{ and } \hat{k}^{13} = 0. \quad (3.233)$$

The Taylor expansion of $|\mathbf{k} - C\hat{\mathbf{G}}|$ used to calculate $\hat{\mathbf{k}}$ in equation 3.231 is

$$|\mathbf{k} - C\hat{\mathbf{G}}| = (1 - C^0) - \epsilon C^1 + O(\epsilon^2), \quad (3.234)$$

which is used again to separate out the zero flow and the perturbation components of $|\mathbf{k} - C\hat{\mathbf{G}}|$ in the first term on the left hand side of the Fokker-Planck equation 3.222.

Now all the expansions that are encountered when solving the Fokker-Planck have been calculated, we can begin to solve equation 3.222. We first look for the solution for zero flow, where $\mathbf{u} = \boldsymbol{\omega} = \mathbf{e} = \mathbf{0}$, $f = f^0$ and $m = m^0$. Using equations 3.223, 3.231 and 3.234, equation 3.222 becomes

$$(1 - C^0) (\mathbf{k} \cdot \nabla f^0 - 2(\mathbf{k} \cdot \mathbf{p})f^0) = \lambda^{-1} \nabla^2 f^0. \quad (3.235)$$

If we define

$$\Lambda_{C2}(z) = \lambda(1 - C^0(z)), \quad (3.236)$$

where C^0 is a function of z given in equation 3.229, and write $\mathbf{p} = (\sin \theta \cos \phi, \sin \theta \sin \phi, \cos \theta)$ and $\mathbf{k} = (0, 0, 1)$, we have the same form as equation 3.13 for Model B (and Case I), with $\Lambda_{C2}(z)$ instead of $\Lambda(z)$. Hence,

$$f^0 = \mu_{\Lambda_{C2}} e^{\Lambda_{C2} \cos \theta}, \text{ with } \mu_{\Lambda_{C2}} = \frac{\Lambda_{C2}}{4\pi \sinh \Lambda_{C2}}. \quad (3.237)$$

The contributions to $\langle \mathbf{p} \rangle^0$ and \mathbf{D}^0 are of the same form as in Model B and Case I, but with $\Lambda_{C2}(z)$ instead of $\Lambda(z)$, shown in equations 3.259 and 3.260 (below).

If we now consider a perturbation from the equilibrium solution, as in equation 3.34, and substitute in the components of $|\mathbf{k} - C\hat{\mathbf{G}}|$, $\hat{\mathbf{k}}$ and C from equations 3.234, 3.231 and 3.229, respectively, the Fokker-Plank equation to order ϵ becomes

$$\begin{aligned} & (1 - C^0)(\mathbf{k}^0 \cdot \nabla f^1 - 2\mathbf{k}^0 \cdot \mathbf{p} f^1) + (1 - C^0)(\hat{\mathbf{k}}^1 \cdot \nabla f^0 - 2\hat{\mathbf{k}}^1 \cdot \mathbf{p} f^0) \\ & - C^1(\mathbf{k}^0 \cdot \nabla f^0 - 2\mathbf{k}^0 \cdot \mathbf{p} f^0) + \eta \boldsymbol{\omega}^1 \cdot (\mathbf{p} \wedge \nabla f^0) \\ & + 2\eta \alpha_0 [\mathbf{p} \cdot \mathbf{e}^1 \cdot \nabla f^0 - 3\mathbf{p} \cdot \mathbf{e}^1 \cdot \mathbf{p} f^0] = \lambda^{-1} \nabla^2 f^1. \end{aligned} \quad (3.238)$$

Since $\hat{\mathbf{k}}^0 = \mathbf{k}$, equation 3.238 becomes

$$\begin{aligned} & \frac{1}{\sin \theta} \frac{\partial}{\partial \theta} \left(\sin \theta \frac{\partial f^1}{\partial \theta} \right) + \frac{1}{\sin^2 \theta} \frac{\partial^2 f^1}{\partial \phi^2} - \Lambda_{C2} \left(\mathbf{k} \cdot \hat{\boldsymbol{\theta}} \frac{\partial f^1}{\partial \theta} - 2 \cos \theta f^1 \right) \\ = & \eta \lambda \left(\boldsymbol{\omega}^1 \cdot \mathbf{p} \wedge \hat{\boldsymbol{\theta}} \frac{\partial f^0}{\partial \theta} + 2\alpha_0 \mathbf{p} \cdot \mathbf{e}^1 \cdot \hat{\boldsymbol{\theta}} \frac{\partial f^0}{\partial \theta} - 6\alpha_0 \mathbf{p} \cdot \mathbf{e}^1 \cdot \mathbf{p} f^0 \right) \\ & - \lambda C^1 \left(\mathbf{k} \cdot \hat{\boldsymbol{\theta}} \frac{\partial f^0}{\partial \theta} - 2 \cos \theta f^0 \right) + \Lambda_{C2} \left(\hat{\mathbf{k}}^1 \cdot \hat{\boldsymbol{\theta}} \frac{\partial f^0}{\partial \theta} - 2\hat{\mathbf{k}}^1 \cdot \mathbf{p} f^0 \right). \end{aligned} \quad (3.239)$$

This can be solved by considering each term on the right hand side separately, as in Model B. For the first terms on the first line of the right hand side, solutions are similar to the other models, but with $\Lambda_{C2}(z)$ instead of $\Lambda(z)$ or $\Lambda_C(z)$, and can be directly quoted. This leaves two new terms to solve for (the 5th term, which includes λC^1 , and the 6th term, which includes by Λ_{C2} , both on the second line of the right hand side). We re-write equation 3.239, setting $\alpha_0 = 0$ and omitting the first three terms on the right hand side, so that we include only the new terms due to phototaxis on that side, hence

$$\begin{aligned} & \frac{1}{\sin \theta} \frac{\partial}{\partial \theta} \left(\sin \theta \frac{\partial f^1}{\partial \theta} \right) + \frac{1}{\sin^2 \theta} \frac{\partial^2 f^1}{\partial \phi^2} + \Lambda_{C2} \left(\sin \theta \frac{\partial f^1}{\partial \theta} + 2 \cos \theta f^1 \right) \\ = & \lambda C^1 \left(\sin \theta \frac{\partial f^0}{\partial \theta} + 2 \cos \theta f^0 \right) \\ & + \Lambda_{C2} \left((\hat{k}^{11} \cos \theta \cos \phi + \hat{k}^{12} \cos \theta \sin \phi) \frac{\partial f^0}{\partial \theta} \right) - 2\Lambda_{C2} \sin \theta \left(\cos \phi \hat{k}^{11} + \sin \phi \hat{k}^{12} \right) f^0, \end{aligned} \quad (3.240)$$

and noting that $\hat{k}^{13} = 0$. Consider a solution of the form

$$f^1 = \lambda C^1 \mu_{\Lambda_{C2}} h_1(\theta), \quad (3.241)$$

for the first term on the right hand side of equation 3.240. On changing variables so that $x = \cos \theta$, equation 3.240 becomes

$$\left((1 - x^2) h_1' \right)' - \Lambda_{C2} \left((1 - x^2) h_1 \right)' = - \left[e^{\Lambda_{C2} x} (1 - x^2) \right]'. \quad (3.242)$$

This is of the same form as equation 3.59 in Model B, hence

$$h_1(x, z) = e^{\Lambda_{C2}x} (K_1(z) - x). \quad (3.243)$$

On using this to find the solution to the Fokker-Planck we have the new parts of the solutions as

$$\langle \mathbf{p} \rangle^{1(1)}(z) = \lambda C^1 \begin{pmatrix} 0 \\ 0 \\ K_6(z) \end{pmatrix}, \quad (3.244)$$

where $K_6(z)$ has the same form as $K_6(z)$ as in equation 3.68 in Model B, but is a function of $\Lambda_{C2}(z)$ instead of $\Lambda(z)$. Likewise, the components of \mathbf{D} are the same as Model B but with Λ_{C2} and λC^1 as the multiplier, as shown in equation 3.260 (see below).

For the penultimate terms on the right hand side of equation 3.240, we try the solution

$$f^{1(2)} = \mu_{\Lambda_{C2}} \Lambda_{C2} (\hat{k}^{11} \cos \phi + \hat{k}^{12} \sin \phi) h_2(\theta), \quad (3.245)$$

so that

$$((1-x^2)h_2')' - \frac{h_2}{(1-x^2)} - \Lambda_{C2}((1-x^2)h_2)' = -x\Lambda_{C2}(1-x^2)^{\frac{1}{2}}e^{\Lambda_{C2}x}. \quad (3.246)$$

Equation 3.246 has the same form as equation 3.43 in Model B, but with an extra x multiplied by the exponential on the right hand side, and with Λ_{C2} instead of Λ . We use the same method of solving, by expanding

$$h_2(x) = \sum_{n=1}^{\infty} \Lambda_{C2}^n H_n(x), \quad \text{and} \quad H_n(x) = \sum_{r=1}^{n+1} \hat{a}_{n,r} P_r^1(x), \quad (3.247)$$

where $\hat{a}_{n,r} = 0$ for $n+1 < r$ or $n, r < 1$. $n+1$ is used in the sum above instead of n in equation 3.46 in Model B, because an extra term in the expansion is required to account for the x multiplier. Using similar analysis to that shown in Section 3.2.2, from Pedley and Kessler [130], which was corrected in Bees and Hill [9] (detailed in Appendix B), we obtain

$$\hat{a}_{n,m} = -\frac{m+2}{(m+1)(2m+3)} a_{n-1,m+1} + \frac{m-1}{(2m-1)m} a_{n-1,m-1} + \frac{\hat{b}_{n,m}}{m(m+1)}, \quad (3.248)$$

where

$$\hat{b}_{n,m} = \frac{2m+1}{2(n-1)!m(m+1)} \int_{-1}^1 (1-x^2)^{\frac{1}{2}} x^n P_m^1(x) dx. \quad (3.249)$$

This can be re-arranged to give

$$\hat{b}_{n,m} = \frac{(2m+1)n}{2(n!)m(m+1)} \int_{-1}^1 (1-x^2)^{\frac{1}{2}} x^n P_m^1(x) dx = nb_{n+1,m}, \quad (3.250)$$

with $b_{n+1,m}$ defined in equation 3.97, and $n+2 \geq m$. Since $b_{n+1,m} = 0$ if $n+m$ is even, $\hat{a}_{n,m} = 0$ for $n+m$ even. We calculate the contribution to the cell swimming direction $\langle \mathbf{p} \rangle$, using 2.8,

$$\langle \mathbf{p} \rangle^{1(2)}(z) = \begin{pmatrix} \hat{k}^{11} \\ \hat{k}^{12} \\ 0 \end{pmatrix} J_7(z) \quad (3.251)$$

where

$$J_7(z) = \frac{4}{3} \pi \Lambda_{C_2}(z) \mu_{\Lambda_{C_2}}(z) \sum_{l=1}^{\infty} \Lambda_{C_2}^{2l}(z) \hat{a}_{2l,1}. \quad (3.252)$$

We calculate the second moments using equation 3.26, where the diagonal terms are zero and $\langle \mathbf{pp} \rangle$ is symmetric. This gives

$$\langle \mathbf{pp} \rangle_{13}^1(z) = \langle \mathbf{pp} \rangle_{31}^1(z) = \hat{k}^{11} J_8(z) \quad \text{and} \quad \langle \mathbf{pp} \rangle_{23}^1(z) = \langle \mathbf{pp} \rangle_{32}^1(z) = \hat{k}^{12} J_8(z), \quad (3.253)$$

with

$$J_8(z) = \frac{4}{5} \pi \Lambda_{C_2}(z) \mu_{\Lambda_{C_2}}(z) \sum_{l=0}^{\infty} \Lambda_{C_2}^{2l+1}(z) \hat{a}_{2l+1,2}. \quad (3.254)$$

The final term on the right hand side in equation 3.240 has the same ϕ dependance as the previous term but with different multipliers, hence we try a solution

$$f^{1(3)} = 2\mu_{\Lambda_{C_2}} \left(\hat{k}^{11} \cos \phi + \hat{k}^{12} \sin \phi \right) h_3(\theta), \quad (3.255)$$

which gives

$$\left((1-x^2)h_3' \right)' - \frac{h_3}{(1-x^2)} - \Lambda_{C_2} \left((1-x^2)h_3 \right)' = -\Lambda_{C_2} (1-x^2)^{\frac{1}{2}} e^{\Lambda_{C_2} x}. \quad (3.256)$$

This is the same as equation 3.43, but with $\Lambda_{C_2}(z)$ instead of $\Lambda(z)$, and so we quote the previous solution from Pedley and Kessler [130] and use it to find the contribution to the mean cell swimming direction,

$$\begin{aligned} \langle \mathbf{p} \rangle^{1(3)} &= 2\mu_{\Lambda_{C_2}} \int_0^{2\pi} \int_0^\pi \left(\hat{k}^{11} \cos \phi + \hat{k}^{12} \sin \phi \right) \begin{pmatrix} \sin \theta \cos \phi \\ \sin \theta \sin \phi \\ \cos \theta \end{pmatrix} \\ &\times \left[\sum_{n=1}^{\infty} \Lambda_{C_2}^n \sum_{r=1}^n a_{n,r} P_r^1(\cos \theta) \right] \sin \theta d\theta d\phi. \end{aligned} \quad (3.257)$$

Evaluating in the same way as Section 3.2.2 gives

$$\langle \mathbf{p} \rangle^{1(3)}(z) = \frac{2J_1(z)}{\lambda} \begin{pmatrix} \hat{k}^{11} \\ \hat{k}^{12} \\ 0 \end{pmatrix}, \quad (3.258)$$

with $J_1(z)$ defined in equation 3.92 for Model B, on changing $\Lambda(z)$ for $\Lambda_{C2}(z)$. The contributions to \mathbf{D} are calculated in a similar fashion and are shown in equation 3.260 below.

Summing the components of the mean cell swimming direction gives

$$\begin{aligned} \langle \mathbf{p} \rangle = & \begin{pmatrix} 0 \\ 0 \\ K_1 \end{pmatrix} + \epsilon \left[\eta J_1 \begin{pmatrix} \omega_2 \\ -\omega_1 \\ 0 \end{pmatrix} - 2\alpha_0 \eta \begin{pmatrix} e_{13}J_4 \\ e_{23}J_4 \\ \frac{3}{2}e_{33}K_4 \end{pmatrix} + \left(J_7 + \frac{2J_1}{\lambda} \right) \begin{pmatrix} \hat{k}^{11} \\ \hat{k}^{12} \\ 0 \end{pmatrix} \right. \\ & \left. + \lambda C^1 \begin{pmatrix} 0 \\ 0 \\ K_6 \end{pmatrix} \right] + O(\epsilon^2). \end{aligned} \quad (3.259)$$

Using the approximation of \mathbf{D} up to order ϵ (equation 3.82) and summing the components gives the dimensionless diffusion tensor as

$$\begin{aligned} \mathbf{D} = & \begin{pmatrix} \frac{K_1}{\Lambda_{C2}} & 0 & 0 \\ 0 & \frac{K_1}{\Lambda_{C2}} & 0 \\ 0 & 0 & K_2 \end{pmatrix} + \epsilon \left[\eta(J_2 - J_1K_1) \begin{pmatrix} 0 & 0 & \omega_2 \\ 0 & 0 & -\omega_1 \\ \omega_2 & -\omega_1 & 0 \end{pmatrix} - 2\alpha_0 \eta \right. \\ & \begin{pmatrix} -\frac{3}{4}e_{33}K_5 + \frac{1}{4}(e_{11} - e_{22})J_6 & \frac{1}{2}e_{12}J_6 & e_{13}(J_5 - K_1J_4) \\ \frac{1}{2}e_{12}J_6 & -\frac{3}{4}e_{33}K_5 - \frac{1}{4}(e_{11} - e_{22})J_6 & e_{23}(J_5 - K_1J_4) \\ e_{13}(J_5 - K_1J_4) & e_{23}(J_5 - K_1J_4) & \frac{3}{2}e_{33}(K_5 - 2K_1K_4) \end{pmatrix} \\ & \left. + \lambda C^1 \begin{pmatrix} K_7 & 0 & 0 \\ 0 & K_7 & 0 \\ 0 & 0 & K_8 - 2K_1K_6 \end{pmatrix} \right. \\ & \left. + \left(J_8 + \frac{2J_2}{\lambda} - K_1 \left(J_7 + \frac{2J_1}{\lambda} \right) \right) \begin{pmatrix} 0 & 0 & \hat{k}^{11} \\ 0 & 0 & \hat{k}^{12} \\ \hat{k}^{11} & \hat{k}^{12} & 0 \end{pmatrix} \right] + O(\epsilon^2). \end{aligned} \quad (3.260)$$

The $K_i(z)$ and $J_i(z)$ are the same as equations 3.84 to 3.96 on changing $\Lambda(z)$ to $\Lambda_{C2}(z)$, where

$$\Lambda_{C2}(z) = \lambda(1 - C^0(z)), \quad (3.261)$$

and $C^0(z)$ is defined in equation 3.229.

3.8.2 Equilibrium solution and linear stability analysis

The equilibrium solution for zero flow $\mathbf{u} = \mathbf{0}$ is computed from the cell conservation equation, where applying the boundary conditions as in Models A and B and integrating equation 3.6 gives

$$\frac{d^2 m}{dz^2} - \frac{d\bar{K}_2}{\bar{K}_1} \frac{K_1(\Lambda_{C2})}{K_2(\Lambda_{C2})} \frac{dm}{dz} = 0. \quad (3.262)$$

The form the equilibrium solution is the same as in Model B and Case I of this model (equations 3.101 and 3.206), the only difference is that now $K_1(z)$ and $K_2(z)$ depend on $\Lambda_{C2}(z)$ instead of $\Lambda(z)$ or $\Lambda_C(z)$. The boundary conditions for m are the same as those in Models A and B.

The linear stability analysis follows the analysis for Model B and C but with different solutions to the Fokker-Planck equation inserted where necessary. We consider a perturbation from equilibrium, shown in equation 3.108, and denote equilibrium solutions from equation 3.262 with superscript 0 and the perturbation components with superscript 1, as before. The Navier Stokes equation is the same as for Models A and B, and is given in equation 2.89, and the Rayleigh number is defined in equation 2.90. The perturbed cell conservation equation at order ϵ becomes, on expanding,

$$\begin{aligned} \frac{\partial n^1}{\partial t} = & -\partial_3 n^0 u_3^1 - \frac{d\bar{K}_2}{\bar{K}_1} \partial_3 n^0 \langle \mathbf{p} \rangle_3^1 - \frac{d\bar{K}_2}{\bar{K}_1} n^0 \partial_i \langle \mathbf{p} \rangle_i^1 - \frac{d\bar{K}_2}{\bar{K}_1} \partial_i n^1 \langle \mathbf{p} \rangle_i^0 \\ & - \frac{d\bar{K}_2}{\bar{K}_1} n^1 \partial_i \langle \mathbf{p} \rangle_i^0 + D_{ij}^0 \partial_i \partial_j n^1 + \partial_i D_{ij}^0 \partial_j n^1 + D_{33}^1 \partial_i \partial_j n^0 + \partial_i D_{i3}^1 \partial_3 n^0. \end{aligned} \quad (3.263)$$

Using the same techniques as in Section 3.3.3 to expand the first order terms from the Fokker-Planck, we obtain

$$\begin{aligned} \partial_i \langle \mathbf{p} \rangle_i^1 = & H_1 \nabla^2 u_3^1 + H_2 \partial_3 \partial_3 u_3^1 - 3\alpha_0 \eta \partial_3 u_3^1 \partial_3 K_4 \\ & + \partial_3 \left(\lambda C^1 K_6(\Lambda) \right) + \left(J_7 + \frac{2J_1}{\lambda} \right) \left(\partial_1(\hat{k}^{11}) + \partial_2(\hat{k}^{12}) \right), \end{aligned} \quad (3.264)$$

$$\begin{aligned} \partial_i D_{i3}^1 = & H_3 \nabla^2 u_3^1 + H_4 \partial_3 \partial_3 u_3^1 - 3\alpha_0 \eta \partial_3 u_3^1 \partial_3 (K_5 - 2K_1 K_4) \\ & + \partial_3 \left(\lambda C^1 (K_8 - 2K_1 K_6) \right) \\ & + \left(J_8 + \frac{2J_2}{\lambda} - K_1 \left(J_7 + \frac{2J_1}{\lambda} \right) \right) \left(\partial_1(\hat{k}^{11}) + \partial_2(\hat{k}^{12}) \right). \end{aligned} \quad (3.265)$$

Substituting equations 3.264 and 3.265 in equation 3.263 and resolving into normal modes

from equation 3.117 gives

$$\begin{aligned}
& \left\{ K_2 \frac{d^2}{dz^2} - \frac{d\bar{K}_2}{\bar{K}_1} K_1 \frac{d}{dz} - \frac{K_1}{\Lambda_{C2}} k^2 - \sigma - \frac{d\bar{K}_2}{\bar{K}_1} \frac{dK_1}{dz} + \frac{dK_2}{dz} \frac{d}{dz} \right\} \Phi(z) \\
& + k^2 \left(\frac{dn^0}{dz} \left(J_8 + \frac{2J_2}{\lambda} - K_1 \left(J_7 + \frac{2J_1}{\lambda} \right) \right) - \frac{d\bar{K}_2}{\bar{K}_1} n^0 \left(J_7 + \frac{2J_1}{\lambda} \right) \right) \frac{C^0}{(1-C^0)n^0} M(z) \\
& - \frac{d\bar{K}_2}{\bar{K}_1} \lambda \left(\frac{dn^0}{dz} K_6 C^1 + n^0 \left(\frac{dK_6}{dz} C^1 + K_6 \frac{dC^1}{dz} \right) \right) \\
& + \lambda \left(\frac{d^2 n^0}{dz^2} C^1 (K_8 - 2K_1 K_6) + \frac{dn^0}{dz} \left((K_8 - 2K_1 K_6) \frac{dC^1}{dz} + C^1 \frac{d(K_8 - 2K_1 K_6)}{dz} \right) \right) \\
= & \left\{ \frac{dn^0}{dz} - \eta \left(\frac{dn^0}{dz} A_1 + \frac{d\bar{K}_2}{\bar{K}_1} n^0 A_2 \right) \frac{d^2}{dz^2} - \eta \left(\frac{d\bar{K}_2}{\bar{K}_1} \frac{dn^0}{dz} A_3 - \frac{d^2 n^0}{dz^2} A_4 \right. \right. \\
& \left. \left. + \frac{d\bar{K}_2}{\bar{K}_1} n^0 \frac{dK_4}{dz} - \frac{dn^0}{dz} \frac{d(K_5 - 2K_1 K_4)}{dz} \right) \frac{d}{dz} + \eta \left(\frac{dn^0}{dz} A_5 - \frac{d\bar{K}_2}{\bar{K}_1} n^0 A_6 \right) k^2 \right\} U(z),
\end{aligned} \tag{3.266}$$

where $A_i(z)$ and $K_i(z)$ are functions of $\Lambda_{C2}(z)$ and are defined in the same way as Models A and B, but with $\Lambda_{C2}(z)$ instead of $\Lambda(z)$ or $\Lambda_C(z)$. C^0 and C^1 are also functions of z , defined in equation 3.229. On writing equation 3.266 so that comparisons with other models can be made, we have

$$\begin{aligned}
& \left\{ P_V(z) \frac{d^2}{dz^2} - \frac{d\bar{K}_2}{\bar{K}_1} K_1(z) \frac{d}{dz} - P_H(z) k^2 - \sigma - \frac{d\bar{K}_2}{\bar{K}_1} \frac{dK_1}{dz} + \frac{dP_V(z)}{dz} \frac{d}{dz} \right. \\
& \left. - P_R(z; d) - P_{R2}(z; d) \frac{d}{dz} \right\} \Phi - \{ P_{M2}(z; d) - k^2 P_{M1}(z; d) \} M(z) \\
= & \left\{ \frac{dn^0}{dz} - \eta P_5(z; d) \frac{d^2}{dz^2} - \eta P_6(z; d) \frac{d}{dz} + \eta P_7(z; d) k^2 \right\} U(z),
\end{aligned} \tag{3.267}$$

where

$$P_H(z) = \frac{K_1(z)}{\Lambda_{C2}(z)}, \quad (3.268)$$

$$P_R(z; d) = \lambda \zeta \chi \kappa e^{2\kappa m^0} (\chi e^{\kappa m^0} - 1) \left[\frac{d\bar{K}_2}{\bar{K}_1} \left(\frac{dn^0}{dz} K_6(z) + n^0 \frac{dK_6(z)}{dz} \right) - \frac{d^2 n^0}{dz^2} (K_8(z) - 2K_1(z)K_6(z)) - \frac{dn^0}{dz} \frac{d}{dz} (K_8(z) - 2K_1(z)K_6(z)) \right] + 2\lambda \zeta \chi \kappa^2 n^0 e^{2\kappa m^0} \left(3\chi e^{\kappa m^0} - 2 \right) \left(\frac{d\bar{K}_2}{\bar{K}_1} K_6(z) n^0 - \frac{dn^0}{dz} (K_8(z) - 2K_1(z)K_6(z)) \right), \quad (3.269)$$

$$P_{R2}(z; d) = \lambda \zeta \chi \kappa e^{2\kappa m^0} \left(\frac{d\bar{K}_2}{\bar{K}_1} K_6(z) n^0 - \frac{dn^0}{dz} (K_8(z) - 2K_1(z)K_6(z)) \right) (\chi e^{\kappa m^0} - 1), \quad (3.270)$$

$$P_{M1}(z; d) = \left[\frac{dn^0}{dz} \left(J_8(z) + \frac{2J_2(z)}{\lambda} - K_1(z) \left(J_7(z) + \frac{2J_1(z)}{\lambda} \right) \right) - \frac{d\bar{K}_2}{\bar{K}_1} n^0 \left(J_7(z) + \frac{2J_1(z)}{\lambda} \right) \right] \frac{C^0(z)}{(1 - C^0(z))n^0}, \quad (3.271)$$

$$P_{M2}(z; d) = \lambda \zeta \chi \kappa e^{2\kappa m^0} \kappa n^0 (3\chi e^{\kappa m^0} - 2) \left[\frac{d\bar{K}_2}{\bar{K}_1} \left(\frac{dn^0}{dz} K_6(z) + n^0 \frac{dK_6}{dz} \right) - \frac{d^2 n^0}{dz^2} (K_8(z) - 2K_1(z)K_6(z)) - \frac{dn^0}{dz} \frac{d}{dz} (K_8(z) - 2K_1(z)K_6(z)) \right] + \lambda \zeta \chi \kappa e^{2\kappa m^0} \left(\kappa \frac{dn^0}{dz} (3\chi e^{\kappa m^0} - 2) + 3\chi \kappa^2 (n^0)^2 e^{\kappa m^0} + 2\kappa^2 (n^0)^2 (3\chi e^{\kappa m^0} - 2) \right) \times \left(\frac{d\bar{K}_2}{\bar{K}_1} K_6(z) n^0 - \frac{dn^0}{dz} (K_8(z) - 2K_1(z)K_6(z)) \right), \quad (3.272)$$

where $n^0 = n^0(z)$ and $m^0 = m^0(z)$. $P_V(z)$, $P_5(z; d)$, $P_6(z; d)$ and $P_7(z; d)$ have the same form as equations 3.119, 3.122, 3.123 and 3.124 in Model B. Equation 3.267 has a similar form to the linear stability equation for Model B (equation 3.118), where all terms on the right hand side and the first six terms on the left hand side of equation 3.267 are the same as those for Model B in equation 3.118, but are now dependent on $\Lambda_{C2}(z)$ instead of $\Lambda(z)$. $P_R(z; d)$ and $P_{M2}(z; d)$ now have a different form and the new version of the model introduces another derivative of Φ multiplied by $P_{R2}(z; d)$. $P_{M1}(z; d)$ in equation 3.267 is a completely new term in this model and is multiplied by k^2 due to derivatives in x and y from the gradient of I appearing in $\hat{\mathbf{k}}(I)$ at order ϵ . If $\chi = 0$ then $\Lambda_{C2} = \lambda$, and the linear stability equation is the same as that in Bees and Hill [9], again allowing some direct numerical comparison.

The no-flow boundary conditions are given in equation 3.125. From equation 2.23 we

have $M = 0$ at $z = 0$, and the no flux boundary conditions becomes

$$\begin{aligned} & \frac{d\bar{K}_2}{\bar{K}_1} K_1 \Phi - K_2 \frac{d\Phi}{dz} + \lambda \zeta \chi \kappa e^{2\kappa m^0} (\chi e^{\kappa m^0} - 1) \frac{dM(z)}{dz} \\ & \times \left(d \frac{\bar{K}_2}{\bar{K}_1} K_6 n^0 - \frac{dn^0}{dz} (K_8 - 2K_1 K_6) \right) \quad \text{on } z = 0, \end{aligned} \quad (3.273)$$

$$\begin{aligned} \text{and} \quad & \frac{d\bar{K}_2}{\bar{K}_1} K_1 \Phi - K_2 \frac{d\Phi}{dz} + \lambda \zeta \chi \kappa e^{2\kappa m^0} \left[\kappa n^0 (3\chi e^{\kappa m^0} - 2) M(z) \right. \\ & \left. + (\chi e^{\kappa m^0} - 1) \frac{dM(z)}{dz} \right] \left(d \frac{\bar{K}_2}{\bar{K}_1} K_6 n^0 - \frac{dn^0}{dz} (K_8 - 2K_1 K_6) \right) \quad \text{on } z = -1. \end{aligned} \quad (3.274)$$

3.9 Numerical results for Model C

In this section, numerical results for Model C, Cases I and II are computed using the same techniques as described in Chapter 2. A range of parameter values, that represent the wider parameter space, are explored, but, to avoid repetition, only results that vary significantly from previous models are shown. Again, the z is scaled with d , so that $z_I = dz$, and the layer depth is $-d \leq z_I \leq 0$.

3.9.1 Model C, Case I

For Case I of Model C, we only consider illumination from above, so that $\boldsymbol{\pi} = \mathbf{k}$. If one sets $\boldsymbol{\pi} = \mathbf{k}$ then the model equations for Model C, Case I in this situation are very similar to those for Model B. The difference is that the function of light intensity that is multiplied by the gravitaxis torque term in the Fokker-Planck equation is different in equation 3.12 for Model B to that used in equation 3.195 for Model C. If we denote this function $g(I)$ in both cases, where $g(I) = h(I)$ in Model B and $g(I)$ is non-dimensional, then

$$g(I) = (1 - \chi I) \quad (\text{Model B}), \quad \text{and} \quad g(I) = (1 - \zeta \chi I (\chi I - 1)) \quad (\text{Model C}) \quad . \quad (3.275)$$

We expect these functions to affect the stability results of the models in qualitatively similar ways. In this section, we compare numerical solutions for a fixed η when ζ and χ are varied. ζ is a new parameter, not present in the previous models. To allow some qualitative comparison between Models B and C, we fix ζ so that the functions $g(I)$ in each model have the same gradient at $g(I) = 0$ (Note that it is impossible to simultaneously set the curves to cross the axis at the same point). $g(I) = 0$ in Model B when $I = \frac{1}{\chi}$ with gradient $-\chi$. For Model C, $g(I) = 0$ at $I = I_0$ when

$$1 = \zeta \chi I (\chi I - 1), \quad \text{so} \quad I_0 = \frac{1 + \left(1 + \frac{4}{\zeta}\right)^{1/2}}{2\chi}, \quad (3.276)$$

where we take the largest positive route. The gradient at this point is given by

$$\frac{dg(I)}{dI} = \zeta\chi(1 - 2\chi I_0), \quad (3.277)$$

so to make the gradients the same at $g(I) = 0$ we set

$$-\chi = \zeta\chi(1 - 2\chi I_0), \text{ hence } \zeta = -2 \pm \sqrt{5}. \quad (3.278)$$

Taking the positive square root to obtain a positive value of ζ gives $\zeta = 0.236$.

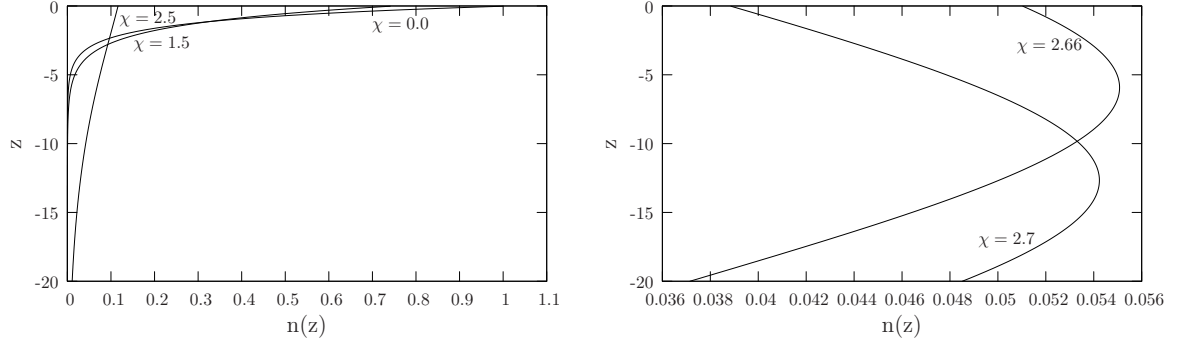


Figure 3.8: Concentration profiles for the equilibrium solution in Model C, Case I, where $d = 20$, $\kappa = 1.0$ and χ varies with $\zeta = 0.236$, so that the gradients of $g(I)$ at $g(I) = 0$ are the same as in Model B.

Figure 3.8 shows equilibrium solutions for $d = 20$ and $\kappa = 1.0$ for various values of χ . The same trends as in Models A and B are seen, where increasing χ moves the maximum of the equilibrium solution down, and the maximum is smallest when the peak is at the midheight of the layer. The only notable difference here is that a higher value of χ (not χ just greater than one) is needed to move the maximum of the equilibrium solution away from $z = 0$. This is because the phototaxis torque strength, ζ , needs to be large, in addition to $I_s > I_c$, so that the light has sufficient effect on cell swimming that cells swim away from the light. Figure 3.9 shows neutral curves corresponding to these equilibrium solutions with $d^2\eta = 4$ and $\zeta = 0.236$. For small $\chi < 1$, small wavenumbers are rapidly stabilized, the critical wavenumber remains non-zero and initially increases. This is the only qualitative difference between the model results, since small wavenumbers are destabilized in Models A and B for $\chi < 1$. As χ increases beyond $\chi = 0.5$ here, we find destabilization of small wavenumbers leads to a zero critical wavenumber, but as χ is increased further ($\chi \geq 2.5$) all wavenumbers are stabilized, and k_c becomes non-zero again. The trend for $\chi > 0.5$ is the same trend as found for $\chi > 0$ in Models A and B, but here higher values of χ ($\chi > 2.5$, compared to $\chi > 1$) are needed for the stability

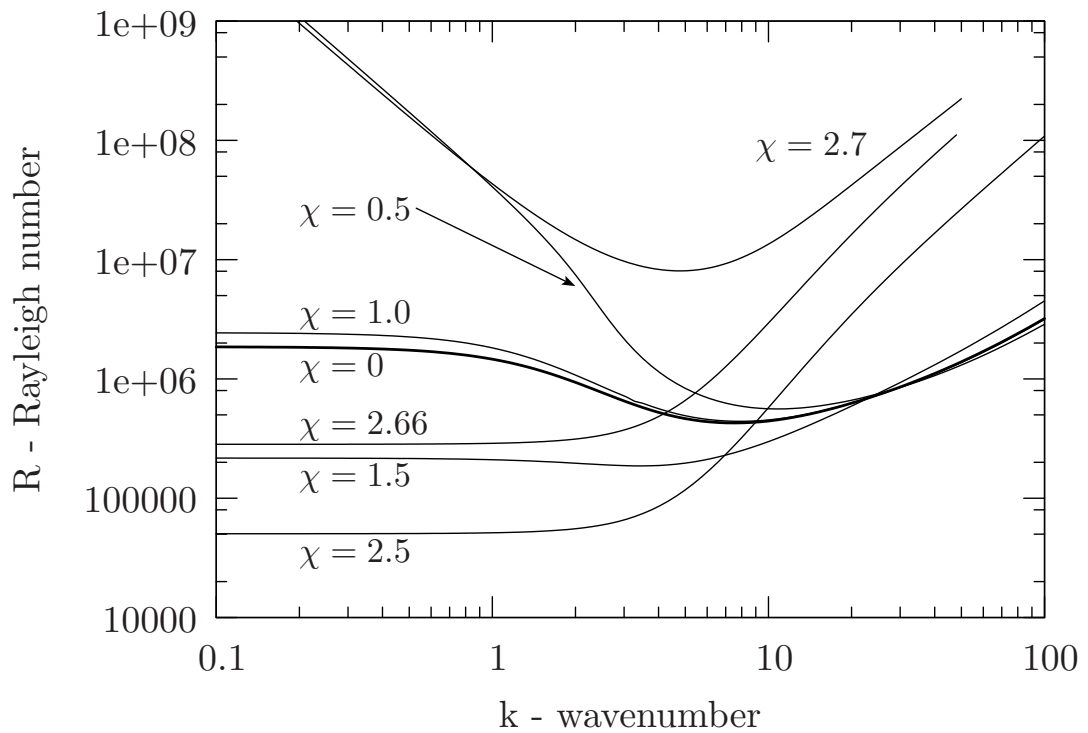


Figure 3.9: Curves of neutral stability for Model C, Case I, where $d = 20$, $\kappa = 1.0$, $d^2\eta = 4$ and χ varies. We choose $\zeta = 0.236$, so that the gradient at $g(I) = 0$ is the same as in Model B.

of the system to increase, because both strong phototaxis and $I_s > I_c$ are required. No oscillatory solution branches were found.

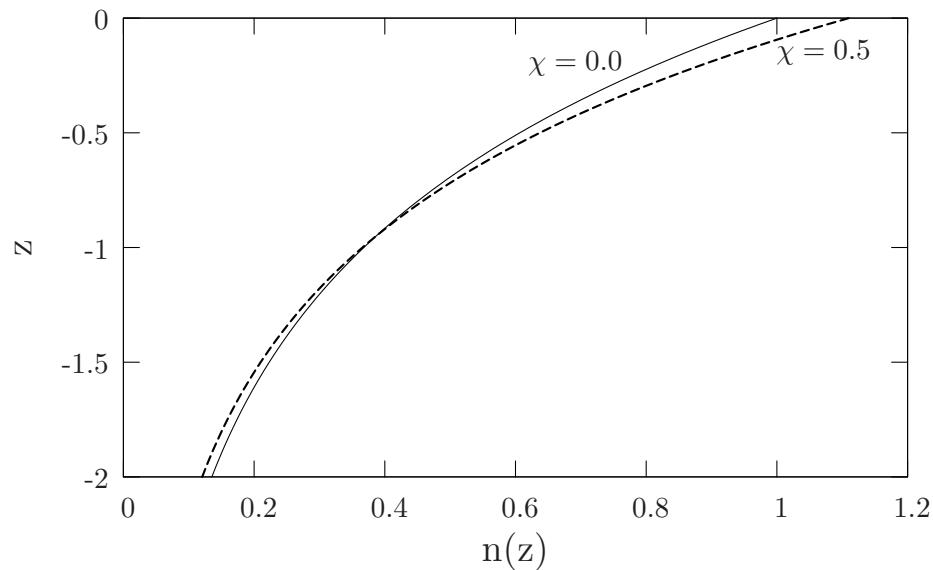


Figure 3.10: Concentration profiles for the equilibrium solution in Model C, Case I, where $d = 20$, $\kappa = 1.0$, $\zeta = 0.236$ and $\chi = 0.5$ (dashed) or $\chi = 0$ (solid line). The z axis is expanded so that only the range $0 \leq z \leq -2.0$ is shown.

To further explore the intriguing stabilization of small wavenumbers for $\chi = 0.5$ compared to $\chi = 0$, which is not found for Models A and B, the equilibrium solutions in the top region of the suspension are expanded and shown in Figure 3.10. The solution for $\chi = 0.5$ has a higher maximum concentration at $z = 0$ compared to $\chi = 0$ and further down the layer the cells are slightly more spread out. This occurs because the function $g(I)$ in Model C increases and then decreases (whereas in Model B the function is monotonically decreasing) as shown in Figure 3.11. The increase in $g(I)$ for Model C means the cells near $z = 0$ act more deterministically in this case compared to Model B, since this is similar to increasing λ , so that gravitaxis increases and the concentration profile is more peaked at $z = 0$. Figure 3.12 shows that using a stress-free boundary condition at $z = 0$ does not significantly stabilize the system for $\chi = 0.5$, indicating that it is the effect of the no-flow boundary that stabilizes the small wavenumbers for small χ in this case.

3.9.2 Model C, Case II

In this section, stability is explored when the two phototaxis parameters, ζ and χ , are varied for $d = 20$, $\kappa = 1.2$ and $d^2\eta = 4$. Equilibrium solutions for the case $\chi = 2$,

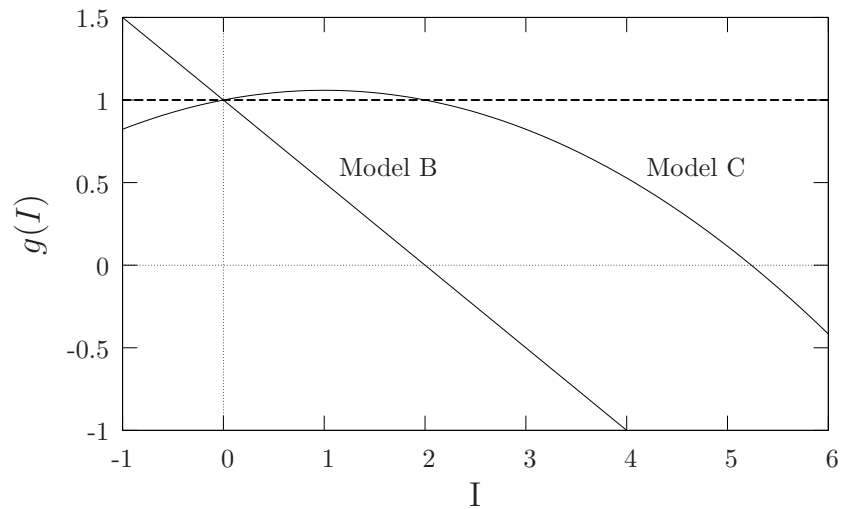


Figure 3.11: Curves for $g(I)$ for Models B and C, where $\zeta = 0.236$ is set so that the gradients at $g(I) = 0$ are the same, and $\chi = 0.5$. The dashed line shows $g(I) = 1$. For $g(I)$ in Model C, when I is around $I = 1$, $g(I) > 1$, while in Model B $g(I) \approx 0.5$ at around $I = 1$. The differences in the function $g(I)$ between these models, where $g(I)$ is monotonically decreasing in Model B but has a maximum in Model C, leads to differences in equilibrium and stability predictions.

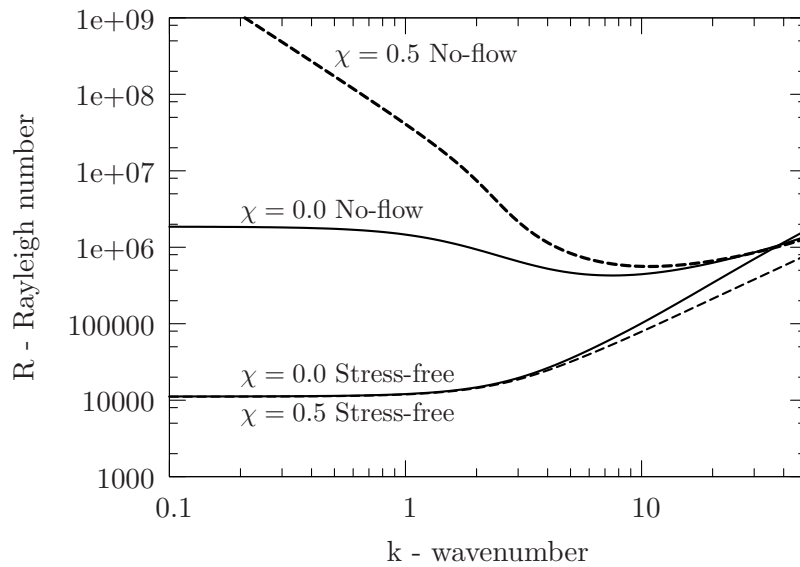


Figure 3.12: Curves of neutral stability for Model C, Case I, where $d = 20$, $\kappa = 1.0$ and $\zeta = 0.236$. $\chi = 0$ is shown for both a no-flow and a stress-free condition (solid lines), and $\chi = 0.5$ with a no-flow or a stress-free condition (dashed lines).

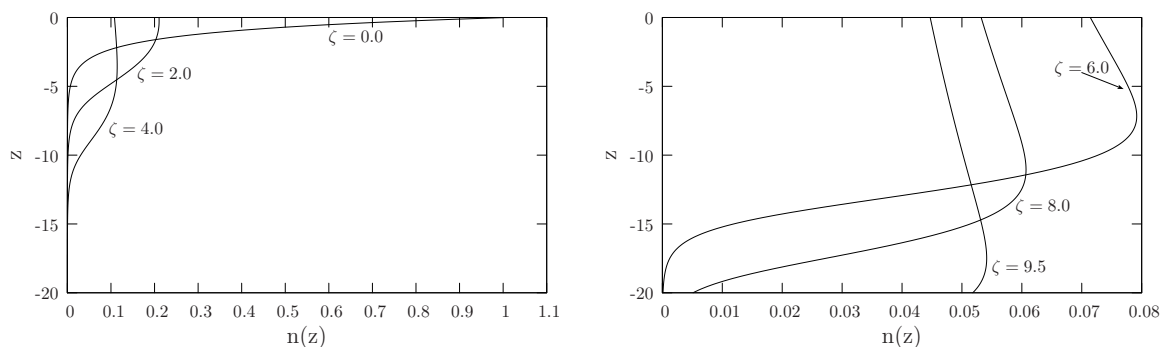


Figure 3.13: Concentration profiles for the equilibrium solution for Model C, Case II, where $d = 20$, $\kappa = 1.2$, $\chi = 2.0$, $d^2\eta = 4$ and ζ varies.

where $I_s > I_c$, and for various ζ values are shown in Figure 3.13. As ζ increases from $\zeta = 0$ the maximum of the concentration profile moves down the fluid layer, as found in previous models. The upper sections of the concentration profiles (above the peak of the distributions) when $\zeta \geq 2$, however, are considerably flatter than those found for $\chi > 1$ in Models A and B, and there is no approximate symmetry in the concentration profile when the maximum is midway down the suspension (which there was for Models A and B). Additionally, the maximum concentration decreases rather than increases as ζ increases when the location of the maximum is located below the mid-point of the domain. This appears to lead to the concentration profiles tending to a uniform distribution for large ζ . The reasons for this are described in Section 3.11. The numerical solutions were difficult to resolve for $\zeta > 9.5$ and, hence, are not shown.

Figure 3.14 shows the associated neutral curves as the phototaxis strength parameter ζ is varied when $\chi = 2$. As ζ increases from $\zeta = 0$ to $\zeta = 4$, the trend in the stability curves is similar to that seen for increasing χ between $0 < \chi < 1$ in Models A and B, where increasing ζ destabilizes the system and the critical wavenumber becomes zero, $k_c = 0$.

Interestingly, this trend continues as ζ increases further, and for approximately $\zeta > 5$ the Rayleigh number for small wavenumbers crosses the line $R = 0$. This is shown in Figure 3.15 for $4 \leq \zeta \leq 8$. This is a smooth transition, implying that under conditions of zero flow, $U = 0$, a destabilizing mechanism still exists for all $R \geq 0$. These non-hydrodynamic modes arise because of sideways swimming due to the x and y components of the gradient of I in the phototaxis torque, even when there is no fluid flow. The case $R = 0$ uncouples the cell dynamics (in the cell conservation equation) from the Navier-Stokes equations. This mechanism is discussed further in Section 3.11.

Figure 3.16 shows growth rate curves for the zero flow version of Case II, where we

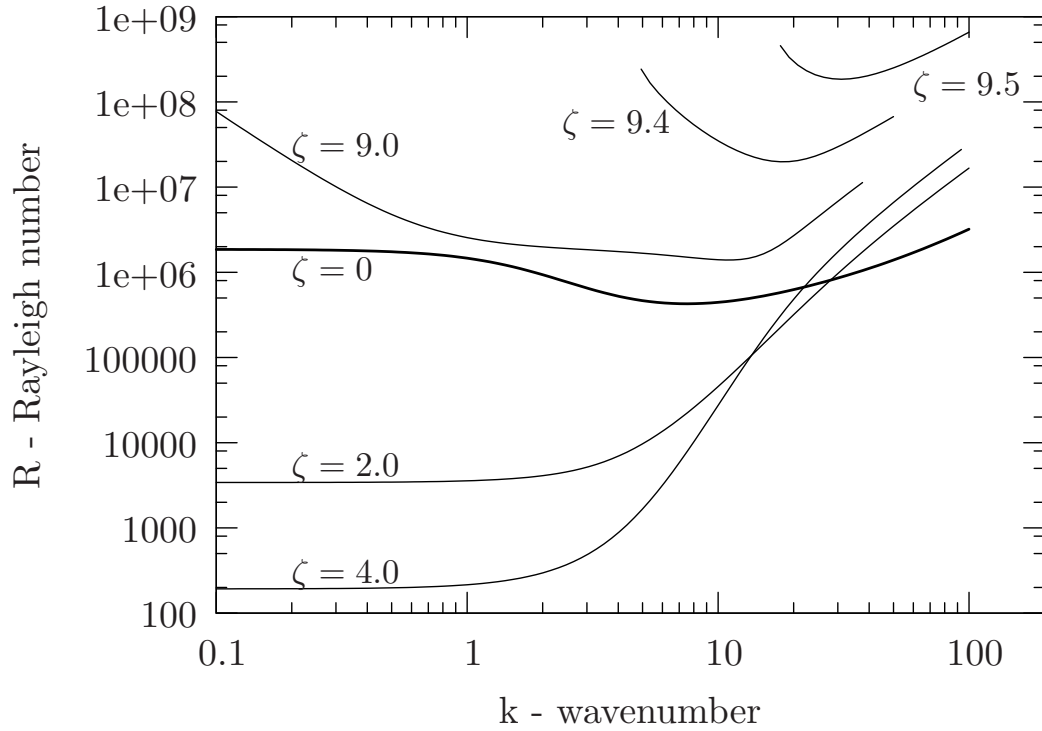


Figure 3.14: Curves of neutral stability for Model C, Case II, where $d = 20$, $\kappa = 1.2$, $\chi = 2.0$, $d^2\eta = 4$ and ζ varies.

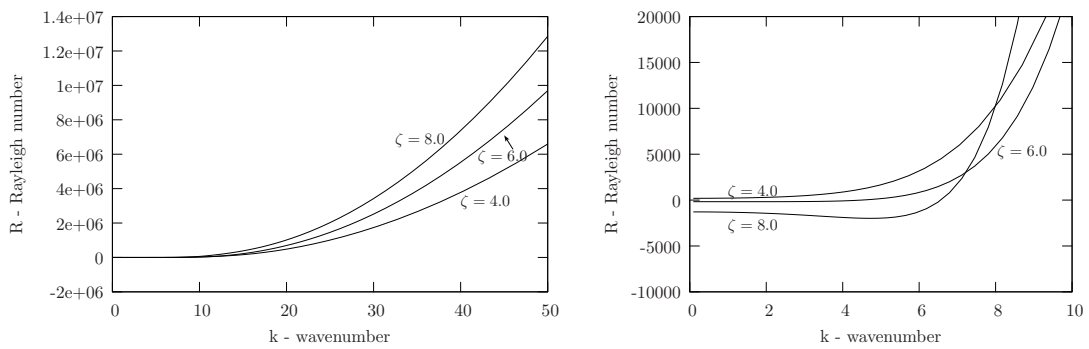


Figure 3.15: Curves of neutral stability for Model C, Case II, where $d = 20$, $\kappa = 1.2$, $\chi = 2.0$, $d^2\eta = 4$ and ζ varies. The curves are not plotted on a log-log scale, since the neutral curves cross the line $R = 0$ for $k \sim O(1)$.

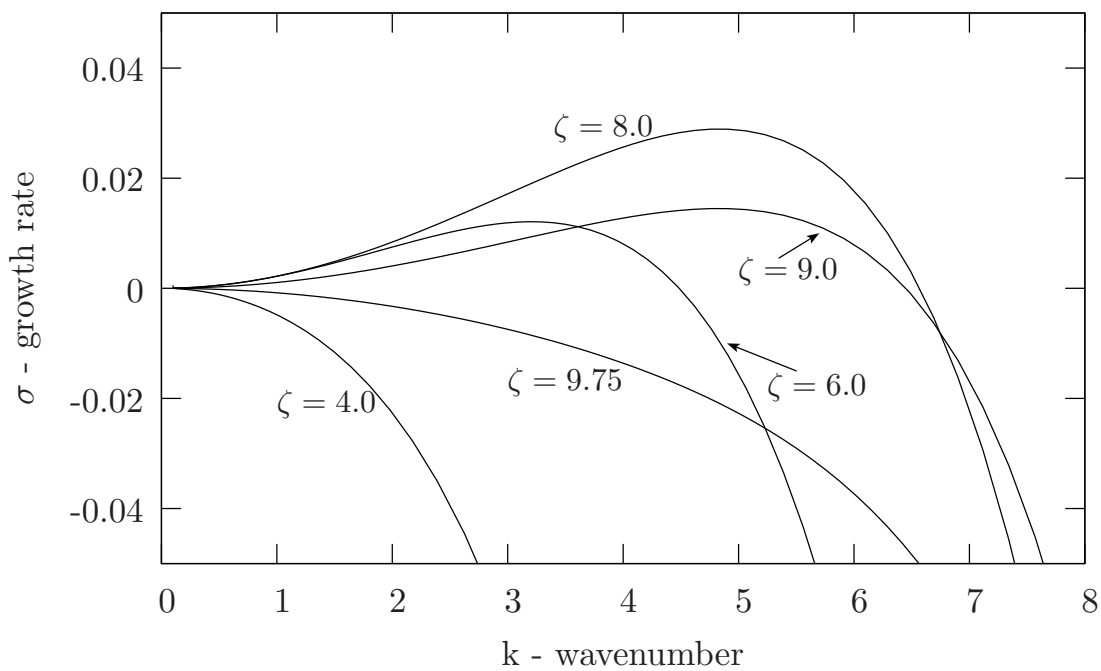


Figure 3.16: Growth rate curves for Model C, Case II when there is no fluid flow, so that $U = R = 0$, $d = 20$, $\kappa = 1.2$, $\chi = 2.0$, $d^2\eta = 4$, and ζ varies. As ζ increases beyond $\zeta = 4.0$, the growth rates becomes positive for some k , but when $\zeta = 9.75$ the growth rates are negative for all k again.

set $U = 0$. The existence of an instability mechanism in the absence of fluid flow is confirmed by the presence of positive growth rates, $\sigma > 0$, for small k when $5 < \zeta < 9.25$. Interestingly, when $\zeta > 9.25$ the growth rates becomes negative again, indicating that these non-hydrodynamic modes only exist when $5 < \zeta < 9.25$ (approximately). If ζ is taken as the eigenvalue instead of R , when $U = 0$, then a neutral curve for ζ versus wavenumber k can be found, as shown in Figure 3.17. For each wavenumber k , when $1 < k < 6$ (approximately), if $5 < \zeta < 9.25$, then the system becomes unstable to non-hydrodynamic modes. For approximately $k < 1$ convergence of the numerical program became difficult and the full neutral curve could not be found. For all parameters values investigated, no oscillatory modes were found.

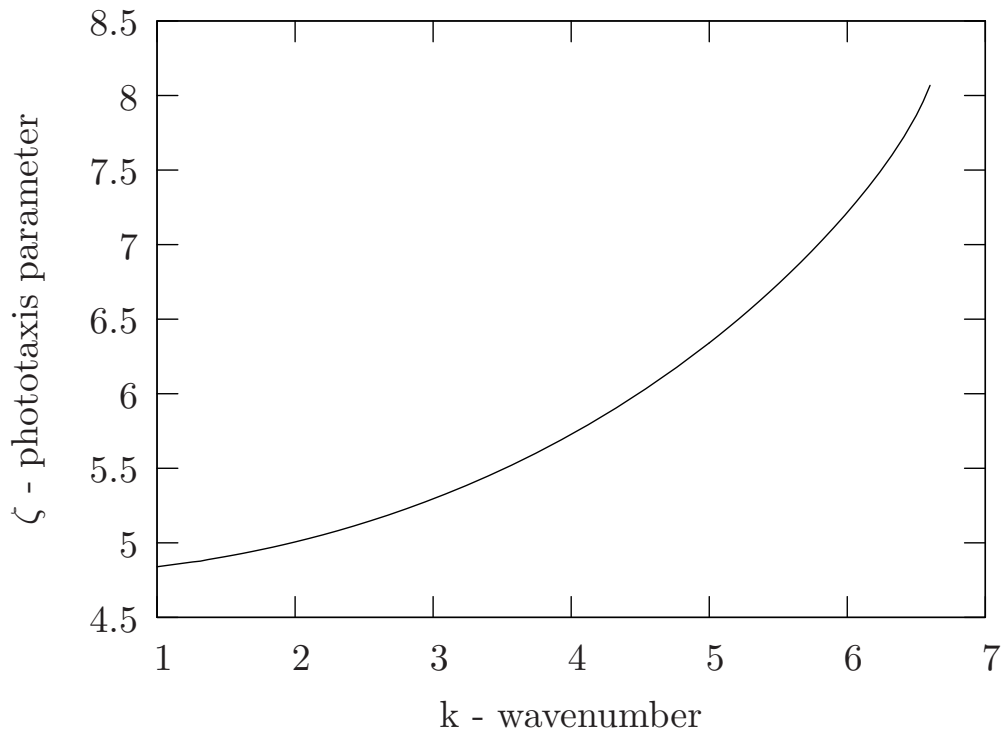


Figure 3.17: Neutral stability curve of wavenumber versus the phototaxis parameter ζ , where ζ is used as the eigenvalue for the case of zero flow, $U = 0$, in Model C, Case II, where $d = 20$, $\kappa = 1.2$, $\chi = 2.0$ and $d^2\eta = 4$.

In Figure 3.14 hydrodynamic modes (with one convection cell) are also shown for $\zeta \geq 9$. The suspension is stabilized as ζ increases from $\zeta = 9$, and the non-zero critical wavenumber k_c increases with ζ . It is unclear where these neutral curves grow from, since hydrodynamic curves for $\zeta < 9$ are very difficult to trace numerically. We expect that they grow from neutral curves that were mode two for smaller values of ζ . The

trend in $\zeta > 9.0$ is similar to that for increasing $\chi > 1$ in Models A and B, in which all wavenumbers are stabilized and k_c increases with χ . However, for the case $\zeta = 9.0$ unstable non-hydrodynamic modes also exist for $R \geq 0$, and it is unclear whether the hydrodynamic or the non-hydrodynamic modes will be the most unstable; which mode one is likely to see will depend on which mode has the largest growth rate. In reality, it is difficult to separate the effects of the non-hydrodynamic and hydrodynamic modes, since for $R > 0$ the non-hydrodynamic modes will eventually also induce fluid flow within the suspension. This could, in turn, lead to the formation of hydrodynamic modes. If $\zeta > 9$ (approximately), Figure 3.16 shows that the non-hydrodynamic modes are stabilized for all wavenumbers and, therefore, in these cases the hydrodynamic modes shown in Figure 3.14 are the most unstable modes of instability.

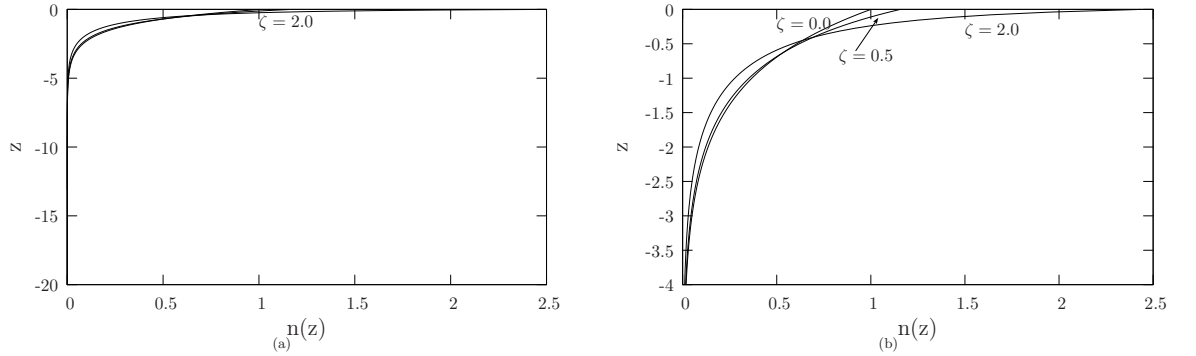


Figure 3.18: Concentration profiles for the equilibrium solution for Model C, Case II, where $d = 20$, $\kappa = 1.2$, $\chi = 0.5$, $d^2\eta = 4$ and ζ varies. In (b) the z -axis is scaled so that only the range $-4 \leq z \leq 0$ is shown.

Figures 3.18 and 3.19 explore the effects of varying the phototaxis torque strength when $\chi = 0.5$, for which $I_s < I_c$ and none of the cells have enough light. For all values of ζ , the peak of the equilibrium profile is at the top of the layer, $z = 0$. The maximum of the peak increases with ζ due to increased swimming upwards, towards the light, when phototaxis is strong. The neutral curves in Figure 3.19 show that this significantly stabilizes wavenumbers $k \leq 60$, and that both the critical wavenumber and the stability increase with increasing ζ . For $\zeta > 2$ solutions are difficult to trace numerically, due to the vast majority of cells collecting in an ever smaller region close to $z = 0$ as ζ gets large.

Trends in equilibrium solutions as χ varies (for constant ζ) are qualitatively the same as those shown for varying χ in Model C, Case I. The maximum concentration first increases at $z = 0$, then decreases as the maximum moves down the fluid layer, and the maximum

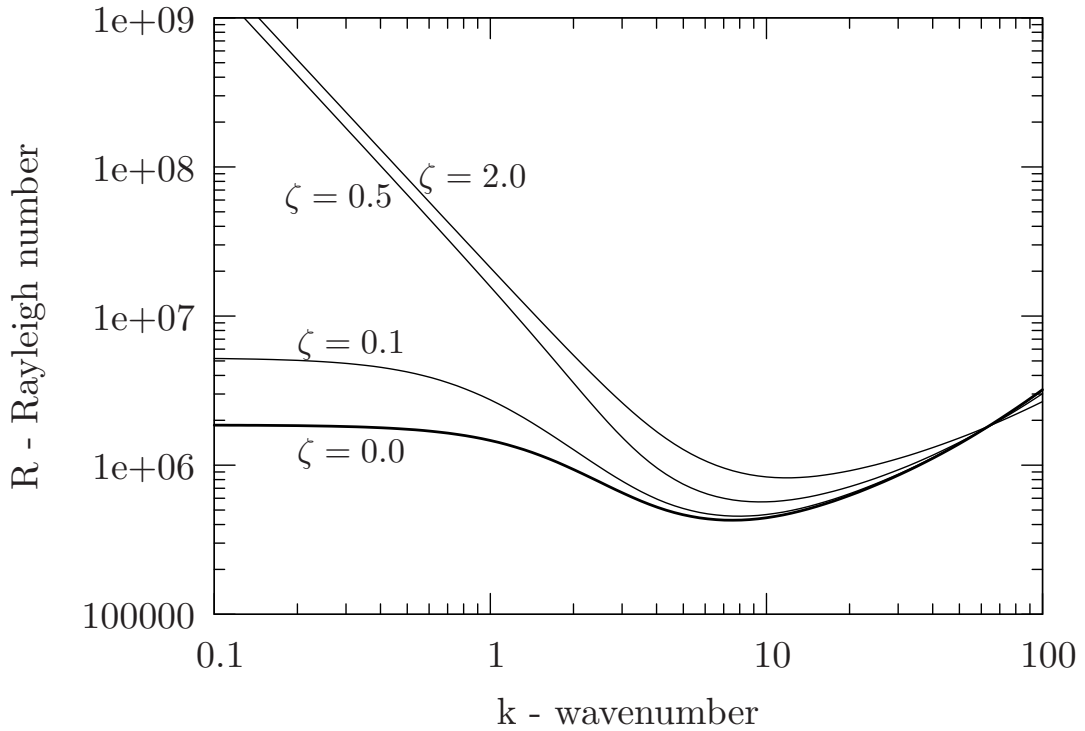


Figure 3.19: Curves of neutral stability for Model C, Case II, where $d = 20$, $\kappa = 1.2$, $\chi = 0.5$, $d^2\eta = 4$, and ζ varies.

concentration is smallest when it occurs at the midheight of the suspension. Compared to Model C, Case I and Models A and B, the top (or bottom, when the maximum is in the lower half of the domain) of the concentration profiles for large χ are much flatter and the shapes are similar to those for varying ζ in Figure 3.13. The smaller the value of ζ , the higher the value of χ needed to move the maximum of the concentration profile down the layer. Figure 3.20 shows curves of neutral stability when $\zeta = 0.1$ and $\zeta = 4.0$ as χ varies. Increasing χ from $\chi = 0$ first stabilizes and then destabilizes the system, as found for Case I. Non-hydrodynamic modes were also found as χ increased from $\chi = 0$. As ζ increases the value of χ at which purely non-hydrodynamic modes first exist (denoted χ_c), with $R = 0$, decreases (for $\zeta = 0.1$, $\chi_c = 10$, and for $\zeta = 4$, $\chi_c = 2.0$). For large χ , hydrodynamic modes were found again, and curves of neutral stability followed the same trends as those for large χ in Models A and B.

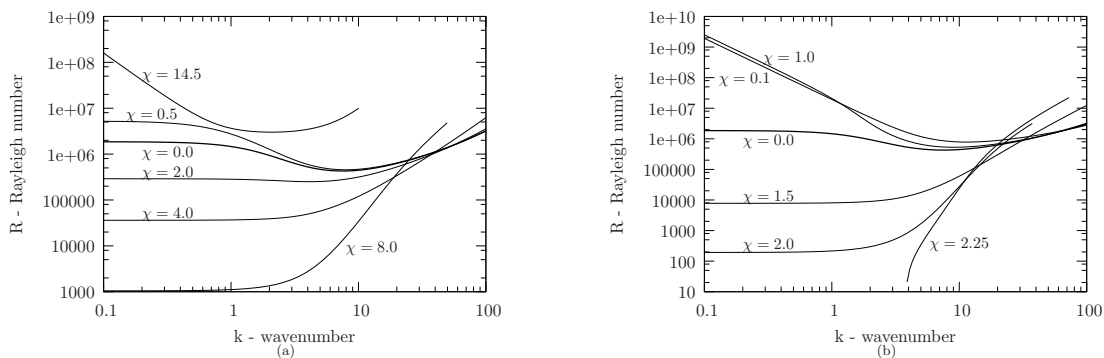


Figure 3.20: Curves of neutral stability for Model C, Case II, where $d = 20$, $\kappa = 1.2$, $d^2\eta = 4$ and χ varies, with $\zeta = 0.1$ in Figure (a) and $\zeta = 4.0$ in Figure (b).

3.10 Model comparisons

In this section, equilibrium solutions and stability results for all models are compared. Model A results were computed using the slightly incorrect values of J_4 and J_5 and so, in order to make direct comparisons, results for Model A in this section have been recalculated with corrected J_4 and J_5 values. For both cases of Model C there are two phototaxis parameters, χ and ζ , whereas for Models A and B there is only χ . Direct comparisons can not be made between Model C and Models A and B, since we have no good way of estimating ζ , but qualitative trends are discussed.

The qualitative trends in equilibrium solutions as χ is varied are similar in Models A and B, as shown in Figure 3.21. For Model C, Cases I and II a similar trend is observed as χ is increased from 1 to $\chi > 1$ for all ζ . However, if $0 < \chi < 1$ then the peak of the equilibrium solution actually increases (compared to the maximum at $\chi = 0$) rather than decreases as χ increases, which is the opposite to what occurs in Models A and B. This increase also occurs as ζ is increased when $\chi < 1$. For Model C, Case II, increasing ζ for $\chi > 1$ decreases the maximum of the concentration profiles even when this maximum is located in the bottom half of the fluid layer, so that for large ζ the concentration distribution is almost uniform. This is not the case for increasing χ in Models A, B and C, in which case the smallest maximum occurs at $z = -\frac{d}{2}$. The equilibrium profiles for Model C, shown in Figure 3.13, are much flatter above the maximum concentration than those shown in Figure 3.21 for Models A and B.

For small $\chi < 1$ results from Model A and B were qualitatively the same, and quantitatively similar, with small wavenumbers destabilized. This is expected, as phototaxis is weak and the equilibrium solutions are very similar. However, for both cases of Model C

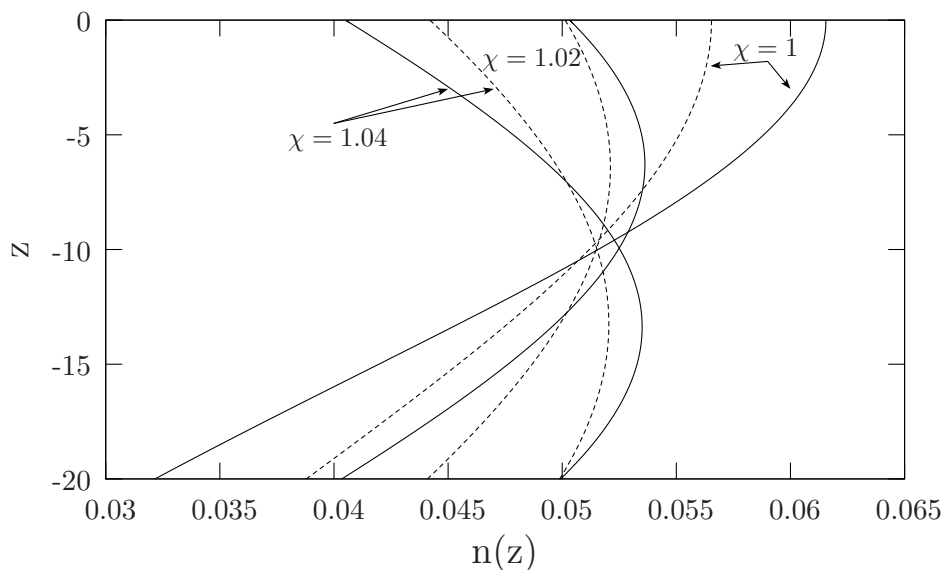


Figure 3.21: A comparison of equilibrium solutions for Model A (solid lines) and Model B (dashed lines), where $d = 20$, $\kappa = 1.2$ and $\chi = 1.0$, $\chi = 1.02$ and $\chi = 1.04$

when $0 < \chi < 1$ small wavenumbers are stabilized rather than destabilized compared to $\chi = 0$. The equilibrium solutions for these cases of Model C also show the opposite trend to Model A and B, with the maximum concentration increasing rather than decreasing as $\chi < 1$ is increased from zero. It is this difference at equilibrium that causes the stabilization effect due to increased (rather than decreased, in Models A and B) fluid damping at the upper surface. This is shown for Model A and Model C, Case I in Figure 3.22.

Stability results for Models A and B for strong phototaxis, χ large, and strong gyrotaxis, η large, are qualitatively similar, although Model B is slightly more stable than Model A. The only qualitative difference between these two models is the double minima appearing for large d and $\chi < 1$ in Model B, but not in Model A, shown in Figure 3.23. Model C, Case I also follows the same trends as Models A and B as χ is increased beyond $\chi = 1$ for a set ζ , although a larger value of χ is needed to stabilize all wavenumbers. This is because both $\chi > 1$ and ζ sufficiently large are needed to make the light intensity and phototaxis torque sufficiently strong enough for the cells to exhibit negative phototaxis.

Surprisingly, Case II of Model C, where the new phototaxis torque depends on the gradient of light intensity, produces very different stability results to all the other models when $\chi > 1$. For a range of values $\zeta > 0$ and $\chi > 1$, and in the absence of any fluid flow, non-hydrodynamic modes are found. The mechanism leading to non-hydrodynamic mode in this model only is presented in Section 3.11. For sufficiently large χ or ζ , hydrodynamic

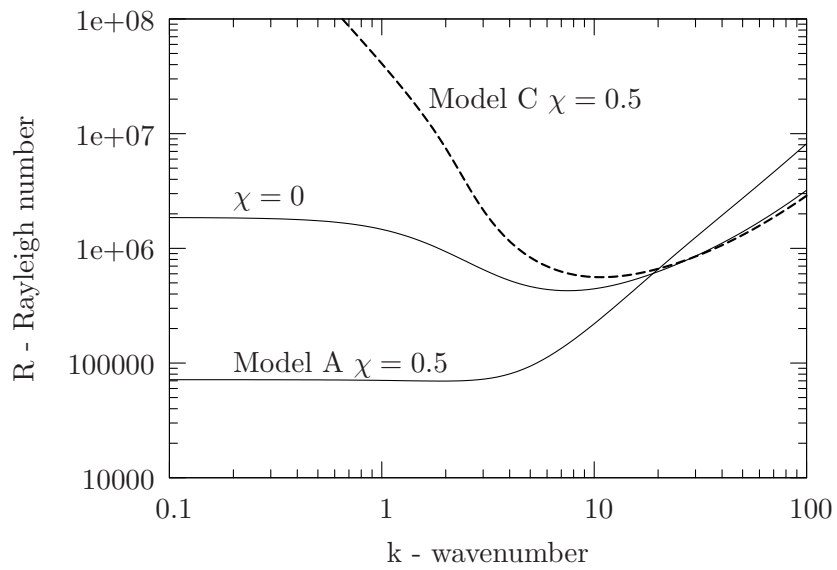


Figure 3.22: A comparison of curves of neutral stability for Model A (solid lines) and Model C, Case I (dashed lines), where $d = 20$, $\kappa = 1.2$ and $\chi = 0$ or $\chi = 0.5$, with $\zeta = 0.236$ in Model C, Case I.

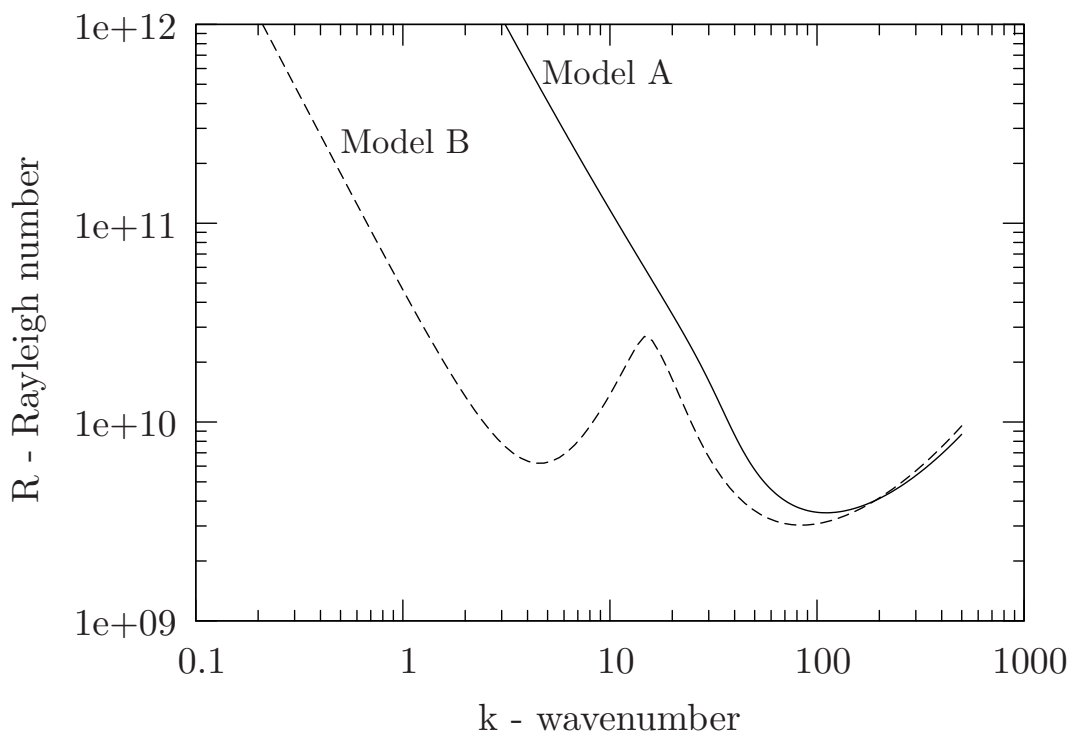


Figure 3.23: A comparison of curves of neutral stability for Model A (solid lines) and Model B (dashed lines), where $d = 200$, $\kappa = 1.2$, $\chi = 32d^{-1}$, and $d^2\eta = 8$

modes can still be found, and these follow the same general trends as in the previous models. If they occur concurrently with non-hydrodynamic modes, the mode with the highest growth rate will be the most unstable, and once ζ or χ is very large the non-hydrodynamic modes are stabilized and the hydrodynamic modes are, again, the most unstable.

3.11 Discussion

In this chapter, Model B, in which the cell either responds to light by acting as though the centre of mass offset varies, and Model C, in which a new torque due to phototaxis is introduced in the torque balance equation, have been explored. Unlike in Model A, the effects of phototaxis in these models are present in the expression for $\dot{\mathbf{p}}$, which introduces new terms dependent on light into the solution of the Fokker-Planck. For both models, the Fokker-Planck equation was solved and the light dependent expressions for $\langle \mathbf{p} \rangle$ and \mathbf{D} were calculated. Following the analysis detailed in Chapter 2, equilibrium solutions were found and perturbed and a linear stability analysis was performed, separately for each model. An analytical equilibrium solution and asymptotic linear analysis for a deep layer were calculated for Model B only. Stability was then assessed numerically for each model. Comparisons are made between models in Section 3.10. Here, any stability trends that were not found in Chapter 2 are explained and model comparisons are further discussed.

For Model B, the trends in equilibrium solution and neutral stability curves as the gyrotaxis parameter, η , and the phototaxis parameter, χ , vary are qualitatively very similar to those found for Model A. As such, the explanations for the trends in critical Rayleigh number and critical wavenumber as χ and η vary, and the explanation of the mechanisms for the overstabilities, discussed in Chapter 2, hold here too. In Model A, cell swimming speed $V_s(I)$ is a function of light intensity, so that if χ is small, cells swim slower than if $\chi = 0$. In Model B, the centre of mass offset, $h(I)$, varies with light intensity, so cells swim less gyrotactically and more stochastically when χ is small compared to when $\chi = 0$. Both result in slightly reduced upwards swimming (negative gravitaxis) and similar equilibrium and stability results for small χ . When $I \approx I_c$, $V_s \approx 0$ in Model A and $h(I) \approx 0$ in Model B, indicating that the cells swim mainly stochastically, with no preferred direction, so $\langle \mathbf{p} \rangle \approx \mathbf{0}$. Thus as I approaches I_c , $V_s(I)$ and $\langle \mathbf{p} \rangle$ approach zero in Models A and B, respectively, and the cell swimming term in the cell conservation equation for both models

also tends to zero. Therefore, $V_s(I)$ and $h(I)$ act in similar ways in Models A and B, and it is not surprising that the models give similar results. The main difference between the models equations for Models A and B is the formulation of the diffusion tensor, which is dependent on light intensity in Model B and not in Model A.

The only qualitative difference between Model A and Model B is the emergence of a second minimum appearing on the neutral curve for small wavenumbers when d is large and χ small in Model B, shown in Figure 3.23. We hypothesize that this is due to the separation of the instabilities caused by phototaxis and gyrotaxis, where the minimum found at small wavenumbers is caused by phototaxis.

In Model C, a new torque due to phototaxis is included in the torque balance equation and two different forms of the torque are explored. In Case I, we consider light from above, where $\boldsymbol{\pi} = \mathbf{k}$, and gradients in light intensity are neglected (by setting $\beta_2 = 0$ in equation 3.191). Thus the torque due to phototaxis is given by $\mathbf{L}_p = f(I)(\mathbf{p} \wedge \mathbf{k})$, where $f(I)$ is a function that determines the strength of the torque. We could write $f(I) = -\chi I$, in which case this version of Model C is the same as Model B, but instead the phototaxis torque is chosen so that it can exist and be consistent even without gyrotaxis. Thus, we define $f(I) = -\zeta\chi(\chi I - 1)$, which is zero both at $I = 0$ and $I = I_c$, so that in the dark and at the desired light intensity, I_c , there is no phototaxis. In both models, the gravitaxis and phototaxis torques are combined, and the function $g(I)$ multiplies the new gravi-phototaxis torque. We set ζ so that the gradients of the function $g(I) = 1 - \chi I$ in Model B and $g(I) = 1 - \zeta\chi(\chi I - 1)$ at $g(I) = 0$ are the same for both models ($\zeta = 0.236$). In Model C (Case I), when $0 \leq \chi < 1$ for $\zeta = 0.236$, $g(I)$ is greater than one for some I , whereas in Model B, $g(I) \leq 1$ for all I . This effectively means that the gravitaxis, or upwards swimming, increases in Model C when $0 < \chi \leq 1$ compared to $\chi = 0$. This causes the equilibrium solutions in this case to have a higher maximum at $z = 0$ for $\chi < 1$ compared to $\chi = 0$, which is the opposite to the trend for Models A and B. The increased maximum concentration at the rigid upper boundary permits less fluid flow associated with any emergent overturning instability (compared to cases where the cells are further spread away from the boundary) and, hence, the system is stabilized when $\chi < 1$. This stabilization is the opposite to the destabilization for $\chi < 1$ found in Models A and B, where a greater spread of cells away from the boundary permitted greater fluid flow associated with overturning, and is the only qualitative difference between those models and Model C, Case I when $\boldsymbol{\pi} = \mathbf{k}$.

If χ is increased above $\chi = 1.0$, the maximum of the equilibrium profile decreases and the system is initially destabilized as the greater spread of cells away from the boundary permits greater fluid flow associated with overturning. This trend was found for increasing χ from zero in Models A and B. In Model C, when the light is bright, large χ , and the torque strong, large $\zeta\chi$, cells near the light source receive too much light and swim downwards. This results in stabilization of all wavenumbers when $\chi > 2.5$. Small wavenumbers are stabilized more than large wavenumbers, resulting in a non-zero critical wavenumber that increases as a function of χ (as described in Section 2.6 for Model A, and also found for Model B). For $\zeta = 0.236$ in Model C, larger values of χ are required for this stabilization compared to Models A and B because both a strong phototactic torque, $\zeta\chi$ large, and bright light, $\chi > 1$, are necessary to move the maximum of the equilibrium profile away from the upper boundary. The effects of illumination in other orientations, such as from the side, have not been considered, but could be investigated using a different form of $\boldsymbol{\pi}$. Interesting instabilities may arise as the cells try to swim towards or away from light at various angles.

Model C, Case II, in which the torque due to phototaxis is dependent on the gradient of light intensity, $\mathbf{L}_p = f(I)(\mathbf{p} \wedge \nabla I)$, produces significantly different results to the previous models. Although equilibrium solutions and associated neutral curves for small ζ or χ for Case II are similar to those found for Case I, we find the surprising result that an instability mechanism exists even in the absence of fluid flow for a range of relatively large values χ and ζ . These non-hydrodynamic modes arise due to shading within the suspension and the mechanism for the instability is as follows. After perturbation, cells in the less concentrated regions receive too much light, due to decreased shading, and swim sideways into the densely concentrated region to avoid the light. Thus the perturbation grows and an instability arises. These modes are only possible because the x and y derivatives arising from ∇I mean that cells can swim horizontally even when $U = 0$. These non-hydrodynamic modes do not exist in Models A or B, and were not found in the gravitaxis, gyrotaxis or phototaxis models of [5, 9, 22, 172]. In those models, when $U = 0$ cells are restricted to swimming purely upwards or downwards, and there is no mechanism for horizontal movement, hence no instabilities can form. The non-hydrodynamic modes may be less stable than the hydrodynamic modes (although to evaluate which is the most unstable mode under different conditions requires knowledge of the respective growth rates). Of course, in reality any aggregations of a finite size such as these will initiate fluid motions,

so that an instability may be initiated non-hydrodynamically but is likely to become a hydrodynamic instability at a later time.

In Section 3.9.2, we found that non-hydrodynamic modes do not exist when ζ is very large. To understand why this is, we examine the equilibrium solutions for large ζ . If ζ is sufficiently large and $\chi > 1$, cells far from $z = 0$ are shaded by cells above and a strong phototaxis torque will enhance the gravitaxis torque and cause these cells to swim upwards very strongly. On the other hand, the cells near $z = 0$ receive too much light and the phototactic torque works in opposition to the gravitactic torque, since negative phototaxis causes the cells swim downwards and gravitaxis causes the cells to swim upwards. These competing torques cause cells for which $I > I_c$ to swim less strongly in a preferred direction than the upwardly swimming cells for which $I < I_c$. This leads to the highly asymmetric concentration distributions that are relatively flat above the maximum of $n(z)$ and sharp below $n(z)$ (seen for $\zeta = 6$ in Figure 3.13). When the phototaxis torque is very strong ($\zeta \geq 9$), the two opposing gravitactic and phototactic torques begin to cancel each other out, so that the cells become ‘indecisive’ and do not swim in any particular direction. Hence, the equilibrium concentration distribution becomes almost uniform for large ζ . In this case, there is no significant unstable density gradient so any perturbation will have very little effect and, in the absence of fluid flow, no instabilities form. Thus we conclude that non-hydrodynamic modes do not exist for large ζ . Furthermore, this indicates that gyrotaxis is the dominant mechanism responsible for the hydrodynamic modes found for large ζ in Figure 3.14, since the gyrotactic instability for bottom heavy cells requires only fluid shear and can occur even when there is not a significant density gradient.

One significant assumption of all three models is that all cells are effectively the same, exhibiting the same swimming speed and critical light intensity I_c . Experimental evidence, such as that by Hill and Häder 1996 [61] and Vladimirov *et al.* 2004 [173], shows that this is not the case for a population of cells. A more realistic model may incorporate a range of values for these key model parameters, as in Bees and Hill 1998 [9] for cell swimming speed V_s . For a more accurate expression of the diffusion tensor \mathbf{D} , the generalized Taylor dispersion theory, as presented by Hill and Bees 2002 [60] for the gyrotaxis only case, could be used. However, the Fokker-Planck equation and the general Taylor dispersion theory give similar results for small flows [60].

Although the three modelling approaches have been presented here separately, it is possible that a combination of these mechanisms is employed by *C. nivalis* for photo-

taxis. The phototactic torque in Model C could potentially be determined mechanically by a change in flagella beat pattern in response to illumination [152], although explicit mechanisms for cell swimming and flagella beating are not considered in this work. We have investigated what happens when each term in the new phototaxis torque in Model C is used separately, but in reality a cell may orientate using both together. The models are consistent with the observation of Häder [52] for *Euglena gracilis* cells, which is that when light is sufficiently bright, negative phototaxis dominates negative gravitaxis, and the cells swim downwards. In Chapter 4, consideration of the issues that arise when comparing experimental and theoretical data are discussed, such as whether the equilibrium solution has time to form during experiments, and whether the effects of mixing have sufficiently subsided. Theoretical results for all three phototaxis models are then compared with experimental results for the green algae *C. nivalis*. Some reasonable agreement is found between results as light is varied, indicating that the models presented here have successfully captured some aspects of photo-gyrotactic pattern formation. It would also be interesting to compare the results from these three models with any future experimental studies of photo-gyrotactic bioconvection as and when they are published.

Chapter 4

An experimental study of the effects of light and concentration on pattern formation

Summary

In this chapter, a quantitative study of bioconvection patterns is presented. A full description of experimental procedures is followed by a discussion of the image analysis processes used to extract data. A novel automated mixing regime was used to standardize the initial distribution of cells at the start of every experiment. The effect of changes in concentration on the initial pattern wavelength λ_0 was explored using a dilution experiment. To our knowledge, this is the first study to quantitatively investigate changes in initial wavelength of bioconvection pattern as a function of light intensity, in which the effects of red light and white light from different orientations are explored. Repeatable trends were found as light intensity varied and, using simple statistical tools, we have deduced whether these trends are statistically significant. Possible explanations for the trends are presented in the discussion and, encouragingly, we find similarities when comparing the experimental results with theoretical predications in Chapter 2.

4.1 Introduction

The first observations of bioconvection patterns in suspensions of micro-organisms date back to at least 1911, when Wagner [174] observed patterns using the green algae species

Euglena viridis. Since then various studies in this area have been conducted, such as Loeffler and Mefferd 1952 [105], and Childress *et al.* [22]. Various studies by Kessler in the 1980s [81, 82, 84] explore the swimming of *Chlamydomonas nivalis*, with a particular focus on the gyrotactic behaviour of these cells. Kessler also qualitatively explored the effects of different light conditions on pattern formation in suspensions of marine green algae *Dunaliella tertiolecta* cells [81] and in suspensions of *Chloromonas rosae* cells [83].

A significant advancement in this area was made by Bees and Hill 1997 [8], who present the first controlled experiments to quantitatively catalogue aspects of bioconvective pattern formation. After mixing the culture, bioconvection patterns were recorded every 10 seconds and the final, long time pattern was also recorded (after around 5-10 minutes). Images were analysed in IDL using Fast Fourier Transforms (FFT) to produce a distribution of wavenumbers of different Fourier densities. A curve was fitted to the Fourier spectra and used to extract the most dominant wavenumber. The initial (first instability to grow) and final pattern wavelength were found as a function of cell concentration and depth and the initial wavelength was compared to model predictions by Bees and Hill [9]. In 2000, Czirók *et al.* [26] used these techniques to explore trends in initial wavelength as a function of depth and concentration in the bacterium *Bacillus subtilis*, using a different fitting function to the Fourier Spectra. These techniques were also used by Pons *et al.* 2002 [138], while studying chemoconvection pattern formation in the Methylene-Blue-Glucose system.

The aim of this investigation is to experimentally analyse the effects of concentration and light on the initial wavelength of the instability formed during pattern formation in a repeatable and rational manner, using the image analysis techniques of Bees and Hill [8] and Czirók *et al.* [26]. This is the first quantitative study on the effect of light on bioconvection patterns. The initial instability that forms before any higher order, non-linear effects occur is of particular interest as this is the only wavelength that can be compared with those predicted by the linear analysis in Chapters 2 and 3. A novel, automated method of mixing was designed in an attempt to decrease the effects of variable mixing that can occur between experiments when performed by hand. This is the first study of its kind to repeat experimental runs, using the same cells, in order to give statistical measures of the standard deviation and standard error of the mean for cells under the same experimental parameters. Crucially, this allowed us to assess whether changes in average initial wavelength as the control parameters varied were statistically significant. Additionally, each experiment was also repeated using different cells to assess whether the

trend was repeatable. This study thus presents improved methods for the quantification of aspects of bioconvection patterns. We then use these methods to investigate previously unexplored changes in bioconvection patterns as light conditions and concentration are varied.

In this chapter, we first give a detailed discussion of the materials and methods used in the experiments. A brief description of the image analysis techniques employed to extract the initial wavelength follows. Experimental results for the effects of varying concentration, light intensity and the position of the light source (whether lit from above or below) for white and red light are then presented, and simple statistical methods are used to analyse these results. For each experiment, the results section concludes with a discussion of the trends found, where hypotheses to explain the observed data are presented. Experimental results are then compared with model predictions from the combined photo-gyrotactic linear bioconvection models presented in Chapters 2 and 3. Estimates of the critical light intensity, I_c , are calculated. The chapter concludes with a summary of results and a general discussion of the work, in which the difficulties in comparing theoretical and model predictions are laid out

4.2 Materials and Methods

4.2.1 Cell Culture

For all the experiments described the motile green alga species *Chlamydomonas nivalis*, strain CCAP 11/51B (recently renamed *Chlamydomonas augustae*), supplied by Sciento, Manchester was used. The algae were suspended in Bold's Basal Medium (BBM) following work by Bees and Hill [8]. Other media, such as TAP (Tri-acetate-phosphorus), could have been used, but we choose BBM since it is easy to produce in the laboratory and provides the necessary nutrients for cellular growth and motility. The cultures of alga cells were stored in either 500 millilitre or 1 litre conical flasks, which were used because the long neck of the flask is useful in concentrating the cells for experimental use. The cultures were sealed with a cotton wool bung inserted in the neck of the flask, which was then covered in tin foil, to avoid contamination while allowing gas exchange. Since these cells are photosynthetic it was necessary to illuminate the cultures, which was done by lighting cultures from above using three strip florescent lights with an intensity of 1900 lux measured just above the flasks of culture. The cells have a 24 hour cycle in which they swim, grow and divide [166].

To control the culture in order to capture the cells swimming at a reasonable time of day, the lights were set on a timer of 16:8 hours on:off.

Each culture was sub-cultured every four weeks to ensure a young, motile and healthy supply of cells. This was the optimal time to allow the cells to divide sufficiently to become concentrated enough for sub-culture. During sub-culture flasks of media were made using the BBM recipe and were then autoclaved at 126⁰C for twenty minutes. Once the new media had cooled sufficiently, one flask of the existing culture was mixed with one flask of the new media over a heat source using a sterile technique.

4.2.2 Concentrating cells

To observe well-defined bioconvection patterns it is desirable to have a sufficiently concentrated suspension of cells. Cultures aged between 2 and 4 weeks (since sub-culture) were used for experimentation. Since *C. nivalis* are negatively gravitactic, and hence swim upwards on average, they can concentrate at the top of a fluid layer using the following procedure. To extract concentrated cells, the flask is filled to the brim with culture and a lump of sterile absorbent cotton wool is inserted in the neck of the flask. The cells swim upwards through the cotton wool and start to sink when they reach the top, but do not sink back through the cotton wool. This creates a region of concentrated cells at the top and, moreover, ensures that the collected cells are good swimmers. This system was typically left for 2-3 days before cells were harvested to ensure a high cell concentration for the experiments. The cells can dehydrate if left on the cotton wool for too long and so concentrated cells older than a week were not used.

4.2.3 Transfer of culture

To record pattern formation, the concentrated cells were extracted from the culture bottles using a pipette and placed in a round Petri dish of diameter 5.2cm. When using a new Petri dish the initial reaction of the cells is to stick to the sides of the Petri dish, which could be due to surfactant and chemicals used in the production of the dish. This would compromise our experiments since we require a culture in which all cells are swimming. To counter this problem we treated new dishes by first washing out the dish with distilled water, then with some dilute culture, before filling with a concentrated culture and leaving for around 24 hours. After this the dishes were washed out with distilled water and dilute culture and were then ready for experimental use. These dishes could then be used again

and again, so long as they were washed with distilled water and dried with lens wipes after use. Before each experimental use the dish was again washed with dilute culture.

4.2.4 Measuring depth and concentration

A standard volume of culture (6.5 mL) was used in each experiment unless otherwise stated. To find the depth of a set volume in a Petri dish we focused from the top of the layer to the bottom of the layer (using a Cole Palmer optical microscope; focus dial divided into 200 segments), keeping a record of how many focus segments were turned. The microscope was calibrated by using the same method to calculate the width of a glass slide, which was also measured using a micrometer. This gives a relation between dial segments and millimeters. Since the volume of culture was also controlled, this gave a relationship between volume and depth of suspension.

Concentration was measured using a colourimeter (WPA CO7500 colourimeter), which is a device used for measuring the amount of light of a certain wavelength that can pass through the sample compared to a reference state, termed absorbance A . In this case we always use the reference as 2 mL of Bold's Basal Medium, so that we measure the absorbance of the cells and not the medium.

To convert the measure of absorption from the colourimeter into a concentration of cells we use Beer's Law, which states that there is a linear relationship between the absorbance of a culture and the cell concentration. To find this linear relationship we calibrate the colourimeter by comparing colourimeter values with cell concentrations measured using a haemocytometer for the same suspension as the culture is diluted. Averaged results, for 5 readings of the haemocytometer and the colourimeter, are plotted in Figure 4.1. We found that for large cell concentrations the curve looked non-linear. This may be because of increased light scattering for high concentrations. We can avoid the problem of the non-linear relationship by discounting any measurements above 0.8, where the trend starts to look non-linear, and ensuring that the measurements we take are always within the accepted linear range of our colourimeter, if necessary by dilution. The calibration curve is shown in Figure 4.1, with standard error of the mean for the colourimeter shown as error bars. The standard error for the haemocytometer was small (not shown).

On fitting a linear curve to the data in Figure 4.1 we find the relationship between the absorbance from the colourimeter A and the concentration (in cells per cm^3 of suspension)

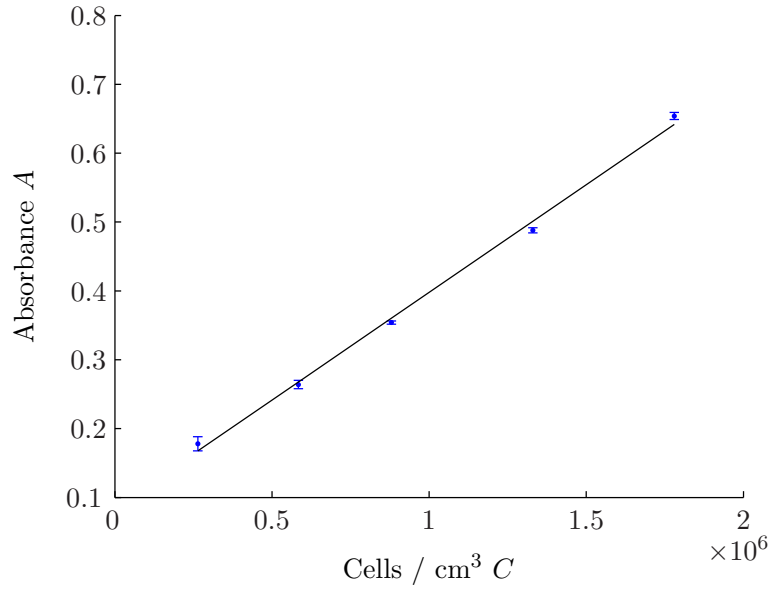


Figure 4.1: Calibrating the absorbance measurement, A , from the colourimeter with cell concentration, C , found using a haemocytometer to count cells.

obtained from the haemocytometer, denoted C , as

$$C = (3.187A - 0.2678) \times 10^6. \quad (4.1)$$

To take the colourimeter measurement we mixed the suspension thoroughly and extracted a 0.5ml sample. This was then diluted with 1.5 mL of Bold's Basal Medium (or diluted more, for higher concentrations), to give a reading that would be in the acceptable linear range of the colourimeter. The sample was shaken well and the reading taken, ensuring the beam was passed through the optically clear side of the cuvette. This process was repeated 5 times and the averaged measure of absorbance was then converted to a concentration of cells using equation 4.1. The concentration measurement had to be taken after the experiment had finished and after the depth has already been measured since the measurement requires culture to be removed from the suspension and not returned.

4.2.5 Culture mixing

For quantitative studies of bioconvection patterns, a uniform distribution of cells in the Petri dish is required at the start of the experiment, so that any pattern that forms will do so from a standardized initial condition. In practise this is difficult to achieve, since residual motions from mixing the cells are generally still present when pattern formation

begins. This can create regions of varying cell concentration or velocity gradients, which will likely affect the wavenumber of the initial pattern, k_0 . These effects from mixing, therefore, create problems when trying to study changes in wavenumber as we vary a parameter, since if mixing is not performed consistently in each case then it is hard to distinguish whether changes in wavenumber are due to changes in parameter values or to different initial distributions.

In previous studies, such as Bees and Hill 1997 [8] and Czirók *et al.* 2000 [26], cultures were mixed by hand and a set mixing routine was used every time. However, there is an element of human error involved in this method, since it is practically difficult to mix in exactly the same way in every case, causing a non-uniform distribution of cells that varies between experiments. This is demonstrated in Bees and Hill [8] in Figure 8, where the initial pattern wavenumber for the same cells under the same conditions varied due to different initial conditions following mixing.

In this study we have designed and implemented an automated mixing device to standardize mixing between experimental runs. This can be seen in Figures 4.3 and 4.4 for light from below and light from above, respectively. It consists of a Vortex mixer (Jencons PLS VX100) plus a flat head attachment with the culture in the Petri dish positioned on a light box (for light from below) or on a board (for light from above) on top of the mixer. The vortex mixer works by running an electric motor, which causes the flat head attachment to oscillate rapidly in a circular motion, creating a rotation in the culture that mixes the cells. We found that an initial thorough mixing followed by a rest period and then another brief mixing was the best way to create a mixed suspension in which the effects of mixing had sufficiently died away before pattern formation had begun. The parameters for this process were investigated to find the optimal mixing regime and are discussed in section 4.4.1. The time at which to begin image capture requires a balance between allowing long enough so that residual fluid motions have died down and not allowing so long that the first traces of pattern formation are missed. This is essential since during image analysis image sets are cleaned by subtracting the first image off the remaining images. Details of the location of the mixing device and its specific role in different situations are discussed below.

This is the first automated and controlled mixing system, to our knowledge, that has been used in bioconvection experiments. It ensures that even if fluid motions are still present in the early stages of pattern formation they are at least consistent every time

the experiment is run, allowing changes in the wavelength to be attributed to culture parameters and not different initial conditions due to mixing in each case.

4.2.6 Calibration of the light source

The lighting for the experiment consisted of either a red or white uniform, diffuse LED array (Advanced Illumination) controlled via a PC. Square lights were used where the intensity of the lights on each edge of the square could be separately controlled by specifying a percentage of the full capacity. Here, the light from each direction was always set to the same percentage, giving uniform light over the surface. To convert these intensity measurements into dimensional units (in lux, which is lumen per meter square) we measure the light at each intensity setting at the surface of the light using a light meter, ensuring that there is no contamination by restricting all other light sources in the room. This calibration is shown in Figure 4.2.

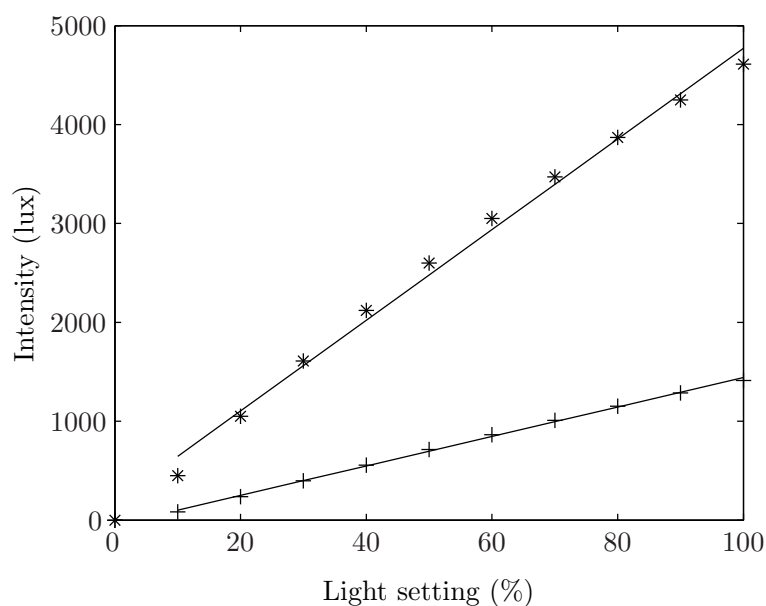


Figure 4.2: Light calibration curves for the red (crosses) and white (stars) light. The relationship between light setting and light intensity I in lux is linear and curves have been fitted to the data. The point $(0, 0)$ is not included in the fit so that the mid-range behaviour, at which the experiments are performed, is captured better.

The conversion is linear and so here we have fitted a line to each data set to give the

conversion equations as

$$I_R = 14.9P - 47.9 \quad (4.2)$$

$$I_W = 45.8P + 186.7 \quad (4.3)$$

where P is the percentage light, I_R and I_W are the light intensities in units of lux for the red and white light, respectively. The point $(0,0)$ is not included in the fit in order to better capture the mid-range behaviour, which the region we are particularly interested in. It is clear that for the two different lights the ranges of dimensional light intensities are not the same. Light intensities are given from here on as those calculated from the linear fit.

4.2.7 Image Capture

The formation of bioconvection patterns during the experiments was recorded using a black and white digital camera (Camtek BW CCD camera) attached to a PC. The experiment and the adjoining computer were located on different work benches to prevent any vibrations from the computer having an effect on the pattern formation. An image capture program, written in C++, was used in which the frequency of image capture and the total number of images taken could be controlled. Image capture began at a specified time after mixing ended and images were taken every 2 seconds until the maximum number of images, typically 30, was reached. The process of the mixing regime followed by image capture is referred to as an experimental run. For each parameter value, such as for every value of light intensity I , n experimental runs were performed with the same cells, with approximately 30 seconds between each run unless otherwise stated.

4.2.8 Varying concentration in the suspension

Investigations into the effect of concentration on the initial pattern wavelength were performed. In all cases depth was kept constant and a standard value of white light at 645 lux was used. Experiments were performed with both light from above and light from below. We started the experiment with the maximum concentration, C_{max} , and performed n experimental runs. A controlled dilute was obtained by replacing 2 mL of culture in the Petri dish with 2 mL of fresh Bold's basal medium, at equilibrated temperature. This was done without moving the Petri dish from its position on the light box, so that positioning and mixing conditions were identical for each concentration. The culture was thoroughly

mixed and left on the light box to re-adjust for 10 minutes before the culture was mixed and the experimental runs re-started. This procedure was repeated, with 2 mL replaced every time, until pattern formation was significantly weaker and the experiment came to an end. Typically 4 or 5 dilutions were required. For each concentration $n = 8$ experimental runs were performed and the complete dilution experiment repeated up to three times in the same way, although the initial concentration in each complete experiment varied due to availability of cells.

4.2.9 Controlling illumination

In this study, we investigate the effects of light when the culture is illuminated from either above or below, which require different experimental set-ups. During all experiments all other lights in the room were turned off and the brightness of the computer monitors dimmed and directed away from the experiment. The lab has no windows so daylight had no effect on the experiment.

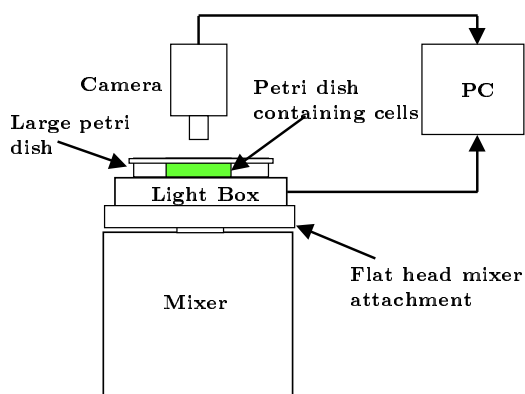


Figure 4.3: A schematic diagram of the experimental set-up for illuminating the culture from below. The suspension, in small Petri dish, is enclosed in a large, lidded Petri dish and attached to the light box. The light box is attached to the vortex mixer via a flat plate attachment and images are recorded with the camera from above. The camera and the light box are controlled via a PC.

Figure 4.3 shows the apparatus when investigating light from below. The dish of culture is placed in a large Petri dish, for stability, and is fixed in place so that images for each run are taken of the same region of the dish. A lid is put on the large Petri dish, enclosing the cells and reducing contamination. This also limits evaporation. The large dish is positioned in the centre of the light box (white or red) and fixed in place. The

light box is in turn attached to the vortex mixer. A spirit level was used to check that the culture was level to avoid any effects of varying depth across the dish. The camera, mounted on a tripod, was positioned above the dish and the focus and aperture were adjusted to give the full range of grey scales in the images. The camera was zoomed in to minimize the effect of the edges of the dish on the image analysis. The camera level was checked using a spirit level. During each experimental run, and between runs, the system was sealed in this way and the only input was using the vortex mixer to mix the suspension and setting the light intensity using the remote controls on the PC.

Figure 4.4 shows the set-up for illumination from above. This requires a significantly different set-up to light from below, where the position of the light and the camera are adjusted as described below. A wooden plank with a Petri dish-sized hole was employed. The dish of cells was inserted directly into this hole and the light was strapped to the plank above the dish to provide illumination from above. The plank was then attached to the mixer, and counterweights were used to balance the plank and make the culture level. This arrangement was necessary due to the space required to image the system from below. To complete the apparatus, the camera was inverted and positioned below the Petri dish.

4.2.10 Statistical Analysis

In order to analyse trends in pattern formation as light conditions and concentration change, we perform some simple statistical tests on the data for the initial wavenumber of the bioconvection pattern. Where appropriate a linear regression analysis was performed (Sigma Plot 8.0) on all data points from each experimental run, not just the averaged wavelength. Correlation coefficients were found and T-tests performed to analyse the probability of incorrectly concluding the existence of an association between the dependent and independent variables. Unpaired T-tests were also used, to see if differences in mean wavelength for different parameters were significant.

4.3 Image Analysis

Each experimental image consists of 768 by 596 pixels. To extract the dominant wavelength in each of the recorded images we follow the analysis of Bees and Hill [9] and Czirók *et al.* [26]. We used the graphics package IDL (version 7.0) to perform the image analysis,

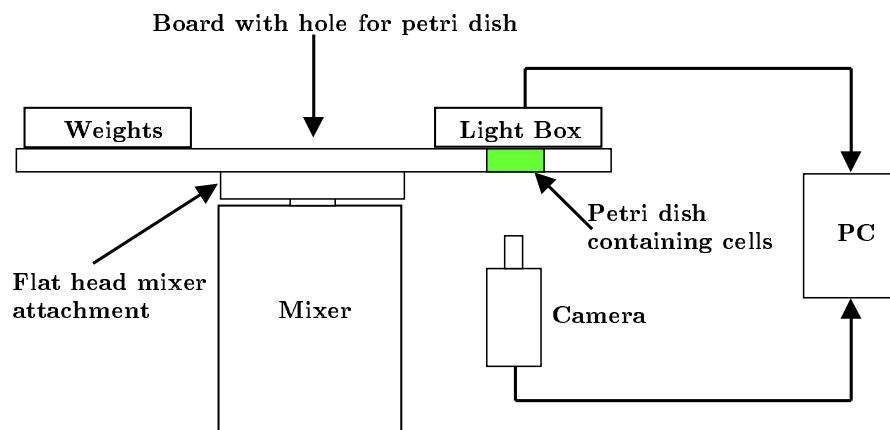


Figure 4.4: A schematic diagram of the experimental set-up for illuminating the culture from above. The suspension, in a small Petri dish, fits snugly into a hole cut in a wooden board. The light is fastened to the board above the dish of cells and the board is balanced on the flat plate attachment of the vortex mixer by using weights to match the light on the other end. The camera is inverted and placed under the dish of cells, so that patterns are recorded from below.

which involves extracting the dominant wavenumber using Fourier transforms. Initially the images contain unwanted information, such as the walls of the dish (in some cases), any imperfections on the surface or lid of the dish, effects of uneven light distribution (although the light source was uniform, there may be effects from other light sources) and the boundary of the image. Subtraction of the first image (taken once the effects of mixing have died away) from every subsequent image eliminates the effects of the first three issues here, and the effect of the boundary of the image can be dealt with by using a smoothing windowing function, as discussed below. A central region sized 512×512 pixels was cut from each image, to create square images for the Fourier transformation. Figure 4.5 (a) shows an example of a bioconvection image for a culture lit from above with white light and Figure 4.5 (b) shows the effect of subtracting the first image. Dark regions indicate high cell concentration.

4.3.1 Fourier transformation

Following the procedure of Bees and Hill 1997 [8], we performed the Fast-Fourier Transform (FFT) algorithm developed by Cooley and Tukey 1965 [24] on the cropped images. Details

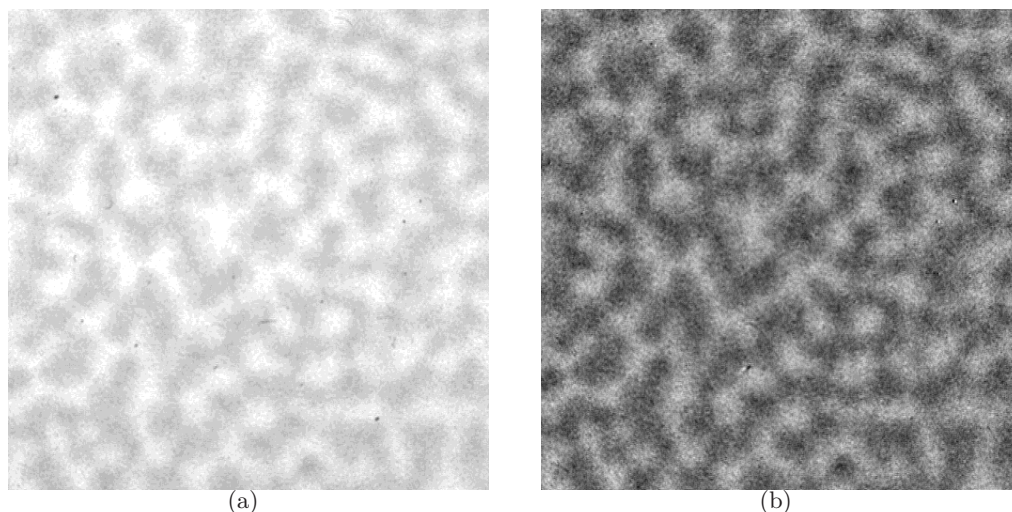


Figure 4.5: A sample bioconvection image in Figure (a) where the culture is illuminated from above with white light, and the same image again in Figure (b) where the first image was subtracted, to reduce the effects of the background, and the image re-scaled. Subtracting the background removes the uneven distribution of light and removes the impurities from the original image, as shown. Dark regions indicate high cell concentration.

of the FFT algorithm can be found in Press *et al.* 1992 [140]. As in Bees and Hill [8], we conclude that the resolution of the image is high enough to use this method, as we have 512×512 pixels and a maximum of approximately 60 wavelengths per picture, giving around 8 pixels per oscillation and, hence, satisfying the Nyquist condition of 2 pixels per oscillation. We use a Hahn windowing function (as in [8] and [26]) to eliminate the effects of the sharp edges of the image [140]. This function has a maximum at the centre of the image and zero at the edges. It weights the information in the centre of the image so that it is more important than information at the edge and enforces periodic smoothing at the boundaries to create a smooth oscillating sequence of the image where the edges join in a continuous fashion. It also removes oscillatory errors from the Fourier spectrum. This windowing is done before the FFT and the Hahn window is given by

$$W_H(x, y) = \frac{1}{4} \left(1 - \cos \frac{2\pi x}{N} \right) \left(1 - \cos \frac{2\pi y}{N} \right), \quad (4.4)$$

where the image is of size $N \times N$.

The Fast Fourier Transform (FFT) takes the real, two-dimensional image array and returns a complex array of the same size. In Fourier space there are various data spread around the origin and it is the distance of these data from the origin that indicate the wavenumber (number of waves in 512 pixels). Furthermore, the position of the data

indicates the direction of the wave, and phase information is also available. We use the data to plot a bar chart for every image, and it is from this that the dominant wavenumber is calculated

4.3.2 Dominant wavenumber extraction

Following the work of Bees and Hill [8], we want to extract the dominant (largest) wavenumber from each image. Bees and Hill [8] fitted an unnormalized double Gaussian distribution to the resulting bar chart from the Fourier spectra with the idea that one Gaussian would fit the noise and the less unstable wavenumbers and another would fit the dominant most unstable wavenumber. They used a least-squares algorithm to fit the double Gaussian to the wavenumber data. Czirók *et al.*, [26] on the other hand, found the spectra had a pronounced tent shape when using a double logarithmic plot of $I(k)$ (Fourier intensity) versus k , which indicates power-law decay for both small and large wavenumbers. This leads them to extract the dominant wavenumber using the fitting function

$$\ln[I(k)] = \alpha |\ln(k) - \ln(k_0)| - \beta \ln(k) + c, \quad (4.5)$$

where k_0 is the dominant wavenumber (the peak of the fit), α and β are fitting parameters that characterize different exponents for small and large wavenumbers and c is a constant. They also note that this is equivalent to separating the logarithms and writing

$$I(k) \approx k^{-\alpha-\beta} \quad \text{when } k < k_0 \quad (4.6)$$

$$I(k) \approx k^{\alpha-\beta} \quad \text{when } k > k_0. \quad (4.7)$$

Since these functions both only provide approximate fits to the bar chart data, it was necessary to compute some analysis of error in this fitting process. We want the fitted curve to fit the general outline of the spectra, and not stipulate that the spectrum has a specified shape. We follow the work of Bees 1996 [7] where two measures of error are calculated, the sum modulus error (ϵ_m), normalized with respect to the area under the graph, and the Kolmogorov-Smirnov statistic (ϵ_{KS}), which describes variations in the trends of cumulative data and measures the cumulative error rather than the total error

sum. These are defined as

$$\epsilon_M = \frac{1}{\sum_{n=0}^{N-1} \rho_n} \sum_{n=0}^{N-1} |\rho_n - \phi(X = n)|, \quad (4.8)$$

$$\epsilon_{KS} = \frac{1}{\sum_{n=0}^{N-1} \rho_n} \max_{n=0..N-1} \sum_{j=0}^n (\rho_n - \phi(X = n)), \quad (4.9)$$

where ρ_n is the Fourier spectrum at wavenumber n and $\phi(X = n)$ is the fitting function distribution that we are using (either the double Gaussian or the double logarithmic). Large ϵ_k indicates the data is not very smooth and large ϵ_{KS} indicates the general trend of the fitting function ϕ is significantly different from the data. As in Bees [7], small values of both statistics implies the curve fit was successful, while larger values of one statistic indicates that the fit should be studied in more detail, and does not necessarily imply an inappropriate curve fit. Then again, large values for both would imply an ineffectual curve fit.

On exploring both methods, we decided to use the double logarithmic function shown in equation 4.5 as in Czirók *et al.* [26], where the constants in equation 4.5 are fitted to the wavenumber data using the least-squares algorithm. The double logarithmic function was chosen over the double Gaussian since in most cases tried it gave a better fit to the data, with smaller errors, and we found that the double Gaussian often did not converge on a fit. For example, for some images in the experiment for red light the double Gaussian did not converge and in general the ϵ_M was twice as large for the double Gaussian compared to the logarithmic function, and ϵ_{KS} was slightly smaller for the logarithmic function compared to the double Gaussian. An example of the double logarithm curve fitting is shown in Figure 4.12 for a culture lit from above with a red light. Occasionally, when the double logarithm function did not provide a close enough fit, we had to estimate the first most unstable wavenumber by hand. This happened only in a very small number of cases, and for the majority of images the double logarithmic curve seems a natural choice. Once the dominant wavenumber k had been estimated it was converted to a wavelength λ using

$$k = \frac{I_w}{\lambda}, \quad (4.10)$$

where I_w is image width in centimeters. Hence, λ has units of cm. We denote the initial wavenumber and wavelength for the pattern formation as k_0 and λ_0 , respectively. It can be difficult to deduce which image contains the initial pattern wavelength because the noise in each image increases with time as the difference between the frame and the background image that was subtracted grows. This was especially true for some white light intensities,

where it became difficult to decipher whether an increase was due to random noise or pattern formation. A consistent approach was used in these cases. Firstly, a wavenumber was only chosen as the initial wavenumber if the Fourier spectrum density was sufficiently larger than the noise, to ensure that the rise was not purely noise. The second condition was that the Fourier spectrum density at this wavenumber grew with time, which indicates the start of pattern formation. Using these image analysis techniques with the curve fitting therefore allows us to investigate changes in initial wavelength as a function of concentration and light intensity for different light positioning and wavelengths.

The time from the end of mixing to the start of pattern formation, t_0 , was also explored. This was calculated for each data set by noting the frame number at which pattern formation was deemed to begin and converting it to a time. Note that since images were taken every 2 seconds, t_0 was a multiple of two but the average t_0 over n runs was not necessarily.

4.4 Results and discussion

In this section, experimental results for the effect of concentration and light intensity on the initial pattern wavelength of bioconvection are presented. Labels RA, CA, CB, LA_{1,2,3} and LB_{1,2,3}, for the different experimental conditions are defined in Table 4.1. Tabulated wavenumbers are normalized to be wavenumbers per dish, since different image widths were used between experiments and this normalization allows wavenumbers to be directly compared. The wavelength in each experiment was calculated by dividing the image width for that experiment by the wavenumber from the Fourier analysis, as in Equation 4.10. For each experiment, the section concludes with a brief discussion of the trends found and, where possible, comparisons with other studies are made.

4.4.1 Exploring the effects of mixing on initial pattern formation

Since our mixing regime is somewhat novel in these types of bioconvection experiments, we first investigate the effects of different mixing regimes on initial pattern formation. In each case explored here, we use the lowest, least vigorous mixing setting (of 200 rpm), since this is sufficient mixing for the culture and too vigorous a mixing can damage the cells and cause the culture to spill.

An ideal mixing is one that produces thoroughly mixed suspensions in which swirling

has subsided sufficiently before pattern formation begins. For light from below we try initially mixing for some time m_1 , leaving the culture to settle for time t_1 before mixing again for time m_2 and then waiting for a time t_2 for swirling to sufficiently decrease before image capture begins. The first mixing thoroughly mixes the culture while leaving for time t_1 allows the fluid motions to subside, and then re-mixing for a short time m_2 is used to mix the cells again, but only very briefly, so that the fluid motions die away quickly.

A little experimentation revealed that $m_1 = 2$ seconds of mixing was adequate to thoroughly mix the suspension whilst minimizing swirling motion, as shown in Figure 4.6. To further optimize the mixing we experimented with different values of t_1 , t_2 and m_2 .

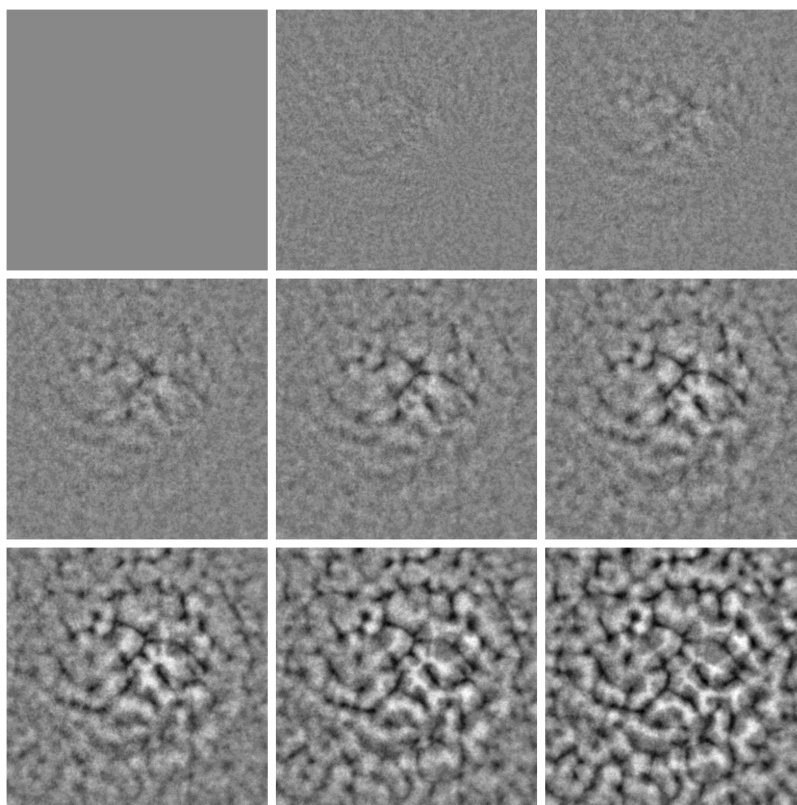


Figure 4.6: Sample bioconvection images where the culture was mixed using $m_1 = 2$, $t_1 = 10$ and $t_2 = m_2 = 0$.

A mixing was deemed acceptable if the pattern appeared to form uniformly and with minimal effects of swirling, so that the pattern appeared after the effects of mixing had subsided and did not follow streamlines. Due to the different geometry of the apparatus, the mixing motion was different when mixed from above and below and when cells were illuminated with a different light source, although mixing was also kept consistent during each experiment. The chosen mixing parameters for each experiment are summarized in

Table 4.1, where the mixing regime is given in seconds and pairs of mixing followed by waiting are shown, i.e. $(m_1, t_1), (m_2, t_2)$, where the last number in the sequence is always how long after the final mixing the image capture begins.

Experiment	Light type	Light orientation	(m_i, t_i) Pairs (seconds)
RA	Red	Above	(4,10),(2,10)
CA	White	Above	(5,2),(3,4),(2,10)*
CB	White	Below	(2,10),(1,12)
LA _{1,2,3}	White	Above	(5,2),(3,4),(2,12)
LB _{1,2,3}	White	Below	(3,10),(1,12)

Table 4.1: A summary of the different mixing methods used in the experimental results. The last column is a sequence of seconds with order mixing, waiting and is either $(m_1, t_1), (m_2, t_2)$ or $(m_1, t_1), (m_2, t_2), (m_3, t_3)$ in cases where more mixing was required. * indicates that the final waiting time was altered when necessary due to pattern formation starting earlier as parameters were varied.

We also found that on varying depth, mixing produced different circulations, which varied the wavelength of the pattern. Therefore, changes in initial wavelength could not be attributed to changes in depth alone. For deep layers, increased swirling caused pattern formation to begin before the swirling has subsided, making it hard to obtain an initial wavelength. Furthermore, if the depth was increased above 5 mm the culture spilt on mixing and images were ruined due to culture appearing on the lid of the dish. For these reasons an appropriate depth was chosen and changes in depth were not investigated. This is clearly a limitation of this mixing method.

Although this novel mixing regime certainly gives consistency, in that we see the same shape of pattern formation in each experimental run, for the same parameters, we still see some after-effects of swirling when pattern formation begins, shown by the pattern not appearing entirely uniform over the dish. Any shear created by the swirling will induce a gyrotactic effect (discussed in Chapters 2 and 3), which could affect the patterns formed. Additionally, the cells swim and focus into concentrated regions whilst the suspension is being mixed and when the flow is in the process of decaying, and this can initiate pattern formation. This is not desirable in these experiments, since if this is the case patterns do not form from equilibrium but are due to concentration variations caused by fluid flow during mixing. However the suspension is mixed there is likely to be at least some residual

fluid motion, such as in Bees and Hill [8] where mixing by hand affects the geometry of the first patterns formed and, hence, the initial wavelength. The current method has the advantage that mixing is controllable and repeatable.

4.4.2 Exploring the effects of concentration on initial pattern wavelength

In this section, the effects of varying the concentration of algae for both light from above and light from below are explored and results are summarized in Table 4.2. Figure 4.7 shows some samples of the evolution of bioconvection patterns when the cells are illuminated from above at 645 lux for different concentrations. There is a clear difference in the patterns formed: the higher concentration image has more waves per image compared to the lower concentration image, hence the initial wavelength is smaller, and earlier pattern onset is found for higher concentrations.

Experiment	I (lux)	C (cells / cm ³)	d (cm)	k_0 /dish	λ_0	S.D.	n
CA	645	8.11×10^6	0.306	28.83	0.1988	0.0185	8
CA	645	5.28×10^6	0.306	23.00	0.2336	0.0209	8
CA	645	3.33×10^6	0.306	20.73	0.2596	0.0228	8
CA	645	1.97×10^6	0.306	16.03	0.2937	0.0255	8
CB	645	6.32×10^6	0.345	33.31	0.1594	0.0341	8
CB	645	3.68×10^6	0.345	28.24	0.1893	0.0344	8
CB	645	1.98×10^6	0.345	22.87	0.2226	0.0287	8
CB	645	0.893×10^6	0.345	22.68	0.2369	0.0181	8

Table 4.2: Summary of results for the initial pattern wavelength, where cell concentration varies. White light from above was used in experiment CA and white light from below in CB. I is light intensity, C concentration, d depth, k_0 /dish the wavenumber of the initial pattern normalized over the dish diameter, λ_0 the initial wavelength, and S.D. the standard deviation calculated over n runs.

For each concentration eight independent data sets were collected and analysed and the wavelengths presented in Figures 4.8 and 4.9 are the mean wavelengths for each concentration over these 8 runs. The error bars indicate the standard error of the means. For both light from above and below, Figures 4.8 and 4.9 show that increasing concentration decreases the initial wavelength of the instability, although wavelengths between experiments cannot be directly compared as different depths were used. For light from above the

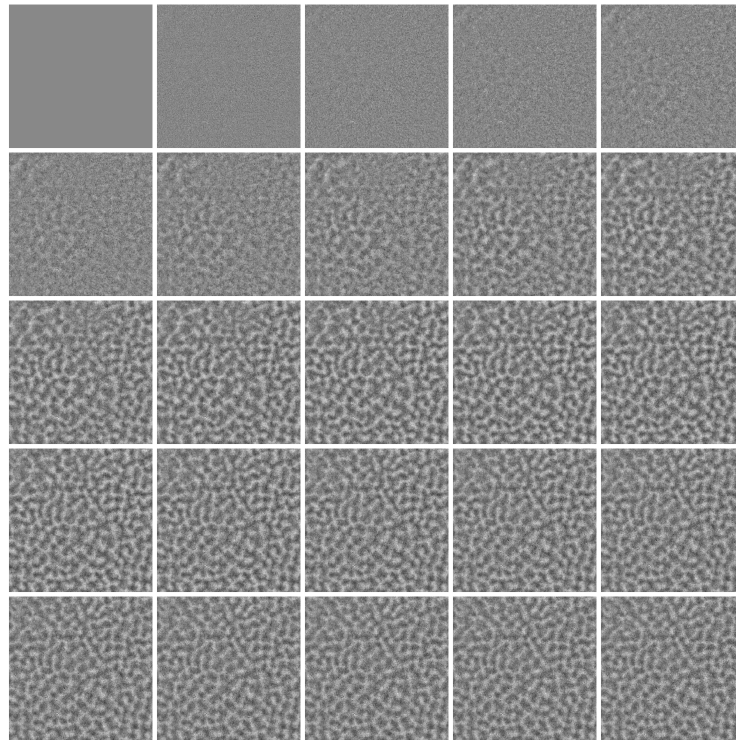
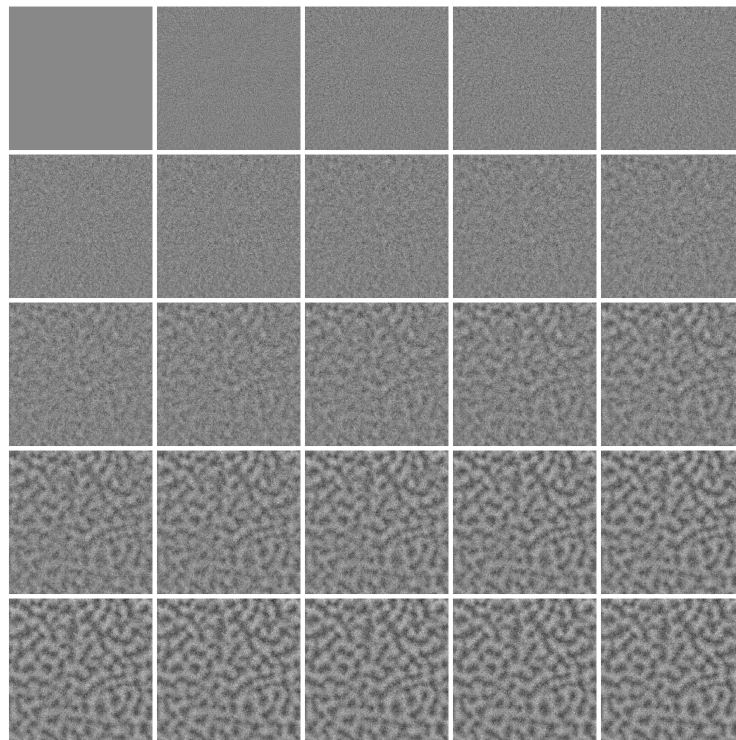
(a) $C = 8.11 \times 10^6$ cells / cm³(b) $C = 3.33 \times 10^6$ cells / cm³

Figure 4.7: Sample images from Experiment CA, with white light illumination from above, $I = 645$ lux, where $d = 0.306$ cm and $I_w = 2.47$ cm. Figure (a) shows a case where concentration $C = 8.11 \times 10^6$ cells / cm³ and Figure (b) a case where $C = 3.33 \times 10^6$ cells / cm³. Images were captured every 2 seconds, starting 10 seconds after mixing ended.

aspect ratio of wavelength to depth was approximately one for the lowest concentration. In the absence of any other indication of trend, a linear regression analysis was performed to fit a straight line to the data. The linear equations and associated correlation statistics are given by

$$\text{Experiment CA: } \lambda_0 = 0.316 - 1.48 \times 10^{-8}C, \text{ with } R = -0.849 (R^2 = 0.721), \quad (4.11)$$

$$\text{Experiment CB: } \lambda_0 = 0.246 - 1.39 \times 10^{-8}C, \text{ with } R = -0.704 (R^2 = 0.496), \quad (4.12)$$

where C is concentration in cells per cm^3 , R is the correlation coefficient. (R^2 is called the coefficient of determination.) The linear fits are shown in Figures 4.8 and 4.9. The correlations coefficients are both $R > 0.7$, but the coefficient of determination for Experiment CB is less than 0.5, indicating that the data have a relatively large spread, and that only approximately 50% of the variability of λ_0 can be explained by the concentration. Using analysis of variance and performing a T-test we found $p < 0.0001$ in both experiments. This is highly significant and indicates that it is very unlikely that there is not a correlation between the concentration and initial wavelength.

Unpaired T-tests between each consecutive concentration for both light from above and from below were performed. For light from above all the p values are small, $p < 0.05$ and give significant results, indicating that the two means compared are significantly different. However, for light from below none of the p values are significant, although some are close, indicating that we cannot conclude whether difference between the means are significant or not. However, on performing the T-tests again on the smallest and second highest concentration, and on the second smallest and the highest concentrations in Table 4.2, we find $p = 0.0038$ and $p = 0.0013$, respectively. These p values are highly significant and imply that difference in these means are unlikely to be caused by random effects. Overall, we conclude that there is negative correlation between concentration and initial pattern wavelength. The data suggest that the correlation is stronger when the culture is illuminated with light from above compared to light from below.

Discussion

Negative correlation between concentration and initial wavelength was also found by Bees and Hill 1997 [8], and on comparison we see wavelengths of a similar order, although exact comparisons are difficult due to differences in concentrations and depths between experiments. Czirók *et al.* 2000 [26] used a two-parameter linear regression on the data of

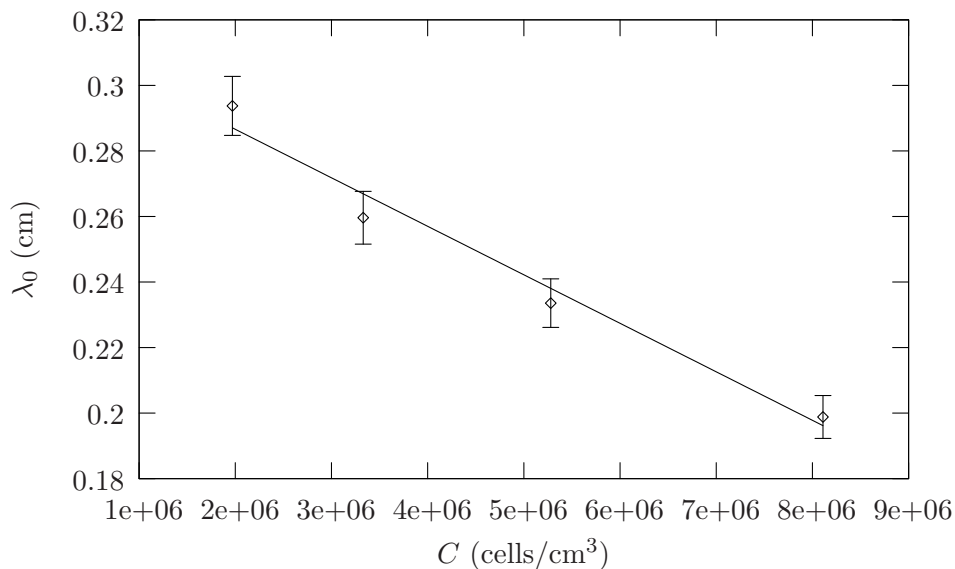


Figure 4.8: Experiment CA: The effects of concentration on dominant initial pattern wavelength for a culture illuminated from above with a white light, where $I = 645$ lux and $d = 0.306$ cm.

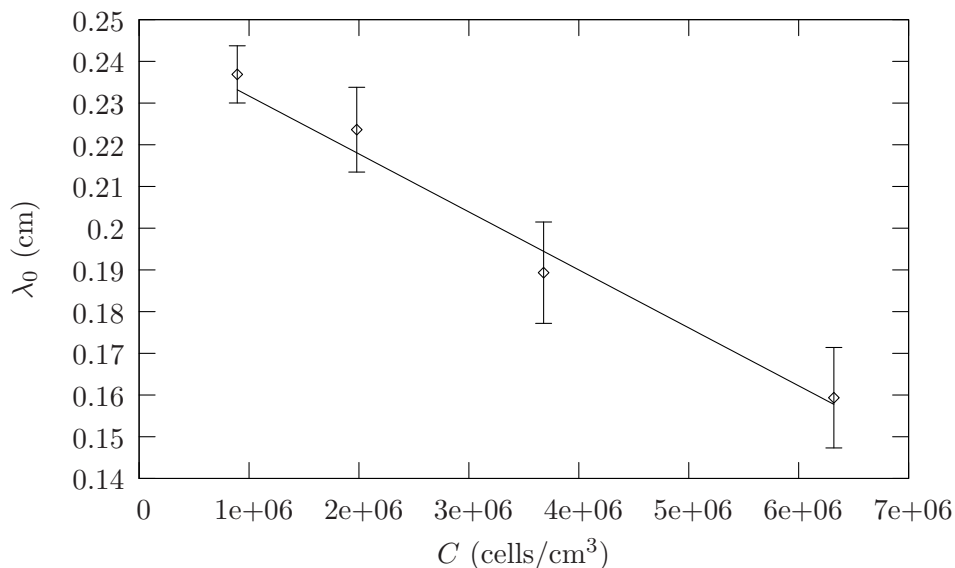


Figure 4.9: Experiment CB: The effects of concentration on dominant initial pattern wavelength for a culture illuminated from below with a white light, where $I = 645$ lux and $d = 0.345$ cm.

Bees and Hill and found that the aspect ratio of depth to wavelength, the characteristic scale of the convection cell, is approximately one as depth varies (although there is quite a large variation). In the present study, we find that for low concentrations this ratio is approximately one, but as concentration decreases the aspects ratio also decreases. Differences may arise since Bees and Hill [8] illuminated with a red light as opposed to white light. Additionally, different wavelengths may have been taken as the initial wavelength, since we captured images every 2 seconds and Bees and Hill [8] every 10 seconds. Czirák *et al.* [26] also found that increasing concentration decreases initial wavelength with cultures of *Bacillus subtilis*. For algae, we hypothesize that the decrease in wavelength that we observe for higher cell concentration occurs through increased gyrotaxis, as in Bees and Hill [8] (since when there are more cells, gyrotactic focussing increases).

4.4.3 Does red light illumination affect the initial pattern wavelength?

Chlamydomonas nivalis cells only have been measured to react to light within a certain range of wavelengths [35, 125]. Nultsch *et al.* [125] measured the action spectra for the photo response of *Chlamydomonas reinhardtii* to light of different wavelengths and found that above around 550 nm there was a considerably reduced response. These data were reproduced and expanded by Foster and Smyth in 1980 [35]. The original Nultsch *et al.* data is reproduced here in Figure 4.10. Since the wavelength of the red light used in our experiments was 660 nm it is unlikely that the cells will exhibit a significant phototactic response. To investigate, we lit the culture of cells from below with the red light and investigated changes in initial wavelength of the resulting pattern as the intensity of the red light increased from $I = 101$ lux. Results are shown in Table 4.3 and plotted in Figure 4.14, where each data point represents the mean of 8 independent measurements taken using the same cells.

An example of the resulting patterns formed under red light with $I = 101$ lux is shown in Figure 4.11, with the corresponding Fourier density against wavenumber plot in Figure 4.12. In this example we note that although the pattern does not appear everywhere in the dish at the same time, due to swirling caused by mixing, the dominant wavenumber can still be extracted, and the double log fit looks like a good fit to the Fourier spectrum data. Figure 4.13 shows a contour plot of the Fourier spectra for the development of all wavenumbers over time. The aspect ratio, of wavelength to suspension depth, was approximately two-thirds for this concentration, for all light intensities.

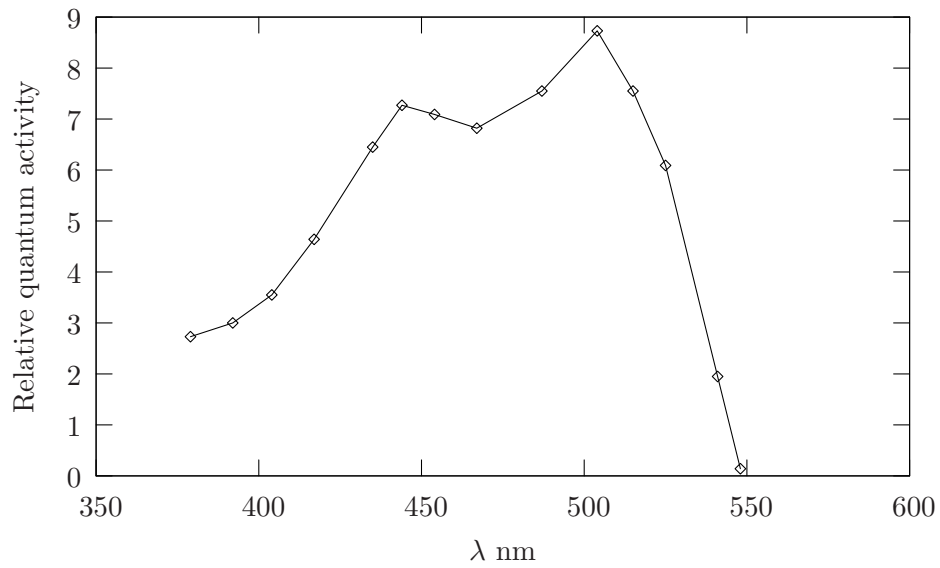


Figure 4.10: Action spectra for *C. reinhardtii* cells; the relationship between wavelength of light, λ nm, and relative response. This figure is reproduced from data in Nultsch *et al.* [125].

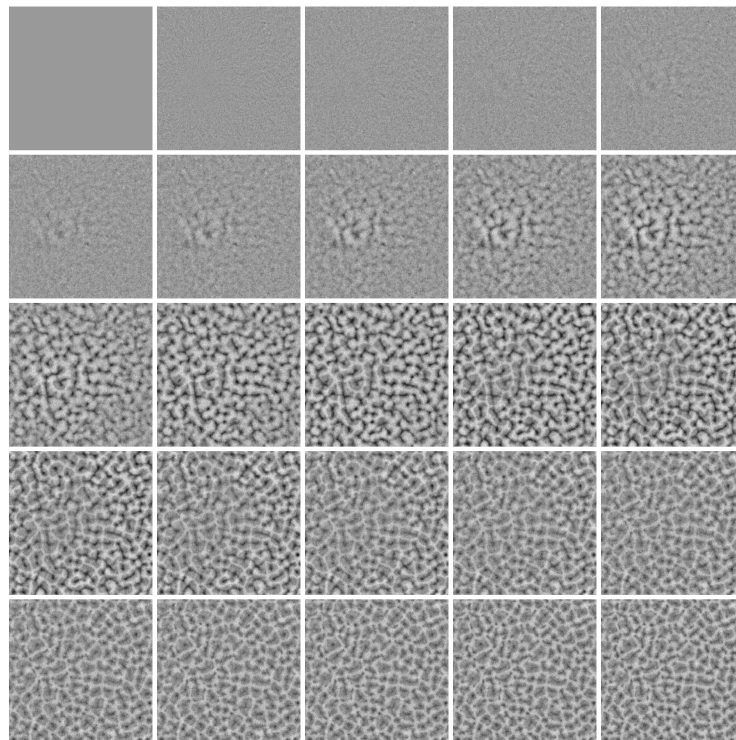


Figure 4.11: Sample images from Experiment RA, with red light illumination from above, $I = 101$ lux, where $C = 5.05 \times 10^6$ cells / cm^3 , $d = 0.306$ cm, and $I_w = 2.33$ cm. Images were captured every 2 seconds, starting 10 seconds after mixing ended.

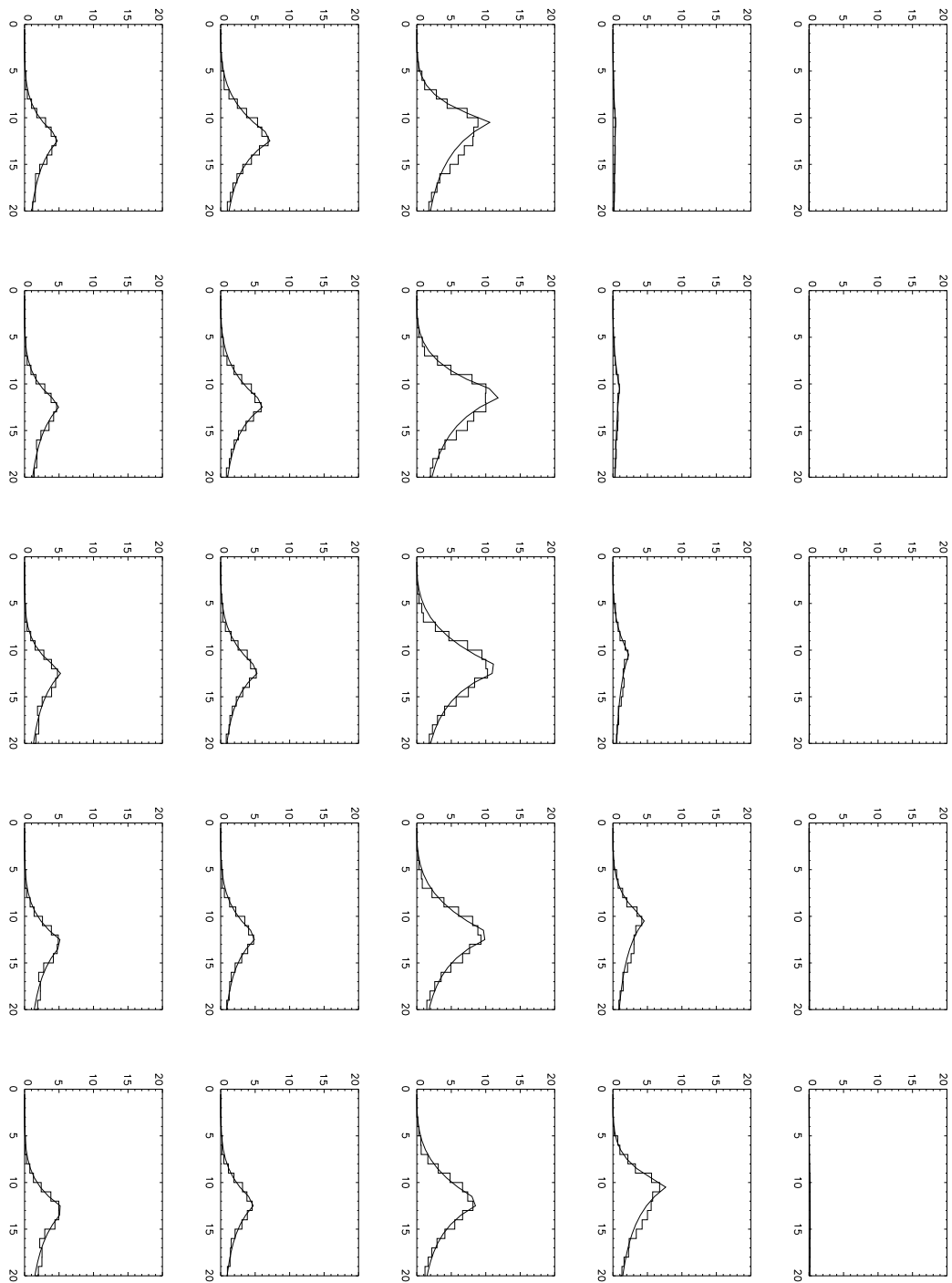


Figure 4.12: A sample set of Fourier spectra from Experiment RA, with red light illumination from above, where $I = 101$ lux, $C = 5.05 \times 10^6$ cells / cm^3 and $d = 0.306$ cm. Images were captured every 2 seconds, starting 10 seconds after mixing ended. The horizontal axis is wavenumber and the vertical axis is Fourier density, and the logarithmic function in equation 4.5 is used as the fitting function.

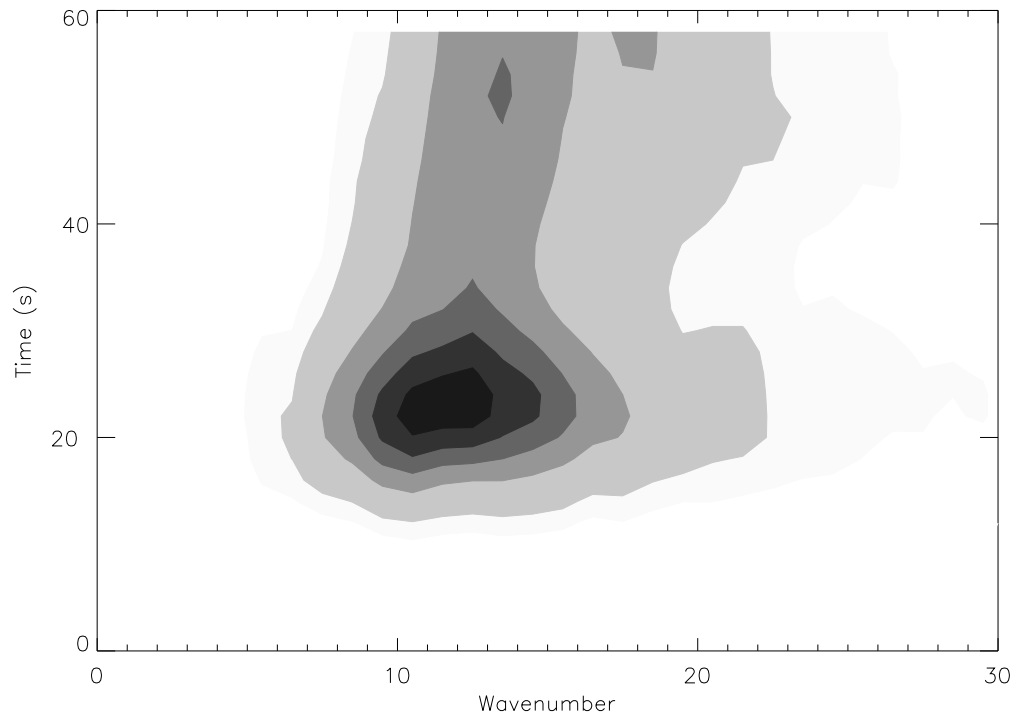


Figure 4.13: A sample contour plot from Experiment RA, with red light illumination from above, where $I = 101$ lux, $C = 5.05 \times 10^6$ cells / cm³ and $d = 0.306$ cm. Images were captured every 2 seconds, starting 10 seconds after mixing ended. Time is measured from the start of image recording, and is not the time since mixing.

Experiment	I (lux)	C (cells / cm ³)	d (cm)	k_0 / dish	λ_0 (cm)	S.D.	n
RA	101	5.05×10^6	0.306	26.26	0.1993	0.0176	8
RA	325	5.05×10^6	0.306	28.33	0.1857	0.0226	8
RA	548	5.05×10^6	0.306	27.31	0.1922	0.0208	8
RA	772	5.05×10^6	0.306	28.09	0.1866	0.0181	8
RA	995	5.05×10^6	0.306	27.61	0.1901	0.0208	8
RA	1220	5.05×10^6	0.306	28.70	0.1837	0.0235	8
RA	1440	5.05×10^6	0.306	27.32	0.1924	0.0226	8

Table 4.3: Summary of results for initial pattern wavelength when the suspension was illuminated with a red light from above. I is light intensity, C concentration, d depth, k_0 /dish the wavenumber of the initial pattern normalized over the dish diameter, λ_0 the initial wavelength, and S.D. the standard deviation calculated over n runs.

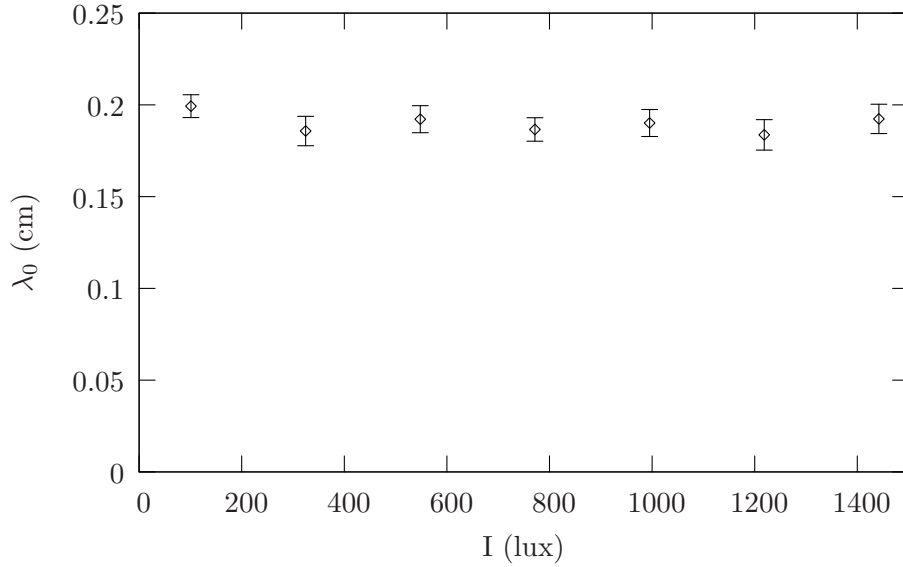


Figure 4.14: Experiment RA: The effect of red light from above on dominant initial pattern wavelength, where $d = 0.306$ cm $C = 5.05 \times 10^6$ cells / cm³. Each point represents the average of eight runs of the experiment and the error bars are the standard error of the mean.

In Figure 4.14 there is no clear trend in the wavelengths as the red light intensity changes, and the data points look to fall either side of a constant value. We use a linear regression and find a very small correlation coefficient of $R = -0.0957$ with a corresponding $R^2 = 0.009162$, implying that there is not significant correlation between the variables. The equation for the fitted line is given by

$$\lambda_0 = 0.193 - 4.33 \times 10^{-6}I, \quad (4.13)$$

where I is light intensity. The probability that we are wrong in saying that the y-intercept coefficient is not zero is very small, $p < 0.0001$, but the probability of being wrong in saying that the gradient is not zero is high, $p = 0.4828$, indicating that there is not sufficient evidence to suggest a non-zero gradient. In any case, the gradient found from the linear regression is very small. We found no significance when comparing the mean wavelength for different light intensities using sets of unpaired T-tests. From all of this information, we conclude that we have found no trend for variations in wavelength of the initial pattern with red light intensity, since the initial wavelength remained approximately the same as the intensity of red light increased between 100 and 1440 lux. We have, therefore, shown that, in terms of pattern formation at least, the cells do not exhibit a photo-response

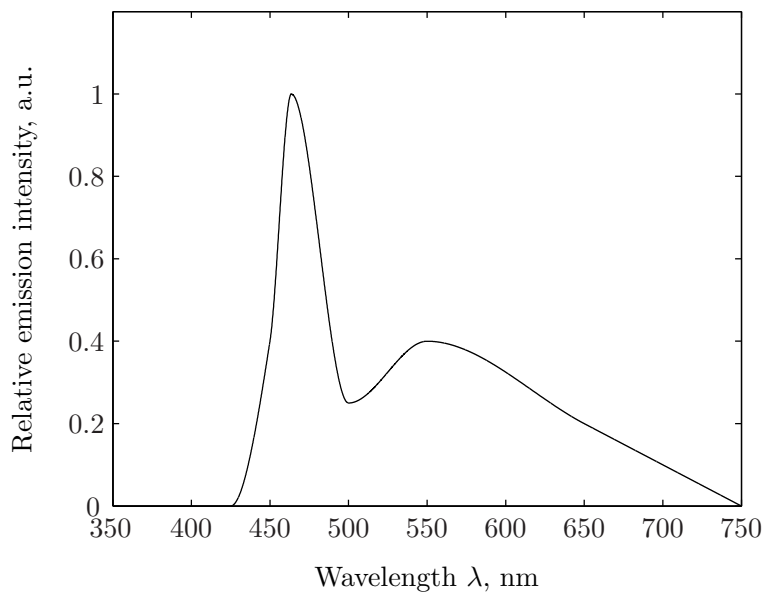


Figure 4.15: Spectrum of the white light box.

to light of wavelength 660 nm, a result which is consistent with observations in Nultsch *et al.* [125], who find a very limited photo-response to light of wavelengths greater than 550 nm. The lack of response means that illumination by red light is equivalent to no illumination, so that data for red light can be thought of as being the case $I = 0$ lux.

Discussion

The average wavelength over all intensities for the red light is $\lambda_0 = 0.19$ cm, which is of the same magnitude as similar experiments in Bees and Hill [8], although it appears to be a little smaller (Bees and Hill reported a value of 0.331 cm for a suspension of concentration $C = 3.60 \times 10^6$ and depth $d = 0.324$ cm). The aspect ratio is approximately two-thirds, and this ratio increases as concentration increases (as increasing concentration decreases initial wavelength when depth is kept constant).

4.4.4 Exploring the effects of white light illumination from below on initial pattern wavelength

The main objective of this study is to investigate the effects of white light from both above and below on the system, and this is performed in this section. The spectrum for the white light box is shown in Figure 4.15, from which is noted that the wavelengths of the light are within the range of response of the cells shown in Figure 4.10.

Using the experimental set-up described in Section 4.2.9, we study the effects of illu-

mination from below. Light intensity I was initially set at 645 lux (10 % of the maximum light intensity) and was increased in increments of 15% of the maximum. For each light intensity n repeats of the experiment were performed with the same cells and from this data the mean wavelength and standard deviation for each light intensity were calculated. n was the same throughout each experiment, but sometimes if images were not recorded properly or there was a problem with one run then this was discounted and n reduced.

Results for the mean wavelength are shown for three independent experiments, with different cells, in Figures 4.16, 4.17 and 4.18 with concentrations of $C = 5.35 \times 10^6$, $C = 5.18 \times 10^6$ and $C = 9.46 \times 10^6$, and $n = 6$, $n = 8$, and $n = 8$, respectively. We denote these experiments Experiment LB1, Experiment LB2 and Experiment LB3 and results are summarized in Table 4.4. Note that LB1 and LB2 have a similar concentration but LB3 has a higher concentration.

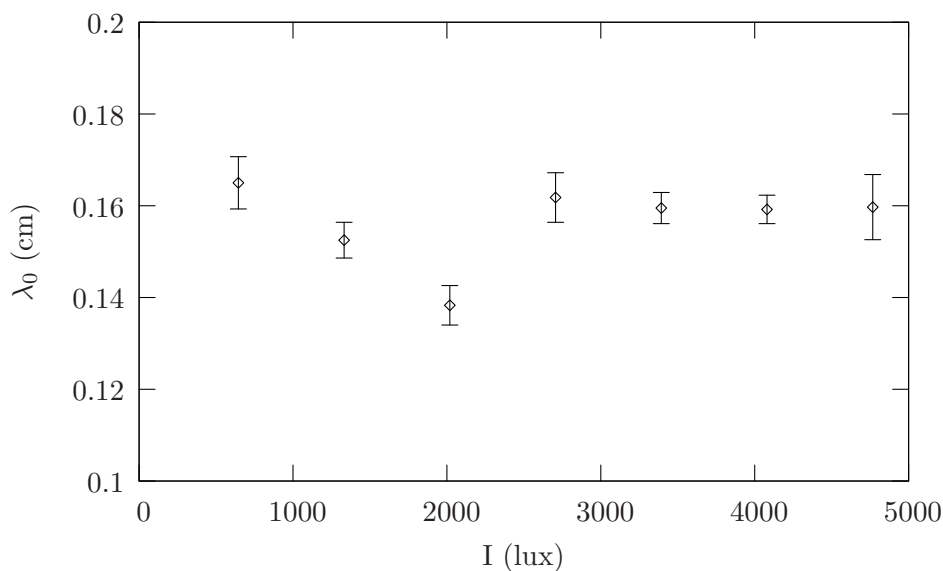


Figure 4.16: Experiment LB1: The effect of white light illumination from below on dominant initial pattern wavelength, where $d = 0.306$ cm and $C = 5.35 \times 10^6$ cells / cm³. Each point represents the average of 6 runs of the experiment, unless otherwise stated in Table 4.4, and the error bars are the standard error of the mean.

Figures 4.16, 4.17 and 4.18 show the same basic trend: a decrease in initial wavelength as light intensity is increased to 2020 lux followed by an increase as light is increased to 2710 lux and then what appears to be a stabilization of wavelengths as light is increased further, with wavelengths beyond 2710 lux looking approximately constant within the

Experiment	I (lux)	C (cells / cm ³)	d (cm)	k_0 / dish	λ_0 (cm)	S.D.	n
LB1	645	5.35×10^6	0.306	31.70	0.1650	0.0139	6
LB1	1330	5.35×10^6	0.306	34.22	0.1525	0.0097	6
LB1	2020	5.35×10^6	0.306	37.79	0.1383	0.0106	6
LB1	2710	5.35×10^6	0.306	32.32	0.1618	0.0131	6
LB1	3390	5.35×10^6	0.306	32.67	0.1595	0.0084	6
LB1	4080	5.35×10^6	0.306	32.72	0.1592	0.0075	6
LB1	4770	5.35×10^6	0.306	32.86	0.1597	0.0173	6
LB2	645	5.18×10^6	0.306	27.26	0.1912	0.0095	8
LB2	1330	5.18×10^6	0.306	30.76	0.1707	0.0178	8
LB2	2020	5.18×10^6	0.306	34.49	0.1544	0.0254	8
LB2	2710	5.18×10^6	0.306	32.27	0.1641	0.0230	8
LB2	3390	5.18×10^6	0.306	32.42	0.1620	0.0170	5
LB2	4080	5.18×10^6	0.306	33.42	0.1582	0.0216	8
LB2	4770	5.18×10^6	0.306	33.37	0.1567	0.0124	8
LB3	645	9.46×10^6	0.306	30.81	0.1727	0.0288	8
LB3	1330	9.46×10^6	0.306	33.59	0.1558	0.0131	8
LB3	2020	9.46×10^6	0.306	40.85	0.1278	0.0168	6
LB3	2710	9.46×10^6	0.306	33.10	0.1582	0.0136	8
LB3	3390	9.46×10^6	0.306	32.83	0.1590	0.0098	8
LB3	4080	9.46×10^6	0.306	33.94	0.1557	0.0203	8
LB3	4770	9.46×10^6	0.306	32.80	0.1600	0.0159	8

Table 4.4: Summary of results for initial pattern wavelength when the suspension was illuminated with a white light from below. I is light intensity, C concentration, d depth, k_0 /dish the wavenumber of the initial pattern normalized over the dish diameter, λ_0 the initial wavelength, and S.D. the standard deviation calculated over n runs.

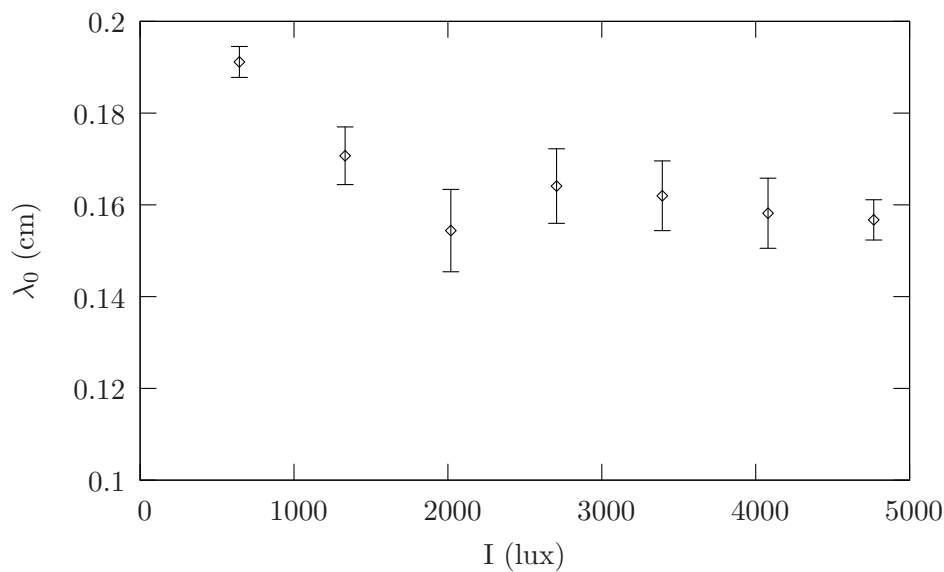


Figure 4.17: Experiment LB2: The effect of white light illumination from below on dominant initial pattern wavelength, where $d = 0.306$ cm and $C = 5.18 \times 10^6$ cells / cm³. Each point represents the average of 8 runs of the experiment, unless otherwise stated in Table 4.4, and the error bars are the standard error of the mean.

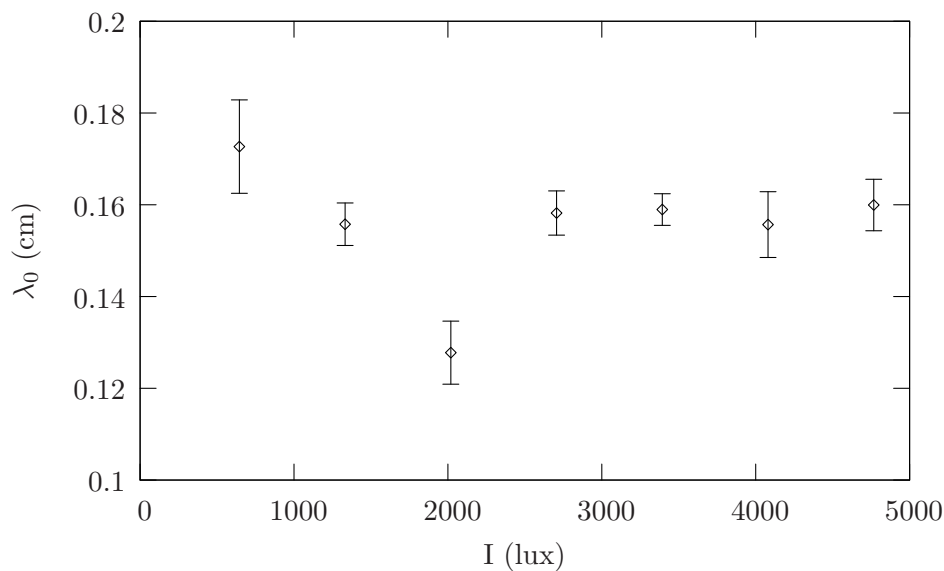


Figure 4.18: Experiment LB3: The effect of white light illumination from below on dominant initial pattern wavelength, where $d = 0.306$ cm and $C = 9.46 \times 10^6$ cells / cm³. Each point represents the average of 8 runs of the experiment, unless otherwise stated in Table 4.4, and the error bars are the standard error of the mean.

range of the error. If the data for red light in Section 4.4.3 for a similar concentration were included as a data point at $I = 0$, since red light does not have an effect, it would also fit with the trend of decreasing wavelength as I is increased to 2020 lux. Although these experiments show the same trend, there is some variability in the quantitative values of the mean wavelengths, which is to be expected due to the difficulty of repeating the same experiment with different cells that may behave slightly differently due to the stage of their life cycle or daily cycle that they are at. Figure 4.17 appears to have a broader spread around the mean than Figure 4.16, as indicated by larger standard deviations. The increase between $I = 2020$ lux and $I = 2710$ lux is also less pronounced than in the other two experiments and the wavelengths are slightly larger. The higher concentration experiment LB3 has a smaller minimum wavelength (at $I = 2020$), as expected since increasing concentration decreases wavelength (see Experiment CA, Section 4.4.2).

Unlike the data for varying concentrations, these are clearly not linear trends and so we must treat the data differently. The data shows a region where the trend looks linear, followed by an increase and then a region that appears stable. Therefore, we perform a linear regression separately on the first three points (for light intensities $I = 645$, $I = 1330$ and $I = 2020$ lux) and then on the following four points for each Figure ($I = 2710$, $I = 3390$, $I = 4080$ and $I = 4770$ lux), denoting the first three data points LB1a, LB2a and LB3a and the later 4 points LB1b, LB2b and LB3b. The linear fits and corresponding R and R^2 values are

$$\text{Experiment LB1a: } \lambda_0 = 0.178 - 1.94 \times 10^{-5}I, \quad \text{with } R = -0.720 \quad (R^2 = 0.518), \quad (4.14)$$

$$\text{Experiment LB2a: } \lambda_0 = 0.208 - 2.68 \times 10^{-5}I, \quad \text{with } R = -0.650 \quad (R^2 = 0.422), \quad (4.15)$$

$$\text{Experiment LB3a: } \lambda_0 = 0.190 - 2.68 \times 10^{-5}I, \quad \text{with } R = -0.613 \quad (R^2 = 0.376), \quad (4.16)$$

where I is light intensity in lux. Experiment LB1a shows the strongest negative correlation, while LB2a and LB3a show weaker correlations. The T-test for both coefficients in all three experiments gave $p < 0.002$. In all cases the analysis of variance T-test gave a significance level of $p < 0.002$ for the probability of being wrong in concluding that there is an association between light intensity and initial wavelength. To test whether the changes in the mean wavelength between the first and last data points in LB1a, LB2a and LB3a are significant we perform an unpaired T-test on each data set. We found a high significance level in each case, $p < 0.05$, indicating that is unlikely that these differences are due to error or normal variation. We conclude that it is unlikely that the light data

can not be used to predict the wavelength data, and we have found a significant negative correlation between light and wavelength for $I \leq 2020$.

The rise in λ_0 between $I = 2020$ lux and $I = 2710$ lux was examined using T-tests and this rise in wavelength was found to be statistical significant in experiments LB1 and LB3, with $p < 0.05$, but was not significant in LB2.

For the second set of points the correlation coefficients are very low, especially for the more concentrated cells in LB3b and, hence, there is no evidence of a correlation between light intensity and wavelength for $I > 2710$. The equations of the linear fits are

$$\text{Experiment LB1b: } \lambda_0 = 0.164 - 9.62 \times 10^{-7}I, \quad \text{with } R = -0.066 \quad (R^2 = 0.0043), \quad (4.17)$$

$$\text{Experiment LB2b: } \lambda_0 = 0.174 - 3.74 \times 10^{-6}I, \quad \text{with } R = -0.166 \quad (R^2 = 0.0274), \quad (4.18)$$

$$\text{Experiment LB3b: } \lambda_0 = 0.157 - 2.87 \times 10^{-7}I, \quad \text{with } R = -0.015 \quad (R^2 = 0.0002). \quad (4.19)$$

In all cases the probability of being wrong in concluding that the y-intercept is non-zero is very small, $p < 0.0001$, but the probability in being wrong in concluding that there is a relationship between the two variables (i.e. that the gradient of the line is non-zero) is very high ($p = 0.760$ for LB1b, $p = 0.391$ for LB2b and $P = 0.934$ for LB3b). These high values, along with the small R values, imply that these data sets are uncorrelated and that there is not sufficient evidence to conclude that light intensity when $I \geq 2710$ lux and initial wavelength vary together in an associated way. This evidence strongly suggests the wavelength remains approximately constant for large I , and so we average all data points for $I \geq 2710$ in LB1b and LB2b separately to obtain $\lambda_{WB1} = 0.1600$ ($SD = 0.0115$) and $\lambda_{WB2} = 0.1600$ ($SD = 0.0184$). For LB3 the average is slightly smaller, as expected, at $\lambda_{LB3b} = 0.1582$ ($SD = 0.0147$). The linear fits are shown in Figure 4.19.

This T-test analysis, together with the linear regression data, leads us to conclude that for illumination from below there is a significant decrease in wavelength as light intensity is increased from 645 lux to 2020 lux, which can be fitted with a linear curve, followed by a significant increase as light is increased further to 2710 lux in 2 cases, and a non-significant increase in the third. Increasing the light intensity beyond this does not give any significant change in wavelength for I up to $I = 4770$ lux. The data for LB2 have a broader spread around the mean. From this we can only conclude that the initial wavelength decreases, stops decreasing and stays at approximately the same level thereon.

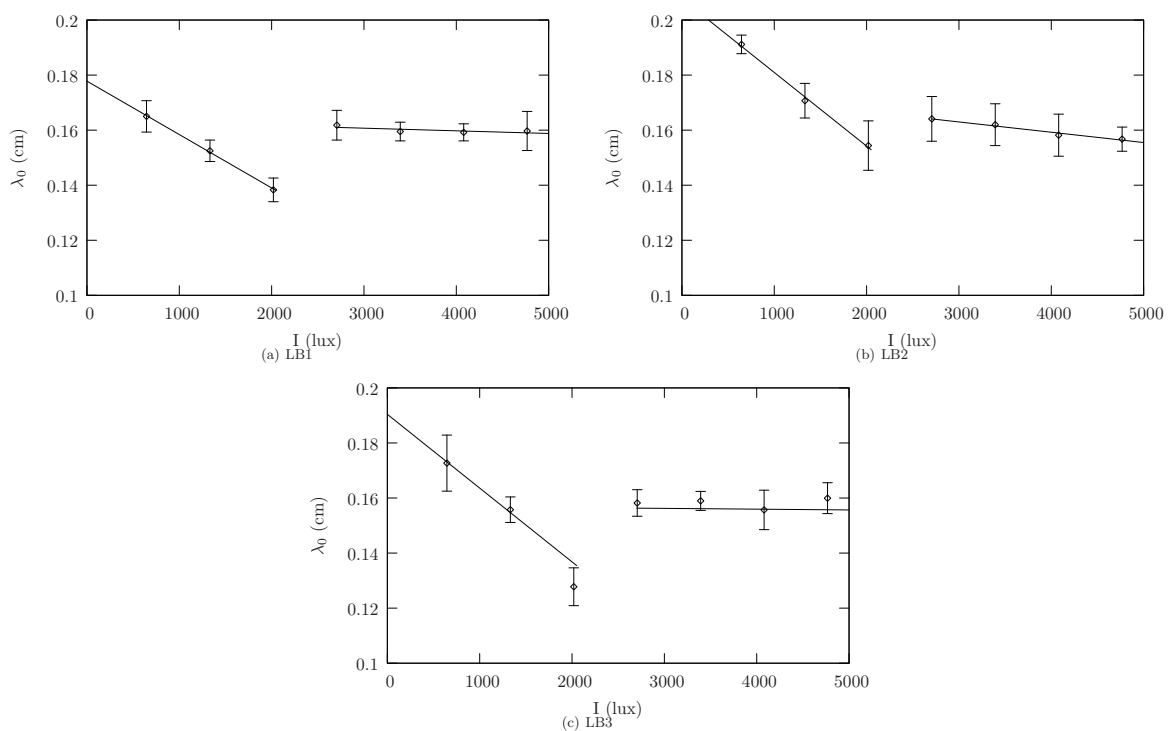


Figure 4.19: The effect of illumination from below on dominant initial pattern wavelength, where linear regression fits have been plotted for all experiments, separately for the first three points and the last four points in each data set.

Discussion

Since cells swim towards a weak light and away from a strong light, there is a preferred light intensity, I_c , between these two behaviours. To explain the remarkable results for illumination from below, we assume that qualitative changes in initial wavelength as the light intensity varies are due to a change between all cells swimming towards the light when $I < I_c$, and cells exhibiting different behaviours (upswimming or downswimming) dependent on location when $I > I_c$. This qualitative change, where wavelength stops decreasing and starts increases as I is increased, occurs in the range $2020 \leq I_c \leq 2710$ lux. We hypothesize that for $I \leq 2020$ lux most cells wish to swim towards the light, thus downwards, to maximize light absorption. If this is the case, positive phototaxis will support any gyrotactic instability that occurs within the fluid, since positive phototaxis will increase cells tilting towards downwelling fluid (as cells will orientate towards the light, which is below). As the light increases from $I = 0$ lux to $I \leq 2020$ lux, the cells will be able to detect the light source more strongly and the phototaxis torque will increase, thus further supporting the gyrotactic instability and increasing gyrotactic focussing and decreasing the wavelength of the initial pattern as I is increased to 2020 lux.

It is also of interest to note that increasing concentration (and, hence, decreasing the light each cell obtains due to shading, see Section 4.4.2) and increasing the light from below from $I = 0$ lux to $I = 2020$ lux initially follow the same trend, of decreasing wavelength. One might expect the opposite trend, since one is akin to decreasing light and the other is an increase in light. However, increased gyrotaxis as concentration increases is the dominant effect in the concentration experiment, and increased gyrotaxis due to increased phototaxis and cell tilting as light intensity increases is the dominant effect in the light experiment. Thus the concentration and light from below experiments show similar trends, both attributed to increased gyrotaxis, even though the light intensity throughout the layer effectively decreases for high concentrations.

We hypothesize that the sudden increase in wavelength as light intensity increases from 2020 lux to 2710 lux is due to light intensity exceeding the critical intensity, $I = 2710 > I_c$, so that the cells' swimming behaviour now depends on location in the layer. Cells far from the light source will still want to move downwards towards the light, as they are shaded by cells below, but now cells lower down near the light source have too much light and are inclined to swim upwards, away from the light. This negative phototaxis will decrease gyrotactic focussing, resulting in an increase of the pattern wavelength.

Increasing light intensity beyond a certain threshold (2710 lux) does not change λ_0 significantly. Presumably this is because the cells near the light source are fully upswimming, so cells concentrate at the upper boundary and there will be an overturning, gravitactic instability. Since cells require to swim upwards, away from the light, gyrotaxis is no longer supported by phototaxis and the gravitactic instability will be dominant for all sufficiently large light intensities.

4.4.5 Exploring the effects of white light illumination from above on initial pattern wavelength

Results for changes in initial pattern wavelength when cultures were illuminated from above are summarized in Table 4.5. Three independent experiments, LA1, LA2 and LA3, were performed on different cells with similar concentrations, ranging from $C = 4.68 \times 10^6$ to $C = 5.69 \times 10^6$ cells per cm^3 and with $d = 0.306\text{cm}$. In each experiment eight experimental runs were conducted for each light intensity, and λ_0 is the mean initial wavelength of those eight repeats, unless otherwise stated (less than eight were recorded in some cases due to problems with the images or the experimental set-up). Figure 4.20 shows an example of a sequence of bioconvection images in Experiment LA1 for two different light intensities, where images are taken 2 seconds apart. It is clear that the images with the higher light intensity have more waves per image and, hence, a smaller wavelength. Fourier spectra for these two image sets are shown in Figures 4.21 and 4.22, where we note that the double logarithmic is a good fit to the data, and time to pattern formation t_0 is longer for the higher light intensity $I = 4770$. Figure 4.23 shows a 3-dimensional plot for the evolution of the Fourier spectrum density and dominant wavenumber over time when $I = 645$ lux. This shows that patterns start to form around 10–20 seconds after recording began, with the Fourier density increasing initially to a maximum and then subsequently decreasing after around 30 seconds.

Figures 4.24, 4.25 and 4.26 show plots of each experiment (for different cells) separately, where initial wavelength is plotted as a function of light intensity. All results show the same basic trend: as light increases from 645 to 1330 lux the initial wavelength, λ_0 , increases and as I is increased beyond $I = 2020$ lux the wavelength decreases. If the data for illumination with red light for a similar concentration were included as $I = 0$ lux (since red light has no phototactic effect), where $\lambda_0 = 0.19$ cm, it would be smaller than the wavelengths for $645 \leq I \leq 1330$, thus would be consistent with the trend of increasing λ_0 as I is increased

Experiment	I (lux)	C (cells / cm ³)	d (cm)	k_0 / dish	λ_0 (cm)	S.D.	n
LA1	645	5.05×10^6	0.306	22.27	0.2352	0.0215	8
LA1	1330	5.05×10^6	0.306	20.41	0.2555	0.0150	8
LA1	2020	5.05×10^6	0.306	22.86	0.2283	0.0142	8
LA1	2710	5.05×10^6	0.306	26.07	0.2012	0.0213	8
LA1	3390	5.05×10^6	0.306	27.68	0.1880	0.0063	8
LA1	4080	5.05×10^6	0.306	30.68	0.1704	0.0131	8
LA1	4770	5.05×10^6	0.306	32.80	0.1592	0.0108	8
LA2	645	4.86×10^6	0.306	24.61	0.2133	0.0214	8
LA2	1330	4.86×10^6	0.306	21.31	0.2456	0.0219	7
LA2	2020	4.86×10^6	0.306	21.70	0.2406	0.0160	7
LA2	2710	4.86×10^6	0.306	22.57	0.2330	0.0277	8
LA2	3390	4.86×10^6	0.306	24.19	0.2197	0.0361	8
LA2	4080	4.86×10^6	0.306	25.30	0.2100	0.0327	8
LA2	4770	4.86×10^6	0.306	27.32	0.1905	0.0067	8
LA3	645	5.69×10^6	0.306	24.42	0.2154	0.0251	8
LA3	1330	5.69×10^6	0.306	19.82	0.2654	0.0295	8
LA3	2020	5.69×10^6	0.306	20.02	0.2632	0.0324	6
LA3	2710	5.69×10^6	0.306	20.83	0.2510	0.0203	8
LA3	3390	5.69×10^6	0.306	21.98	0.2378	0.0192	7
LA3	4080	5.69×10^6	0.306	24.28	0.2132	0.0172	7
LA3	4770	5.69×10^6	0.306	26.28	0.2022	0.0332	8

Table 4.5: Summary of results for initial pattern wavelength when the suspension was illuminated with a white light from above. I is light intensity, C concentration, d depth, k_0 /dish the wavenumber of the initial pattern normalized over the dish diameter, λ_0 the initial wavelength, and S.D. the standard deviation calculated over n runs.

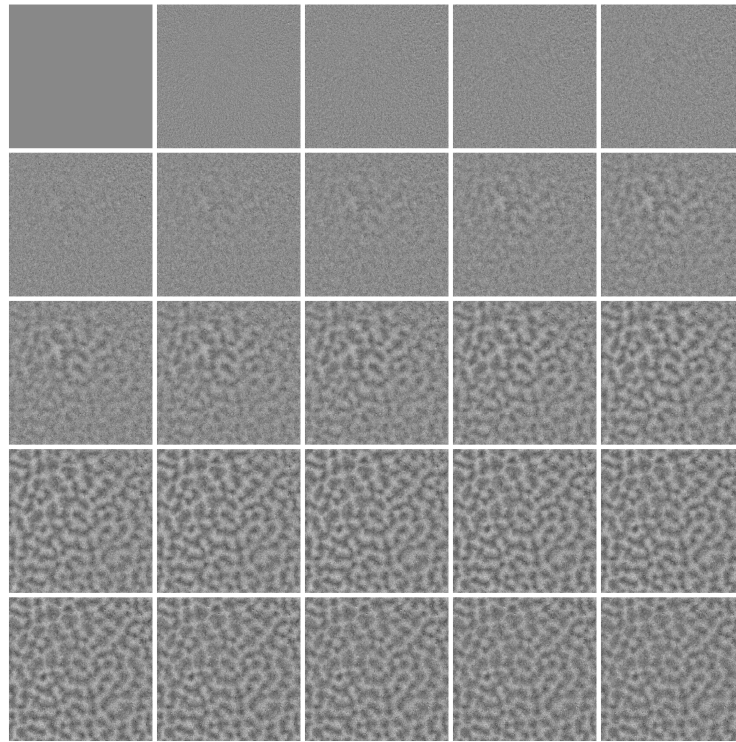
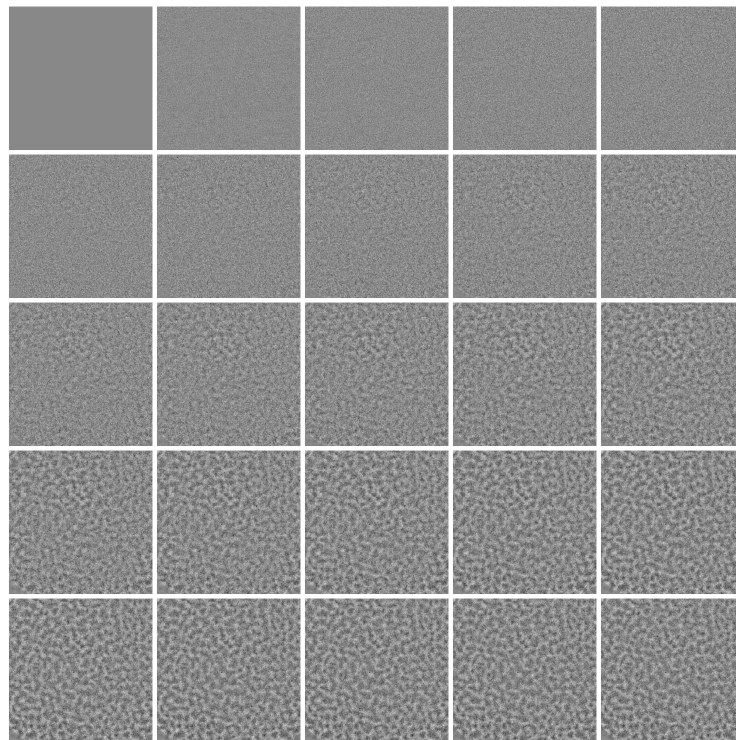
(a) $I = 645$ lux(b) $I = 4770$ lux

Figure 4.20: Sample images from Experiment LA1, with white light illumination from above, where $C = 5.05 \times 10^6$ cells / cm³, $d = 0.306$ cm and $I_w = 2.47$ cm. Figure (a) shows a case where $I = 645$ lux and Figure (b) a case where $L = 4770$ lux. Images were captured every 2 seconds, starting 12 seconds after mixing ended.

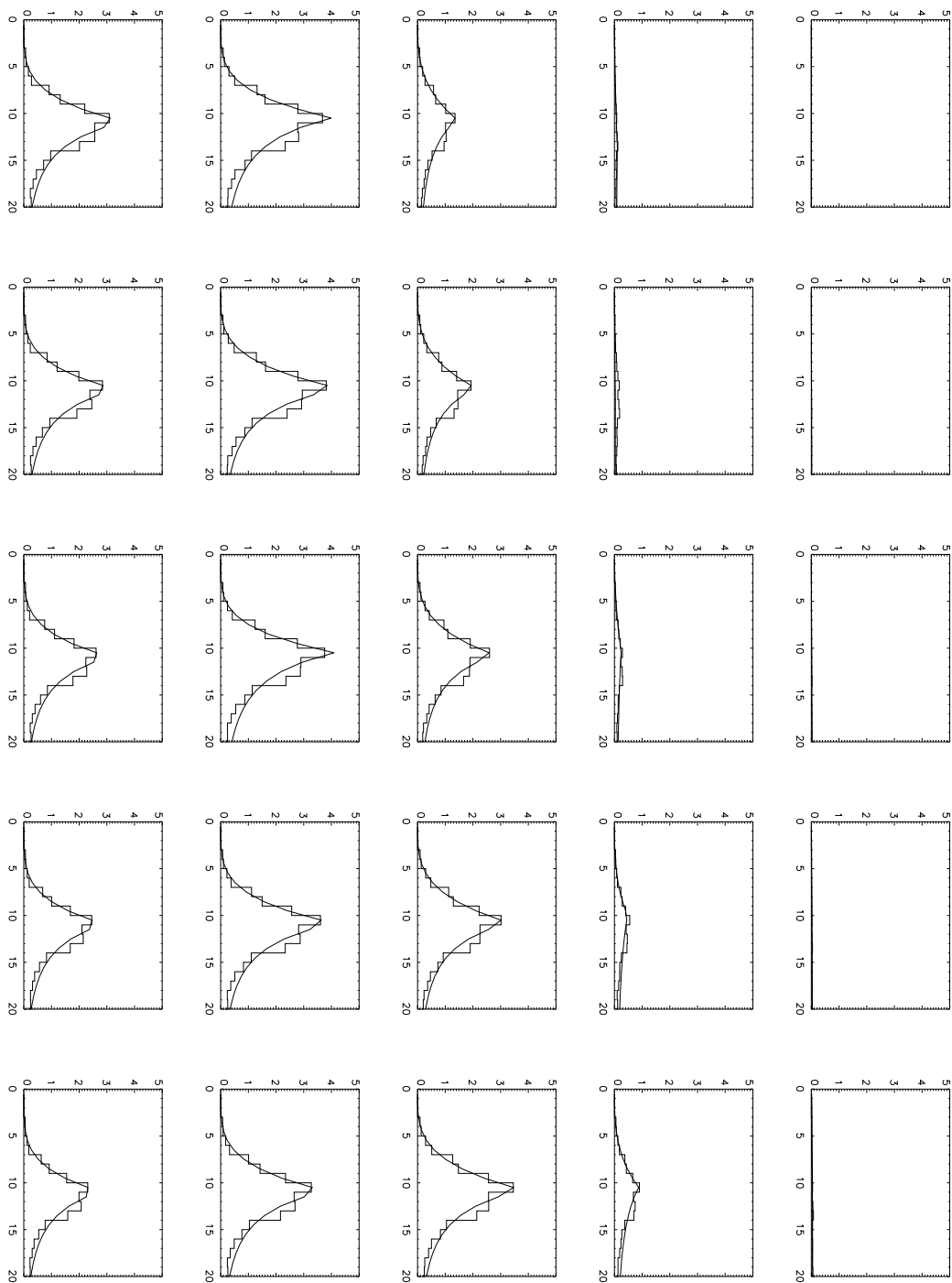


Figure 4.21: A sample set of Fourier spectra from Experiment LA1, with white light illumination from above, where $I = 645$ lux, $C = 5.05 \times 10^6$ cells / cm^3 and $d = 0.306$ cm. Images were captured every 2 seconds, starting 12 seconds after mixing ended. The horizontal axis is wavenumber and the vertical axis is Fourier density, and the logarithmic function in equation 4.5 is used as the fitting function.

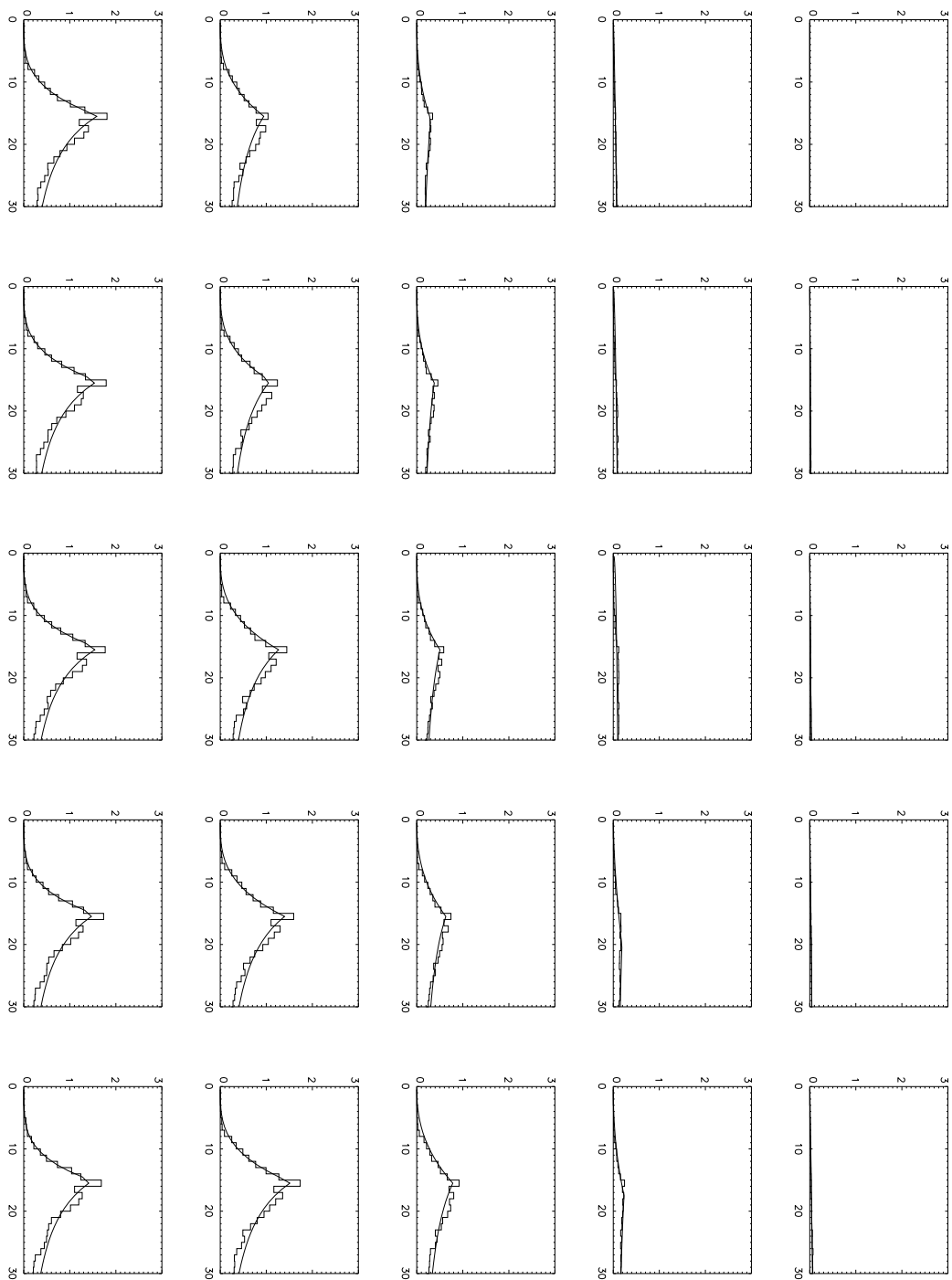


Figure 4.22: A sample set of Fourier spectra from Experiment LA1, with white light illumination from above, where $I = 4770$ lux, $C = 5.05 \times 10^6$ cells / cm^3 and $d = 0.306$ cm. Images were captured every 2 seconds, starting 12 seconds after mixing ended. The horizontal axis is wavenumber and the vertical axis is Fourier density, and the logarithmic function in equation 4.5 is used as the fitting function.

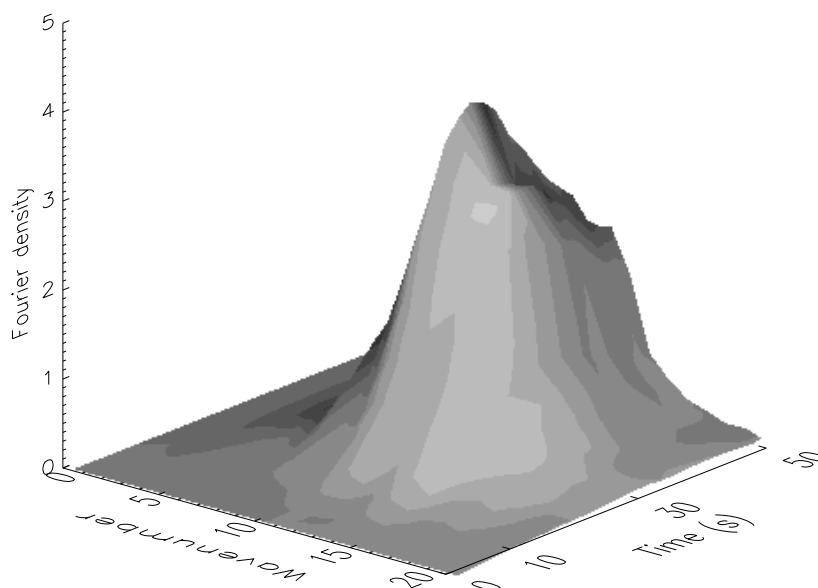


Figure 4.23: A sample 3D surface from Experiment LA1, with white light illumination from above, where $I = 645$ lux, $C = 5.05 \times 10^6$ cells / cm³ and $d = 0.306$ cm. Images were captured every 2 seconds, starting 12 seconds after mixing ended. ‘Time’ is time since recording started.

to $I = 1330$ lux. The initial increase in the wavelength is most pronounced in Experiment LA3, with λ_0 increasing from 0.215 to 0.265, whilst the subsequent decrease is clearer in Experiment LA1 (decreasing from 0.255 to 0.159, compared to a drop of approximately 0.055 – 0.063 in the other two experiments). LA1 is the most extreme data set, with the highest wavelength for $I = 645$ lux and the lowest for $I = 4770$ lux. The wavelengths for $I = 1330$ lux and $I = 2020$ lux in experiments LA2 and LA3 and very similar to each other, causing these curves to level off around the maximum, unlike LA1, where the fall in wavelength is more rapid once $I > 1330$ lux. The aspect ratios of wavelength to depth were between 0.5 and 1.0. Although all the data sets show the same basic trend, the strength of this trend and the absolute values of λ_0 vary between them. This is likely to be due to the different concentrations and cell cultures used, since different cells are unlikely to behave in exactly the same way.

We investigate the trends using similar techniques to the case for light from below. Comparing the mean wavelengths for $I = 675$ and $I = 1330$ lux using an unpaired T-test it was found that the increase in wavelength was significant, with $p < 0.05$, in every case. We perform a linear regression analysis but exclude the first data point, since it does

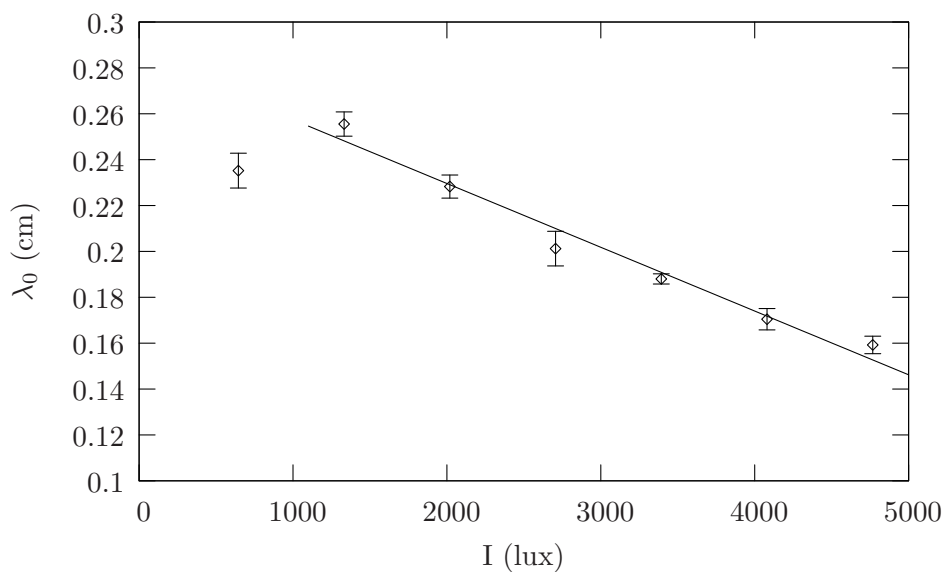


Figure 4.24: Experiment LA1: The effect of white light illumination from above on dominant initial pattern wavelength, where $d = 0.306$ cm and $C = 5.05 \times 10^6$ cells / cm³. A linear regression fit is plotted for all points except the first, $I = 645$ lux.

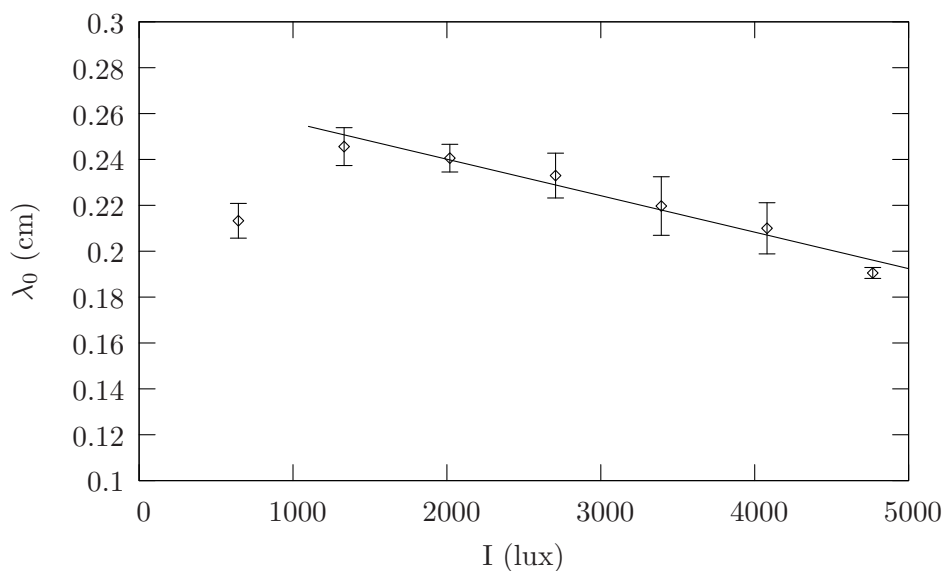


Figure 4.25: Experiment LA2: The effect of white light illumination from above on dominant initial pattern wavelength, where $d = 0.306$ cm and $C = 4.86 \times 10^6$ cells / cm³. A linear regression fit is plotted for all points except the first, $I = 645$ lux.

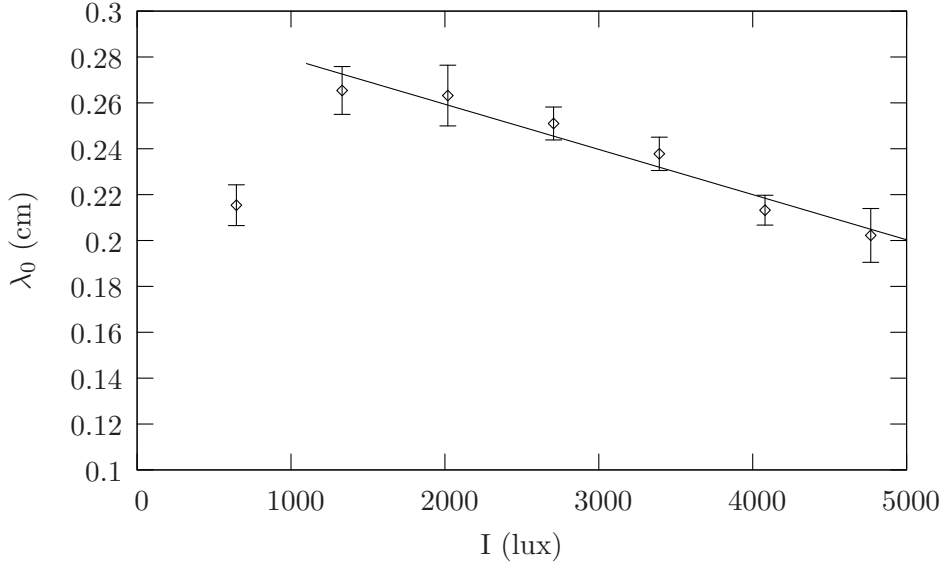


Figure 4.26: Experiment LA3: The effect of white light illumination from above on the dominant initial pattern wavelength, where $d = 0.306$ cm and $C = 5.69 \times 10^6$ cells / cm³. A linear regression fit is plotted for all points except the first, $I = 645$ lux.

not form part of the decreasing linear trend. This gives the equation of the line and the correlation coefficient in each case as

$$\text{Experiment LA1: } \lambda_0 = 0.285 - 2.78 \times 10^{-5}I, \text{ with } R = -0.915 \text{ (} R^2 = 0.837 \text{),} \quad (4.20)$$

$$\text{Experiment LA2: } \lambda_0 = 0.272 - 1.59 \times 10^{-5}I, \text{ with } R = -0.604 \text{ (} R^2 = 0.351 \text{),} \quad (4.21)$$

$$\text{Experiment LA3: } \lambda_0 = 0.299 - 1.97 \times 10^{-5}I, \text{ with } R = -0.688 \text{ (} R^2 = 0.474 \text{).} \quad (4.22)$$

The correlation is high in LA1 and not as high in the other two experiments. The T-test for each coefficient in the linear equation returned significance values of $p < 0.0001$ for all values over all three experiments and, likewise, using the analysis of variance test we find the probability of being wrong in concluding an association between the variables as $p < 0.0001$. Using an unpaired T-test the difference in λ_0 for $I = 1330$ and $I = 4770$ lux was found to be significant in all three experiments, with p ranging between $0.0001 < p < 0.0013$ and, hence, this decrease in initial wavenumber as I increases from 1330 lux to 4770 lux appears to be a significant trend.

Therefore, we find that increasing light intensity from $I = 645$ lux to $I = 1330$ lux repeatedly produces a significant increase in the initial wavelength of the resulting pattern and increasing I further up to $I = 4770$ lux significantly decreases the initial wavelength, and this decrease is approximately linear. The linear fits are plotted in Figures 4.24, 4.25

and 4.26. The initial wavelengths were of the same order as for illumination from below all light intensities

Discussion

We hypothesize that the increase in wavelength between $I = 645$ lux and $I = 1330$ lux can be explained as follows. For these intensities, $I < I_c$, all the cells want to swim towards the light and, hence, upswimming via phototaxis increases as the signal of light received increases. This increased upswimming leads to a higher concentration of cells close to the upper boundary for $I = 1330$ lux compared to $I = 645$ lux, forming a dense sublayer which is unstable to smaller wavenumbers. Gyrotaxis is also decreased, as cells swim strongly upwards, thus the large wavelengths become more unstable at $I = 1330$ lux compared to $I = 645$ lux, and wavelength increases as I is increased from 645 to 1330 lux.

If I is increased from $I = 1330$ lux to $I = 4770$ lux the initial pattern wavelength decreases as I increases. We assume that light intensities greater than 1330 lux are above the critical light intensity, I_c . Thus, starting from a uniform distribution of cells, negative phototaxis is sufficient to overcome negative gravitaxis, as found by Häder 1987 [52], and the cells near the top swim downwards due to too much light, whilst those lower down swim upwards due to shading, creating a concentrated sublayer somewhere within the layer, which moves down as the light intensity increases. This creates a stable region overlying an unstable region of fluid and, since the sublayer is denser than the fluid below, an instability arises. We hypothesize that the initial most unstable wavelength decreases as I increases from 1330 lux to 4770 lux for two reasons. Firstly, the inclination of cells near the light source to swim downwards as light intensity increases supports gyrotaxis, since downwelling is increased. This is similar to what happens when the culture is illuminated from below with intensity $I < I_c$, in which case gyrotaxis is supported, causing the cells to swim downwards. Secondly, as light intensity increases from 1330 lux to 4770 lux, the unstable region below the sublayer decreases in size, and large wavelength instabilities that use the whole fluid layer have a reduced space to circulate, thus are stabilized more than small wavelength instabilities. This causes a smaller wavelength to be the most unstable for higher light intensities compared to lower light intensities, so long as $I > I_c$. Note that we assume a different value of the critical light intensity to the value of I_c for light from below in Section 4.4.4. This is discussed further in Section 4.6.

4.4.6 Exploring the start time of pattern formation, t_0

It is also of interest to investigate the start time of pattern formation, t_0 , as light intensity changes for white light. Additionally, we investigate if there is any difference in start time between white light and red light. The start time of pattern formation is measured from when mixing ends, and so the values presented here cannot be directly compared to Figure 4.12, for example, where time indicates time after image capture began. For red light we only investigate one light intensity, since we deduced there is no effect on initial wavelength when red light intensity changes. We take the eight runs from Experiment RA where $I = 325$ lux and find the average t_0 . For white light from above and below, we chose two sample experiments, LA1 and LB1, and find t_0 for every run. t_0 is averaged for each light intensity and results are summarized in Table 4.6 and plotted in Figure 4.27. It should be noted that start time can only be a multiple of 2, since images were taken every 2 seconds, but the t_0 values used are averaged over 8 runs of the experiment for each light intensity.

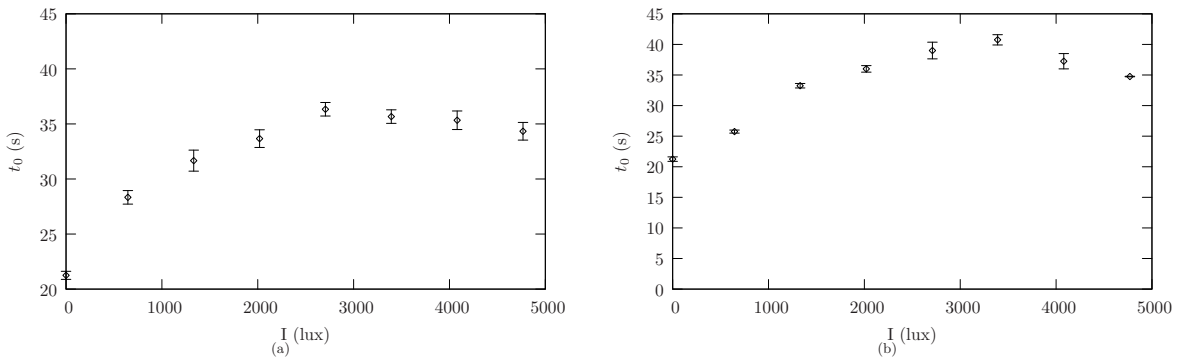


Figure 4.27: Plots of average initial start time t_0 for (a) Experiment LB1 and (b) Experiment LA1 for different light intensities, where the average start time for $I = 325$ lux for the red light experiment RA is included as $I = 0$ lux, since red light has no effect on photo-motility. In both cases, $d = 0.306$ cm, and for LA1 and LB1 images were captured every 2 seconds, starting 12 seconds after mixing ended.

For Experiment LB1, the time to pattern formation at the lowest light intensity, $I = 645$ lux, was approximately 28.33 seconds. t_0 then increased as I increases, reaching a maximum of $t_0 = 36.33$ seconds at $I = 2710$ lux. As I increase above $I = 2710$, the time to pattern formation then stayed approximately the same, at around 35 – 36 seconds. For light from above, Experiment LA1 shows pattern formation was delayed as I was increased from $t_0 = 25.75$ seconds at $I = 645$ lux to 40.75 seconds at $I = 3390$ lux, but when I_0

Experiment	C (cells / cm ³)	d (cm)	I (lux)	Mean t_0 (s)
LB1	5.35×10^6	0.306	645	28.33
LB1	5.35×10^6	0.306	1330	31.67
LB1	5.35×10^6	0.306	2020	33.67
LB1	5.35×10^6	0.306	2710	36.33
LB1	5.35×10^6	0.306	3390	35.67
LB1	5.35×10^6	0.306	4080	35.33
LB1	5.35×10^6	0.306	4770	34.33
LA1	5.05×10^6	0.306	645	25.75
LA1	5.05×10^6	0.306	1330	33.25
LA1	5.05×10^6	0.306	2020	36
LA1	5.05×10^6	0.306	2710	39
LA1	5.05×10^6	0.306	3390	40.75
LA1	5.05×10^6	0.306	4080	37.25
LA1	5.05×10^6	0.306	4770	34.75
RA	5.05×10^6	0.306	325	21.25

Table 4.6: Summary of initial start time t_0 for the Experiments LA1 and LB1 and for a sample red light intensity $I = 325$ lux from Experimental RA. I is light intensity, C concentration, d depth and t_0 measures the total time from the end of mixing to the start of pattern formation.

is increased further to $I = 4080$ lux and 4770 lux, t_0 decreased and pattern formation happened a little earlier ($t_0 = 34.75$ at $I = 4770$ lux).

When using red light, pattern formation occurred after approximately 21 seconds, earlier than for any of the white light intensities for light from above or below. If red light is treated as $I = 0$, since we found that cells do not respond to red light, then for both light from below and from above including these data points as $I = 0$ supports the trends in t_0 for $I < 2710$ lux and $I < 3390$ lux, respectively. These data have been plotted in Figure 4.27.

Discussion

In Section 4.4.4 it is hypothesized that as I increases above $I = 2710$ with illumination from below, $I > I_c$ and the overturning instability at the upper boundary is the dominant instability mechanism. An overturning instability is likely to take longer to form than a gyrotactic instability, which could explain why we see a later start time for pattern formation for $I > 2710$ lux compared to smaller intensities, and why start time t_0 remains approximately constant for $I > 2710$ lux. However, it is hypothesized in Section 4.4.4 that as I is increased from 645 lux to 2020 lux gyrotaxis increases, in which case we would actually expect to the time to pattern formation to decrease, not increase, at $I = 2020$ lux compared to $I = 645$ lux. It may be that the cells take longer to generate an unstable density gradient under brighter light (as I increases) as they spend less time swimming upwards compared to predominantly gravitactic cells, since for $I < I_c$ in a suspension illuminated from below cells will wish to swim downwards.

In Section 4.4.5 it was hypothesized that for $I > 1330$ lux with illumination from above gyrotaxis increases, which would decrease time to pattern formation and could explain the trend in start time for $I > 3390$ lux shown in Figure 4.27. However, the light intensity at which t_0 is maximal, $I = 3390$ lux, does not correlate with the light intensity at which the wavelength is maximal, $I = 1330$ lux, and we would expect these values to be the same if increasing gyrotaxis were the cause of decreased time to pattern formation. This may be because under strong illumination from above, when $I > I_c$, it takes the cells longer to achieve the equilibrium distribution due to conflicting orientation biases (gravitaxis causes the cells to swim upwards and negative phototaxis causes the cells to swim downwards when $I > I_c$), as for light from below when $I < I_c$.

There are many possible explanations for the trends in t_0 for light from above and

below. In addition to those discussed above, the cells may swim slower the longer they are in the dish, so that a larger change in conditions is needed to compensate for the slower cells in order to reduce or increase the average time to pattern formation. For I close to I_c there is likely to be gravitaxis and gyrotaxis both causing the instability, which for light from below may mean that t_0 increases even when gyrotaxis increases because overturning is still the dominant mechanism. For light from above, it may be that t_0 only starts decreasing when gyrotaxis has sufficiently increased to become the main destabilizing mechanism.

The start time t_0 was estimated manually, due to relatively few discrete images captured, and thus was only accurate within 2 seconds, but this aspect of pattern formation deserves to be explored more fully using computational techniques with more regular image capture.

4.5 Comparing experiment results with predictions from the three photo-gyrotaxis models

Results for the combined photo-gyrotactic models in Chapters 2 and 3 explore the effects of changing the phototaxis parameters χ and ζ for cultures of cells illuminated from above. χ is the ratio of the light intensity at the source, I_s , to the critical light intensity, I_c (above which the cells swim up, and below which they swim down) and, hence, $\chi = \frac{I_s}{I_c}$. $\chi = 0$ can be thought of as the case of no light, $I_s = 0$, and increasing χ is like increasing the light intensity (or decreasing the critical light intensity of the cells). The neutral curves for the model results in Chapters 2 and 3 provide an estimate for the critical Rayleigh number R_c and corresponding critical wavenumber k_c (the minimum wavenumber on the neutral curve, at which the growth rate is zero). On the other hand, in the experimental study the initial dominant wavenumber, k_0 , clearly has a non-zero growth rate and occurs for a set Rayleigh number determined by the experimental concentration and layerdepth, which is not the same as the critical Rayleigh number (since $R > R_c$ needed for pattern formation). Although this makes direct comparisons between theory and experimental results difficult, the predicted critical wavenumber k_c at $R = R_c$ may be related to the fastest growing observed wavenumber, k_0 , so that trends in k_0 as I varies experimentally and k_c as χ is increased numerically can be compared for illumination from above.

There are some issues that need to be considered before making any comparisons.

Most importantly, have the effects of mixing sufficiently diminished before pattern formation begins? Furthermore, has the equilibrium distribution, as found in the models, had sufficient time to form before the onset of pattern formation? To establish whether mixing effects would have diminished we use a similar argument to Hill *et al.* 1989 [63] and Bees and Hill 1997 [8] and assume that the Petri dish is in solid body rotation with angular velocity $\mathbf{\Omega}$ until the mixing stops and the container instantaneously comes to rest. The time for spin down is of the order $O(E^{-1/2}|\mathbf{\Omega}|^{-1})$, where $E = \frac{\nu}{\Omega H^2}$ is the Ekman number (ν is the viscosity and H the layer depth). The timescale for the decay of the residual fluid motion is also $O(E^{-1/2}|\mathbf{\Omega}|^{-1})$. If we convert the speed of the mixer from units of r.p.m to units of angular velocity, s^{-1} , then we have $|\mathbf{\Omega}| = 20.94 s^{-1}$, and if we assume we have a shallow layer with $H = 0.306$ cm and kinematic viscosity $\nu = 10^{-2} \text{ cm}^2 s^{-1}$ then $E = 5.1 \times 10^{-3}$. This gives $O(E^{-1/2}|\mathbf{\Omega}|^{-1}) = 0.69$ seconds, hence the decay is approximately 0.69 seconds, and since we waited 10-12 seconds before recording, and the patterns started tens of seconds after that, we conclude that the flow was likely to have diminished sufficiently before pattern formation began. As for the formation of the equilibrium solution, if the average cell swimming speed is $63 \mu m s^{-1}$, as in Hill and Häder [61], and the cells are swimming upwards an average of 56% of the time (calculated from Bees *et al.* 1998 [11]), then if the layer is 3mm deep a cell swimming at full speed upwards would take approximately 48 seconds to swim the whole depth, and an average cell, only swimming up 56% of the time, would take approximately 85.7 seconds. This implies that the cells may not have sufficient time to form the equilibrium distributions that were used in the phototaxis models because pattern formation began before 48 seconds in all cases.

To compare experimental data and the theoretical predictions we convert all the parameters into the same non-dimensional form. To do this we use expressions from the models in Chapters 2 and 3 for the scaled layer depth d , equation 2.47, and the Rayleigh number, equation 2.90, both in Section 2.3, and N from Section 2.2.3.

$$d = \frac{K_1 H}{K_2 V_n \tau}, \quad (4.23)$$

$$\begin{aligned} R &= \frac{vg \nabla \rho \kappa_1 H^4 N}{\nu \rho V_n^2 \tau} \\ &= \frac{vg \nabla \rho \kappa_1^2}{\nu \rho V_n^2 \tau} \left(\frac{H^5 \bar{n}}{1 - e^{-\kappa_1 H}} \right), \quad \text{since} \end{aligned} \quad (4.24)$$

$$N = \frac{\kappa_1 H \bar{n}}{1 - e^{-\kappa_1 H}} \quad \text{and} \quad (4.25)$$

$$\kappa_1 = \frac{K_1}{K_2 V_n \tau}. \quad (4.26)$$

τ is the direction correlation time, V_n the swimming speed, H the depth of the layer, ρ fluid density, $\nabla\rho$ the difference in density between the cell and fluid, v is the cell volume, g acceleration due to gravity, ν the kinematic viscosity and \bar{n} the mean cell concentration. N is the scaling for concentration, substituted into Equation 4.24. λ is a constant defined in equation 2.30 in Chapter 2, and K_1 and K_2 are from the equilibrium, zero flow solution to the Fokker-Planck equation when $\lambda = 2.2$ in every case (so that they are constant in Models B and C, even when λ is not), and are defined in Table 2.2. This value of λ was chosen to be the same as in Pedley and Kessler 1990 [130], and is calculated by Hill and Häder 1996 [61]. We choose a value of $\tau = 5$ seconds and choose the gyrotactic orientation parameter, B_n (defined in equation 2.28), as $B_n = 6.3$ seconds, taken from Jones [73]. In the models, the gyrotaxis parameter η has the expression

$$\eta = \frac{B_n V_n^2 \tau \kappa_1^2}{d^2}, \quad (4.27)$$

from equation 2.30 in Section 2.2.3. Choosing parameters from Table 2.1 in Section 2.2, we have $\eta = 16d^{-2}$. For all the other parameters we use those stated in Table 2.1 in Chapter 2. Using these conversions for the experimental data provides d and R , as shown in Table 4.7. We also convert the dimensional wavelengths found in the experiments to dimensionless wavelengths by scaling with depth H . Non-dimensional initial wavelength is denoted $\tilde{\lambda}_0$, and we calculate the non-dimensional initial wavenumber \tilde{k}_0 using $\tilde{k}_0 = \frac{2\pi}{\tilde{\lambda}_0}$. Figure 4.28 and Table 4.7 show the results of Experiment LA1, where the dimensional wavelengths have been converted to non-dimensional wavelengths.

Theoretical predictions for critical wavenumber, k_c , and Rayleigh number, R_c , are made with parameter values $d = 34.6$ and $\eta = 16d^{-2}$ using methods outlined in Section 2.3 and used again in Chapter 3. κ is a measure of the absorbance and is given by $\kappa = \alpha^* H N$ in equation 2.19, Section 2.2.3, where α^* is the cellular extinction coefficient. To calculate the cellular extinction coefficient we use the relationship $A = \alpha^* C l$, where A is absorption per suspension, C the concentration of the suspension and l the path length. This can be calculated using the data for calibrating the colourimeter, where absorbance A is known for various concentration and the width of the colourimeter cuvette is 1 cm, hence $l = 1$ cm. Thus, we find a range for α^* per cell as

$$3.67 \times 10^{-7} \text{ cm}^2 \leq \alpha^* \leq 6.74 \times 10^{-7} \text{ cm}^2 \quad (4.28)$$

Note that this is a different range to that used for *C. reinhardtii* in Chapter 5. Using $\alpha^* = 3.67 \times 10^{-7} \text{ cm}^2$, since this is the mode of the range, and averaging the mean

Experiment	I (lux)	λ_0 (cm)	$\tilde{\lambda}_0$	\tilde{k}_0	d	$R(\times 10^6)$
LA1	645	0.2352	0.7687	8.23	34.6	2.18
LA1	1330	0.2555	0.8351	7.55	34.6	2.18
LA1	2020	0.2283	0.7460	8.45	34.6	2.18
LA1	2710	0.2012	0.6576	9.64	34.6	2.18
LA1	3390	0.1880	0.6144	10.24	34.6	2.18
LA1	4080	0.1704	0.5570	11.34	34.6	2.18
LA1	4779	0.1592	0.5159	12.23	34.6	2.18
RA	Any (red)	0.190*	0.6209	10.12	34.6	2.18

Table 4.7: Results from experiment LA1 with white light from above and RA with red light from above, where wavelength has been converted into non-dimensional wavenumbers in order to compare with theoretical results. In RA the star indicates that, since no dependence on intensity was found with red light, the wavelength is the mean of all measurements for all light intensities.

concentration over the three experiments with illumination from above to obtain N , gives $\kappa = 20.3$. Examples of the model predictions for the critical wavenumber and Rayleigh number are shown in Table 4.8.

Figure 4.29 shows plots of the critical wavenumber as χ varies for Models A and B, where $\eta = 16d^{-2}$ and $\kappa = 20.3$. Results for Model C, where a new torque due to phototaxis was included in the torque balance, are more difficult to compare because this model requires two phototaxis parameters, ζ and χ , and it is not obvious how these can be determined. Two versions of Model C were explored in Chapter 3, and here we just compare the more realistic Case II. For this model, we found the surprising result that for a range of values of ζ and χ , non-hydrodynamic modes exist, which occur even in the absence of fluid flow. In the experiments in this chapter, fluid flow was present and so experimental results cannot be compared with theoretical results for Model C, and from herein only comparisons with Models A and B are made. An experiment to investigate whether these non-hydrodynamics modes exist could be conducted by suspending alga cells in a soft agar gel, in which there would be limited fluid flow.

For $d^2\eta = 16$ the critical wavenumber k_c for no light in all of the Models ($\chi = 0$) is $k_c = 45.3$, which is around a factor of 4 higher compared to the initial most unstable mode \tilde{k}_0 for red light data (equivalent to no light; $\tilde{k}_0 = 10.12$; see Section 4.4.3). The

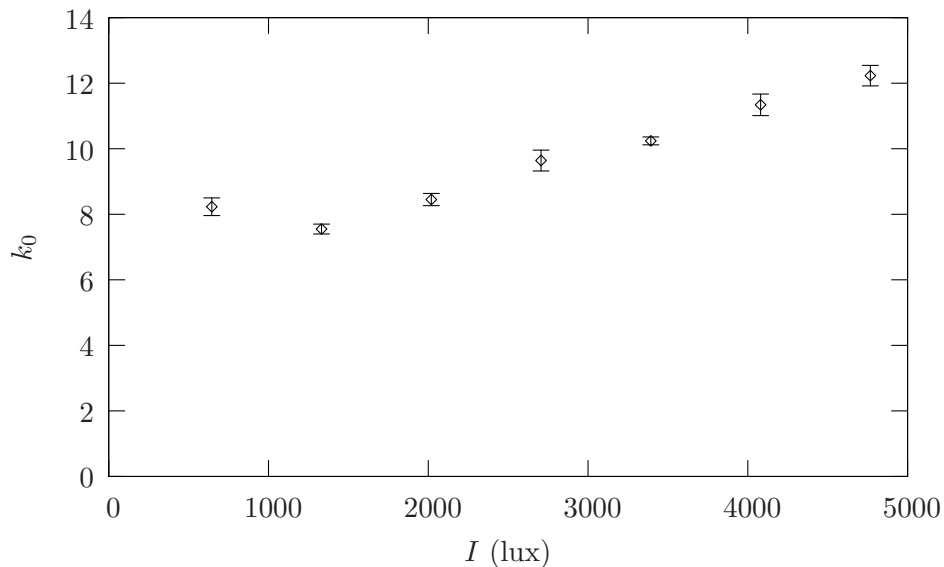


Figure 4.28: Results from experiment LA1, where the dimensional wavelengths have been non-dimensionalized, for comparison with the theoretical predictions, and converted to a non-dimensional wavenumber, \tilde{k}_0 . Again, each point is the mean of 8 initial wavenumbers from the experimental data (see Table 4.5 for more details).

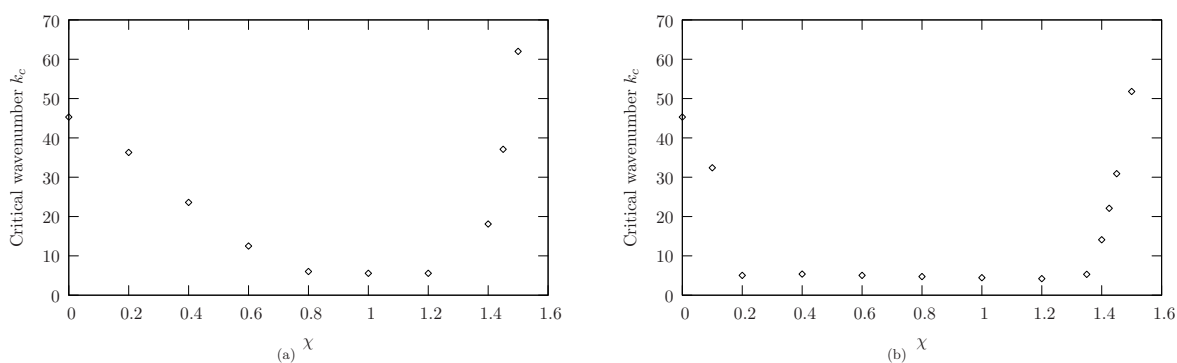


Figure 4.29: Critical wavenumber, k_c , plotted against χ for Model A in Figure (a) and for Model B in Figure (b), where $\kappa = 20.3$ and $d = 34.6$.

Model	d	$d^2\eta$	χ	κ	k_c	R_c
A	34.6	16	0	20.3	45.3	2.77×10^6
A	34.6	16	0.6	20.3	12.5	1.32×10^6
A	34.6	16	1.0	20.3	5.57	4.02×10^5
A	34.6	16	1.2	20.3	5.57	2.71×10^5
A	34.6	16	1.4	20.3	18.1	1.09×10^7
A	34.6	16	1.45	20.3	37.1	3.63×10^7
A	34.6	16	1.5	20.3	62.0	9.16×10^7
B	34.6	16	0	20.3	45.3	2.77×10^6
B	34.6	16	0.1	20.3	32.4	2.64×10^6
B	34.6	16	0.2	20.3	5.04	1.83×10^6
B	34.6	16	0.6	20.3	5.04	7.17×10^5
B	34.6	16	1.0	20.3	4.45	3.17×10^5
B	34.6	16	1.2	20.3	4.21	2.36×10^5
B	34.6	16	1.4	20.3	14.1	1.16×10^7
B	34.6	16	1.45	20.3	30.9	3.95×10^7
B	34.6	16	1.5	20.3	51.8	1.01×10^8

Table 4.8: Theoretical predictions of critical wavenumber, k_c , and critical Rayleigh number, R_c , for Models A and B.

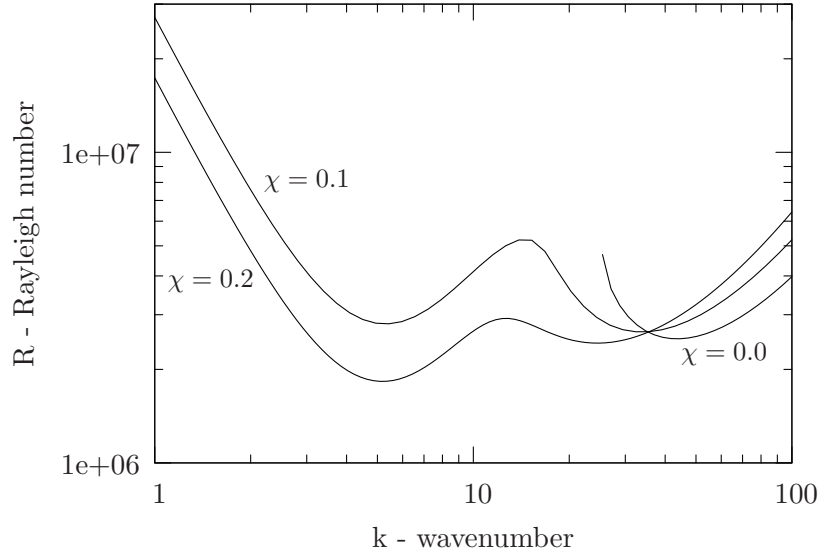


Figure 4.30: Curves of neutral stability for Model B, where $d = 20$, $\kappa = 20.3$, $d^2\eta = 16$ and $\chi = 0.0$, $\chi = 0.1$ and $\chi = 0.2$. The critical wavenumber k_c moves from the minimum at large k to the minimum for small k for $\chi = 0.2$, causing a jump in k_c in Figure 4.29.

corresponding critical Rayleigh number was found to be $R_c = 2.77 \times 10^6$ for all of the models, which is very close to the experimental value of $R = 2.18 \times 10^6$. If η is reduced to $d^2\eta = 4$ then $k_c = 13.22$, which is approximately the same order as the red light data (data not shown). For $d^2\eta = 16$, Models A and B predict a decrease in k_c with increasing χ from $\chi = 0$ followed by an increase for some value of $\chi > 1$ (see Figure 4.29), a trend also seen the experimental data for \tilde{k}_0 as I increases (see Figure 4.28). Critical wavenumber appears to remain almost constant once the minimum value of k_c is reached, until $\chi > 1.25$. For Model B, a double minima appears on the neutral curve as χ is increased from $\chi = 0$ to $\chi = 0.1$, shown in Figure 4.30. As χ increases from $\chi = 0.1$ to $\chi = 0.2$ the minimum for smaller k is smaller than the minimum for larger k , so that the value of k_c moves to the smaller minima and there is a sudden decrease in k_c in Figure 4.29 between $\chi = 0.1$ and $\chi = 0.2$. This double minima was not found for Model A and explains the differences in the rate of decrease of k_c as χ increases for Model B in Figure 4.29. The minimum critical wavenumber and minimum Rayleigh number are $k_c = 5.57$ and $R_c = 1.49 \times 10^5$ in Model A, and $k_c = 4.21$ and $R_c = 2.20 \times 10^5$ in Model B. In the experimental data the average minimum initial wavenumber, \tilde{k}_0 , was found to be between $7.33 < \tilde{k}_0 < 7.88$ for $I = 1330$ lux over the three experiments, which is, encouragingly, of the same order as the model predictions.

In Models A and B the critical wavenumber started to increase as χ increased above $\chi = 1.25$ for both models. The critical wavenumber at $\chi = 1.5$ was $k_c = 62.0$ in Model A and $k_c = 51.8$ in Model B, which are both greater than k_c for the case of no light, $\chi = 0$. For comparison, the mean wavenumbers for $I = 4770$ lux in the experiments ranged between $9.72 < \tilde{k}_0 < 12.23$. The increase in \tilde{k}_0 appears to be linear in the experiments but the theory suggests a higher order polynomial or an exponential distribution for increases in k_c when χ is large. The critical Rayleigh number, R_c , also increased rapidly with increasing χ in both models, reaching 9.16×10^7 at $\chi = 1.5$ in Model A. For the values of χ used, we see a larger range for k_c values than was found experimentally for \tilde{k}_0 , where the theoretical range for critical wavenumber was $0 < k_c < 62.0$ for $0 \leq \chi \leq 1.5$ over all models, compared to an experimental range for dominant initial wavenumber of $7.33 < \tilde{k}_0 < 12.23$. For $\chi > 1.5$ for both models, tracing neutral curves became very difficult.

We conclude that the general trend of an initially decreasing and then increasing critical wavenumber, k_c , or dominant initial wavenumber, \tilde{k}_0 , in the experiments, as the phototaxis parameter, χ , or the light intensity, I , is increased from zero is found for both models A and B and the experimental data. A more detailed discussion of the issues involved in comparing theoretical and experimental results is presented in Section 4.7.

4.6 Predicting I_c from Experiments

The experimental trends for light from above and from below can be used to estimate the critical light intensity, I_c . We assume that qualitative changes of pattern wavelength with light intensity are due to the cells either all swimming towards the light, when $I < I_c$, or some swimming towards and some away, when $I > I_c$. For light from below, results in Section 4.4.4 indicate that this occurs when the wavelength reaches a minimum in the range $2020 < I < 2710$ lux, hence we estimate $2020 < I_c < 2710$ lux. A more precise estimate cannot be found because it is not clear what happens when I is between these two intensities. For light from above, the qualitative behavioural change occurs approximately when the wavelength reaches a maximum at $I = 1330$ lux. To calculate an estimate for the critical light intensity I_c we fit a linear curve to the two data points $I = 645$ lux and $I = 1330$ lux and separately for the remaining data points for experiments LA1, LA2 and LA3 in Section 4.4.5. We assume that the point at which these lines meet is the critical light intensity, I_c , since this is the point at which we assume the cells near the light

Experiment	Curve fit for $645 \leq I \leq 1330$ lux	Curve fit for $2020 \leq I \leq 4770$	I_c (lux)
LA1	$3.0 \times 10^{-5}I + 0.22$	$-2.5 \times 10^{-5}I + 0.27$	909
LA2	$4.7 \times 10^{-5}I + 0.18$	$-1.8 \times 10^{-5}I + 0.28$	1538
LA3	$7.3 \times 10^{-5}I + 0.17$	$-2.3 \times 10^{-5}I + 0.31$	1458

Table 4.9: Summary of curve fitting results when cells are illuminated with a white light from above for the three experiments in Section 4.4.5. Separate curves were fit for the data points $I = 645$ lux and $I = 1330$ lux and for the data points $I \geq 2020$ lux. The point at which the curves meet, for each experiment, is used as an estimate of I_c .

source change from swimming towards the light to swimming away from the light. This is summarized in Table 4.9, and gives a value for the critical light intensity of $I_c = 1302$ lux, averaged over the three light from above experiments.

The estimated critical light intensity for light from above is not within the range of the estimated I_c for light from below. To understand why this is, we consider the location of a cell's light-detecting apparatus. Currently, information on the location of the eye-spot which detects the signal of light intensity is controversial (discussed in Ruffer and Nultsch 1985 [149]), probably because it varies between different species and strains of *Chlamydomonas*. In the simple phototaxis response and orientation model of Hill and Vincent [64], it is assumed that for *C. nivalis* the eye-spot is located at an angle of 45° to the major axes of the cell. Hill and Vincent use their simple orientation model with a double beamed light source, where each light is at 45° on either side of the vertical, to show that the mean signal of light the cell receives over one rotation is smaller when the cell is swimming away from the light than if the cell were swimming towards the light with the eye-spot more inclined towards the vertical. If we also assume the eye-spot is at 45° to the major axis then if cells are upswimming on average, due to gravitaxis, then, using the results of Hill and Vincent, less light is received by cells over one rotation if the suspension is illuminated from below compared to being illuminated from above, due to shading of the eye-spot by the cell body. Thus, a higher light intensity would be required to induce negative phototaxis when illuminated from below compared to from above, and this could explain why I_c is higher when the culture illuminated from below. However, if the eye-spot is located approximately at the equator of the cell, as supported by experimental evidence (Gruber and Rosario 1974 [51] Ruffer and Nultsch 1985 [149]), this theory does not hold. In this case, we hypothesize that since the pyrenoid, in which dense starch is stored, and

other organelles are located towards the rear of the cell, the eye-spot is also more shaded when illuminated from below than from above, hence a higher critical light intensity is needed to cause negative phototaxis and to change the trend in initial wavelength.

4.7 Conclusions

In this chapter, techniques have been employed and developed to quantitatively record aspects of bioconvection patterns and to investigate initial wavelength as a function of concentration and light intensity in two orientations (illumination from above and below). To produce repeatable results using fully motile cells, a methodology for sub-culturing and concentrating the cells was used and methods of measuring depth and concentration were calibrated and implemented. The same depth, of approximately 0.306 cm, was used in all experiments (except the concentration experiment with light from below, Experiment CB). A novel, automated mixing method was used to control the initial concentration distribution from which patterns form. Using the image capture and analysis methods designed by Bees and Hill 1997 [8] and modified by Czirák *et al.* 2000 [26], a Fourier analysis was performed on each image and a suitable curve fitted to the wavenumber distribution in order to extract the most dominant wavenumber. The initial wavenumber (the first instability to grow) before any non-linear fully developed pattern appeared was of particular interest here, as these wavelengths can be compared to the trends found from the photo-gyrotactic models (as shown in Section 4.5). Trends were found in initial wavenumber as concentration or light intensity was varied. To our knowledge, this is the first study that repeats each experiment, both with the same cells and with different cells, allowing some simple statistical analysis of trends and significance of changes in average wavelength for varying experimental parameters to be explored. Using experimental data, an estimate for the light related parameter I_c was calculated, which curiously differed between illumination from above and below.

We found that for a set light intensity when the culture was illuminated either from above or below, the initial wavelength of the most dominant mode, λ_0 , decreased as concentration increased. This was also found by Bees and Hill [8], and we hypothesize that it is due to increased gyrotaxis for higher concentrations. We also found that cultures do not respond to changes in red light intensity, an observation which is consistent with observations by Nultsch *et al.* 1971 [125]. To our knowledge, we found the first statis-

tically significant trends for initial pattern wavelength as a function of light intensity for cultures illuminated from either above or below. In the case of illumination from below, the wavelength of the initial most unstable mode decreased as light intensity was increased from $I = 645$ lux to $I = 2020$ lux, then increased as intensity increased from 2020 lux to 2710 lux, and for $I \geq 2710$ lux the initial wavelength stayed approximately constant. For light from above, initial wavelength increased between 645 lux and 1330 lux and decreased as light intensity increased between 1330 lux and 4700 lux. These trends are explored in Sections 4.4.4 and 4.4.5 and were found to be repeatable using different cell cultures.

In Section 4.5 experimental results for light from above were compared to theoretical predictions from the photo-gyrotaxis models presented in Chapters 2 and 3. Since the phototaxis parameter χ cannot be directly related to light intensity I , and experiments use $R > R_c$, whereas numerics predict k_c at R_c (discussed in Section 4.5), it is the general trends as these parameters change that are of particular interest. Promising consistency between theoretically predicted critical wavenumbers, k_c , and experimentally observed dominant initial wavenumbers, \tilde{k}_0 , was found. Theoretical and experimental techniques both revealed the same basic trends, where k_c and \tilde{k}_0 decrease when I or χ is increased from zero, and then increase when $I > 1330$ lux experimentally, or $\chi > 1.25$ numerically. The observed critical wavenumbers were within a multiple of 4 of the predicted initial wavenumbers, with the critical Rayleigh number for $I = 0$ of the same order as the experimental Rayleigh number. Although the models and the experiments both show an increase in critical (or initial) wavenumber as light increases sufficiently, the models show a much more rapid increase in k_c when $I > I_c$, compared to the increase in \tilde{k}_0 . This could be because in our model each cell has the same critical light intensity and so will act in the same way once $I > I_c$, whereas if the critical light intensity varied between cells then this change would be smoothed out somewhat.

Comparisons between theoretical and experiment results are difficult and there are many limitations. On the experimental side, isolating the very first instability can be difficult, and there is often more than one significant initial instability. Although we have produced a consistent mixing methodology, there is still some vanishingly small effect of the mixing that causes the initial distribution of cells to be non-uniform, and fluid motions inevitably also remain and contribute to the onset of pattern formation. The Rayleigh number used in experiments also has to be greater than R_c , meaning we are comparing an initial dominant wavenumber \tilde{k}_0 from experiments that is above the neutral

curve to a theoretical critical wavenumber k_c lying on the neutral curve. On the theoretical side, the prediction of k_c comes from finding an equilibrium distribution and perturbing, but in section 4.5 we suggest that there would not be time for the formation of this equilibrium state. The aim of the work was to investigate the effects of light using these two independent methods, theory and experiment, without trying to match them together using data fitting or parameter extrapolation, and to this end we are satisfied that the main trends are consistent between methods.

Unlike previous studies, such as Bees and Hill [8] and Czirók *et al.* [26], the time evolution of the patterns over a sufficiently long period was not investigated because the long periods of time that would be needed to perform a large number of experimental runs on each culture would be unfeasible, since cell swimming and pattern formation may be affected by many hours of continuous experimentation. The effects of evaporation would also need to be considered if experiments were conducted over long periods. It would be interesting to investigate long term pattern formation for the photo-gyrotactic system in the future. Refinement of the trends around what appear to be the critical values of I should also be explored to try and provide a more accurate estimate of I_c for future use in models and elsewhere. Techniques to analyse other aspects of the patterns formed under different light intensities, such as their geometry, could also be developed to build up a thorough understanding of the system and the mechanisms at play during photo-gyrotactic bioconvection.

Chapter 5

Modelling hydrogen production in suspensions of *Chlamydomonas reinhardtii*.

Summary

In this chapter, a simple mechanistic model for the system of hydrogen production in the green algae species *Chlamydomonas reinhardtii* is constructed. The biology and biochemistry of the hydrogen producing system are discussed in detail and key modelling assumptions and hypotheses are outlined. A description of the model is presented, in which the model is built up component-wise, based on analysis of experimental evidence. A description of parameter estimation for each model parameter then follows, and a suitable non-dimensionalized is presented. Standard numerical model results are computed and discussed. In Chapter 6, we investigate varying the parameter values. We then optimize the total yield of hydrogen gas produced over a set time using different input functions of external sulphur.

5.1 Introduction

In this study, we construct a mathematical model of sulphur-deprived hydrogen production in *Chlamydomonas reinhardtii*. The focus of this work is to construct the model mechanistically, using our knowledge of the biology and biochemistry behind the reactions of the system, as oppose to indulging in fitting a model with many degrees of freedom

to data. In this way, we aim to produce a simple model that reflects the main physical mechanisms of the system, without including all details, with parameter values from independent experiments, where available. Although we aim for a simple model, it will be sufficiently complex to ensure all the key mechanisms are included. Before constructing the model, it is necessary to begin with a detailed discussion of the biological mechanisms and interplays that are fundamental to hydrogen production.

In this work, the term ‘system’ is used to describe a typical bio-reactor set-up, in which a concentration of cells are suspended in 1 litre of medium within a sealed container. The term ‘cell’ is used in descriptions of an individual organism.

5.1.1 Background

Although the ability of the unicellular microorganism *Chlamydomonas reinhardtii* to produce hydrogen gas has been known for over 60 years (Gaffron and Rubin, 1942 [37]) until recently it remained largely a biological curiosity due to the fact that the hydrogen producing iron-hydrogenase is highly sensitive to oxygen co-produced from the photosynthetic pathway (Ghirardi *et al.* 1997 and 2000 [39, 41]). The growing need for an environmentally friendly, renewable energy source has accelerated this area of research. Recently, Melis *et al.* 2000 [114] discovered a new two stage process where partial deactivation of oxygen evolving photosystem II (PSII) occurs in response to sulphur deprivation, hence separating oxygen and hydrogen production in time. It is this system that is modelled here, and to understand how it works we first consider the basic photosynthetic pathways and reactions.

Under normal conditions, PSII uses light energy to split water into oxygen, protons and electrons. The electrons are passed along the photosynthetic chain on the thylakoid membrane, running through proton pumps that pump protons into the enclosed thylakoid lumen, until they reach PSI where they are further energized by light and passed onto a ferredoxin complex. These electrons are then used to reduce NADP^+ to NADPH, an electron carrier that is used to transport electrons to the Calvin cycle, which fixes carbon dioxide. ATP is produced when the protons that have been pumped into the thylakoid lumen run through ATP synthetase. ATP is an energy form vital for cell survival and is also used in the Calvin cycle. The Calvin cycle, too, is essential for the survival of the cell, because it makes carbon skeletons used for growth and repair of cellular material. Protein is constructed via the Calvin cycle by combining these carbon skeletons with

internal sulphur. A detailed description of these process can be found in (Madigan *et al.* 2003 [107]). A very simple schematic diagram showing the main cellular process is shown in Figure 5.1.

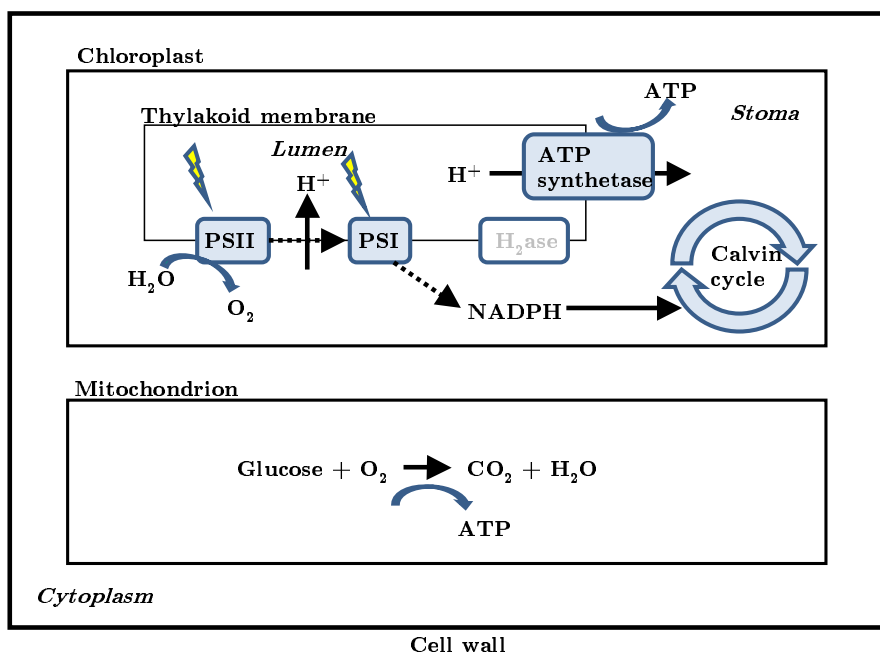


Figure 5.1: A schematic diagram showing the basic internal structure of a *C. reinhardtii* cell. For the labels, roman font indicates membranes (thylakoid, and those that enclose the chloroplast and mitochondrion) and italic font indicates interiors, such as the stroma and the cytoplasm. Dashed arrows indicated electron flow. The photosynthetic chain is located across the thylakoid membrane, enclosing the thylakoid lumen. Photosystem II (PSII) uses light energy to split water into protons, oxygen gas and electrons, that are passed along the photosynthetic chain. Concurrently, protons are pumped into the chloroplast lumen as the energized electrons run through proton pumps. These protons are then released through an ATP synthetase, generating usable energy in the form of ATP. Reductant NADPH is generated in a light-dependant step at PSI and is used in carbon fixation during the Calvin cycle. In aerobic respiration, glucose made via the Calvin cycle is oxidized to produce carbon dioxide and water and ATP is produced. Anaerobic respiration can occur to supplement aerobic respiration if necessary. This occurs through the break down of glucose without oxygen (glycolysis) in the cytoplasm of the cell. The hydrogenase is inactive under normal conditions.

During the water splitting process the reaction-centre D1 proteins in Photosystem II are damaged and need to be replaced (Mattoo *et al.* 1987 [110]). Sulphur is an essential

component of the D1 proteins, so in the absence of sulphur, D1 protein biosynthesis is impeded and the PSII repair cycle is blocked (Wykoff *et al.* 1998 [179]). Thus, the quantity of oxygen produced from PSII under these conditions is dramatically reduced, although production continues at a low level (Melis *et al.* 2000 [114]). Aerobic respiration and the activity of PSI, which is required for ATP generation and to energize electrons to pass to the appropriate electron sink (the Calvin cycle via NADPH, or the hydrogenase), are not directly affected by sulphur deprivation [16, 28, 114, 183]. After approximately 24 hours, the rate of oxygen produced from photosynthesis is less than the rate of oxygen used in respiration [41, 92, 114, 182]. In a sealed container, the cells then use up any remaining dissolved oxygen in the medium, and the ratio of respiration to photosynthesis is sufficient to ensure that the culture becomes anaerobic [41, 92, 114, 182]. The oxygen sensitive iron-hydrogenase enzyme on the thylakoid membrane is then expressed, and hydrogen gas is produced for approximately 100 hours in the light [90, 92, 114, 182, 183]. If sulphur is re-added to the culture when hydrogen production ends the cells can repair and return to normal; additional cycles of oxygen production under sulphur sufficiency and hydrogen production under sulphur-deprivation can then occur after a suitable recuperation time for cells (Ghirardi *et al.* 2000 [41]).

Recent research by various groups demonstrates that anaerobiosis alone is not sufficient for the cells to produce hydrogen gas: the Calvin cycle also has to be inactivated [156, 176, 182]. Under sulphur deprivation the protein Rubisco, which is a necessary enzyme in carbon fixation via the Calvin cycle and contains sulphur [107], is broken down and not synthesized; 60 hours after sulphur deprivation began Rubisco could not be detected in the suspension (White and Melis 2006 [176] and Zhang *et al.* 2002 [182]). Both White and Melis [176] and Zhang *et al.* [182] suggest that sulphur deprivation causes Rubisco breakdown, which disables the ability of the cells to use the Calvin cycle (via NADPH) as the electron sink for reductant (electrons) generated on the thylakoid membrane during photosynthesis. Thus an alternative electron sink must be used, as discussed below.

Under sulphur-deprived conditions (compare Figures 5.2 and 5.3) the cell is not able to make sufficient energy in the form of ATP using oxidative photosynthesis, due to a decline in PSII activity. Furthermore, the lack of oxygen produced by PSII in a sealed system causes a reduction in the rate of oxygenic respiration, hence less energy in the form of ATP can be produced than under normal conditions. When the cells become anaerobic they start a fermentative mechanism, where internal reserves of endogenous

substrate, such as starch and protein, are broken down to allow production of ATP and energy in the form of NADH (Happe *et al.* 2002 [55]). This is a less preferable process than oxygenic respiration and normal photosynthesis because energy production is less efficient, by an order of magnitude, and significant quantities of harmful reducing equivalents from fermentation may be produced [80, 107]. The catabolism of endogenous substrate during fermentation also causes the cells to change shape and shrink during hydrogen production (Zhang *et al.* 2002 [182]). Thus there is a metabolic switch between an aerobic state with photosynthetic growth and an anaerobic state characterized by fermentation, H₂ production and culture shrinkage (Hemschemeier *et al.* 2008 [58]).

The electrons acquired during fermentation enter the electron-transport chain by donation between PSII and PSI at the plastoquinone pool [38, 48, 162], and continue on the electron transport chain to PSI. These free electrons are harmful to the cells, since they can cause oxidative damage and, hence, need to be removed. During dark fermentation ethanol acts as an electron sink for the reducing equivalents produced, but ethanol is harmful to the cell (Kennedy *et al.* 1992 [80]). In the light, under sulphur deprivation, the partially active respiratory chain does not suffice as an electron sink, and neither does the Calvin cycle. To prevent the production of these harmful end products, the iron-hydrogenase acts as the major electron sink, by re-oxidizing potentially harmful electrons produced from both the PSII-dependent (via water splitting) and the PSII-independent (reducing agents from fermentation) pathways, which are transferred to the hydrogenase via the light dependant PSI pathway (Happe *et al.* 2002 [55], Fouchard *et al.* 2005 [36], Melis *et al.* 2002 [114]). Thus the hydrogenase produces H₂ gas in the light, which can leave the cell. In this way, hydrogen production saves the life of the cell, but does so at a cost because it uses protons from the thylakoid lumen to combine with electrons, decreasing the proton gradient across the thylakoid membrane required for ATP production (Happe *et al.* 2002 [55]).

In addition to this linear electron flow, cells can perform cyclic photophosphorylation, where electrons reach PSI and are cycled back to the plastoquinone pool to run through the electron transport chain again to order to increase ATP production. Whether this happens significantly during hydrogen production is still under debate [90, 93, 114]. Kruse *et al.* [93] find that inhibiting cyclic electron transport increases electron supply to the iron hydrogenase, since cyclic photophosphorylation competes with the hydrogenase for electrons, but we found no other quantitative data on how this affects hydrogen production.

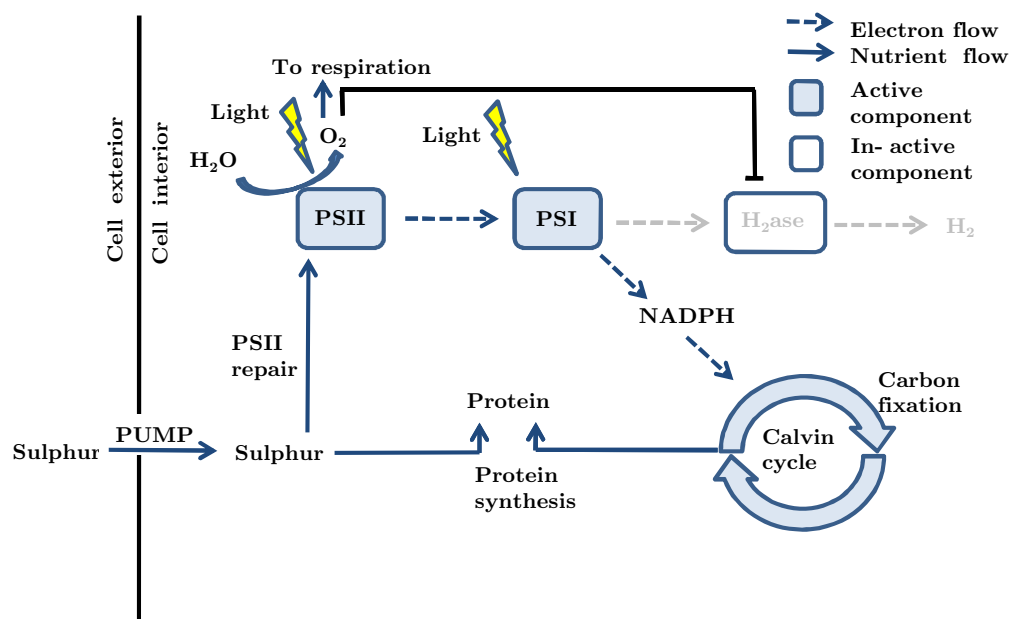


Figure 5.2: **Normal conditions.** Electron flow (dashed arrows) from PSII to PSI causes protons to be pumped into the thylakoid lumen for use in ATP synthetase. Sufficient sulphur levels allow maximal PSII repair and activity and oxygen produced from water splitting inhibits (thick black line) the activity of the iron-hydrogenase. Electrons are used to generate NADPH, which is used in the Calvin cycle for carbon fixation, and carbon skeletons can be combined with sulphur to produce protein. Light grey arrows and text indicate an inactive pathway or process.

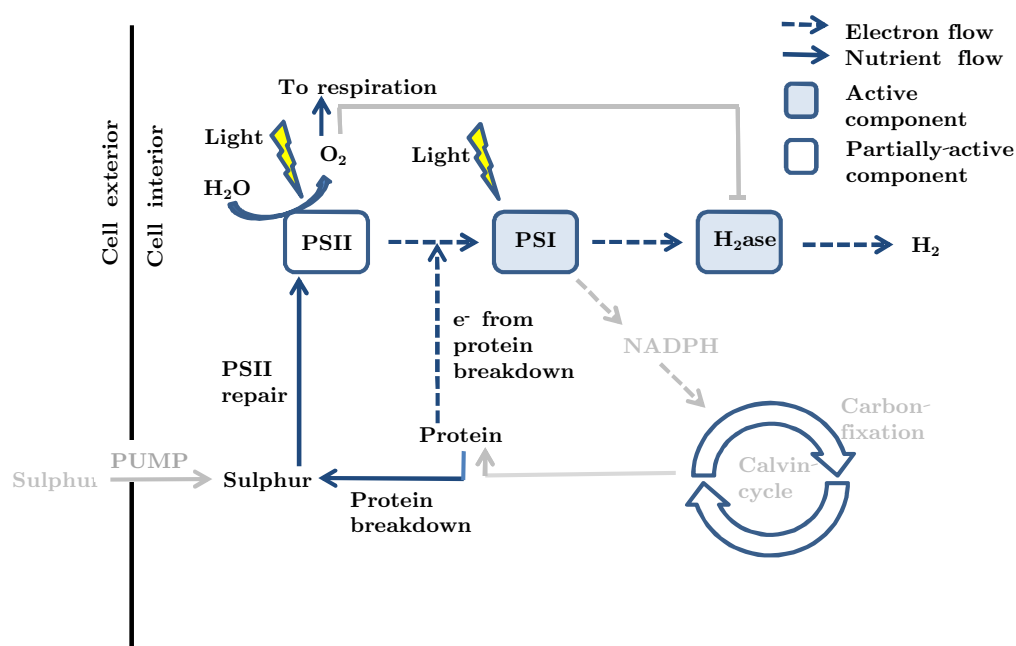


Figure 5.3: **Sulphur deprivation.** PSII activity decreases due to a lack of available internal sulphur. Protein is broken down, giving minimal quantities of sulphur, which are used in the repair of PSII, and electrons, which are donated to the photosynthetic pathway at the plastoquinone pool between PSII and PSI [38, 48, 162]. Due to low Calvin cycle activity, caused by Rubisco depletion, electrons are passed to the iron-hydrogenase under anaerobic conditions and hydrogen gas is evolved. Again, light grey arrows and text indicate an inactive pathway or process.

For this reason, we do not consider cyclic electron transport in this work.

What substrate, or combination of substrates, is catabolized during anaerobic fermentation is still under discussion. In Melis *et al.* [114] protein was thought to be the main, and maybe the only, provider of electrons, but later work showed the importance of starch in hydrogen production [139, 156, 182]. In fact, protein breakdown is two-fold: in addition to releasing electrons, protein also breaks down to release small amounts of bioorganic sulphur, which are used to repair PSII and allow the photosynthetic chain to run, albeit at a low level (Melis *et al.* 2000 [114]). This is essential for the cell, since it needs to keep photosynthesis active for ATP production, and it has been found that if PSII is not running at all, even a donation of electrons at the level of the plastoquinone pool cannot provide enough energy for the survival of the cell (Zhang *et al.* 2002 [182]). Starch production increases 8 – 10 fold in the initial stages of hydrogen production (Posewitz *et al.* 2004 [139]) and is subsequently used as a substrate for respiration (Fouchard *et al.* 2005 [36]). Many studies, such as Zhang *et al.* 2002 [182], show that both protein and starch are catabolized during H₂ production, but which is the main source of electrons, and what effect this catabolism has on other cellular activities, is still under investigation.

It is well documented that hydrogen production stops after around 120 – 140 hours of sulphur deprivation [90, 92, 114, 182, 183]. It is believed that hydrogen production ceases because the endogenous substrate available to the cell for catabolism is depleted; the cells have effectively used up as much of their internal reserves as possible (discussed in Melis [111]).

This relatively simple description seems appropriate to capture the main behaviour of the system. However, it should be noted that the dynamics are likely to be more complex. Much work is in progress to try to unravel these complex metabolic pathways [36, 59, 139, 156].

5.1.2 Challenges to commercial hydrogen production

Although the work of Melis and co-workers demonstrates dramatic improvements in hydrogen yield (previously hydrogen gas was only produced for a few seconds, Gaffron and Rubin [37]), the process still has problems that prevent commercial exploitation of green algae for hydrogen production. The total yield of gas per volume of cells is too low for commercial production, and is much lower than that which the photosynthetic oxygen generating capacity of the cell suggests (Melis 2002 [111]). The cells are very inefficient,

wasting up to 80% of the sunlight that they absorb, meaning they are not utilizing the resources available (Polle *et al.* 2002 [135]). In addition, there is a large downtime associated with the process due to sulphur-cycling between anaerobic sulphur-deprived hydrogen production and aerobic, sulphur-replete recovery periods (Ghirardi *et al.* 2000 [41]). This two stage hydrogen producing system is currently too expensive, in terms of both cost and land area (Melis 2002 [111], Melis 2007 [112])

Attempts to solve these problems using genetic engineering are currently underway. *C. reinhardtii* cells use chlorophyll antenna complexes to harvest light and transfer the light energy to the reactor centre of the chlorophyll for use in photosynthesis [107]. These antennae are large and absorb more light than can be used by the cell (Melis *et al.* 1998 [113], Polle *et al.* 2002 [135]). Thus, in a suspension of cells illuminated from above, the cells close to the surface absorb and waste a large proportion of the light (up to 95 %; Polle *et al.* 2003 [136]), while strongly attenuating the light received by cells deeper down and further from the light source [113, 121, 122]. This reduces photon use efficiencies and photosynthetic productivity, hence hydrogen production. Many studies have shown that truncating the chlorophyll antenna size (using mutants such as *tla1* isolated by Polle *et al.* [136]) creates a more even spread of light through a suspension layer, thus reducing the wastage of light (in terms of photons) and increasing the photosynthetic activity [12, 113, 135, 135]. Polle *et al.* [135] and Melis [111] suggests that this truncated antenna and increased photosynthetic activity efficiency could increase hydrogen production per volume of culture, since hydrogen production depends both on light and photosynthetically derived electrons. As yet, no work has demonstrated a positive impact of reduced chlorophyll antenna size on hydrogen production. Flynn *et al.* [33] are selecting mutants and engineering alga cells with a higher oxygen tolerance, in which case cells would be able to produce hydrogen gas perhaps even under aerobic conditions. Variations of the culture parameters are also being investigated to try and improve yield [88, 90–92, 167, 182]. Kosourov *et al.* 2002 [92] and Zhang *et al.* 2002 [182] investigate the effects of additions of minimal external sulphur concentrations to the media at $t = 0$ on hydrogen yields and start time. Kosourov *et al.* 2005 [89] investigate the effects of re-addition of external sulphates during hydrogen production. Kim *et al.* 2006 [88] and Hahn *et al.* 2004 [53] explore the effects of changing light intensity and Kosourov *et al.* 2003 [91] study the effects of pH on hydrogen production. Hydrogen production under different growth conditions are compared by Kosourov *et al.* [90].

5.1.3 Previous modelling methodologies

Various models of hydrogen production from green algae have been proposed. Jo *et al.* 2006 [72] published a statistical study in which Response Surface Methodology (RSM) (where a sequence of designed experiments is used to obtain an optimal response) was used to evaluate the relationship between a set of controllable experimental factors and observed responses. A second-order model was fitted to experimental data using a least-squares technique and a polynomial expression for specific growth rate as a function of ammonium, phosphate and sulfate and for hydrogen production rate as a function of ammonium, phosphate and pH were found. These functions were then optimized over parameter space and contour plots were used to show the optimal parameter values for maximal growth and hydrogen production. The maximum rate of hydrogen production was 1.22 times higher than Melis *et al.* [114] but 0.95 times lower than Kosourov *et al.* [92].

Jorquera *et al.* 2008 [75] constructed a mathematical model consisting of 17 differential equations with 34 rate constants and 77 kinetic orders to describe a metabolic map of the hydrogen production process, which included aspects such as photosynthetic components, fermentation processes and mitochondrial reactions. Due to difficulties in parameter estimation, order estimates were used. A sensitivity analysis of the overall response of the system to variations in parameters was conducted to analyse which parameters could increase hydrogen production, with the aim of identifying possible targets for protein engineering. In investigating parameter sensitivity, good qualitative agreement was found between the model and experimental results on pH [91] and sulphate re-addition [89], but not with results for hydrogenase expression in [91].

Park and Moon 2007 [126] constructed a discrete model of aspects of the photosynthetic processes involved in hydrogen production, which had multi-states dependent on discrete events such as sulphur deprivation. These discrete states have a similar effect to the switch functions used to describe qualitative changes of behaviour in the new model described in Section 5.2. Park and Moon's model consisted of 11 differential equations and numerical techniques were used for parameter estimation from experimental data and to find the optimal light intensity for hydrogen production (found as $238 \mu\text{E m}^{-2}\text{s}^{-1}$) [126].

5.1.4 Modelling methodology in this study

For the model for hydrogen production presented in this work, the system is simplified further (compared to previous models mentioned in Section 5.1.3), and we construct the

first mechanistic model of its kind from a careful consideration of the essential mechanisms for the whole system (methodology outline is discussed at the start of Section 5.1). The model needs to include sufficient detail to capture the main behavioural traits of the system. In particular, we need to model external sulphur transport into the cell [181] and the use and release of sulphur within the cell, along with the catabolism and synthesis of endogenous substrate [92]. Oxygen is modelled due to the sensitivity of the hydrogen producing iron-hydrogenase [39, 41], and culture growth and shrinkage are also shown to be significant during hydrogen production [182]. Finally, hydrogen gas produced clearly also needs to be modelled. Therefore, our model has six variables; using any less revealed inconsistencies between the model and experimental data. This mechanistic approach leads to fewer variables and fewer parameters than in Jo *et al.* [72], Jorquera *et al.* [75] and Park and Moon [126]. As in those models, parameter estimation and determining functional forms for this novel model are a considerable challenge. The objective here is to produce a model that exhibits the same qualitative trends in behaviour as the biological system and not try to refine parameter values to obtain quantitative agreement.

By constructing a mathematical model for hydrogen production, in tandem with experimental studies, we hope to be able to capture the main mechanistic features of the system and then use the model to make clear predictions that will help bio-fuel scientists and engineers to enhance yield and efficiency of the algal cultures. This work may help guide experimental studies and optimize experimentation time by giving focus to the experiments. Comparisons between model predictions and experimental results should be made. Agreement may lead to strategies for improving the viability of algal hydrogen production for commercialization. Disagreement will necessitate model refinements. The process of model construction also means we gain a thorough understanding of the interactions and behaviour of the system we are modelling.

5.1.5 Hypotheses

We aim to use the novel mechanistic model to test hypotheses suggested in the experimental work to see if the explanations given for the experimental data are fully self-consistent and sufficient to explain the trends in behaviour under different culture conditions. The hypotheses are as follows:

- **Hypothesis 1:** Increases in initial rates of H₂ production per mole of chlorophyll for values of initial external sulphur at $t = 0$ (denoted S_0) up to $S_0 = 25 \mu\text{M}$, when

compared to $S_0 = 0 \mu\text{M}$, are due to higher levels of residual PSII activity passing more electrons to the iron hydrogenase for hydrogen production (Kosourov *et al.* 2002 [92]).

- **Hypothesis 2:** Decreases in initial specific rates of hydrogen production per mole of chlorophyll for initial external sulphur concentrations for $S_0 = 25 \mu\text{M}$ and above in [92] and $S_0 = 50 \mu\text{M}$ and above in [182] are due to increased light limitation caused by increased cell volume fraction (Kosourov *et al.* 2002 [92], Zhang *et al.* 2000 [182]).
- **Hypothesis 3:** When initial sulphur concentration is $S_0 = 50 \mu\text{M}$ the yield of hydrogen gas increases overall but the rate of hydrogen production per cell decreases due to light limitation, implying that increased hydrogen yield for $S_0 = 50 \mu\text{M}$ is due to there being more cells to produce the hydrogen (Zhang *et al.* 2000 [182]).
- **Hypothesis 4:** There is a mid-range of light intensities ($60\text{--}200 \mu\text{ E m}^{-2} \text{ s}^{-1}$) which cause an earlier onset of hydrogen production (compared to the case $60 \mu\text{ E m}^{-2} \text{ s}^{-1}$) due to faster sulfate consumption (caused by increased photo-damage), resulting in a prolonged period of hydrogen production. Increased chlorophyll concentration for light intensities close to $200 \mu\text{ E m}^{-2} \text{ s}^{-1}$ means that more electrons are released and this, together with the prolonged period of production, creates higher yields of hydrogen gas as light is increased from 60 to $200 \mu\text{ E m}^{-2} \text{ s}^{-1}$ (Kim *et al.* 2006 [88]).
- **Hypothesis 5:** Above a critical light intensity, between $200\text{--}300 \mu\text{ E m}^{-2} \text{ s}^{-1}$, the rate of PSII photo-damage is increased yet further and chlorophyll decomposition happens rapidly. This now decreases the overall yield of hydrogen gas, so that total hydrogen yield over a set time period saturates as light increases beyond the critical light intensity. Thus the critical light intensity is optimal for hydrogen production over a set period. (Kim *et al.* 2006 [88]).

These hypotheses will be discussed in Section 5.6 and Chapter 6 as and when these issues arise in the model results.

In this study, we first discuss the modelling assumptions before building up the model component-wise. We then present a discussion of parameter measurement and estimation. The model is solved numerically and model results are compared to published experimental studies. In Chapter 6, parameter sensitivity is investigated, and the results of this are used to make some predictions for improving yields of hydrogen gas. Finally, we test novel strategies for controlled sulphur titration, with the aim of improving yield, continuity and ease of application of the cycling of cultures between the sulphur-replete, photosynthetic aerobic phase and the sulphur-deprived, hydrogen producing, fermentative anaerobic phase. We conclude, in Section 6.3, with a discussion of the work and ideas for further study.

5.2 Model construction

Since this work focuses on building a simple rational model for a very complex system, there are naturally aspects that will not be included. We aim not to model the complete system but to produce a rational model for the main mechanistic features.

The model consists of a set of differential equations to explore what recent research suggests are the core-components of the H_2 producing system. Here the model is constructed component-wise to provide a clear statement of our assumptions. We model the metabolites sulphur, s , protein, p , and oxygen, ω , as concentrations in units of micromolar, μM , and model hydrogen gas in units of millimeter of gas produced per litre of culture. Cell division and size are modelled together as cell volume fraction, denoted Λ . This avoids explicitly modelling the effects of sulphur-deprivation on cell division, as well as changes in individual cell shape and size. To construct the model we consider the total amounts of these substrates per volume of culture, so we use $s\Lambda$, $p\Lambda$ and so on.

Figure 5.4 shows a simple schematic diagram of how the system has been modelled. Solid arrows represent a transfer of mass and dashed arrows show an effect on the receiving variable (for example, we say that oxygen has an effect on hydrogen production, but not that oxygen *becomes* hydrogen).

5.2.1 Main modelling assumptions

To begin, we assume that we have an asynchronous cell population, where the cells used in the bio-reactor are first grown under continuous illumination and, hence, are a variety

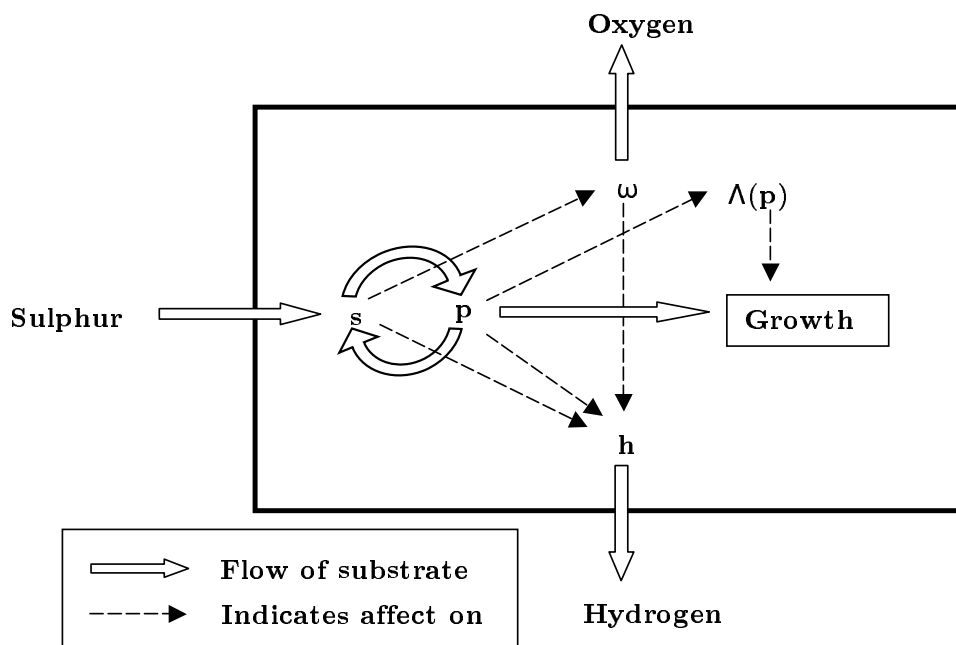


Figure 5.4: A simple schematic diagram of the variables in the novel mechanistic model, showing the interactions between them. The box indicates the system, consisting of a suspension of cells in a sealed container. Oxygen diffuses out of the cell and is either lost from the suspension under super-saturation, or used up in respiration (not shown). Hydrogen gas bubbles off and leaves the cell and is collected in a measuring device. Sulphur is used to make PSII which is damaged during oxygen release, hence sulphur is lost from the model when used in PSII repair. Protein is produced from carbon skeletons produced via the Calvin cycle, which in turn requires the light-dependent activity of PSII to provide NADPH and ATP. PSI is intrinsic to the system and is not modelled explicitly, so is not included in this diagram.

of randomly selected sizes and shapes at time $t = 0$. This is so that comparisons can be made with experimental data in [92, 114, 182], and seems reasonable since we model total cell volume fraction instead of individual cells. For simplicity, we model the bio-reactor as a cubical container, filled with 1 L of culture. For comparison with the bio-reactor used by Kosourov *et al.* [92], we use two-sided illumination from the side at a light intensity of $300 \mu\text{E m}^{-2} \text{s}^{-1}$. Although the shape of our bio-reactor is not identical to that used in Kosourov *et al.* [92], this is a first step in making a rational, realistic model. Initially, we assume that the culture is instantaneously and completely mixed, so that each cell receives the average light as though it samples over all space at each time, t . This is used for simplicity in the light function. In the basic model, we do not consider the effects of cell swimming, a non-uniform distribution of cells, or flow occurring in the bio-reactor. We also assume that the bio-reactor has been purged of oxygen before the start of the experiment. This simplifies the initial condition of oxygen, which would otherwise be difficult to quantify.

We assume that protons are not limited outside of the thylakoid lumen, since protons are present in water (at pH 7.0, water contains 10^{-7}M protons, and at equilibrium $\text{H}_2\text{O} \rightleftharpoons \text{H}^+ + \text{OH}^-$). The suspension is sealed from the start and there is no external source of oxygen. This is essential for hydrogen production due to the sensitivity of the hydrogenase to oxygen. Additionally, we stipulate that oxygen can leave the suspension when supersaturation occurs and this gas is collected and so cannot re-enter the suspension at a later time. The cell membrane is thin, hence we assume the timescale for oxygen diffusion into and out of the cells is small, allowing us to model internal and external oxygen concentrations as the same and not distinguish between the two. This is different to the way we model sulphur, as external and internal sulphur separately (S and s , respectively), because sulphur is present in large, charged molecules (sulphates) that are actively, rather than passively, transported into the cell via an energy dependant process (Yildiz *et al.* 1994 [181]). Spatial compartmentalization within the cell is not considered.

A key assumption in this model is that the only endogenous substrate catabolized to donate electrons to the hydrogen pathway is protein, and starch is not modelled explicitly. We assume that the cells have sufficient starch to maintain anaerobiosis under sulphur deprivation (through the oxygen scavenging by aerobic respiration, which uses starch in the form of glucose). Although this is a simplification of the system, it is used to de-couple the activity of photosynthesis from the carbon cycle, glucose pathways and fermentative

respiration as far as possible. Including these pathways would make the model considerably more complex and would not enhance the understanding of the main mechanisms sufficiently to warrant inclusion. The assumption seems reasonable, since there is evidence of sufficient protein breakdown to provide the source of reductant for the hydrogenase pathways (Melis *et al.* 2000 [114]). It is also protein, not starch, that provides small amounts of sulphur to keep PSII running at a low level. A discussion of the possible effects of including starch is presented in Chapter 6. Protein is modelled as total protein in the cell due to insufficient data on concentrations of specific proteins. Internal sulphur is modelled as free sulphur within the cell that is readily available for use. Finally, we assume that, except for sulphur, the culture has all the nutrients it needs to grow, divide and produce hydrogen gas.

Additional modelling assumptions are discussed in the following sections as and when required.

5.2.2 Internal concentrations

We start by considering the internal concentrations of protein and sulphur within the cell. For both these concentrations we expect to have depletion and production. The term for internal sulphur is

$$\begin{aligned} \frac{d(s\Lambda)}{dt} &= \text{uptake}(S, s, \Lambda) - \text{repair}(s, \Lambda, L(\Lambda)) + \beta \times \text{protein breakdown}(p, \omega, \Lambda) \\ &- \beta \times \text{protein production}(s, \Lambda, L(\Lambda)), \end{aligned} \quad (5.1)$$

where s is internal sulphur, S is external sulphur and p is protein, all measured in micromolar, μM . Λ cell volume fraction, in non-dimensional units, and $L(\Lambda)$ is a yet-to-be specified light function which is dependent on cell volume fraction (see Section 5.2.6).

Explaining this expression term by term, an obvious gain of internal sulphur comes from sulphur taken into the cell from the medium in an active energy dependent process. Yildez *et al.* [181] find that the rate of uptake of sulphur by the cell, in the form of sulphates, depends on the amount of sulphate available and the total internal sulphur in the cell; uptake rate varied for cells that were starved of sulphur prior to incubation compared with normal, non-starved cells. We have

$$\text{uptake}(S, s, \Lambda) = \Lambda \frac{\alpha(s)S}{\beta(s) + S}, \quad (5.2)$$

where $\alpha(s)$ and $\beta(s)$ are functions for the maximum uptake rate and the value of the substrate concentration when the rate is half of its maximum, respectively. The form of

equation 5.2 is chosen because the data in Yildez *et al.* [181] clearly suggest that for a set value of internal sulphur, where α and β are constant, the uptake function has Michaelis-Menten form: uptake is almost constant when S is large, and acts like $\frac{1}{\beta}$ when S is small. To account for the changes in the maximum uptake rate and corresponding substrate concentration as internal sulphur varies, which was found by [181], α and β are modelled as functions of internal s .

If we make the assumption that in the Yildez *et al.* [181] data the starved cells have an internal sulphur concentration of $s = 0$ and the non-starved cells have the normal amount of internal sulphur, defined as s_0 , then on the basis of the existing data the following function forms fit the data in [181] well:

$$\alpha(s) = a \exp\left(-\frac{Gs}{s_0}\right), \quad (5.3)$$

$$\beta(s) = b_1 + b_2 \left(\frac{s}{s_0}\right). \quad (5.4)$$

In the expression for $\alpha(s)$, equation 5.3, a is the maximum uptake rate of external sulphur. Yildiz *et al.* [181] show that this maximum rate is 206 fmol s⁻¹ per 10⁵ cells, and this is obtained when the cells have been starved of sulphur, so $s = 0$. We take this as the value for a , on converting the units to μM per hour (per cell volume fraction), hence $a = 14,800 \mu\text{M h}^{-1}$. The maximum rate of uptake of external sulphur for non-starved cells is $\alpha = 20.8 \text{ fmol s}^{-1}$ per 10⁵ cells in Yildez *et al.* [181]. If we assume that internal sulphur s has not changed from s_0 at this point then $s = s_0$, so $\alpha(s_0) = 20.8 \text{ fmol s}^{-1}$ per 10⁵ and, using this with the calculated value of a , equation 5.3 gives

$$\alpha(s_0) = 20.8 \text{ fmol s}^{-1} \text{ per } 10^5 \text{ cells} = a \exp(-G), \text{ hence } G = \ln(9.90) = 2.29. \quad (5.5)$$

When $s = s_0$ for non-starved cells in Yildiz *et al.* [181], the substrate concentration at which the uptake rate is half of the maximum, defined here as the function $\beta(s)$, was 16.7 μM , so that $\beta(s = s_0) = 16.7 \mu\text{M}$. For the starved cell, where we assume that they have no internal sulphur, $s = s_0 = 0$, this value of substrate was $\beta(s = 0) = 2.2 \mu\text{M}$. Fitting the linear curve for substrate concentration against internal sulphur, $\beta(s)$ in equation 5.4, to these two data points for $s = 0$, $\beta = 2.2 \mu\text{M}$ and $s = s_0$, $\beta = 16.7 \mu\text{M}$ gives $b_1 = 2.2 \mu\text{M}$ and $b_2 = 14.5$.

Thus the uptake function in equation 5.1 is

$$\text{uptake}(S, s, \Lambda) = a\Lambda \frac{\exp\left(-\frac{Gs}{s_0}\right) S}{b_1 + \frac{b_2}{s_0} s + S}. \quad (5.6)$$

Cell volume fraction Λ is included in equation 5.6 because more cells will take up more sulphur.

Sulphur is used in the repair of photosystem II, with PSII activity depending ‘strictly on sulphur availability’ (Zhang *et al.* 2002 [182]), thus we account for this repair as a loss term in the equation for internal sulphur (the second term on the right hand side in equation 5.1). We assume that damage to PSII is proportional to light intensity (since rate of PSII activity is proportional to light intensity), so the demand for sulphur for use in repair is also linearly dependent on light. The rate of repair of PSII must also be proportional to the amount of sulphur available. We use a Heaviside function to denote that above a critical level of sulphur (in normal, sulphur-replete conditions), the repair occurs at a constant rate, $k_1 s_0$. We chose the critical level to be the normal sulphur concentration of a cell, s_0 . A ramp function can be defined as $R(s, s_0) = sH(s_0 - s) + s_0H(s - s_0)$, where H denotes a Heaviside function, and is illustrated in Figure 5.5. Since equation 5.1 is for total sulphur for all cells in the suspension, we multiply by Λ (as more cells require more sulphur for repair). Hence,

$$\text{repair}(s, \Lambda, L(\Lambda)) = -k_1 \Lambda (sH_{PSII}(s_0 - s) + s_0H_{PSII}(s - s_0))L(\Lambda), \quad (5.7)$$

where k_1 is the rate constant for this process. H_{name} is used to describe a Heaviside function that models any arbitrary process, ‘name’, which is ‘PSII’ in this case.

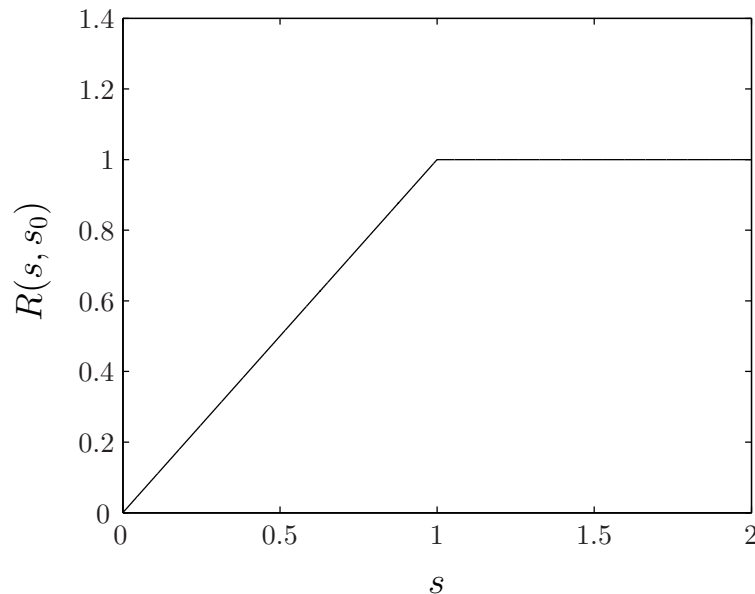


Figure 5.5: An example of a ramp function $R(s, s_0) = sH_1(s_0 - s) + s_0H(s - s_0)$, where $s_0 = 1.0$, used to model the rate of sulphur used to repair PSII in equation 5.7.

There is significant interaction between protein and sulphur within the cell. Proteins consist of chains of amino acid sequences, two of which (cysteine and methionine) each contain one mole of sulphur per mole of amino acid. Protein acts as a store of sulphur molecules, so that when sulphur is plentiful some is stored in protein. In sulphur-deprived or anoxic conditions protein can be broken down to release sulphur. We need two terms in the sulphur equation to describe this: a loss term for the process of sulphur storage in protein and a gain term for sulphur released by the catabolism of protein during anaerobic fermentation. These complete equation 5.1, where β indicates that one mole of protein contains β moles of sulphur. This breakdown and production of protein also provides two terms in the protein equation, so that

$$\frac{d(p\Lambda)}{dt} = -\text{protein breakdown}(p, \omega, \Lambda) + \text{protein production}(s, \Lambda, L(\Lambda)). \quad (5.8)$$

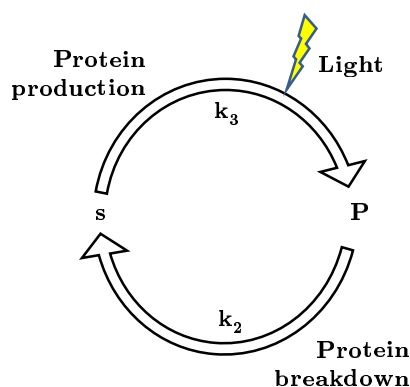


Figure 5.6: A simple schematic diagram to show the cyclic relationship between protein and sulphur. Protein is produced at a rate k_3 and broken down at a rate k_2 (omitting the conversion factor β). Note that sulphur is not directly made into protein - it combines with carbon skeletons made from the Calvin cycle via NADPH, which is produced from light dependent photosynthesis.

We assume that protein breakdown depends on both how much protein is available and on oxygen concentration, because protein breakdown (via fermentation) is an emergency survival response to adverse, anaerobic conditions (Happe *et al.* 2002 [55]). Here, we model this using a switch function such that protein breakdown only occurs when oxygen is below the critical level ω_p . We also stipulate that there is a base level of protein, denoted p_r , necessary for the survival of the cell, and that the base level concentration cannot be broken

down (shown experimentally in Kosourov *et al.* 2002 [92], where hydrogen production stops whilst some cellular protein is still present). To model this we use $(p - p_r)$ in all the protein breakdown terms to imply that when $p = p_r$ no more protein is available for breakdown. If $p = p_r$ in equation 5.12 then the only term that could potentially lead to $p < p_r$ is the term due to changes in protein concentration as the cell volume fraction varies (the term for protein production is always positive). However, since p_r is less than the amount of protein below which the cell volume fraction shrinks at a constant rate ($p_r < p_1$; Table 5.1), then when $p = p_r$, $-\frac{d\Lambda}{dt} > 0$ and there are no sink terms in equation 5.12. Thus protein is bounded below by p_r and $p \geq p_r$ always. For simplicity, we propose the linear relationship

$$\text{protein breakdown}(p, \omega, \Lambda) = k_2(p - p_r)\Lambda H_{Ferment}(\omega_p - \omega), \quad (5.9)$$

where k_2 is the rate constant for protein breakdown.

For the protein production term, we assume a linear dependence on the amount of sulphur available for the cell to convert into protein, relative to the normal amount of sulphur in the cell, s_0 : protein is made at a rate $\frac{k_3 s}{s_0}$. Protein production is dependent on carbon skeletons produced from the Calvin cycle. The Calvin cycle, in turn, needs NADPH in order to run, and NADPH is created from the light-dependent electron transfer that occurs during photosynthesis. For this reason, we also stipulate the protein production is light-dependent and we assume that the effect of light on this chain of events is linear.

The electrons running through the photosystems are potentially harmful to the cells and so must be employed [107]. Under normal conditions, electrons are donated to NADPH which is used in the Calvin cycle. However, under sulphur deprivation, Rubisco, which is a crucial enzyme necessary for the Calvin cycle to run, is broken down, and the Calvin cycle can no longer act as an electron sink (White and Melis 2006 [176]). Hence, under sulphur deprivation, the hydrogenase, in anaerobic conditions, or ethanol production otherwise, will remove the electrons (Happe *et al.* 2002 [55]). We assume that the cell can only use one of these pathways at a time, as shown in Figure 5.7. In reality, the cell may use a combination if conditions allow (i.e. anaerobic and Rubisco replete). This assumption is realized by using a switch function $H_{Calvin}(s - s_1)$ to stipulate that protein is only produced when electrons are donated to NADPH and the Calvin cycle is on (as protein needs carbon skeletons produced by the Calvin cycle), i.e. when the other two electron sinks are off. The switch seems a reasonable way of closing the system and allows us to compute a simple model without including details of the Calvin cycle, which would further complicate

the system. This switch depends on sulphur, since a lack of sulphur causes Rubisco to breakdown and not be synthesized, hence deactivating the Calvin cycle [176, 182]. We stipulate that the Calvin cycle is active when internal sulphur concentration is greater than a critical level s_1 , $s > s_1$. We assume that sufficient Rubisco breakdown to stop the Calvin cycle happens within the timescale for sulphur changing from the normal amount of sulphur in the cell, s_0 , to the critical switch level, s_1 . Hence,

$$\text{protein production}(s, \Lambda, L(\Lambda)) = \frac{k_3 s \Lambda}{s_0} H_{Calvin}(s - s_1) L(\Lambda). \quad (5.10)$$

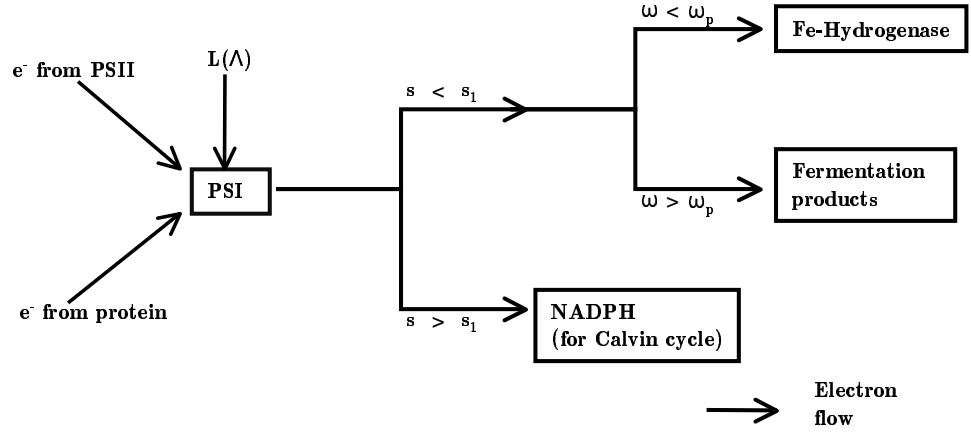


Figure 5.7: A simple schematic diagram of the transport of electron flow from photosystem I, via electrons donated from PSII and from protein breakdown, to the final location. Where the electrons end up is decided by the oxygen and sulphur switches, as shown.

Separating the differentials on the left hand sides of equations 5.1 and 5.8 and substituting in equations 5.6, 5.7, 5.9 and 5.10 gives the rate of change of internal sulphur concentration,

$$\begin{aligned} \frac{ds}{dt} = & a \frac{\exp\left(-\frac{Gs}{s_0}\right) S}{b_1 + \frac{b_2}{s_0} s + S} - k_1 (s H_{PSII}(s_0 - s) + s_0 H_{PSII}(s - s_0)) L(\Lambda) \\ & + \beta k_2 (p - p_r) H_{Ferment}(\omega_p - \omega) - \frac{\beta k_3}{s_0} s H_{Calvin}(s - s_1) L(\Lambda) - \frac{s}{\Lambda} \frac{d\Lambda}{dt}, \end{aligned} \quad (5.11)$$

and the equation for internal protein concentration as

$$\frac{dp}{dt} = -k_2 (p - p_r) H_{Ferment}(\omega_p - \omega) + \frac{k_3}{s_0} s H_{Calvin}(s - s_1) L(\Lambda) - \frac{p}{\Lambda} \frac{d\Lambda}{dt}. \quad (5.12)$$

The last terms in equation 5.11 and equation 5.12 are the terms for cell growth and division.

5.2.3 External sulphur concentration

The equation for the rate of change of external sulphur will consist of two terms: the sulphur uptake by the cells from equation 5.6 and some arbitrary input of external sulphur as a function of time, $\text{INPUT}(S, h, \frac{dh}{dt}, t) = I(S, h, \frac{dh}{dt}, t)$. Hence,

$$\frac{d(S(1 - \Lambda))}{dt} = -\text{uptake}(S, s, \Lambda) + I\left(S, h, \frac{dh}{dt}, t\right). \quad (5.13)$$

We use $S(1 - \Lambda)$ because we consider sulphur in the solution, not in the cells. Expanding and rearranging gives

$$\frac{dS}{dt} = -\frac{1}{1 - \Lambda}\text{uptake}(S, s, \Lambda) + \frac{S}{1 - \Lambda}\frac{d\Lambda}{dt} + \frac{I(S, h, \frac{dh}{dt}, t)}{1 - \Lambda}. \quad (5.14)$$

The uptake function is given in equation 5.6 and, hence,

$$\frac{dS}{dt} = -\frac{a\Lambda}{1 - \Lambda}\frac{\exp\left(-\frac{Gs}{s_0}\right)S}{b_1 + \frac{b_2}{s_0}s + S} + \frac{S}{1 - \Lambda}\frac{d\Lambda}{dt} + \frac{I(S, h, \frac{dh}{dt}, t)}{1 - \Lambda}, \quad (5.15)$$

where the input function, $I(S, h, \frac{dh}{dt}, t)$, will be specified in Chapter 6.

5.2.4 Oxygen concentration

One of the key aspects of this model is that we treat internal and external oxygen concentrations as the same, denoted ω , as discussed in Section 5.2.1. During normal cellular photosynthesis PSII produces oxygen, some of which is consumed by respiration in the mitochondrion. Therefore, a simple equation for the change in oxygen concentration is

$$\frac{d\omega}{dt} = \text{photosynthesis}(s, \Lambda, L(\Lambda)) - \text{respiration}(\omega, \Lambda) - \text{loss}(\omega) \quad (5.16)$$

The loss term will be explained below. Oxygen is produced by photosystem II during photosynthesis, where water is split to produce protons, electrons and oxygen, so that



As previously discussed, under sulphur limited conditions this water splitting reaction slows down due to a lack of sulphur for the protein biosynthesis needed to repair the PSII complex. Therefore, we model oxygen produced from photosynthesis as dependent on how much sulphur is available for repair, and we use a simple linear function form for this. This has the same form as the repair of PSII function in equation 5.7, since they model different aspects of the same process (sulphur used in repair compared to oxygen produced

from that repair), so we also use a heaviside function to denote that under sulphur-replete conditions, above a critical level of sulphur, s_0 , oxygen is produced from PSII at a constant rate k_6 . When $s < s_0$, oxygen is produced at a rate proportional to the amount of sulphur in the cell relative to the normal amount, $\frac{s}{s_0}$. Clearly, photosynthesis also depends on light, hence

$$\text{photosynthesis}(s, \Lambda, L(\Lambda)) = k_6 \Lambda \left(\frac{s}{s_0} H_{PSII}(s_0 - s) + H_{PSII}(s - s_0) \right) L(\Lambda) \quad (5.18)$$

The term is multiplied by Λ since the amount of oxygen produced scales with the quantity of cells

Respiration remains relatively unaffected by sulphur deprivation, at least for early times (the rate of oxygen use does not decrease significantly in the first 70 hours, Melis *et al.* [114]). We assume that respiration is not affected by sulphur deprivation and its activity depends only on how much oxygen is available for use. As previously discussed in Section 5.2.1, in doing this we are assuming that respiration always has sufficient glucose and carbon dioxide to scavenge any remaining oxygen. We use the same form of the equation as in photosynthesis, so that under normal oxygen conditions, $\omega > \omega_1$, oxygenic respiration is constant, and for ω below ω_1 respiration levels decrease. Hence,

$$\text{respiration}(\omega) = k_5 [\omega H_{Resp}(\omega_1 - \omega) + \omega_1 H_{Resp}(\omega - \omega_1)] \Lambda. \quad (5.19)$$

The H_2 producing system must be sealed to prevent atmospheric O_2 entering, which would stop the hydrogenase functioning. However, O_2 gas can leave the system via the pipe that collects the H_2 gas, so that when the culture has become saturated with oxygen, oxygen will be forced to leave. Thus we also need a loss term to ensure a realistic saturation behaviour in the oxygen balance equation. We use a term that dictates that above the saturation value of oxygen in water, χ , oxygen will leave at a rate v_{O_2} , and we cap the term using a switch function so that oxygen cannot re-enter the system. Hence,

$$\text{loss}(\omega) = v_{O_2} (\omega - \chi) H_{Loss}(\omega - \chi). \quad (5.20)$$

Thus, the full expression for the oxygen balance reads:

$$\begin{aligned} \frac{d\omega}{dt} &= k_6 \Lambda \left(\frac{s}{s_0} H_{PSII}(s_0 - s) + H_{PSII}(s - s_0) \right) L(\Lambda) \\ &- k_5 \Lambda [\omega H_{Resp}(\omega_1 - \omega) + \omega_1 H_{Resp}(\omega - \omega_1)] - v_{O_2} (\omega - \chi) H_{Loss}(\omega - \chi). \end{aligned} \quad (5.21)$$

5.2.5 Growth and decay of cell volume fraction

Under normal, sulphur-replete conditions a culture of cells will grow and divide in the light. It has also been found that in the aerobic stage of sulphur deprivation, before hydrogen is produced, some cellular growth and division occurs (Kosourov *et al.* 2002 [92] and Melis *et al.* 2000 [114]. Zhang *et al.* [183]) show that under sulphur deprivation cell division is limited but cellular growth occurs, causing the cells to change from ellipsoidal to large spheres in the aerobic phase. They also show that during hydrogen production the cells shrink and become smaller spheres, caused by the substantial catabolism of internal substrates. Clearly these changes in cell number and cell volume should be included in a rational model of hydrogen production. We do not model cell division and cell growth explicitly. Rather, we model cell volume fraction defined by

$$\Lambda = \frac{NV_{\text{cell}}}{V_{\text{container}}}, \quad (5.22)$$

where N is the number of cells, V_{cell} is the volume of one cell and $V_{\text{container}}$ is the volume of the container.

Growth occurs when carbon skeletons produced by the Calvin cycle are used in constructing proteins, glucose and cellular material. Protein production also requires sulphur. We work with the hypothesis that carbon skeletons produced by the Calvin cycle, through NADPH production by photosynthesis, combine with available sulphur to make cellular proteins that are used for cell growth and division [107]. Hence, we model growth as dependant on protein concentration. Since protein production is a function of light intensity in equation 5.10, and since growth is a function of protein in equation 5.24, then growth depends indirectly on light intensity. There is also a dependance on Λ , since growth and division depend on the current cell volume fraction:

$$\frac{d\Lambda}{dt} = \text{growth and decay}(p, \Lambda). \quad (5.23)$$

At this stage there are many different functional forms we could chose to represent the growth and decay function. We could use a combination of heaviside functions, or construct a smooth version of this function. For simplicity and consistency with the other functions in the model, we construct a piecewise linear function out of Heaviside functions, such that

$$\begin{aligned} \text{growth and decay}(p, \Lambda) = & \Lambda [r_{\text{exp}}H_{G2}(p - p_2) + H_{G2}(p_2 - p)H_{G1}(p - p_1)] \\ & \times c_1(p - p_0) - r_{\text{decay}}H_{G1}(p_1 - p)]. \end{aligned} \quad (5.24)$$

In equation 5.24, r_{exp} is the maximum growth rate, r_{decay} is the maximum decay rate, p_2 the protein concentration required for constant growth, p_1 the protein concentration below which the cells shrink at a constant rate, p_0 is the protein concentration when growth rate is zero and c_1 is the gradient of the linear part of the function. If we calculate c_1 we can write equation 5.24 as

$$\begin{aligned} \text{Growth and decay}(p, \Lambda) = & \Lambda [r_{exp}H_{G2}(p - p_2) \\ & + \frac{r_{exp}(p - p_0)}{(p_2 - p_0)}H_{G2}(p_2 - p)H_{G1}(p - p_1) - r_{decay}H_{G1}(p_1 - p)]. \end{aligned} \quad (5.25)$$

We choose this function so that growth/decay rate are constant above/below critical levels of protein and there is some linear transition between these two states, as data in Kosourov *et al.* 2002 [92] suggest (see Figure 5.8). This significantly differs from the usual models

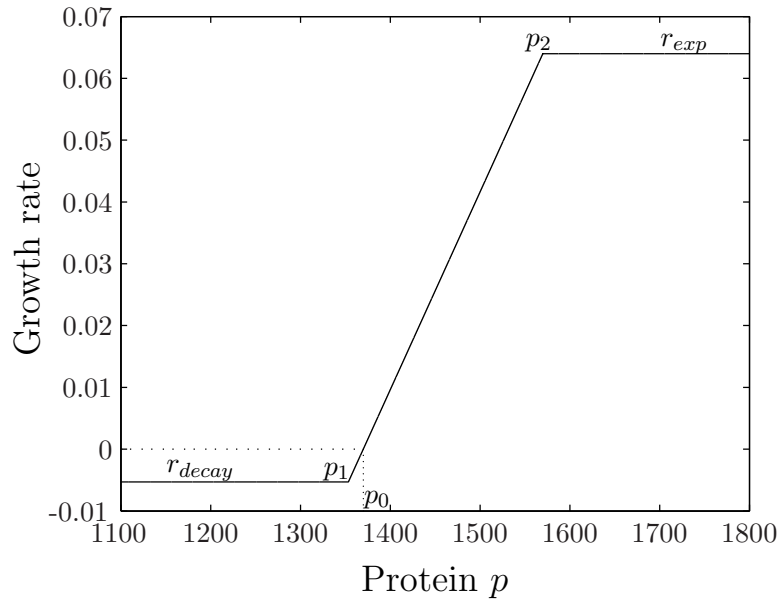


Figure 5.8: The function for growth dependent on protein, shown with the standard parameter values in Table 5.1

of algae or bacteria growth, where a logarithmic growth phase is followed by a stationary phase, since we want to include the effects of culture shrinkage as well as growth.

A smooth version of equation 5.25 could be

$$\text{growth and decay}(p, \Lambda) = \frac{r_{exp}(p^n - p_0^n)}{p_h^n + p^n}. \quad (5.26)$$

This function form was tried and we found that it does not make a considerable difference to the model, hence we use the piecewise approach for consistency with other modelling aspects.

We could limit cell growth here by not allowing the cell volume fraction to rise above the maximum packing capacity of spheres, K_Λ , using

$$\left(1 - \frac{\Lambda}{K_\Lambda}\right), \quad (5.27)$$

but since we do not expect the cell volume fraction to even be close to K_Λ we do not include this limiting factor in the model.

5.2.6 The effects of culture density on light availability

Due to cell growth and cell division the optical density of the culture will change during hydrogen production, which will have an impact on the photosynthetic chain. Since we include cell growth and division in the model, we also need to include the effect that this growth has on the available light.

Light intensity is modelled on the basis of the Beer-Lambert law as in Duysens 1956 [29]. This is the same relationship that we use in the phototaxis modelling in Chapters 2 and 3, based on work by Vincent and Hill [172]. The assumptions in Section 2.2.2 are used, where we assume that all cells are homogenous and transmit light equally in all directions, and we neglect the effects of multiple scattering. This is a self-shading model, where cells close to the light source absorb light before it reaches those further away. We consider illumination from the side at $x = 0$, so that light only varies in the x direction between $x = 0$ and $x = d$, where d is the width of the bio-reactor. Light intensity, I , is given by

$$I(x) = I_0 \exp^{-\int_x^0 [k_w + k_{chl}n(x)]dx}, \quad (5.28)$$

where I_0 is the light intensity at the source, k_w is the absorbance of the medium and k_{chl} is the absorbance of the cells (the cellular extinction coefficient). If we make the simplifying assumption that $n(x) = n_0$, so the concentration is uniform through the layer, and define $\tilde{C}_L = \frac{k_w}{n_0} + k_{chl}$, then

$$I(x) = I_0 \exp^{\tilde{C}_L n_0 x}. \quad (5.29)$$

If we further assume that the culture is instantaneously well mixed then averaging over the width is the same as averaging over time. Here we are assuming that the culture is well mixed in such a way that the timescale for a cell to sample the illumination over all space in the bio-reactor is small compared to the timescale for hydrogen production (tens of seconds compared to over 100 hours). Thus we approximate that each cell at every time

receives the average light it would receive if it surveyed all space instantaneously, so

$$\langle I \rangle_t = \langle I \rangle_d = \frac{1}{d} \int_{-d}^0 I_0 \exp \tilde{C}_L n_0 x \, dx. \quad (5.30)$$

Note that if we were considering a non-mixed solution, so that the cells form an exponential distribution or plumes, as in static cultures, then this assumption would not hold and hydrogen yield would be affected. Looking at the relative magnitudes of k_w and $k_{chl}n_0$, we note that $k_w \ll k_{chl}n_0$, so we can approximate $\tilde{C}_L \approx k_{chl}$.

To convert n_0 into cell volume fraction we divide \tilde{C}_L by the volume of a single cell, since

$$\Lambda = n_0 V_{cell}, \quad (5.31)$$

and write

$$C_L = \frac{\tilde{C}_L}{V_{cell}} = \frac{k_{chl}}{V_{cell}}. \quad (5.32)$$

So far we have specified that as cell volume fraction decreases, the amount of light, hence the functioning of the light dependent processes, increases, so that as Λ tends to zero the light on average each cell receives and uses tends to I_0 . However, it is well documented that as light is greatly increased the photosynthetic reaction rate saturates; if the cells are given more light beyond the light saturation point, I_{sat} , they do not increase their rate of photosynthetic activity (Leverenz *et al.* 1990 [100]). In this case, light is not the limiting factor in the photosynthetic reaction rates. We include this at the level of the integral in equation 5.30 by imposing a cut off function for the total light when $I > I_{sat}$. Hence, the useable light, $L(\Lambda)$, is defined from equation 5.30, substituting in equation 5.32, as

$$L(\Lambda) = \frac{1}{d} \int_{-d}^0 [I_0 \exp^{x C_L \Lambda} H(I_{sat} - I_0 \exp^{x C_L \Lambda}) + I_{sat} H(I_0 \exp^{x C_L \Lambda} - I_{sat})] dx. \quad (5.33)$$

Using Heaviside functions to define the limits of the integrals, equation 5.33 becomes

$$L(\Lambda) = \left(\frac{I_0}{C_L d \Lambda} [\exp(-C_L l \Lambda) - \exp(-C_L d \Lambda)] + \frac{I_{sat} l}{d} \right) H(d - l) + I_{sat} H(l - d), \quad (5.34)$$

where

$$l = \frac{1}{C_L \Lambda} \ln \left(\frac{I_{sat}}{I_0} \right). \quad (5.35)$$

We normalize equation 5.34 using the value of this function calculated for the experimental case in Kosourov *et al.* [92] from which the light-dependent parameters were obtained. This

is because this value of the light function is intrinsically included in the light dependent parameters, and we want a measure of the light as the cell volume fraction changes relative to the light intensity at which those parameters were measured. Thus we set $L = 1$ for the ‘standard’ experimental case, so L is normalized and non-dimensional when included in the model terms. We denote the value of the light function in the experimental case in [92] as L_{e1} , where $L_{e1} = 6.05 \mu\text{mol m}^{-2} \text{s}^{-1}$, and write non-dimensional $\tilde{L}(\Lambda)$ (where $\tilde{L}(\Lambda) = \frac{L(\Lambda)}{L_{e1}}$), on dropping tildes, as

$$L(\Lambda) = \frac{\left(\frac{I_0}{C_L d \Lambda} [\exp(-C_L l \Lambda) - \exp(-C_L d \Lambda)] + \frac{I_{sat} l}{d}\right)}{L_{e1}} H(d - l) \quad (5.36)$$

$$+ \frac{I_{sat}}{L_{e1}} H(l - d).$$

Furthermore, we define non-dimensional parameters

$$\tilde{I}_{sat} = \frac{I_{sat}}{L_{e1}}, \quad \tilde{I}_0 = \frac{I_0}{L_{e1}} \quad \text{and} \quad D_C = C_L d, \quad (5.37)$$

and re-write equation 5.36, on dropping the tildes and substituting in the non-dimensional expression for l , as

$$L(\Lambda) = \left(\frac{I_0}{D_C \Lambda} \left[\exp\left(-\text{Ln}\left(\frac{I_{sat}}{I_0}\right)\right) - \exp(-D_C \Lambda)\right] + \frac{I_{sat} \text{Ln}\left(\frac{I_{sat}}{I_0}\right)}{D_C \Lambda}\right) \quad (5.38)$$

$$\times H\left(1 - \frac{1}{D_C \Lambda} \text{Ln}\left(\frac{I_{sat}}{I_0}\right)\right) + I_{sat} H\left(\frac{1}{D_C \Lambda} \text{Ln}\left(\frac{I_{sat}}{I_0}\right) - 1\right).$$

Figure 5.9 shows this function for different values of I_0 .

This function is a factor in all the terms related to photosynthesis: namely, the use of sulphur to repair PSII, oxygen produced from PSII, and hydrogen production. It is also a factor in protein production because although protein production, and the Calvin cycle that creates the carbon skeletons, can happen in the dark, the Calvin cycle can only produce carbon skeletons if NADPH is available, which is produced from the light reactions of photosynthesis [107]. Since light is included in protein production, we do not explicitly include light in the growth term (because growth is dependent on protein, which is in turn dependent on light).

5.2.7 Hydrogen production

So far, hydrogen has not appeared in the model. This is because it has had no feedback into the other model equations and is modelled as a product, or an output, of the system.

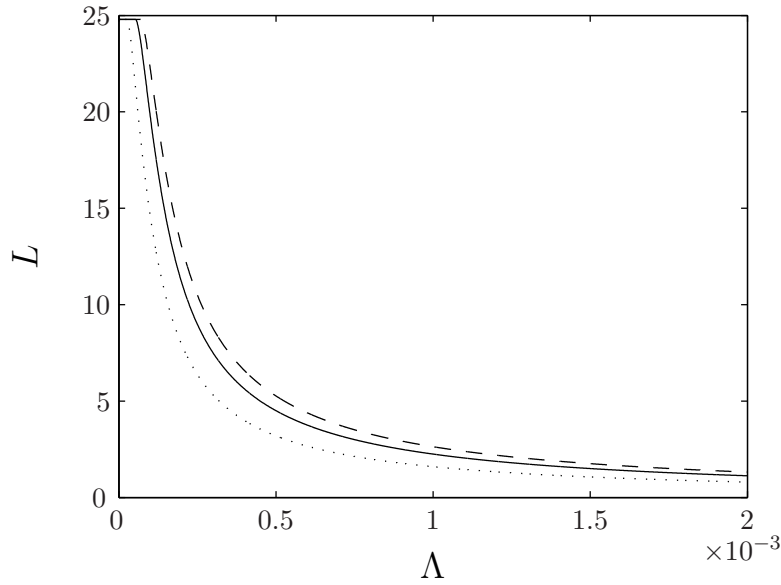


Figure 5.9: The normalized light function $L(\Lambda)$, where $I_{sat} = 150$ and $I_0 = 49.6$ (dotted), $I_0 = 99.2$ (solid) and $I_0 = 148.8$ (dashed lines).

The general form of the equation for hydrogen production is

$$\begin{aligned} \frac{dh}{dt} = & \Lambda \times \text{O}_2 \text{ sensitivity}(\omega) \times [\text{PSII-dependent}(s) + \text{PSII-independent}(p)] \quad (5.39) \\ & \times \text{Light}(\Lambda) \times \text{Calvin cycle activity}(s), \end{aligned}$$

where cell volume fraction Λ is multiplied by all terms as we require the total rate of hydrogen production from all the cells in the bio-reactor. k_4 is the rate constant of hydrogen production, which has units of mL h^{-1} .

The sensitivity of the hydrogen producing iron-hydrogenase to oxygen is well documented [92, 111, 114]. We model this using a simple switch function indicating that when oxygen is above a critical level, ω_2 , no hydrogen can be produced, hence

$$\text{O}_2 \text{ sensitivity}(\omega) = H_{Sensitivity}(\omega_2 - \omega). \quad (5.40)$$

The quantity of hydrogen gas produced also depends on the availability of electrons passed to iron hydrogenase [36, 55]. Thus we model H_2 production as dependent on the sum of electrons coming from internal protein catabolism (the PSII-independent pathway) and electrons coming from the residual level of the PSII water splitting activity (the PSII-dependent pathway), as shown in equation 5.39. In modelling these separate electron donations using addition, we assume that they happen independently. We do not include

the effects of cyclic phosphorylation, in which electrons are cycled around the electron transport chain instead of being passed to the hydrogenase.

Kosourov *et al.* [92] hypothesize that hydrogen production stops at around 100 hours because the cells have catabolized as much of its internal substrate as possible. If no substrate is available for catabolism, there will be no electrons from the PSII-independent pathway. Thus we define the PSII-independent term as dependent on protein and write

$$\text{PSII-independent}(p) = (1 - E_L) \frac{(p - p_r)}{p_h}, \quad (5.41)$$

where p_r is the base level of protein for cellular survival, below which hydrogen production is not possible. E_L is the fraction of electrons that come from the PSII-dependent pathway when initial external sulphur is zero. PSII activity is modelled as linear in sulphur in the oxygen equation, equation 5.21, and so the same form is used for PSII-dependent term, hence

$$\text{PSII-dependent}(s) = E_L \frac{s}{s_h}, \quad (5.42)$$

The specifications of the heaviside functions for rate of PSII activity, i.e. that PSII works at a constant rate when $s \geq s_0$, are not necessary because the Calvin switch indicates that hydrogen production only occurs when $s < s_0$ anyway. The constants p_h in equation 5.41 and s_h in equation 5.42 are the levels of protein and sulphur during the initial stages of residual PSII activity and hydrogen production (in Kosourov *et al.* [92]), and are used to normalize these expressions so that they measure electron donation during hydrogen production relative to electron donation in initial stage of hydrogen production when there is no external sulphur. These normalizations are necessary as they ensure that these terms are dimensionless, since all units are contained in the rate constant k_4 in equation 5.44.

The final considerations in the hydrogen term are, firstly, that hydrogen production depends on available light, since the light-dependent PSI complex passes electrons to the iron hydrogenase. Thus we multiply the entire hydrogen term in equation 5.39 by the function for light, $L(\Lambda)$, as defined in equation 5.57. Secondly, we include the Calvin cycle switch function $H_{Calvin}(s)$ to stipulate that hydrogen production can only occur when the preferred electron sink, the Calvin cycle, is not operating and protein is not produced. The flow of electrons to the various electron sinks is shown in Figure 5.7. Hence,

$$\text{Calvin cycle activity}(s) = H_{Calvin}(s_1 - s). \quad (5.43)$$

This is the same (but opposite s and s_1 dependencies) switch function, H_{Calvin} , used in the term for protein production in equation 5.10, since we are modelling that either

protein, ethanol or hydrogen is produced from the electron pathway through PSI, and a full description of the modelling processes for this switch can be found in Section 5.2.2. Using this switch neatly closes the system from further modelling, and the full hydrogen equation thus stipulates that anaerobiosis alone is not sufficient for hydrogen production; the Calvin cycle also needs to be inactivated. This also eliminates the possibility of a sealed, densely concentrated container of cells producing hydrogen due to increased cell volume fraction leading to anaerobiosis through light limitation (in agreement with Zhang *et al.* [182]).

Thus the full hydrogen equation is

$$\frac{dh}{dt} = k_4 \Lambda H_{Sensitivity}(\omega_2 - \omega) \left(E_L \frac{s}{s_h} + (1 - E_L) \frac{(p - p_r)}{p_h} \right) L(\Lambda) H_{Calvin}(s_1 - s). \quad (5.44)$$

5.2.8 The standard model, SM

Putting together all the model equations yields the standard model. The word form of the model equations is

$$\frac{d(S(1 - \Lambda))}{dt} = -\text{uptake}(S, s, \Lambda) + I \left(S, h, \frac{dh}{dt}, t \right) \quad (5.45)$$

$$\begin{aligned} \frac{d(s\Lambda)}{dt} &= \text{uptake}(S, s, \Lambda) - \text{repair}(s, \Lambda, L(\Lambda)) + \text{protein breakdown}(p, \omega, \Lambda) \\ &\quad - \text{protein production}(s, \Lambda, L(\Lambda)) \end{aligned} \quad (5.46)$$

$$\frac{d(p\Lambda)}{dt} = -\text{protein breakdown}(p, \omega, \Lambda) + \text{protein production}(s, \Lambda, L(\Lambda)) \quad (5.47)$$

$$\frac{d\omega}{dt} = \text{photosynthesis}(s, \Lambda, L(\Lambda)) - \text{respiration}(\omega, \Lambda) - \text{loss}(\omega) \quad (5.48)$$

$$\frac{d\Lambda}{dt} = \text{growth and decay}(p, \Lambda) \quad (5.49)$$

$$\begin{aligned} \frac{dh}{dt} &= \Lambda \times \text{O}_2 \text{ sensitivity}(\omega) \times [\text{PSII-dependent}(s) + \text{PSII-independent}(p)] \\ &\quad \times \text{light}(\Lambda) \times \text{Calvin cycle activity}(s) \end{aligned} \quad (5.50)$$

The full version of the model is

$$\begin{aligned} & \text{EXTERNAL SULPHUR} \\ \frac{dS}{dt} &= -\frac{a\Lambda}{1-\Lambda} \frac{\exp\left(-\frac{Gs}{s_0}\right) S}{b_1 + \frac{b_2}{s_0} s + S} + \frac{S}{1-\Lambda} \frac{d\Lambda}{dt} + \frac{I(S, h, \frac{dh}{dt}, t)}{1-\Lambda}, \end{aligned} \quad (5.51)$$

$$\begin{aligned} & \text{INTERNAL SULPHUR} \\ \frac{ds}{dt} &= a \frac{\exp\left(-\frac{Gs}{s_0}\right) S}{b_1 + \frac{b_2}{s_0} s + S} - k_1(sH_{PSII}(s_0 - s) + s_0H_{PSII}(s - s_0))L(\Lambda) \\ & + \beta k_2(p - p_r)H_{Ferment}(\omega_p - \omega) - \frac{\beta k_3}{s_0} sH_{Calvin}(s - s_1)L(\Lambda) - \frac{s}{\Lambda} \frac{d\Lambda}{dt}, \end{aligned} \quad (5.52)$$

$$\begin{aligned} & \text{PROTEIN} \\ \frac{dp}{dt} &= -k_2(p - p_r)H_{Ferment}(\omega_p - \omega) + \frac{k_3}{s_0} sH_{Calvin}(s - s_1)L(\Lambda) - \frac{p}{\Lambda} \frac{d\Lambda}{dt}, \end{aligned} \quad (5.53)$$

$$\begin{aligned} & \text{OXYGEN} \\ \frac{d\omega}{dt} &= \Lambda \left[k_6 \left(\frac{s}{s_0} H_{PSII}(s_0 - s) + H_{PSII}(s - s_0) \right) L(\Lambda) \right. \\ & \left. - k_5(\omega H_{Resp}(\omega_1 - \omega) + \omega_1 H_{Resp}(\omega - \omega_1)) \right] - v_{O_2}(\omega - \chi)H_{Loss}(\omega - \chi), \end{aligned} \quad (5.54)$$

$$\begin{aligned} & \text{CELL VOLUME FRACTION} \\ \frac{d\Lambda}{dt} &= \Lambda \left[r_{exp}H_{G2}(p - p_2) + \frac{r_{exp}(p - p_0)}{(p_2 - p_0)}H_{G2}(p_2 - p)H_{G1}(p - p_1) \right. \\ & \left. - r_{decay}H_{G1}(p_1 - p) \right], \end{aligned} \quad (5.55)$$

$$\begin{aligned} & \text{HYDROGEN} \\ \frac{dh}{dt} &= k_4\Lambda H_{Sensitivity}(\omega_2 - \omega) \left(E_L \frac{s}{s_h} + (1 - E_L) \frac{(p - p_r)}{p_h} \right) \\ & \times L(\Lambda)H_{Calvin}(s_1 - s), \end{aligned} \quad (5.56)$$

where $L(\Lambda)$ is the normalized light function

$$\begin{aligned} L(\Lambda) &= \left(\frac{I_0}{D_C\Lambda} \left[\exp\left(-\text{Ln}\left(\frac{I_{sat}}{I_0}\right)\right) - \exp(-D_C\Lambda) \right] + \frac{I_{sat}\text{Ln}\left(\frac{I_{sat}}{I_0}\right)}{D_C\Lambda} \right) \\ & \times H\left(1 - \frac{1}{D_C\Lambda}\text{Ln}\left(\frac{I_{sat}}{I_0}\right)\right) + I_{sat}H\left(\frac{1}{D_C\Lambda}\text{Ln}\left(\frac{I_{sat}}{I_0}\right) - 1\right). \end{aligned} \quad (5.57)$$

5.3 Parameter Estimation

Since this is the first mechanistic model of this kind for the hydrogen producing algal system, specifying parameters for use in the model has been a difficult task, especially due to the difficulty in physically measuring some of these values. Although we have tried to find appropriate values from *independent data resources* this has not always been possible, in which case we have estimated a range of parameters from minimal fitting procedures.

There are 32 parameters in total and in this section we describe how the values or ranges are obtained for all parameters that have not already been discussed. Parameters taken directly from publications, which only require unit conversions to be in correct form, are shown directly in Table 5.1.

5.3.1 The critical values s_0 , s_1 , ω_1 , ω_2 , ω_p and p_r

The normal level of free sulphur in the cell, s_0 , was difficult to quantify. Using data for total sulphur content of wild type cells from Hiriart 2006 [67], we calculate a value of internal sulphur as approximately 100,000 μM . However, this value is clearly too large since we expect that much of the sulphur in the cell is not free and is contained in other complexes that can not be used. Considerations of the data for sulphur transport across the cell wall (Yildez *et al.* [181]) and behaviour of the system for values of external sulphur of 100 μM (Zhang *et al.* [182] and Kosourov *et al.* [92]) suggests s_0 is an order of magnitude lower. For these reasons we typically set $s_0 = 15,000 \mu\text{M}$, although we also vary this value between 10^3 and $10^5 \mu\text{M}$.

Parameter s_1 quantifies the switch between the Calvin cycle being used as the electron sink, when Rubisco is sufficient, to the hydrogen or ethanol electron sinks being used instead. An upper bound for s_1 is the normal level of sulphur in a cell, s_0 . A lower bound could be the level of internal sulphur at which hydrogen production begins, since at that point sufficient Rubisco must have broken down. When hydrogen production begins the level of oxygen production from PSII has approximately decreased by a factor of 5 (Zhang *et al.* 2002 [182]). Since we model oxygen production from PSII as linearly dependent on sulphur, we estimate that internal sulphur has also fallen by a factor of 5 at this point, hence

$$\frac{s_0}{5} \leq s_1 \leq s_0. \quad (5.58)$$

We set the standard value of s_1 as $s_1 = \frac{s_0}{2}$, because Rubisco and sulphur levels both rapidly reduce by a factor of two before hydrogen production begins, after which anaerobiosis is the necessary condition for hydrogen production to begin. We choose a slightly smoother switch for this function so that around the switch value, s_1 , hydrogen production and the Calvin cycle can both be used as an electron switch. The gradient of the switch is denoted s_g .

For ω_1 , the level of oxygen required for full aerobic respiration, a value of $\omega_1 = 1.18$

μM was obtained from Forti and Caldiroli 2005 [34]. ω_2 , the sensitivity of the iron hydrogenase to oxygen, was extrapolated from data in Flynn *et al.* 2002 [33]; when oxygen is below 2% (partial pressure of 0.02 atm), hydrogen production began. To convert this into concentration of oxygen we use Henry's Law,

$$p_{atm} = k\omega_2, \quad (5.59)$$

where p_{atm} is partial pressure measured in atm, and k is a constant measured in L.atm/mol. Using $k = 769.2$ L. atm/mol from Sander and Lin 2002 [104] gives

$$\omega_2 = 2.60 \times 10^{-5} \text{ M} = 26 \mu\text{M}. \quad (5.60)$$

ω_p is the oxygen level when protein breakdown begins. We set this to be the same as the oxygen level when hydrogen production starts, so that $\omega_p = \omega_2$, since there is evidence that hydrogen production and endogenous substrate catabolism are coordinated [111].

p_r , the base level of protein needed for survival of a cell, is calculated using data from Kosourov *et al.* [92]. We take p_r as the value of protein at which hydrogen production stops for the case $S = 0.0\mu\text{M}$, converting into units of μM , and also convert from per mL of culture to per cell using chlorophyll data. This gives $p_r = 206.0 \mu\text{M}$.

The growth function for Λ also requires switch values but, for convenience, these are discussed in the growth parameters section (Section 5.3.4).

5.3.2 Parameters in the sulphur equations

Parameters in the uptake function, equation 5.6, are discussed in Section 5.2.2.

k_2 is the rate constant for the breakdown of protein to release sulphur under stressed conditions. Due to a lack of other available data, we use protein data from Figure 5 of Kosourov *et al.* [92], re-produced here in Figure 5.10, which shows that substantial net protein breakdown occurs between 40 and 66 hours and again between 100 and 120 hours. We assume an exponential decay of total protein during breakdown and further assume that when protein breaks down there is no protein production. Using the exponential decay assumption we write

$$p_{final} = p_{initial} \exp(-k_2(t_{final} - t_{initial})) \quad (5.61)$$

where $p_{initial/final}$ and $t_{initial/final}$ are the protein and time at the start/end of each breakdown period, respectively. Substituting values for the first protein breakdown period,

$40 \leq t \leq 66$, from Kosourov *et al.* [92] into equation 5.61 gives $k_2 = 0.0267 \text{ h}^{-1}$, and from the second protein breakdown period we calculate $k_2 = 0.0973 \text{ h}^{-1}$. Thus, we assume that the rate of protein breakdown is in the inclusive range between these values,

$$0.0267 \text{ h}^{-1} \leq k_2 \leq 0.0973 \text{ h}^{-1}. \quad (5.62)$$

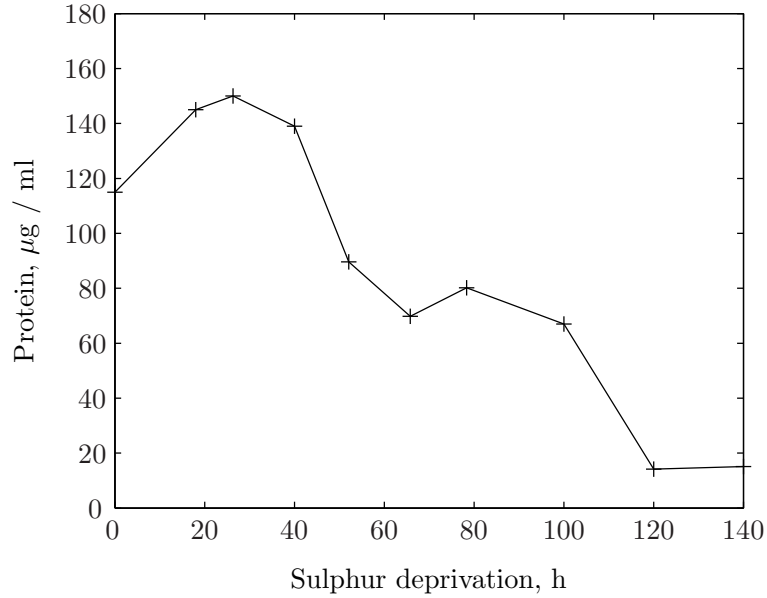


Figure 5.10: Reproduced protein data for $S_0 = 0 \text{ } \mu\text{M}$ from Figure 5 for unsynchronized cells in Kosourov *et al.* [92].

Parameters k_3 and k_1 are linked and so k_3 is explained first and then used to calculate k_1 . The presence of the light term in the protein and sulphur terms complicates the estimation so we calculate upper and lower bounds for k_1 and k_3 by assuming $L(\Lambda) = L_1$ is constant (hence Λ is constant, Λ_1). We then use the maximum and minimum values of L_1 and Λ to calculate the ranges of k_1 and k_3 .

k_3 is the rate constant for protein produced from sulphur. In the early stages of hydrogen production we assume no protein breakdown or hydrogen production. Hence, equation 5.12 simplifies to

$$\frac{d(p\Lambda)}{dt} = \frac{k_3}{s_0} s \Lambda_1 L_1. \quad (5.63)$$

If we set the half life of sulphur to be $t_{1/2}$ then at $t = t_{1/2}$ equation 5.63 becomes

$$\left(\frac{\frac{d(p\Lambda)}{dt}}{\Lambda_1 L_1} \right)_{(t=t_{1/2})} = \frac{k_3}{2}. \quad (5.64)$$

We set the half life of sulphur $t_{1/2}$ to be the half life of the oxygen production in Melis *et al.* [114], since we model both oxygen produced and internal sulphur used in repairing PSII linearly. Again, we use data from Figure 5b in Kosourov *et al.* [92] for $S = 0 \mu\text{M}$ to obtain $\frac{d(p\Lambda)}{dt}$ and the value of $\Lambda_1 L_1$ at $t = 0$ and $t = t_{1/2}$, to give an approximate range for k_3 as

$$51.7 \mu\text{M h}^{-1} \leq k_3 \leq 61.1 \mu\text{M h}^{-1}. \quad (5.65)$$

We use the same method to find k_1 , again assuming no external sulphur and no protein breakdown in the initial stages of sulphur deprivation, and assuming that $L(\Lambda) = L_1 =$ constant. If $s < s_0$ then the equation for internal sulphur, equation 5.11, becomes

$$\frac{d(s\Lambda_1)}{dt} = - \left(k_1 + \frac{k_3\beta}{s_0} \right) s\Lambda_1 L_1. \quad (5.66)$$

Solving equation 5.66 and evaluating for $s = \frac{s_0}{2}$ at $t = t_{1/2}$ gives

$$k_1 = \frac{- \left(\frac{1}{t_{1/2}} \ln \left(\frac{1}{2} \right) + \frac{k_3\beta}{s_0} \right)}{L_1}. \quad (5.67)$$

Using a constant value of $L(\Lambda)$ is somewhat of an approximation, because cell volume fraction and, hence, light intensity, do change between $t = 0$ and $t = t_{1/2}$. The presence of the $\frac{1}{\Lambda}$ in the light function would make equation 5.66 unsolvable if light were not set as a constant; this simple method provides an order estimate for k_1 . At $t = 0$, we calculate light as $L_1 = 1$ from Kosourov *et al.* [92], and at $t = t_{1/2}$ we use the cell volume fraction at $t = t_{1/2}$ from Kosourov *et al.* [92] to calculate $L_1 = 0.846$. Using the maximum and minimum values of L_1 and k_3 as previously calculated, along with standard values for s_0 and β , we calculate a range for k_1 as

$$0.0376 \text{ h}^{-1} \leq k_1 \leq 0.0451 \text{ h}^{-1}. \quad (5.68)$$

The final parameter in this section is β , which is the number of moles of sulphur present in one mole of protein. An upper bound for the value of β is found by calculating the number of sulphur-containing amino acids in an average protein chain, since these amino acids each contain one sulphur mole. Abundant Rubisco proteins are used to obtain an order estimate and a weighted average is calculated from large Rubisco subunit data in Thompson *et al.* 1995 [165] and small subunit data in Goldschmidt-Clermont and Rahire 1986 [49] (there is not a one-to-one ratio of these proteins). We find β is bounded above by 15. However, the value generally used is of an order of magnitude lower than this, since not all the sulphur will be freely available and some will likely be bound up in other compounds.

5.3.3 Parameters in the oxygen and hydrogen equations

k_6 is the rate constant in the equation for oxygen production from photosynthesis. It is the normal rate of photosynthesis (when $s > s_0$). We find this value from Kosourov *et al.* [92] (in units of $\mu\text{moles O}_2 (\text{mg Chl})^{-1} \text{h}^{-1}$) by assuming that a normal rate of photosynthesis occurs at the start of the sulphur deprivation. The chlorophyll concentration at $t = 0$ was approximately $10 \mu\text{g/mL}$, thus we can calculate the rate of photosynthesis per litre of suspension (of concentration 4.5×10^6 cells per mL) as $2800 \mu\text{M h}^{-1}$. This value contains intrinsic information about cell number and size, but since we model these aspects as non-constant, we need to divide this value by the initial cell volume fraction at $\Lambda(t = 0)$. For a concentration of 4.5×10^6 , from [92], cell volume fraction $\Lambda(t = 0) = 0.00225$. Hence,

$$k_6 = 1,240,000 \mu\text{M h}^{-1}. \quad (5.69)$$

The constant rate of respiration in equation 5.19 occurs when $\omega > \omega_1$, and is given by $k_5\omega_1$, shown in Section 5.2.4. $k_5\omega_1$ is also found from Kosourov *et al.* [92], using the same conversion method as for k_6 , hence

$$k_5\omega_1 = 311,111 \mu\text{M h}^{-1} \Rightarrow k_5 = 264,000.0 \text{h}^{-1}. \quad (5.70)$$

The saturation value of oxygen, denoted χ , we find from Weiss 1970 [175] to be $253.0 \mu\text{M}$ at 22°C and atmospheric pressure of 710 atmospheric pressure (measured in millimeters of mercury). A range for χ can be calculated using other temperature and atmospheric pressures from the tables based on calculations of Weiss 1970 in [101].

v_{O_2} is the oxygen mass transfer coefficient and gives an indication of how quickly excess oxygen (that is, oxygen above the saturation value) can leave the culture by bubbling off. This parameter has been difficult to estimate due to the complexity of bubble formation in suspensions and the need to calculate it specifically for the container involved. To obtain an order estimate, we use a value for the oxygen mass transfer coefficient of the surface layer of waste water as $d_s/l_s = 0.13 \times 10^{-3} \text{cm s}^{-1}$ (Molder *et al.* 2005 [119]). For our 1L cubical container

$$v_{\text{O}_2} = 0.13 \times 10^{-3} \times 3600 \text{ cm h}^{-1} \times \frac{100 \text{ cm}^2}{1000 \text{ cm}^3} \text{ per side} = 0.0468 \text{ h}^{-1} \text{ per side}. \quad (5.71)$$

k_4 is the rate constant for the production of hydrogen gas measured in mL per hour. Due to a lack of available data we estimate this from initial rates of hydrogen production Table II in Kosourov *et al.* [92] for unsynchronized cultures. Although not ideal, it still

allows us to compare our hydrogen yield for long times and for different amounts of external sulphur with experimental data. We take the specific initial rate of hydrogen production in μ moles \cdot mg Chl⁻¹ \cdot h⁻¹ and multiply by the amount of chlorophyll in one litre of culture to obtain the rate of H₂ produced per litre of culture. This gives

$$5.74 \mu\text{moles} \cdot \text{mg Chl}^{-1} \cdot \text{h}^{-1} = 57.4 \mu\text{moles} \cdot \text{L}^{-1} \cdot \text{h}^{-1}. \quad (5.72)$$

We convert the units of hydrogen to mL⁻¹, using $33 \mu\text{moles H}_2 = 1 \text{ mL}$ (from [92]). Since we model cell volume fraction explicitly in equation 5.44, we divide by the cell volume at the start of hydrogen production, which is $\Lambda = 0.00293$ in [92]. We must also divide by the value of the light function $L(\Lambda)$ at $\Lambda = 0.00293$, because k_4 is multiplied by $L(\Lambda)$ in equation 5.44. (Note: this is not necessary for the other light dependent parameters, as in those cases $L(\Lambda) = 1$ at the value of Λ at which those parameters are measured). This gives

$$k_4 = 773 \text{ mL h}^{-1}. \quad (5.73)$$

s_h and p_h are the normalizations of the PSII-dependent and PSII-independent electron pathways, respectively. They are used in equations 5.41 and 5.42 to normalize the hydrogen equation so that at the start of hydrogen production, T_H , $\frac{dh}{dt} = k_4$ in equation 5.44. Thus s_h and p_h are chosen as the concentrations of sulphur and protein at the start time of hydrogen production in Kosourov *et al.* [92]. This gives $p_h = 1260 \mu\text{M}$. At T_H , PSII activity is approximately one-sixth of normal PSII activity [92], so we assume that sulphur has decreased by the same factor, as PSII is linearly dependent on internal sulphur. Hence,

$$s_h = \frac{s_0}{6}. \quad (5.74)$$

E_L is the fraction of electrons coming from the PSII-dependent pathway. We set $E_L = 0.75$, using the suggestion that 70 – 80% of electrons come from PSII-dependent and the remaining 20 – 30% come from the PSII-independent pathway in Fouchard *et al.* 2005 [36].

5.3.4 Parameters in the cell volume fraction equation

The maximum growth rate for *C. reinhardtii* in TAP media was found as $r_{exp} = 0.0373 \text{ h}^{-1}$ in Jo *et al.* 2006 [72]) and $r_{exp} = 0.074 \text{ h}^{-1}$ in Fischer *et al.* 2006 [32]), indicating that the cultures grow between 3.73 and 7.4 % per hour, giving a range

$$0.0373 \text{ h}^{-1} \leq r_{exp} \leq 0.074 \text{ h}^{-1}. \quad (5.75)$$

We can also calculate a growth rate from Kosourov *et al.* [92] using chlorophyll data over the first 20 hours (since it is stated the cell volume fractions acts in the same way as chlorophyll concentration) for various concentrations of external sulphur and find the maximum growth rate of the culture as $r_{exp} = 0.064 \text{ h}^{-1}$. Encouragingly, this growth rates is within the range in equation 5.75, and we use $r_{exp} = 0.064 \text{ h}^{-1}$ from Kosourov *et al.* [92] as the standard value, for consistency with calculations of other parameters.

In the absence of any other data, we compute the maximum decay rate parameter r_{decay} from the chlorophyll data of unsynchronized cells when $S = 50 \mu\text{M}$ in Kosourov *et al.* [92] (since this concentration of external sulphur results in the highest rate of shrinking). The shrinkage in chlorophyll concentration occurs over 120 hours, so to find the rate per hour we use

$$(1 - r_{decay})^{120} = \frac{\text{Final Chl}}{\text{Initial Chl}}, \quad (5.76)$$

which, on substituting in values from [92], gives

$$r_{decay} = 0.0053 \text{ h}^{-1}. \quad (5.77)$$

p_0 , the protein concentration when the growth rate is zero, is also calculated from Kosourov *et al.* [92], and is set to be the protein concentration at which the chlorophyll content changes from increasing to decreasing, as zero growth rate must occur in the period in which the culture changes between growth and decay.

To fix a value for p_2 , the protein level needed for constant growth, we assume that before the start of the sulphur deprivation there is an optimal concentration of protein that each cell maintains; additional protein produced from sulphur is used for growth. Thus we take the value of protein at $t = t_0$ in Figure 5 of Kosourov *et al.* [92] as the level of protein required for steady growth, hence $p_2 = 1570 \mu\text{M}$ (on converting units).

p_1 is the protein concentration below which decay occurs at a constant rate, r_{decay} . At this point the linear part of the growth and decay function in equation 5.25 (the second term) will meet the straight line $-r_{decay}$, shown in Figure 5.8. Thus, setting $p = p_1$ and equating the linear component in equation 5.25 with $-r_{decay}$ gives

$$\frac{r_{exp}(p_1 - p_0)}{(p_2 - p_0)} = -r_{decay}, \quad (5.78)$$

and substituting in values for r_{decay} , r_{exp} , p_0 and p_2 gives

$$p_1 = -\frac{r_{decay}}{r_{exp}}(p_2 - p_0) + p_0 = 1350 \mu\text{M}. \quad (5.79)$$

Note that the parameters r_{decay} , p_0 , p_1 and p_2 are all calculated from Kosourov *et al.* [92]. This is not ideal, since we also wish to compare model results to this data, but is necessary to give order estimates in the absence of other data.

5.3.5 Parameters in the light function

If we assume we have a litre of culture in a cube then the width of the container is $d = 10$ cm. To find the cellular extinction coefficient, k_{chl} , we take an average of the mass extinction coefficients of *C. reinhardtii* under different wavenumbers presented in Berberoglu *et al.* 2008 [12], converting to units of $\text{m}^2 \text{kg}^{-1}$. Converting from dry cell weight in kg m^{-3} to cells m^{-3} , using $\frac{1\text{kg}}{\text{m}^3} = 7.60 \times 10^{12} \frac{\text{cells}}{\text{m}^3}$, from [12], gives the cellular extinction coefficient as

$$k_{chl} = 1.315 \times 10^{-6} \text{ cm}^2, \text{ hence } C_L = \frac{k_{chl}}{V_{cell}} = 2630 \text{ cm}^{-1}. \quad (5.80)$$

Leverenz *et al.* 1990 [100] show light saturation curves for *C. reinhardtii*, plotting light intensity against oxygen production rate. Significantly, this experiment was conducted with a relatively dilute concentration of cells in a thin layer, thus there are no effects of shading in the culture. This allows us to use the curve to estimate the light saturation point for the cells, I_{sat} , directly. The control curve shows an initial clear linear increase in oxygen production rate as light intensity increases, followed by a stationary phase when light intensity is high. To find I_{sat} we fit a piecewise linear curve to the data in [100], extrapolating forwards from the linear phase and backwards from the stationary phase. The light intensity at which the linear phase meets the stationary phase is the saturation of light intensity point, and is found as $I_{sat} = 150 \mu\text{mol m}^{-2}\text{s}^{-1}$. Using the scalings for I_{sat} in equation 5.37 gives non-dimensional $\tilde{I}_{sat} = 24.8$, where herein we drop the tilde.

We use $600 \mu\text{mol m}^{-2}\text{s}^{-1}$ as a standard dimensional value of I_0 for comparison with Kosourov *et al.* [92], which comes from two light sources, one at each side, of $I_0 = 300 \mu\text{mol m}^{-2}\text{s}^{-1}$. Doubling light intensity is the same as including a light source at either side when the cells are uniformly distributed and well mixed (as described in Section 5.2.1). The standard, non-dimensional value is $I_0 = 99.2$.

5.3.6 Standard parameter values

Parameters are summarized in Table 5.1, where a brief description of what each parameter measures, the standard value, unit, range and reference from which the parameter was

found or extrapolated from are tabulated.

Notation	Parameter	Standard Value	Unit	Range	Reference
s_0	Normal level of sulphur in a cell	15,000*	μM	$10^3 - 10^5$	[67]
s_1	Sulphur level above which Calvin cycle is active	7500*	μM	3000 – 15,000*	[182]
ω_1	Oxygen required for full respiration	1.18	μM	0.75 – 2.0	[34]
ω_2	Oxygen required to stop H_2 production	26.0	μM	13 – 39*	[33]
ω_p	Oxygen level below which protein breakdown occurs	26.0	μM	13 – 39*	[33]
χ	Oxygen saturation in water	253.0	μM	200 – 300	[101, 175]
k_1	Rate constant for PSII repair	0.041*	h^{-1}	0.0376 – 0.0451*	[92, 114]
k_2	Rate constant for protein breakdown	0.08*	h^{-1}	0.0267 – 0.0973*	[92]
k_3	Rate constant for protein production	56.4*	$\mu\text{M h}^{-1}$	51.7 – 61.1*	[92, 114]
k_4	Rate constant for hydrogen production	773.0	mL h^{-1}	595.0 – 1068.0	[92]
k_5	Rate constant for oxygen consumption by respiration	264000.0	h^{-1}	247,000- 281,000*	[92]
k_6	Rate constant for oxygen production from PSII	1240000.0	h^{-1}	1,000,000- 1,480,000*	[92]
v_{O_2}	Oxygen mass transfer coefficient	0.374	N/A	0.03 – 0.5	[119]
a	Rate constant for S uptake over normal cell volume	14,800	$\mu\text{M h}^{-1}$	12,500 – 17,100	[181]
G	Rate constant for sulphur uptake	2.29	μM^{-1}	1.77 – 2.99	[181]
b_1	Rate constant for sulphur uptake	2.2	μM	1.3 – 3.1	[181]
b_2	Rate constant for sulphur uptake	14.5	N/A	14.5 – 19.8	[181]
β	Average moles of sulphur in one mole of protein	0.5*	N/A	0.1 – 15.0	[49, 165]
r_{exp}	Maximum growth rate	0.064	h^{-1}	0.037 – 0.064	[32, 72, 92]
r_{decay}	Maximum rate for cell decay	0.0053	h^{-1}	0.001 – 0.01*	[92]

Continued over page

Notation	Parameter	Standard Value	Unit	Range	Reference
p_0	Protein level when growth is zero	1370.0	μM	1240 – 1770	[92]
p_1	Protein below which maximum decay occurs	1350.0	μM	1180 – 1690	[92]
p_2	Protein required for maximum growth	1570.0	μM	1480 – 1650	[92]
p_r	Basic protein needed for cell survival	206.0	μM	100 – 300*	[92]
d	Width of the bio-reactor	10.0	cm	1 – 100	N/A
C_L	Measure of absorbance of the cells	2630.0	cm^{-1}	2000 – 6000*	[12]
I_{sat}	Non-dimensional saturation level of light	24.8	N/A	20 – 30.0	[100]
I_0	Non-dimensional light intensity at the source	99.2	N/A	0.0 – 200.0	[92]
s_h	Normalization of PSII-dependent electron pathway	2,500	μM	1,250-3,750*	[92]
p_h	Normalization of PSII-independent electron pathway	1260	μM	1000 - 1400*	[92]
E_L	Fraction of electrons from PSII-dependent path	0.75	N/A	0.7 – 0.8	[36]
s_g	Gradient of Rubisco switch function	25.0*	N/A	1 – 100*	N/A

Table 5.1: Table of standard model parameters. Estimates parameters, such as those calculated using the model, are marked with a star. The range of values is calculated either using error bars given in the original data, using different values from data to estimate the range or by simply estimating. This has been necessary in some of the more difficult to estimate (or measure) parameters, and is also denoted with a star. The reference refers either to the publication in which the parameter can be found, or the publication from which the value was derived from.

5.4 Non-dimensionalization of the standard model

First we non-dimensionalize the standard model shown in equations 5.51 to 5.56. We chose the scalings

$$\tilde{t} = k_1 t, \quad \tilde{S} = \frac{S}{b_2}, \quad \tilde{s} = \frac{s}{s_0}, \quad \tilde{p} = \frac{k_2 p}{k_3}, \quad \tilde{\omega} = \frac{\omega}{\chi}, \quad \tilde{h} = \frac{k_1 h}{k_4}. \quad (5.81)$$

Λ and $L(\Lambda)$ are already dimensionless. The scaling for time is chosen so that one non-dimensional time unit corresponds to approximately one day, so $\tilde{t} = 1$ approximates to $t = 24.4$ hours and, for convenience, we scale with k_1 (instead of choosing a non-dimensionalization so that exactly 24 hours is one non-dimensional time unit). The sulphur scaling of s_0 is chosen so that $s = 1$ initially (under normal sulphur conditions) and parameters relating to the normal level of sulphur in the cell range from 0 to 1. External sulphur and protein scalings are used for convenience in the respective equations and oxygen is scaled with the super-saturation value. The hydrogen scaling removes the rate k_4 from the non-dimensional form of the model and scales with the new time scale k_1 .

By substituting in the scalings in equation 5.81, and dropping tildes, the non-dimensional version of the standard model is:

$$\frac{dS}{dt} = \frac{-A_1 \Lambda}{1 - \Lambda} \frac{S e^{-Gs}}{1 + B(s + S)} + \frac{S}{1 - \Lambda} \frac{d\Lambda}{dt} + \frac{I(S, h, \frac{dh}{dt}, t)}{1 - \Lambda}, \quad (5.82)$$

$$\frac{ds}{dt} = \frac{A_2 S e^{-Gs}}{1 + B(s + S)} - (s H_{PSII}(1 - s) + H_{PSII}(s - 1)) L(\Lambda) \quad (5.83)$$

$$+ K_3 ((p - P_R) H_{Ferment}(\Omega_2 - \omega) - s L(\Lambda) H_{Calvin}(s - S_1)) - \frac{s}{\Lambda} \frac{d\Lambda}{dt},$$

$$\frac{dp}{dt} = K_2 (s L(\Lambda) H_{Calvin}(s - S_1) - (p - P_R) H_{Ferment}(\Omega_2 - \omega)) - \frac{p}{\Lambda} \frac{d\Lambda}{dt}, \quad (5.84)$$

$$\frac{d\omega}{dt} = \Lambda [K_6 (s H_{PSII}(1 - s) + H_{PSII}(s - 1)) L(\Lambda) \quad (5.85)$$

$$- K_5 (\omega H_{Resp}(\Omega_1 - \omega) + \Omega_1 H_{Resp}(\omega - \Omega_1))] - V_L (\omega - 1) H_{Loss}(\omega - 1),$$

$$\frac{d\Lambda}{dt} = \Lambda (R_G H_{G2}(p - \gamma_2) + R_G P_G (p - \gamma_0) H_{G2}(\gamma_2 - p) H_{G1}(p - \gamma_1) \quad (5.86)$$

$$- R_D H_{G1}(\gamma_1 - p)),$$

$$\frac{dh}{dt} = \Lambda H_{Sensitivity}(\Omega_2 - \omega) H_{Calvin}(S_1 - s) [E_L S_H s L(\Lambda) \quad (5.87)$$

$$+ (1 - E_L) P_H (p - P_R)] L(\Lambda),$$

Heaviside function	Value of g used
H_{PSII}	1000
$H_{Ferment}$	10
H_{Calvin}	25
H_{Resp}	200
H_{Loss}	200
$H_{Sensitivity}$	1000
H_{G1}	1500
H_{G2}	1500
H_{light}	1000

Table 5.2: The values of the gradients, g , used in each tanh function. Here, H_{light} is the Heaviside function used in the expression for light intensity in equation 5.57.

where $I(S, h, \frac{dh}{dt}, t)$ is the non-dimensional input function and

$$\begin{aligned}
 A_1 &= \frac{a}{k_1 b_1}, & B &= \frac{b_2}{b_1}, & A_2 &= \frac{ab_2}{k_1 b_1 s_0}, & K_3 &= \frac{\beta k_3}{k_1 s_0}, & K_2 &= \frac{k_2}{k_1}, & (5.88) \\
 K_6 &= \frac{k_6}{k_1 \chi}, & K_5 &= \frac{k_5}{k_1}, & V_L &= \frac{v_{0_2}}{k_1}, & \Omega_1 &= \frac{\omega_1}{\chi}, & \Omega_2 &= \frac{\omega_2}{\chi}, \\
 D_C &= dC_L, & P_R &= \frac{k_2 p_r}{k_3}, & P_G &= \frac{k_3}{(p_2 - p_0)k_2}, & \gamma_0 &= \frac{k_2 p_0}{k_3}, \\
 \gamma_1 &= \frac{k_2 p_1}{k_3}, & \gamma_2 &= \frac{k_2 p_2}{k_3}, & R_G &= \frac{r_{exp}}{k_1}, & R_D &= \frac{r_{decay}}{k_1}, \\
 S_1 &= \frac{s_1}{s_0}, & S_H &= \frac{s_0}{s_h}, & P_H &= \frac{k_3}{k_2 p_h}.
 \end{aligned}$$

To improve the convergence of the numerical program, we use tanh function approximations for the sharp Heaviside functions. For example, we use

$$H_{Sensitivity}(\Omega_2 - \omega) = 0.5[1.0 + \tanh(g \times (\Omega_2 - \omega))], \tag{5.89}$$

The value g that multiplies the argument of the tanh function determines the steepness of the function (how close to a Heaviside it is). To avoid creating more parameters, we set g in every case to be sufficiently large so that the switches are always steep. To fix a value of g for each Heaviside function, g was increased until increasing g any further did not significantly affect the model results. The values of g used in the numerical solutions are shown in Table 5.2.

Table 5.3 shows standard values for the non-dimensional parameters, where the ranges are calculated using the range (either calculated or otherwise) of the dimensional param-

eters in Table 5.1.

5.4.1 Initial conditions

The initial condition for each variables at time t_0 is denoted using a subscript 0. We set $s_0 = 1$, the normal level of sulphur in a cell, $p_0 = 2.227$, the level of protein at the start of the experiment in Kosourov *et al.* [92], and we vary external sulphur S_0 . Since we assume that the culture has been purged of oxygen at the start of the experiment, as discussed in Section 5.2.1, $\omega_0 = 0$. We also set $h_0 = 0$ at $t = 0$. For comparison with Kosourov *et al.* [92] we set the initial cell volume fraction as $\Lambda_0 = 0.00225$. In this chapter, we set the input of external sulphur function, $I(S, h, \frac{dh}{dt}, t) = 0$ in equation 5.82; non-zero forms of this are investigated in Chapter 6.

5.5 Numerical model results for the standard parameter values

In this section, we solve the model and present results for the set of standard parameter values in Table 5.3. Due to the complexity of the system it is not easy to solve analytically. We take a numerical approach and solve in Matlab. Here follows a brief description of the numerical scheme, followed by a numerical check in which numerical solutions are compared to analytical solutions for a much reduced system at early times.

5.5.1 Numerical Method

To solve numerically, an in-built numerical solver in Matlab was used. Initially, a fourth order Runge-Kutta method was tried (ode45), but rapid variations in the solution due to the switch functions cause the system to be stiff and, hence, mean that this scheme is slow to run as very small time steps are required. For the results presented in this section, a scheme called ode15s was used. ode15s employs a modified backward Euler (BE) method for a step from (y_n, t_n) to (y_{n+1}, t_{n+1}) , where the standard BE is of the form

$$y_{n+1} = y_n + (\Delta t)f(t_{n+1}, y_{n+1}), \quad (5.90)$$

where Δt is a small time-step. This is an implicit scheme and, although it requires solving a set of non-linear equations at every time step, it is much more numerically stable than an explicit method. The truncation error when using the backward Euler (BE) method to

Dimensionless parameter	Definition	Description	Standard Value	Range
S_1	$\frac{s_1}{s_0}$	Ratio of s required for Calvin cycle to normal s	0.5	0.2 – 1.0
Ω_1	$\frac{\omega_1}{\chi}$	Scaled oxygen switch ω_1	0.0047	0.0025 – 0.01
Ω_2	$\frac{\omega_2}{\chi}$	Scaled oxygen switch ω_2	0.103	0.0433 – 0.195
P_R	$\frac{k_3}{k_2 p_c}$	Scaled protein required for survival p_r	0.292	0.0437 – 0.565
K_2	$\frac{k_2}{k_1}$	Scaled protein breakdown rate	1.95	0.592 – 2.59
K_3	$\frac{\beta k_3}{k_1 s_0}$	Scaled measure of rate of p production	0.0459	0.0057 – 25.4
K_5	$\frac{k_5}{k_1}$	Scaled respiration rate	6.44×10^6	5.48×10^6 – 7.47×10^6
K_6	$\frac{k_6}{k_1 \chi}$	Scaled photosynthesis rate	1.2×10^5	7.39×10^4 – 1.97×10^5
V_L	$\frac{v_{02}}{k_1}$	Scaled oxygen mass transfer	9.12	0.665 – 13.3
A_1	$\frac{a}{k_1 b_1}$	Scaled ratio of uptake rates	1.64×10^5	8.94×10^4 – 3.5×10^5
B	$\frac{b_2}{b_1}$	Ratio of S uptake rates	6.59	3.39 – 14.2
A_2	$\frac{ab_2}{k_1 b_1 s_0}$	Scaled ratio of sulphur uptake rates	159.0	9.39 – 6480
R_G	$\frac{r_{exp}}{k_1}$	Scaled growth rate	1.56	0.82 – 2.39
R_D	$\frac{r_{decay}}{k_1}$	Scaled decay rate	0.129	0.0221 – 0.266
P_G	$\frac{k_3}{k_2(p_2 - p_0)}$	Scaled protein gradient	3.52	0.699 – 5.9
γ_0	$\frac{k_2 p_0}{k_3}$	Scaled protein switch p_0	1.94	0.542 – 2.58
γ_1	$\frac{k_2 p_1}{k_3}$	Scaled protein switch p_1	1.91	0.516 – 3.18
γ_2	$\frac{k_2 p_2}{k_3}$	Scaled protein switch p_2	2.23	0.647 – 3.11
D_C	dC_L	Scaled measure of absorption	26300	2×10^3 – 6×10^5
I_{sat}	$\frac{I_{sat}}{L_{e1}}$	Normalized light saturation	24.8	20 – 30.0
I_0	$\frac{I_0}{L_{e1}}$	Normalized light intensity at source	99.2	0.0 – 200.0
S_H	$\frac{s_0}{s_h}$	Non-dimensional reciprocal of s_h	6.0	4.0 – 12.0
P_H	$\frac{k_3}{k_2 p_h}$	Non-dimensional reciprocal of p_h	0.560	0.380 – 2.29
E_L	E_L	Fraction of electrons from PSII-dependent path	0.75	0.7 – 0.8

Table 5.3: Table of all non-dimensional parameter values. Parameters that were already non-dimensionalized are included here for completeness. A short description of each parameter is included, and the ranges are calculated from the ranges of the dimensional parameters.

order k may be approximated to leading order as

$$\frac{1}{k+1} \nabla^{k+1} y_{n+1}.$$

In order to increase numerical stability, the traditional BE approach in equation 5.90 is modified in ode15s to include a term of the form $\kappa(y_{n+1} - y_{n+1}^{(0)})$, where κ is a scalar parameter and $y_{n+1}^{(0)}$ is the initial guess [157]. The resulting equations are called the Numerical Differentiation Formulas (NDFs). The extra term included in equation 5.90 can be written as $(y_{n+1} - y_{n+1}^{(0)}) = \nabla^{k+1} y_{n+1}$, which is approximately the leading order term in the truncation error of 5.90. This should improve the numerical stability and reduce the error (more details can be found in [157]). The implicit scheme for solving the equation for y_{n+1} at every time step uses a simple Newton iteration. We specify an initial time-step of 0.001, after which the solver specifies the remaining time steps. We set the relative and absolute error tolerances to 10^{-8} and solve over an interval $t = 0$ to t_{end} . Solutions are then plotted for each variable separately.

5.5.2 A numerical check

We solve a simplified version of the standard model in equations 5.82 to 5.87 in order to compare analytical and numerical solutions at early times, which can help verify the numerical code. We consider the case of no growth, ($\frac{d\Lambda}{dt} = 0$), no additional external sulphur, $S_0 = S = 0$, and we remove the loss term in the oxygen equation. We also neglect the effects of light. This gives the simplified model as

$$\frac{dS}{dt} = 0, \quad (5.91)$$

$$\frac{ds}{dt} = -(sH_{PSII}(1-s) + H)PSII(s-1) \quad (5.92)$$

$$+ K_3((p - P_R)H_{Ferment}(\Omega_2 - \omega) - sH_{Calvin}(s - S_1)),$$

$$\frac{dp}{dt} = K_2(sH_{Calvin}(s - S_1) - (p - P_R)H_{Ferment}(\Omega_2 - \omega)), \quad (5.93)$$

$$\frac{d\omega}{dt} = \Lambda[K_6(sH_{PSII}(1-s) + H_{PSII}(s-1)) \quad (5.94)$$

$$- K_5(\omega H_{Resp}(\Omega_1 - \omega) + \Omega_1 H_{Resp}(\omega - \Omega_1))],$$

$$\frac{d\Lambda}{dt} = 0, \quad (5.95)$$

$$\begin{aligned} \frac{dh}{dt} = & \Lambda H_{Sensitivity}(\Omega_2 - \omega)H_{Calvin}(S_1 - s) [E_L S_H s L(\Lambda) \\ & + (1 - E_L)P_H(p - P_R)]. \end{aligned} \quad (5.96)$$

To solve analytically, solutions can be built up piecewise. We consider what happens in the system initially, starting with the initial conditions $S_0 = 0$, $s_0 = 1$, $p_0 = 2.227$, $\omega_0 = 0$, $h_0 = 0$ and $\Lambda_0 = 0.00225$. In the first regime, at very early times, since $\omega = 0$ at $t = 0$, H_{Resp} is on, oxygen increases rapidly and is governed by the simple equation

$$\frac{d\omega}{dt} = \Lambda_0 [K_6 - K_5\omega], \quad (5.97)$$

until $\omega > \Omega_1$ (which happens very fast as Ω_1 is small), after which H_{Resp} switches off and oxygen is used in respiration at a constant rate. After this, in the second regime, oxygen is produced at a constant rate, $K_5\Omega_1$. We find that, as there is no external sulphur, internal sulphur decreases. Thus the $H_{PSII}(1 - s)$ switches are on and the $H_{PSII}(s - 1)$ switches are off. In this regime, internal sulphur will be sufficiently high for the Calvin cycle to operate, since $s > S_1$, so $H_{Calvin}(S_1 - s) \approx 0$ and protein, not hydrogen, is produced. Thus $\frac{dh}{dt} = 0$. This reduces the system at early times to

$$\frac{dS}{dt} = 0, \quad \frac{ds}{dt} = -s - K_3s, \quad \frac{dp}{dt} = K_2s, \quad \frac{d\omega}{dt} = \Lambda[K_6s - K_5\Omega_1], \quad \frac{d\Lambda}{dt} = 0, \quad \frac{dh}{dt} = 0. \quad (5.98)$$

Solving gives

$$S = 0, \quad s = \exp[-(K_3 + 1)t], \quad p = -\frac{K_2 \exp[-(K_3 + 1)t]}{(1 + K_3)} + c_2, \quad (5.99)$$

$$\omega = -\frac{\Lambda_0 K_6}{1 + K_3} \exp[-(1 + K_3)t] - K_5\Omega_1\Lambda_0 t + c_3, \quad h = 0, \quad \Lambda = \Lambda_0,$$

where $c_2 = p_0 + \frac{K_2}{1+K_3}$ and $c_3 = \Omega_1 + \frac{\Lambda_0 K_6}{1+K_3}$ are constants of integration calculated from the initial conditions.

For the third regime, we consider what happens when $s < S_1$. In this case, internal sulphur has decreased so the Calvin switch term will be $H_{Calvin}(S_1 - s) \approx 1$ and protein production will stop. The reduced model at the time the third regime begins, $t_3 = 0.663$, for which $s < S_1$, then becomes

$$\frac{dS}{dt} = 0, \quad \frac{ds}{dt} = -s, \quad \frac{dp}{dt} = 0, \quad \frac{d\omega}{dt} = \Lambda[K_6s - K_5\Omega_1], \quad \frac{d\Lambda}{dt} = 0, \quad \frac{dh}{dt} = 0. \quad (5.100)$$

which can be solved to give

$$S = 0, \quad s = d_1 \exp[-t], \quad p = d_2, \quad (5.101)$$

$$\omega = -d_1\Lambda_0 K_6 \exp[-t] - K_5\Lambda_0 t + d_3, \quad h = 0, \quad \Lambda = \Lambda_0,$$

where d_1 , d_2 and d_3 are constants of integration that can be calculated using the values s , p and ω at time $t_3 = 0.663$. We plot these three analytical solution regimes with the

numerical solution for the simplified system in equations 5.91 to 5.96 for $t < 4$ in Figure 5.11, and find good agreement between the analytical solution and the numerics until approximately $t = 3.5 - 4$. After this, more terms would be required in equations 5.100 to proceed further analytically. From here on, the model solutions are computed numerically.

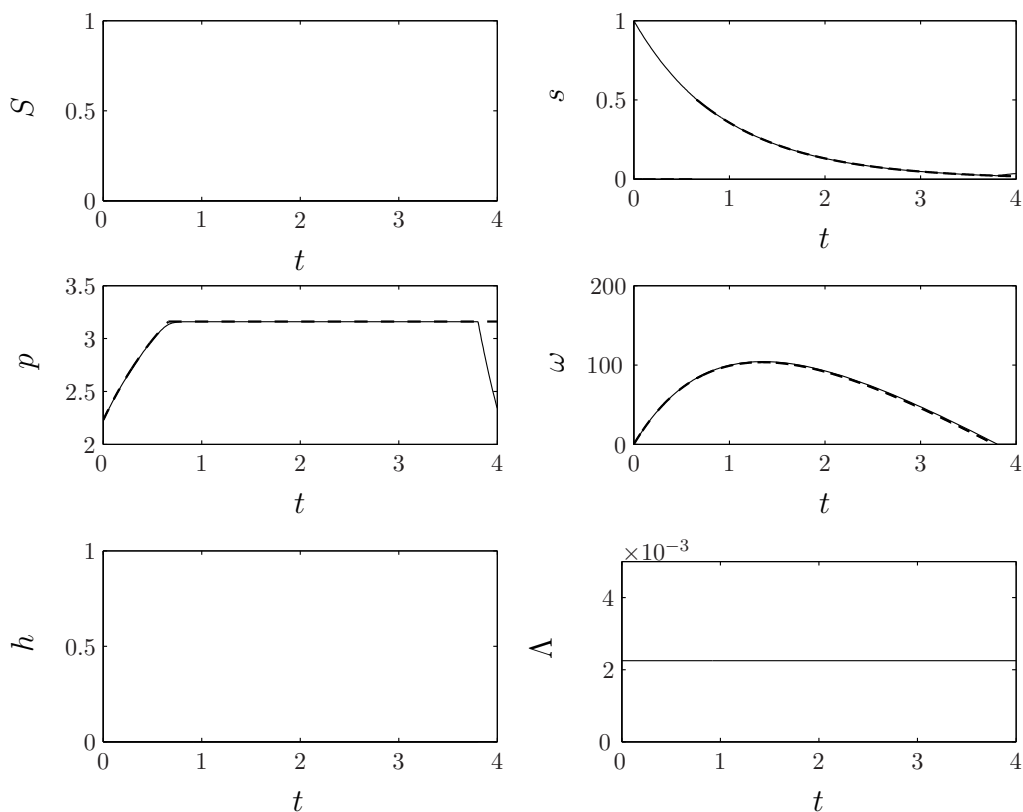


Figure 5.11: Numerical (solid lines) and analytical (dashed lines) solutions for a simplified version of the model. Good agreement is found between numerical and analytical solutions for early times, $t < 4$.

5.5.3 The sulphur-deprived case

Figure 5.12 shows the results for the standard model under sulphur deprivation, where the external sulphur concentration at the start of the experiment is $S_0 = 0 \mu M$. This corresponds to a typical experimental case where cells are grown in a sulphur-replete media, washed in a solution buffer and transferred to a sulphur-free media at time $t = 0$. The time range is $0 \leq t \leq 10$ in non-dimensional units, which corresponds to an end time of approximately 10 days (244 hours).

To explain these results chronologically, first observe that initial internal sulphur starts to decrease since it is used in protein production and PSII repair, and $S = 0$, so no sulphur

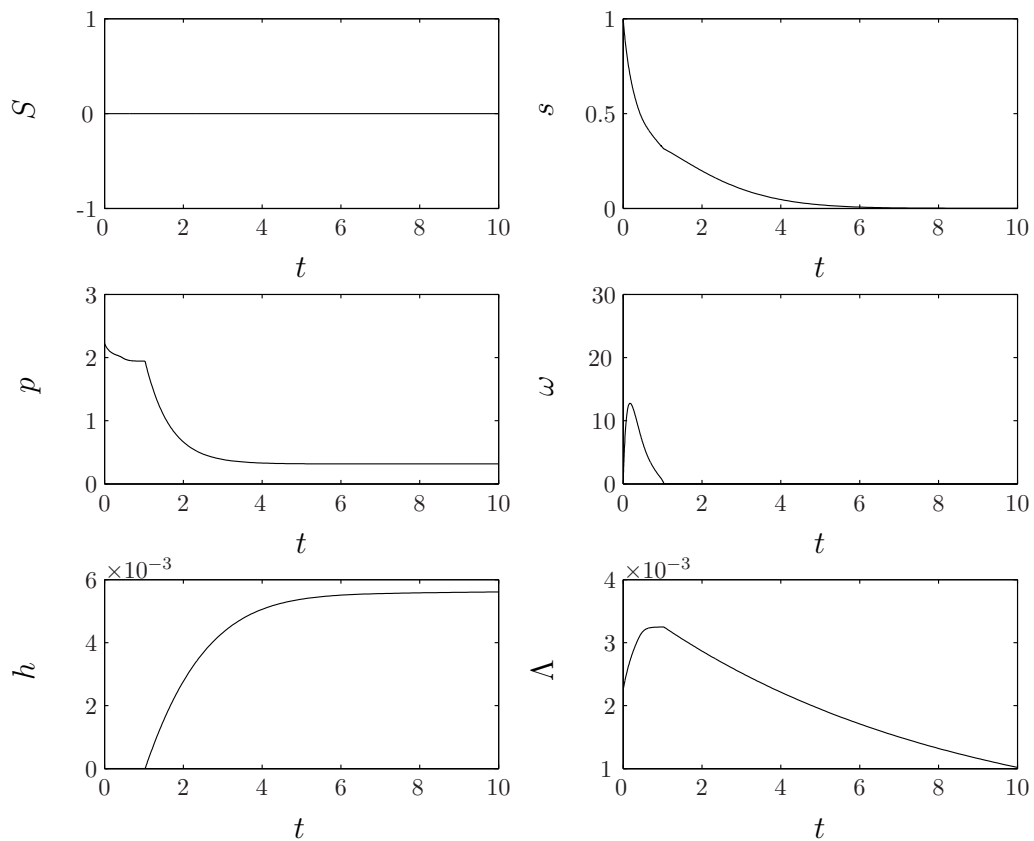


Figure 5.12: Results for the model with standard parameter values under sulphur deprivation, with initial condition $S_0 = 0$.

can be taken up from the media. Oxygen levels initially increase due to a higher rate of oxygen produced by photosynthesis than oxygen used in respiration. During this period the cell volume fraction increases, but when $s < S_1$, where $S_1 = 0.5$, growth slows down, as sufficient protein is not produced via the Calvin cycle. As s decreases further the photosynthesis rate falls below the respiration rate and the cells start using up all free oxygen in the system. A period of anaerobiosis (where the rate of oxygen produced from photosynthesis is less than or the same as the rate of oxygen used in respiration, and the oxygen in the media has also been used) begins after approximately 1 day ($t = 1$). As oxygen levels decrease below Ω_2 , fermentative protein breakdown begins, because low levels of photosynthetic activity mean the cells can no longer fulfil the energy production requirements. Small amounts of sulphur are released from this breakdown within the cells, so the internal sulphur curve continues to fall, but less rapidly than when $\omega > \Omega_2$. Hydrogen production begins after one day, as the system is now sufficiently low on oxygen, $\omega < \Omega_2$, and the Calvin cycle is not available to act as an electron sink, $s < S_1$.

During the hydrogen production phase protein and cell volume fraction decrease due to catabolism of endogenous substrate. Note that p reaches P_R , the base level of protein needed for cell survival, between 2 and 4 days. However, protein breakdown continues to supply electrons and sulphur to the photosynthetic pathway because the shrinking cell volume fraction causes oscillations in p around P_R (as Λ decreases, p increases transiently, so $p > P_R$). Thus more protein becomes available for breakdown as the cells shrink, so that the total protein in the system, $p\Lambda$, decreases in this period (not shown), and electrons for the hydrogenase are still released from protein even when p is close to P_R .

Initial hydrogen production rate is rapid, but the rate of production decreases with time due to reduction of cell volume fraction, decrease of sulphur (needed for repair of the PSII-dependent pathway to provide electrons to the hydrogenase), and decreasing endogenous substrate (protein) to supply the electrons. After around 6 days the cells runs out of internal sulphur, PSII activity stops and only minimal amounts of hydrogen are now produced from the few electrons released from the PSII-independent pathway as cells shrink. Between 6 and 8 days after sulphur deprivation began, hydrogen production stops and the cells continue to shrink and will eventually die. The final yield of gas after ten days is 106 mL H₂/L culture.

For direct comparison with Kosourov *et al.* 2002 [92] we obtain results for the standard model with $S_0 = 0$ and an end time of $t = 5.74$ (140 hours). At this time there is still some

hydrogen production, although very little (only another 3 mL is made) and the yield is 103 mL H₂/L culture. Kosourov *et al.* [92] suggests production has stopped at 140 hours, with a yield of 71.7 mL H₂/L culture. Data for $S_0 = 0 \mu\text{M}$ re-produced from Kosourov *et al.* [92] is shown in Figure 5.14.

Since the culture may not have been purged of oxygen at the start of the experiment, we investigate the effects of using the initial condition $\omega_0 \neq 0$ instead of $\omega_0 = 0$. Using values of ω_0 up to 100, which corresponds to 25,300 μM in dimensional units (which is, anyway, much beyond the saturation of oxygen in water χ), does not have significant effect on the model results. The maximum change in hydrogen yield at $t = 10$ only varied by 0.01%.

5.5.4 The sulphur-replete case

Figure 5.13 shows the model results for a sulphur-replete, sealed system. Although this is not the situation we shall generally consider, we present the results for the normal situation to check that the model functions as expected when sulphur-replete.

In Figure 5.13, external sulphur concentration decreases as sulphates are transported into the cell and a corresponding increase in internal sulphur is also found. Protein initially varies little and settles to an almost constant level and oxygen is produced. Under these ‘normal’ conditions, which are good for growth, there is a rapid increase in cell volume fraction in the first two days, with a doubling time of 21 hours, compared to an experiment range of 9.4 – 18.6 hours calculated from data in Fischer *et al.* 2006 [32] and Jo *et al.* 2006 [72]. After two days, light limitation, caused by increased shading as cell volume fraction increases, decreases oxygen production from PSII, causing the system to become anaerobic. To create sufficient energy for cell survival under anaerobiosis, fermentation begins, during which protein is broken down. Unlike the sulphur-deprived system, hydrogen production is not observed as sulphur levels are high and the Calvin cycle acts as the electron sink. Fermentation causes a decrease in protein and thus cell volume fraction, and as cell volume fraction decreases the effects of light limitation decrease, so that each cell receives more light as Λ decreases. Since the system is sulphur-replete, the rate of oxygen production increases and the system becomes aerobic when Λ has sufficiently decreased. This in turn creates a subsequent period of cellular growth and protein production, which occurs until increasing light limitation as Λ increases causes a subsequent period of anaerobiosis. Hence, under sulphur-replete, sealed conditions, oscillations in s , p , ω and Λ are found,

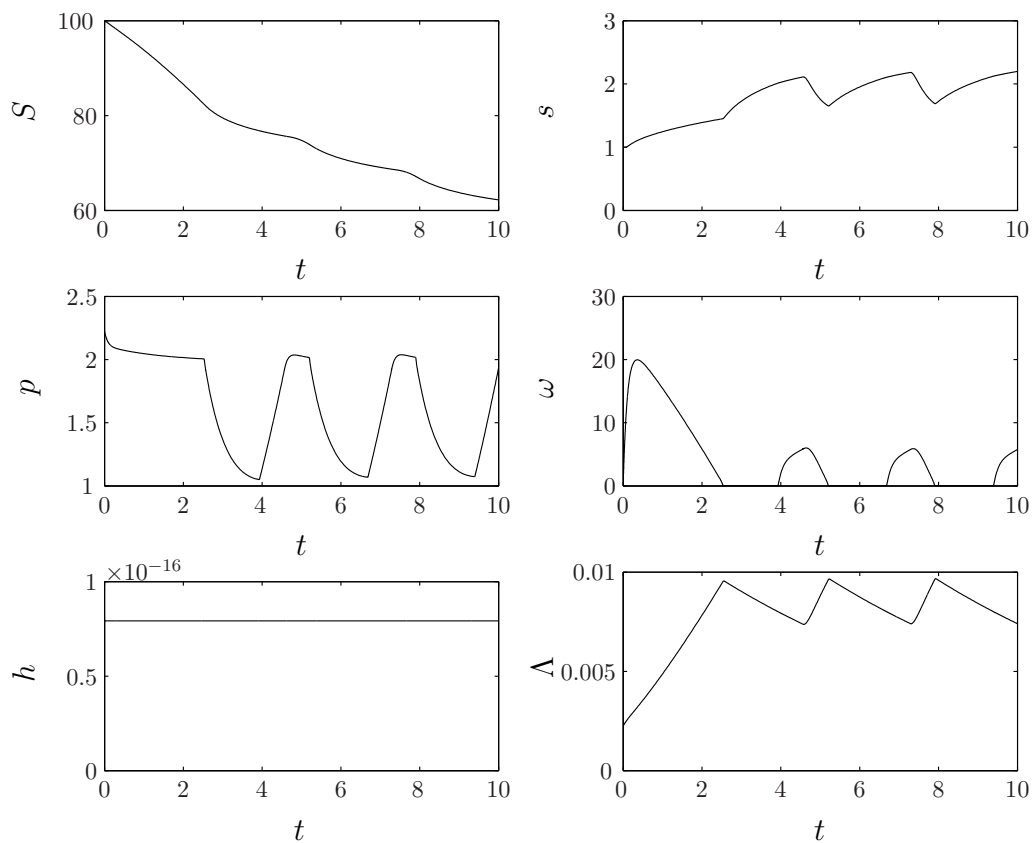


Figure 5.13: Results for the model with standard parameter values under sulphur-replete conditions, with initial condition $S_0 = 100$ in non-dimensional units.

with no hydrogen produced. The period of these oscillation is approximately 66 hours.

5.5.5 Varying the initial concentration of external sulphur, S_0

Kosourov *et al.* 2002 [92] and Zhang *et al.* 2002 [182] find that re-suspending the cells in media with minimal concentrations of external sulphur increases the yield of hydrogen gas compared to cells re-suspended in fully sulphur-deprived media. Data re-produced from Kosourov *et al.* [92] for initial conditions of external sulphur of $S_0 = 0 \mu\text{M}$, $S_0 = 25 \mu\text{M}$ and $S_0 = 50 \mu\text{M}$ are shown in Figure 5.14.

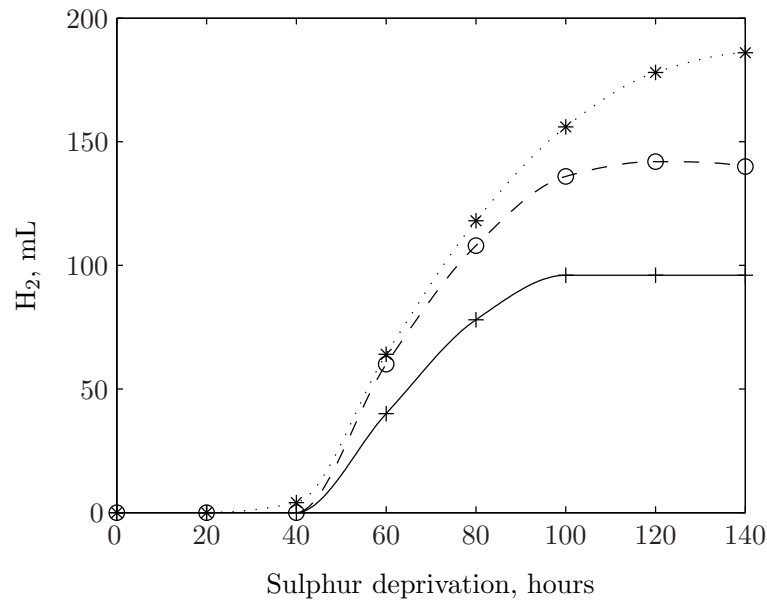


Figure 5.14: Data reproduced from Figure 6b in Kosourov *et al.* 2002 [92] for hydrogen production per 1.2 L of unsynchronized culture against time, where the cultures were deprived of sulphur at $t = 0$, and data points every 20 hours were manually measured from smooth curves in [92]. Solid lines with crosses are $S_0 = 0 \mu\text{M}$, dashed lines with circles are $S_0 = 25 \mu\text{M}$, and dotted lines with stars indicate $S_0 = 50 \mu\text{M}$.

To investigate, we present model results where the initial external sulphur concentration S_0 is varied, shown in Figure 5.15. The results for S_0 slightly greater than zero are similar to those for $S_0 = 0$, but as S_0 increases further internal sulphur and protein begin to decrease later. These slower decays allow the cell volume fraction to increase for longer, compared to the case $S_0 = 0$, leading to higher culture density when $S_0 > 0$. More oxygen is produced due to both higher sulphur levels available for PSII repair and a higher cell volume fraction. This, combined with a later decay in p and s , leads to a later onset of anaerobiosis and hydrogen production and a slightly later end time of production for

$S_0 > 0$. For larger values of S_0 , such as $S_0 = 3.45$ ($50 \mu\text{M}$ in dimensional units), yields of hydrogen gas are significantly larger after ten days: $h = 237 \text{ mL H}_2/\text{L culture}$ for $S_0 = 3.45$ compared to $h = 106 \text{ mL H}_2/\text{L culture}$ for $S_0 = 0$. Initial rates of hydrogen production per culture appear to have increased, but whether this is due to higher hydrogen production per cell, or simply due to more cells, is discussed in Section 5.5.6.

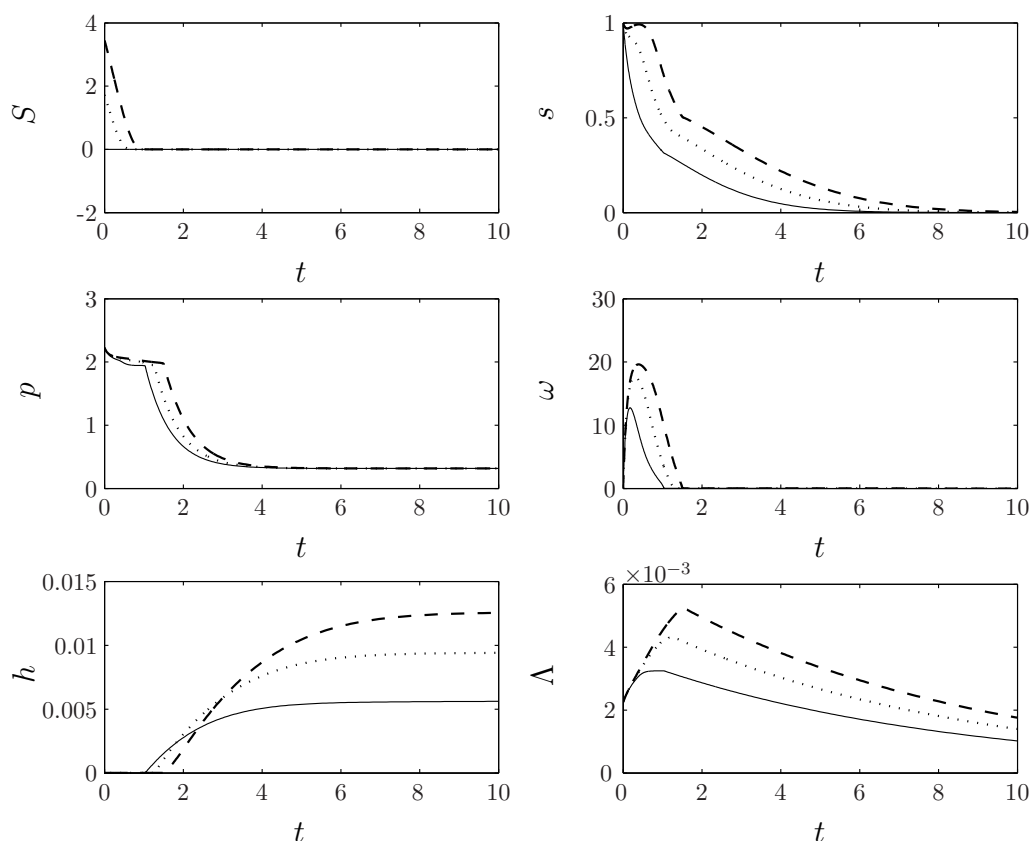


Figure 5.15: Results for the model with standard parameter values, with initial conditions of external sulphur of $S_0 = 0$ (solid lines), $S_0 = 1.725$ (dotted lines) and $S_0 = 3.45$ (dashed lines). These correspond to $0 \mu\text{M}$, $25 \mu\text{M}$, and $50 \mu\text{M}$, respectively.

Again, to compare with Kosourov *et al.* 2002 [92] for unsynchronized cells we obtain results for $t = 5.74$: for $S_0 = 1.725$ ($25 \mu\text{M}$), $h = 168 \text{ mL H}_2/\text{L culture}$, and for $S_0 = 3.45$ ($50 \mu\text{M}$), $h = 213 \text{ mL H}_2/\text{L culture}$, compared to $h = 127 \text{ mL H}_2/\text{L culture}$ for $25 \mu\text{M}$, and $h = 159 \text{ mL H}_2/\text{L culture}$ for $50 \mu\text{M}$ in [92]. Both this model and [92] indicate that increasing S_0 increases yield, although the simulation results are 58% and 101% higher, for $25 \mu\text{M}$ and $50 \mu\text{M}$ compared to $S_0 = 0 \mu\text{M}$, respectively. For $S_0 = 1.725$, hydrogen production starts after $t = 36.4$ hours, compared to $t = 43 - 47$ hours in Kosourov *et al.* [92], and for $S_0 = 3.45$ start time is $t = 45.2$ hours compared to $43 - 49$ hours. Again,

the trend is the same (increasing S_0 delays onset of hydrogen production), and overall agreement is promising. The data also match trends seen in Zhang *et al.* 2002 [182]. The end times for hydrogen production in the simulations are also in the same range as in [92].

Figure 5.16 shows results from the standard model for just the hydrogen yield and cell volume fraction for a range of different values for initial external sulphur. Increasing S_0 from zero to $S_0 = 6.9$ delays the start time of hydrogen production and increases yield at time $t = 10$ but, as S_0 is increased further, yields decrease until S_0 is so high that hydrogen is not produced in this time frame (as the start time also increases with S_0). Increase in yield for small S_0 can in part be attributed to the culture attaining higher cell volume fractions under these conditions, and will be discussed further in Section 5.5.6.

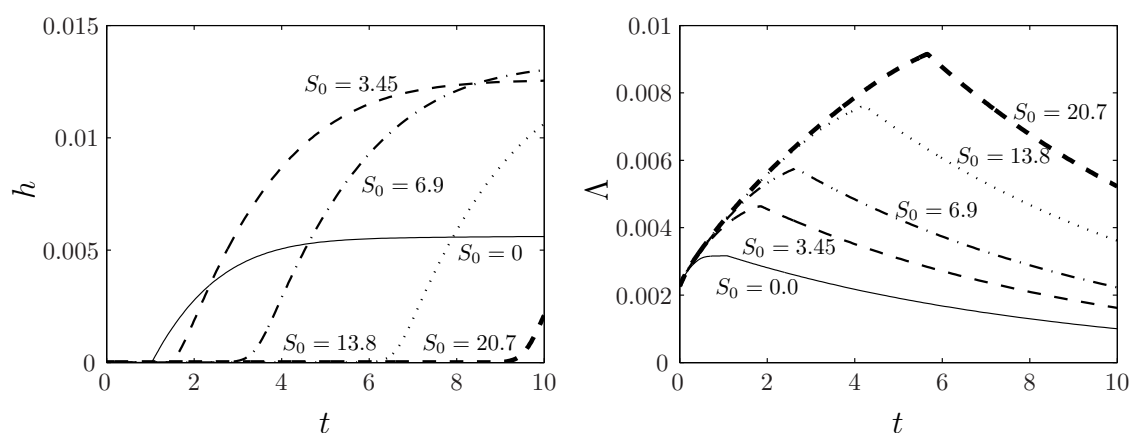


Figure 5.16: Hydrogen and cell volume fraction curves for the model with standard parameter values and with initial conditions $S_0 = 0$ (solid lines), 3.45 (dashed lines), 6.9 (dot-dashed lines), 13.8 (dotted lines), and 20.7 (thick dashed lines).

In Figure 5.17 we plot curves for total hydrogen yield at time $t = T$ as initial external sulphur S_0 is varied for a range of values of T . For $T = 5.74$, increasing S_0 from zero first increases yield significantly but then decreases yield when S_0 is large. If S_0 is too large no hydrogen is produced. The maximum of this curve corresponds to 214 mL H_2/L culture at $S_0 = 3.7$ (i.e. $53.65 \mu\text{M}$). For $T = 10$ a higher yield of hydrogen is obtained and the curve is seen to level off for intermediate values of S_0 . This ridge may be a balance between a later start time and a higher cell volume fraction as S_0 increases from zero. The optimal S_0 is now $S_0 = 6.19$ (i.e. $89.8 \mu\text{M}$) with $h = 246 \text{ mL } H_2/L$ culture.

For $T = 15$, we obtain a wider range of S_0 for which hydrogen is produced, as expected. However, we do not obtain significantly more hydrogen than for $T = 10$ (only a 3.46% increase). Interestingly, undulations can be observed on the curve (see simulation in Figure

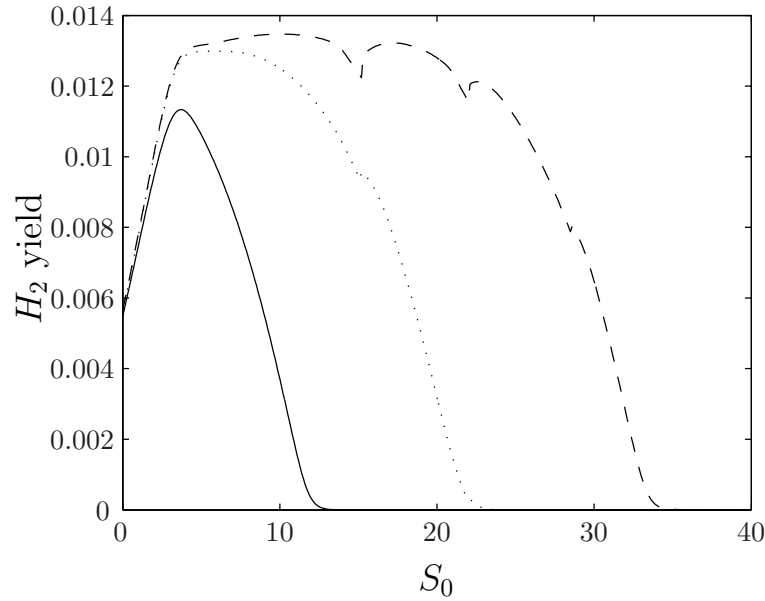


Figure 5.17: Hydrogen yield at time $t = T$ as a function of initial condition S_0 where $T = 5.74$ (solid line), $T = 10$ (dotted line) and $T = 15$ (dashed line).

5.17).

Figure 5.18 plots model results for values of S_0 around one of these undulating regions. Increasing S_0 from $S_0 = 15.2$ increases the internal sulphur concentration but, for the values of S_0 plotted, the onset time to anaerobiosis is approximately the same (see Figure 5.18). For the smaller value of $S_0 = 15.2$, protein increases slower than for the larger values and s falls below S_1 at an earlier stage. Hence, the Calvin cycle switches off sooner and less growth occurs for $S_0 = 15.2$ compared to $S_0 = 18.5$ and $S_0 = 22$, leading to a later start time, T_H , for $S_0 = 18.5$ and $S_0 = 22.0$, as the cells grow instead of producing hydrogen for a longer period. Surprisingly, however, the overall yield is higher for $S_0 = 18.5$, despite the later start time, due to increased cell volume fraction. Further increasing S_0 to $S_0 = 22.0$ increases cell volume fraction further but results in a lower yield at time $T = 15$, because the increase in T_H reduces the time between $T_H \leq t \leq T$ in which hydrogen can be produced. Thus the undulations in the curve are caused by the balances between later start time T_H potentially decreasing yield and higher cell volume fraction increasing yield as S_0 is increased, and occur only after subsequent periods of anaerobiosis, when differences in the switch functions around S_1 as S_0 varies affect growth.

Results are shown in Figure 5.19 for the effect of initial external sulphur concentration S_0 on start time for hydrogen production, T_H . To plot this we record the first time that hydrogen levels are greater than a tolerance value (since $\omega_0 = 0$ and H_2 is initially produced

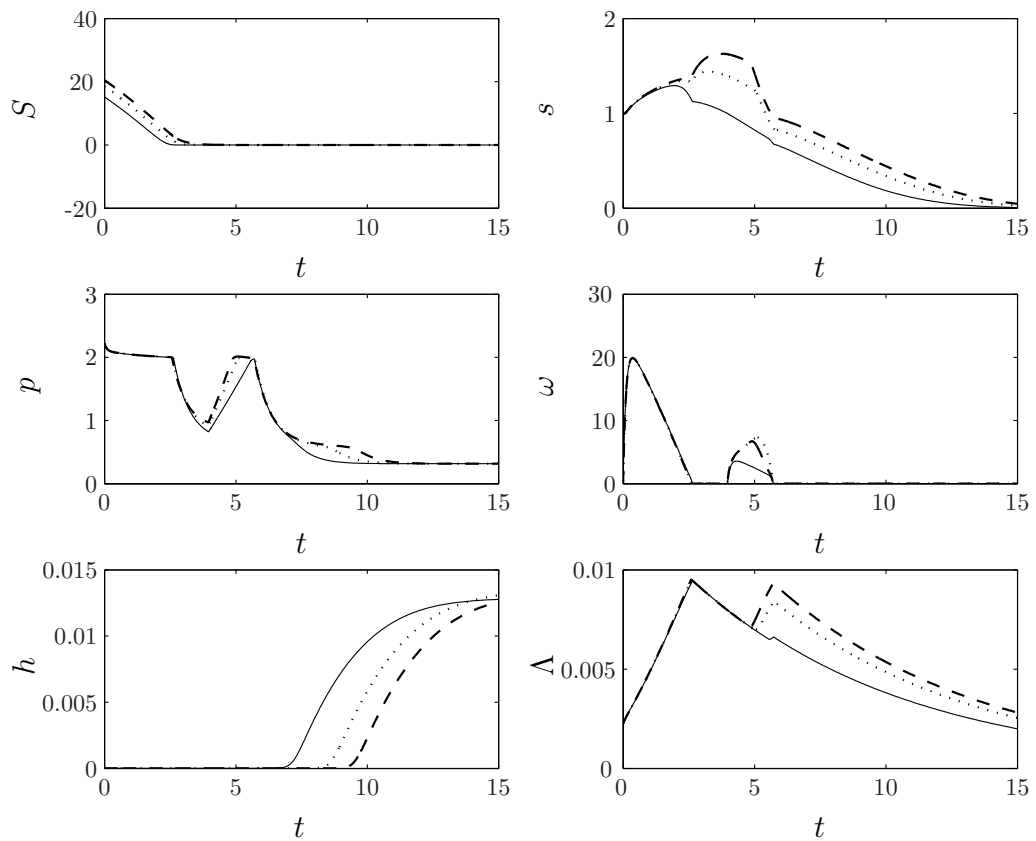


Figure 5.18: Results for the model with standard parameter values where $T = 15$, with initial conditions of $S_0=15.2$ (solid line), $S_0 = 18.5$ (dotted) and $S_0 = 22.0$ (dashed). These results illustrate the behaviour of the model for values of S_0 around the undulating regions on the curve for hydrogen yield as a function of S_0 in Figure 5.17.

transiently before respiration rapidly consumes all the oxygen produced by photosynthesis). We set the tolerance to be $\text{tol} = 10^{-5}$. The curve increases on average, showing that increasing the initial amount of external sulphur delays the onset of hydrogen production. The change in gradient of the curve around $S_0 = 5$ is due to T_H changing from being critically dependant on oxygen (since for small S_0 , $s < S_1$ before $\omega < \Omega_2$), to being mainly dependent on sulphur (since the cell becomes anaerobic and there is a delay before $s < S_1$ and the Calvin cycle stops).

We also observe small kinks on the curve. These are due to the behaviour of the system around $s = S_1$. For sufficiently large S_0 , around $s = S_1$, sulphur increases and there will be a period where $s > S_1$ and aerobiosis occurs again, allowing a small amount of growth which, in turn, decreases s more rapidly than for smaller S_0 when there is no growth. This results in a smaller value of T_H compared to that for slightly smaller values of S_0 . However, if S_0 is increased further, sulphur increases more and the period of aerobic growth is elongated, so that the system takes longer to get to $s < S_1$ and the onset of H_2 production is delayed, thus T_H increases. This decrease and subsequent increase in T_H as S_0 is increased and $s \approx S_1$ is a transient effect when the system moves from anaerobic to subsequent aerobic periods, and produces the small kinks on the curve in Figure 5.19.

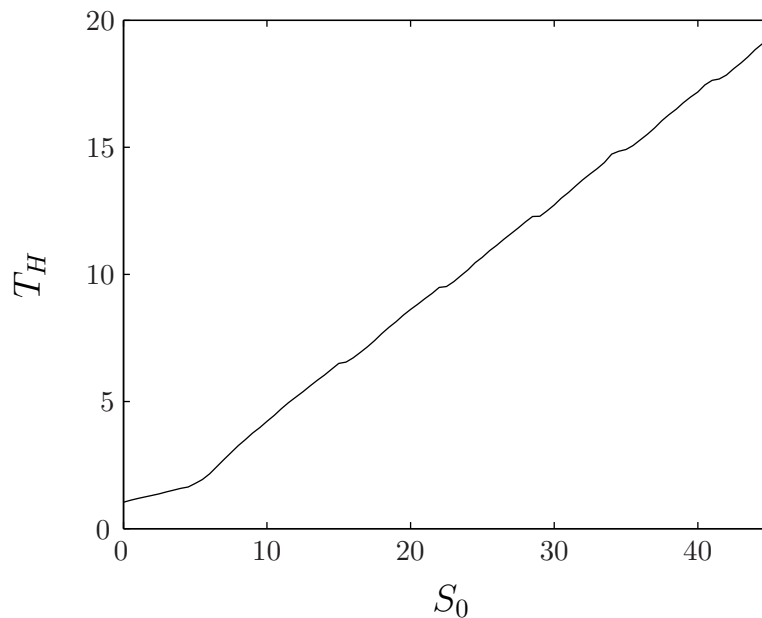


Figure 5.19: Initial amount of external sulphur, S_0 , plotted against the start time of hydrogen production, T_H .

5.5.6 Comparing initial rates of hydrogen production as S_0 varies

To understand the trends in yield as S_0 is increased from zero, we investigate the initial rates of hydrogen production as S_0 is varied. We plot rates of hydrogen production in the first 14.6 hours (0.6 non-dimensional time units) as a function of S_0 . For simplicity, we define hydrogen production rate as

$$H_2 \text{ rate} = \frac{h_{(T_H+0.6)}}{0.6(\Lambda_{(T_H+0.6)} + \Lambda T_H)/2}, \quad (5.102)$$

where we average Λ over the initial hydrogen production period to get hydrogen rate per unit of cell volume fraction per non-dimensional time unit. This is plotted in Figure 5.20 and is comparable to data in Kosourov *et al.* [92], who measured the hydrogen production rate per mole of chlorophyll in the initial 10 – 15 hours of production.

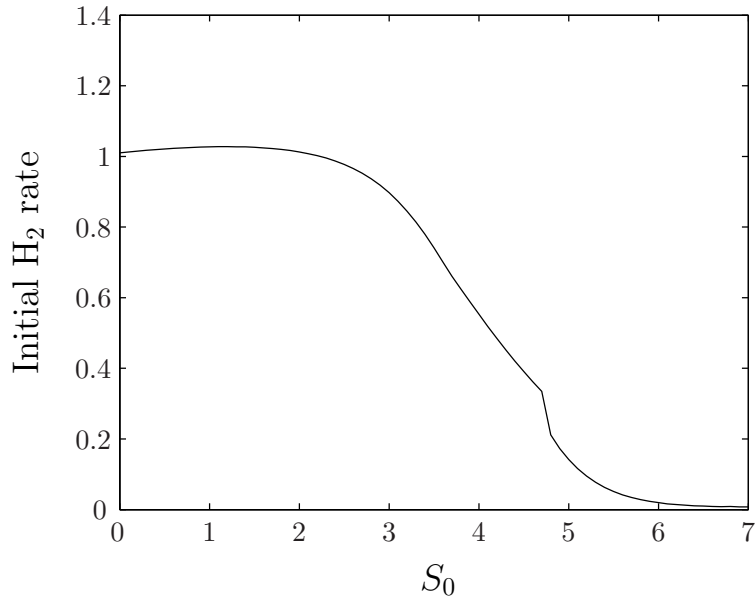


Figure 5.20: Initial rates of hydrogen production (in the first 14.6 hours) plotted against the initial amount of external sulphur.

Figure 5.20 shows there is a very slight increase in the initial rate of hydrogen production as S_0 is increased from zero up to approximately $S_0 = 1.5$, and thereafter the curve decreases and reaches very low levels at $S_0 = 6$. The sharp decrease around $S_0 = 4.8$ is caused by hydrogen production changing from being predominantly oxygen dependent to predominantly sulphur dependent (since for higher S_0 , $\omega < \Omega_2$ before $s < S_1$, so that hydrogen production is initially slow as the Calvin cycle is the main electron sink).

These results show that there is an optimal initial value for external S_0 for improving the rate of hydrogen produced per cell ($0 < S_0 < 2$), which is different to the optimal for

improving yield at time T ($S_0 = 6.19$ for $T = 10$). Thus methods of optimization of the hydrogen production system depend on what is required: more hydrogen per cell or more hydrogen produced over a fixed period.

5.5.7 Varying the initial cell volume fraction, Λ_0

Here, we explore what affect changing the initial cell volume fraction has on the final yield of hydrogen produced. We find that for $S_0 = 0$ and $S_0 = 3.45$ the time to anaerobiosis decreases with increasing Λ_0 but the time to hydrogen production stays the approximately the same. This is because a greater cell volume fraction means any oxygen produced up quicker in respiration, but internal sulphur is used slower due to increased light limitation slowing down PSII activity and repair. The delay between anaerobiosis onset and hydrogen production starting was seen in Kosourov *et al.* [92], and here is due to the time it takes for s to reach S_1 , since the Calvin cycle will still be operating when anaerobiosis begins. We see higher yields for $\Lambda_0 = 0.0045$ and $\Lambda_0 = 0.00225$ compared to $\Lambda_0 = 0.00125$ under these conditions (see Figure 5.21), and we find that the hydrogen start time initially decreases and then increases as Λ_0 is increased from 0.00125. For $S_0 = 0$ we see a yield of $h = 247$ mL H₂/L culture for $\Lambda_0 = 0.0045$ compared to 106 mL H₂/L culture when $\Lambda_0 = 0.0025$, but for $S_0 = 3.45$ there is less of an increase for $\Lambda_0 = 0.0045$: $h = 249$ mL H₂/L culture for $\Lambda_0 = 0.0045$ compared to 237 mL H₂/L culture for $\Lambda_0 = 0.0025$, shown in Figure 5.21.

This yield does not increase significantly if Λ_0 is increased beyond $\Lambda_0 = 0.0045$, since there is a significant delay in the start of hydrogen production after anaerobiosis is reached (as light limitation for high cell volume fraction decreases the rate of sulphur used in repairing PSII, so that the Calvin cycle is still in operation when $\omega < \Omega_2$).

5.6 Discussion

In this chapter, a simple mechanistic model to describe hydrogen production in green algae has been constructed. By modelling in a mechanistic way we have significantly simplified this incredibly complicated system to just six variables (compared to Jorquera *et al.* [75] with 17): internal and external sulphur, s and S , respectively, protein, p , oxygen, ω , cell volume fraction, Λ and hydrogen gas, h . Key assumptions have been made that are necessary for the modelling process and the impact of these will be further explored in Chapter 6. Parameter values have been found from independent experimental data,

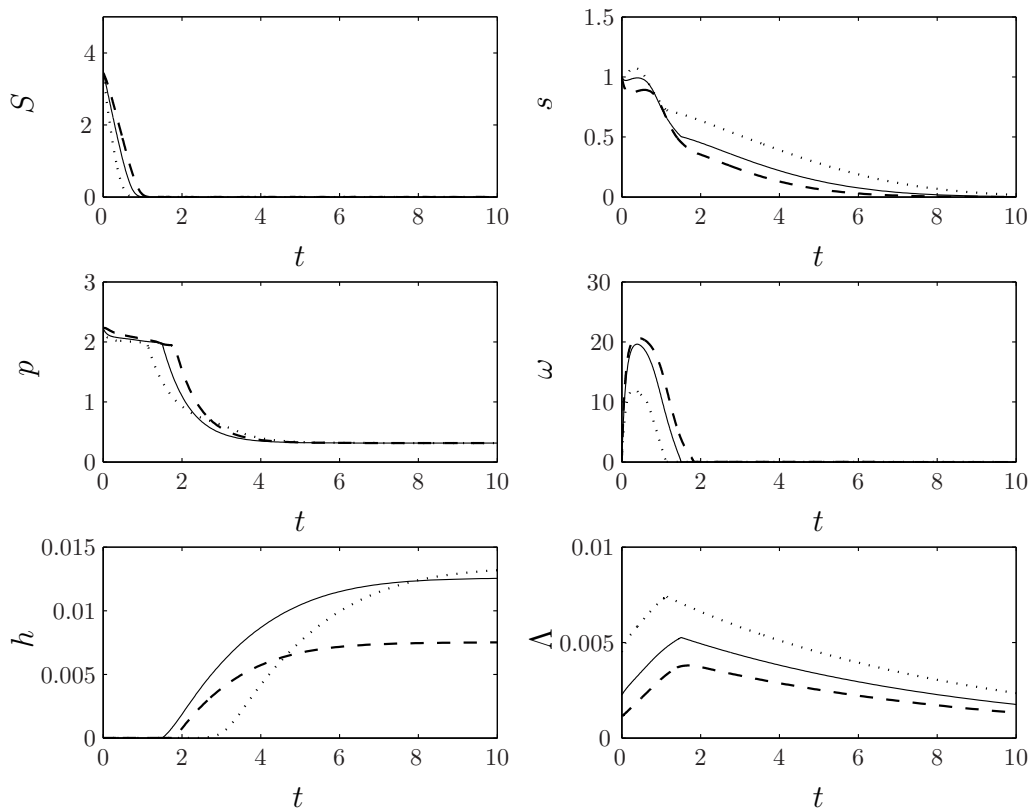


Figure 5.21: Results for the model with standard parameter values, with initial condition $S_0 = 3.45$ and $\Lambda_0 = 0.00225$ (solid lines), $\Lambda_0 = 0.0045$ (dotted lines) and $\Lambda_0 = 0.001125$ (dashed lines).

where possible, or else we have estimated a range of values. The model was then non-dimensionalized using suitable scalings. A numerical scheme in Matlab was used to solve the model and this was verified by comparison with a closed form analytical solution for a much reduced system. Results for the standard values of the parameters and with a range of initial conditions were computed in Section 5.5.

The experimental studies of Kosourov *et al.* 2002 [92], Zhang *et al.* 2002 [182] and Melis *et al.* 2000 [114] guided the construction of the model in Section 5.2. Encouragingly, good agreement was obtained between these experimental results and model simulations for the case of sulphur deprivation, $S = 0 \mu\text{M}$. The model predicts a start time for hydrogen production, T_H , of approximately $T_H = 24$ hours compared to $T_H = 27$ hours in Zhang *et al.* [182] and $T_H = 40$ hours in Kosourov *et al.* [92]. In simulation results, hydrogen production begins almost as soon as the system became anaerobic when $S = 0 \mu\text{M}$, which is consistent with observations by Zhang *et al.* [182], but Kosourov *et al.* [92] found a slight delay between onset of anaerobiosis and hydrogen production. The predicted hydrogen yield from the model is in the same range as Kosourov *et al.* [92] (106 mL H_2/L culture after 140 hours, compared to an average of 71.7 mL H_2/L culture in [92]), and we also find that hydrogen production stops in approximately the same time range. Model results can not be directly compared to other experimental papers, as different experimental conditions were used. Hydrogen production also followed the same trends as experiments, with an initially high rate which gradually levels off. Endogenous substrate, modelled as protein in this model, is catabolized during anaerobic hydrogen production. This releases both electrons for the hydrogenase pathway via donation at PSI and minimal quantities of internal sulphur, which are used to repair PSII, which then also passes electrons to PSI. Thus hydrogen production depends on electrons passed to PSI by both of these protein-dependent mechanisms (shown by PSII-dependent and PSII-independent terms in equation 5.44), and the model shows that as protein available for electron donation and PSII repair decreases, the hydrogen production rate also decreases and eventually stops. This explanation is consistent with results provided by Kosourov *et al.* [92].

Under sulphur-replete conditions, the model results show that no hydrogen is produced even when the system becomes anaerobic due to light limitation caused by a high cell volume fraction. This is consistent with the observation in Zhang *et al.* [182], where a concentrated culture in a sealed container became anaerobic as cell volume fraction increased, but only inactive hydrogenase was found: no hydrogen was produced.

The model predicts that as the initial concentration of external sulphur, S_0 , increases from zero the hydrogen yield after a set period at first increases: for $S_0 = 25 \mu\text{M}$ and $S_0 = 50 \mu\text{M}$ the model predicted final yields of hydrogen of 177.4 mL H_2/L culture and $h = 213 \text{ mL H}_2/\text{L}$ culture, respectively. For the same initial concentrations of sulphur, Kosourov *et al.* [92] measure average yields of 127 mL H_2/L culture and 159 mL H_2/L culture. For higher values of S_0 we also find a later onset time of hydrogen production, T_H , and, as S_0 gets very large, a decrease in yield over a set time, T , as the time in which hydrogen can be produced, $T_H < t < T$, is much reduced. These trends in yield as S_0 increases from zero are consistent with trends demonstrated in experimental papers [92, 182]. The delay between onset and anaerobiosis and hydrogen production predicted for $S > 0 \mu\text{M}$ are due to slower sulphur decay causing an extended period of Calvin cycle activity, so that the hydrogenase was not the preferred electron sink in the initial period of anaerobiosis.

We find that as S_0 is increased from zero, the initial rate of hydrogen production remains approximately constant for $0 \mu\text{M} \leq S_0 \leq 43.5 \mu\text{M}$ and decreases thereafter. The simulations are consistent with observations from Zhang *et al.* [182] and the rationale in Hypothesis 3, that increasing S_0 from zero increases hydrogen yield, but does not significantly increase initial rate per cell and, hence, increased yields for intermediate $S_0 > 0 \mu\text{M}$ are ultimately due to larger cell volume fraction. This is supported by the fact the hydrogen yield (at a set time, $T = 10$) increases as the cell volume fractions increases in both the simulations and Zhang *et al.* [182] (and in Kosourov *et al.* [92] when $S_0 \geq 25 \mu\text{M}$) even when the initial rate of production decreases. However, Kosourov *et al.* [92] found an increase in rate of initial hydrogen production as S_0 increased from zero to $25 \mu\text{M}$, and hypothesize that the increase in rates for $0 < S_0 \leq 25$ are due to increased residual levels of PSII due to higher internal sulphur (Hypothesis 1 in Section 5.1.5). This increase in rates was not found in our simulations, thus our model simulations are consistent with Hypothesis 3 and inconsistent with Hypothesis 1.

In the simulations, increasing S_0 beyond $S_0 = 43.5 \mu\text{M}$ decreases the initial rate of hydrogen production, so that at approximately $S_0 = 87 \mu\text{M}$ the rate is only 1.95% of the rate at $S_0 = 0 \mu\text{M}$. This is due to increased light limitation caused by higher cell volume fraction, which is itself caused by higher internal sulphur concentration, for $S_0 > 43.5 \mu\text{M}$ compared to for $S_0 < 43.5 \mu\text{M}$. This is consistent with the trends found by Kosourov *et al.* [92] and Zhang *et al.* [182] for large S_0 . Thus the simulations are consistent with

Hypothesis 2: the initial rate of hydrogen production decreases for $S_0 > 43.5 \mu\text{M}$ compared to $S_0 < 43.5 \mu\text{M}$ due to increased light limitation caused by large cell volume fraction.

Increasing the cell volume fraction from zero initially decreases the time to hydrogen production and then increases it when Λ is large. Kosourov *et al.* [92] also see an earlier onset with increasing Λ_0 , but they did not see a later onset as Λ_0 gets very large. However, it is possible that this trend could be seen experimentally if very large Λ_0 were used. The results for varying cell volume fraction in Section 5.5.7, where large Λ_0 can increase the yield of hydrogen gas dependent on S_0 , suggest that an optimal yield of hydrogen could be obtained by optimizing the initial cell volume fraction of the culture Λ_0 in tandem with optimizing S_0 .

In Chapter 6, a parameter sensitivity analysis is performed for a range of parameter values. The model is then used to innovate new ways of optimizing the total yield of hydrogen gas produced from sulphur-deprived green *C. reinhardtii* cells over a set period. Further consideration of the modelling assumptions and the viability of the novel mechanistic model are discussed at the conclusion of this work, in Section 6.3.

Chapter 6

Investigating parameter sensitivity and optimizing hydrogen yield for the mechanistic hydrogen model

Summary

In this chapter, a parameter sensitivity analysis for the hydrogen production model presented in Chapter 5 is performed. This is used to suggest parameters that could be used to increase yields of hydrogen gas. Novel strategies for re-addition of external sulphur are then innovated, tested and compared in order to find the strategy and corresponding parameter values that gives the highest yield of hydrogen gas over a set period.

6.1 Parameter sensitivity

In this section, we test the sensitivity of the model to the parameters using the standard initial conditions, with initial sulphur $S_0 = 3.45$, which corresponds to approximately 50 μM . We set S_0 to be non-zero so that changing parameters associated with sulphur uptake have an effect on the system. We investigate varying all the parameters within the ranges given in Table 5.3 and plot results to $t = 10$ with standard values for the other parameters.

6.1.1 Parameters in the sulphur uptake equation

Scaled parameters for sulphur uptake, A_1 and B , appear in the external sulphur function in equation 5.83 and A_2 is equivalent, and dependent on, A_1 in the internal sulphur equation.

We find that varying B within its range has little effect on the model results. Decreasing A_1 causes the rate of sulphur uptake to decrease, so the cells take longer to use up all available sulphur. This appears to be an advantage to the cells because they keep their internal sulphur levels higher for longer, since external sulphur is slowly taken in and does not run out as quickly, allowing more protein production and more cell growth and division. This causes anaerobiosis and hydrogen production to begin slightly later, but due to higher cell volume fractions the overall yields of H_2 production are higher. This shows that limiting the amount of sulphur the cells can take in can give higher yields of H_2 gas, but this needs to be balanced with later onset of hydrogen production, and although yields are not much higher here, correct manipulation of this variable may produce significantly higher yields. Increasing A_1 has the opposite effect, with lower yields of hydrogen gas produced even though onset of production is earlier.

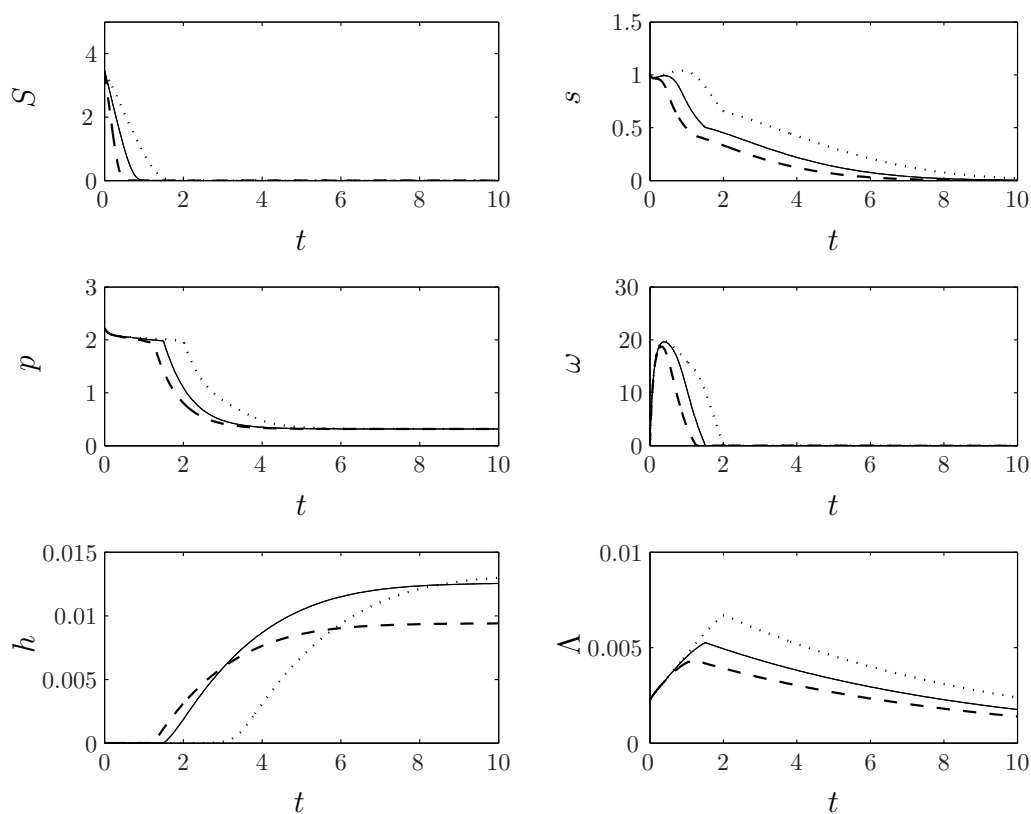


Figure 6.1: Model results when the sulphur uptake parameter A_1 is increased (dashed lines) and decreased (dotted lines) by a factor of 2, compared to model results for the standard parameter values (solid lines).

6.1.2 Parameters in substrate equations for sulphur and protein

K_3 is a non-dimensionalized, scaled version of the protein production rate k_3 and it multiplies the terms relating to protein breakdown and protein production in the sulphur equation. Varying K_3 in the lower range of the parameter has little effect on the system, but setting $K_3 = 25.4$, at the upper end of the range, causes sulphur and protein levels to stay at almost constant levels, and hydrogen is not produced in the time range $0 \leq t \leq 10$ because the system does not become anaerobic. P_R is the non-dimensional protein level required for cell survival. Varying this within the range given in Table 5.3 also has little significant effect on the system. However, we expect that increasing P_R to a high value would have a profound effect on the system, since it could lead to a situation where cell volume fraction shrinkage does not occur as the cell needs to maintain a high level of protein for survival. This situation would be unrealistic.

K_2 is the ratio of protein breakdown (to release sulphur) to sulphur used to repair PSII. It multiplies the protein breakdown and production terms in the protein equation, as K_3 does in the sulphur equation. Increasing K_2 implies greater protein production leading to sustained higher levels of protein and more rapid culture growth compared to the standard case (see Figure 6.2). This leads to earlier onset of both anaerobioses and hydrogen production. An increase also results in earlier protein breakdown and earlier cell shrinkage, which creates slightly higher internal sulphur concentration and we see a slight increase in yield and a more rapid decrease in p . Decreasing K_2 from the standard value causes lower cell growth and a later onset of hydrogen production and we see a smaller yield. These results suggest that yield could be slightly improved by increasing protein production in the early stages and protein breakdown in the latter stages. However, how much this could improve the yield is unclear since we only see a small increase in yield, and rapid protein breakdown will lead to hydrogen production stopping earlier. Also, this term would really need to be varied in parallel with K_3 , since if protein breakdown increases sulphur released from protein breakdown in the sulphur equation should also increase, although we do find that varying K_2 and K_3 together produces similar results to varying K_3 alone (results not shown).

6.1.3 Parameters relating to oxygen and hydrogen production

K_6 and $K_5\Omega_1$ are the non-dimensionalized parameters for normal rate of photosynthesis and respiration, respectively. Increasing K_6 from the standard value implies a higher rate

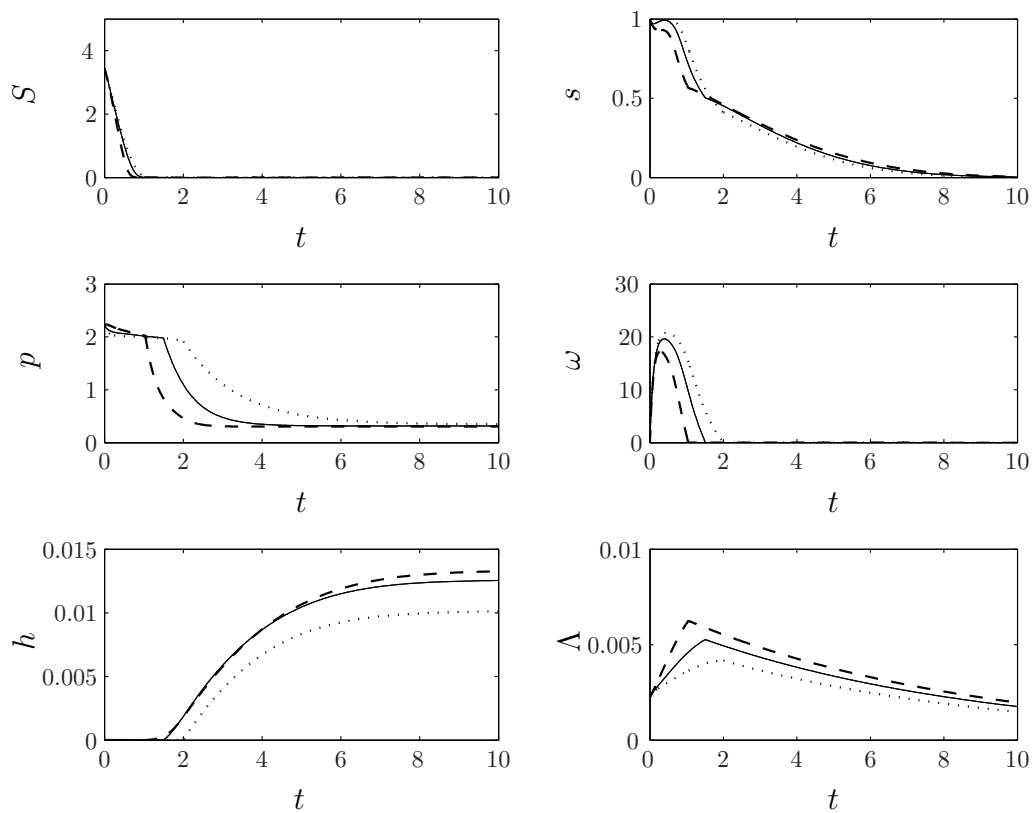


Figure 6.2: Model results when K_2 is increased (dashed lines) and decreased (dotted lines) by a factor of 2, compared to model results for the standard parameter values (solid lines).

of photosynthesis leading to more oxygen produced. Hence, anaerobiosis is reached later and hydrogen production is delayed. The cell volume also increases for a longer period during sulphur deprivation but, since more sulphur is used up in oxygenic PSII repair and it takes longer to reach anaerobiosis, there is less sulphur available initially by the time hydrogen production begins, and hydrogen production stops at approximately the same time as for the standard value of K_6 . This, combined with a later start time and increased light limitation due to larger cell volume fraction, reduces the yield of hydrogen as K_6 is increased, and is shown in Figure 6.3. If K_6 is decreased within the specified range in Table 5.3, less oxygen is produced from PSII and anaerobiosis occurs sooner, but hydrogen production begins later than in the standard case as internal sulphur is used up slower, so that there is a delay after anaerobiosis is reached until $s < S_1$. This means the cell volume fraction is smaller when H_2 production begins and this, combined with a reduction in available protein and sulphur for PSII, means there is a smaller yield of hydrogen gas. Varying K_5 naturally has the opposite effect; increasing from the standard value means more respiration and anaerobiosis is reached quicker and decreasing gives a lower rate of respiration so hydrogen production starts later. Varying Ω_1 , the non-dimensionalized oxygen level required for full respiration, follows the same trends as altering K_5 since the rate constant for respiration is $K_5\Omega_1$. Figure 6.3 shows results for varying K_6 .

Setting V_L , the scaled oxygen loss due to super saturation, to the top of the range in Table 5.3 has very little effect on the system, where less of a build up of oxygen occurs, but this quantitative difference in oxygen concentration does not significantly affect the time for anaerobiosis. Decreasing V_L within the range, however, causes a large build up of oxygen and delays the onset of hydrogen production, leading to a decreased yield of hydrogen gas.

Moving on to the hydrogen equation, the simulation results were found to be insensitive to Ω_2 , the scaled switch value, and P_H , a normalized parameter for rate of hydrogen production from the PSII-independent pathway. Varying S_H , the residual level of PSII activity in the culture, had a more significant effect. Increasing S_H from the standard value led to more hydrogen production (and a decrease, less) due to a higher residual level of PSII activity providing more electrons to the hydrogenase pathway. However, in reality S_H can not be varied independently of the parameter K_6 for oxygen production from PSII, since an increase in electron production from PSII would also cause an increase in oxygen and the system may not remain anaerobic. It does, however, suggest that if one

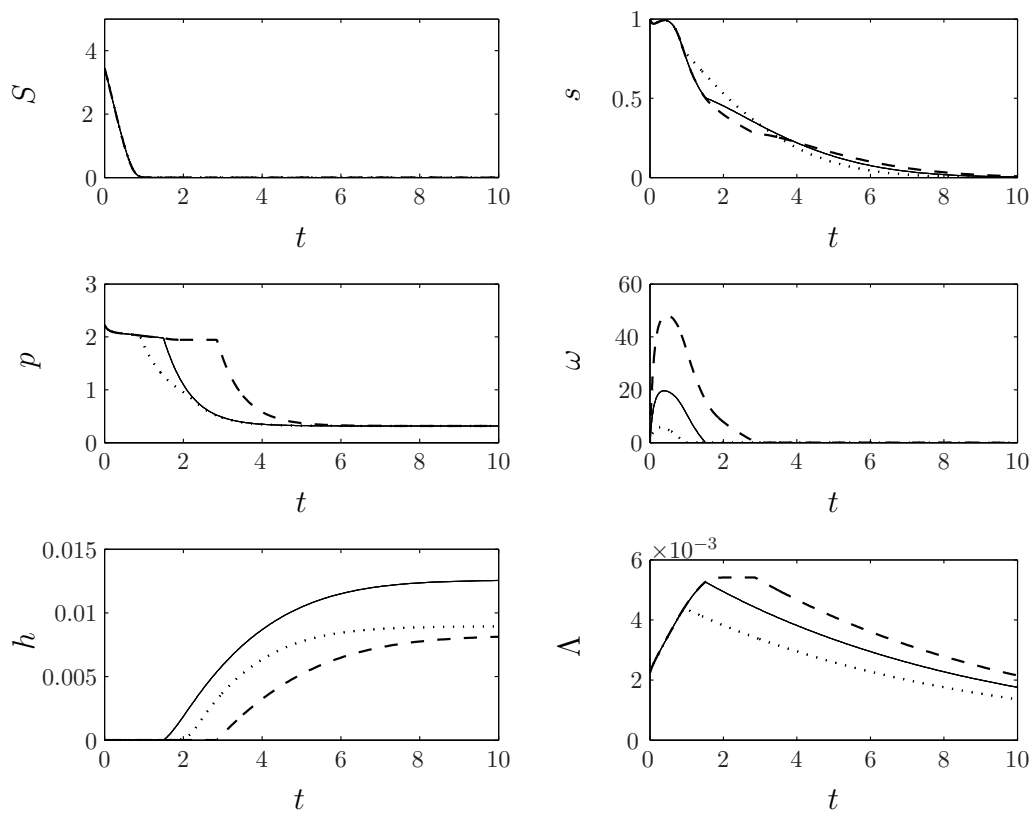


Figure 6.3: Model results when K_6 is increased (dashed lines) and decreased (dotted lines) by a factor of 2, compared to model results for the standard parameter values (solid lines).

can increase the residual PSII activity and keep the system anaerobic then yields may be improved, as Kosourov *et al.* [92] suggest. Increasing E_L , which increases the number of electrons coming from this pathway, has the same effect as increasing S_H , since they are multiplied together in the model equation (equation 5.87). Interestingly, increasing E_L not only increases electrons coming to PSII but also decreases electrons coming from protein breakdown (since we use $1 - E_L$ in the PSII-independent term), implying that PSII is a more efficient pathway for electron donation to the iron-hydrogenase.

The final parameter to consider here is S_1 , the sulphur level below which Rubisco has sufficiently decayed and hydrogen production replaces the Calvin cycle as the electron sink under anaerobiosis. Results for varying S_1 by a factor of 2 are shown in Figure 6.4.

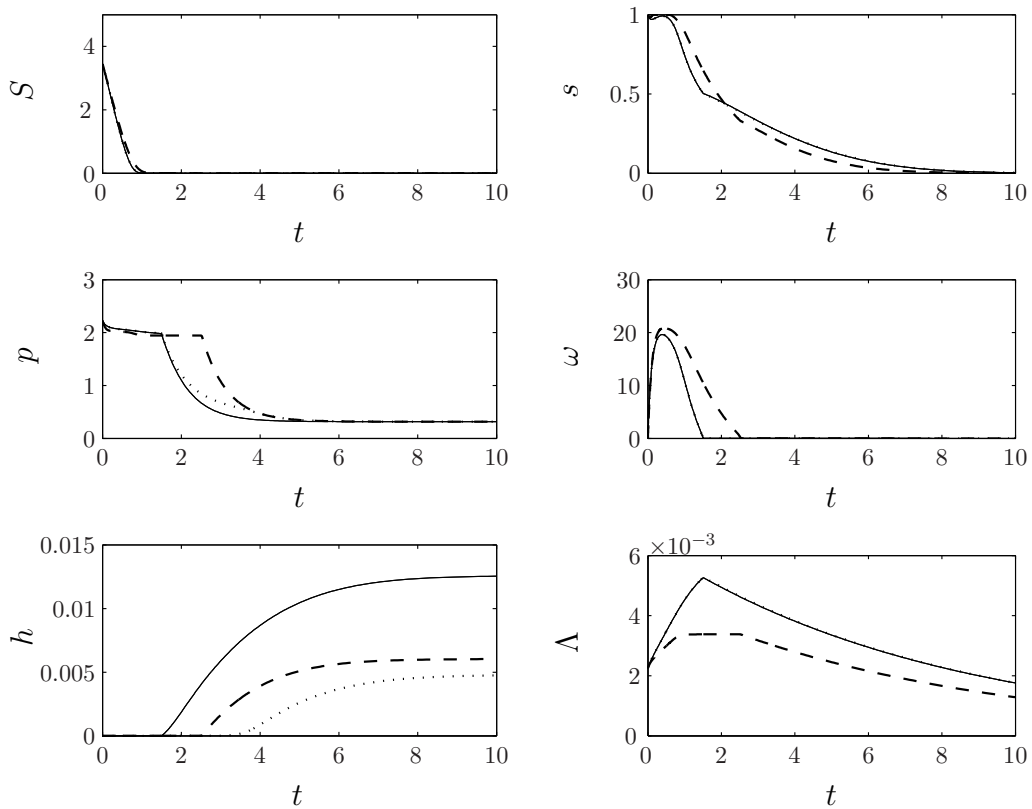


Figure 6.4: Model results when S_1 is increased (dashed lines) and decreased (dotted lines) by a factor of 2, compared to model results for the standard parameter values (solid lines).

These results show that if S_1 increases from $S_1 = 0.5$ then, even though the system could theoretically produce hydrogen gas when there is more sulphur around, we see a later onset of hydrogen production. In this case, growth is severely limited, since protein can not be produced when $S < S_1$. This means we have an aerobic period of damage to the cell during which neither the Calvin cycle nor the hydrogen pathway can act as the electron

sink. Limited growth causes internal sulphur to be used up slower in repairing PSII than in the standard case and the onset of anaerobiosis and, hence, hydrogen production, is delayed. The delay in anaerobiosis in turn delays fermentative protein breakdown, which delays in the release of sulphur from this process and by the time hydrogen production begins, internal sulphur levels are actually lower than in the standard case. This, combined with the decreased cell volume fraction and later onset of H_2 production, results in reduced yields.

Decreasing S_1 from $S_1 = 0.5$ does not affect the s , ω or Λ curves, as shown in Figure 6.4, but does cause a later onset of hydrogen gas production, as once anaerobiosis begins the system also requires sulphur levels to drop below S_1 so that the Calvin cycle is deactivated. This causes a smaller yield of hydrogen gas as production only starts once the cell volume fraction has been shrinking for some time and significant protein and sulphur degradation have occurred, so protein levels for electron donation to the hydrogenase during H_2 production are lower. This is similar to results seen in Kosourov *et al.* [92], where there is a delay period between anaerobiosis and hydrogen production, and suggests that we could replicate those results by decreasing S_1 to approximately $S_1 = 0.25 - 0.4$.

6.1.4 Parameters in the growth equation

The scaled growth rate, R_G , does not have a significant effect when varied within the appropriate range, and nor did varying P_G , the gradient of the growth rate curve plotted in Figure 5.24. Varying R_D , the scaled rate of shrinkage of the cells under hydrogen producing conditions, showed that an increase causes more rapid culture decay, hence slightly lower yields of hydrogen gas. A decrease caused a slower decay, hence slightly more hydrogen was produced. However, these differences in yield were relatively small and this parameter did not have a very profound effect on the system when altered within the range in Table 5.3.

On increasing γ_2 , the protein required for full exponential growth of the culture, we see no significant changes in the standard model. Decreasing γ_2 causes an increase in growth and earlier onset of hydrogen production coupled with earlier protein breakdown. This leads to an increase in hydrogen yield in the $t = 10$ time frame, suggesting that if the cells were able to produce optimal growth with less available protein one would see a higher yield. However, this situation is unlikely to arise due to protein being necessary for cellular growth. One way to increase growth is to increase the dimensional parameter k_3 ,

the rate of protein production. Doing this allowed more culture growth and a considerably increased yield of hydrogen gas. It is feasible that such genetic modification of protein production could increase yields.

Like for many pairs of parameters, varying γ_1 , the protein level below which the culture shrinks at a constant rate, and γ_0 , protein levels when growth rate is zero, have similar but opposite effects. Increasing γ_1 within the range in Table 5.3 produces results qualitatively like decreasing γ_0 , since increasing the level at which cells shrink at the maximum rate is similar to decreasing the level at which growth stops. Increasing γ_1 , hence decreasing γ_0 , within the designated range has very little effect on the system. However, decreasing γ_1 by a factor of two, which is within the range in Table 5.3, causes s , ω , p , h and Λ to alternate between increasing and decreasing periods. Culture shrinkage begins at the same time as γ_1 is decreased, but since the protein level required for maximum shrinkage rate is lower, the cells continue to shrink at a faster rate than for higher values of γ_1 , and cell volume fraction decreases rapidly. This causes protein concentration to rapidly increase, which, in turn, stops shrinkage and results in a periods of culture growth. This causes oscillations where periods of anaerobiosis alternate with aerobic periods and the yield of hydrogen gas is significantly reduced. These trends were not seen in any of the experimental papers, implying that this would be an unrealistic value of this parameters to use and, hence, these results are not shown.

6.1.5 Investigation into the light parameters I_0 , I_{sat} and D_C .

Varying I_{sat} , the saturation value of light, and I_0 , the light intensity at the source, give qualitatively similar results since both control how much light can be used in the light-dependent reactions. Results for varying I_0 are shown in Figure 6.5.

Decreasing I_0 from the standard value causes the cells to photosynthesize and, hence, grow at a lower rate (although the cell volume fractions are very similar in both cases, probably because the length of time the culture grows for is similar). Thus internal sulphur is used up in repair slightly lower and there is a delay in the hydrogen production start time, even though the time to anaerobiosis is similar. The hydrogen yield for smaller I_0 is lower than the standard case because of this later start time causing protein and cell volume fraction at the onset of production to be lower than in the standard case, and there is a reduced activity of the photosynthetic chain passing electrons to the hydrogenase due to a lack of light. This is as expected and is shown in Figure 6.5.

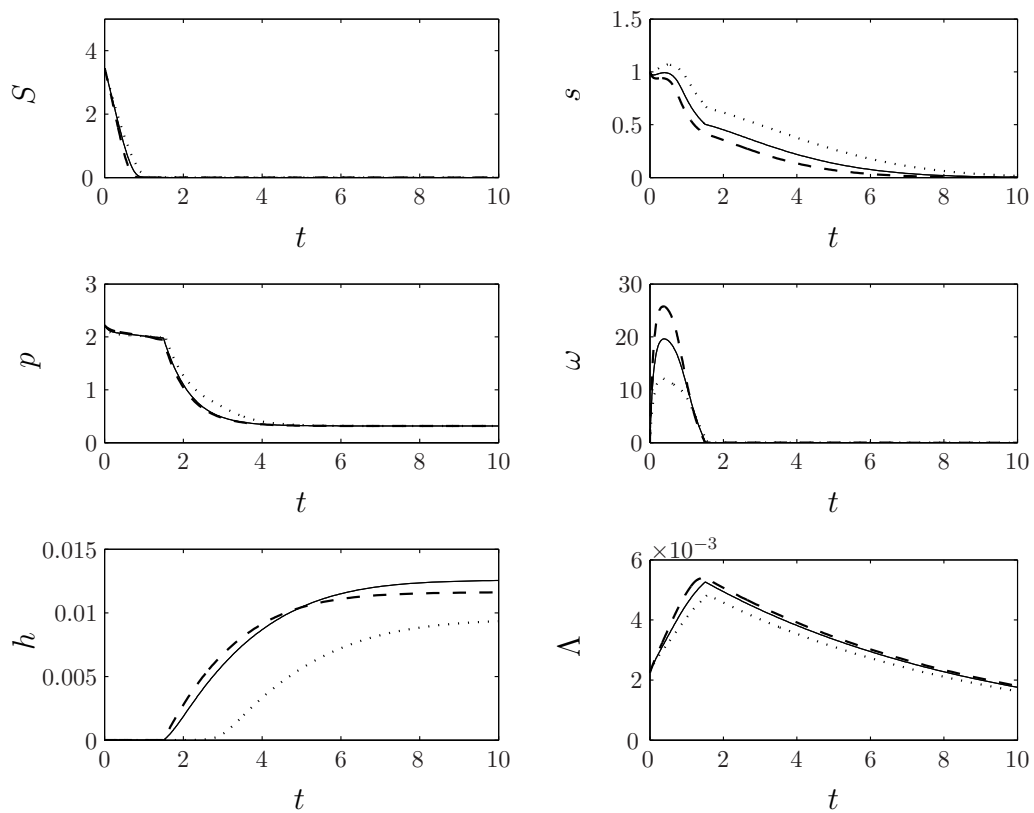


Figure 6.5: Model results when I_0 is increased (dashed lines) and decreased (dotted lines) by a factor of 2, compared to model results for the standard parameter values (solid lines)

Increasing I_0 from the standard value means the cells can photosynthesize and, hence, grow more rapidly, and we see a slight increase in cell volume fraction. This increased photosynthesis means the cells use up their reserves of internal sulphur to repair PSII at a higher rate, so that sulphur decreases quicker, but increased oxygen produced from PSII combined with this rapid sulphur decrease means the system becomes anaerobic at approximately the same time as the standard case. Hydrogen production begins at approximately the same time and we see a slight increase in initial rate. However, hydrogen is not produced for as long because increased PSII activity when more light is available uses more internal sulphur to repair PSII and, hence, s declines faster when the light intensity is greater than the standard value. Thus electrons coming from PSII for hydrogen production run out quicker than in the standard case. This increased rate of sulphur used PSII repair is due to increased photo-damage under strong illumination. Overall, these conditions surprisingly lead to a slightly reduced yield when compared to the standard model case due to rapid photo-damage of PSII, even though the cell volume fraction and available light have increased.

The standard value of I_0 that we use is at the large end of the realistic range and, therefore, we have found that increasing light intensity from zero significantly increases hydrogen yield at time $t = 10$ only up to a point. Beyond a critical level, we obtain a decrease in hydrogen yield over a set period. We also find that greater light intensities give earlier start times for hydrogen production. Comparison with experimental studies, such as that presented by Kim *et al.* [88], reveals the same trends, which are discussed in Section 6.3.

Melis [111] and Polle *et al.* [135] suggest that truncating the chlorophyll antenna size can improve the yield of hydrogen gas since cells closer to the light will not absorb, and waste, so much of the available light, with the implication that cells further away from the light will get more light on average. The appropriate parameter is the measure of light absorbance by the cells, which is modelled by D_C . In an opposite fashion to I_0 , decreasing D_C provides more light on average and a greater initial rate of hydrogen production. However, for large I_0 and small D_C , a slight decrease in yield is obtained due to increased photodamage (this is the same effect as increasing I_0). This appears to contradict the predictions of Melis [111] and Polle *et al.* [135], but if we employ a smaller value of I_0 , such as $I_0 = 300 \mu\text{mol m}^{-2}\text{s}^{-1}$, then we find that decreasing D_C does indeed increase yield, and increasing D_C decreases yield, as shown in Figure 6.6. This is discussed further

in Section 6.3.

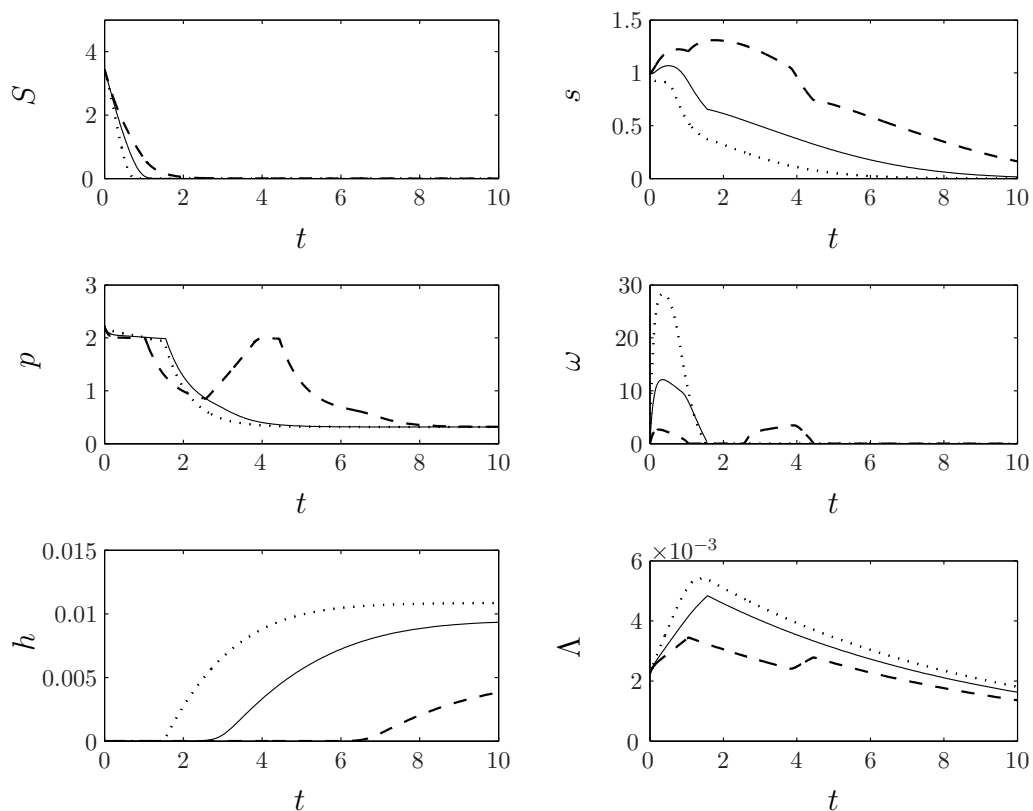


Figure 6.6: Model results when D_C is decreased (dotted lines) and increased (dashed lines) by a factor of 2 for $I_0 = 300 \mu\text{mol m}^{-2}\text{s}^{-1}$, compared to model results for the standard parameter values (solid lines)

6.1.6 Brief conclusions from parameter sensitivity analysis

In this section, we have found that the model is insensitive to several parameters. Here, we outline only the parameters that may improve the yield of hydrogen, with the hope that experimentalists and engineers will investigate methods to improve these aspects of the cells. Only non-dimensional parameters that have realistic biological interpretations and can be altered independently of other parameters are considered here. They are as follows:

- S_H, E_L . Increasing the electrons coming from the residual level of PSII activity increases the yield of hydrogen gas in the model, as suggested in Hypothesis 1 from Kosourov *et al.* [92]. In reality, yield can only be increased in this way if the increase in PSII activity does not cause the system to become aerobic.

- γ_2 (switch value for maximal growth). If the cells could be modified so that initiation of growth requires less protein then total yield might be increased. However, this is unrealistic since proteins are required for cellular growth. Further investigation into starch and other requirements for growth should be made. We also found that increasing the dimensional parameter k_3 , the rate constant for protein production from carbon skeletons and sulphur, increased growth and, hence, increased yield. Therefore, hydrogen yield could be improved by increasing protein production rate in early stages of sulphur deprivation.
- I_0, I_{sat}, D_C . Increasing the light parameters I_0 and I_{sat} , or decreasing D_C , can increase yields up to a optimal value, but if they are increased any further high levels of photo-damage occur and the system uses up internal sulphur quickly, causing the yield to decrease. Thus, there is an optimal light intensity to maximize hydrogen yield at a given time.

6.2 Optimizing the yield of hydrogen gas

Since we find good agreement between the model and experimental results we now aim to use the model to innovate novel strategies for improving the yield of hydrogen and to make comparisons between them. It is hoped that these strategies will be tested, which will help to either support or refute the model, and that they will give focus to experimental studies on improving yield in algal cultures.

The idea of ‘optimizing’ hydrogen production has been discussed recently in the literature [72, 75, 126]. Current ideas to improve the viability and efficiency of hydrogen production are discussed in the introduction. They centre around varying light [88], external sulphur concentrations [92, 182], and growth conditions [90], as well as genetically modifying the cells so they are either more tolerant to oxygen or have smaller chlorophyll antennas [93, 111, 135]. Ghirardi *et al.* [41] show that cycling between sulphur-replete and sulphur-deprived conditions causes the cells to make hydrogen production under nutrient stress and then repair and rebuild during sulphur sufficiency. Cycles of anaerobic hydrogen production and cellular breakdown followed by aerobic respiration and cell growth are observed, but efficiency of this process is low due to the large down time associated with

the re-building, aerobic phase, and the fact that the yield decreases in subsequent cycles of hydrogen production.

A key point to discuss is what does one really mean by ‘optimization’? The optimal strategy will depend on what is required from the system, whether this be a higher rate of H₂ production per cell, or an earlier start time of H₂ production, or simply the largest volume of H₂ gas collected over a set time period. Strategies will not necessarily be the same when optimizing in these different ways, as shown in Section 5.5, where optimal S_0 varies depending on whether the highest initial rate per cell or the highest yield of gas is required. For commercialization purposes, continuity and ease of implementation should also be addressed.

In this work, we aim to optimize hydrogen production by controlling the sulphur-cycling regime to minimize downtime and produce the maximum volume of hydrogen gas over a set time. We want to show that hydrogen production can happen more effectively and efficiently by controlling the addition of external sulphur to the media. This is just one aspect of the process available for optimization, but we can show that interesting and useful results can be obtained by studying this sulphur dependence in isolation. We try various functional forms for re-addition of sulphur into the media and compare yields and sustainability between them. The dimensionless sulphur input function, $\text{INPUT}(S, h, \frac{dh}{dt}, t) = f(S, h, \frac{dh}{dt}, t)$, enters the model in the differential equation for external sulphur as $I(S, h, \frac{dh}{dt}, t)$ in equation 5.82, and, in general, will depend on a combination of S , h , $\frac{dh}{dt}$ and t . Hence,

$$\frac{d(S(1 - \Lambda))}{dt} = -\text{uptake}(S, s, \Lambda) + f\left(S, h, \frac{dh}{dt}, t\right). \quad (6.1)$$

A summary of the different functional forms of the optimization function $f(S, h, \frac{dh}{dt}, t)$ can be found in Table 6.1, and each of these functions is explored in the following sections.

In choosing functional forms for $f(S, h, \frac{dh}{dt}, t)$ we want sulphur addition to allow periods of anaerobic hydrogen production cycling with aerobic growth, since continuous hydrogen production is non-sustainable (see Sections 5.1 and 5.5). We also want the sulphur addition strategies to be easily implementable in industry. This means strategies can only depend on variables that could be measured without disrupting the system, which is why we have chosen h and $\frac{dh}{dt}$. Furthermore, we want the strategies to be run continuously without having to remove sulphur or any other products (excluding hydrogen) from the system. The current state-of-the-art cycling method developed by Ghirardi and coworkers [41] necessitates changing the medium of the cells to remove excess sulphur and requires that

Function name	Definition	Section
Two-stage	Cycles of $\begin{cases} S = 0.0 \mu\text{M} \text{ for } t_1 \text{ hours, followed by} \\ S = 900 \mu\text{M} \text{ for } t_2 \text{ hours} \end{cases}$	6.2.2
Sine wave	$A (1 + \sin [2\pi Ft - \frac{\pi}{2}])$	6.2.3
Square wave	$A \times Sq(t, F, P)$	6.2.4
Gradient switch	$a_1 \times H (h_c - \frac{dh}{dt}) (h > 0)$	6.2.5
Linear switch	$(\frac{dh}{dt} \frac{(a_1 - a_2)}{h_c} + a_2) (\frac{dh}{dt} < h_c) (h > 0)$	6.2.6
Two-step switch	$[a_1 H (h_c - \frac{dh}{dt}) H (\frac{dh}{dt} - h_{c2}) + a_2 H (h_{c2} - \frac{dh}{dt})] (h > 0)$	6.2.6
Two-stage feedback spike	$\begin{cases} f(S, h, \frac{dh}{dt}, t) = a_1 (\frac{dh}{dt} < h_c) (h > 0) \\ \text{if } \frac{dh}{dt}(T) > h_{tol} \text{ and } \frac{dh}{dt}(T + 1) > h_{tol}, \\ \text{or Re-start model at } T + 1 \text{ with} \\ I_C = [S_I s(T + 1) p(T + 1) \omega(T + 1) h(T + 1) \Lambda(T + 1)] \\ \text{if } \frac{dh}{dt}(T) > h_{tol} \text{ and } \frac{dh}{dt}(T + 1) < h_{tol}. \end{cases}$	6.2.7

Table 6.1: Summary of functional forms used as input functions in equation 6.1 in an attempt to optimize hydrogen yield. $Sq(t)$ is the square wave function and H a Heaviside. Parameters are defined in the relevant section.

the cells are washed before re-suspension. Such a strategy is time consuming and means the system can not be left to run continuously. A simpler, less disruptive system, where sulphur is only ever added, would make industrial scale hydrogen production from alga cells more feasible.

We need to choose a suitable long time for the optimization to run so that a few oscillations in sulphur input can occur and to ensure that we are not just seeing effects of an early, unsustainable production. For this reason, and to compare with the results in Ghirardi *et al.* [41] (which runs to $t = 14.7, 360$ hours) we optimize the hydrogen yield at $t = 15$, which corresponds to approximately 15 days. We also discuss the sustainability of the optimal solution as it is usually clear in 15 days whether the production will continue or not.

To minimize computer processing time and for clarity, we optimize with as few optimization parameters in the function $f(S, h, \frac{dh}{dt}, t)$ as possible. We set $S_0 = 0$ for all different optimization functions and then for the function that, on optimizing, gives the highest yield of hydrogen, the yield is optimized again with varying S_0 . Other variations in initial conditions are not investigated.

Below we describe the optimization process, after which each optimization is discussed

individually and analyzed.

6.2.1 Numerical optimization

The optimization process was implemented numerically in Matlab with the aim of finding the value of the optimization parameters that give the highest yield of hydrogen, h , at $t = 15$. We use the Simplex method (Matlab procedure ‘fminsearch’), where the simplex consists of $n + 1$ vectors that form its vertices, where n is the number of optimization parameters. For example, for a two parameter optimization the simplex is a triangle. (The above procedure regime actually minimizes a function, and so to maximize the hydrogen yield we minimize $-h$.) At each step in the algorithm a new point on or near the simplex is generated and the value of this new point is compared to the function values at the vertices. If this value is smaller than any of those on the simplex one of the vertices is replaced by the new point. This is done iteratively until the diameter of the simplex is less than the tolerance that has been set. For these results we use a tolerance of 10^{-4} and specify that no more than 200 iterations should be performed. Since this procedure does not find the global minimum, it is necessary to find a suitable start guess for the optimization. This was achieved by selecting a sufficiently fine grid and calculating an array of the hydrogen yield as the parameters are independently varied. The global minimum in this array was then found using Matlab, and this was used as the initial guess. For the two parameter case, surfaces or contour maps can be plotted to reveal the approximate location of the global minimum. For three or more parameters this was not possible and one variable was fixed in surface and contour plots.

6.2.2 Two-stage sulphur cycling (as in Ghirardi *et al.* [41])

One very simple way to cycle sulphur is used in Ghirardi 2000 *et al.* [41] where a two stage sulphur cycling method is implemented. The cells are incubated in a sulphur free medium for 100 hours and then transferred to a sulphur rich medium (approximately 0.9 mM) for a period of 30 hours. At the end of this period the cells are then washed and re-suspended again in the sulphur-deprived medium for 100 hours, after which the cycle is repeated. Data from Ghirardi *et al.* [41] for the two-stage cycling is reproduced in Figure 6.7. This is an extreme cycling, where the cells are completely sulphur-deprived for a set time, t_1 , incubated in sulphur-replete conditions for a time t_2 and then removed, washed and put back into $S = 0$ conditions for another period of t_1 and so on. We simulate

these conditions using the model with standard parameter values. Results are shown in Figure 6.8 using the external sulphur concentration in sulphur-replete conditions, S_R , as $S_R = 62.1$, which is equivalent to 0.9 mM.

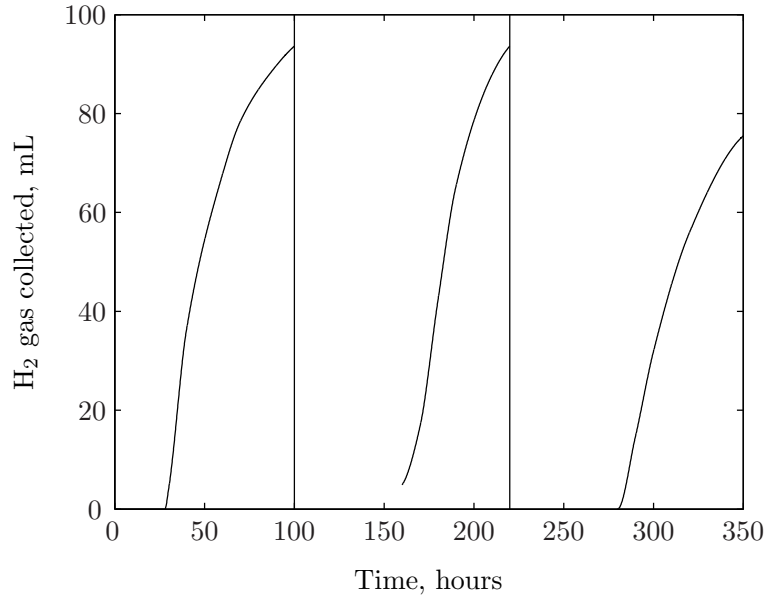


Figure 6.7: Data reproduced from Ghirardi *et al.* [41] for hydrogen production using the two-stage sulphur cycling method, where cells are deprived of sulphur at $t = 0$ and re-suspended in a sulphur-replete medium for 30 hours at $t = 100$ and $t = 220$ hours, before being deprived of sulphur once more.

On comparing the hydrogen data with those of Ghirardi *et al.* [41] we find that the trends in hydrogen production are similar. Both studies see phases of anaerobic hydrogen production followed by aerobic phases during sulphur-replete conditions. During sulphur-deprivation there is a short time in which the cultures become anaerobic, after which hydrogen is produced. The only difference between the simulations and results in [41] is that in the model in each of the first three cycles of sulphur deprivation slightly more hydrogen produced than in the previous cycle, whereas in Ghirardi *et al.* [41] hydrogen production either stays the same as the previous stage (as in the second run) or decreases (as in the final run). This discrepancy suggests that cellular repair in the model happens quicker than in reality. The ‘repair’ parameter in the model is k_3 , the rate of protein production, since protein production re-builds cellular material. Since estimation of k_3 was difficult and we had no concrete value to base this on, from literature, we can explore the effects of decreasing k_3 to slow down cellular repair. Results of this are shown in Section 6.2.9 and are compared to results for the new cycling methods discussed in Section 6.2.7.

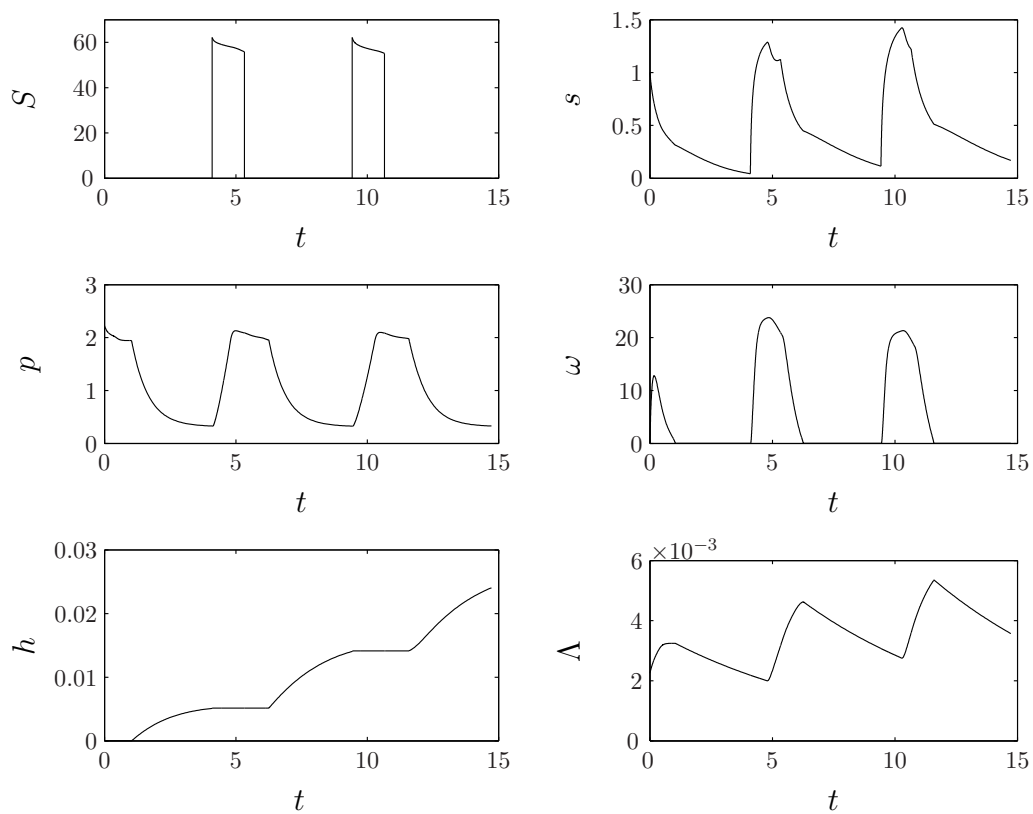


Figure 6.8: Results for the model with standard parameters using the two-stage cycling regime from Ghirardi *et al.* [41] until $t = 14.7$. Here, $S_R = 62.1$ ($S_R = 0.9$ mM) in sulphur-replete conditions, and $t_1 = 4.1$, $t_2 = 1.23$

For now, we vary the parameters t_1 and t_2 , the time in sulphur-deprivation and time in sulphur-replete condition, respectively, to optimize hydrogen yield at $t = 15$. We find that the maximum hydrogen produced at $t = 15$ is $h = 0.0248$, which is $h = 468$ mL H₂/L culture, compared to 455 mL H₂/L culture in Ghirardi *et al.* [41], and requires $t_1 = 3.04$ and $t_2 = 0.941$. The cycling these parameters produce is shown in Figure 6.9 for long time $t = 40$. This provides a slight improvement on the yield using the parameter values in Ghirardi *et al.* [41] since these values cause more cycles to occur in the time frame because the periods of sulphur-replete and sulphur-deprived incubation are shorter. Notably, it is clear that the optimal strategy has both $t_1 > 0$ and $t_2 > 0$, indicating that cycling is necessary for maximal hydrogen production.

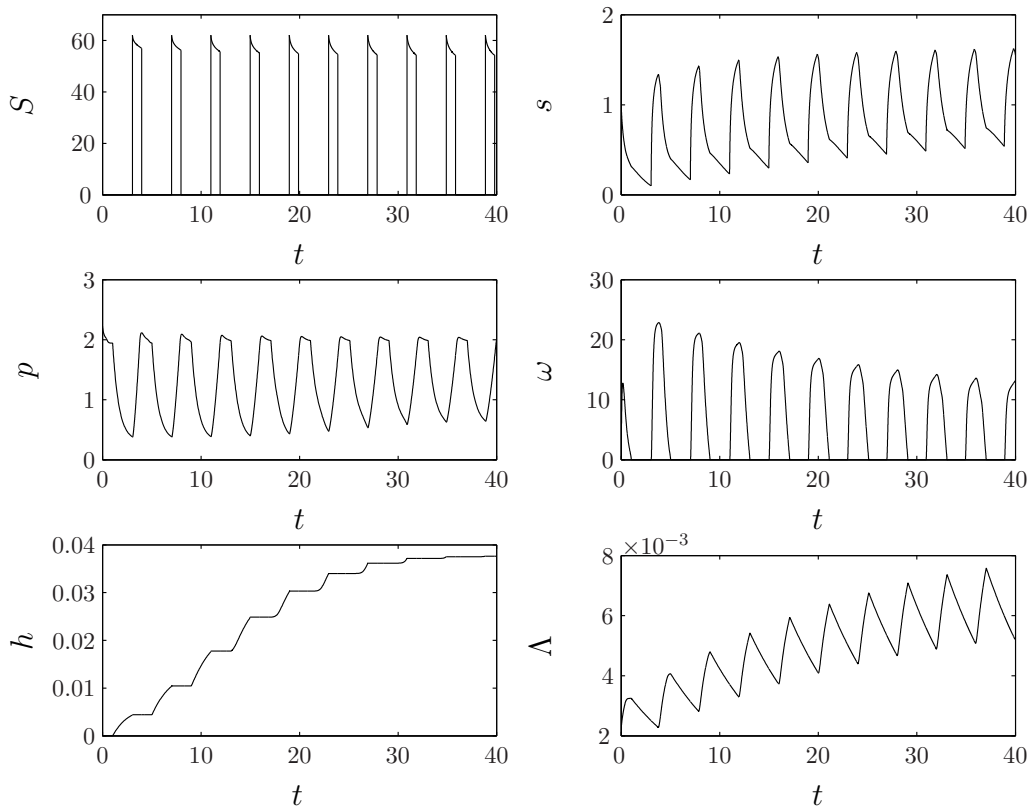


Figure 6.9: Model results to $t = 40$ using optimal parameters $t_1 = 3.04$, $t_2 = 0.941$ with $S_R = 62.1$ for the two-stage cycling from Ghirardi *et al.* [41].

Although this is the optimal strategy for hydrogen yield at approximately 15 days, if we run the model with optimal t_1 and t_2 until 40 days we see that the yield actually starts to decrease in each cycle, as shown in Figure 6.9 and found by Ghirardi *et al.* [41]. This is because the periods of hydrogen production are actually relatively short, and the aerobic periods, in which cell volume fraction and internal sulphur increase, are long. Internal

sulphur builds during the sulphur-replete conditions faster than it can be used under sulphur deprivation, so that sulphur increases on average and eventually $s > S_1$, and the Calvin cycle is always active and used as an electron sink instead of the iron-hydrogenase, and hydrogen production grinds to a halt.

6.2.3 Sulphur cycling using a sine wave

Now the two-stage cycling method has been explored, we begin to formulate new methods to cycle sulphur. We try a simple method where the rate of sulphur addition to the media follows a sine wave and is not dependant on the activity of the system. We propose the optimization function

$$f(t) = A \left(1 + \sin \left[2\pi Ft - \frac{\pi}{2} \right] \right), \quad (6.2)$$

where A is amplitude and F is frequency. Clearly, $f(0) = 0$ and $f(s) \geq 0 \forall t$, so that sulphur is only ever added, not removed as in the two-stage method.

Figure 6.10 shows a contour plot for A , F and hydrogen yield at time unit $t = 15$. The contour is fairly complicated and appears to have two main regions: an oscillating region that on average steadily increases as F decreases for a constant A and then reaches a maximum, and a relatively high ridge for small A and all values of F . The narrow ridge is actually a region of parameter space where the yield of hydrogen produced is quite high but is non-sustainable, since if we optimize for longer this region does not increase in height, as shown in Figure 6.12 for $t = 40$, and is barely visible. This shows that adding a minimal quantity of external S increases the yield but does not produce cycles, which is akin to varying S_0 , and is not what we were looking for.

Using an array for A , F and hydrogen yield to calculate an initial guess, we find the optimal strategy for the sine wave (taking hydrogen yield at $t = 15$) to be $F = 0.154$ and $A = 1.088$ with a yield of $h = 0.0227$, which is 428 mL H₂/L culture. Model results using the optimal strategy parameters A and F are shown in Figure 6.11. The highest yield is not achieved by simply adding more and more S , hence increasing A , because that would lead to a normal, sulphur-replete system.

The cycling shown in Figure 6.11 looks similar to two-stage cycling, with periods of aerobiosis allowing cellular repair and culture growth, causing a downtime in hydrogen production, oscillating with anaerobic fermentation, hydrogen production and culture shrinkage. The main difference between methods is that this production is continuous and

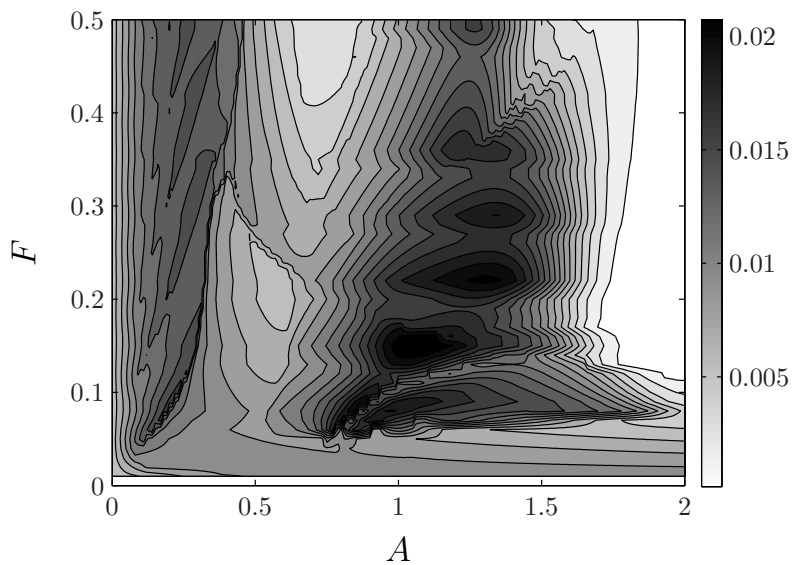


Figure 6.10: Contour plot of optimal hydrogen yield at $t = 15$ using the sine wave sulphur input, with $S_0 = 0$, varying amplitude and frequency. The maximum yield is $h = 0.0227$.

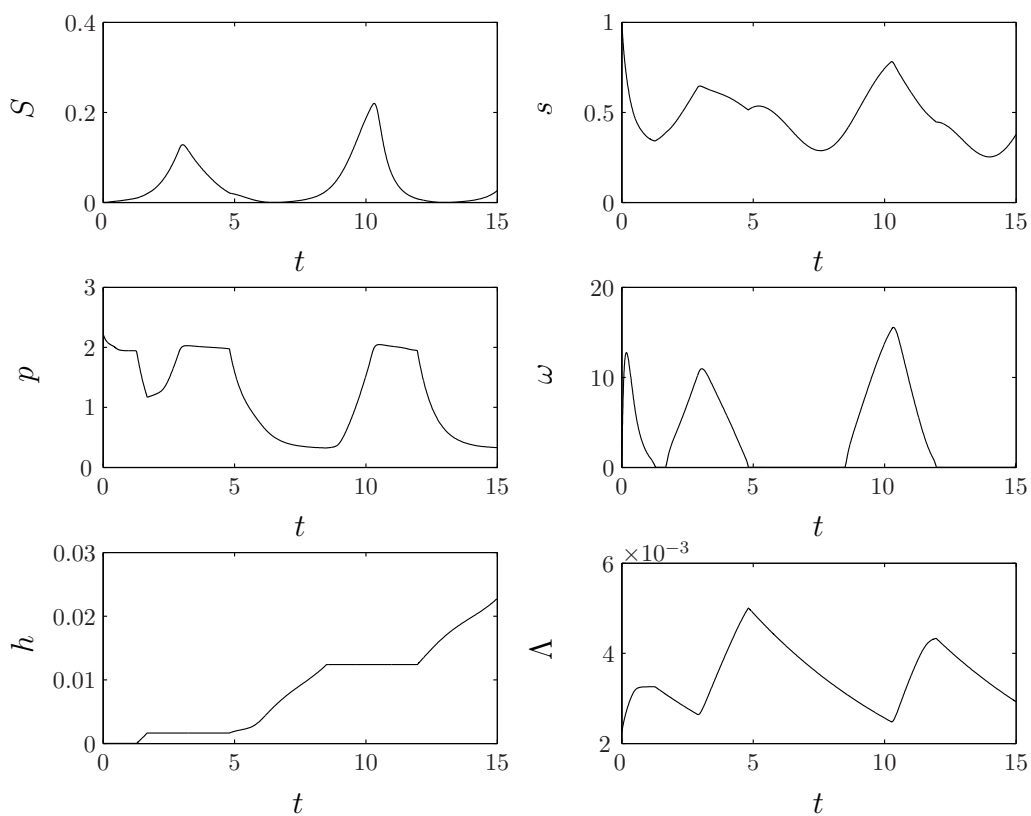


Figure 6.11: Model results to $t = 15$ using optimal parameters $F = 1.09$ and $A = 0.154$ for the sine wave sulphur input.

does not involving removing sulphur from the medium and washing the cells. Although the yield of hydrogen is slightly less than when using the two-stage method, it confers an advantage because it would be easier to run using an automated system, without the need for human interference.

We expect that as we increase the time at which we measure hydrogen yield, the surfaces or contour plots will become smoother because differences in the stage of the cycling at which the yield is recorded are less significant compared to the size of the yields. This is certainly true when $t = 40$, shown in Figure 6.12. The model solutions for this longer time also look very similar, with optimal parameter values of $F = 0.157$ and $A = 1.167$ and a maximum $h = 0.0644$ (1214 mL H₂/L culture). The slightly different values for F and A is due to the point in the cycle at which the hydrogen yield is taken.

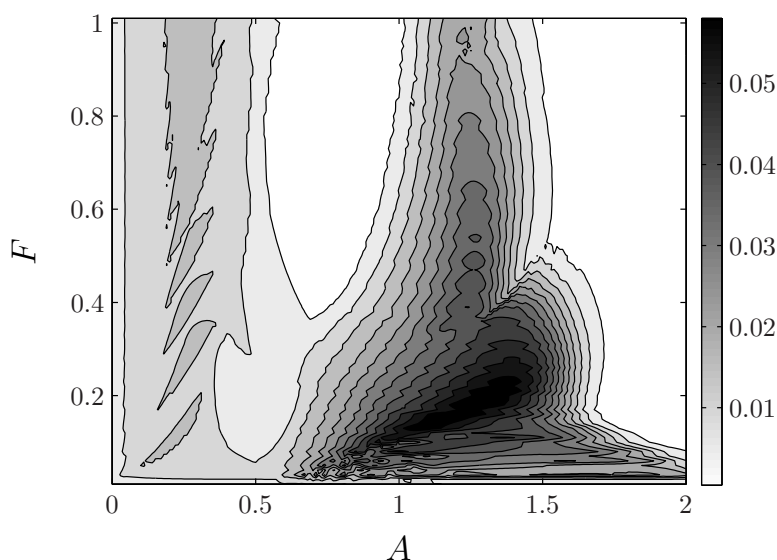


Figure 6.12: Contour plot of optimal hydrogen yield at $t = 40$ using the sine wave sulphur input, with $S_0 = 0$, varying amplitude and frequency. The maximum yield is $h = 0.064$.

In conclusion, the sine wave sulphur input gives an optimal cycling behaviour with yields that are just shy of the optimized yield using the two-stage cycling method in Section 6.2.2. The cycling here has the advantage of being continuously applied since no sulphur has to be removed from the bio-reactor.

6.2.4 Sulphur cycling using a square wave

A square wave function can also be used to optimize hydrogen production. The advantage of using the square wave function is that we can enforce periods where no sulphur is added

and periods where it is added at a constant rate. The square wave, however, gives us an additional parameter; we now have amplitude A , frequency F and a parameter P which determines what percentage of time the function is non-zero. P has the range $0 \leq P \leq 100$. An example of a square wave is shown in Figure 6.13 where in this case $A = 2$, $F = 2$ and $P = 25$.

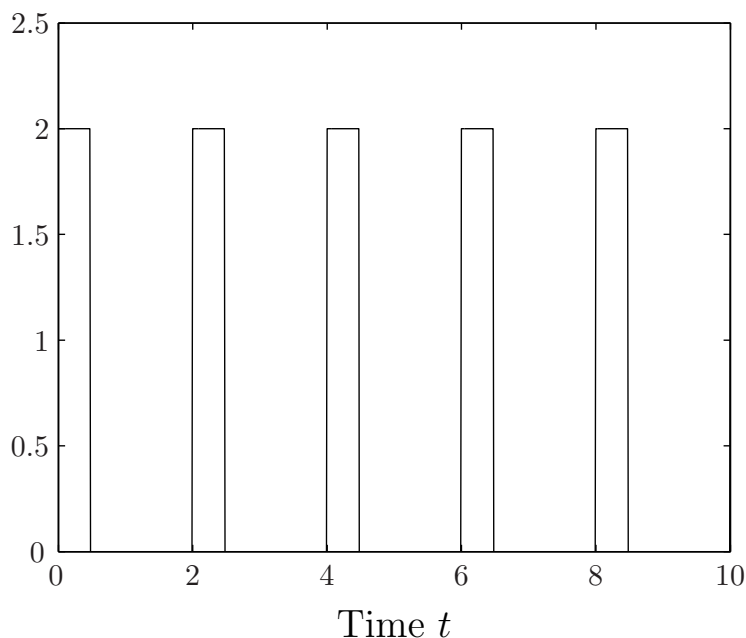


Figure 6.13: An example of a square wave function used in the optimization where $A = 2$, $F = 2$ and $P = 25$.

To make an initial estimate to start the optimization process we calculate an array of yields dependent on A , F and P and select the maximum of this discrete set. Optimizing then gives us a maximum yield of 0.0265 (approximately 500 mL H₂/L culture), when $A = 35.2$, $F = 5.11$ and $P = 3.44$.

If we set $F = 5.11$ and plot A and P parameter space then Figure 6.15 shows that instead of there being one optimal strategy there are actually many that give the maximal yield to three significant figures, shown by the curving region at which h is maximal. Here, if P , the percentage of the square wave that sulphur is added for, is decreased then the rate of sulphur addition, A , must be increased to keep the yield approximately the same. Thus decreasing P with increasing A gives a curved region in parameter space where the optimal yield of 500 mL H₂/L culture (to three significant figures) can be achieved. The optimal strategy shown in Figure 6.14 is just one example of an optimal strategy which attains the maximum yield. The downtime for cellular repair has been decreased by adding

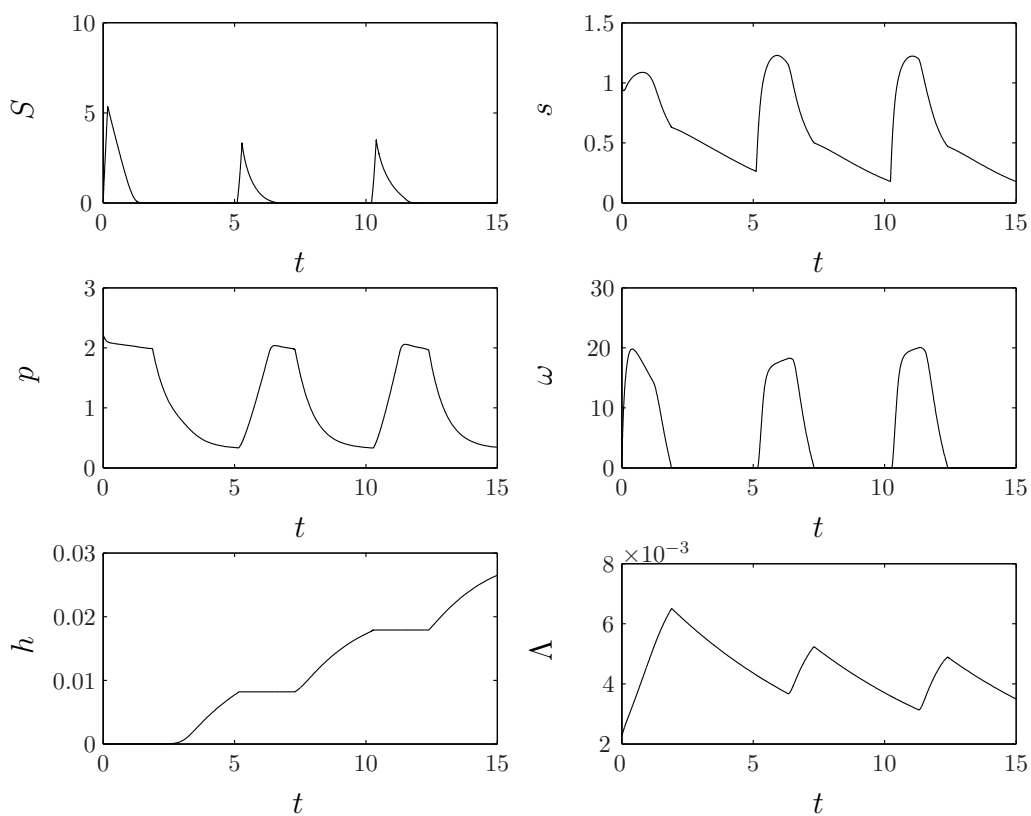


Figure 6.14: Model results to $t = 15$ using optimal parameters $F = 5.11$, $A = 35.2$ and $P = 3.44$ for the square wave sulphur input.

S quickly for a short period but the rate of hydrogen production in the anaerobic phase is still relatively low compared to results for varying S_0 in Section 5.5.5 (see Figure 5.16). We also note that in Figure 6.14 Λ is slightly decreasing on average and so this system is not sustainable long term.

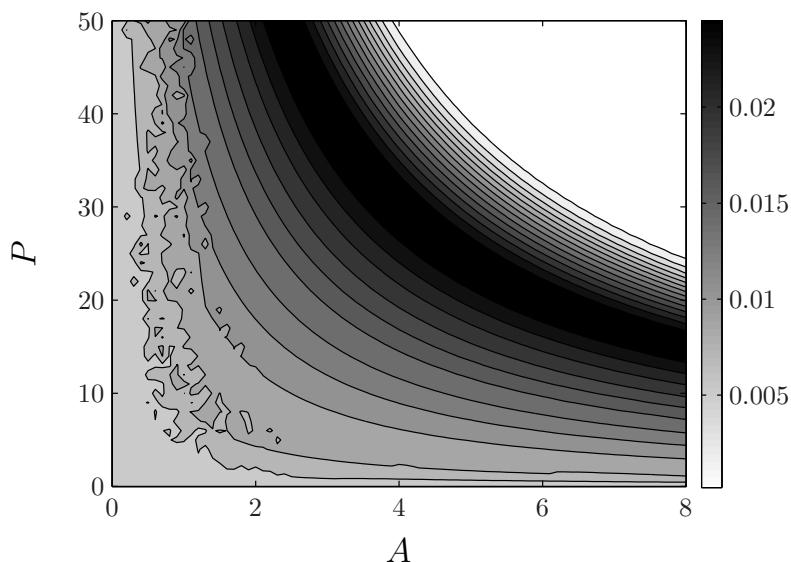


Figure 6.15: Contour plot of optimal hydrogen yield at $t = 15$ using the square wave sulphur input, with $S_0 = 0$, varying A and P and setting $F = 5.11$. The maximum yield is $h = 0.0265$.

Using this square wave optimization function we have thus improved the amount of hydrogen gas produced in 15 days (from 468 mL H_2 /L culture in the two-stage cycling to 500 mL H_2 /L culture here) but not by a significant amount. Ideally we would like to be able to improve this yield further. However, sulphur is only added and not removed, which is an improvement on the method of Ghirardi *et al.* [41].

6.2.5 Controlling sulphur addition using the gradient of H_2 production: a gradient switch function

The two functions used to optimize hydrogen yield so far have no feedbacks relating sulphur addition to the hydrogen production. We expect that the best way to optimize hydrogen production will be to have some kind of feedback mechanism where external sulphur is added dependant on the system state. Since we want this strategy to ultimately be tested and used in bio-reactor conditions, it is important to choose a method that can be easily implemented, so our function depends only on model variables that can be measured easily:

hydrogen and gradients of hydrogen production (which will be measured anyway during production).

As a first attempt, we choose a functional form that stipulates that sulphur is added to the culture when the gradient of hydrogen production gets below a certain level, h_c . The idea is that sulphur will be added at a time when hydrogen production is just starting to decrease, so that the cells are kept in the phase of most rapid H_2 production. We hope that regime could be tested in an experimental bio-reactor where H_2 measurements are taken and gradients calculated over time, and when the rate of H_2 production starts decreasing external sulphur can be re-added at a constant rate, a_1 . The functional form we use is

$$f\left(h, \frac{dh}{dt}\right) = a_1 H\left(h_c - \frac{dh}{dt}\right) (h > 0), \quad (6.3)$$

where $h > 0$ is used to specify no sulphur is added before hydrogen production begins and H indicates a Heaviside function.

The model results at $t = 15$ for the optimal parameter values are shown in Figure 6.16, and the surface plot for hydrogen yield is shown in Figure 6.17. A region where a few steep peaks are present is clearly seen in Figure 6.17, and we find that if h_c is small hydrogen production is low, and if a_1 is large the culture becomes aerobic and yields are small. On optimizing, we find a maximum of $h = 0.0221$ at $h_c = 0.0031$ and $a_1 = 1.412$. This corresponds to approximately 417mL H_2 /L culture.

This method actually gives a slightly smaller yield of hydrogen than the sine wave and square wave oscillations, as well as the two-stage method of Ghirardi *et al.* [41]. To understand why, we analyze Figures 6.16 and 6.17 in more detail:

1. Initially no sulphur is added and we see normal sulphur-deprived behaviour leading to hydrogen production. When $\frac{dh}{dt} < h_c$, at approximately $t = 1.4$, sulphur is added at a rate a_1 until the gradient increases above h_c , and sulphur is added in small amounts to maintain the hydrogen gradient.
2. During hydrogen production, increased light availability, as the culture shrinks, coupled with a non-decreasing internal sulphur curve, cause the rate of photosynthesis to increase. Thus the culture becomes aerobic, and hydrogen production stops abruptly at time $t = 3.33$.

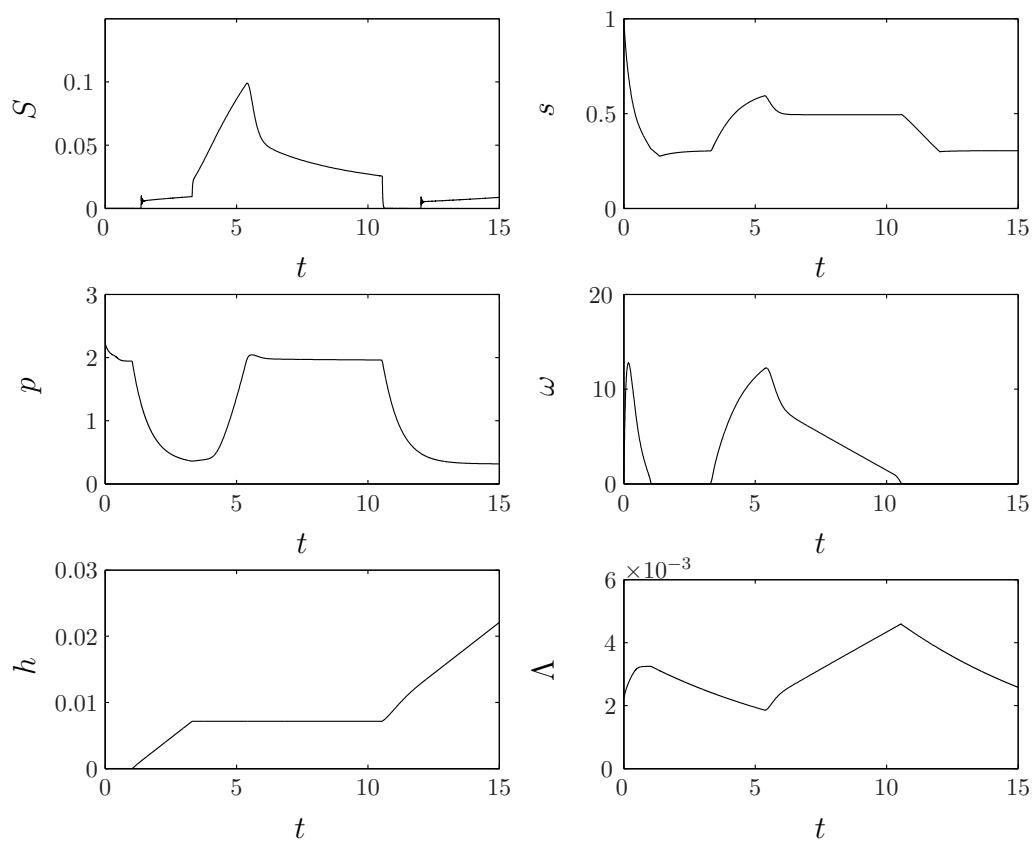


Figure 6.16: Model results to $t = 15$ using optimal parameter values $h_c = 0.0031$ and $a_1 = 1.4117$ for the hydrogen gradient switch sulphur input.

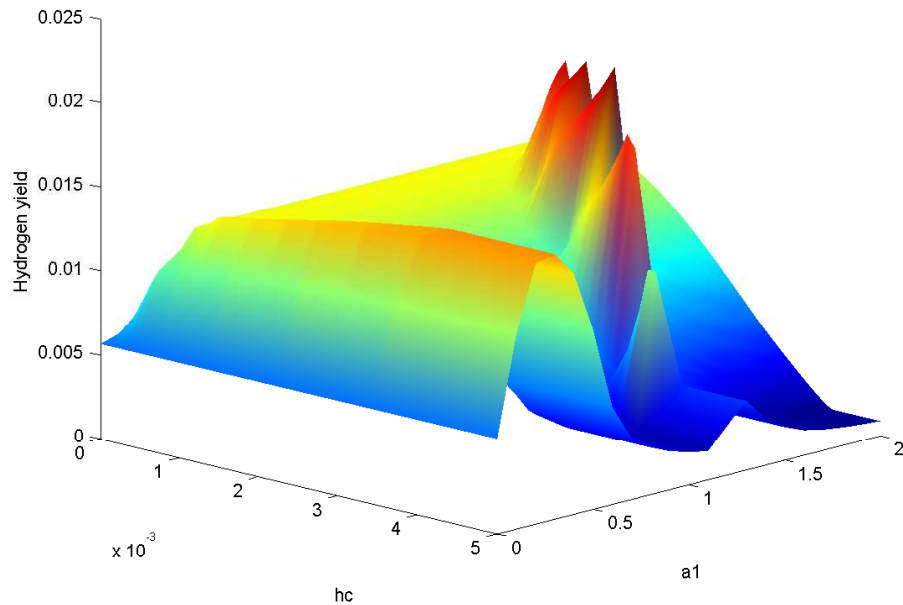


Figure 6.17: Surface plot of optimal hydrogen yield at $t = 15$ using the hydrogen gradient switch sulphur input, with $S_0 = 0$, varying a_1 and h_c . The maximum yield is $h = 0.0221$.

3. During this second aerobic phase, oxygen levels rise and sulphur is added continuously at the rate a_1 (since $\frac{dh}{dt} = 0 < h_c$). This leads to an initially sharp build up of external sulphur followed by a steady increase in S once the external sulphur starts to be taken into the cell. Thus internal sulphur concentration also increases and the cells re-build, so that p and Λ increase.
4. External sulphur concentration continues to increase while the cell volume fraction is relatively small, but demand for external S increases as Λ increases and so, although sulphur continues to be added at a constant rate, the concentration S will start to decrease (at $t = 5.41$) as Λ increases.
5. Internal sulphur decreases due to increasing Λ , and s levels off close to $s = S_1 = 0.5$, due to a balance in sulphur added and sulphur used, causing growth rate to decrease as the system is close to the minimum sulphur required for growth, S_1 . Slower growth causes the oxygen curve to start decreasing less rapidly at approximately

$t = 6.3$ (see Figure 6.16), as the constant level of internal sulphur in this period supports a steady rate of oxygen production from PSII. This steady rate of oxygen production means the cells take longer to reach anaerobiosis than for the first sulphur-deprivation cycle, in which oxygen production rate decreased as s decreased rapidly. Protein levels stay approximately constant in this period as no fermentation occurs under aerobic conditions, and there is enough light and sulphur available for minimal protein production to facilitate growth.

6. The cells become anaerobic again at $t = 10.55$ in Figure 6.16 because lower than normal sulphur levels, $s < S_0$, combined with increasingly low light levels as Λ increases, decreases oxygen production from PSII. Hydrogen production restarts around this time ($t = 10.55$) and since $\frac{dh}{dt} > h_c$ no external sulphur is added, any remaining external sulphur is used up quickly and $S = 0$ at $t = 10.61$. As before, s decreases until s settles at a constant level and anaerobic fermentation causes p and Λ to decrease.
7. When $\frac{dh}{dt} < h_c$ again, steps 1-6 repeat and we see cycles of sulphur addition for hydrogen gradient maintenance followed by periods of repair that last until the system becomes anaerobic again.

The level at which s stabilizes in the constant periods (described in step 5 above) is determined by the parameter S_1 in the Calvin switch $H_{Calvin}(s; S_1)$ which determines whether protein production or hydrogen production is used as the main electron sink. The gradient s_g of this smoothed switch function H_{Calvin} is crucial, because for protein to increase and for cellular growth we require $s > S_1$, but for H_2 production we require $s < S_1$. Slackness in the switch is necessary so that at the onset of anaerobiosis, when s is close to but slightly greater than S_1 , the switch allows a sufficient amount of hydrogen to be made to stop the addition of sulphur and allow $\frac{dh}{dt}$ to increase. Cycling can not be achieved if s_g is too large (in which case hydrogen is only made in minimal quantities if s is slightly larger than S_1) as in this case at the onset of anaerobiosis s is close to S_1 and such a small amount of hydrogen is produced that $\frac{dh}{dt}$ remains less than h_c , and sulphur is added again very soon after hydrogen production begins. If this is the case, re-addition of sulphur causes the system to become aerobic again almost immediately, and hydrogen is only produced transiently after the initial period of production. This is a limitation of

using this functional form.

In this novel process, sulphur is added first to maintain the gradient of hydrogen production and then added during a period of cellular repair where no hydrogen is produced. By stipulating that sulphur is added at the rate a_1 when $\frac{dh}{dt} = 0$ we are saying something quite different to the two-stage cycling, where external sulphur was removed and there followed a period where internal sulphur was used up and the culture became anaerobic. With the new optimization function, the addition of sulphur for repair does not stop until hydrogen production resumes, which can only happen if the culture becomes anaerobic. The culture can only become anaerobic by keeping a relatively low internal sulphur concentration and decreasing light available due to increased cell volume fraction (which decreases oxygenic photosynthesis). Thus there is a delicate balance between giving the cells enough external sulphur to repair and not giving them too much so that anaerobiosis and hydrogen production are not restarted. This causes a relatively long down time compared to the two-stage cycling and causes the overall hydrogen yield to be lower at $t = 15$, even though hydrogen is produced at a higher rate during periods of production.

6.2.6 Controlling sulphur input using the gradient of H₂ production: a linear and a two-step switch function

The previous optimization function only allowed hydrogen to be added at one rate, so the same rate was used to maintain the hydrogen gradient during hydrogen production and for the repair of the cells during the aerobic phase. In the hope of decreasing the downtime between periods of hydrogen production, we consider separating these two rates; we optimize for a different rate when $\frac{dh}{dt}$ is small compared to when it is close to h_c . There are many forms that this function could take and we begin by considering a linear term where the rate of sulphur addition varies according to how far away $\frac{dh}{dt}$ is from the critical gradient. This optimization function has the form

$$f\left(h, \frac{dh}{dt}\right) = \left(\frac{dh}{dt} \frac{(a_1 - a_2)}{h_c} + a_2\right) \left(\frac{dh}{dt} < h_c\right) (h > 0), \quad (6.4)$$

where a_1 , a_2 and h_c are parameters used to optimize the yield. An example of this function is shown in Figure 6.18. A surface plot of h_c against a_2 for the optimal value of $a_1 = 0.0002$ is very similar the surface in Figure 6.17 for the gradient switch in Section 6.2.5. This is because a_2 is small and the culture actually jumps from making hydrogen at a rate around h_c to stopping production due to the onset of aerobiosis, and the solution never properly

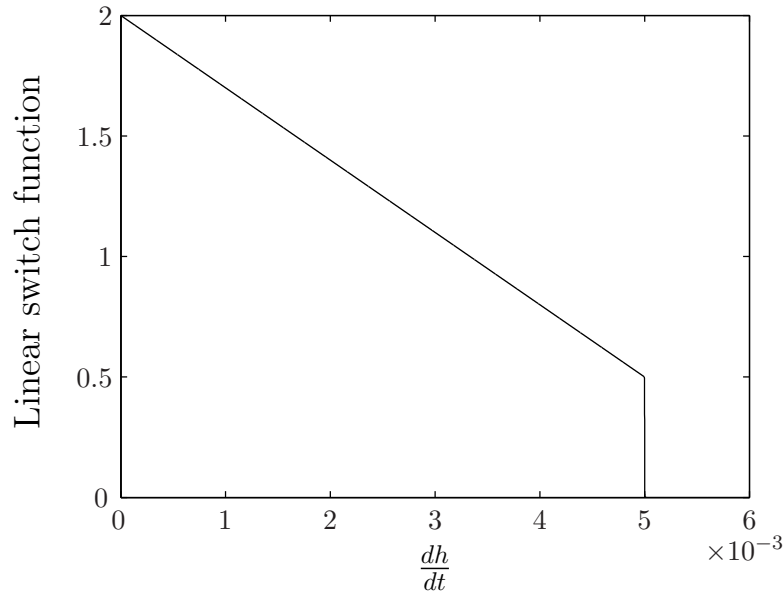


Figure 6.18: An example of the linear switch sulphur input dependant on $\frac{dh}{dt}$, where $h_c = 0.005$, $a_1 = 0.5$ and $a_2 = 2$.

experiences the linear regime.

Finding an initial guess for the optimization using the method described in Section 6.2.4, we find the optimal parameter values to be $a_1 = 0.936$, $a_2 = 0.0661$ and $h_c = 0.006$ with a yield of $h = 0.0249$ (470 mL H₂/L culture) at $t = 15$. However, we found that this is a regime that stops producing hydrogen gas at around 14 days i.e. there is no cycling. This is clear if we look at the long term behaviour in Figure 6.19. The optimal solution that continues for long times was found to be $a_1 = 0.0002$, $a_2 = 1.44$ and $h_c = 0.0051$ with a maximum of $h = 0.0234$ (441 mL H₂/L culture). This solution is also shown in Figure 6.19, where curves look very similar to those in Section 6.2.5 for the gradient switch function, except for the small bump that appears on the S curve around $t = 10$. This is due to a variable rate of S addition as the gradient of h changes in the initial stages of hydrogen production. In addition, external sulphur is always added so is never zero, as for the gradient switch function, because S is added at a low rate even when $\frac{dh}{dt}$ is close to h_c .

This variable rate function has only increased hydrogen yield at $t = 15$ by a very small amount (441 mL H₂/L culture compared to 417 mL H₂/L culture for the gradient switch in Section 6.2.5) and there is still a long downtime between periods of hydrogen production.

One may imagine that to decrease the downtime using this linear switch function, the rate of S addition, a_2 , could be increased to facilitate faster growth during the aerobic period, since this would lead to earlier onset of anaerobiosis. Increasing a_2 for the linear

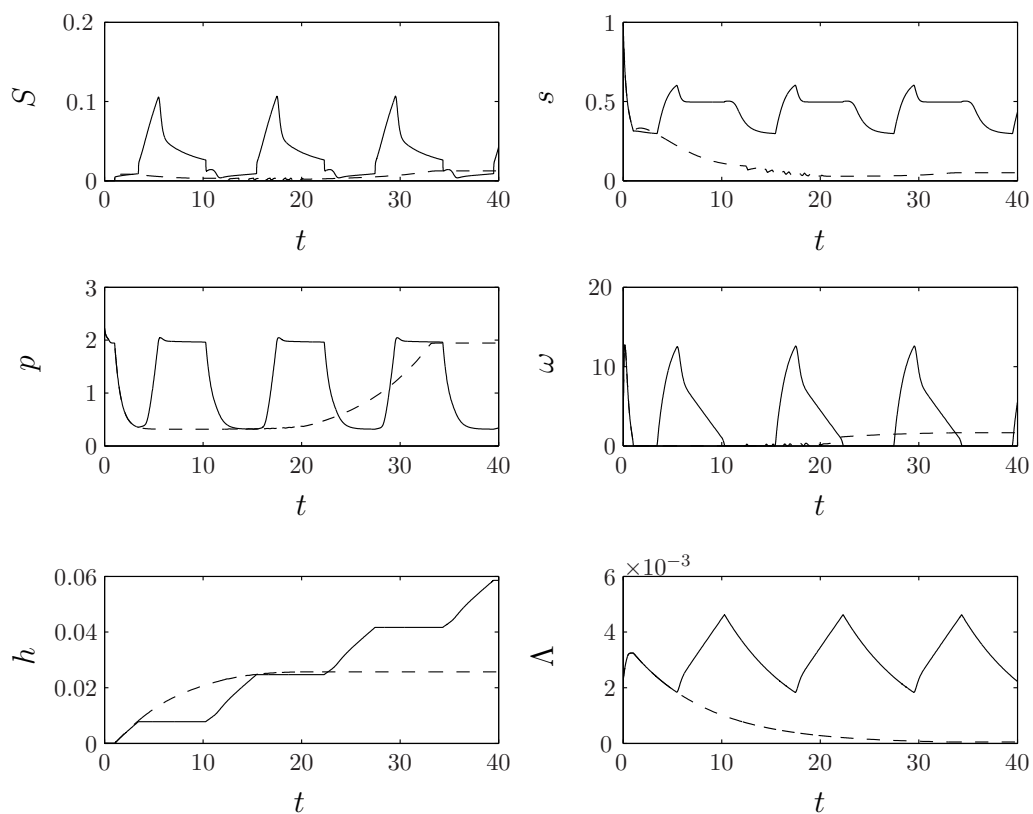


Figure 6.19: A comparison of optimization strategies for the linear switch sulphur input, with optimal parameters $a_1 = 0.0002$, $a_2 = 1.44$ and $h_c = 0.0051$ (solid lines), and $a_1 = 0.936$, $a_2 = 0.0661$ and $h_c = 0.006$ (dashed lines). The dashed line optimization is not continuous and for long times it is no longer optimal and hydrogen production stops around $t = 14$

switch function causes earlier onset of aerobic conditions, because s is kept slightly higher due to the increase in gradient of $f\left(h, \frac{dh}{dt}\right)$. Sulphur is then added at a rate a_2 until hydrogen production recommences, and the cells reach anaerobiosis quicker, thus downtime is decreased. Hydrogen production is initially at a low rate $s \approx S_1$, so some electrons are used in the operational Calvin cycle. In this case, the linear input function specifies that sulphur will be added at a rate close to the large a_2 value, and internal sulphur increases. This causes the culture to quickly become aerobic again, stopping hydrogen production soon after it begins. Therefore, we can not use this function to decrease the downtime between cycles because attempting to do this by increasing a_2 , which decreases downtime, leads only to transient oscillations in hydrogen production. The yield is still lower than in the two-stage cycling case, so further improvements to the optimization function are required.

To overcome the problem of high sulphur addition in the early stages of hydrogen production we try a two-step function, where sulphur is added at one rate when $\frac{dh}{dt}$ is large and another when $\frac{dh}{dt}$ is small. Thus as soon as hydrogen production resumes after the second aerobic period the high rate of sulphur addition, a_2 , switches to a low rate, a_1 , eliminating the problem of the system becoming aerobic again very quickly. The new two-step rate function has the form

$$f\left(h, \frac{dh}{dt}\right) = \left[a_1 H\left(h_c - \frac{dh}{dt}\right) H\left(\frac{dh}{dt} - h_{c2}\right) + a_2 H\left(h_{c2} - \frac{dh}{dt}\right) \right] (h > 0) \quad (6.5)$$

with optimization parameters rates a_1 and a_2 and critical gradients h_c and h_{c2} . This gives four optimization parameters. However, we find that the optimization process is relatively insensitive to h_{c2} , so long as it is sufficiently small so as not to add sulphur at a high rate during initial hydrogen production. This is shown in Figure 6.20, where large $h_{c2} = 0.001$ stops further cycles of hydrogen production. For this reason we set $h_{c2} = 0.0001$ and find the optimal values of a_1 , a_2 and h_c .

We find that $a_1 = 0.522$, $a_2 = 1.868$ and $h_c = 0.0051$ give the maximum yield of hydrogen gas at $t = 15$, where $h = 0.0304$ (573 mL H₂/L culture). This is a significant improvement on the yield using the two-stage sulphur input of Ghirardi *et al.* [41] in Section 6.2.2, and the other methods tried so far. Figure 6.20 (solid lines) shows very similar cycling behaviour to the linear switch function in Figure 6.19, but here increasing the rate of sulphur added during the repair period, but not during the hydrogen production, allows the cells to repair and grow quicker and, hence, decreases the downtime between hydrogen production cycles. Optimizing a_1 for gradient maintenance also allows for a high

gradient of production without too much additional sulphur, so that the system remains aerobic.

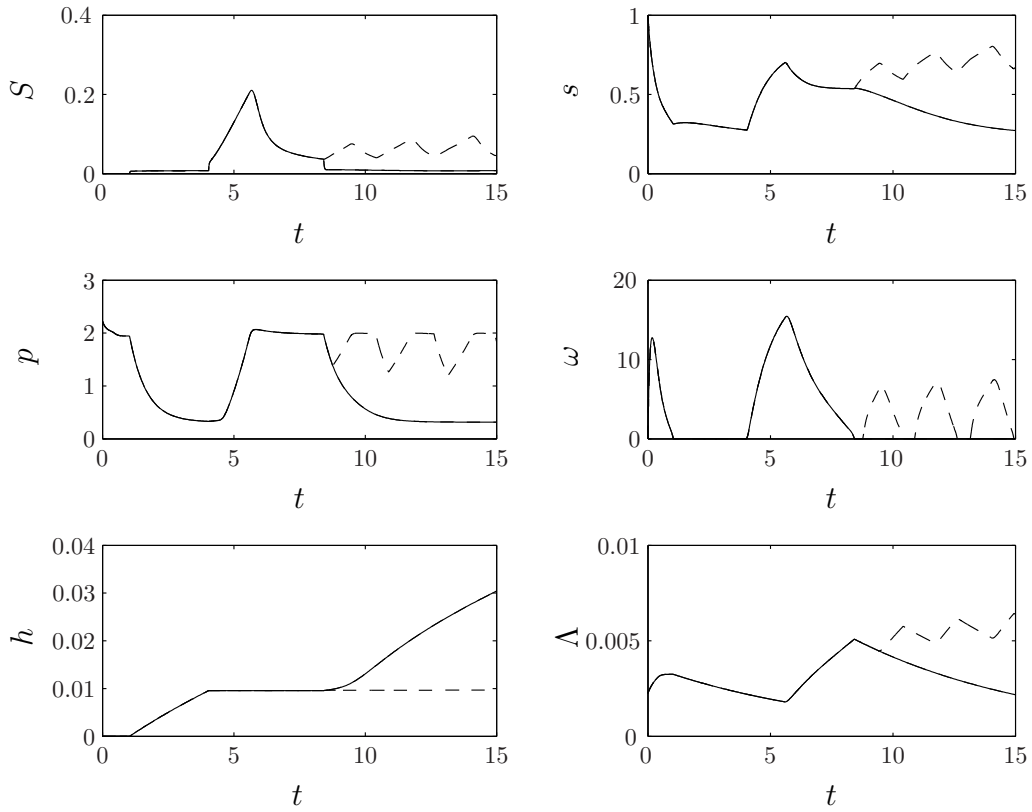


Figure 6.20: Model results to $t = 15$ using optimal parameters $a_1 = 0.522$, $a_2 = 1.868$, $h_c = 0.0051$ and $h_{c2} = 0.0001$ (solid lines) with $h_{c2} = 0.001$ (dashed lines) for the two-step sulphur input. For the larger value of h_{c2} we see oscillations in S , s , p , ω and Λ , but no further hydrogen production after the initial period.

We can investigate this new function further by plotting three surfaces with one parameter set to the optimal value on each. If we set $h_c = 0.0051$ and plot the surface for a_1 versus a_2 (Figure 6.21) then we see a fairly smooth surface with a well defined maximum.

Figure 6.22 shows two contour plots where either a_1 or a_2 is set to the optimal value, and h_c and the remaining parameter are varied. While in both cases there are clear values of a_1 and a_2 that give a maximal h to three significant figures, a range of values of h_c , $h_c \geq 0.0051$ were found for this maximum. Physically, this implies that the optimal yield of hydrogen gas is obtained when sulphur is added at a rate a_1 as soon as hydrogen production begins. This is shown in Figure 6.20 where the external sulphur curve shows that after the repair cycle, S does not drop to zero but instead stays at a low level. The

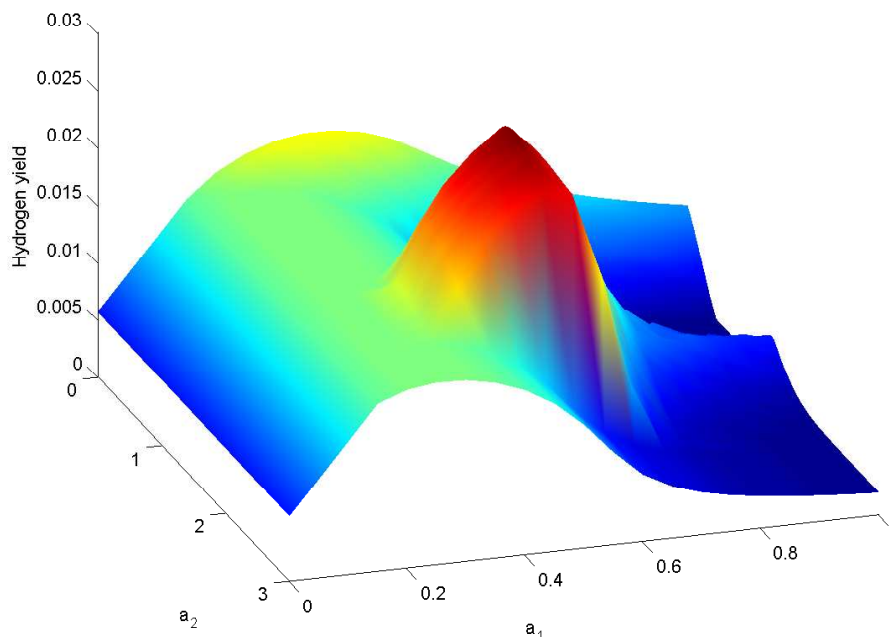


Figure 6.21: Surface plot of optimal hydrogen yield at $t = 15$ using the two-step sulphur input, with $S_0 = 0$ and $h_c = 0.0051$, varying a_1 and a_2 . The maximum yield is $h = 0.0304$.

optimal solution is, therefore, $a_1 = 0.0552$, $a_2 = 0.187$ and $h_c \geq 0.0051$.

This two-step switch helps to maximize the yield of hydrogen gas by decreasing the downtime due to a faster repair of cells in the aerobic phase. However, the strategy is not ideal since sulphur is added at a rate a_2 until increased cell volume fraction and decreased photosynthesis lead to anaerobiosis and hydrogen production again, ($\frac{dh}{dt} > 0$), which may cause an unnecessary delay.

6.2.7 A novel two-stage feedback spike sulphur input function

Although the previously discussed optimizations can be used to increase the amount of hydrogen gas produced in 15 days when compared to the two-stage method of Ghirardi *et al.* [41], we aim to improve the yield further by reducing the downtime associated with the cycling.

A more efficient method may be a two-stage process where sulphur is added at a rate a_1 to maintain a gradient h_c and, when the culture eventually becomes aerobic and hydrogen production stops, a set amount S_I of sulphur is added to the bio-reactor in one go (in a ‘spike’). The cells then use up the sulphur S_I for repair and there is a phase where no

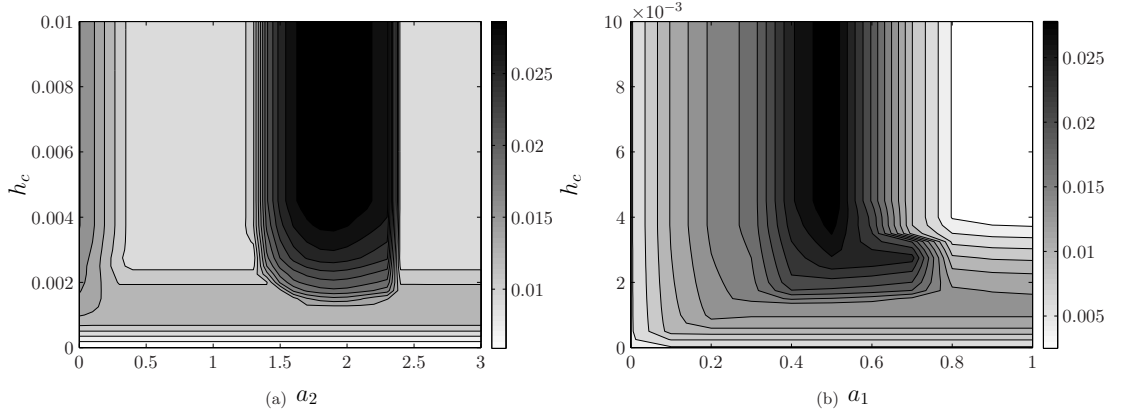


Figure 6.22: Contour plot of optimal hydrogen yield at $t = 15$ using the two-step sulphur input, with $S_0 = 0$. In Figure (a) $a_1 = 0.552$, and a_2 and h_c are varied, and in Figure (b) $a_2 = 1.87$, and a_1 and h_c are varied. The maximum yield is $h = 0.0304$.

sulphur is added, the cells are starved of external sulphur and eventually anaerobiosis and hydrogen production resume. This function should decrease the downtime as sulphur is not added right up until hydrogen production begins. It should also facilitate rapid repair.

This new function has three optimization parameters: the critical gradient, h_c , the rate of addition to maintain the gradient, a_1 , and the amount of sulphur to be added when the system becomes aerobic and stops producing hydrogen, S_I . Since it would be difficult and probably expensive to measure oxygen continuously in bio-reactor conditions, we stipulate that if the gradient of hydrogen production is decreasing then S_I of sulphur is added. Thus if $\frac{dh}{dt}(T) > h_{tol}$ and $\frac{dh}{dt}(T + 1) < h_{tol}$, then S_I of sulphur is added to the system at time step $T + 1$, where h_{tol} is a small parameter.

The algorithm for this optimization differs from the others because we wish to vary the initial conditions at $t = 0$ or timestep $T + 1$ depending on the behaviour of the system. We perform simulations for the chosen parameters from $t = 0$ to $t = 15$, and $\frac{dh}{dt}(T)$ and $\frac{dh}{dt}(T + 1)$ are calculated at every time step T . If the conditions for adding S_I of sulphur are met at $T + 1$ then the program is re-started from the time corresponding to the $T + 1$ timestep with the new initial conditions $S_0 = S_I$ and the other variables taking the values they had at $T + 1$, and the program is run until $t = 15$. The loop is repeated until the conditions for sulphur re-addition are not satisfied at any time step and the complete solution to $t = 15$ has been found. The hydrogen yield at $t = 15$ is then output.

We can write this function as

$$f\left(S, h, \frac{dh}{dt}, t\right) : \begin{cases} f(S, h, \frac{dh}{dt}, t) = a_1 \left(\frac{dh}{dt} < h_c\right) (h > 0) \\ \text{if } \frac{dh}{dt}(T) > h_{tol} \text{ and } \frac{dh}{dt}(T+1) > h_{tol}, \\ \text{or Re-start model at } T+1 \text{ with} \\ I_C = [S_I \ s(T+1) \ p(T+1) \ \omega(T+1) \ h(T+1) \ \Lambda(T+1)] \\ \text{if } \frac{dh}{dt}(T) > h_{tol} \text{ and } \frac{dh}{dt}(T+1) < h_{tol}. \end{cases} \quad (6.6)$$

Here, I_C are the initial conditions and the model is restarted from $T+1$ when the initial conditions are reset. The value of h_{tol} is set to ensure that no sulphur is added before any hydrogen has been produced in the initial stages and that sulphur is only added when the culture changes from anaerobic ($\frac{dh}{dt} > 0$) to aerobic ($\frac{dh}{dt} = 0$) conditions.

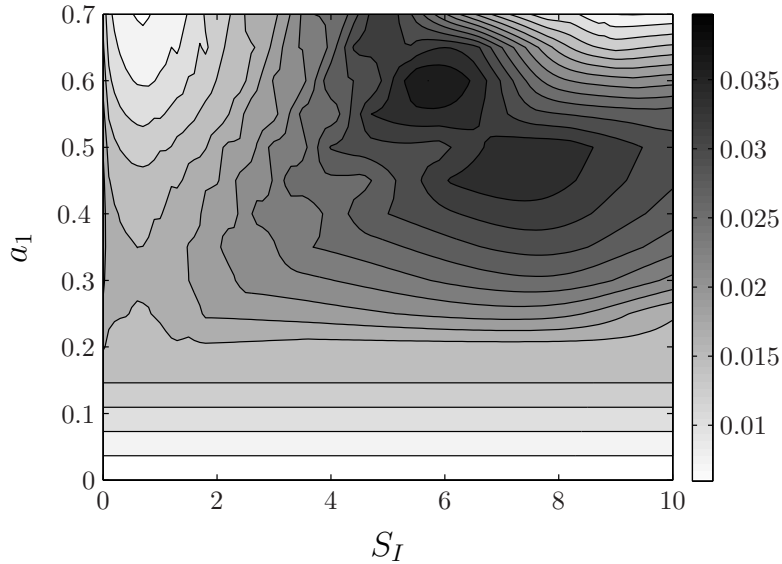


Figure 6.23: Contour plot of optimal hydrogen yield at $t = 15$ using the feedback spike optimization function, with $S_0 = 0$ and $h_c = 0.0051$, varying S_I and a_1 . The maximum yield is $h = 0.0386$.

Using a sensible initial guess, we find optimal parameter values of $h_c = 0.0051$, $S_I = 5.75$ and $a_1 = 0.614$, with $h = 0.0386$ (728 mL H_2 /L culture) at $t = 15$. This value of h is a significant improvement on the optimal value obtained using the two-stage cycling from [41] (468 mL H_2 /L culture). Figure 6.23 shows the surface for varying S_I and a_1 when $h_c = 0.0051$. The key in this optimization is to add sulphur at a high enough rate to keep the hydrogen gradient large, but not at such a high rate that the system becomes aerobic. Likewise, for S_I the key is to add enough sulphur to allow the culture to repair and regrow sufficiently so that substantial hydrogen production can occur, but to not add

too much sulphur, otherwise the system will stay aerobic for too long and the hydrogen production phase will be delayed.

As for the two-step sulphur input in Section 6.2.6, on plotting surfaces for varying h_c with either parameter we find that the maximum h to three significant figures can be found for a range of values of h_c (it is not unique). The optimal hydrogen yield at $t = 15$ is obtained for $h_c \geq 0.0051$. Since the hydrogen gradient never gets as high as 0.0051, this means that sulphur is added at a constant rate a_1 during hydrogen production (so that addition of s begins as soon as hydrogen production starts) and S_I of sulphur is added when the gradient of hydrogen production decreases.

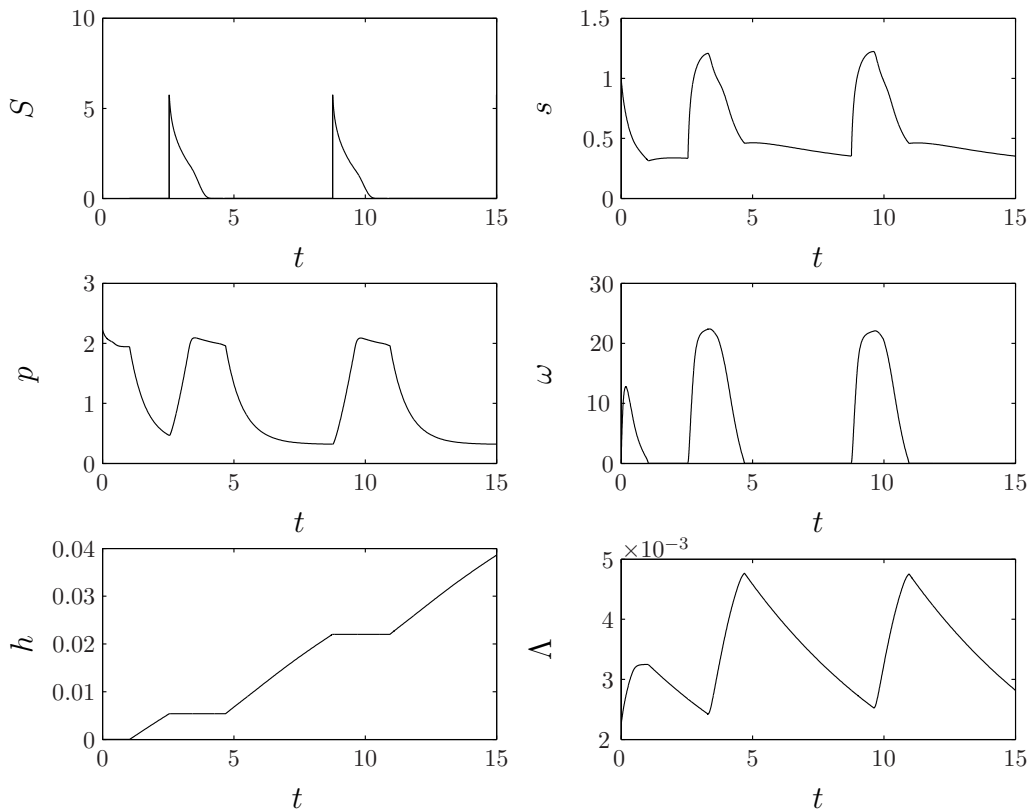


Figure 6.24: Model results to $t = 15$ using optimal parameters $S_I = 5.75$, $h_c = 0.0051$ and $a_1 = 0.614$ for the feedback spike cycling method. A significant increase in yield at $t = 15$ is seen compared to the previous optimization functions.

Figure 6.24 shows the model run with this new sulphur addition regime using the optimal parameters. Initially, we see the same behaviour as the sulphur deprivation system in Figure 5.12 but we also see a larger gradient in hydrogen production due to the re-addition of sulphur at the constant rate a_1 . Figure 6.25 shows a close up of external sulphur levels, where one can see that sulphur is added to produce an almost constant,

very low level of S during periods of hydrogen production. Again, the quasi-constant level of sulphur in the cell, combined with the increased photosynthesis due to an increase in available light as the cell volume fraction decreases, leads to a period of aerobiosis, which immediately stops H_2 production. At time step $T + 1$, S_I of external sulphur is added and in this aerobic, downtime period the cells use that sulphur to repair and grow. Once all the sulphur is used the system becomes anaerobic, as before, and hydrogen production starts again at a high rate (approximately $3.63 \text{ mL } H_2 \text{ (L culture)}^{-1} \text{ h}^{-1}$).

The initial period of hydrogen production is shorter than the subsequent periods due to a smaller cell volume fraction. This decreases the overall yield at $t = 15$ significantly. A strategy for improving this aspect is discussed in Section 6.2.8.

It is clear from the graphs in Figure 6.24 for s , p and Λ that this process is sustainable and could run like this for many more days. Using the values of a_1 , h_c and S_I that gave the maximal hydrogen yield at $t = 15$ to simulate behaviour until $t = 40$ we find that this is indeed the case, with steady oscillations of period 152 hours (not counting the first, shorter period of hydrogen production) continuing until $t = 40$, at which time the yield is $1978 \text{ mL } H_2/\text{L culture}$. This suggests that optimizing with this sulphur input function until $t = 40$ would give very similar optimal parameter values as those found for $t = 15$. This new method also allows the bio-reactor to be run continuously without the need to re-suspend the cells and change the media from sulphur-replete to sulphur-deprived (as in the current two-stage method of Ghirardi *et al.* [41]). This makes the system easy to implement, more efficient and less time consuming.

6.2.8 Optimizing the initial sulphur concentration, S_0

Results from the feedback spike cycling method in Section 6.2.7 show that the first period of hydrogen production is shorter than the subsequent periods due to a smaller cell volume fraction. Here, we try to improve the overall yield of hydrogen in 15 days by increasing the initial amount of sulphur from $S_0 = 0$. We optimize hydrogen yield using the feedback spike function with three parameters by setting $h_c = 0.0051$ and varying S_0 , a_1 and S_I . We also optimize hydrogen yield using two-stage Ghirardi cycling by varying the amount of sulphur the cells get in the sulphur-deprived period (which was previously zero), denoted S_D . Optimizing S_0 and S_D in each case is slightly different: for the two-stage case we stipulate that the cells are given S_D of sulphur every time they are re-incubated in the sulphur-‘deprived’ conditions, and for the feedback spike method we vary the one-off initial

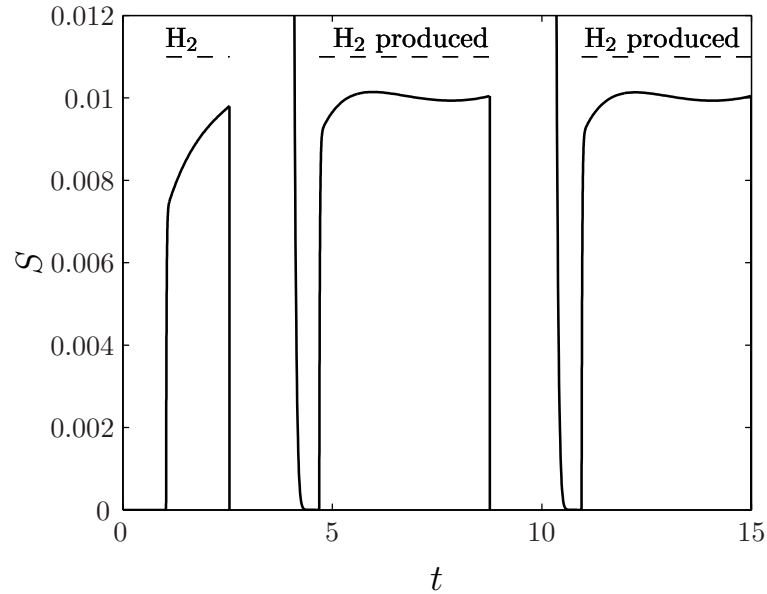


Figure 6.25: Model results to $t = 15$ using optimal parameters $S_I = 5.751$, $h_c = 0.0051$ and $a_1 = 0.614$ for the feedback spike cycling method: a close up of the external sulphur (S) behaviour. The dashed line indicated periods in which hydrogen gas is produced.

amount of sulphur given to the system before hydrogen production begins.

We find the optimal parameters for the two-stage method at $t = 15$ as $t_1 = 4.88$, $t_2 = 0.172$ and $S_D = 3.521$, with $h = 0.0293$ (554 mL H_2 /L culture). For these parameters, we find an improvement in yield and a shorter period in sulphur-replete conditions, since cells are given sulphur during the ‘deprived’ conditions as well, combined with a longer period in sulphur depleted conditions, since it takes the cells longer to commence hydrogen production.

The optimal parameters for the feedback spike cycling with $h_c = 0.0051$ are $a_1 = 0.557$, $S_I = 6.54$ and $S_0 = 2.81$, giving the highest yield of hydrogen at $t = 15$ found so far: $h = 0.0423$ (798 mL H_2 /L culture), shown in Figure 6.26. We see that the first short cycle has been replaced by a longer period of hydrogen production due to $S_0 \neq 0$ providing conditions for increased growth in the initial aerobic phase. Thus the cell volume fraction is larger than when $S_0 = 0$, and it takes longer for decreasing Λ to increase the light each cell receives sufficiently to cause the system to become aerobic and for H_2 production to stop H_2 . Only two cycles of hydrogen production are seen in 15 days, significantly reducing the downtime of the system and ensuring hydrogen is produced at a maximal rate for as long as possible. Variations in s , p and Λ indicate that this oscillation works continuously, as enough repair and regrowth occurs even though the downtime for the system is reduced.

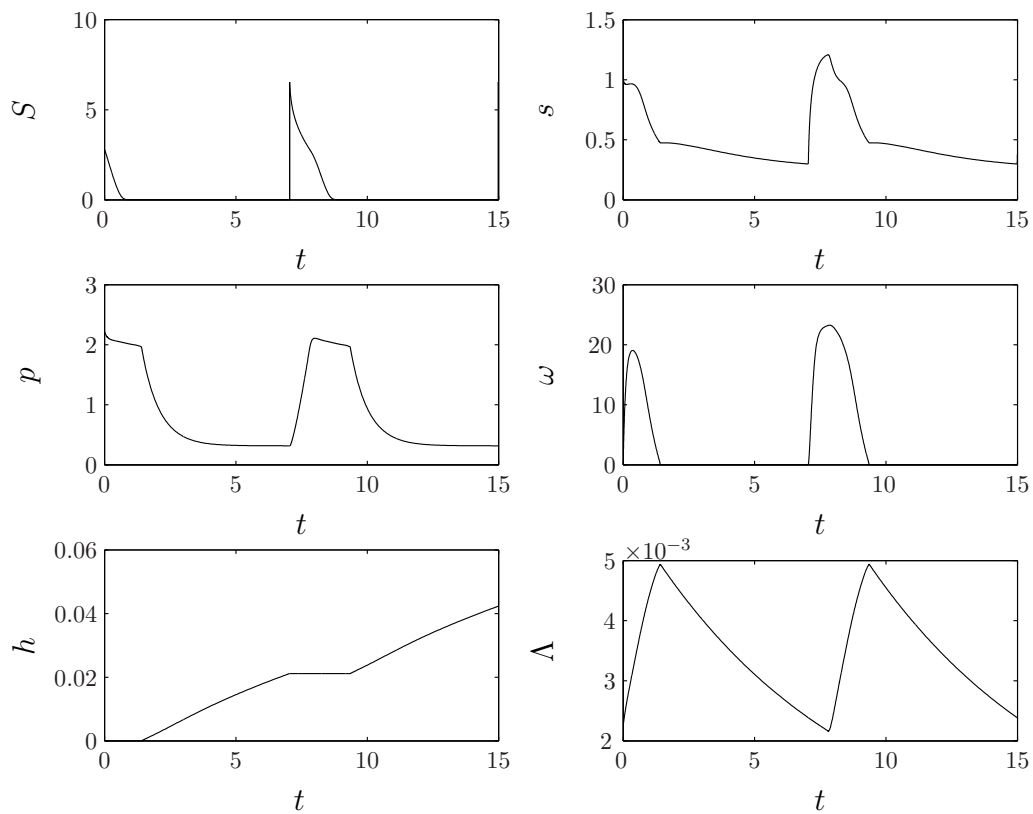


Figure 6.26: Model results to $t = 15$ using optimal parameters $S_0 = 2.81$, $h_c = 0.0051$, $S_I = 6.54$ and $a_1 = 0.557$ for the feedback spike cycling method, where the initial condition for external sulphur was also varied.

Again, this strategy produces more hydrogen gas than all the strategies tried so far; the yield is significantly higher than that found from the two-stage method of Ghirardi *et al.* [41].

6.2.9 Investigating k_3 , the dimensional rate constant for protein production.

As discussed in Section 6.1.4, we expect that if we reduce k_3 , the rate of protein production, the two-stage sulphur cycling, with t_1 and t_2 as used by Ghirardi *et al.* [41], will produce results that are more similar to those in [41], with H₂ yield decreasing in the third cycle of hydrogen production. Indeed, we find that decreasing k_3 leads to a decrease in hydrogen yield per cycle with time, because the cells do not increase protein levels enough to grow in the sulphur-replete periods. Investigating this further, we plot a curve in Figure 6.27 to show the how the difference in hydrogen yield per cycle between the second and third cycles of hydrogen production, h_{23} , changes as k_3 is varied when $t_1 = 4.1$ and $t_2 = 1.23$, as in Ghirardi *et al.* [41]. Negative regions on the curve indicate hydrogen yield per cycle decreases. For small values of k_3 , the yield decreases in each cycle due to the cells not having enough time to repair, as repair is slower. As k_3 is increased so also does h_{23} as sufficient repair occurs during the aerobic phase and cell volume fraction increases on average, which increases yields. Finally, when repair rate k_3 is large we see another region where h_{23} decreases. This is due to fast repair facilitating a high cell volume fraction, so that more sulphur is taken in to the cells and increasing internal sulphur causes the culture to take longer to reach anaerobiosis and, hence, produce a lower yield in the allowed time frame. The curve suggests that there is an optimal value of k_3 to increase yields in subsequent cycles. However, issues of sustainability need to be addressed.

Here, we consider decreasing k_3 to slow down repair, possibly to provide better agreement with results in Ghirardi *et al.* [41]. We also investigate the feedback spike cycling with a reduced k_3 to see if the method still produces more hydrogen gas than the two-stage method.

In the original system k_3 was used to estimate the parameter k_1 . Previously we employed a value of k_1 approximately mid way in the range of k_1 values. If we halve k_3 the range of values for k_1 becomes

$$0.0386 < k_1 < 0.0458. \quad (6.7)$$

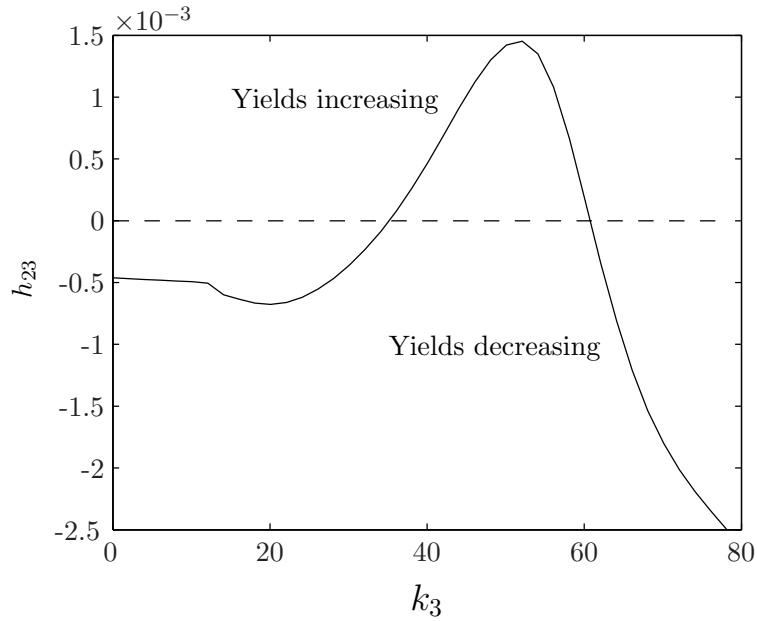


Figure 6.27: The difference in yield per cycle between the second and third cycles of hydrogen production, h_{23} , as a function of the rate of protein production, k_3 . Negative regions indicate a decrease in yield per cycle. Here, $t_1 = 4.1$ and $t_2 = 1.23$ as in Ghirardi *et al.* [41].

This range is not significantly different from the previous range for k_1 in Table 5.3, so we conclude that it is reasonable to alter k_3 without varying k_1 .

Proceeding with the optimization, using half the standard value of k_3 we find the optimal two-stage cycling to be $t_1 = 3.51$ and $t_2 = 2.22$, with a maximum $h = 0.0189$ (356 mL H₂/L culture). Decreasing k_3 means the cells make protein and, hence, repair at a slower rate, so the period of repair and growth, t_2 , is longer. Thus the overall yield is lower due to increased downtime for culture repair.

If we use half the value of k_3 and optimize the feedback method we find optimal parameters $h_c = 0.0051$, $a_1 = 0.497$ and $S_I = 10.75$, with a hydrogen yield at $t = 15$ of $h = 0.0317$ (598 mL H₂/L culture). This yield is significantly higher than that obtained from the two-stage case because during period of hydrogen production the rate of production is higher due to the addition of sulphur at a rate a_1 . This additional of sulphur means protein concentration and residual PSII activity are relatively high compared to in the two-stage case, thus contributing more electrons to the hydrogenase. The cells need more external sulphur, S_I , than for the standard value of k_3 , since the cellular repair is slower and less efficient (protein produced per mole of sulphur has reduced). This results in only

two cycles instead of three. We conclude that the novel strategy produces more hydrogen even if k_3 is reduced, with the ratio of yield from the feedback spike method to yield from the two-stage method approximately the same.

6.2.10 Summary of Optimization Results

A comparison of the different optimization functions with hydrogen yield optimized at 15 days is shown in Figure 6.28, where hydrogen yield was also optimized using non-zero S_0 for the two-stage feedback spike function, denoted ‘Feedback spike S_0 ’. The results have been put in order, largest to smallest. It is clear that the optimization function that gives the highest yield of hydrogen at $t = 15$ is the new two-stage feedback spike function, with $S_0 \neq 0$. Results are summarized in Table 6.2.

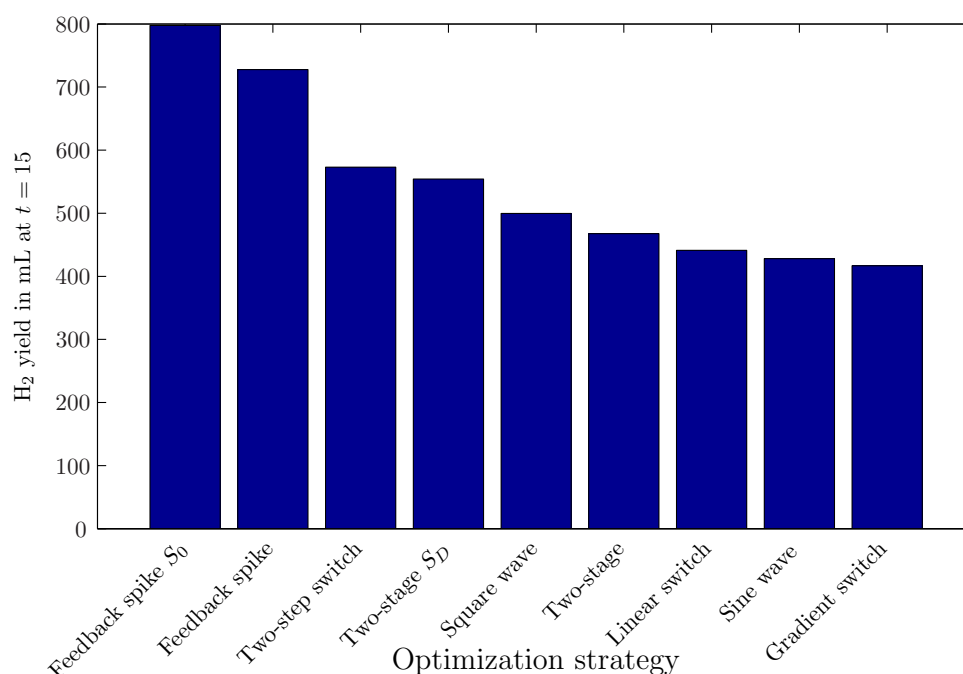


Figure 6.28: A bar chart to show the values of hydrogen in mL H₂/L culture at approximately 15 days for the different optimization strategies tested. Standard parameter values from Table 5.3 were used.

6.3 Discussion

In this chapter, a parameter sensitivity analysis for the mechanistic hydrogen model constructed in Chapter 5 was performed and conclusions on which parameters could be used

Function	t_1	t_2	S_D	k_3	Total yield (mL H ₂ /L culture)
Two-stage	3.04	0.941	0	56.4	468
Two-stage	4.88	0.172	3.52	56.4	554
Two-stage	3.51	2.22	0	28.2	356
Function	A	F	P	k_3	Total Yield (mL H ₂ /L culture)
Sine Wave	0.154	1.09	N/A	56.4	428
Square Wave	35.2	5.11	3.44	56.4	500
Function	a_1	h_c	a_2	k_3	Total Yield (mL H ₂ /L culture)
Gradient switch	1.41	0.0031	N/A	56.4	417
Linear switch	0.0002	0.0051	1.44	56.4	441
Linear switch*	0.936	0.006	0.0660	56.4	470
Two-step switch	0.522	0.00532	1.87	56.4	573
Function	a_1	h_c	S_I	k_3	Total Yield (mL H ₂ /L culture)
Feedback spike	0.614	0.0051	5.75	56.4	728
Feedback spike	0.497	0.0051	10.7	28.2	598
Feedback spike ($S_0 = 2.81$)	0.557	0.0051	6.54	56.4	798

Table 6.2: The yield of hydrogen gas at $t = 15$. The * indicates that this optimal strategy is non-sustainable, as discussed in the relevant section.

to increase hydrogen yield were drawn from this analysis. The two-stage sulphur cycling regime used by Ghirardi *et al.* 2000 [41] was then implemented on the model and comparisons with experimental data were explored. In Section 6.2 the total yield of hydrogen produced after approximately 15 days was optimized using a range of different strategies to input external sulphur into the system. These strategies were compared, and the yield of hydrogen gas was found to be much higher when using a novel strategy compared to using the two-stage cycling of Ghirardi *et al.* [41].

On conducting a parameter sensitivity analysis, we found that doubling the electrons coming to the hydrogenase from the residual photosystem II activity could be used to increase yield, compared to using the standard value in Table 5.3, by 97.5% after 244 hours when $S_0 = 50 \mu\text{M}$. Whether it is possible to increase the electrons coming to the hydrogenase without the increase in PSII activity causing the cell to become aerobic again is not clear. However, the model suggests that providing more electrons to the photosynthetic chain could increase yield, which is consistent with the notion in Kosourov *et al.*, that increasing residual PSII activity could increase hydrogen yield. Doubling the dimensional rate of protein production allowed more growth and, hence, also increased hydrogen yield (compared to the standard value) by 37.22% after 244 hours when $S_0 = 50 \mu\text{M}$.

Simulation results show that increasing light intensity from $I_0 = 49.6$ to $I_0 = 99.2$ causes an earlier onset of hydrogen production and higher yields of hydrogen, due to longer production time combined with a higher cell volume fraction and electron release, even though sulphur decays quicker than for lower light. Although the effects of light on PSII and PSI were modelled, the subsequent effect on start time of H_2 production and overall H_2 yield as a function of light were not obvious, as these are due to a combination of factors, and so comparisons can be made with hypotheses in Chapter 5. Kim *et al.* 2006 [88] find similar trends in hydrogen yield and start time as the light intensity varies. They attribute earlier start time for high light intensities ($60 - 200 \mu \text{E m}^{-2} \text{s}^{-1}$) to a faster use of sulphur, and they attribute increasing yield with increasing light intensity to an earlier start time combined with a higher chlorophyll content, which increases electron release during photosynthesis (Hypothesis 5 in Chapter 5). The first part of Hypothesis 5 clearly holds in our model; an earlier start time when light intensity increases is due to faster internal sulphur decrease (modelled by sulphur use to repair PSII), causing the hydrogenase to be active at earlier times, which in turn allows the cells to make hydrogen

for a longer period. The second part is more difficult to entangle. Whereas the hypothesis states that more chlorophyll itself is made as light increases to release electrons, the model shows that cell volume fraction as a whole increases and that, independently, the residual level of PSII and PSI activity are able to increase due to increased light energy, both of which cause more electrons to be released for use by the hydrogenase. These are very similar processes and both result in increased hydrogen yield due to increased electron release as more light becomes available, thus we conclude that the model is consistent with Hypothesis 5.

Although increasing light to $I_0 = 99.2$ increases yield, we find the unexpected result that high light intensities, such as $I_0 = 198.4$, decrease the yield of hydrogen gas. Kim *et al.* 2006 [88] hypothesize that increasing light intensity beyond $200 \mu\text{Em}^{-2}\text{s}^{-1}$ reduces yields of hydrogen gas because the rate of PSII damage increases in conditions of bright light. Similar results are found in other papers, with hydrogen yield initially increasing with I_0 and then decreasing when I_0 is large (e.g. Hahn *et al.* 2004 [53]). We model that increased light causes sulphur to be used in the repair of PSII more rapidly, since PSII gets damaged more as light increases. These high levels of photo-damage to PSII cause internal sulphur to run out quickly and this, in turn, leads to lower yield than for lower light intensities, even though PSII activity is increased and cell volume fraction is larger (both of which actually increased the yield of H_2 for $I = 99.2$ compared to $I = 49.6$). Although we did not expect to find a decrease in yield for high light intensity, the model results are consistent with Hypothesis 6 by Kim *et al.* [88] and we are satisfied that our modelling of light produces similar trends to those exhibited experimentally. The simulation results suggest that hydrogen production saturates as light intensity is increased and, hence, that there is an optimal light intensity (e.g. approximately $I_0 = 300 \mu\text{mol m}^{-2}\text{s}^{-1}$ for $S_0 = 50 \mu\text{M}$ with illumination from both sides) that can be employed for maximal hydrogen production. This is the same order as the optimal light intensity predicted by Park and Moon 2006 [126] ($238 \mu\text{E m}^{-2} \text{s}^{-1}$).

Melis [111] and Polle *et. al* [135] suggest that decreasing the absorbance of each cell, D_C , allows each cell to receive more light on average, increasing photosynthetic activity which may also increase the yield of hydrogen. This may be realized by genetically modifying the size of the light collecting antennae complexes within the chloroplasts of the cell. Such a conclusion is consistent with our model results as long as the light intensity at the source, I_0 , is not too high, or D_C not too small; the model results provide increases in

yield as D_C is decreased, but if D_C is too small hydrogen yield decreases due to increased photo-damage. This photo-damage is the same effect as found for high light intensities in Kim *et al.* 2006 [88] and Hahn *et al.* 2004 [53], and in this model and the model of Park and Moon [126], but is not predicted as an effect of decreased absorbance by Melis *et al.* 1998 [113] or Polle *et al.* 2002 [135]. The discrepancy between the model results and the predictions could be due to the over simplified instantaneous mixing assumption, quantitative differences in parameter values, or it could be that photo-damage at very low absorbance had not been considered in the context of decreasing absorbance.

The main aim of this work was to innovate new methods for providing external sulphur to increase hydrogen yields. In particular, we have aimed to improve the viability of the system by designing continuous input methods that do not necessitate changes of media or disruption to the bio-reactor. We employed an optimization procedure that maximized hydrogen yields after approximately 15 days by varying the optimization parameters, achieved numerically using a simplex method implemented Matlab. In total we tested seven methods and found the maximum yield was obtained using the new two-stage feedback spike method, where cells are given sulphur at a rate a_1 to maintain a gradient of hydrogen h_c and, once hydrogen production halts, S_I of external sulphur is added to the media in one go. This allows periods of rapid hydrogen production coupled with a short downtime for the repair and rebuilding of the cells. Optimizing this method with initial sulphur, S_0 , we found the maximum yield to be 798 mL H₂/L culture, compared to 468 mL H₂/L culture for the standard two-stage method of Ghirardi *et al.* [41]. The novel method appears robust, as it is a feedback mechanism that responds to the current state of the system at any time, and long time simulations show that cycles of hydrogen production and repair can continue indefinitely without the need to change the optimal parameters. We envisage that the sulphur addition could be automated using computer software to measure $\frac{dh}{dt}$ and control the addition of S . This would improve the cost and efficiency of the system. As previously discussed, optimization depends on what is required from the system. To extend this work, the hydrogen production start time or yield of gas per cell could also be optimized.

To our knowledge, this is the first simple mechanistic model of this system, and although we do not model the complex photosynthetic pathway in detail, we find good reasonable agreement between the model predictions and the experimental results, despite avoiding ‘fitting’ the model directly to the data. One aspect that we have not modelled

is the role of starch in this process, mainly because it is not yet fully understood and would add further complications to the system. Instead, we model endogenous substrate as protein only, since this acts in a similar way to starch in donating electrons to the hydrogenase and, additionally, when protein is broken down it releases small amounts of sulphur that are used to repair PSII. This makes the modelling processes considerably simpler than if starch were included. If starch were modelled, hydrogen production would depend on electrons from starch degradation as well as protein breakdown. We would not assume that the cell has sufficient glucose (stored as starch) to maintain anaerobiosis for hydrogen production, and aerobic respiration would have an explicit dependency on starch. In addition, we would need to model how starch builds up under sulphur deprivation compared to normal growth conditions (see Posewitz *et al.* 2004 [139]), and would model the Calvin-cycle explicitly in terms of carbon skeletons stored as starch, used in protein biosynthesis and broken down into glucose and used in respiration. It is possible that including starch could affect the time at which hydrogen is first produced and the frequency of the optimal oscillations to a small degree. Including starch was not within the scope of this work but it would be interesting to build into the model at a later stage.

The switch $H_{Calvin}(s; S_1)$, present in the model terms for protein and hydrogen production, was used to close the system to avoid explicitly modelling features of the Calvin cycle. The switch was also necessary to avoid hydrogen production in a sealed system with a high concentration of cells that turns anaerobic due to low light, since experimentally hydrogen production does not occur here (Zhang *et al.* 2002 [182]). We justified use of the switch by explaining how Rubisco breaks down under sulphur deprivation, which disables the Calvin cycle and causes the iron-hydrogenase to be the main electron sink [55,58,176]. Thus hydrogen production requires both anaerobiosis and the Calvin cycle to be inactive and protein production requires the Calvin cycle to be active. Using this switch in the model when initial external sulphur was set to minimal values did not have a large qualitative affect on the system compared to model results computed without the switch: using the switch, hydrogen production was delayed and initial rates of hydrogen production decreased for $S_0 \geq 25 \mu\text{M}$. This switch also creates the situation whereby when oxygen is low and the cell is essentially anaerobic but sulphur is high (such as in a light limited but not sulphur-deprived system, where $\omega < \omega_2$ and $s > S_1$) protein is broken down during fermentation but still produced at very low levels in the Calvin cycle. Whether it is feasible to have protein production and protein breakdown occurring concurrently, it does not

significantly affect the system because when the system is anaerobic and sulphur-replete net protein is decreasing, as more protein is used than is produced. We expect that the novel sulphur input processes described in Section 6.2 would still be a viable method for increasing the yield of hydrogen gas, even if the Calvin cycle was modelled in a different way. Further investigation of the viability of this switch and other methods to model this concept should be investigated in conjunction with the starch aspects discussed above.

The term for sulphur used to repair PSII in equation 5.7 does not appear elsewhere in the model, implying that this sulphur is lost from the system once it has been used to rebuild PSII and is not released when PSII is damaged. This seems a reasonable assumption since sulphur will be contained in proteins that might not be able to release the sulphur as they become damaged, and if sulphur were re-released during PSII damage then sulphur deprivation would not lead to hydrogen production, which would be inconsistent with experimental results.

The assumption of thorough and instantaneous mixing, so that the cells receive an average light as if they have sampled all space, should also be explored, since experimental mixing is not likely to be this thorough. If the cells are not thoroughly mixed then the cells further from the light source will receive very little light, the hydrogen yield may be lower and the effects of decreasing absorption of the cells (as suggested by Melis [111]) may be more pronounced. However, if the culture were not mixed then swimming behaviour of the cells would cause them to not be uniformly distributed throughout the culture. This would have an effect on the spatial distribution of light intensities. The model could be expanded by considerations of flow within the bio-reactor due to non-uniform cell concentration caused by cell swimming.

Future directions of this work will be of model development and experimentation. The predictions of novel optimal hydrogen production processes presented herein should be tested experimentally. The results would either support the model or suggest model improvements. New experimental methodologies and techniques should also be used to obtain more accurate parameter estimates. Various other aspects of hydrogen production could be optimized, such as bio-reactor shape, culture mixing, light conditions and initial cell volume fraction. We envisage a new two-stage hydrogen production process with real time computational adjustments to obtain optimal sulphur cycling conditions for maximum hydrogen yield. This system should be readily adaptable to other strains of algae with increased hydrogen production potential.

Chapter 7

Concluding remarks

Microorganism species display a large and diverse range of behavioural traits and biochemical processes that operate over many different length and time scales. In this thesis, we have used various modelling techniques in tandem with experimental studies, where possible, to separately explore two phenomena: bioconvection, in which the orientation mechanisms of individual cells cause collective motions involving many millions of cells, and the internal cellular processes leading to hydrogen production by sulphur-deprived *Chlamydomonas reinhardtii*. We have shown that modelling these systems by considering the main mechanistic interactions, and subsequently obtaining parameter estimates from independent data, is a valuable tool for exploration of such problems and for making predictions of organism behaviour under different conditions.

In Chapters 2 and 3 we presented three different novel modelling approaches to introduce phototaxis into the stochastic, gyrotactic model of Pedley and Kessler 1990 [130] for a suspension layer of finite depth. Model A was a photokinesis-like model, in which cell swimming speed varied as a function of light intensity, $V_s(I)$. In Model B the centre of mass offset of each cell varied as a function of light intensity, $h(I)$. A new phototaxis torque, $\mathbf{L}_p(I)$, was introduced to the gyrotactic torque balance equation in Model C, and two forms of this new torque were explored in Case I and Case II. In this study, *C. nivalis* cells were investigated in detail, although these models are applicable to a wide range of microorganism species. For all models, a linear stability analysis was completed and solutions were found numerically (and asymptotically for Models A and B). The parameters controlling phototaxis, χ and ζ (in Model C), and gyrotaxis, η , were of significant interest in this study. In all three models, for sufficiently large values of the phototaxis parameter, χ (or ζ in Model C), the maximum of the concentration profile at equilibrium

was located below $z = 0$, creating a gravitationally stable region overlying an unstable region that increased in size as χ or ζ increased. For Models A, B, and C (Case I), similar stability results were found for most parameter values: for all values of η , sufficiently large χ stabilized all wavenumbers and resulted in a non-zero critical wavenumber. In these cases, penetrative bioconvection, where fluid motions from the unstable region penetrated into the stable region causing the whole fluid layer to become unstable, occurred unless the stable layer was so large that a mode two solution was preferred. Two different instability mechanisms (one for small χ and one for large χ) when gyrotaxis was sufficiently strong (large η) were found and discussed. The overstability for small χ arose due to gyrotactic cells in the shear flow at the rigid upper boundary re-orientating to swim away from the downwelling fluid (as found by Hill *et al.* 1989 [63] for gyrotactic cells). The overstability for large χ was due to a combination of self-shading and gyrotaxis within the suspension, which caused the cells near the light source to swim backwards, away from the downwelling fluid. Interestingly, Model C (Case II), in which cells react to local gradients in light intensity, produced radically different stability results: non-hydrodynamic modes, which exist even in the absence of any fluid flow, arose due to self-shading of cells within the suspension. Such modes have not been found previously for phototactic, gravitactic or gyrotactic bioconvection problems.

The three combined photo-gyrotactic models represent a significant advancement in moving towards a realistic and rational model of bioconvection under illumination. It is possible that gyrotactic microorganisms use a combination of the three modelled mechanisms to photo-orientate, and so models which incorporate two or more of the photo-gyrotactic modelling approaches should be investigated. It is hoped that these models can be used as a framework for studies of pattern formation under various conditions for a diverse range of microorganism species.

In Chapter 4, a robust experimental framework was described and used to conduct controlled, repeatable experiments to investigate the effects of concentration and light intensity on wavelengths of pattern formation. The proposed framework could be used for a variety of experimental investigations of bioconvection with different species, and in this study we explored the initial, dominant pattern to form from a well mixed distribution of *C. nivalis*. Experiments were repeated both with the same cells and with different cells, allowing simple statistical measures to be calculated, and a novel automated mixing was designed and implemented to minimize differences in initial conditions between

experiments. The dominant wavelength was extracted using Fourier analysis. Trends in initial wavelength as concentration varied were consistent with those found by Bees and Hill 1997 [8]. Variations in red light illumination intensity were found to have no significant effect on the resulting pattern wavelength, which is consistent with measurements in Nultsch *et al.* 1971 [125]; cells do not respond phototactically to red light (wavelengths of approximately 660 nm). However, initial pattern wavelength was found to vary as a function of white light intensity, and the resulting trends were dependent on the direction of illumination. The dependence on light intensity of the most unstable wavelength of the well developed pattern has yet to be investigated, and it would certainly be interesting to explore aspects of pattern shape and formation as non-linear effects come into play. Comparisons between experimental results and model predictions for Models A and B were made and, encouragingly, some good agreement was found. Further experimental work is required in order to assess whether the non-hydrodynamic modes predicted by Model C (Case II) actually occur. This could be achieved by exploring pattern formation in soft agar gels, in which there would be limited fluid flow.

In Chapter 5, a novel model to describe hydrogen production in suspensions of sulphur-deprived *C. reinhardtii* was built from a careful consideration of the relevant intracellular mechanisms. Parameters were found from independent data sources, where possible, and good agreement was found between model results and experimental data of previous studies [92, 114, 182]. In Chapter 6, a full parameter sensitivity analysis highlighted those parameters that could potentially increase the yield of hydrogen. The work concluded with an optimization study in which various sulphur input functions were used in an attempt to maximize the total hydrogen yield after approximately 15 days. One such function, which adds sulphur to the bio-reactor at a constant rate during hydrogen production and then in a block addition once hydrogen production stops, was found to significantly increase the yield of hydrogen gas compared to the maximum obtained using the current state-of-the-art two-stage cycling of Ghirardi *et al.* 2000 [41]. In addition, this proposed sulphur input regime can be run continuously without the need for periodic medium changes, as was required in the discontinuous two-stage method [41]. It is hoped that the increased yield and the easy implementation of the feedback mechanism for the addition of sulphur, which could be controlled via an automated system, will improve the commercial viability of hydrogen production and could be used for a variety of microorganism species. Model extensions and the need to test optimization predictions experimentally were discussed in

Chapter 6.

In this thesis, the phenomena of bioconvection and hydrogen production have been considered separately. However, there are at least two ways in which bioconvection and hydrogen production may interact. Firstly, the deposition and consumption of internal reserves of starch by hydrogen-producing cells changes both the cellular morphology and the individual cell's centre of mass offset, thus varying the gyrotactic and gravitactic behaviour. The intriguing effects of hydrogen production on bioconvective pattern formation have not yet been investigated. Including the effects of hydrogen production in a model for photo-gyrotactic bioconvection (possibly through the parameters for cell eccentricity, α_0 , and centre of mass offset, h) would not be straightforward, not least because of the large range of length and time scales involved. Bioconvection patterns with the scale of centimeters form within tens of seconds due to the behaviour of individual cells with scales of micrometers, whereas hydrogen production occurs as a result of microscopic intracellular processes, and changes in shape and mass distribution occur over many tens of hours. Additionally, linear analysis of the current photo-gyrotactic models predicts only the first most unstable mode to grow from equilibrium (usually within 30 seconds); aspects of long term fully non-linear plume and pattern formation have not been explored and, hence, slow changes in model parameters due to hydrogen production would not be captured. The centre of mass offset varied between individuals, $h(I)$, in Model B, but the time scale for changes in h due to light were much smaller than the time scale for changes in h due to hydrogen production. A first step towards including the effects of hydrogen production on bioconvection could be to use a photo-gyrotactic model to investigate stability for a range of realistic values of α_0 and h that occur during sulphur-deprivation. Predicted stability trends could be compared to experimental results by performing bioconvection experiments (as described in Chapter 4) and measuring cell eccentricity and centre of mass offset at various intervals during hydrogen production. However, this may be complicated by the fact that hydrogen producing cells need to be kept in a sealed container, and a suitable motile species that can produce both hydrogen gas and patterns would need to be found.

Secondly, bioconvection can affect hydrogen production, since in an unmixed suspension of motile hydrogen-producing cells, plume formation would lead to an uneven distribution of light throughout the bio-reactor. The population would be unsynchronized and the rate of hydrogen production for each cell would depend on the cell's location. Uneven

light distribution caused by plume formation could possibly be included in the term for light intensity, $L(\Lambda)$, in the hydrogen production model in Chapter 5 by changing the assumption that the suspension is well mixed. However, this would not be straightforward, since it would require designing a model for long term plume formation (over many hours) within a bio-reactor. Experimental investigation would be more straightforward: the yield of hydrogen produced by a suitable motile algal species could be measured in two identical bio-reactor set-ups, where the suspension is mixed in one and not in the other. What effect cell swimming and plume formation has on the overall yield of hydrogen gas remains to be seen and could provide an interesting and potentially valuable avenue of future research.

Appendix A

Analytic equilibrium solution for the case of weak absorption in Models A and B

In Section 2.3.3 for Model A and Section 3.3.1 for Model B an analytic equilibrium solution is found for the case of weak absorption, $\kappa \ll 1$. On expanding for small κ the form of the equilibrium solution to be solved in equations 2.61 and 3.106 is

$$\frac{dn}{dz} - G_1 \left[\int_z^0 n(z) dz - C \right] n(z) = 0, \quad (\text{A.1})$$

where the constant G_1 is defined by

$$G_1 = d\kappa \text{ in Model A, and } G_1 = \frac{d\bar{K}_2}{\bar{K}_1} \lambda \kappa \text{ in Model B.} \quad (\text{A.2})$$

To solve, we first divide equation A.1 by $n(z)$, so that

$$\frac{1}{n(z)} \frac{dn(z)}{dz} = G_1 \int_z^0 n(z) dz - G_1 C. \quad (\text{A.3})$$

Differentiating with respect to z gives

$$\frac{n''n - (n')^2}{n^2} = -G_1 n, \quad (\text{A.4})$$

where the dash denotes differentiation with respect to z . We set

$$p(n) = \frac{dn}{dz}, \text{ so that} \quad (\text{A.5})$$

$$\frac{d^2n}{dz^2} = \frac{dp}{dz} = \frac{dp}{dn} \frac{dn}{dz} = p'p, \quad (\text{A.6})$$

where p' indicates p differentiated with respect to n . Substituting equations A.5 and A.6 into equation A.4 gives

$$p'pn - p^2 = -G_1n^3. \quad (\text{A.7})$$

We define $r(n)$ so that

$$r(n) = p^2, \text{ hence } \frac{dr}{dn} = \frac{d(p^2)}{dp} \frac{dp}{dn} = 2pp'. \quad (\text{A.8})$$

Substituting equation A.8 into A.7 gives

$$r' - \frac{2r}{n} = -2G_1n^2, \text{ hence } \left(\frac{r}{n^2}\right)' = -2G_1. \quad (\text{A.9})$$

Integrating this expression gives

$$\left(\frac{r}{n^2}\right) = -2G_1n + K^2, \quad (\text{A.10})$$

where K^2 is a constant of integration. Converting equation A.10 back to being in terms of n using equations A.5 and A.8 gives

$$(n')^2 = p^2 = r = -2G_1n^3 + K^2n^2, \quad (\text{A.11})$$

hence

$$\frac{dn}{dz} = (-2G_1n^3 + K^2n^2)^{1/2}. \quad (\text{A.12})$$

On integrating with respect to z we can write equation A.12 as

$$\int \frac{dn}{(-2G_1n^3 + K^2n^2)^{1/2}} = z + A, \quad (\text{A.13})$$

where A is a constant of integration. We make the substitution $m^2 = K^2 - 2G_1n$, so that

$$n = \frac{K^2 - m^2}{2G_1} \text{ and } dm = -G_1(K^2 - 2G_1n)^{-1/2}dn. \quad (\text{A.14})$$

Substituting equation A.14 into equation A.13 gives

$$-2 \int \frac{dm}{K^2 - m^2} = z + A. \quad (\text{A.15})$$

Integrating equation A.15 gives

$$-\frac{1}{K} \text{Ln} \left| \frac{K+m}{K-m} \right| = z + A. \quad (\text{A.16})$$

On re-arranging, equation A.16 becomes

$$m = \frac{-K(1 - e^{-K(z+A)})}{1 + e^{-K(z+A)}}. \quad (\text{A.17})$$

Multiplying top and bottom by $e^{\frac{K(z+A)}{2}}$ gives

$$m = -K \tanh\left(\frac{K}{2}(z+A)\right). \tag{A.18}$$

Using the relation of m to n in equation A.14 we can write n as

$$n = \frac{K^2}{2G_1} \left(1 - \tanh^2\left(\frac{K}{2}(z+A)\right)\right), \text{ hence } n = \frac{K^2}{2G_1} \operatorname{sech}^2\left(\frac{K}{2}(z+A)\right). \tag{A.19}$$

To obtain the solution in the same form as in Ghorai and Hill 2005 [46], we first differentiate equation A.19 with respect to z

$$n' = -\frac{K^3}{2G_1} \frac{\sinh\left(\frac{K}{2}(z+A)\right)}{\cosh^3\left(\frac{K}{2}(z+A)\right)}. \tag{A.20}$$

Substituting equation A.20 into equation A.3 and re-arranging gives

$$-K \tanh\left(\frac{K}{2}(z+A)\right) = G_1 \int_z^0 \frac{K^2}{2G_1} \operatorname{sech}^2\left(\frac{K}{2}(z+A)\right) dz - G_1 C. \tag{A.21}$$

Solving the integration yields the relationship

$$\tanh\left(\frac{KA}{2}\right) = \frac{G_1 C}{K}. \tag{A.22}$$

On expanding equation A.19 using trigonometric identities we have

$$n(z) = \frac{K^2}{2G_1} \left[\frac{1}{\cosh\left(\frac{Kz}{2}\right) \cosh\left(\frac{KA}{2}\right) + \sinh\left(\frac{Kz}{2}\right) \sinh\left(\frac{KA}{2}\right)} \right]^2, \text{ hence} \tag{A.23}$$

$$n(z) = \frac{K^2}{2G_1} \frac{\operatorname{sech}^2\left(\frac{Kz}{2}\right) \operatorname{sech}^2\left(\frac{KA}{2}\right)}{\left(1 + \tanh\left(\frac{Kz}{2}\right) \tanh\left(\frac{KA}{2}\right)\right)^2}. \tag{A.24}$$

Expanding sech in terms of tanh and using equation A.22 gives

$$\operatorname{sech}^2\frac{KA}{2} = 1 - \tanh^2\frac{KA}{2} = 1 - \frac{G_1^2 C^2}{K^2}. \tag{A.25}$$

Substituting equation A.25 into equation A.24 and re-arranging, we have

$$n(z) = \frac{\frac{K^2}{2G_1} [(K^2/G_1^2) - C^2] \operatorname{sech}^2(Kz/2)}{[(K/G_1) + C \tanh(Kz/2)]^2}. \tag{A.26}$$

This is the analytic solution for Models A and B given in equations 2.62 and 3.107, respectively, where the constant G_1 for each model is shown in equation A.2. Also note equation A.26 is the same as in Ghorai and Hill 2005 [46], except for a different constant G_1 .

All that remains is to find the transcendental equation from which the constant K can be calculated. To calculate K we substitute the expression for $n(z)$ in equation A.19 into the normalization condition in equation 2.64, given by

$$\int_{-1}^0 n(z) dz = d^{-1} (1 - e^{-d}). \tag{A.27}$$

This gives

$$\frac{K^2}{2G_1} \int_{-1}^0 \operatorname{sech}^2 \left(\frac{K}{2}(z+A) \right) dz = d^{-1} (1 - e^{-d}), \quad (\text{A.28})$$

which can be evaluated to give

$$\frac{K}{G_1} \left[\tanh \frac{KA}{2} - \tanh \frac{K(A-1)}{2} \right] = d^{-1} (1 - e^{-d}). \quad (\text{A.29})$$

Using equation A.22 and the half angle identity for tanh in equation A.29 yields

$$\frac{K}{G_1} \left[\frac{G_1 C}{K} - \frac{\frac{G_1 C}{K} - \tanh \frac{K}{2}}{1 - \frac{G_1 C}{K} \tanh \frac{K}{2}} \right] = d^{-1} (1 - e^{-d}). \quad (\text{A.30})$$

Re-arrangement and simplification of equation A.30 leads to

$$\tanh \frac{K}{2} \left[-\frac{G_1 C^2}{K} + \frac{K}{G_1} + d^{-1} (1 - e^{-d}) \frac{G_1 C}{K} \right] = d^{-1} (1 - e^{-d}). \quad (\text{A.31})$$

Hence the transcendental equation from which K can be calculated is

$$\left(\frac{K^2}{G_1^2} - C^2 + d^{-1} (1 - e^{-d}) C \right) \tanh \left(\frac{K}{2} \right) - \frac{d^{-1} (1 - e^{-d}) K}{G_1} = 0. \quad (\text{A.32})$$

Appendix B

Solving terms in the Fokker-Planck equation using associated Legendre polynomials

In Section 3.2 solutions to the Fokker-Planck equation for the case of no-flow and for a first order perturbation are found by considering each term separately, as in Pedley and Kessler 1990 [130] and Bees and Hill 1998 [9]. Many of the resulting equations can be solved using Legendre polynomials, and so here the relevant aspects of Legendre's associated equation are introduced and then used to solve one of the terms of the Fokker-Planck equation as an example.

B.1 Definitions and identities for associated Legendre polynomials

Legendre's associated equation is defined as

$$((1-x^2)y')' + \left[r(r+1) - \frac{\mu^2}{(1-x^2)} \right] y = 0, \quad (\text{B.1})$$

where $x \in [-1, 1]$, $y(x)$ finite at the end points, $0 \leq r$ and $\mu \in \mathbb{Z}$. If we substitute $y(x) = (1-x^2)^{\frac{\mu}{2}} u(x)$ and then divide by $(1-x^2)^{\frac{\mu}{2}}$ we have Legendre's equation differentiated μ times, and we can write

$$y(x) = P_r^\mu(x) = (1-x^2)^{\frac{\mu}{2}} \frac{d^\mu}{dx^\mu} P_r(x), \quad (\text{B.2})$$

where $P_r(x)$ are Legendre polynomials and P_r^μ are associated Legendre polynomials. The latter are orthogonal in the lower index, so that

$$\int_{-1}^1 P_r^k P_m^k dx = \delta_r^m \frac{2}{2r+1} \frac{(r+k)!}{(r-k)!}, \tag{B.3}$$

where $0 \leq k \leq r, m$, and are also orthogonal in the upper index, so that

$$\int_{-1}^1 \frac{P_k^r P_k^m}{1-x^2} dx = \delta_r^m \frac{1}{m} \frac{(k+m)!}{(k-m)!}, \tag{B.4}$$

where $1 \leq r \leq m \leq k$. Recurrence relations for these associated Legendre polynomials are given in Arfken 1985 [3]:

$$P_r^{m+1} - \frac{2mx}{(1-x^2)^{\frac{1}{2}}} P_r^m + [r(r+1) - m(m-1)] P_r^{m-1} = 0, \tag{B.5}$$

$$(2r+1)x P_r^m = (r+m) P_{r-1}^m + (r-m+1) P_{r+1}^m, \tag{B.6}$$

$$(2r+1)(1-x^2)^{\frac{1}{2}} P_r^m = P_{r+1}^{m+1} - P_{r-1}^{m+1}, \tag{B.7}$$

$$(2r+1)(1-x^2)^{\frac{1}{2}} P_r^m = (r+m)(r+m-1) P_{r-1}^{m-1} - (r-m+1)(r-m+2) P_{r+1}^{m-1}, \text{ and} \tag{B.8}$$

$$(1-x^2)^{\frac{1}{2}} P_r^{m'} = \frac{1}{2} P_r^{m+1} - \frac{1}{2} (r+m)(r-m+1) P_r^{m-1}. \tag{B.9}$$

B.2 An example of using associated Legendre polynomials to solve a term in the Fokker-Planck equation

For the first order perturbation for spherical cells the flow term, the first on the right hand side of equation 3.41, can be written as

$$((1-x^2)G_n')' - \frac{G_n}{(1-x^2)} - ((1-x^2)G_{n-1}')' = -\frac{(1-x^2)^{\frac{1}{2}} x^{n-1}}{(n-1)!}, \tag{B.10}$$

as shown in Section 3.2.2. Equation B.10 has the form of an associated Legendre polynomial of order one, in which case $\mu = 1$ in equation B.1, and so we define

$$G_n(x) = \sum_{r=1}^n a_{n,r} P_r^1(x), \tag{B.11}$$

where $a_{n,r} = 0$ for $n < r$ or $n, r < 1$. Substituting B.11 into equation B.10 and using the definition of Legendre's associated equation in equation B.1 gives

$$-\sum_{r=1}^n a_{n,r} r(r+1) P_r^1 - \sum_{r=1}^{n-1} a_{n-1,r} \frac{d}{dx} ((1-x^2) P_r^1) = -(1-x^2)^{\frac{1}{2}} \frac{x^{n-1}}{(n-1)!}. \tag{B.12}$$

To proceed, we substitute the recurrence relations in equation B.5 and B.8 into equation B.9, on setting $m = 1$, which gives

$$(1 - x^2)P_r^{1'} = xP_r^1 - \frac{r(r+1)}{(2r+1)}(P_{r+1}^1 - P_{r-1}^1). \quad (\text{B.13})$$

Using this expression in equation B.12 gives

$$\begin{aligned} & \sum_{r=1}^n a_{n,r} r(r+1)P_r^1 + \sum_{r=1}^{n-1} a_{n-1,r} \left[-xP_r^1 - \frac{r(r+1)}{2r+1} (P_{r+1}^1 - P_{r-1}^1) \right] \\ &= (1 - x^2)^{\frac{1}{2}} \frac{x^{n-1}}{(n-1)!}. \end{aligned} \quad (\text{B.14})$$

If $m = 1$ then equation B.6 can be written

$$xP_r^1 = \frac{(r+1)P_{r-1}^1 + rP_{r+1}^1}{2r+1}, \quad (\text{B.15})$$

which can be applied to equation B.14 to give

$$\begin{aligned} & \sum_{r=1}^n a_{n,r} r(r+1)P_r^1 - \sum_{r=1}^{n-1} a_{n-1,r} \left[\frac{r+1}{2r+1} P_{r-1}^1 + \frac{r}{2r+1} P_{r+1}^1 + \frac{r(r+1)}{2r+1} (P_{r+1}^1 - P_{r-1}^1) \right] \\ &= (1 - x^2)^{\frac{1}{2}} \frac{x^{n-1}}{(n-1)!}. \end{aligned} \quad (\text{B.16})$$

If we then multiply by P_m^1 we can integrate from $x = -1$ to $x = 1$ using equation B.3 to give

$$a_{n,m} = -\frac{m+2}{(m+1)(2m+3)} a_{n-1,m+1} + \frac{m-1}{(2m-1)m} a_{n-1,m-1} + \frac{b_{n,m}}{m(m+1)} \quad (\text{B.17})$$

where

$$b_{n,m} = \frac{2m+1}{2(n-1)!m(m+1)} \int_{-1}^1 (1-x^2)^{\frac{1}{2}} x^{n-1} P_m^1(x) dx, \quad (\text{B.18})$$

as shown in equations 3.47 and 3.48. The solution to equation B.10 can now be calculated using the values of $a_{n,r}$ (calculated from equation B.17, with $b_{n,m}$ given in equation 3.49) together with the known expressions for $P_r^1(x)$ in the expression for $G_n(x)$ in equation B.11.

Appendix C

Definitions of constants used in the asymptotic analysis for a deep layer and weak illumination for Model B

Table C.1 summarizes the definitions of parameters that are needed in equation 3.188 for the asymptotic analysis of Model B. Values are calculated using the standard values $\lambda = 2.2$ and $\alpha_0 = 0.2$, which are used throughout Chapters 2 and 3.

Parameter	Definition	Typical value
$K_{(1,0)}$	$\coth \lambda_0 - \frac{1}{\lambda_0}$	0.570
$K_{(1,-1)}$	$\frac{\lambda_1 (\cosh^2 \lambda_0 - 1 - \lambda_0^2)}{\lambda_0^2 \sinh^2 \lambda_0}$	-0.344
$K_{(2,0)}$	$1 - \coth^2 \lambda_0 + \frac{1}{\lambda_0^2}$	0.156
$K_{(2,-1)}$	$\frac{-2\lambda_1 (\sinh \lambda_0 \cosh^2 \lambda_0 - \sinh \lambda_0 - \lambda_0^3 \cosh \lambda_0)}{\lambda_0^3 \sinh^3 \lambda_0}$	0.186
$K_{(4,0)}$	$K_{(2,0)} - \frac{K_{(1,0)}}{\lambda_0}$	-0.103
$K_{(4,-1)}$	$K_{(2,-1)} - \frac{K_{(1,-1)}}{\lambda_0} + \frac{K_{(1,0)}\lambda_1}{\lambda_0^2}$	0.0833
$K_{(5,0)}$	$-\frac{2}{\lambda_0} \left[1 + K_{(2,0)} - \frac{4K_{(1,0)}}{\lambda_0} \right]$	-0.108
$K_{(5,-1)}$	$-\frac{2}{\lambda_0} \left(K_{(2,-1)} - \frac{4}{\lambda_0} \left(K_{(1,-1)} - \frac{K_{(1,0)}\lambda_1}{\lambda_0} \right) \right)$ $+ \frac{2\lambda_1}{\lambda_0^2} \left(1 + K_{(2,0)} - \frac{4K_{(1,0)}}{\lambda_0} \right)$	0.0966
$J_{(1,0)}$	$\frac{\lambda_0^2}{3 \sinh(\lambda_0)} \sum_{l=0}^{\infty} \lambda_0^{2l+1} (z) a_{2l+1,1}$	0.452

Continued over page

Parameter	Definition	Typical value
$J_{(1,-1)}$	$\frac{\lambda_0}{3} \left(\lambda_0 \operatorname{cosech}(\lambda_0) - \lambda_0 \lambda_1 \coth(\lambda_0) \operatorname{cosech}(\lambda_0) \right) \\ \times \sum_{l=0}^{\infty} \lambda_0^{2l+1}(z) a_{2l+1,1} + \frac{\lambda_0}{\sinh(\lambda_0)} \sum_{l=0}^{\infty} \lambda_1^{2l+1}(z) a_{2l+1,1} \Bigg)$	-0.0225
$J_{(2,0)}$	$\frac{\lambda_0^2}{5 \sinh(\lambda_0)} \sum_{l=1}^{\infty} \lambda_0^{2l}(z) a_{2l,2}$	0.159
$J_{(2,-1)}$	$\frac{\lambda_0}{5} \left((\lambda_0 \operatorname{cosech}(\lambda_0) - \lambda_0 \lambda_1 \coth(\lambda_0) \operatorname{cosech}(\lambda_0)) \right. \\ \left. \times \sum_{l=1}^{\infty} \lambda_0^{2l}(z) a_{2l,2} + \frac{\lambda_0}{\sinh(\lambda_0)} \sum_{l=1}^{\infty} \lambda_1^{2l}(z) a_{2l,2} \right)$	-0.163
$J_{(4,0)}$	$\frac{\lambda_0^2}{3 \sinh(\lambda_0)} \sum_{l=0}^{\infty} \lambda_0^{2l+1}(z) \tilde{a}_{2l+1,1}$	-0.227
$J_{(4,-1)}$	$\frac{\lambda_0}{3} \left(\lambda_0 \operatorname{cosech}(\lambda_0) - \lambda_0 \lambda_1 \coth(\lambda_0) \operatorname{cosech}(\lambda_0) \right) \\ \times \sum_{l=0}^{\infty} \lambda_0^{2l+1}(z) \tilde{a}_{2l+1,1} + \frac{\lambda_0}{\sinh(\lambda_0)} \sum_{l=0}^{\infty} \lambda_1^{2l+1}(z) \tilde{a}_{2l+1,1} \Bigg)$	0.114
$J_{(5,0)}$	$\frac{\lambda_0^2}{5 \sinh(\lambda_0)} \sum_{l=0}^{\infty} \lambda_0^{2l}(z) \tilde{a}_{2l,2}$	-0.166
$J_{(5,-1)}$	$\frac{\lambda_0}{5} \left(\lambda_0 \operatorname{cosech}(\lambda_0) - \lambda_0 \lambda_1 \coth(\lambda_0) \operatorname{cosech}(\lambda_0) \right) \\ \times \sum_{l=0}^{\infty} \lambda_0^{2l}(z) \tilde{a}_{2l,2} + \frac{\lambda_0}{\sinh(\lambda_0)} \sum_{l=0}^{\infty} \lambda_1^{2l}(z) \tilde{a}_{2l,2} \Bigg)$	0.0195
$A_{(1,0)}$	$J_{(1,0)} K_{(1,0)} - J_{(2,0)} + \alpha_0 (J_{(5,0)} - K_{(1,0)} J_{(4,0)} - 3(K_{(5,0)} - 2K_{(1,0)} K_{(4,0)}))$	0.0862
$A_{(1,-1)}$	$J_{(1,0)} K_{(1,-1)} + J_{(1,-1)} K_{(1,0)} - J_{(2,-1)} + \alpha_0 (J_{(5,-1)} - K_{(1,0)} J_{(4,-1)} - K_{(1,-1)} J_{(4,0)} - 3(K_{(5,-1)} - 2K_{(1,0)} K_{(4,-1)} - 2K_{(1,-1)} K_{(4,0)}))$	0.0114
$A_{(2,0)}$	$J_{(1,0)} - \alpha_0 (J_{(4,0)} - 3K_{(4,0)})$	0.436
$A_{(2,-1)}$	$J_{(1,-1)} - \alpha_0 (J_{(4,-1)} - 3K_{(4,-1)})$	0.00453
$A_{(3,0)}$	$3\alpha_0 K_{(4,0)}$	-0.0618
$A_{(3,-1)}$	$3\alpha_0 K_{(4,-1)}$	0.0500
$A_{(4,0)}$	$3\alpha_0 (K_{(5,0)} - 2K_{(1,0)} K_{(4,0)})$	0.00537
$A_{(4,-1)}$	$3\alpha_0 (K_{(5,-1)} - 2K_{(1,0)} K_{(4,-1)} - 2K_{(1,-1)} K_{(4,0)})$	-0.0415
$P_{(H,0)}$	$\frac{K_{(1,0)}}{\lambda_0}$	0.259
$P_{(H,-1)}$	$\frac{K_{(1,-1)}}{\lambda_0} - \frac{K_{(1,0)} \lambda_1}{\lambda_0^2}$	0.103
$P_{(5,0)}$	$A_{(1,0)} + \frac{K_{(2,0)} A_{(2,0)}}{K_{(1,0)}}$	0.205
$P_{(6,0)}$	$\frac{K_{(2,0)} A_{(3,0)}}{K_{(1,0)}} - A_{(4,0)}$	-0.0223

Continued over page

Parameter	Definition	Typical value
A_K	$\frac{1}{K_{(2,0)}} \left(K_{(2,-1)} - \frac{K_{(2,0)}K_{(1,-1)}}{K_{(1,0)}} \right)$	1.79
C_K	1.0	1.0
N_K	$\frac{1}{K_{(1,0)}} \left(K_{(1,-1)} - \frac{K_{(1,0)}K_{(2,-1)}}{K_{(2,0)}} \right)$	-1.79

Table C.1: Summary of constants needed to compute the asymptotic solution for Model B in equation 3.188, where $\alpha_0 = 0.2$. From equation 3.138, $\lambda_0 = \lambda$ and $\lambda_1 = -\chi_{-1}\lambda$, where we use $\lambda = 2.2$ and $\chi_{-1} = 1$. $a_{i,j}$ and $\tilde{a}_{i,j}$ are defined in equations 3.97 and 3.98. $K_{(i,0)}$ and $J_{(i,0)}$ are equivalent to the values of K_i and J_i when $\Lambda(z) = \lambda$, i.e. the values of K_i and J_i when $\chi = 0$. These are the (corrected) values of K_i and J_i used in Bees and Hill 1998 [9], shown in Table 2.2 in Chapter 2.

References

- [1] Z. Alloui, T. H. Nguyen, and E. Bilgen. Bioconvection of gravitactic microorganisms in a vertical cylinder. *International Communications in Heat and Mass Transfer*, 32(6):739 – 747, 2005.
- [2] Z. Alloui, T. H. Nguyen, and E. Bilgen. Stability analysis of thermo-bioconvection in suspensions of gravitactic microorganisms in a fluid layer. *International Communications in Heat and Mass Transfer*, 33(10):1198 – 1206, 2006.
- [3] G. Arfken. *Mathematical methods for Physicists*. Academic Press Inc., London, 3rd edition, 1985.
- [4] C. Ascoli, M. Barbi, C. Frediani, and A. Mur. Measurements of *Euglena* motion parameters by laser light scattering. *Biophysical Journal*, 24(3):585 – 599, 1978.
- [5] G. K. Batchelor. The stress system in a suspension of force-free particles. *Journal of Fluid Mechanics*, 41(3):545–570, 1970.
- [6] R. N. Bearon and D. Grunbaum. Bioconvection in a stratified environment: experiments and theory. *Physics of Fluids*, 18(12):127102(14), 2006.
- [7] M. A. Bees. *Non-linear pattern generation in suspensions of swimming microorganisms*. PhD thesis, University of Leeds, 1996.
- [8] M. A. Bees and N. A. Hill. Wavelengths of bioconvection patterns. *Journal of Experimental Biology*, 200(10):1515–1526, 1997.
- [9] M. A. Bees and N. A. Hill. Linear bioconvection in a suspension of randomly swimming, gyrotactic micro-organisms. *Physics of Fluids*, 10(8):1864–1881, 1998.

- [10] M. A. Bees and N. A. Hill. Non-linear bioconvection in a deep suspension of gyrotactic swimming micro-organisms. *Journal of Mathematical Biology*, 38:135–168, 1999.
- [11] M. A. Bees, N. A. Hill, and T. J. Pedley. Analytical approximations for the orientation distribution of small dipolar particles in steady shear flows. *Journal of Mathematical Biology*, 36:269–298, 1998.
- [12] H. Berberoglu, L. Pilon, and A. Melis. Radiation characteristics of *Chlamydomonas reinhardtii* cc125 and its truncated chlorophyll antenna transformants tla1, tlax and tla1-cw+. *International Journal of Hydrogen Energy*, 33(22):6467 – 6483, 2008.
- [13] H. C. Berg. *Random Walks in Biology*. Princeton University Press, 1983.
- [14] C. J. Brokaw, D. J. Luck, and B. Huang. Analysis of the movement of *Chlamydomonas* flagella: the function of the radial-spoke system is revealed by comparison of wild-type and mutant flagella. *Journal of Cell Biology*, 92(3):722–732, 1982.
- [15] J. Buder. Zur kenntnis der phototaktischen richtungsbewegungen. *Jahrbuch fur wissenschaftliche Botanik*, 58:105–220, 1917.
- [16] H. Cao, L. Zhang, and A. Melis. Bioenergetic and metabolic processes for the survival of sulfur-deprived *Dunaliella salina* (Chlorophyta). *Journal of Applied Phycology*, 13:25–34(10), 2001.
- [17] D. M. Casey, T. Yagi, R. Kamiya, and G. B. Witman. DC3, the smallest subunit of the *Chlamydomonas* flagellar outer dynein arm-docking complex, is a redox-sensitive calcium-binding protein. *Journal of Biological Chemistry*, 278(43):42652–42659, 2003.
- [18] J. R. Cash and D. R. Moore. A high order method for the numerical solution of two-point boundary value problems. *BIT*, 20(1):44–52, 1980.
- [19] S. Chandrasekar. *Hydrodynamic and Hydromagnetic Stability*. Clarendon, Oxford University Press, 1961.
- [20] R. J. Charlson, S. G. Warren, J. E. Lovelock, and M. O. Andreae. Oceanic phytoplankton, atmospheric sulphur, cloud albedo and climate. *Nature*, 326:655–661, 1987.

- [21] S. Childress. *Mechanisms of swimming and flying*. Cambridge University Press, Cambridge, 1981.
- [22] S. Childress, M. Levandowsky, and E. A. Spiegel. Pattern formation in a suspension of swimming microorganisms: equations and stability theory. *Journal of Fluid Mechanics*, 69(3):591–613, 1975.
- [23] S. Childress and E. A. Spiegel. Pattern formation in a suspension of swimming microorganisms: nonlinear aspects. In D. Givoli, M. J. Grote, and G.C. Papanicoulao, editors, *A Celebration of Mathematical Modeling: The Joseph B. Keller Anniversary Volume*, 2004 (based on the previous version from 1978).
- [24] J. W. Cooley and J. W. Tukey. An algorithm for the machine calculation of complex Fourier series. *Mathematics of Computation*, 19(90):297–301, 1965.
- [25] H. Crenshaw. Orientation by helical motion: III Microorganisms can orient to stimuli by changing the direction of their rotational velocity. *Bulletin of Mathematical Biology*, 55(1):231 – 255, 1993.
- [26] A. Czirók, I. M. Jánosi, and J. O. Kessler. Bioconvective dynamics: dependence on organism behaviour. *Journal of Experimental Biology*, 203(21):3345–3354, 2000.
- [27] R. Datar, J. Huang, P.-C. Maness, A. Mohagheghi, S. Czernik, and E. Chornet. Hydrogen production from the fermentation of corn stover biomass pretreated with a steam-explosion process. *International Journal of Hydrogen Energy*, 32(8):932 – 939, 2007.
- [28] J. P. Davies, F. Yildiz, and A. R. Grossman. Mutants of *Chlamydomonas* with aberrant responses to sulfur deprivation. *Plant Cell*, 6(1):53–63, 1994.
- [29] L. N. M. Duysens. The flattening of the absorption spectrum of suspensions, as compared to that of solutions. *Biochimica et Biophysica Acta*, 19:1–12.
- [30] P. G. Falkowski, M. E. Katz, A. H. Knoll, A. Quigg, J. A. Raven, O. Schofield, and F. J. R. Taylor. The evolution of modern eukaryotic phytoplankton. *Science*, 305(5682):354–360, 2004.
- [31] P. Fay and R. M. Cox. Oxygen inhibition of nitrogen fixation in cell-free preparation of blue-green algae. *Biochimica et Biophysica Acta*, 143:562–569, 1967.

- [32] B. Fischer, M. Wiesendanger, and R. I. L. Eggen. Growth condition-dependent sensitivity, photodamage and stress response of *Chlamydomonas reinhardtii* exposed to high light conditions. *Plant Cell Physiology*, 47(8):1135–1145, 2006.
- [33] T. Flynn, M. L. Ghirardi, and M. Seibert. Accumulation of O₂-tolerant phenotypes in H₂-producing strains of *Chlamydomonas reinhardtii* by sequential applications of chemical mutagenesis and selection. *International Journal of Hydrogen Energy*, 27:1421–1430(10), 2002.
- [34] G. Forti and G. Caldiroli. State transitions in *Chlamydomonas reinhardtii*. The role of the meyer reaction in state 2-to-state 1 transition. *Plant Physiology*, 137(2):492–499, 2005.
- [35] K. W. Foster and R. D. Smyth. Light antennas in phototactic algae. *Microbiology and Molecular Biology Reviews*, 44(4):572–630, 1980.
- [36] S. Fouchard, A. Hemschemeier, A. Caruana, T. Pruvost, J. Legrand, T. Happe, G. Peltier, and L. Cournac. Autotrophic and mixotrophic hydrogen photoproduction in sulfur-deprived *Chlamydomonas* cells. *Applied Environmental Microbiology*, 71(10):6199–6205, 2005.
- [37] H. Gaffron and J. Rubin. Fermentative and photochemical production of hydrogen in algae. *Journal of General Physiology*, 26:219–240, 1942.
- [38] R. P. Gfeller and M. Gibbs. Fermentative metabolism of *Chlamydomonas reinhardtii*: II. Role of plastoquinone. *Plant Physiology*, 77(2):509–511, 1985.
- [39] M. Ghirardi, R. Togasaki, and M. Seibert. Oxygen sensitivity of algal H₂-production. *Applied Biochemistry and Biotechnology*, 63:141–151, 1997.
- [40] M. L. Ghirardi, A. Dubini, J. Yu, and P.-C. Maness. Photobiological hydrogen-producing systems. *Chemical Society Review*, 38:52–61, 2009.
- [41] M. L. Ghirardi, L. Zhang, J. W. Lee, T. Flynn, M. Seibert, E. Greenbaum, and A. Melis. Microalgae: a green source of renewable H₂. *Trends in Biotechnology*, 18(12):506 – 511, 2000.
- [42] S. Ghorai and N. A. Hill. Development and stability of gyrotactic plumes in bioconvection. *Journal of Fluid Mechanics*, 400:1–31, 1999.

- [43] S. Ghorai and N. A. Hill. Periodic arrays of gyrotactic plumes in bioconvection. *Physics of Fluids*, 12(1):5–22, 2000.
- [44] S. Ghorai and N. A. Hill. Wavelengths of gyrotactic plumes in bioconvection. *Bulletin of Mathematical Biology*, 62:429–450, 2000.
- [45] S. Ghorai and N. A. Hill. Axisymmetric bioconvection in a cylinder. *Journal of Theoretical Biology*, 219(2):137 – 152, 2002.
- [46] S. Ghorai and N. A. Hill. Penetrative phototactic bioconvection. *Physics of Fluids*, 17(7):074101, 2005.
- [47] S. Ghorai and N. A. Hill. Gyrotactic bioconvection in three dimensions. *Physics of Fluids*, 19(5):054107, 2007.
- [48] M. Gibbs, R. P. Gfeller, and C. Chen. Fermentative metabolism of *Chlamydomonas reinhardtii*: III Photoassimilation of acetate. *Plant Physiology*, 82(1):160–166, 1986.
- [49] M. Goldschmidt-Clermont and M. Rahire. Sequence, evolution and differential expression of the two genes encoding variant small subunits of ribulose biphosphate carboxylase/oxygenase in *Chlamydomonas reinhardtii*. *Journal of Molecular Biology*, 191(3):421 – 432, 1986.
- [50] I. S. Gradshteyn and I. M. Ryzhik. *Tables of Integrals, Series and Products*. Academic Press Inc., English edition, 1980.
- [51] H. E. Gruber and B. Rosario. Variation in eyespot ultrastructure in *Chlamydomonas reinhardtii* (ac-31). *Journal of Cell Science*, 15(3):481–494, 1974.
- [52] D.-P. Häder. Polarotaxis, gravitaxis and vertical phototaxis in the green flagellate *Euglena gracilis*. *Archives of Microbiology*, 147:79–83, 1987.
- [53] J. J. Hahn, M. L. Ghirardi, and W. L. Jacoby. Effect of process variables on photosynthetic algal hydrogen production. *Journal of Biotechnology Progress*, 20(3):989 – 991, 2004.
- [54] P. C. Hallenbeck and J. R. Benemann. Biological hydrogen production; fundamentals and limiting processes. *International Journal of Hydrogen Energy*, 27(11-12):1185 – 1193, 2002.

- [55] T. Happe, A. Hemschemeier, M. Winkler, and A. Kaminski. Hydrogenases in green algae: do they save the algae's life and solve our energy problems? *Trends in Plant Science*, 7(6):246–250, 2002.
- [56] F. R. Hawkes, R. Dinsdale, D. L. Hawkes, and I. Hussy. Sustainable fermentative hydrogen production: challenges for process optimisation. *International Journal of Hydrogen Energy*, 27(11-12):1339 – 1347, 2002.
- [57] P. Hegemann and B. Bruck. Light-induced stop response in *Chlamydomonas reinhardtii*: occurrence and adaptation phenomena. *Cell Motility and the Cytoskeleton*, 14(14):501 – 515, 1989.
- [58] A. Hemschemeier, S. Fouchard, L. Cournac, G. Peltier, and T. Happe. Hydrogen production by *Chlamydomonas reinhardtii*: an elaborate interplay of electron sources and sinks. *Planta*, 227(2):397–407, 2008.
- [59] A. Hemschemeier and T. Happe. The exceptional photofermentative hydrogen metabolism of the green alga *Chlamydomonas reinhardtii*. *Biochemical Society Transactions*, 33(Pt 1):39–41, 2005.
- [60] N. A. Hill and M. A. Bees. Taylor dispersion of gyrotactic swimming micro-organisms in a linear flow. *Physics of Fluids*, 14(8):2598–2605, 2002.
- [61] N. A. Hill and D.-P. Häder. A biased random walk model for the trajectories of swimming micro-organisms. *Journal of Theoretical Biology*, 186:503–526, 1997.
- [62] N. A. Hill and T. J. Pedley. Bioconvection. *Fluid Dynamics Research*, 37(1-2):1 – 20, 2005.
- [63] N. A. Hill, T. J. Pedley, and J. O. Kessler. Growth of bioconvection patterns in a suspension of gyrotactic micro-organisms in a layer of finite depth. *Journal of Fluid Mechanics*, 208:509–543, 1989.
- [64] N. A. Hill and R. V. Vincent. A simple model and strategies for orientation in phototactic microorganisms. *Journal of Theoretical Biology*, 163(2):223 – 235, 1993.
- [65] P. Hillmer and H. Gest. H₂ metabolism in the photosynthetic bacterium *Rhodospseudomonas capsulata*: H₂ production by growing cultures. *Journal of Bacteriology*, 129(2):724–731, 1977.

- [66] E. J. Hinch and L. G. Leal. Note on the rheology of a dilute suspension of dipolar spheres with weak brownian couples. *Journal of Fluid Mechanics*, 56(4):803–813, 1972.
- [67] V. P. Hiriart-Baer, C. Fortin, D.-Y. Lee, and P. G. C. Campbell. Toxicity of silver to two freshwater algae, *Chlamydomonas reinhardtii* and *Pseudokirchneriella sub-capitata*, grown under continuous culture conditions: influence of thiosulphate. *Aquatic Toxicology*, 78(2):136–148, 2006.
- [68] S. Holmes. *Henderson’s dictionary of biological terms*. Longmans, London and New York, 9th edition, 1985.
- [69] J.S. Hyams and G.G. Borisy. Isolated flagellar apparatus of *Chlamydomonas*: characterization of forward swimming and alteration of waveform and reversal of motion by calcium ions in vitro. *Journal of Cell Science*, 33(1):235–253, 1978.
- [70] I. M. Jánosi, A. Czirók, D. Silhavy, and A. Holczinger. Is bioconvection enhancing bacterial growth in quiescent environments? *Environmental Microbiology*, 4(9):525–531, 2002.
- [71] I. M. Jánosi, J. O. Kessler, and V. K. Horváth. Onset of bioconvection in suspensions of *Bacillus subtilis*. *Physical Review E*, 58(4):4793–4800, 1998.
- [72] J. H. Jo, D. S. Lee, and J. M. Park. Modeling and optimization of photosynthetic hydrogen gas production by green alga *Chlamydomonas reinhardtii* in sulfur-deprived circumstance. *Biotechnology Progress*, 22(2):431–437, 2006.
- [73] M. S. Jones. *Hydrodynamics of Bi-flagellate Locomotion*. PhD thesis, University of Leeds, 1995.
- [74] M. S. Jones, L. le Baron, and T. J. Pedley. Biflagellate gyrotaxis in a shear flow. *Journal of Fluid Mechanics*, 281:137–158, 1994.
- [75] O. Jorquera, A. Kiperstok, E. A. Sales, M. Embiruçu, and M. L. Ghirardi. S-systems sensitivity analysis of the factors that may influence hydrogen production by sulfur-deprived *Chlamydomonas reinhardtii*. *International Journal of Hydrogen Energy*, 33(9):2167 – 2177, 2008.
- [76] K. Josef, J. Saranak, and K. W. Foster. Ciliary behavior of a negatively phototactic *Chlamydomonas reinhardtii*. *Cell Motility and the Cytoskeleton*, 61:97–111, 2005.

- [77] K. Josef, J. Saranak, and K. W. Foster. Linear systems analysis of the ciliary steering behavior associated with negative-phototaxis in *Chlamydomonas reinhardtii*. *Cell Motility and the Cytoskeleton*, 63(12):758–777, 2006.
- [78] R. Kamiya and G. B. Witman. Submicromolar levels of calcium control the balance of beating between the two flagella in demembranated models of *Chlamydomonas*. *Journal of Cell Biology*, 98:97–107, 1984.
- [79] E. Kamke. *Differentialgleichungen Lösungsmethoden und Lösungen*, volume 1. Akademische Verlagsgesellschaft Geest and Portig K.-G., Leipzig, 1967.
- [80] R. A. Kennedy, M. E. Rumpho, and T. C. Fox. Anaerobic metabolism in plants. *Plant Physiology*, 100(1):1–6, 1992.
- [81] J. O. Kessler. Co-operative and concentrative phenomena of swimming micro-organisms. *Contemporary Physics*, 26(2):147–166, 1985.
- [82] J. O. Kessler. Hydrodynamic focusing of motile algal cells. *Nature*, 313:218–220, 1985.
- [83] J. O. Kessler. The external dynamics of swimming micro-organisms. *Progress in Phycological Research*, 4:258–305, 1986.
- [84] J. O. Kessler. Individual and collective fluid dynamics of swimming cells. *Journal of Fluid Mechanics*, 173:191–205, 1986.
- [85] J. O. Kessler. Path and pattern - the mutual dynamics of swimming cells and their environment. *Comments on Theoretical Biology*, 212:85–108, 1989.
- [86] J. O. Kessler, G. D. Burnett, and K. E. Remick. Mutual dynamics of swimming microorganisms and their fluid habitat. In P. L. Christiansen, M. P. Sørensen, and A. C. Scott, editors, *Nonlinear Science at the Dawn of the 21st Century*, volume 542 of *Lecture Notes in Physics*, Berlin Springer Verlag, pages 409–426, 2000.
- [87] J.O. Kessler. Gyrotactic buoyant convection and spontaneous pattern formation in algal culture. In M.G. Verlarde, editor, *Non-equilibrium cooperative phenomena in physics and related fields*, New York: Plenum, pages 241–248, 1984.
- [88] J. P. Kim, C. D. Kang, T. H. Park, M. S. Kim, and S. J. Sim. Enhanced hydrogen production by controlling light intensity in sulfur-deprived *Chlamydomonas*

- reinhardtii* culture. *International Journal of Hydrogen Energy*, 31(11):1585 – 1590, 2006.
- [89] S. Kosourov, V. Makarova, A. S. Fedorov, A. Tsygankov, M. Seibert, and M. L. Ghirardi. The effect of sulfur re-addition on H₂ photoproduction by sulfur-deprived green algae. *Photosynthesis Research*, 85:295–305, 2005.
- [90] S. Kosourov, E. Patrusheva, M. L. Ghirardi, M. Seibert, and A. Tsygankov. A comparison of hydrogen photoproduction by sulfur-deprived *Chlamydomonas reinhardtii* under different growth conditions. *Journal of Biotechnology*, 128(4):776 – 787, 2007.
- [91] S. Kosourov, S. Seibert, and M. Ghirardi. Effects of extracellular pH on the metabolic pathways in sulfur-deprived, H₂-producing *Chlamydomonas reinhardtii* cultures. *Plant Cell Physiology*, 44(2):146–155, 2003.
- [92] S. Kosourov, A. Tsygankov, M. Seibert, and M. Ghirardi. Sustained hydrogen photoproduction by *Chlamydomonas reinhardtii*: effects of culture parameters. *Biotechnology and Bioengineering*, 78(7):731–740, 2002.
- [93] O. Kruse, J. Rupprecht, K.-P. Bader, S. Thomas-Hall, P. M. Schenk, G. Finazzi, and B. Hankamer. Improved photobiological H₂ production in engineered green algal cells. *Journal of Biological Chemistry*, 280(40):34170–34177, 2005.
- [94] A. V. Kuznetsov. The onset of bioconvection in a suspension of gyrotactic microorganisms in a fluid layer of finite depth heated from below. *International Communications in Heat and Mass Transfer*, 32(5):574 – 582, 2005.
- [95] A. V. Kuznetsov. Thermo-bioconvection in a suspension of oxytactic bacteria. *International Communications in Heat and Mass Transfer*, 32(8):991 – 999, 2005.
- [96] L. G. Leal and E. J. Hinch. The rheology of a suspension of nearly spherical particles subject to brownian rotations. *Journal of Fluid Mechanics*, 55(4):745–765, 1972.
- [97] C.-M. Lee, P.-C. Chen, C.-C. Wang, and Y.-C. Tung. Photohydrogen production using purple nonsulfur bacteria with hydrogen fermentation reactor effluent. *International Journal of Hydrogen Energy*, 27:1309–1313(5), 2002.
- [98] G. F. Leedale. *Euglenoid Flagellates*. Englewood Cliffs: Prentice-Hall, 1967.

- [99] M. Levandowsky, W. S. Childress, E. A. Spiegel, and S. H. Hunter. A mathematical model of pattern formation by swimming microorganisms. *Journal of Eukaryotic Microbiology*, 22(2):296–306, 1975.
- [100] J. Leverenz, S. Falk, C.-M. Pilström, and G. Samuelsson. The effects of photoinhibition on the photosynthetic light-response curve of green plant cells (*Chlamydomonas reinhardtii*). *Planta*, 182(1):161–168, 1990.
- [101] M. E. Lewis. *Dissolved Oxygen (version 2.1): U.S. Geological Survey Techniques of Water-Resources Investigations, book 9, chapter A6, section 6.2*, volume accessed 04/2007 from <http://pubs.water.usgs.gov/twri9A6/>. 2006.
- [102] J. Lighthill. *Mathematical biofluidynamics*. Philadelphia: SIAM, 1975.
- [103] J. Lighthill. Flagellar hydrodynamics. *SIAM Review*, 18(2):161–230, 1976.
- [104] S.-T. Lin and S.I. Sandler. Henry’s law constant of organic compounds in water from a group contribution model with multipole corrections. *Chemical Engineering Science*, 57(14):2727 – 2733, 2002.
- [105] J. B. Loeffler and R. B. Mefferd. Concerning pattern formation by free-swimming microorganisms. *The American Naturalist*, 86(830):325–329, 1952.
- [106] P. S. Lovely and F. W. Dahlquist. Statistical measures of bacterial motility and chemotaxis. *Journal of Theoretical Biology*, 50:477–496, 1975.
- [107] M. Madigan, J. M. Martinko, and J. Parker. *Brock biology of microorganisms*. Prentice Hall, 10th edition, 2003.
- [108] A. Manela and I. Frankel. Generalized Taylor dispersion in suspensions of gyrotactic swimming micro-organisms. *Journal of Fluid Mechanics*, 490:99, 2003.
- [109] P. C. Matthews. A model for the onset of penetrative convection. *Journal of Fluid Mechanics*, 188:571–583, 1988.
- [110] A. K. Mattoo and M. Edelman. Intramembrane translocation and posttranslational palmitoylation of the chloroplast 32-kDa herbicide-binding protein. *Proceedings of the National Academy of Sciences of the United States of America*, 84(6):1497–1501, 1987.

- [111] A. Melis. Green alga hydrogen production: progress, challenges and prospects. *International Journal of Hydrogen Energy*, 27:1217–1228, 2002.
- [112] A. Melis. Photosynthetic H₂ metabolism in *Chlamydomonas reinhardtii* (unicellular green algae). *Planta*, 226:1075–1086, 2007.
- [113] A. Melis, J. Neidhardt, and J. Benemann. *Dunaliella salina* (chlorophyta) with small chlorophyll antenna sizes exhibit higher photosynthetic productivities and photon use efficiencies than normally pigmented cells. *Journal of Applied Phycology*, 10:515–525, 1998.
- [114] A. Melis, L. Zhang, M. Forestier, M. Ghirardi, and M. Seibert. Sustained photobiological hydrogen gas production upon reversible inactivation of oxygen evolution in the green alga *Chlamydomonas reinhardtii*. *Plant Physiology*, 122(1):127–136, 2000.
- [115] N. H. Mendelson. *Bacillus subtilis* macrofibres, colonies and bioconvection patterns use different strategies to achieve multicellular organization. *Environmental Microbiology*, 1(6):471–477, 1999.
- [116] N. H. Mendelson, A. Bourque, K. Wilkening, K. R. Anderson, and J. C. Watkins. Organized cell swimming motions in *Bacillus subtilis* colonies: patterns of short-lived whirls and jets. *Journal of Bacteriology*, 181(2):600–609, 1999.
- [117] S. S. Merchant, S. E. Prochnik, O. Vallon, E. H. Harris, S. J. Karpowicz, G. B. Witman, A. Terry, A. Salamov, L. K. Fritz-Laylin, L. Marechal-Drouard, W. F. Marshall, L.-H. Qu, D. R. Nelson, A. A. Sanderfoot, M. H. Spalding, V. V. Kapitonov, Q. Ren, P. Ferris, E. Lindquist, H. Shapiro, S. M. Lucas, J. Grimwood, J. Schmutz, P. Cardol, H. Cerutti, G. Chanfreau, C.-L. Chen, V. Cognat, M. T. Croft, R. Dent, S. Dutcher, E. Fernandez, H. Fukuzawa, D. Gonzalez-Ballester, D. Gonzalez-Halphen, A. Hallmann, M. Hanikenne, M. Hippler, W. Inwood, K. Jabbari, M. Kalanon, R. Kuras, P. A. Lefebvre, S. D. Lemaire, A. V. Lobanov, M. Lohr, A. Manuell, I. Meier, L. Mets, M. Mittag, T. Mittelmeier, J. V. Moroney, J. Moseley, C. Napoli, A. M. Nedelcu, K. Niyogi, S. V. Novoselov, I. T. Paulsen, G. Pazour, S. Purton, J.-P. Ral, D. M. Riano-Pachon, W. Riekhof, L. Rymarquis, M. Schroda, D. Stern, J. Umen, R. Willows, N. Wilson, S. Lana Zimmer, J. Allmer, J. Balk, K. Bisova, C.-J. Chen, M. Elias, K. Gendler, C. Hauser, M. R. Lamb, H. Ledford, J. C. Long, J. Minagawa, M. D. Page, J. Pan, W. Pootakham, S. Roje, A. Rose, E. Stahlberg, A. M. Terauchi,

- P. Yang, S. Ball, C. Bowler, C. L. Dieckmann, V. N. Gladyshev, P. Green, R. Jorgensen, S. Mayfield, B. Mueller-Roeber, S. Rajamani, R. T. Sayre, P. Brokstein, I. Dubchak, D. Goodstein, L. Hornick, Y. W. Huang, J. Jhaveri, Y. Luo, D. Martinez, W. C. A. Ngau, B. Otilar, A. Poliakov, A. Porter, L. Szajkowski, G. Werner, K. Zhou, I. V. Grigoriev, D. S. Rokhsar, and A. R. Grossman. The *Chlamydomonas* genome reveals the evolution of key animal and plant functions. *Science*, 318(5848):245–250, 2007.
- [118] P. Metzger and C. Largeau. *Botryococcus braunii*: a rich source for hydrocarbons and related ether lipids. *Applied Microbiology and Biotechnology*, 66(5):486–496, 2005.
- [119] E. Mölder, A. Mashirin, and T. Tenno. Measurement of the oxygen mass transfer through the air-water interface. *Environmental Science and Pollution Research*, 12(2):66–70, 2005.
- [120] N. M. Morel-Laurens and M. E. Feinleib. Photomovement in an ‘eyeless’ mutant of *Chlamydomonas*. *Photochemistry and Photobiology*, 37:189–194, 1983.
- [121] J. Naus and A. Melis. Changes of photosystem stoichiometry during cell growth in *Dunaliella salina* cultures. *Plant Cell Physiology*, 32(4):569–575, 1991.
- [122] J. Neidhardt, J. R. Benemann, L. Zhang, and A. Melis. Photosystem-II repair and chloroplast recovery from irradiance stress: relationship between chronic photoinhibition, light-harvesting chlorophyll antenna size and photosynthetic productivity in *Dunaliella salina* (green algae). *Photosynthesis Research*, 56:175–184, 1998.
- [123] T. Nguyen-Quang, T. H. Nguyen, F. Guichard, A. Nicolau, G. Szatmari, G. LePelec, M. Dusser, J. Lafossee, J. L. Bonnet, and J. Bohatier. Two-dimensional gravitactic bioconvection in a protozoan (*Tetrahymena pyriformis*) culture. *Zoological Science*, 26(1):54–65, 2009.
- [124] W. Nultsch and D.-P. Häder. Photomovement in motile microorganisms. *Photochemistry and Photobiology*, 47(6):837–869, 1988.
- [125] W. Nultsch, G. Throm, and I. von Rimscha. Phototaktische untersuchungen an *Chlamydomonas reinhardtii* dangeard in homokontinuierlicher kultur. *Archiv von Mikrobiologie*, 80:351–369, 1971.

- [126] W. Park and I. Moon. A discrete multi states model for the biological production of hydrogen by phototrophic microalga. *Biochemical Engineering Journal*, 36(1):19–27, 2007.
- [127] G. J. Pazour, O. A. Sineschekov, and G. B. Witman. Mutational analysis of the phototransduction pathway of *Chlamydomonas reinhardtii*. *Journal of Cell Biology*, 131(2):427–440, 1995.
- [128] T. J. Pedley, N. A. Hill, and J. O. Kessler. The growth of bioconvection patterns in a uniform suspension of gyrotactic micro-organisms. *Journal of Fluid Mechanics*, 195:223–237, 1988.
- [129] T. J. Pedley and J. O. Kessler. The orientation of spheroidal microorganisms swimming in a flow field. *Proceedings of the Royal Society of London. Series B. Biological Sciences*, 231(1262):47–70, 1987.
- [130] T. J. Pedley and J. O. Kessler. A new continuum model for suspensions of gyrotactic micro-organisms. *Journal of Fluid Mechanics*, 212:155–182, 1990.
- [131] T. J. Pedley and J. O. Kessler. Hydrodynamic phenomena in suspensions of swimming microorganisms. *Annual Review of Fluid Mechanics*, 24(1):313–358, 1992.
- [132] J. R. Platt. “Bioconvection Patterns” in cultures of free-swimming organisms. *Science*, 133:1766–1767, 1961.
- [133] M. S. Plesset and H. Winet. Bioconvection patterns in swimming microorganism cultures as an example of Rayleigh-Taylor instability. *Nature*, 248:441–443, 1974.
- [134] M. Polin, I. Tuval, K. Drescher, J. P. Gollub, and R. E. Goldstein. *Chlamydomonas* swims with two “gears” in a eukaryotic version of run-and-tumble locomotion. *Science*, 325(5939):487–490, 2009.
- [135] J. E. Polle, S. Kanakagiri, E. Jin, T. Masuda, and A. Melis. Truncated chlorophyll antenna size of the photosystems—a practical method to improve microalgal productivity and hydrogen production in mass culture. *International Journal of Hydrogen Energy*, 27(11-12):1257–1264, 2002.
- [136] J. E. Polle, S. D. Kanakagiri, and A. Melis. *tla1*, a dna insertional transformant of the green alga *Chlamydomonas reinhardtii* with a truncated light-harvesting chlorophyll antenna size. *Planta*, 217:49–59, 2003.

- [137] L. R. Pomeroy. The ocean's food web, a changing paradigm. *BioScience*, 24(9):499–504, 1974.
- [138] A. J. Pons, F. Sagues, M. A. Bees, and P. G. Sorensen. Quantitative analysis of chemoconvection patterns in the methylene-blue-glucose system. *The Journal of Physical Chemistry B*, 106(29):7252–7259, 2002.
- [139] M. C. Posewitz, S. L. Smolinski, S. D. Kanakagiri, A. Melis, M. Seibert, and M. L. Ghirardi. Hydrogen photoproduction is attenuated by disruption of an isoamylase gene in *Chlamydomonas reinhardtii*. *The Plant Cell*, 16:2151–2163, 2004.
- [140] W. H. Press, S. A. Teukolsky, B. P. Flannery, and W. T. Vetterling. *Numerical Recipes in FORTRAN: The Art of Scientific Computing*. Cambridge University Press, second edition, 1992.
- [141] R. Prince and H. Kheshgi. The photobiological production of hydrogen: potential efficiency and effectiveness as a renewable fuel. *Critical Reviews in Microbiology*, 31:19–31, 2005.
- [142] E. M. Purcell. Life at low reynolds number. *American Journal of Physics*, 45(1):3–11, 1977.
- [143] J. M. Rallison. The effects of brownian rotations in a dilute suspension of rigid particles of arbitrary shape. *Journal of Fluid Mechanics*, 84(2):237–263, 1978.
- [144] W. J. Robbins. Patterns formed by motile *Euglena gracilis var. bacillaris*. *Bulletin of the Torrey Botanical Club*, 79(2):107–109, 1952.
- [145] A. M. Roberts. The external dynamics of swimming micro-organisms. *Nature*, 828:375–376, 1970.
- [146] A. M. Roberts. Geotaxis in motile micro-organisms. *Journal of Experimental Biology*, 53(3):687–699, 1970.
- [147] A. M. Roberts. Mechanisms of gravitaxis in *Chlamydomonas*. *Biology Bulletin*, 210:78–80, 2006.
- [148] A. M. Roberts and F. M. Deacon. Gravitaxis in motile micro-organisms: the role of fore-aft body asymmetry. *Journal of Fluid Mechanics*, 452:405–423, 2002.

- [149] U. Ruffer and W. Nultsch. High-speed cinematographic analysis of the movement of *Chlamydomonas*. *Cell Motility and the Cytoskeleton*, 5(3):251–263, 1985.
- [150] U. Ruffer and W. Nultsch. Comparison of the beating of *cis*- and *trans*-flagella of *Chlamydomonas* held on micropipettes. *Cell motility and the cytoskeleton*, 7:87–93, 1987.
- [151] U. Ruffer and W. Nultsch. Flagellar photoresponses of *Chlamydomonas* cells held on micropipettes: I. Change in flagellar beat frequency. *Cell Motility and the Cytoskeleton*, 15(3):162–167, 1990.
- [152] U. Ruffer and W. Nultsch. Flagellar photoresponses of *Chlamydomonas* cells held on micropipettes: II. Change in flagellar beat pattern. *Cell Motility and the Cytoskeleton*, 18(4):269–278, 1991.
- [153] U. Ruffer and W. Nultsch. Flagellar photoresponses of *Chlamydomonas* cells held on micropipettes: III. Shock responses. *Botanica Acta*, 108:255–265, 1995.
- [154] U. Ruffer and W. Nultsch. Flagellar photoresponses of *ptx1*, a nonphototactic mutant of *Chlamydomonas*. *Cell Motility and the Cytoskeleton*, 37(2):111–119, 1997.
- [155] U. Ruffer and W. Nultsch. Flagellar coordination in *Chlamydomonas* cells held on micropipettes. *Cell Motility and the Cytoskeleton*, 41(44):297–307, 1998.
- [156] T. Ruhle, A. Hemschemeier, A. Melis, and T. Happe. A novel screening protocol for the isolation of hydrogen producing *Chlamydomonas reinhardtii* strains. *BMC Plant Biology*, 8(1):107–119, 2008.
- [157] L. F. Shampine and M. W. Reichelt. The MATLAB ODE suite. *SIAM Journal of Scientific Computing*, 18(1):1–22, 1997.
- [158] O. Sineshchekov. Photoreception in unicellular flagellates: bioelectric phenomena in phototaxis. *Light in Biology and Medicine*, II(4):523–532, 1991.
- [159] A. Spitzbart and N. Macon. Numerical differentiation formulas. *The American Mathematical Monthly*, 64(10):721–723, 1957.
- [160] K. D. Stewart and K. R. Mattox. Comparative cytology, evolution and classification of the green algae with some consideration of the origin of other organisms with chlorophylls a and b. *Botanical Review*, 41(1):104–135, 1975.

- [161] B. Straughan. *Mathematical Aspects of Penetrative Convection*. Longman Scientific and Technical, 1993.
- [162] T. S. Stuart and H. Gavron. The mechanism of hydrogen photoproduction by several algae II. The contribution of photosystem II. *Planta*, 106:101–112, 1972.
- [163] M. Taheri and E. Bilgen. Bioconvection of gravitactic micro-organisms in rectangular enclosures. *International Journal of Heat and Mass Transfer*, 50(23-24):4652 – 4660, 2007.
- [164] C. C. Taylor, I. L. Dryden, and R. Farnoosh. The K-function for nearly regular point processes. *Biometrics*, 57(1):224–231, 2001.
- [165] M. D. Thompson, C. D. Paavola, T. R. Lenvi, and J. S. Gantt. *Chlamydomonas* transcripts encoding three divergent plastid chaperonins are heat-inducible. *Plant molecular biology*, 27(5):1031–1035, 1995.
- [166] A. M. Tomson and R. Demets. *Sexual communication in the green alga Chlamydomonas eugametos*. PhD thesis, University of Amsterdam, 1989.
- [167] A. Tsygankov, I. Kosourov, S. Tolstygina, M. Ghirardi, and M. Seibert. Hydrogen production by sulfur-deprived *Chlamydomonas reinhardtii* under photoautotrophic conditions. *International Journal of Hydrogen Energy*, 31(11):1574 – 1584, 2006.
- [168] I. Tuval, L. Cisneros, C. Dombrowski, C. W. Wolgemuth, J. O. Kessler, and R. E. Goldstein. Bacterial swimming and oxygen transport near contact lines. *Proceedings of the National Academy of Sciences of the United States of America*, 102(7):2277–2282, 2005.
- [169] M. van Dyke. *Perturbation methods in Fluid mechanics*. Academic Press, New York, USA, 1968.
- [170] G. Veronis. Penetrative convection. *Journal of Astrophysics*, 137:641–663, 1963.
- [171] R. V. Vincent. *Mathematical modelling of phototaxis in motile microorganisms*. PhD thesis, University of Leeds, 1995.
- [172] R. V. Vincent and N. A. Hill. Bioconvection in a suspension of phototactic algae. *Journal of Fluid Mechanics*, 327:343–371, 1996.

- [173] V. A. Vladimirov, M. S. C. Wu, T. J. Pedley, P. V. Denissenko, and S. G. Zakhidova. Measurement of cell velocity distributions in populations of motile algae. *Journal of Experimental Biology*, 207(7):1203–1216, 2004.
- [174] H. Wager. On the effect of gravity upon the movements and aggregation of *Euglena viridis*, Ehrb., and other micro-organisms. *Philosophical Transactions of the Royal Society of London. Series B*, 201:333–390, 1911.
- [175] R. F. Weiss. The solubility of nitrogen, oxygen, and argon in water and seawater. *Deep-Sea Research*, 17:721–735, 1970.
- [176] A. L. White and A. Melis. Biochemistry of hydrogen metabolism in *Chlamydomonas reinhardtii* wild type and a rubisco-less mutant. *International Journal of Hydrogen Energy*, 31(4):455 – 464, 2006.
- [177] J. A. Whitehead and M. M. Chen. Thermal instability and convection of a thin fluid layer bounded by a stably stratified region. *Journal of Fluid Mechanics*, 40(3):549–576, 1970.
- [178] G. Witman. *Chlamydomonas* phototaxis. *Trends in Cell Biology*, 3:403–408, 1993.
- [179] D. D. Wykoff, J. P. Davies, A. Melis, and A. R. Grossman. The regulation of photosynthetic electron transport during nutrient deprivation in *Chlamydomonas reinhardtii*. *Plant Physiology*, 117(1):129–139, 1998.
- [180] Y. Yamamoto, T. Okayama, K. Sato, and T. Takaoki. Relation of pattern formation to external conditions in the flagellate, *Chlamydomonas reinhardtii*. *European Journal of Protistology*, 28(4):415–420, 1992.
- [181] J. P. Yildiz, F. H. Davies and A. R. Grossman. Characterization of sulfate transport in *Chlamydomonas reinhardtii* during sulfur-limited and sulfur-sufficient growth. *Plant Physiology*, 104(3):981–987, 1994.
- [182] L. Zhang, T. Happe, and A. Melis. Biochemical and morphological characterization of sulfur-deprived and H₂-producing *Chlamydomonas reinhardtii* (green alga). *Planta*, 214(4):552–561, 2002.
- [183] L. Zhang and A. Melis. Probing green algal hydrogen production. *Philosophical Transactions of the Royal Society of London B: Biological Sciences*, 357(1426):1499–1507, 2002.